

INTERFACE SCIENCE AND TECHNOLOGY

# Advanced Chemistry of Monolayers at Interfaces

---

TRENDS IN METHODOLOGY  
AND TECHNOLOGY

Toyoko Imae  
*Editor*



# **Advanced Chemistry of Monolayers at Interfaces**

Trends in Methodology and Technology

---

# INTERFACE SCIENCE AND TECHNOLOGY

Series Editor: ARTHUR HUBBARD

---

*In this series:*

- Vol. 1: Clay Surfaces: Fundamentals and Applications  
Edited by F. Wypych and K.G. Satyanarayana
- Vol. 2: Electrokinetics in Microfluids  
By Dongqing Li
- Vol. 3: Radiotracer Studies of Interfaces  
Edited by G. Horányi
- Vol. 4: Emulsions: Structure Stability and Interactions  
Edited by D.N. Petsev
- Vol. 5: Inhaled Particles  
By Chiu-sen Wang
- Vol. 6: Heavy Metals in the Environment: Origin, Interaction and Remediation  
Edited by H.B. Bradl
- Vol. 7: Activated Carbon Surfaces in Environmental Remediation  
Edited by Teresa J. Bandosz
- Vol. 8: Tissue Engineering: Fundamentals and Applications  
By Yoshito Ikada
- Vol. 9: Particles at Interfaces: Interactions, Deposition, Structure  
By Zbigniew Adamczyk
- Vol. 10: Interface Science in Drinking Water Treatment:  
Theory and Applications  
Edited by G. Newcombe and D. Dixon
- Vol. 11: Surface Complexation Modelling  
Edited by Johannes Lützenkirchen
- Vol. 12: Theory of Colloid and Interfacial Electric Phenomena  
By Hiroyuki Ohshima
- Vol. 13: Sorbent Deformation  
By A.V. Tvardovskiy
- Vol. 14: Advanced Chemistry of Monolayers at Interfaces:  
Trends in Methodology and Technology  
Edited by Toyoko Imae

INTERFACE SCIENCE AND TECHNOLOGY—VOLUME 14

---

# Advanced Chemistry of Monolayers at Interfaces

## Trends in Methodology and Technology

Edited by

Toyoko Imae

Graduate School of Science and Technology  
Keio University  
3-14-1 Hiyoshi, Kohoku-ku  
Yokohama 223-8522, Japan



Amsterdam • Boston • Heidelberg • London • New York • Oxford  
Paris • San Diego • San Francisco • Singapore • Sydney • Tokyo  
Academic Press is an imprint of Elsevier



Academic Press is an imprint of Elsevier  
84 Theobald's Road, London WC1X 8RR, UK  
Radarweg 29, PO Box 211, 1000 AE Amsterdam, The Netherlands  
The Boulevard, Langford Lane, Kidlington, Oxford OX5 1GB, UK  
30 Corporate Drive, Suite 400, Burlington, MA 01803, USA  
525 B Street, Suite 1900, San Diego, CA 92101-4495, USA

First edition 2007

Copyright © 2007 Elsevier Ltd. All rights reserved

No part of this publication may be reproduced, stored in a retrieval system or transmitted in any form or by any means electronic, mechanical, photocopying, recording or otherwise without the prior written permission of the publisher

Permissions may be sought directly from Elsevier's Science & Technology Rights Department in Oxford, UK: phone (+44) (0) 1865 843830; fax (+44) (0) 1865 853333; email: [permissions@elsevier.com](mailto:permissions@elsevier.com). Alternatively you can submit your request online by visiting the Elsevier web site at <http://elsevier.com/locate/permissions>, and selecting *Obtaining permission to use Elsevier material*

#### Notice

No responsibility is assumed by the publisher for any injury and/or damage to persons or property as a matter of products liability, negligence or otherwise, or from any use or operation of any methods, products, instructions or ideas contained in the material herein. Because of rapid advances in the medical sciences, in particular, independent verification of diagnoses and drug dosages should be made

ISBN: 978-0-12-372570-7

ISSN: 1573-4285

For information on all Academic Press publications  
visit our website at [books.elsevier.com](http://books.elsevier.com)

Printed and bound in The Netherlands

07 08 09 10 11 10 9 8 7 6 5 4 3 2 1

Working together to grow  
libraries in developing countries

[www.elsevier.com](http://www.elsevier.com) | [www.bookaid.org](http://www.bookaid.org) | [www.sabre.org](http://www.sabre.org)

ELSEVIER

BOOK AID  
International

Sabre Foundation

# Contents

<b>Preface</b>	<b>xi</b>
<b>1 Scanning Tunneling Microscopy for Self-Assembled Monolayers</b>	<b>1</b>
<i>P. Brodard and H. Fukumura</i>	
1. Introduction for scanning tunneling microscopy	1
1.1. Principle	1
1.2. Apparatus	4
1.3. Sample Preparation	7
2. Structure of monolayers	8
2.1. Brief History	8
2.2. Recognition of Atoms	9
2.3. Recognition of Chirality	12
3. Dynamics of molecular layers	12
3.1. Desorption and Re-adsorption	12
3.2. Chemical Reactions	14
4. Spectroscopic techniques combined with STM	17
4.1. Current/Voltage Spectroscopy	17
4.2. Raman Spectroscopy	18
5. Future directions	20
<b>2 Monolayer Properties Probed by Surface Forces Measurements</b>	<b>23</b>
<i>Andra Dedinaite</i>	
1. Introduction	23
2. Function of the basic surface forces apparatus	24
2.1. Determining Separation Between Surfaces	24
2.2. Determining Forces Between Surfaces	26
2.3. Other Surface Forces Measuring Techniques	27
3. Development of the SFA	27
4. Monolayers of surfactants and lipids	31
4.1. Langmuir–Blodgett Films	32
5. Polyelectrolytes on surfaces	37
5.1. Polyelectrolytes on Oppositely Charged Surfaces	39
5.2. Polyelectrolyte Brushes	42
6. Summary	47

<b>3</b>	<b>Surface Plasmon Optics for the Characterization of Biofunctional Architectures</b>	<b>55</b>
	<i>Fang Yu, Danfeng Yao, Jing Liu, Danica Christensen, Rolf Lauterbach, Harald Paulsen, and Wolfgang Knoll</i>	
1.	Introduction	55
2.	Theoretical background	56
2.1.	Excitation of Surface Plasmon Modes	56
2.2.	Surface Plasmon Field-Enhanced Fluorescence Spectroscopy	58
2.3.	Surface Plasmon Field-Enhanced Diffraction	60
3.	Instrumental	61
4.	Application of SPR and SPFS in bio-affinity analysis	62
4.1.	Nonspecific Binding	63
4.2.	Surface Regeneration	64
4.3.	Avidity of IgG Binding	65
4.4.	SPFS Detection of Extremely Diluted Antigen Densities	67
4.5.	Layer-By-Layer Assembly of Proteins	68
4.6.	Affinity Determination Between hIL8 and Its Antibody Fragments	69
4.7.	Anchoring of Light-Harvesting Complex II Via a His-Tag	73
4.8.	Ionic Strength Dependence of PNA/DNA Hybridization	74
5.	Surface plasmon diffraction sensor	78
5.1.	Diffraction Enhancement by Surface Plasmon Fields	78
5.2.	Quadratic Effect of Diffraction Intensity	80
5.3.	SPDS for Oligonucleotide Hybridization	81
6.	Conclusion	82
<b>4</b>	<b>Probing Surfactant Adsorption at the Solid–Solution Interface by Neutron Reflectometry</b>	<b>87</b>
	<i>J. Penfold and R. K. Thomas</i>	
1.	Introduction	87
2.	Neutron reflectivity	89
2.1.	Basic Principles and Equations	89
2.2.	Application to the Solid–Solution Interface	92
2.3.	Relationship to Other Techniques	96
3.	Surfactant systems	99
3.1.	Adsorption of Nonionic Surfactants onto Hydrophilic Surfaces	99
3.2.	Adsorption of Ionic Surfactants onto Hydrophilic Surfaces	101
3.3.	Mixed Surfactant Adsorption	103
3.4.	Adsorption onto Hydrophobic Surfaces	106
3.5.	Adsorption onto Functionalized Surfaces	106
3.6.	More Complex Surface Structures	107
3.7.	Polymer/Surfactant Adsorption	109
4.	Summary and future prospects	112

<b>5</b>	<b>Near-Field Scanning Optical Microscopy of Lipid Membranes</b>	<b>117</b>
	<i>Bret N. Flanders and Robert C. Dunn</i>	
1.	Introduction	117
2.	Near-field scanning optical microscopy	118
3.	Near-field studies of submicron membrane domains	121
3.1.	Monolayers	121
3.2.	Bilayers and Multi-Layer Lipid Films	127
3.3.	Live Cell Measurements	133
4.	Conclusions and future Ddirections	138
<b>6</b>	<b>Micro/Nanolithography Using Self-Assembled Monolayers (SAMs)</b>	<b>141</b>
	<i>O. Takai and K. Hayashi</i>	
1.	Self-assembled monolayers (SAMs)	141
1.1.	What is SAM?	141
1.2.	Usefulness of SAMs in Lithography	143
2.	Preparation of SAMs by chemical vapor deposition (CVD)	144
2.1.	Structure and Formation Mechanism of Organosilane SAMs	144
2.2.	Preparation Method of SAMs by CVD	146
3.	Microlithography using SAMs	151
3.1.	Photodegradation of Organosilane SAMs by VUV Light	151
3.2.	Photopatterning of SAMs	156
4.	Nanolithography using SAMs	157
4.1.	Principle of Nanolithography with SPM	158
4.2.	SPNL of SAMs	159
5.	Applications of micro/nanopatterned SAMs	167
5.1.	Application of Organosilane SAMs to Transferring of Nanopatterns	168
5.2.	Application of Nanopatterned Substrates to Immobilization Surfaces of Molecules	168
5.3.	Application of Patterned SAMs to Circuit Formation	169
<b>7</b>	<b>Highly Fluorinated Langmuir, Langmuir–Blodgett and Gibbs Monolayers</b>	<b>177</b>
	<i>Marie Pierre Krafft</i>	
1.	Introduction	177
2.	Specific physico-chemical characteristics of fluorinated chains	178
3.	Monolayers of fluorinated surfactants	178
3.1.	Langmuir Monolayers	178
3.2.	Langmuir–Blodgett Monolayers	180
3.3.	Gibbs Monolayers	180
4.	Monolayers of semifluorinated alkanes	181
4.1.	Langmuir Monolayers	181
4.2.	Langmuir–Blodgett Monolayers	182
4.3.	Surface Freezing	183

5.	Mixtures of fluorinated and hydrogenated amphiphiles	183
5.1.	Lateral Phase Separation	183
5.2.	Vertical Phase Separation	185
6.	Potential use of fluorinated monolayers in biological sciences	186
6.1.	Lung Surfactant	186
6.2.	Two-Dimensional Protein Crystallization	187
7.	Potential use of fluorinated monolayers in materials science	188
<b>8</b>	<b>Structure and Physicochemical Properties of Polyalkylsiloxane Monolayers Prepared onto the Solid Substrate</b>	<b>193</b>
	<i>T. Koga and A. Takahara</i>	
1.	Introduction	193
2.	Fabrication of micropatterned organosilane monolayers	195
2.1.	Formation of Organosilane Monolayers at the Air/Water Interface	195
2.2.	Phase Separation of Mixed Monolayers at Air/Water Interface	198
2.3.	Fabrication of Multi-Phase Organosilane Monolayers through Chemisorption and Photolithography Process	201
3.	Dependence of the molecular aggregation state of organosilane monolayers on preparation methods	207
4.	Applications of organosilane monolayers	210
4.1.	Site-Specific Polymerization of Methacrylate Monomers	210
4.2.	Site-Specific Immobilization of Charged Microparticles	212
4.3.	Tribological Control	212
5.	Conclusion	215
<b>9</b>	<b>Homo- and Hybrid-Monolayers of Dendritic Polymers</b>	<b>219</b>
	<i>Toyoko Imae, Masaki Ujihara, and Mariko Hayashi</i>	
1.	Introduction	219
2.	Homo-monolayers of dendritic polymers	220
3.	Hybrid-monolayers of dendritic polymers with linear polymers	227
4.	Hybrid-monolayers of dendritic polymers with inorganic nanoparticles	234
5.	Conclusion	238
<b>10</b>	<b>Infrared Reflection Absorption Spectroscopy of Monolayers at the Air–Water Interface</b>	<b>247</b>
	<i>Jiayin Zheng and Roger M. Leblanc</i>	
1.	Introduction	247
2.	In situ infrared reflection absorption spectroscopy (IRRAS) of Langmuir films	248
2.1.	Background	248
2.2.	Application	250

3.	Polarization modulation reflection absorption spectroscopy (PM-IRRAS) of Langmuir films	263
3.1.	Theory of PM-IRRAS on Dielectrics	263
3.2.	Applications	266
4.	Conclusion	273
<b>11</b>	<b>Measurement of Complex Formation and Aggregation at the Liquid–Liquid Interface</b>	<b>277</b>
	<i>Hitoshi Watarai</i>	
1.	Introduction	277
2.	Measurement of liquid–liquid interface	278
2.1.	High-Speed Stirring Method	278
2.2.	Centrifugal Liquid Membrane Method	280
2.3.	Two-Phase Stopped Flow Method	281
2.4.	Interfacial Reflection Spectrometry	281
2.5.	Micro-Two-Phase Sheath Flow Method	281
2.6.	Raman Spectroscopy of the Interface	283
2.7.	Optical Chirality Measurement of the Interface	287
2.8.	Single Molecule Probing at the Interface	289
2.9.	Magnetophoretic Velocimetry of Microdroplets	292
3.	Interfacial complexation and aggregation	295
3.1.	Interfacial Catalysis in Metal Extraction Kinetics	295
3.2.	Interfacial Aggregation at the Liquid–Liquid Interface	301
4.	Concluding remarks	305
<b>12</b>	<b>Monolayers on Air/Solid Interfaces: Vibrational Spectroscopy and Atomic Force Microscopy Studies</b>	<b>309</b>
	<i>Yukihiro Ozaki, Shin-ichi Morita, Yoshiaki Hirano, and Xiaoling Li</i>	
1.	Introduction	309
2.	Infrared and atomic force microscopy studies of LB films	311
2.1.	An Infrared Study of LB Films of Cadmium Stearate	311
2.2.	Infrared and AFM Studies of LB Films of 2-Alkyl-7,7,8,8-tetracyanoquinodimethane	313
2.3.	Infrared and AFM Studies of Time-Dependent Changes in Molecular Orientation, Structure, and Morphology in One-Layer LB Films of Alkyl-TCNQ	315
2.4.	Structural Characterization of Mixed-Stack Charge Transfer Films of Octadecyl-TCNQ and 5,10-Dimethyl-5,10-dihydrophenazine Prepared by the LB Technique and Donor Doping: Molecular Orientation and Structure and Morphology Investigated by Infrared Spectroscopy, X-ray Diffraction, and AFM	321
3.	SERS studies on monolayer films	323

3.1.	SERS Studies on Metallophthalocyanine Self-Assembled Films on Different Organic-Monolayer-Modified Films	325
3.2.	SERS Studies on Metalloporphyrin Self-Assembled Films on Organic-Monolayer-Modified Substrates	330
3.3.	An SERS Study on the Orientation of an Atactic Poly(methyl methacrylate) Thin Film on a Silver Substrate	333
4.	AFM studies on monolayer films	337
4.1.	AFM Studies on Metalloporphyrin LB Films	337
4.2.	An <i>In Situ</i> AFM Study on Morphological Changes in an LB Film of Cadmium 10,12-Pentacosadiynoate during Polymerization	339
5.	Infrared and visible absorption spectroscopy studies on J- and H-aggregates in LB films of merocyanine dye	340
5.1.	Formation and Assignments of Red- and Blue-Shifted Bands in LB Films of MS	341
5.2.	Out-of-Plane and In-Plane Orientations of MS Transition Dipole Moments in J- and H-Aggregates	343
5.3.	Intramolecular Charge Transfer of MS in J- and H-Aggregates	346
5.4.	Conformation and Orientation of Hydrocarbon Chains of MS in J- and H-Aggregates	348
5.5.	Whereabout, Conformation, and Orientation of AL <sub>18</sub> Added as a Third Component in Mixed LB Films	352
	<b>Subject Index</b>	<b>361</b>

## Preface

The monolayer science started from the investigation of adsorption monolayers on water and solid surfaces, which was developed by scientists as represented by Gibbs and Langmuir. The early researches were based on thermodynamics, and two-dimensional (surface) thermodynamic theories were established. The monolayer investigation furthermore evolved into Langmuir and Langmuir–Blodgett monolayers, which are an insoluble monolayer at air/water interface and its transfer film on solid substrate, respectively, and later into self-assembled monolayers. It should be noticed that the evolution of monolayer science involves intensively the development of methodologies in surface science, which made it possible to obtain the information at nano-scale level. The pioneering technique is a scanning probe microscopy, which enabled molecular ordering to visualize at an atomic scale. Secondly, the development of surface spectroscopy was enhanced by taking advantage of surface plasmon resonance phenomenon and allowed the highly supersensitive detection of molecular species at interface. Nanotechnology, that is, technology at nano-scale was developed in the last part of the 20th century, and it is one of key sciences in the 21st century. In this way the nanotechnology is supported by the development of monolayer science and surface methodologies.

This book describes the advanced chemistry of monolayers at interfaces. Especially the recent trends of methodology and technology are focused upon. The book introduces the methodologies of scanning probe microscopy, surface force instrumentation, surface spectroscopy, surface plasmon optics, reflectometry, and near-field scanning optical microscopy. The modern interface reaction method and the lithographic technology are also included. Such methodologies and technologies are indispensable in supersensitive and nano-scale sciences such as monolayer science. Those are applied to monolayers of surfactants, amphiphiles, polymers, dendrimers, enzymes, and proteins, which serve many uses. The researches range in different types of monolayers like adsorption, Langmuir, Langmuir–Blodgett, and self-assembled monolayers at air/liquid, liquid/liquid, liquid/solid, and air/solid interfaces. Recent monolayer chemistry runs on experiment, theory, and simulation at static and dynamic viewpoints, extends to analyses at not only steady state but also time-resolved state, and takes in bottom-up and top-down techniques. This book covers such research fields and regions. The book aims at contributing to the further development in research of academic and professional researchers, to the further knowledge of the students and to the further technological advancement in engineers' specialized field.

This page intentionally left blank

## Chapter 1

# Scanning Tunneling Microscopy for Self-Assembled Monolayers

P. Brodard, H. Fukumura\*

*Department of Chemistry, Graduate School of Science, Tohoku University, 6-3 Aoba Aramaki, Sendai, Miyagi 980-8578, Japan*

## 1. INTRODUCTION FOR SCANNING TUNNELING MICROSCOPY

### 1.1. Principle

Among all the different types of surface imaging techniques, the scanning tunneling microscope (STM) presents the best spatial resolution and versatility. In fact, atoms and molecules can be literally touched one by one, thus opening new ways for investigating them [1]. The first and most amazing ability of the STM is to provide three-dimensional images of individual molecules and their environment at the atomic level. However, many other experiments can be conducted with an STM, as for instance manipulating particles, performing local spectroscopy, and even chemically modifying the sample. In a sense, STM has made it possible to act directly on atoms and molecules for the first time. This is the ultimate step of spatial resolution for chemistry, like femtosecond techniques are the ultimate step of time resolution for chemical reactions [2].

The basic principle of scanning tunneling microscopy (STM) is based on the tunneling current between a metallic tip, which is sharpened to a single atom point, and a conducting material (Fig. 1). A small bias voltage (mV to V) is applied between an atomically sharp tip and the sample.

---

\*Corresponding author. E-mail: fukumura@orgphys.chem.tohoku.ac.jp

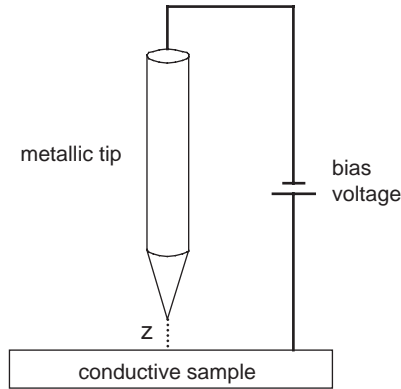


**Fig. 1.** Basic principle of the scanning tunneling microscopy technique.

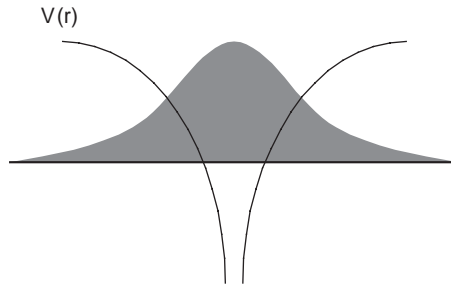


**Fig. 2.** Wave function of a valence electron in the Coulomb potential well  $V(r)$ .

If  $z$ , the distance between the tip and the sample, is large, no current flows. However, when the tip is brought very close ( $< 10 \text{ \AA}$ ) without physical contact, a current (pA to nA) flows across the gap between the tip and the sample. Such current, which is called tunneling current, is the result of the overlapping wave functions between the tip atom and surface atoms. Electrons can tunnel across the vacuum barrier separating the tip and sample in the presence of a small bias voltage. The magnitude of the tunneling current is extremely sensitive to the gap distance between the tip and the sample. As we measure the current with the tip moving across the surface, atomic information of the surface can be mapped out.

To understand how STM works, it is vital to know what is tunneling current, and how it is related to all the experimental observations. Tunneling current is originated from the wavelike properties of particles (electrons, in this case) in quantum mechanics. When an electron is incident upon a vacuum barrier with potential energy larger than the kinetic energy of the electron, there is still a non-zero probability that it may traverse the forbidden region and reappear on the other side of the barrier. It is shown by the leak out electron wave function in Fig. 2.

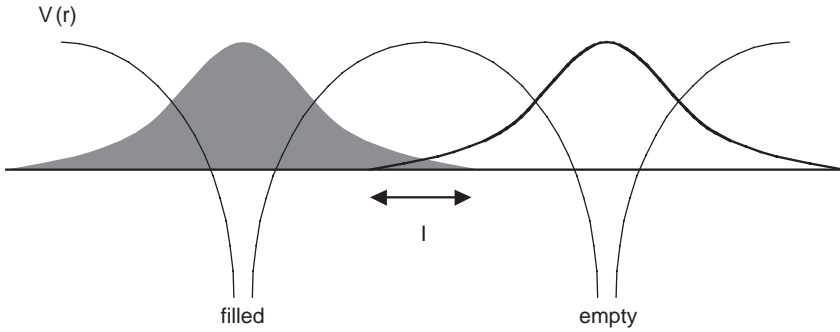


**Fig. 3.** Tunneling current  $I$  through vacuum between two atoms.

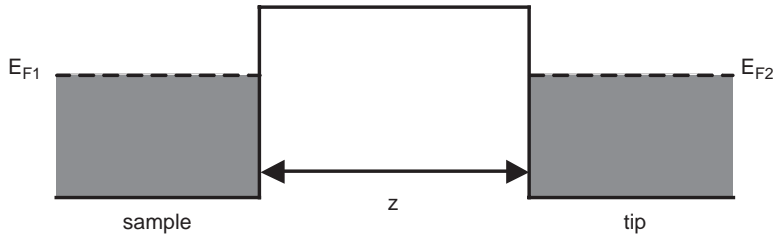


**Fig. 4.** Energy levels in two metals separated by a vacuum barrier.

If two conductors are so close that their leak out electron wave functions overlap, then an electron can tunnel back and forth through the vacuum or potential barrier between them, generating a tunneling current (Fig. 3).

In a metal, the potential barriers between the atoms in the interior are quenched and electrons move freely in the conduction bands. In other words, electrons exist within an energy range, designated by the shaded areas in Fig. 4, up to the respective Fermi levels,  $E_{F1}$  and  $E_{F2}$ . If an insulator, or indeed a vacuum, is inserted between two metals, an energy barrier appears. In our STM scheme, the thickness of the barrier corresponds to the tip-sample gap,  $z$ .

When a small voltage  $V$  is applied between the tip and the sample, the shape of the energy barrier changes. A difference between the Fermi levels  $E_{F1}$  and  $E_{F2}$  creates empty states on the right, generating a driving force for the electrons to tunnel across the barrier from the left side (Fig. 5).

Quantum mechanics allows a few electrons to traverse the barrier if the thickness  $z$  is small. The probability that an electron will cross the barrier is the tunneling current ( $I$ ) flowing across the vacuum gap, and it decays exponentially with the barrier width  $z$  as

$$I \propto e^{-2Kz} \quad (1)$$

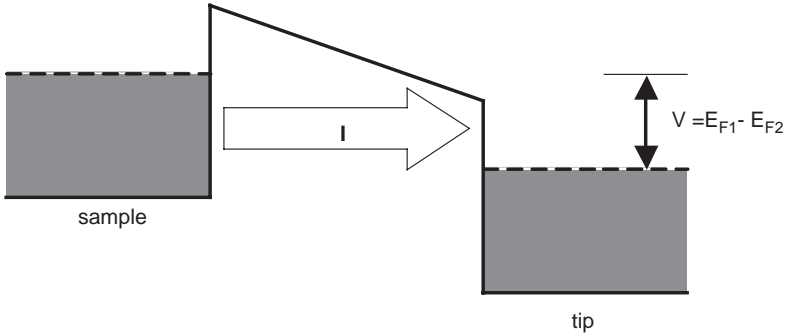


**Fig. 5.** Tunneling current  $I$  through vacuum when a bias voltage  $V$  is applied.

where  $z$  is the distance between tip and sample.  $K$ , which is the inverse decay length of the electronic wave functions at the Fermi level, is given by

$$K = \frac{\sqrt{2m(V - E)}}{h} \quad (2)$$

where  $m$  is the mass of the electron,  $E$  the energy of the state,  $V$  the potential in the barrier and  $h$  the Planck's constant. As a consequence, very small changes in the tip-sample separation induce large changes in the tunneling current. Therefore, the sensitivity to vertical distance is extremely high. Moreover, the tunneling current is only carried by the outermost tip atom: the atoms that are second nearest carry only a negligible amount of the current. In other words, the sample surface is scanned by a single atom only.

## 1.2. Apparatus

In order to obtain an image of the surface of the sample, the STM tip slowly scans across the surface at a distance of only an atom's diameter. This is represented in Fig. 6.

Two different modes of imaging have been developed: the constant current mode and the constant height mode. In the first experiment, the tip is scanned across the surface at constant tunnel current  $I_T$ , maintained at a pre-set value by continuously adjusting the vertical tip position with the feedback voltage  $V_z$ . In the case of an electronically homogeneous surface, constant current essentially means constant tip-sample distance  $z$  (Fig. 7).

On the other side, on surface portions with small unevenness, the tip can be rapidly scanned at constant  $z$ -position. Such "current images" allow much faster scanning than in the constant current mode, but a separate calibration of current/height is required. This mode is presented in Fig. 8.

The tip is moved across the surface by using a piezoelectric element. A voltage applied to two electrodes contracts the piezoelectric material in between, and the typical total excursion of a piezo is usually in the range of

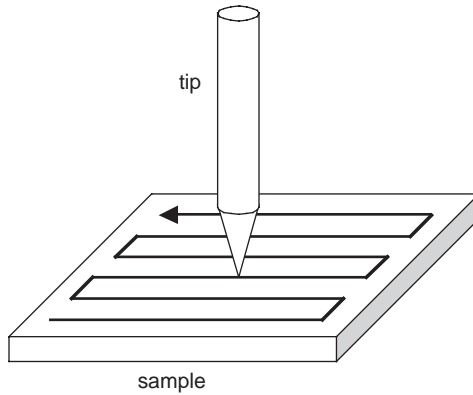


**Fig. 6.** The STM tip scans the sample surface in order to create an image.

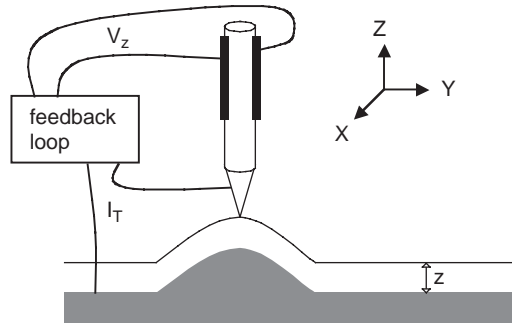


**Fig. 7.** Constant current mode of imaging with STM.

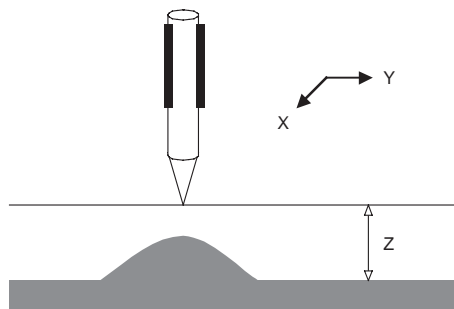


**Fig. 8.** Constant height mode of imaging with STM.

micrometers. Originally, the STM tip was mounted on a three-part piezo element (Fig. 9), with three different piezo bars used to move the tip in all the three dimensions of space.

However, nowadays a piezo tube is more commonly used. In this geometry, the inner and outer surfaces of a tube of piezoelectric material are coated with

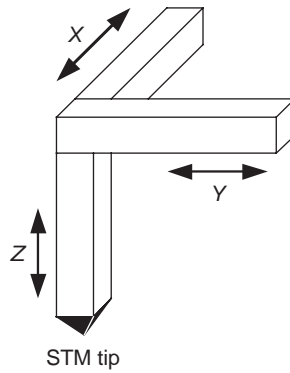


**Fig. 9.** STM tip mounted on a three-parts piezo element.

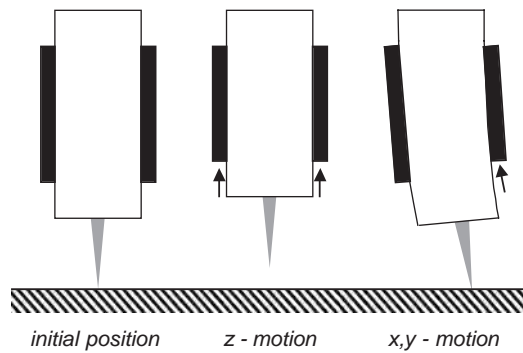


**Fig. 10.** Principle of operation of a piezo tube.

a thin metal electrode. The outside is separated into four sections, which are electrically isolated from each other. For the lateral motion of scanning, the voltage is applied across the tube, while for the vertical motion, the voltage is applied between the inside and the outside of the tube (Fig. 10).

Different metals and different processes can be used to prepare the tips. Mechanically cleaved platinum/iridium tips (4:1) provide very sharp atomically resolved images, and furthermore they are cheap, easy to prepare, and stable. However, the exact shape of the tip differs from one experiment to another: the high resolution is achieved by randomly created minitips of potentially atomic size rather than by a perfect cone decreasing to a single atom end. In addition, the general shape of the tip is not conical, which can be necessary in some optical setups for coupling with spectroscopy. Therefore, a lot of effort has been done to produce reproducible electrochemically etched tips. The basic setup is depicted in Fig. 11.

Some papers on how to prepare Pt/Ir tips have been published, with end curvature of the tip smaller than 100 nm [3]. Tungsten tips are somehow easier to fabricate, and tip radius of about 20 nm have been reported [4–6]. Silver tips

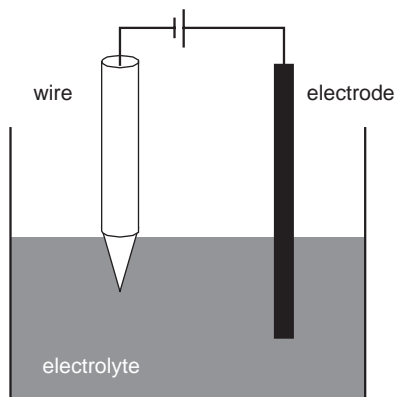


**Fig. 11.** Basic scheme to prepare tips by electrochemical etching.

can also be obtained [7–9], but silver is not very stable under ambient conditions because of oxidation. Finally, gold tips can be difficult to work with, mainly due to the inherent softness of the metal [10].

### 1.3. Sample Preparation

Organic molecules with long alkyl chains are known to form monolayers on definite solid surfaces by self-adsorption. Highly oriented pyrolytic graphite (HOPG), which presents an atomically flat surface that can be cleaned mechanically, is the substrate of choice. However, in some spectroscopic experiments using an inverse microscope for instance, a transparent sample is required. In these cases, a quartz glass substrate covered by a thin layer of indium tin oxide (ITO,  $\sim 100$  nm) can be used. The surface is not as flat as with HOPG, but the sample is transparent and conductive, an obvious requirement for STM. Typical self-adsorbed molecules are stearic acid, dioctadecyl ether, and dioctadecyl selenide dissolved in 1-phenyloctane.

After preparing the surface of HOPG by cleaving one layer of graphite, the substrate is installed onto the piezoelectric scanner of the STM head. Subsequently, a few microliters of solution are deposited on the substrate with a micropipette, immediately forming a physisorbed monolayer. A freshly cleaved tip is then manually approached to the surface at a distance of about 0.5 mm, and the feedback mechanism is turned on. The automatic approaching mechanism brings the tip to a very close distance above the monolayer, namely about 1 nm, with the end of the tip into the solution drop. Fig. 12 presents the experimental setup for imaging this kind of monolayer at the solid–liquid interface. Note that the tip is immersed in the supernatant solution during scanning.

The main advantage of this solid–liquid setup is that the experiment can be carried out in air, which is normally unstable due to the condensation of water on the tip and/or onto the sample. Water is highly conductive, and since the

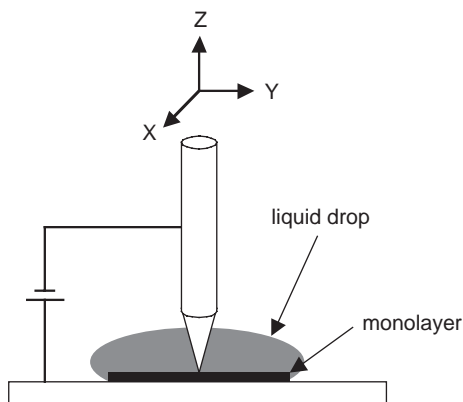


**Fig. 12.** Experimental setup for STM studies at the solid–liquid interface.

STM experiment relies on the tunneling current through an insulator (the gap between the tip and the sample), high vacuum is generally required to stabilize the tunneling current. However, with the tip dipped into a non-conductive organic solvent, no water can disturb the experiment, and the expensive and potentially troublesome equipment for high vacuum is not necessary.

## 2. STRUCTURE OF MONOLAYERS

### 2.1. Brief History

Although the initial applications of STM were focused on the imaging of semiconductor, inorganic, and metal surfaces, it has recently become possible to study physisorbed organic molecules, immobilized by the formation of densely packed two-dimensional layers, at the solid–liquid interface. In 1990, McGonigal et al. published the first direct STM images of a self-adsorbed monolayer of long-chain alkanes at the solid–liquid interface [11]. Though this kind of system had already been studied using different methods, it was the first direct observation of the true ordering of these adsorbed layers. However, they found that the apparent atomic resolution was related to graphite lattice substrate, and the organic molecules only enhance locally the tunneling current. Nevertheless, the general pattern of adsorption for several *n*-alkanes was observed, revealing highly ordered parallel rows of molecules. In this experiment, the molecule axis with respect to the direction of a piled-up column often called a lamella was perpendicular. Rabe and Buchholz have later found that the adsorbed molecular axes with respect to the column direction depend on functional groups at the alkyl chain ends [12]. During the next 10 years, many other reports on this subject have been published. This efficient approach to reduce the mobility of molecules, a prerequisite for high-quality imaging at room temperature, has stimulated STM investigations under ambient conditions at the solid–liquid

interface [13–16]. Actually, STM has the potential to provide images of the two-dimensional ordering of monolayers at interfaces on a sub-molecular scale, which is summarized in some reviews [17,18].

## 2.2. Recognition of Atoms

There have been many attempts to recognize elements under STM. It has been proposed that the polarizability of atoms and functional groups plays a key role in the contrast mechanism when highest occupied molecular orbital (HOMO) and lowest unoccupied molecular orbital (LUMO) levels of the adsorbed molecules are energetically far from the Fermi level of the substrate [19,20]. Another paper showed that ionization potentials seem to correlate to the STM image contrast for a series of functionalized alkanes [21]. The geometric configuration of functional groups is found to play an important role in the image contrast [22]. In the case of aromatic molecules, resonant tunneling through a potential well formed in physisorbed molecules is believed to explain the conductivity of molecules [23]. In another case, the HOMO or LUMO of adsorbed molecules was apparently coupled with the Fermi level of the substrate, and this was proposed as the dominant mechanism controlling the tunneling current through the molecules [24]. Thus, the contrast mechanism for physically adsorbed molecules at liquid–solid interfaces still remain obscure. One problem in the quantitative study of image contrast in self-assembled monolayers is that the conductivity through adsorbed molecules is highly affected by the shape of tunneling probes. Therefore, it is necessary to develop a method which is independent of the probe shape in order to study the image contrast.

Padowitz et al. have shown that dihexadecyl ether ( $\text{CH}_3(\text{CH}_2)_{15})_2\text{O}$  and dihexadecyl sulfide ( $\text{CH}_3(\text{CH}_2)_{15})_2\text{S}$  molecules can be co-adsorbed on graphite surface and are distinguishable in STM image due to the strong image contrast of sulfur atoms with methylene group [25,26]. A series of dioctadecyl chalcogenides were also found to form monolayers, and the structure of pure and mixed monolayers were systematically investigated [27]. For this series of molecules, a new analytical method is proposed for comparison of images obtained with different conditions. Fig. 13 shows examples of STM images of these molecules. Assuming that the fluctuations of alkyl chains of these adsorbed molecules were the same, the distribution of the brightness was normalized with respect to both the distribution curve peak position and the distribution width.

This normalization procedure is rationalized as follows [27]. According to the treatment by Tersoff and Hamann [28,29], the conductivity between a tunneling probe and a surface is represented with the following equation:

$$\sigma = CR^2\rho_0^v \exp(-2Kz) \quad (3)$$

where  $C$  is the constant,  $R$  the curvature radius of the probe,  $\rho_0^v$  the surface local density of state,  $K$  the inverse decay length of tunneling electrons in vacuum, and  $z$  the gap between the probe and the surface. When we observe long alkyl

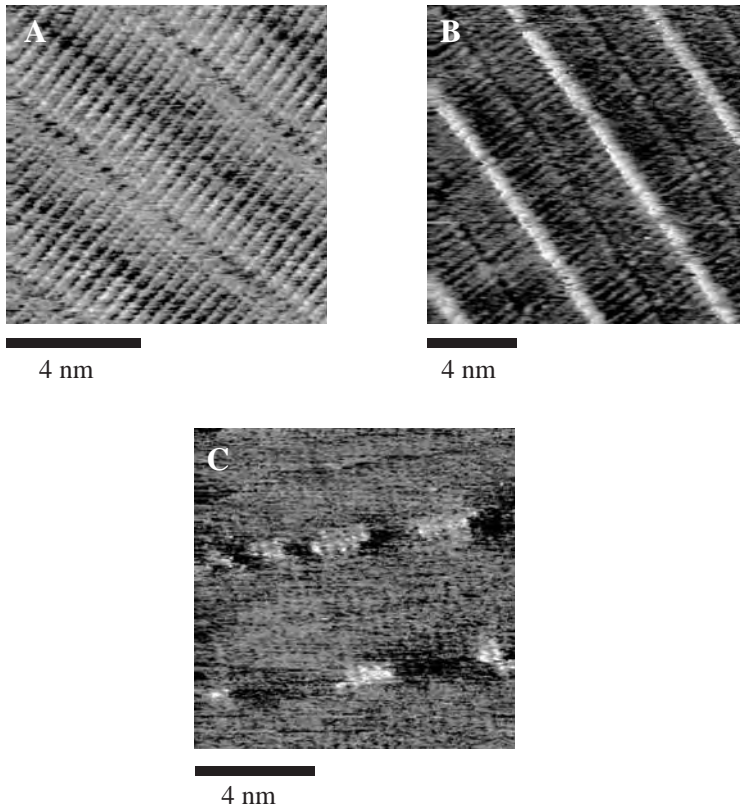


**Fig. 13.** STM images of dioctadecyl ether (A), dioctadecyl selenide (B) and a mixture of A and B (C).

chains adsorbed onto a graphite surface at room temperature, the gap  $z$  is thermally fluctuating and its distribution would be represented by a normal stochastic process. Thus the observation frequency to have the distance  $z_i$  should follow a Gaussian function, and thus expressed by:

$$N_i = N_0 \exp\{-(z_i - z_0)^2/s\} \quad (4)$$

where  $s$  is the width of the distribution involving temperature as a parameter. Assuming that the term corresponding to the fluctuation  $K(z_i - z_0)$  is reasonably small, we obtain the following equation from Eqs. (3) and (4):

$$N_i = N_0 \exp\{-(\sigma_i - \sigma_0)^2/8s^2K^2\sigma_0^2\} \quad (5)$$

It should be noted here that both the curvature radius and local density of states are canceled out by taking the ratio between  $\sigma_i$  and  $\sigma_0$ . This means that the frequency  $N_i$  as a function of conductivity  $\sigma_i$  presents an inverse parabolic curve when it is plotted with a logarithmic scale. This is consistent with the curves shown in Fig. 14, if we consider that the height required to keep a

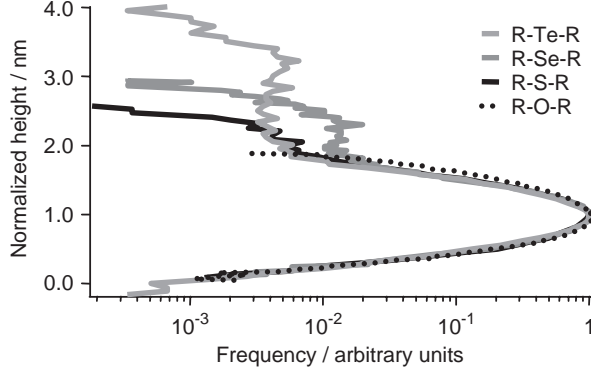


**Fig. 14.** Normalized distribution curves of co-adsorbed dioctadecyl chalcogenides monolayers.

constant current is proportional to the conductivity. A full width at half maximum (fwhm) of the conductivity distribution can be calculated with the following equation:

$$\Delta\sigma_{\text{fwhm}} = 4sK\sigma_0 \quad (6)$$

It is clear that both  $\Delta\sigma_{\text{fwhm}}$  and  $\sigma_0$  are proportional to  $R^2\rho_0^v$  from Eqs. (3) and (6), which means that these values depend on the probe shape and the local density of states at the surface. However, if we normalize the conductivity  $\sigma_0$  with the width  $\Delta\sigma_{\text{fwhm}}$ , the value should give a constant depending on the fluctuation of the observed surface. Therefore, we can cancel the effect of the tunneling probe shape if we take the same fluctuating surface as standard.

Now we consider a situation in which another atomic species X having a different local density of states  $\rho_0^x$  is mixed with alkyl chains with the local density of states  $\rho_0^{\text{CH}}$ . Then its conductivity is represented by the following equation:

$$\sigma_0^x = CR^2\rho_0^x \exp(-2kz) \quad (7)$$

Assuming that the kinetic energy of tunneling electrons ( $k$ ) does not depend on the atomic species, we can obtain the following equation:

$$\sigma_0^x/\sigma_0^{\text{CH}} = (\rho_0^x/\rho_0^{\text{CH}}) \exp\{-2k(z_0^x - z_0^{\text{CH}})\} \quad (8)$$

This can be reduced to the following simple equation when the sizes of X and CH are considered to be similar:

$$\sigma_0^x/\sigma_0^{\text{CH}} = \rho_0^x/\rho_0^{\text{CH}} \quad (9)$$

Thus we can compare a local density of states of each atom after the normalization using both  $\Delta\sigma_{\text{fwhm}}^{\text{CH}}$  and  $\sigma_0^{\text{CH}}$ , even though the tip radius is different.

Fig. 14 shows the distribution curves of co-adsorbed monolayers of R-S-R, R-Se-R, and R-Te-R with R-O-R, which were normalized based on the

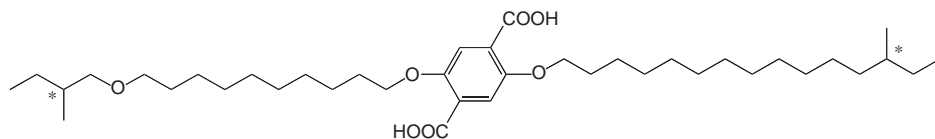


**Fig. 15.** Structure of the terephthalic acid derivative.

curves related to the alkyl chain of dioctadecyl ether of each sample. It should be noted, however, that we can compare atoms in question only when the interactions between the atoms and the substrate are similar.

### 2.3. Recognition of Chirality

A chiral terephthalic acid derivative, 2,5-bis[10-(2-methylbutoxy)decyloxy]terephthalic acid (Fig. 15), with two identical stereogenic centers, has been investigated by De Feyter et al. [18].

The chirality and conformation have been simultaneously studied. The chirality of the monolayer can be observed in various ways: in regions of the monolayer where the alkoxy chains are fully extended, the STM images exhibit a clear modulation of the contrast along the lamellae. The unit cells of this contrast modulation are mirror images for both enantiomers, which means that each enantiomer forms its characteristic enantiomorphous monolayer structure. In addition, the orientation of the lamella axes with respect to the graphite lattice provide another indication of the chirality of the monolayer: the angle between a lamella axis and a graphite reference axis is  $-3.7^\circ$  and  $+3.7^\circ$  for the (*S*) and (*R*) enantiomers, respectively. In summary, the two-dimensional ordering of monolayers of chiral molecules is found to express the chirality of individual molecules too.

## 3. DYNAMICS OF MOLECULAR LAYERS

### 3.1. Desorption and Re-adsorption

As described in a pioneering work by Rabe and Buchholz, self-assembled monolayers are known to be dynamic [12]. The boundaries of lamellae are unstable and moving within the time scale of a conventional STM imaging system, which clearly indicates that molecules in self-assembled monolayers are repetitively desorbed to and re-adsorbed from the liquid phase. Of course, the motion of individual molecules is too fast to be observed, however, collective motion of molecules can be visualized over nanometer ranges. Stabel et al. investigated the self-assembled monolayers of alkylated octathiophene derivatives at the solution-graphite interface [30]. Small domains in the monolayers were overtaken by large domains and eventually disappeared, as expected from the Ostwald ripening process, which explains domain growth by reduction of the interfacial potential energy.

Dynamic processes in two component monolayers have also been studied. Hibino et al. investigated mixtures of fatty acids having alkyl chains of different lengths [15,31]. They found that molecular motion within monolayers often occurred at the liquid–solid interface and adsorption of fatty acids with longer alkyl chains was preferential. Gesquiere et al. observed the dynamics in the self-assembled monolayers of isophthalic acid derivatives with a speed of two frames per second and found that non-fluorinated molecules progressively replaced the fluorinated molecules [32]. These dynamic processes were always initiated at the domain boundary due to the local instability of adsorption. Fluctuation dynamics in physisorbed monolayers apparently occurring without rearrangement of whole monolayers have also been reported. Stabel et al. observed “fuzzy” images of alkylated anthraquinone derivatives within loosely packed monolayers, the cause of which was attributed to the significantly large free volume [33]. Padowitz et al. studied the exchange process between alkylated ether and thioether in monolayers with the compounds in solution [25,26]. The residence time of the thioether molecules in the monolayers depended on the neighboring adsorbates owing to differences in the weak intermolecular interactions. Cousty et al. also observed monolayer structures formed with binary mixtures of *n*-alkanes and found point defects due to the insertion of short alkanes among long alkane molecules [34]. These structural fluctuations were found to occur randomly but never induced co-operative molecular motion leading to a large-scale fluctuation within the assembly.

When 1-pyrenehexadecanoic acid (PHDA) and 4,4'-dipyridyl (4Bpy) are co-adsorbed at the solution–graphite interface, interesting domino-like molecular reorientation in the self-assembled monolayers was observed [35]. A single defect due to anti-parallel molecular orientation was found to propagate itself over 10 molecules, enlarging the fluctuation region due to co-operative molecular motion as shown in Fig. 16. Because  $\pi$ - $\pi$  interaction affects the crystal structure of large aromatic halves, e.g., pyrene and perylene, it is expected to influence desorption and adsorption dynamics through similar interactions.

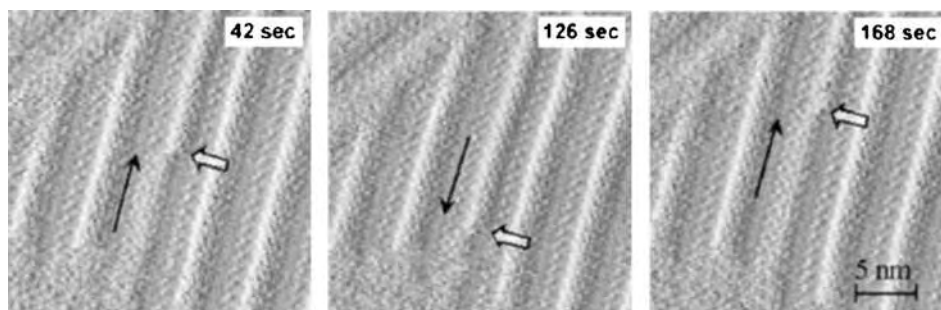


**Fig. 16.** A series of STM images of the same area of 1-PHDA and 4Bpy co-adsorbed monolayers.

The co-operative structural fluctuation in self-assembled monolayers is also considered to be dominated by the  $\pi$ - $\pi$  interaction between the pyrene units. The  $\pi$ - $\pi$  interaction involves a move of electronic charge between molecules, often leading to the formation of intermolecular donor-acceptor complexes. This kind of interaction can also affect the structure of self-assembled monolayers [36].

### 3.2. Chemical Reactions

Polymer industries depend on the spontaneous polymerization of molecules into chains in response to an appropriate trigger. Polymerization reaction under STM was first observed by Grim et al., although the reaction itself was not induced with a current from the tunneling probe [37]. Recently, by using an STM tip, Okawa and Aono have successfully initiated and terminated the linear propagation of the chain polymerization of a diacetylene compound into a polydiacetylene compound at any chosen point with a spatial precision of about 1 nm [38].

A self-ordered monomolecular layer of 10,12-nonacosadiynoic acid molecules (NCDA,  $C_{29}H_{50}O_2$ , Fig. 17), adsorbed on a graphite surface, is used as starting material. In a typical STM image of the monomolecular layer, a linear array of diacetylene moieties of the self-ordered molecules can be clearly observed as a couple of bright lines. This molecular species polymerizes in a three-dimensional solid state, and this reaction can be induced by local stimulation with the STM tip. First, an artificial defect in the form of a 6-nm-wide hole is generated at a predetermined position in the monomolecular layer by placing the STM tip at this position and applying a 5 V pulsed sample bias during 10  $\mu$ s. Then, scanning from top to bottom with a negatively pulsed sample bias ( $-4$  V, 5  $\mu$ s), applied when the scanning tip passed a certain point, causes a bright line to appear between the point and the artificial defect. This bright line represents a polymerized polydiacetylene nanowire, as confirmed by structural analysis. The same area is once more scanned, applying another negatively pulsed sample bias when the tip passed another certain point indicated by the other certain point. From these experimental results, they conclude that the STM-induced chain polymerization propagates on both sides of the point of stimulation. The polymerization results in polydiacetylene compounds that behave as conjugated linear polymers and should function as electrically conductive “nanowires” upon transfer of charge from the surroundings. Therefore, this technique should be useful for interconnecting nanostructures, enabling the electrodes of a single-electron transistor, for example, to be wired up even if it is nanometer-sized. This new method opens up possibilities for the fabrication of novel molecular nanoelectronic devices and should help to take molecular nanoelectronics beyond the present silicon-based-device technology.

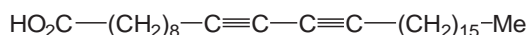


**Fig. 17.** 10,12-Nonacosadiynoic acid (NCDA).

Although the above-mentioned research concerning inducement of such localized organic chemical reactions have been carried out in the solid–air interface, STM can also be applied to the solid–liquid interface as described before. STM in the solid–liquid interface allows us to get rid of influence of water and various contaminants in air to preserve clean interfaces, resulting in obtaining clear molecular images even without a vacuum chamber. Furthermore, one of the advantages of STM in the solid–liquid interface is the potentiality to add chemical reactants in the solvent. Making the best use of such advantages [39], STM could induce various organic reactions such as addition, substitution, and polymerization reactions in nano-scale. Nishio et al. have induced a polymerization reaction by STM in a monolayer of a diacetylene derivative at the solid–liquid interface and investigated the effects of ionic species dissolved in the solution on the reaction probability [40].

The same STM setup as in Fig. 12 is used. The STM tip is immersed into the drop of liquid, and probes the solid–liquid interface. All the STM measurements are carried out under ambient conditions at a room temperature. A drop of saturated solution of NCDA (see Fig. 17) in phenyloctane is deposited on a clean surface of graphite. Fig. 18 shows a STM image of the monolayer of the acid adsorbed on the graphite surface together with a model structure. A few lines of the lamellae arranging orderly can be observed clearly, and the width of each lamella is in accordance with the molecular length of NCDA. The longest horizontal bright lines correspond to the long alkyl chains of NCDA,  $(\text{CH}_2)_{15}$ , while the shortest are the  $(\text{CH}_2)_8$  chains. The diagonal portions reflect the diacetylene part of NCDA, and two NCDA molecules form hydrogen bonding (dark lines). The distance between two adjacent molecules in the lamellae is  $4.5 \text{ \AA}$ .

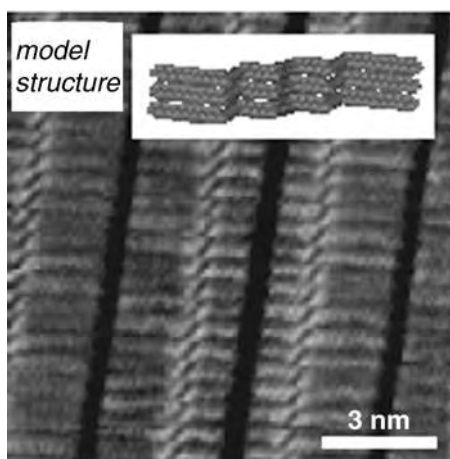


**Fig. 18.** STM image of a monolayer of 10,12-nonacosadiynoic acid adsorbed on graphite.

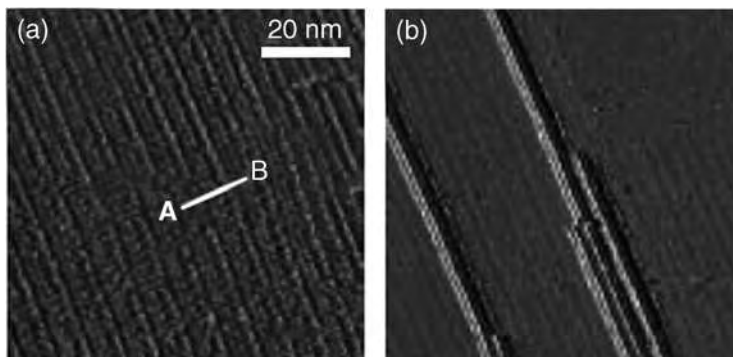


**Fig. 19.** 80 nm  $\times$  80 nm STM images of a monolayer of NCDA in phenyl octane deposited on graphite, (a) before and (b) just after the impression of a pulsed voltage on the STM tip.

Polymerization is induced with the STM tip. STM images of the monolayer of NCDA before and just after applying a positive pulsed bias voltage of 4 V are shown in Fig. 19. In Fig. 19a, a number of parallel lines corresponding to the diacetylene portions of NCDA molecules are observed.

A 30 ms pulsed bias voltage is applied in succession over five diacetylene lines along the line A–B in the figure, resulting in successful inducement of the polymerization reaction as shown in Fig. 19b. Considering the quite similar conditions with the conventional solid state polymerization of diacetylene compounds, the polymer is supposed to be polydiacetylene, although no conclusive evidence has been obtained from the STM image. The polymerized lines are brighter than the other lines where no polymerization took place. This is mainly due to development of  $\pi$ -conjugated systems by forming polydiacetylene. The maximum polymerization length along the diacetylene lines is more than 200 nm, reaching the end of the domain of the monolayer. The reaction also occurs at a portion about 30 nm away from the region where the pulsed voltage has been applied. The threshold of the pulsed voltage for polymerization is 2 V, whereas the reaction probability increases with increasing the absolute value of the voltage.

In order to investigate the effect of ionic additives on the STM-induced polymerization,  $10^{-2}$  M of tetramethylammonium perchlorate,  $N(\text{CH}_3)_4\text{ClO}_4$ , is dissolved in the solution. Fig. 20 shows the spatial distribution of the probability of the polymerization reaction at various bias voltages without and with  $N(\text{CH}_3)_4\text{ClO}_4$ , respectively. The reaction probability is defined as the average number of lines polymerized by a single pulse in each region separated by an interval of 10 nm. The threshold of the applied voltage is  $\pm 2$  V, independently of the presence of tetramethylammonium perchlorate. However, at more than  $\pm 2$  V, the addition of  $N(\text{CH}_3)_4\text{ClO}_4$  expands the reaction region and increases the reaction probability, regardless of the sign of the bias voltage applied.

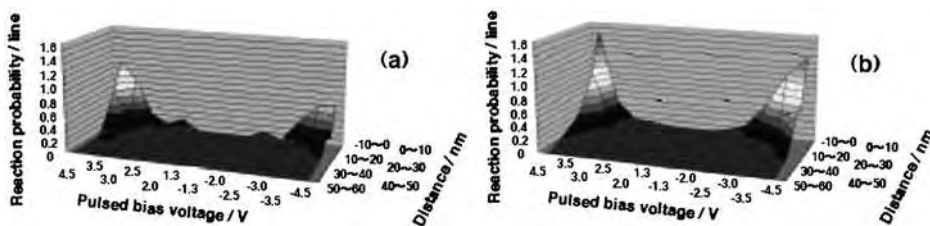


**Fig. 20.** Spatial distribution of the probability of the polymerization at various bias voltage (a) without and (b) with tetramethylammonium perchlorate.

As mentioned above, polymerization is observed at portions far away from where the pulsed voltage is applied. This could be explained by the following hypothesis: on applying a positive pulsed voltage of several volts between the STM tip and the graphite surface, electrons are injected from the tip into the liquid. These electrons are accelerated due to the strong electric field ranging from  $10^8$  to  $10^{10}$   $\text{V m}^{-1}$  formed between the tip and the graphite surface. The accelerated electrons then come into collision with various species in the liquid to yield secondary electrons from them, inducing a so-called electron avalanche [39]. Furthermore, the electron avalanche occurs more frequently at lower applied voltages with the presence of ionic compounds. The same process may participate in the polymerization reaction induced by STM in the solid–liquid interface. In addition, the effect of  $\text{N}(\text{CH}_3)_4\text{ClO}_4$  on the polymerization reaction is found even when a negative pulsed bias is applied, suggesting that the positive ions also contribute to the polymerization reaction. In addition, the threshold voltage of 2 V is smaller than that for the solid–air interface (4 V). While direct excitation to the  $T_1$  state of diacetylene by tunneling electrons occurs at the solid–air interface [41], a different mechanism takes place at the solid–liquid interface. The polymerization is probably induced through the multiple vibrational excitation of NCDA by incessant collisions with charged carriers activated by the effects of strong electric field involving the electron avalanche.

## 4. SPECTROSCOPIC TECHNIQUES COMBINED WITH STM

### 4.1. Current/Voltage Spectroscopy

In tunneling spectroscopy, the tip position is fixed and the current is recorded as a function of the potential difference between the tip and sample. At positive voltage bias, the majority of electrons tunnel elastically from filled tip states to empty sample states. An adsorbate perturbs the sample density of states in a unique way, and therefore produces a different tunneling current than the bare sample. Additional information can be extracted from tunneling spectra by considering the effect of inelastic tunneling processes on the current. When the energy of a tunneling electron is sufficient to excite a quantized molecular vibration, the electron can tunnel inelastically and leave the molecule in a

vibrationally excited state. Inelastic tunneling represents an additional tunneling channel which, when accessible, increases the differential conductance of the tunnel junction. Typical vibrational mode energies are 0–500 meV. Metals provide a relatively smooth and substantial density of states in this region near the Fermi level. Such properties are desirable for discriminating vibrational peaks from electronic contributions to the spectra.

Lauhon and Ho have reported the vibrational spectrum of an acetylene ( $C_2H_2$ ) molecule adsorbed on a copper surface measured with tunneling spectroscopy [42]. The spectrum is an average of 20 scans at 9.5 K, and the tunneling gap is set to 250 mV. A Cu background spectrum has been subtracted from the spectrum. The peak corresponds to the C–H stretch mode, taken at positive and negative bias. The peak intensity at 357 mV is 1.7 times greater than the peak intensity at  $-357$  mV. Similar junction bias asymmetries have been observed in macroscopic IETS spectra. This effect may be qualitatively understood by noting that the electrons have a higher probability of tunneling before losing a vibrational quantum energy (at positive bias) than after (at negative bias).

## 4.2. Raman Spectroscopy

A conventional atomic force microscope (AFM) tip, suitably coated with gold, can provide spatially selective enhancement of a Raman signal using the surface enhanced Raman scattering (SERS) effect [43]. The SERS effect exploits a property of nanometer-sized metal particles or surface grains: incident laser photons are absorbed into the metal particles through oscillations of surface plasmons [44]. When this effect couples with molecules in close proximity, an efficient pathway to transfer energy to the molecular vibrational modes opens, generating Raman photons. The enhancement is maximized when the metal grains are smaller than the incident laser wavelength and when the metal has the optical properties to generate surface plasmons. The greatest enhancements are observed with silver, gold, and copper with grain diameters between 10 and 200 nm. In addition to this electromagnetic field enhancement, there is an additional chemical enhancement that results when a molecule coordinates with the surface metal particle and forms charge transfer states with the energy levels of the metal. This results in a charge transfer transition in the visible wavelength region and a surface localized resonance Raman enhancement [45]. For example, enhancement factors of  $10^8$  to  $10^{14}$  have been reported with molecules absorbed on a silver substrate [46]. However, the spatial resolution of this AFM tip enhanced Raman spectroscopy yet remains in the range of nanometers. On the other hand, using STM allows to determine the morphology of surfaces down to the atomic level. STM tip enhanced Raman spectroscopy is therefore a very promising tool for spectroscopic investigations with sub-molecular resolution [47].

In actual experimental setup for the combination of STM with Raman spectroscopy, there are essentially two optical detection methods as shown in

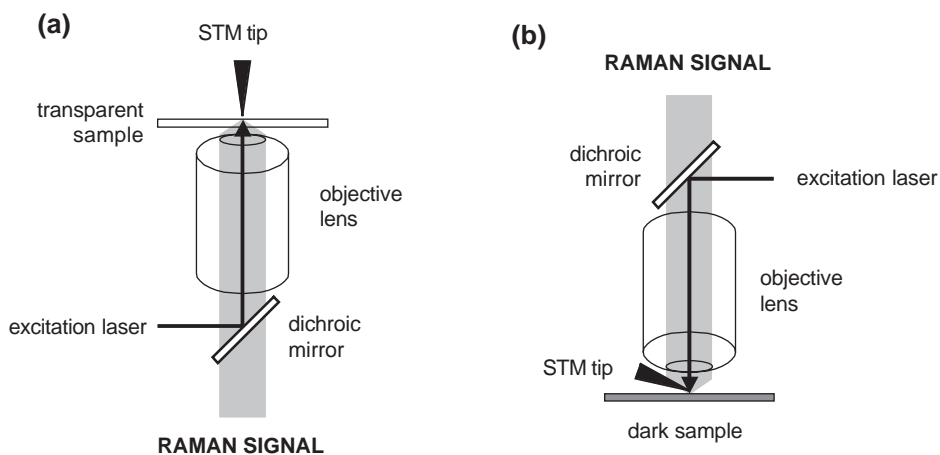


**Fig. 21.** Schematic representation of the inverse (a) and reflective (b) microscope setup.

**Fig. 21.** In the case of inverse type microscopy, laser light is focused by the objective onto a transparent sample from bottom. The scattered light is collected through the same objective and discriminated from the excitation light by a dichroic mirror. Then the light is refocused into the spectrograph and detected by photodetectors. Alternatively, the collected light can be directed to binoculars for visual checking using white illumination light from above the sample, either vertically (bright field) or from the side (dark field). The advantage of such an inverse type microscope is that the top of the sample remains free, which can be used for installing a conventional STM head. On the other hand, such an experiment requires a substrate that is both conducting and transparent, and the only easily available sample fulfilling these conditions is ITO deposited on quartz that is usually not atomically flat.

In the case of reflective type setup, the key element is the high magnification ( $100\times$ ), large numerical aperture (NA 0.76), long working distance (6 mm) objective with a special concave end lens in order to let some free space for the STM tip. This setup allows us to use atomic flat graphite substrates and thus self-assembled monolayers are easily observed with atomic scale resolution. In addition, Raman spectra of 1-phenyloctane and *n*-octylcyclohexane have been successfully measured although the amount of samples was very small ( $25\ \mu\text{l}$ ). The ability as both an STM and a Raman spectrometer of this system is demonstrated by using a simple HOPG surface as shown in **Figs. 22 and 23**.

For Raman scattering measurement, a freshly cleaved sample is directly illuminated with the Ar-ion laser, and the resulting spectrum, accumulated during 10 min, is shown in **Fig. 23**. The band at  $1580\ \text{cm}^{-1}$  corresponds to the in-plane C–C breathing mode of the whole graphite lattice, namely the  $E_{2g}$  mode. The band at  $2730\ \text{cm}^{-1}$  is an overtone of a lower-energy vibration, and

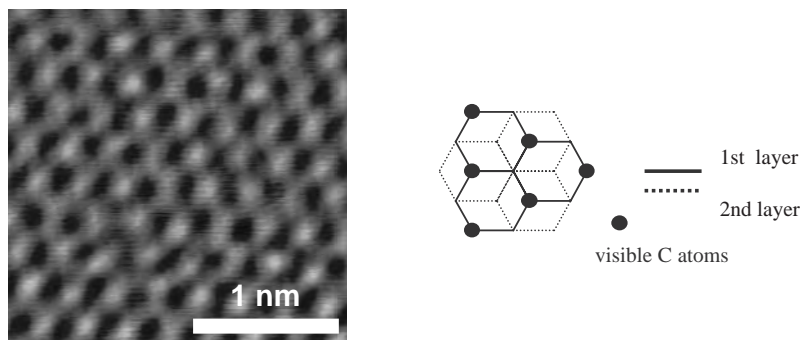


**Fig. 22.** An STM image of a HOPG surface obtained with the reflective type setup.

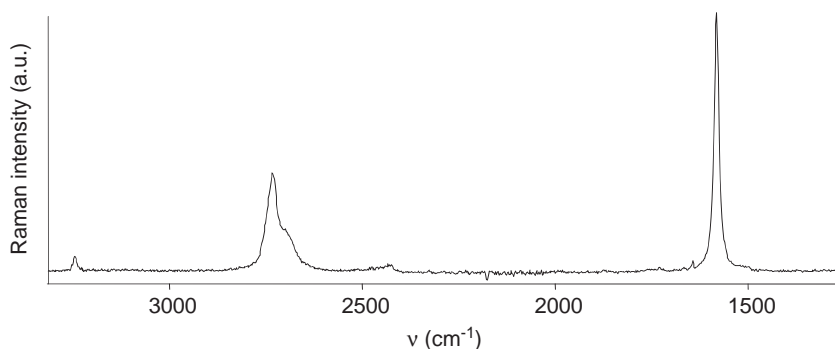


**Fig. 23.** Raman spectrum of the surface of HOPG.

the two remaining small peaks ( $2430$  and  $3240\text{ cm}^{-1}$ ) are a combination band and an additional overtone, respectively. Thus, the reflective type confocal Raman spectrometer has more versatility in choosing a substrate.

## 5. FUTURE DIRECTIONS

By combining vibrational spectroscopy with STM, *in situ* characterization of single molecules can be achieved. However, the STM is not only capable of imaging, but also of local chemical modifications: injecting electrons to the sample can induce vibrational excitation, and even break or form bonds. This ability to directly visualize molecules as well as their controlled reactions opens up a new field of research for chemistry. In fact, STM allows us to visualize quantum mechanics [1]. By using nanosystems specifically designed for specific problems, we are actually working like Nature does. Life is built on nanofunctionality: senses, metabolism, and even growth take place on the nanometer scale. In addition, the small energies required for local activation are in the thermal energy (kT) range. All the elements are now at our disposal to finally build functionality from the bottom up [48].

In this chapter, we did not touch another important area studying excited state dynamics with sub-molecular-level spatial resolution. There are already a few pioneering works in this field [49,50]. Generally, fluorescence is more sensitive than Raman scattering and therefore it would be easier to detect fluorescence than Raman. However, fluorescence of adsorbed molecules can be quenched by the substrate graphite and probe metals due to energy and electron transfer. To overcome these problems, we need to develop further instruments and materials fitting to the fluorescence detection under the STM condition. We do strongly hope the era will come soon that allows us to observe real-time excited state dynamics with sub-molecular resolution in the self-assembled monolayers.

## REFERENCES

- [1] W. Ho, *J. Chem. Phys.*, 117 (2002) 11033.
- [2] A. H. Zewail, *J. Phys. Chem. A*, 104 (2000) 5660.
- [3] I. H. Musselman and P. E. Russell, *J. Vac. Sci. Technol. A*, 8 (1990) 3558.
- [4] J. P. Ibe, P. P. J. Bey, S. L. Brandow, R. A. Brizzolara, N. A. Burnham, D. P. DiLella, K. P. Lee, C. R. K. Marrian and R. J. Colton, *J. Vac. Sci. Technol. A*, 8 (1990) 3570.
- [5] M. Fotino, *Rev. Sci. Instrum.*, 64 (1993) 159.
- [6] M. Klein and G. Schwitzgebel, *Rev. Sci. Instrum.*, 68 (1997) 3099.
- [7] A. A. Gorbunov, B. Wolf and J. Edelmann, *Rev. Sci. Instrum.*, 64 (1993) 2393.
- [8] K. Dickmann, F. Demming and J. Jersch, *Rev. Sci. Instrum.*, 67 (1996) 845.
- [9] M. Iwami, Y. Uehara and S. Ushioda, *Rev. Sci. Instrum.*, 69 (1998) 4010.
- [10] L. Libioulle, Y. Houbion and J.-M. Gilles, *J. Vac. Sci. Technol. B*, 13 (1995) 1325.
- [11] G. C. McGonigal, R. H. Bernhardt and D. Thomson, *J. Appl. Phys. Lett.*, 57 (1990) 28.
- [12] J. P. Rabe and S. Buchholz, *Science*, 253 (1991) 424.
- [13] R. Heinz, A. Stabel, J. P. Rabe, G. Wegner, F. C. De Schryver, D. Corens, W. Dehaen and C. Stilling, *Angew. Chem. Int. Ed. Engl.*, 33 (1994) 2080.
- [14] B. Venkataraman, J. J. Breen and G. W. Flynn, *J. Phys. Chem.*, 99 (1995) 6608.
- [15] M. Hibino, A. Sumi and I. Hatta, *Jpn. J. Appl. Phys.*, 34 (1995) 3354.
- [16] D. M. Cyr, B. Venkataraman and G. W. Flynn, *Chem. Mater.*, 8 (1996) 1600.
- [17] L. C. Giancarlo and G. W. Flynn, *Annu. Rev. Phys. Chem.*, 49 (1998) 297.
- [18] S. De Feyter, A. Gesquiere, M. M. Abdel-Mottaleb, P. C. M. Grim, F. C. De Schryver, C. Meiners, M. Sieffert, S. Valiyaveetil and K. Mullen, *Acc. Chem. Res.*, 33 (2000) 520.
- [19] J. K. Spong, H. A. Mizes, L. J. LaComb, Jr, M. M. Dovek, J. E. Frommer and J. S. Foster, *Nature*, 338 (1989) 137.
- [20] D. M. Cyr, B. Venkataraman, G. W. Flynn, A. Black and G. M. Whitesides, *J. Phys. Chem.*, 100 (1996) 13747.
- [21] C. L. Claypool, F. Faglioni, W. A. Goddard, III, H. B. Gray, N. S. Lewis and R. A. Marcus, *J. Phys. Chem. B*, 101 (1997) 5978.

- [22] D. G. Yablou, J. Guo, D. Knapp, H. Fang and G. W. Flynn, *J. Phys. Chem. B*, 105 (2001) 4313.
- [23] M. D. Watson, F. Jackel, N. Severin, J. P. Rabe and X. Mullen, *J. Am. Chem. Soc.*, 126 (2004) 1402.
- [24] H. Uji-i, S. Nishio and H. Fukumura, *Chem. Phys. Lett.*, 408 (2005) 112.
- [25] D. F. Podowitz and B. W. Messmore, *J. Phys. Chem. B*, 104 (2000) 9943.
- [26] D. F. Padowitz, D. M. Sada, E. L. Kemer, M. L. Dougan and W. A. Xue, *J. Phys. Chem. B*, 106 (2002) 593.
- [27] H. Fukumura, D. I-i, H. Uji-i, S. Nishio, H. Sakai and A. Ohuchi, *Chem. Phys. Chem.*, 6 (2005) 2383.
- [28] J. Tersoff and D. R. Hamann, *Phys. Rev. Lett.*, 50 (1983) 1998.
- [29] J. Tersoff and D. R. Hamann, *Phys. Rev. B*, 31 (1985) 805.
- [30] A. Stabel, R. Heinz, F. C. De Schryver and J. P. Rabe, *J. Phys. Chem.*, 99 (1995) 505.
- [31] M. Hibino, A. Sumi and I. Hatta, *Thin Solid Films*, 594 (1996) 281.
- [32] A. Gesquiere, M. M. Abdel-Mottaleb, S. De Feyter, F. C. De Schryver, M. Sieffert, K. Mullen, A. Calderone, R. Lazzaroni and J. L. Bredas, *Chem. Eur. J*, 6 (2000) 3739.
- [33] A. Stabel, R. Heinz, J. P. Rabe, G. Wegner, F. C. De Schryver, D. Corenes, W. Dehaen and C. Suling, *J. Phys. Chem.*, 99 (1995) 8690.
- [34] J. Cousty and L. P. Van, *Phys. Chem. Chem. Phys.*, 5 (2003) 599.
- [35] H. Uji-i, M. Yoshidome, J. Hobley, K. Hatanaka and H. Fukumura, *Phys. Chem. Chem. Phys.*, 5 (2003) 4231.
- [36] S. Nishio, M. Yoshidome, H. Uji-i, J. Hobley, H. Fukumura and K. A. Zachariasse, *Chem. Lett.*, 33 (2004) 1506.
- [37] P. C. M. Grim, S. De Feyter, A. Gesquiere, P. Vanoppen, M. Rucker, S. Valiyaveetil, G. Moessner, K. Mullen and F. C. De Schryver, *Angew. Chem. Int. Ed. Engl.*, 36 (1997) 2601.
- [38] Y. Okawa and M. Aono, *Nature*, 409 (2001) 683.
- [39] H. Uji-i, K. Hatanaka, J. Hobley and H. Fukumura, *Appl. Phys. Lett.*, 79 (2001) 2660.
- [40] S. Nishio, D. I-i, H. Matsuda, M. Yoshidome, H. Uji-i and H. Fukumura, *Jpn. J. Appl. Phys.*, 44 (7B), (2005) 5417.
- [41] M. Bertault, J. L. Fave and M. Schott, *Chem. Phys. Lett.*, 62 (1979) 161.
- [42] L. J. Lauhon and W. Ho, *Rev. Sci. Instrum.*, 72 (2001) 216.
- [43] A. Hartschuh, E. J. Sanchez, X. S. Xie and L. Novotny, *Phys. Rev. Lett.*, 90 (2003) 095503.
- [44] S. Habuchi, M. Cotlet, R. Gronheid, G. Dirix, J. Michiels, J. Vanderleyden, F. C. De Schryver and J. Hofkens, *J. Am. Chem. Soc.*, 125 (2003) 8446.
- [45] K. Shibamoto, K. Katayama and T. Sawada, *J. Photochem. Photobiol. A*, 158 (2003) 105.
- [46] S. Nie and S. R. Emory, *Science*, 275 (1997) 1102.
- [47] B. Pettinger, B. Ren, G. Picardi, R. Schuster and G. Ertl, *Phys. Rev. Lett.*, 92 (2004) 096101.
- [48] G. Binnig and H. Rohrer, *Rev. Mod. Phys.*, 71 (1999) S324.
- [49] M. M. J. Bischoff, M. C. M. M. van der Wielen and H. van Kempen, *Surf. Sci.*, 400 (1998) 127.
- [50] E. J. Sanchez, L. Novotny and X. S. Xie, *Phys. Rev. Lett.*, 82 (1999) 4014.

## Chapter 2

# Monolayer Properties Probed by Surface Forces Measurements

Andra Dedinaite<sup>a,b,\*</sup>

<sup>a</sup>*Department of Chemistry, Surface Chemistry, Royal Institute of Technology, Drottning Kristinas väg 51, Stockholm SE-100 44, Sweden*

<sup>b</sup>*Institute for Surface Chemistry, Box 5607, Stockholm SE-114 86, Sweden*

### 1. INTRODUCTION

The interferometric surface forces apparatus (SFA) has played a major role in the discovery and experimental investigation of a variety of surface forces since the early seventies. It has now served its scientific purpose in surface chemistry for more than 30 years. The SFA was envisaged by Tabor and Winterton [1] and later developed by Tabor and Israelachvili [2] and Israelachvili and Adams, and Klein [3–5]. Considerable development of the basic technique has occurred since then, and this has opened new perspectives in studying matter in confinement.

This chapter aims at reviewing the main development milestones of the SFA and look back at some of the most important experimental achievements in studying monolayers at interfaces with the SFA. It is structured as follows. In Section 2 the function of the basic SFA is described. This has been excellently done by several authors before [6–9]; however, we feel that it is a necessary part of the review since it helps to appreciate the development of the SFA that is reviewed in Section 3. Further sections are devoted to an overview of experimental achievements obtained using the SFA. A particular emphasis is put on monolayer studies of surfactants and lipids (Chapter 4) where intriguing behaviour of hydrophobic monolayers and forces between hydrophilic monolayers, including specific interactions, are discussed. In Chapter 5 forces generated by

---

\*Corresponding author. E-mail: andra.dedinaite@surfchem.kth.se

polyelectrolytes on oppositely charged surfaces and forces due to polyelectrolyte brushes are discussed. These are of considerable importance in understanding colloidal stability. More to this, as we will see, the knowledge of polyelectrolyte behaviour on surfaces empowers us to understand biotechnological systems, such as protein-repelling surfaces.

## 2. FUNCTION OF THE BASIC SURFACE FORCES APPARATUS

The SFA consists of a hermetically closed stainless steel chamber that can be filled with any transparent liquid or gas of choice. Mica is a preferred substrate in the SFA, though other surfaces, such as single-crystal sapphire plates have also been used [10]. In the SFA, the force acting between the surfaces, mounted in a crossed cylinder configuration, as a function of surface separation is measured. The data obtained are normally plotted as force,  $F_c(D)$ , normalised by the undeformed geometric mean radius of the surfaces,  $R$ . This quantity is related to the free energy of interaction per unit area,  $G_f$ , between two flat surfaces at the same separation [11]:

$$\frac{F_c(D)}{R} = 2\pi G_f(D) \quad (1)$$

### 2.1. Determining Separation between Surfaces

The separation between the surfaces and the refractive index of thin films (e.g., liquid film, polymer adsorption layer, monolayer) are determined by using multiple beam interferometry [6–8]. In order to do so, two mica surfaces that are a few micrometres thin, atomically smooth and of equal thickness are silvered on their back side and glued silvered side down on semi-cylinders of optically polished silica, and positioned in a crossed cylinders configuration. This configuration is locally equivalent to a sphere near a flat. If such surfaces are brought close together and white light is directed perpendicularly on one of the silvered surfaces, some light will pass through the silver layer and it will then be multiply reflected between the two silver mirrors (see Fig. 1). For some wavelengths constructive interference will occur and only these wavelengths will be passed through the upper silver mirror. If the passed light will be directed into a spectrometer, it will be split into bands of discrete wavelengths and thus fringes of equal chromatic order (FECO) can be observed and their wavelengths can be accurately determined. The FECO wavelengths depend on the thickness,  $T$ , of the mica sheets and the separation between the two mica surfaces,  $D$ . When a thin film is introduced between the surfaces, the fringes shift to longer wavelengths. The surface separation is determined with the accuracy of 0.1 nm by comparing the wavelengths of fringes when the two surfaces are in mica–mica

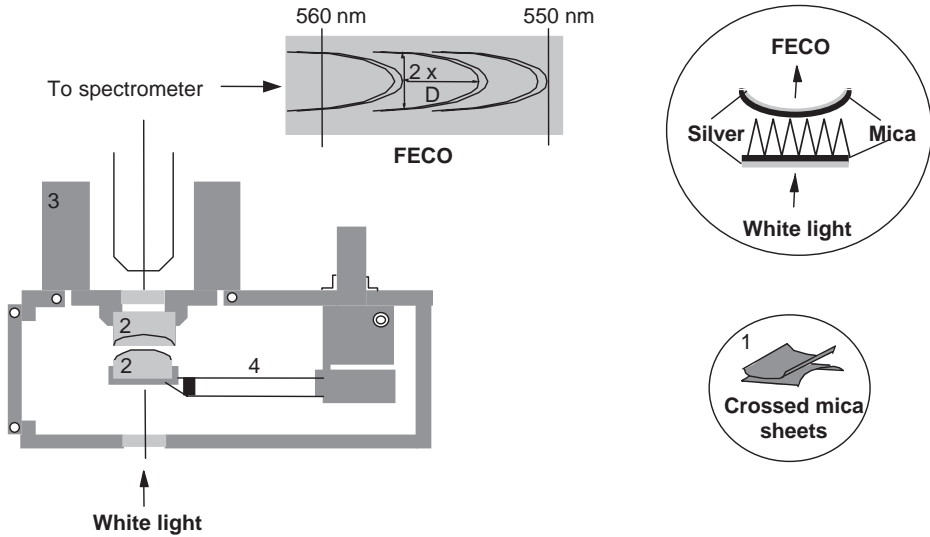


**Fig. 1.** Schematic representation of the main features of the interferometric surface forces apparatus. Crossed mica sheets (1) are glued onto semi-cylinder optically polished silica discs (2). One of the discs is attached to a piezoelectric crystal tube (3), and another to the force measuring double cantilever spring (4). White light passes through the window positioned in the bottom of the apparatus and reflects between two silver mirrors. Constructive interference occurs for some wavelengths and the fringes of equal chromatic order are passed through the upper silver mirror to the spectrometer where they can be viewed and their wavelengths determined. Adapted from Ref. [9]. © 1996, with permission from Elsevier.

contact and some distance apart. From the wavelengths the refractive index can also be determined. For a symmetric three-layer interferometer the distance can be calculated from [6]

$$\tan\left(\frac{2\pi\mu D}{\lambda_n^D}\right) = \frac{2\bar{\mu} \sin(\pi\phi)}{(1 + \bar{\mu}^2) \cos(\pi\phi) \pm (\bar{\mu}^2 - 1)} \quad (2)$$

In Eq. (2):

- $\mu$  the refractive index of the medium,
  - $\bar{\mu}$   $\mu_m/\mu$ ,
  - $\mu_m$  the refractive index of mica at the wavelength  $\lambda_n^D$ ,
  - $n$  the fringe order that equals the number of antinodes in the standing wave,
  - $\lambda_n^D$  the wavelength of fringe  $n$  when the surfaces are separated a distance  $D$ ,
  - $\lambda_n^0$  the wavelength of fringe  $n$  when the surfaces are in contact,
  - $\lambda_{n-1}^0$  the wavelength of fringe  $n-1$  when the surfaces are in contact,
- The signs “+” and “-” refers to  $n$  being odd and even, respectively.

Refractive index determination of a thin film relies on the fact that odd and even fringes depend in a different way on the refractive index of the intervening medium between the surfaces. Thus, by measuring the wavelengths of fringes  $n$ ,  $n-1$  and  $n-2$  with the surfaces in contact and the wavelengths of fringes  $n$  and  $n-1$  with the surfaces separated, it is possible to determine the refractive index and from this calculate the adsorbed amount on each surface,  $\Gamma$ , by using the relation [12]:

$$\Gamma = \frac{D(n - n_b)}{2dn/dc} \quad (3)$$

In Eq. (3):

$n$	the refractive index of the adsorbed layer,
$n_b$	the refractive index of the bulk solution,
$D$	the surface separation,
$dn/dc$	the refractive index increment.

## 2.2. Determining Forces between Surfaces

In the SFA, the distance between the surfaces is controlled by use of a three-stage mechanism of increasing sensitivity: a coarse motor, a fine motor and a piezoelectric crystal tube, the latter allowing for distance control with an accuracy of 0.1 nm. The movement of the piezoelectric crystal tube is calibrated at large surface separations where no force is acting between the surfaces. For calibration it is an acceptable approximation that the expansion of the piezoelectric crystal ( $\Delta D$ ) is linear in response to an applied voltage ( $\Delta V$ ):

$$\Delta D = c\Delta V \quad (4)$$

where  $c$  is the proportionality constant.

The force,  $F_c(D)$ , is determined by virtue of multiple beam interferometry. The piezoelectric crystal is expanded or contracted by a known amount  $\Delta D$  and subsequently the actual distance by which the surfaces move is determined interferometrically. Any difference between the expected distance of motion and the actual distance that the surfaces moved with respect to each other,  $\Delta D_0$ , when multiplied by the spring constant,  $k$ , gives, according to Hooke's law, the difference between the forces at the initial and the final separations,  $\Delta F_c$ :

$$\Delta F_c = k(\Delta D_0 - \Delta D) = k(c\Delta V - \Delta D) \quad (5)$$

There are several force measuring spring designs offered in the SFA, the most commonly used being single or double cantilever springs. A double cantilever spring design is advantageous over a single cantilever spring for measuring strong adhesive forces, since it prevents the surfaces from rolling over each other when the spring bends [13]. The spring constant can be varied over a

broad interval from  $1 \times 10^2$  to  $1 \times 10^5$  N/m, thus allowing to accurately measure both strong and weak surface interaction forces. With the spring constant of  $1 \times 10^2$  N/m and surfaces with a radius of  $2 \times 10^{-2}$  m the detection limit of the forces is  $10^{-7}$  N or, when normalised by the radius,  $5 \times 10^{-3}$  mN/m.

### 2.3. Other Surface Forces Measuring Techniques

Up to date, besides the SFA, several non-interferometric techniques have been developed for direct measurements of surface forces between solid surfaces. The most popular and widespread is atomic force microscopy, AFM [14]. This technique has been refined for surface forces measurements by introducing the colloidal probe technique [15,16]. The AFM colloidal probe method is, compared to the SFA, rapid and allows for considerable flexibility with respect to the used substrates, taken into account that there is no requirement for the surfaces to be neither transparent, nor atomically smooth over macroscopic areas. However, it suffers an inherent drawback as compared to the SFA: It is not possible to determine the absolute distance between the surfaces, which is a serious limitation, especially in studies of soft interfaces, such as, e.g., polymer adsorption layers. Another interesting surface forces technique that deserves attention is measurement and analysis of surface and interaction forces (MASIF), developed by Parker [17]. This technique allows measurement of interaction between two macroscopic surfaces and uses a bimorph as a force sensor. In analogy to the AFM, this technique allows for rapid measurements and expands flexibility with respect to substrate choice; however, it fails if the absolute distance resolution is required.

It is appropriate to mention here that the SFA and other techniques available for measuring surface forces have been reviewed before and the interested reader is referred to some excellent papers [9,18–20].

## 3. DEVELOPMENT OF THE SFA

Since the beginning, the SFA technique experienced major interest from the scientific community, due to the opportunities that it has opened in surface chemical science. It has been used extensively for studying various systems, and along with this it has been developed to answer increasingly complex scientific questions. Today several types of the SFA are available, all suited for specific surface chemistry purposes. The SFA Mark II [4,5] and Mark IV [21] (see Fig. 2) were particularly designed for measuring forces acting normal to the surfaces.

In fact, the SFA was initially developed for practically probing the DLVO theory, and DLVO forces were successfully measured in electrolyte solutions and colloidal systems [4,22]. However, the applications of the apparatus were not restricted to this. Detailed and accurate information was obtained on thickness and refractive index profiles of thin films [6], simple liquid molecular structuring



**Fig. 2.** Photographic image of the surface forces apparatus Mark IV and images of FECO fringes when the mica surfaces are close to contact (1), and when they are in adhesive contact (2). Figure adapted from <http://www.rsphysse.anu.edu.au/SFA/>, with permission. From the Australian National University, Tim Wetherell.

in confinements [23–26] and packing in complex liquids, such as micellar solutions [27], polyelectrolyte solutions, liquid crystalline phases [28–30] and polyelectrolyte–surfactant mixtures [31,32]. Vapour condensation in slits was studied [13], and interaction forces between surfaces coated with Langmuir–Blodgett (LB) monolayers [33], and polymers [34–36] were characterised.

Later, the SFA was developed to suit an even broader range of measurements, and in 1985 Israelachvili reported a set-up of the SFA with vibrating upper surface suited for viscosity measurements of liquids confined between the surfaces [37].

During the eighties and nineties the SFA has been further developed to study the dynamic properties of thin films trapped between surfaces in order to understand molecular origins of friction and wear. Retaining its capability of measuring normal forces, the SFA was equipped with a lateral sliding mechanism which allowed the surfaces to be sheared past each other with various frequencies and lateral amplitudes. Several versions of the tribological SFA have been designed [20, 38–43], the most broadly known, commercialised version being Israelachvilis Mark III SFA (SFA3<sup>TM</sup>, Surforce, USA) [44]. Numerous exciting measurements have been performed using the tribological SFA. For instance, lubrication forces between surfaces bearing polymer brushes have been measured [45], and friction in asymmetric systems consisting of one stationary solid mica surface and one polymeric surface sliding over the mica or

vice versa have been reported [46, 47], dramatic reduction in friction when surface interactions are mediated by polyelectrolytes with possible implications for biolubrication have been demonstrated [48], lubrication and wear properties of polyelectrolytes that are important as biomedical materials, hyaluronan and hylan [49], and normal and shear forces between mica and model membrane surfaces with adsorbed hyaluronan [50] have been measured, to mention but a very few.

For the reader interested in shear and friction studies using the SFA, an excellent overview of the advances in this area up to 1998 is given by Kumacheva [51]. The recent developments of the tribological SFA have allowed for the study of tribology at the molecular and atomic scale [20].

Most SFA's, irrespective of version and design, are operated manually. However in the extended SFA (eSFA) Heuberger et al. [52–54] succeeded in modifying SFA3<sup>TM</sup> such that a fully automated version of the SFA has been created. In this apparatus up to 150 interference fringes can be simultaneously tracked over a wide spectral range and the distance is calculated in real time. Multiple beam interferometry spectra are analysed using a fast spectral correlation (FSC) method, which provides unprecedented precision and simplified extraction of information. Precise temperature control improves instrumental stability [53]. The eSFA control software (Acquisoft) allows to program several different experiments in advance with predetermined timing, thus automated measurements with the eSFA are typically performed at night, with no human intervention. In addition to the benefit of being fully automated the eSFA is claimed to outperform the manual SFA's in the distance measurement precision (0.05–0.25 Å), measurable distance range (0–100 μm), sampling rate and overall accuracy [52]. A thorough description of the operational principals and technical details of the eSFA can be found in Ref. [52–54] and on the webpage [55].

Though the SFA is a superior technique for static and dynamic force measurements, measured forces present an average value over the collective action of molecules in the whole surface interaction area (typically ~100 μm<sup>2</sup>) and the important direct structural information on the molecular level of the molecules in confinement is lacking. In order to enable this there has been numerous attempts to combine the SFA with other techniques capable of providing such information. For instance, Cosgrove et al. have designed a parallel plate SFA suited for simultaneous force and neutron reflectivity measurements [56, 57] and simultaneously studied forces between adsorbed polymer layers as well as their structure by neutron reflectivity. Idziak et al. have united synchrotron X-ray scattering and the SFA [58, 59] in order to permit simultaneous measurement of forces and structures of liquid crystals under static and flow conditions. Recently, Israelachvili et al. [60, 61] have reported on the second-generation X-ray SFA (XSFA-II) that allows simultaneous X-ray scattering and direct force measurements. A schematic representation of the XSFA-II chamber is given in Fig. 3. The apparatus is designed such that it allows both for multiple beam interferometry of white light and for X-ray diffraction in the same optical

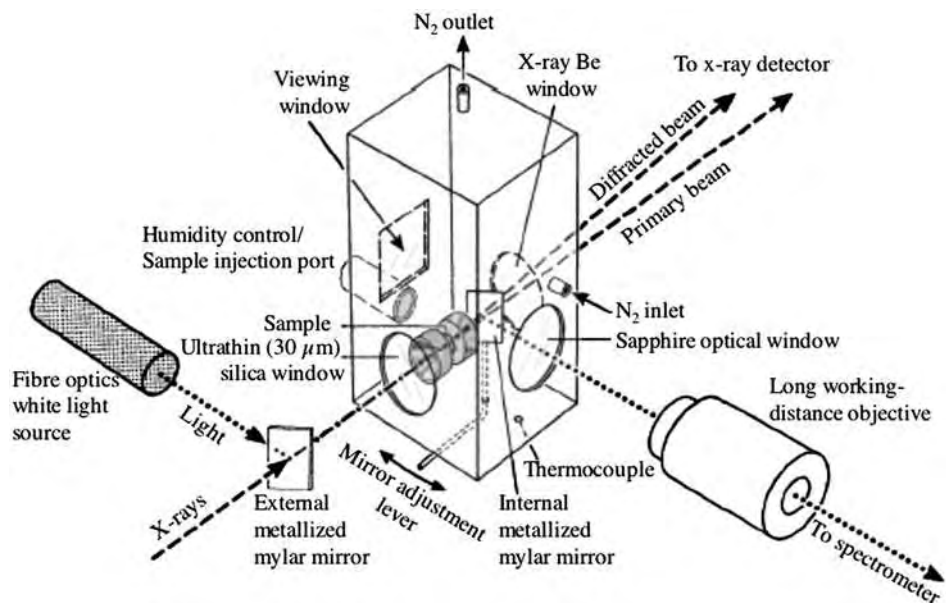


**Fig. 3.** Schematic illustration of the XSFA-II that enables all basic capabilities of the SFA simultaneously with X-ray diffraction measurements. Redrawn with permission from Ref. [61]. © 2002, American Institute of Physics.

path due to the presence of 30- $\mu\text{m}$ -thick mylar mirrors coated with a thin layer of Al, instead of the traditionally used silver mirrors that are not transparent for the X-rays.

Müller et al. [62] have measured optical properties of a thin dye layer adsorbed on mica surfaces in the SFA by analysing the resonance wavelength, and the size and width of the transmission peak at the resonance wavelength from a Fabry–Perot interferometer. An attempt of application of *in situ* laser spectroscopic technique in the SFA has been undertaken by Neuman et al. [63] who, by fluorescence recovery after photobleaching method, for the first time directly measured the molecular mobility in surfactant monolayers confined between two solid surfaces. Frantz and co-workers [64] have combined the tribological SFA with nonlinear optical spectroscopy. The authors employed a fibre-optic interferometer (FOI) as an alternative way to monitor the relative positions of the surfaces and thus it could be done without the silver mirrors otherwise used in the SFA (see Section 2.1). This provided conditions in which full illumination for the spectroscopy of the buried interface was achieved. In this way the SFA can be placed in the path of an Nd-YAG laser light for studies of the linear response or the second harmonic and sum-frequency generation from the material confined between the two surfaces.

The prevalence of mica as a substrate in the SFA has long been perceived as one of the limitations of the SFA. Partly, because of the technological need to

use other materials relevant to applications. There have been numerous attempts to broaden the scope of the substrates used in the SFA. For instance, two single-crystal sapphire plates have been successfully employed for the SFA measurements by Horn et al. [10]. Parker and Christenson have succeeded in measuring forces between a metal (silver) surface and mica [65]. Mica has been modified by LB deposition [66–68], LB cellulose films have been prepared for the SFA studies [69], self-assembled monolayers have been used [70], amorphous silica has been deposited on mica to yield smooth surfaces [71], surfaces activated by gas plasma treatment has been followed by silanation and plasma polymerisation [72, 73]. Recently, plasma enhanced chemical vapour deposition of silicon nitride layers have been suggested as a generic substrate for the SFA [74].

However, in an attempt to integrate the SFA and spectroscopic techniques, the use of silver for optical interferometry has been seen as a drawback due to the fact that it precluded sufficient excitation source intensity to illuminate the buried interface. In order to circumvent this problem Mukhopadhyay and co-workers in an experimental set-up where the SFA was combined with fluorescence correlation spectroscopy (FCS) used, instead of silver, multilayer dielectric coatings that allowed simultaneous interferometry and fluorescence measurements in different regions of the optical spectrum [75]. Using this set-up they succeeded in measuring diffusion in molecularly thin films with single-molecule sensitivity.

Another alternative to using multiple beam interferometry for surface separation determination was offered by Stewart [76] who coupled a capacitance sensor to the SFA Mark IV to measure the deflection of the double cantilever force measuring spring. The capacitance dilatometry method enables the study of opaque surfaces at the same time as the distance and force normalised to the radius resolution remain equal to that of the regular SFA, or even better [77]. However, using this method, the absolute separation cannot be determined.

Even though the SFA technique is close to 40 years old, we can see that the basic concept remains very useful and that novel developments occur regularly. Thus, one can expect that the coming years will offer many exiting developments of the SFA, and that this will increase our understanding of matter confined in narrow gaps. Perhaps, the most interesting perspective is the combination of force studies, including friction and molecular spectroscopy. The initial attempts in this area are indeed promising.

#### 4. MONOLAYERS OF SURFACTANTS AND LIPIDS

Since the origination of the SFA technique mica has been utilised as a preferred substrate because of the convenience of this substrate. However, the fundamental and practical interest of mica surfaces interactions in liquids and gases is quite limited. It was of great interest to develop a broad range of substrates of various

chemistries, while retaining the advantages offered by mica (transparency, atomic smoothness, chemical and physical robustness). With this need in mind several surface modification procedures have been developed.

## 4.1. Langmuir–Blodgett Films

One surface modification procedure that was used early on was the classical LB deposition, which allows one or several layers to be deposited in a controlled manner. This procedure has been utilised to prepare non-polar surfaces [33], phospholipid bilayers [78, 79] and cellulose surfaces [69], just to mention a few. In the next two subsections we will discuss some results obtained using surfaces modified by LB-technique, and compare with similar surfaces obtained by other means. The focus in the first section is on the long-range attraction between non-polar surfaces in water, whereas the second section deals with short-range repulsive and attractive interactions between monolayers exposing various polar groups or including biologically active molecules.

### 4.1.1. Hydrophobic monolayers

Long-range attractive interactions between hydrophobic surfaces in aqueous solutions have puzzled the scientific community since the first measurements by the SFA of an exponentially decaying long-range attraction about an order of magnitude greater than the expected van der Waals dispersion force, in the range of 0–8 nm. This force was suggested to be the “hydrophobic interaction” and first reported by Israelachvili and Pashley [80, 81] (Fig. 4).

Later an exceptionally long-range attractive force between mica surfaces made hydrophobic by LB deposition of a monolayer of dimethyldioctadecylammonium bromide (DODAB) was measured by Christenson and Claesson [82]. It was shown to be an exponentially decaying force with a decay-length of 12–13 nm in the distance range 20–80 nm. This force was noted to be up to 100 times stronger than the expected van der Waals attraction (Fig. 5).

Since then many researchers have undertaken an effort to elucidate the origin of the force acting between hydrophobic surfaces. With this purpose the dependence of the force on electrolyte and pH [72, 83–87], temperature [84], and dissolved gas has been investigated using a variety of hydrophobic monolayer preparation methods for force measurements such as adsorption from surfactant solution [80, 81], LB deposition [88, 89], silanation [72, 73], combination of LB deposition and silanation [68], and finally, self-assembly of thiols on gold [90, 91] have been tested. The work of Wood and Sharma [68, 92, 93] in particular showed that it is not only the hydrophobicity that is playing a role in defining the range of attractive interactions between hydrophobic surfaces but also the structure of the hydrophobic monolayers is of utmost importance, since with polymerised monolayer of octadecyltriethoxysilane (OTE), no attraction longer than 20 nm was seen.

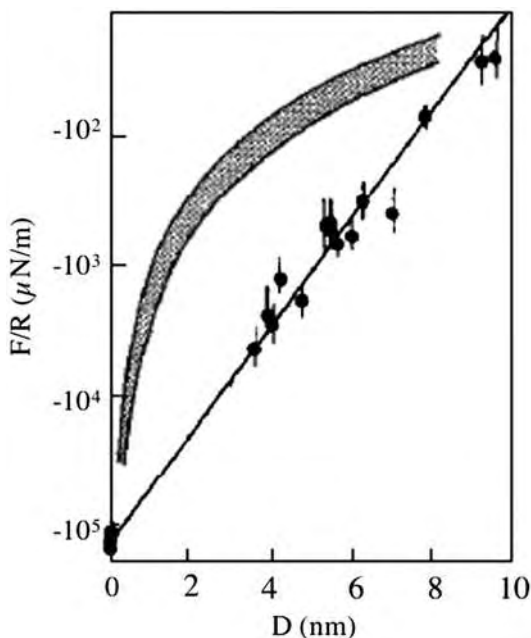


**Fig. 4.** Attractive force law deduced from forces measured between mica surfaces immersed in CTAB solutions. Each point is the difference between the measured force and the expected DLVO interaction. For comparison, from Lifshitz theory calculated van der Waals force-law for two mica surfaces and two hydrocarbon surfaces in water is shown as shaded area. Adapted from Ref. [81]. © 1984, with permission from Elsevier.

To date there is no clear agreement regarding the origin, distance dependence and the magnitude of the force acting between hydrophobic surfaces. However, thanks to a number of recent efforts it becomes clear that certain hydrophobic surfaces do not show the very long-range attraction though the short-range attraction is always present and is stronger than the expected van der Waals force. In certain cases the attractive force is clearly caused by microscopic bubbles [86]. However, in many cases there is no evidence of presence of bubbles, but nevertheless, the exponentially decaying attraction is measured in the range of 20–100 nm. The origin of this force is still unclear.

The interferometric SFA has served as an invaluable tool in studying the “hydrophobic attraction” among other things due to the fact that it is the only technique available today that enables direct observation of occurrence of cavitation. For instance, recently Lin et al. [89] employed a dynamic surface forces measurement method to study interactions between DODAB LB coated surfaces. High-speed camera images of FECO revealed that there are no bubbles on the surfaces prior to contact. However, short-lived cavities, typically lasting 3  $\mu$ s before disappearing, have been observed to form upon separation (Fig. 6).

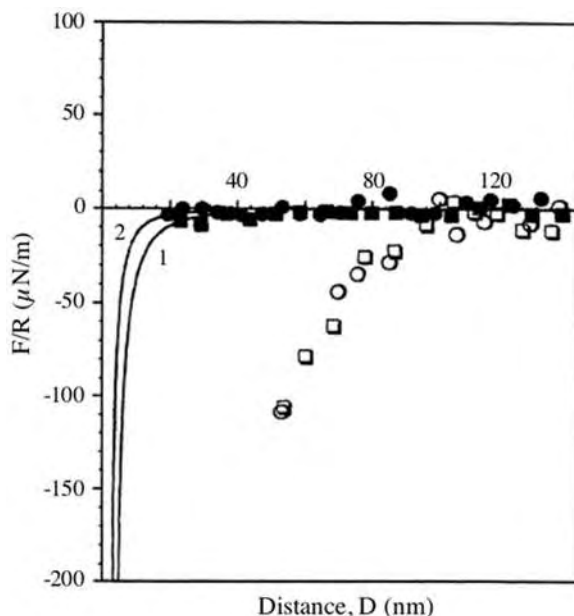


**Fig. 5.** Force measured in water between LB films of DODAB deposited on mica. Data plotted in open symbols. The different symbols denote separate series of measurements. Forces measured in water (pH = 5.6) between mica surfaces coated with polymerised monolayers of OTE (different filled symbols represent separate series of measurement). The solid lines show the van der Waals forces expected between mica surfaces (1) and hydrocarbon surfaces (2) across water. Redrawn with permission from Ref. [92]. © 1995, VPS. Publishers and Brill Academic Publishers.

The phenomenon of cavitation was also observed by Christenson and Claesson [82], around 20 years ago, who used DODAB LB films and the equilibrium method for forces measurements. The direct measurement of forces between hydrophobic surfaces in water were rather recently thoroughly reviewed by the above authors [94] and the reader who is interested in this intriguing topic is referred to this review and many references therein.

#### 4.1.2. *Hydrophilic monolayers*

Interactions between hydrophilic monolayers have deserved considerable attention due to their importance in understanding phenomena that govern stability and fusion of biological membranes. For instance, Claesson et al. [95] have characterised the forces acting between dihexadecylphosphate (DHP) monolayers supported by dioctadecyldimethylammonium chloride hydrophobised mica and compared the stability of DHP layers on hydrophobic mica surfaces. The authors demonstrated that less than 2% of all DHP molecules deposited onto hydrophobised mica surfaces are charged at pH 5–6. The

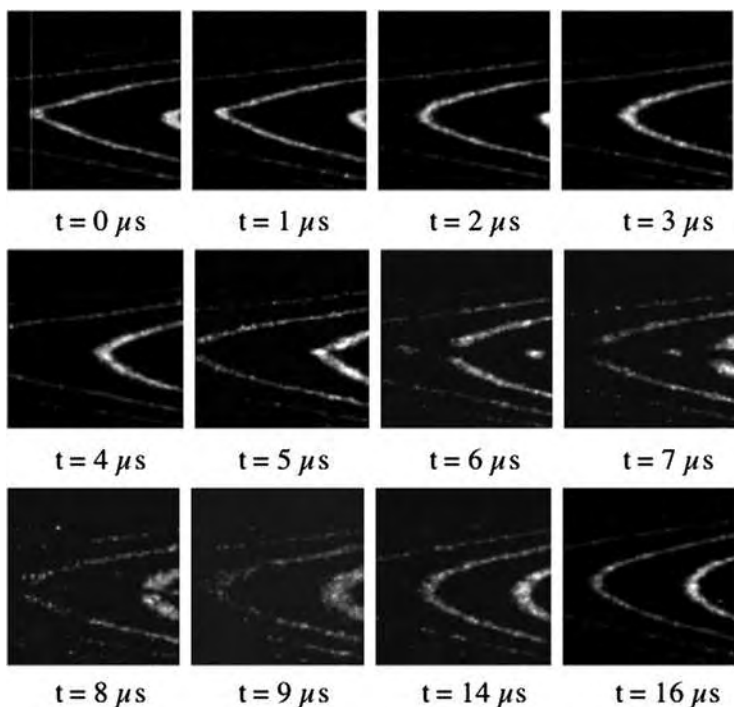


**Fig. 6.** Development and disappearance of a refractive index discontinuity in the FECO, revealing a transient vapour bridge during the jump apart from adhesive contact of the DODAB surfaces in water, shown frame by frame. Times are relative to  $t = 0$ , defined as the time when separation is started. Reprinted with permission from Ref. [89]. © 2005, American Chemical Society.

interlayer interactions at pH 5–6 are repulsive at large separations; the attractive van der Waals force was considerable at separation less than 2 nm. With increasing NaCl concentration the surface charge density was shown to increase and the adhesion between the layers was decreasing. At pH 9.5, when sodium was the dominant counterion, a repulsive force prevented the surfaces from coming into adhesive contact (Fig. 7). This force is of the same origin as the repulsive hydration forces observed between phospholipids bilayers [78] and between mica surfaces carrying adsorbed hydrated ions [96] and normally referred to as a hydration force, since it is thought to be due to work needed to dehydrate polar groups. However, it has been argued [97, 98] that the main repulsive force contribution is due to steric confinement preventing in-and-out motion of molecules, which causes an unfavourable reduction in entropy when two surfaces bearing adsorbed molecules are close together. Most likely, both dehydration and confinement effects contribute to the short-range repulsion.

It was not possible to induce fusion of the DHP layers under any conditions studied, which is in contrast to dihexadecyldimethylammonium ion bilayers

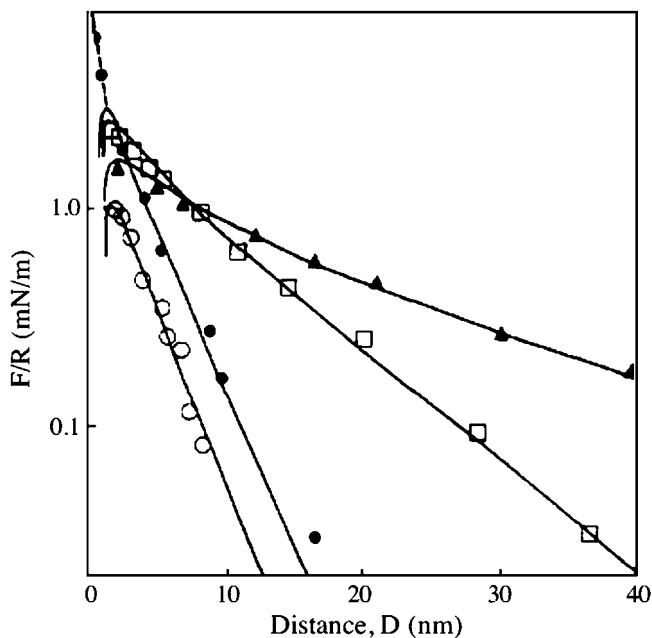


**Fig. 7.** Force normalised by radius as a function of surface separation between layers of DHP deposited onto hydrophobised mica surfaces measured in NaCl solutions of  $2 \times 10^{-4}$  M ( $\blacktriangle$ ),  $1 \times 10^{-3}$  M ( $\square$ ),  $1 \times 10^{-2}$  M ( $\circ$ ), at pH 5.2–5.7. At pH 9.5 no attraction was observed at any separation. The solid lines are force curves calculated from DLVO theory. The dashed line represents the part of the force curve that cannot be explained by the DLVO theory. This is a repulsive hydration force. Reprinted with permission from Ref. [95]. © 1989, American Chemical Society.

studied by Pashley et al. [99] who found that bromide ions decreased cohesion within bilayers allowing the outer layer to be squeezed out.

Force–distance curves between monolayers of monoglycerides, monoolein and monopalmitin, deposited on hydrophobically modified mica were determined using the surface force technique. It was demonstrated that the interactions between the monoglyceride films change with the state of the hydrocarbon chain, the headgroup being the same. In transition from the more condensed state to the more fluid state the attraction between the monolayers decreased whereas the repulsion increased [100].

Interactions between both phospholipid [101–106] and monoglyceride [107, 108] bilayers have been extensively studied by osmotic stress techniques. By comparing the forces acting between monoglyceride layers deposited on solid surfaces, measured by an SFA [100], and results obtained using osmotic stress technique [107], it can be seen that there is a qualitative agreement between the two techniques, the most significant difference being the lower repulsive force at short separations observed between deposited layers as compared to free bilayers.

Specificity and selectivity observed in biological systems is extraordinarily precise and has not been surpassed using synthetic molecules. These phenomena have been of considerable scientific interest for a long time due to their importance for living systems and for their potential in a multitude of technical applications, e.g., biosensors. It has been demonstrated by indirect methods that receptor–ligand surface properties and their microenvironment significantly influence their performance, however, direct measurements were required in order to obtain knowledge on precise molecular effects. The SFA has enabled such measurements that have been performed using streptavidin and biotin [109] between oriented protein monolayers formed by protein attachment to functionalised lipid monolayers (see Ref. [110] and references therein). These measurements successfully captured both long-range and short-range interactions between receptor–ligand coated surfaces (Fig. 8).

As seen in Fig. 8 the long-range interactions between streptavidin and avidin surfaces are dominated by electrical double-layer repulsion. At separations less than 55 Å the surfaces jump into strong adhesive contact under the influence of the specific short-range attractive force, independent of biotin concentration on the surfaces. At 33°C the lipids that carry biotin and avidin are in fluid state and the receptors and ligands diffuse along the surfaces. This explains the occurrence of a non-equilibrium steric force arising due to the fact that the receptor and ligand groups are not initially aligned and the biotin groups undergo a configurational search for the bound equilibrium orientation. This example demonstrates the detail of information that can be obtained using the SFA technique for studying molecular surface interactions.

Another exciting example is that of interactions measured between one oriented streptavidin monolayer and poly(ethylene glycol) (PEG) grafted on a lipid bilayer [111]. Using the SFA it was demonstrated that at low compressive force the interactions between biotin and PEG are repulsive but they turn attractive when the polymer is pressed into the protein layer by applying higher loads, and then the adhesion is sufficiently strong to rip the lipid-grafted PEG from the bilayer during separation.

## 5. POLYELECTROLYTES ON SURFACES

The SFA was initially utilised for experimentally probing the DLVO theory of colloidal stability, i.e., the attractive van der Waals force and the repulsive electrical double-layer force [4]. It proved to be a perfect tool for this purpose and even further, it revealed a host of phenomena that do not fall into the framework of the DLVO theory but are of utmost importance for explaining colloidal stability. For instance, short-range repulsive hydration forces between hydrophilic surfaces [96, 112] and surprisingly long-range attractive forces between non-polar surfaces [80, 81, 94]. The rich behaviour encountered when studying interactions between polymer-coated surfaces was also explored [113, 114], as well as the forces acting between polyelectrolyte-coated surfaces [115].

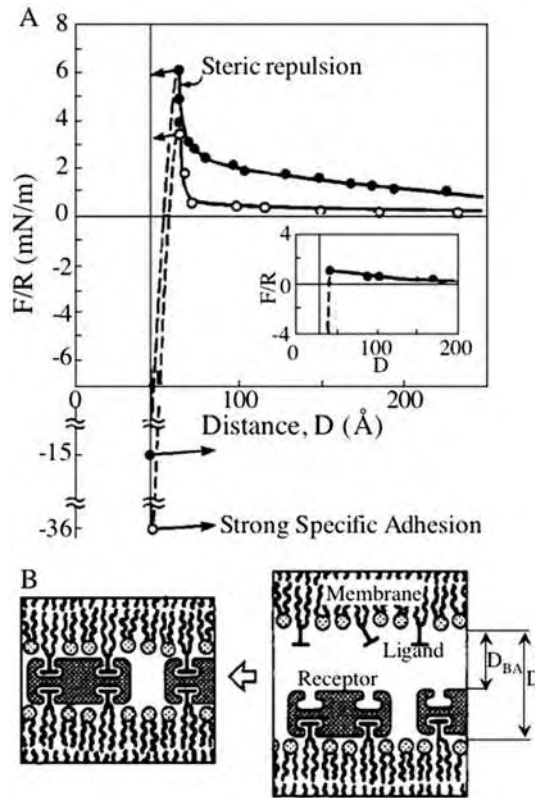


**Fig. 8.** (A) Force normalised by radius as a function of surface separation for a streptavidin surface interacting with 5% ( $\circ$ ) and 0.5% ( $\bullet$ ) biotin surface in 0.3 mM salt at pH 7.2 and 33°C, at approach rates higher than 10  $\text{\AA}/\text{s}$ . The equilibrium force profile measured at approach rates less than 10  $\text{\AA}/\text{s}$  is shown in the inset. It demonstrates the absence of time-dependent steric barrier. (B) Illustration of the biotin and streptavidin molecular arrangement during approach and in strong adhesive contact. Redrawn with permission from Ref. [109]. © 1994, American Chemical Society.

In the latter case the total interaction, which is what can be measured, is affected by the net charge of the surface and the adsorbed layer, ion-ion correlations, bridging interactions and steric confinement of the polymer chain [116]. We note that polyelectrolytes are often present as additives in colloidal dispersions and the character of the forces generated by the polyelectrolyte adsorption layers has a paramount influence on stability of these colloidal systems. With the aim to illustrate what can be learnt about polyelectrolyte adsorption layers using the SFA, we will look at the influence of the polyelectrolyte charge density on the forces acting between surfaces coated with polyelectrolytes. We will consider an example where the polyelectrolyte charge density is varied by a systematic

change in composition, and another example where pH is used to change the charge density of a weak polyelectrolyte.

### 5.1. Polyelectrolytes on Oppositely Charged Surfaces

Cationic polyelectrolytes with various charges have been synthesised by using two monomers: [3-(2-methylpropionamido)propyl]trimethylammonium chloride (MAPTAC) and acrylamide (AM). Interactions between surfaces coated with such polymers have been investigated for the charge densities of 100% (poly-MAPTAC), 30% (AM-MAPTAC-30), 10% (AM-MAPTAC-10) and 1% (AM-MAPTAC-1). These polyelectrolytes have been used for studying adhesion between two polyelectrolyte-coated surfaces, and between one such surface and a bare surface in air [117]. Interestingly, two adhesion mechanisms were found. Bridging attraction dominated for highly charged polyelectrolytes whereas entanglement effects were of importance for low charge density polyelectrolytes. The adhesions found were very high, several thousands of mN/m in some cases. This resulted in changes in the adsorbed layer upon separation, and material transfer from polyelectrolyte-coated surfaces to initially bare ones. The effect on surface interactions in aqueous solutions of the same set of polyelectrolytes has also been investigated. Here we will only recapitulate the results when these polyelectrolytes were adsorbed on negatively charged mica surfaces from low ionic strength (0.1 mM) salt solution, and the situation at the charge neutralisation point, i.e., where no or only an extremely weak electrical double-layer force can be detected (Fig. 9).

With the highly charged polyelectrolyte, poly-MAPTAC and 30% charged polyelectrolyte, AM-MAPTAC-30, the long-range forces are similar, i.e., hardly any long-range interactions are observed until a bridging attraction pulls the surfaces into a very close contact. This attraction is observed at separations below 15–10 nm [118]. The position of the attractive minimum is located at a separation of 1 nm for the 100% charged polyelectrolyte and the steric force encountered here is of a hard-wall type. Thus, at low ionic strength we note that a highly charged polyelectrolyte adopts a very flat conformation with an intimate contact of its positively charged segments with the negatively charged sites available on the surface. This gives evidence that there is a good match between the spacing between charges on the surface and on the polyelectrolyte. On the other hand, the position of the attractive minimum for the 30% charged polyelectrolyte is shifted to larger distances, 3–4 nm, and this indicates that AM-MAPTAC-30 adopts a less flat conformation as compared to poly MAPTAC. It seems likely that the uncharged segments form many short loops on the surface. The pull-off force required to separate the surfaces from the adhesive minimum position is  $100 \pm 50$  mN/m for the 100% charged polyelectrolyte and only 2–5 mN/m for the 30% charged polyelectrolyte.

A reduction in polyelectrolyte charge density to 10% results in further increase in adsorbed layer thickness. The steep steric repulsion is now

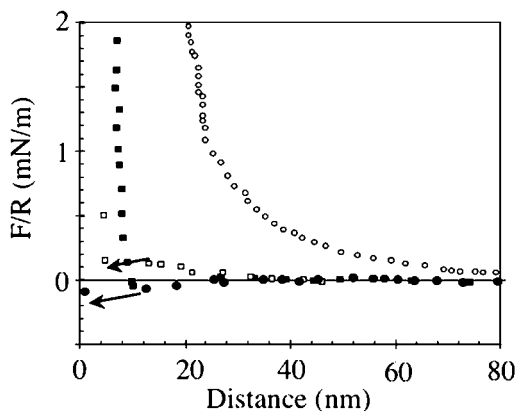


**Fig. 9.** Force normalised by radius as a function of surface separation between mica surfaces coated with polyelectrolytes of various charge densities. The forces were measured across an aqueous 0.1 mM KBr solution. The polyelectrolytes were poly-MAPTAC ( $\bullet$ ), AM-MAPTAC-30 ( $\square$ ), AM-MAPTAC-10 ( $\blacksquare$ ) and AM-MAPTAC-1 ( $\circ$ ). Adapted with permission from Ref. [118]. © 2002, American Chemical Society.

encountered at separations of about 10 nm and the pull-off force is further decreased to 0.5–1 mN/m [119]. For the 1% charged polyelectrolyte a long-range steric force dominates the surface interactions and there is no adhesion force present [120]. Clearly, the layer thickness (as sketched in Fig. 10) and compressibility decreases with increasing charge density of the polyelectrolyte, at the same time as the adhesion force is increasing, as also predicted by Monte Carlo simulations [121].

There is a range of parameters other than polyelectrolyte charge density that has an important influence on the generated surface interactions, for instance, counterion valency and ionic strength of solution [121–123], the order of addition of polyelectrolyte and salt [124], polyelectrolyte concentration [125], presence of surfactants [31, 119, 126], and finally, the chemical structure of the polyelectrolyte itself [127]. A rich literature is available on these topics (see Ref. [115] and references therein).

Another illustration of how the SFA can be used to understand polyelectrolyte adsorption layer properties will consider chitosan, a polyelectrolyte that is very appealing for practical use due to its natural origin and non-toxicity [128], acceptance in food [128, 129], biodegradability and biocompatibility, [130] antibacterial and fungistatic activity [129, 131].

The properties of chitosan in solution depend on molecular weight, degree of deacetylation, pH and ionic strength. Here we will only discuss a highly deacetylated chitosan, degree of deacetylation of 90–95% [132]. Such chitosan is highly positively charged at pH 3.8. The interaction forces measured in chitosan-free 0.01% acetic acid solution are dominated by a long-range

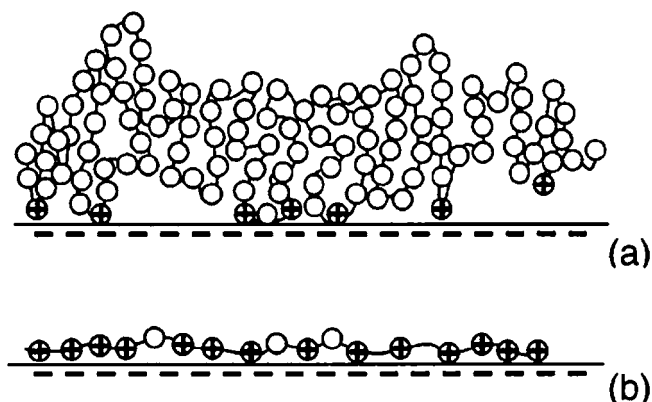


**Fig. 10.** Schematic representation of conformation of polyelectrolyte (a) with a low charge, and (b) high charge density with the charge spacing similar to that present on a surface. Reprinted with permission from Ref. [118]. © 2002, American Chemical Society.

electrical double-layer force and a van der Waals attraction at separations below 5 nm (Fig. 11A). Adsorption of chitosan onto the mica surfaces results in an increase in the measured double-layer force and development of a strong steric force at distances below 10 nm (Fig. 11B). Thus, from the increased electrical double-layer force it can be deduced that chitosan brings a surplus of positive charges to the mica surface.

The change of solution pH to 4.9 does not change the measured interactions considerably, it only causes the expected decrease in Debye length. A further increase in pH to 6.2 results in complete removal of the double-layer force indicating that, at this pH, chitosan-coated mica surfaces carry a net zero charge, thus the charges in the partly neutralised chitosan layer balances the negative mica surface charge. Even further, increase in solution pH further to 9.1 causes the electrical double-layer force to re-appear and the adsorption layer to swell. At this pH chitosan carries a low charge, not sufficient to compensate for the negative mica lattice charge and this affects the adsorbed layer conformation. Fig. 12 illustrates how the structure of the adsorbed chitosan layer varies with the pH.

It is worth noting that, if the chitosan–mica system that has experienced the history of step-wise increasing pH is returned to pH 3.8 and the forces are re-measured, then it is found that the forces are very similar to those originally observed at this pH value (Fig. 11). Hence, it is concluded that only very few chitosan molecules may have desorbed and the layer is practically intact. This is very important since it points to the possibility of using chitosan for surface coating and modification in a broad range of environmental conditions.

We have chosen to discuss only a few examples of how polyelectrolyte adsorption layers can be studied by employing the SFA. However, the interest

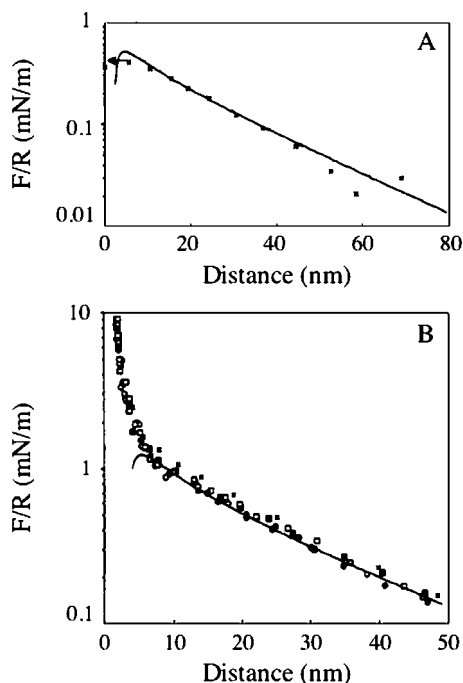


**Fig. 11.** (A) Force normalised by radius as a function of surface separation between mica surfaces in 0.01 wt.% acetic acid solution (pH 3.8). The arrow indicates a jump from a force barrier into molecular contact. (B) Forces between mica surfaces coated with chitosan across 0.01 wt.% acetic acid solution (pH 3.8). Two sets of measurements are shown. Filled and open symbols represent the forces measured on approach and separation, respectively, after 24 h of adsorption. The crosses represent the forces measured at pH 3.8 after the cycle of exposing chitosan adsorption layers for solutions of increasing alkalinity and measuring forces at pH 4.9, 6.2 and 9.1. The solid lines represent theoretically calculated DLVO forces. Redrawn with permission from Ref. [132]. © 1992, American Chemical Society.

in polyelectrolyte-mediated surface interactions has been huge over the past decades and there is a large body of valuable literature that can be found. The topic has been recently reviewed and we refer the interested reader for further discussion on this topic to the paper by Claesson et al. [115].

## 5.2. Polyelectrolyte Brushes

Polyelectrolyte brushes are macromolecular monolayers where the chains are attached by one end on the surface and, at the same time, the chains carry a considerable amount of charged groups. Such polyelectrolyte structures have received thorough theoretical treatment, and experimental interest has been vast due to the potential of brushes for stabilising colloidal particle dispersions or for

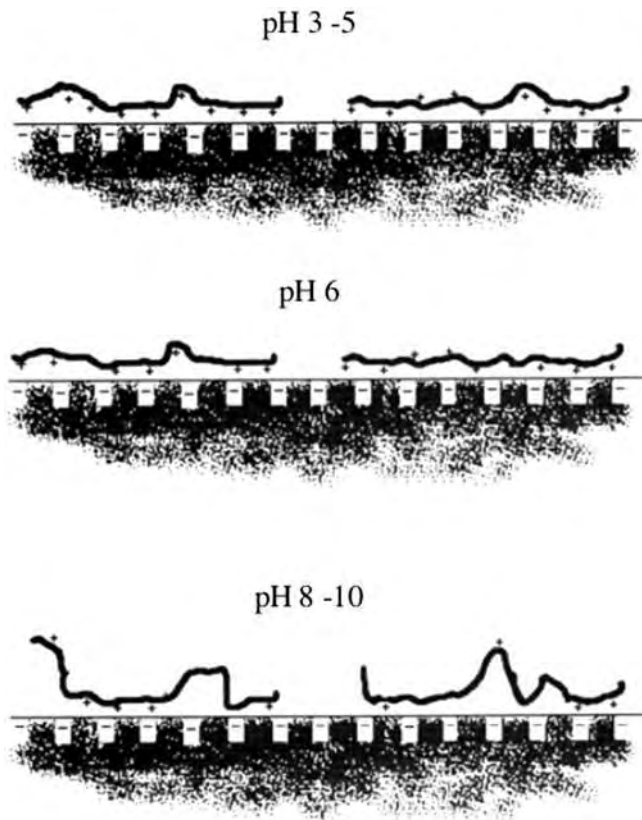


**Fig. 12.** Schematic representation of how the structure of the adsorbed chitosan layer varies with the solution pH. Reprinted with permission from Ref. [132]. © 1992, American Chemical Society.

friction control [48]. The structure of polyelectrolyte brushes anchored to surfaces [133, 134], and how the structure is influenced by polyelectrolyte charge density, chain length and graft density has been theoretically investigated in detail [135]. The effects of ionic strength [135–137], multivalent ions [138], the nature of the charged groups [136, 139, 140] (weak or permanent charges) and solvent quality [140, 141] have also been considered in a large number of theoretical publications. Works treating the effect of the elasticity of the underlying substrate to which the polyelectrolytes are grafted [142], or surface curvature effects [143] can also be found. Experimental results on dense and significantly charged polyelectrolyte brushes are scarce due to extreme difficulty in preparing such brushes. However, success in making highly charged and dense polyelectrolyte brushes by first preparing a dense neutral polymer (polystyrene) brush and then charging it by sulphonation reaction on an interface allowed measurements of the segment density profile for polyelectrolyte brushes [144]. One

important feature of polyelectrolyte brushes is that most of the counterions to the polyelectrolytes are incorporated within the brush layer, which is a consequence of the strong Coulombic attraction. When the polyelectrolyte brushes are grafted onto neutral walls the chains are highly extended, mainly due to the excess osmotic pressure due to the mobile counterions.

The forces acting between surfaces carrying grafted polyelectrolyte chains have been predicted [133, 145–148]. It is typically found that the outermost part of the force curve has a decay-length equal to that of a double-layer force. This force is due to overlap of the diffuse ionic clouds that extend beyond the surface of the brush layer. At smaller separations, but starting prior to direct brush layer contact, counterions are redistributing to become further incorporated within the brush layer, and the layer responds by contracting. At this stage the resulting force depends crucially on the ionic strength of the surrounding solution. Zhulina and co-workers distinguish between three cases, the osmotic regime, the salt dominance regime and the quasi-neutral regime [145]. When the concentration of counterions within the brush is larger than the concentration of ions in bulk solution we have the osmotic regime. In this case the force is due to the osmotic pressure of mobile counterions within the brush. In this regime the force (between flat plates) vary with separation,  $D$ , to the power of  $D^{-1}$ . When the salt concentration in bulk is larger than the concentration of counterions in the brush we encounter the salt dominance regime. The osmotic pressure of the added salt contributes significantly to the forces that now depend on distance as  $D^{-2}$ . At very high salt concentrations electrostatic forces become insignificant and the force is governed by the osmotic pressure of the polyelectrolyte segments. Under theta conditions this results in a force varying with separation to  $D^{-3}$ . It is important to note that when the brush layer will be compressed the concentration of counterions within the layer will increase. Hence, one may enter into different regimes as the compression progresses, and the resulting force curve may be rather complex. We further note that the effect of salt is more complex when the polyelectrolyte brushes are built by weak polyelectrolytes. In this case the salt concentration also affects the degree of dissociation within the brush layer, as discussed by Zhulina [145]. One consequence is that the osmotic regime is significantly smaller compared to the situation with polyelectrolyte brushes having permanent charges. The distance dependence of the force in this regime is also altered and, due to reduction in the charge density of the brush with decreasing separation, now goes as  $D^{-0.5}$ [145].

Polyelectrolytes can form brushes on solid–liquid interfaces [149, 150] through adsorption [151] or by forming covalent bonds via chemical grafting [152, 153]. The main challenges for experimentalists studying polyelectrolyte brushes lay in understanding molecular arrangements and forces of interactions in such brushes under various conditions. Important questions to answer are the extension of a brush layer, forces between brush layers and segment density profiles as a function of ionic strength, brush density, fraction of free counterions per chain and chain segment number. The SFA has been extensively

used in studies attempting to answer these questions. There are several reports on direct measurements of the forces acting between brush polyelectrolyte monolayers [149, 150, 154–157]. For instance, Kurihara et al. [149] investigated interactions between anionic chain-end-anchored monolayers of poly (metacrylic acid) (PMA), a weak polyelectrolyte, as a function of pH and background electrolyte concentration. It was demonstrated that at low pH in water, where PMA is charge neutral and adopts a hypercoiled conformation, surface interactions could be described by the diffuse electrical double-layer model applicable for normal solid surfaces. At higher pH and higher inert salt concentrations, an increase in both the range and magnitude of the surface interactions was observed. These variations were attributed to the ionisation of PMA that forces the polyelectrolyte to adopt a more extended conformation. Interactions between such polyelectrolyte-grafted surfaces are complex and affected by structural changes of the polyelectrolyte, salt-promoted ionisation and condensation of counterions. For instance, at elevated pH, when the chains of PMA are strongly ionised, an addition of salt results in both further increase in chain ionization and screening of Coulombic interactions. These two phenomena causes opposite trends in surface interactions. The former effect was found to dominate and thus increased repulsive forces at low pH and strong compressions were measured. At high pH and weak compression, the latter effect was dominant and the repulsive force decreased with increasing salt concentrations.

Abraham et al. [157] studied interactions between hydrophobically anchored strongly charged polyelectrolyte brushes as a function of salt concentration. The authors used a hydrophobic–hydrophilic diblock poly(*tert*-butyl methylacrylate-*b*-poly(glycidyl methacrylate sodium sulphonate) (PtBMA-*b*-PGMAS) and showed that the measured interactions are a combination of electrostatic and steric forces. As expected, a decrease in the range of the measured force with increase in added salt concentration is due to electrostatic screening. However, the added salt effect is less pronounced than the one observed for regular charged surfaces. At low salt conditions, the long-range interactions can be quantitatively described by classical electrical double-layer theory, whereas long-range forces with added salt deviate from those expected using classical considerations. Moreover, a long-range electrical double-layer force due to overlapping counterion clouds may not always be observed when two polyelectrolyte brushes are brought together.

In another study, Balastre et al. [158] investigated hydrophobically grafted NaPSS brushes on mica surfaces at various salt concentrations and showed that at none of the salt concentration any exponentially decaying force could be detected and thus long-range electrostatic interactions as described by classical Poisson–Boltzmann theory were excluded. There were two regimes of polyelectrolyte brush behaviour observed. In the “salted” brush regime the interaction range of the surfaces shifted to progressively larger distances with decreasing salt concentration due to decreasing screening and increasing electrostatic excluded-volume repulsion. In the “osmotic brush” regime the measured forces

between the brush layers showed almost no dependence on salt concentration. The authors succeeded in fitting the data for the polymers of different molecular size into general force curve profiles for the “osmotic” and “salted” brush, based on equations from the scaling theory and corroborated the validity of this theory in both regimes (Figs. 13 and 14).

In conclusion, the SFA technique has been able to provide valuable experimental information on the forces acting between polyelectrolyte brushes. The general behaviour is now rather well established and the experimental data can in most cases be rationalised by considering predictions based on scaling arguments.

Finally, we note that in a very recent work Heuberger et al. investigated protein-resistant copolymer monolayers of PEG grafted to poly(L-lysine) (PLL) (PLL-g-PEG) in terms of the role of water in surface grafted PEG layers [159], interaction forces and morphology [160], compressibility, temperature dependence and molecular architecture [161]. PEG is often used in biomedical applications in order to create protein-resistant surfaces but the mechanisms responsible for the protein-repelling properties of PEG are not fully understood.

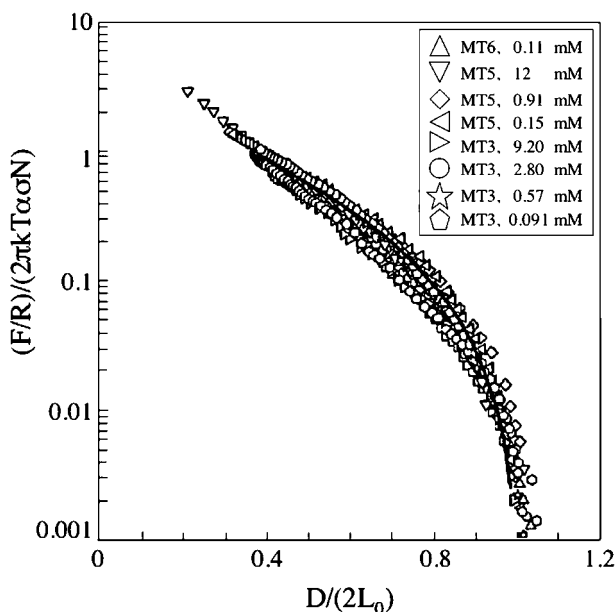


**Fig. 13.** A universal curve of force profiles in the osmotic brush regime, incorporating data for three different molecular weights. One force curve is shown for each salt concentration. The separations are normalised by twice the equilibrium brush height at the corresponding salt concentration, and the measured force  $F/R$  is normalised by the prefactor  $(2\pi kT\alpha\alpha N)$ , which is derived from the scaling theory. The solid line is a fit based on equations from this theory (see Ref. [158]). Redrawn with permission from Ref [158]. © 2002, American Chemical Society.

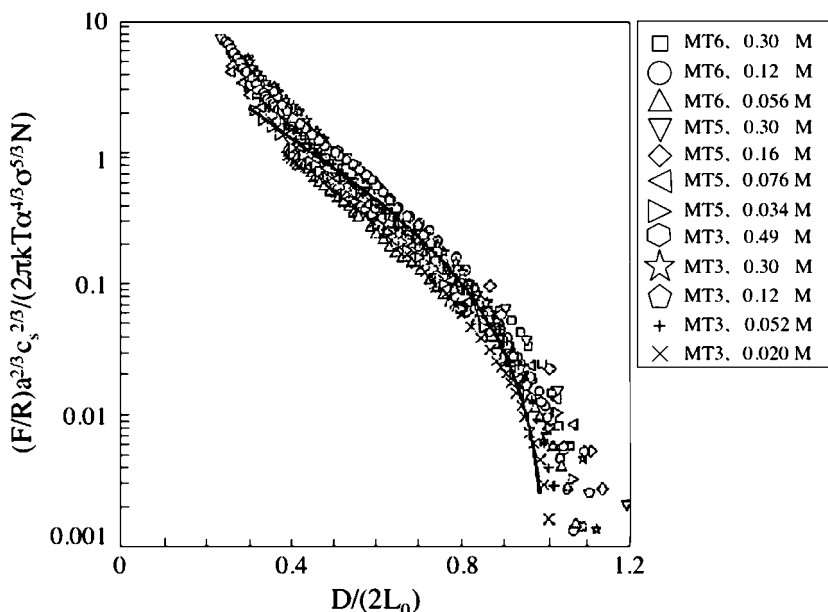


**Fig. 14.** A universal force curve in the salted brush regime, incorporating data for three molecular weights. One curve is shown for each salt concentration. The separation is normalised by twice of the equilibrium brush height at the corresponding salt concentration, and the measured force,  $F/R$ , is multiplied by the prefactor  $a^{2/3}c_s^{2/3}/(2\pi kT\sigma^{5/3}\alpha^{4/3}N)$ , which is derived from the scaling theory. The solid line is a fit based on equations from this theory (see Ref. [158]). Redrawn with permission from Ref. [158]. © 2002, American Chemical Society.

Heuberger and co-workers obtained, by using eSFA, a very intriguing result. Their data indicate that there exists a fine structure embedded within the established steric repulsion of PEG in the brush regime (Fig. 15) [159] arising due to restriction of the conformational space of the PEG/water complex, which causes quantisation of the steric force observed in the SFA. The presence of this water-induced restricted conformation space was suggested to have implications in protein adsorption since in order to adsorb a protein induces a local deformation, which necessitates a restriction of the PEG and protein conformational space, which is energetically and kinetically unfavourable [159, 160].

## 6. SUMMARY

In a review like this it is impossible to refer to even a small fraction of all the interesting work that has been done with the SFA. Anyway, I hope to have illustrated some selected areas in which the SFA has played a major role for increasing our understanding. It is fascinating to see how the development of the “basic SFA” is continued in many laboratories. One clear focus of modern

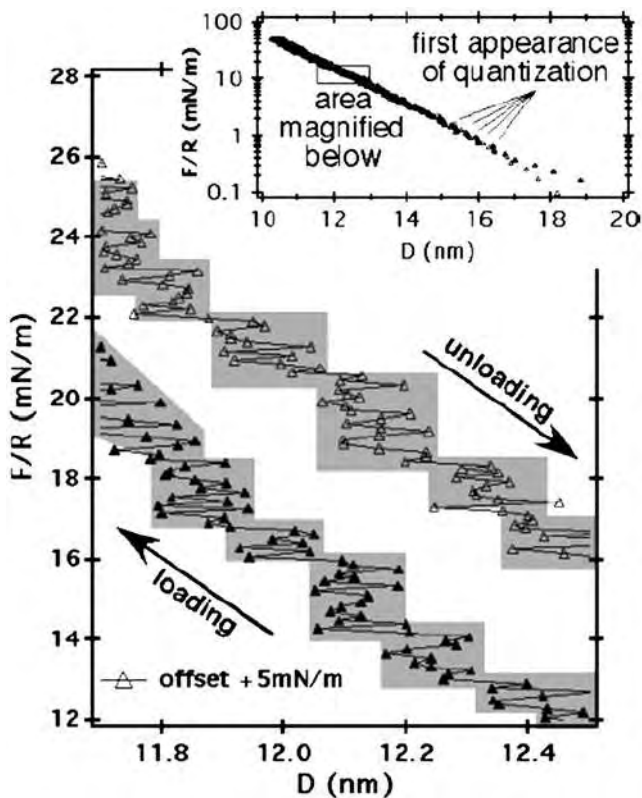


**Fig. 15.** Force normalised by radius as a function of surface separation measured on approach ( $\blacktriangle$ ) and separation ( $\triangle$ ). The separation curve is graphically offset by 5 mN/m for clarity. The picture shows magnified region of the surface forces curve. The inset shows the entire surface forces curve. Reprinted with permission from Ref. [159]. © 2004 American Chemical Society.

developments is towards studies of dynamic phenomena, another is to combine the SFA with spectroscopy in order to gain further molecular understanding of matter in confinement. The coming years will be exciting and promise new developments that will allow us to develop our understanding of colloids, biophysical systems and complex liquids at and between interfaces.

## REFERENCES

- [1] D. Tabor and R. H. S. Winterton, Proc. R. Soc. London, A312 (1969) 435.
- [2] J. N. Israelachvili and D. Tabor, Proc. R. Soc. London, A331 (1972) 19.
- [3] J. Klein, J. Chem. Soc., Faraday Trans. 1, 79 (1983) 99.

- [4] J. N. Israelachvili and G. E. Adams, *J. Chem. Soc., Faraday Trans. 1*, 74 (1978) 975.
- [5] J. N. Israelachvili and G. E. Adams, *Nature*, 262 (1976) 774.
- [6] J. N. Israelachvili, *J. Colloid Interface Sci.*, 44 (2), (1973) 259.
- [7] P. N. Luckham, *Powder Technology*, 58 (1989) 75.
- [8] R. Tadmor, C. Nianhuan and J. N. Israelachvili, *J. Colloid Interface Sci.*, 264 (2), (2003) 548.
- [9] P. M. Claesson, T. Ederth, V. Bergeron and M. V. Rutland, *Adv. Colloid Interface Sci.*, 67 (1996) 119.
- [10] R. G. Horn, D. R. Clarke and M. T. Clarkson, *J. Mater. Res.*, 3 (1988) 413.
- [11] B. V. Derjaguin, *Kolloid Zeits*, 69 (1934) 155.
- [12] J. A. de Feijter, J. Benjamins and F. A. Veer, *Biopolymers*, 17 (1978) 1759.
- [13] H. K. Christenson, *J. Colloid Interface Sci.*, 121 (1988) 170.
- [14] G. Binnig, C. F. Quate and C. Gerber, *Phys. Rev. Lett.*, 56 (1986) 930.
- [15] W. A. Ducker, T. J. Senden and R. M. Pashley, *Nature*, 353 (1991) 239.
- [16] W. A. Ducker, T. J. Senden and R. M. Pashley, *Langmuir*, 8 (1992) 1831.
- [17] J. L. Parker, *Prog. Surf. Sci.*, 47 (1994) 205.
- [18] P. M. Claesson, *Surface Forces Apparatus: Studies of Polymers, Polyelectrolytes and Polyelectrolyte-Surfactant Mixtures at Interfaces* (P. Dubin and R. Farinato, eds.), *Colloid-Polymer Interactions: From Fundamentals to Practice*, Wiley, New York, 1999, p. 287.
- [19] J. N. Israelachvili, *Acc. Chem. Res.*, 20 (1987) 415.
- [20] S. Granick, *Science*, 253 (1991) 1347.
- [21] J. L. Parker, H. K. Christenson and B. W. Ninham, *Rev. Sci. Instrum.*, 60 (10), (1989) 3135.
- [22] J. N. Israelachvili, *Intermolecular and Surface Forces*, Second Edition, Academic Press, London, 1992.
- [23] H. K. Christenson and C. E. Blom, *J. Chem. Phys.*, 86 (1987) 419.
- [24] H. K. Christenson, *J. Chem. Phys.*, 78 (1983) 6906.
- [25] H. K. Christenson, *J. Dispersion Sci. Technol.*, 9 (1988) 171.
- [26] H. K. Christenson, D. W. R. Gruen, R. G. Horn and J. N. Israelachvili, *J. Chem. Phys.*, 87 (1987) 1834.
- [27] P. Kékicheff and P. Richetti, *Prog. Colloid Polym. Sci.*, 88 (1992) 8.
- [28] R. G. Horn, J. N. Israelachvili and E. Perez, *J. Physique*, 42 (1981) 39.
- [29] P. Petrov, S. J. Miklavic, U. Olsson and H. Wennerström, *Langmuir*, 11 (1995) 3928.
- [30] P. Petrov, U. Olsson, H. K. Christenson, S. J. Miklavic and H. Wennerström, *Langmuir*, 10 (1994) 988.
- [31] P. M. Claesson, A. Dedinaite, E. Blomberg and V. G. Sergeev, *Ber. Bunsenges. Phys. Chem.*, 100 (1996) 1008–1013.
- [32] A. Dedinaite, P. M. Claesson and M. Bergström, *Langmuir*, 16 (12), (2000) 5257.
- [33] P. M. Claesson, C. E. Blom, P. C. Herder and B. W. Ninham, *J. Colloid Interface Sci.*, 114 (1986) 234–242.
- [34] J. Klein and P. Luckham, *Nature*, 300 (1982) 429.
- [35] J. Klein and P. F. Luckham, *Macromolecules*, 17 (1984) 1041.
- [36] P. Luckham and J. Klein, *J. Chem. Soc., Faraday Trans.*, 86 (1990) 1363.

- [37] J. N. Israelachvili, *J. Colloid Interface Sci.*, 110 (1985) 263.
- [38] A. M. Homola, J. N. Israelachvili, M. L. Gee and P. M. McGuiggan, *J. Tribol.*, 111 (1989) 675.
- [39] J. N. Israelachvili, P. M. McGuiggan and A. M. Homola, *Science*, 240 (1988) 189.
- [40] G. Luengo, F.-J. Schmitt, R. Hill and J. N. Israelachvili, *Macromolecules*, 30 (1997) 2482.
- [41] J. Peachey, J. Van Alsten and S. Granick, *Rev. Sci. Instrum.*, 62 (1991) 463.
- [42] J. Van Alsten and S. Granick, *Phys. Rev. Lett.*, 61 (22), (1988) 2570–2573.
- [43] J. Klein, D. Perahia, S. Warburg and L. J. Fetters, *Nature*, 352 (1991) 143.
- [44] J. N. Israelachvili and P. M. McGuiggan, *J. Mater. Res.*, 5 (1990) 2223.
- [45] J. Klein, Y. Kamiyama, H. Yoshizawa, J. N. Israelachvili, G. H. Fredrickson, P. Pincus and L. J. Fetters, *Macromolecules*, 26 (1993) 5552–5560.
- [46] M. Heuberger, G. Luengo and J. N. Israelachvili, *J. Phys. Chem.*, 103 (1999) 10127.
- [47] G. Luengo, M. Heuberger and J. Israelachvili, *J. Phys. Chem.*, 104 (2000) 7944.
- [48] U. Raviv et al., *Nature*, 425 (2003) 163.
- [49] B. Marcel, C. Nianhuan and J. Israelachvili, *J. Biomed. Mater. Res. A*, 71A (1), (2004) 6.
- [50] R. Tadmor, C. Nianhuan and J. Israelachvili, *Macromolecules*, 36 (25), (2003) 9519.
- [51] E. Kumacheva, *Prog. Surf. Sci.*, 58 (2), (1998) 75.
- [52] M. Heuberger, *Rev. Sci. Instrum.*, 72 (3), (2001) 1700.
- [53] M. Heuberger, J. Vanicek and M. Zäch, *Rev. Sci. Instrum.*, 72 (9), (2001) 3556.
- [54] M. Zäch, J. Vanicek and M. Heuberger, *Rev. Sci. Instrum.*, 74 (1), (2003) 260.
- [55] Heuberger, M., The extended Surface Forces Apparatus (eSFA). [http://www.surface.mat.ethz.ch/research/surface\\_forces/extended\\_SFA2004](http://www.surface.mat.ethz.ch/research/surface_forces/extended_SFA2004)
- [56] T. Cosgrove, P. F. Luckham, R. M. Richardson, J. R. P. Webster and A. Zorbakhsh, *Colloids and Surfaces A*, 86 (1994) 103–110.
- [57] T. Cosgrove, A. Zorbakhsh, P. F. Luckham, M. L. Hair, and J. R. P. W. Webster, *Faraday Discussions Volume Date 1994, 98(Polymers at Surfaces and Interfaces)*, (1995) 189–201.
- [58] S. H. J. Idziak, C. R. Safinya, R. S. Hill, K. E. Kraiser, M. Ruths, H. E. Warriner, S. Steinberg, K. S. Liang and J. N. Israelachvili, *Science*, 264 (1994) 1915–1918.
- [59] S. H. J. Idziak and Y. Li, *Curr. Opin. Colloid Interface Sci.*, 3 (1998) 293.
- [60] Y. Golan, A. Martin-Herranz, Y. Li, C. R. Safinia and J. Israelachvili, *Phys. Rev. Letters*, 86 (2001) 1263–1266.
- [61] Y. Golan, M. Seitz, C. Luo, A. Martin-Herranz, M. Yasa, Y. Li and C. R. Safinya, *Rev. Sci. Instrum.*, 73 (2002) 2486–2488.
- [62] C. Müller, P. Mächtle and C. A. Helm, *J. Phys. Chem.*, 98 (1994) 11119.
- [63] R. D. Neuman, S. Park and P. Shahn, *J. Colloid Interface Sci.*, 172 (1995) 257.
- [64] P. Frantz, F. Wolf, X.-D. Xiao, Y. Chen, S. Bosch and M. Salmeron, *Rev. Sci. Instrum.*, 68 (1997) 2499–2504.
- [65] J. L. Parker and H. K. Christenson, *J. Chem. Phys.*, 88 (12), (1988) 8013.
- [66] Y. L. Chen, C. A. Helm and J. N. Israelachvili, *Langmuir*, 7 (1991) 2694.
- [67] C. E. Herder, B. W. Ninham and H. K. Christenson, *J. Chem. Phys.*, 90 (1989) 5801.

- [68] J. Wood and R. Sharma, *Langmuir*, 10 (1994) 2307.
- [69] M. Holmberg, J. Berg, S. Stemme, L. Ödberg, J. Rasmusson and P. Claesson, *J. Colloid Interface Sci.*, 186 (1997) 369–381.
- [70] J. Penansky, H. M. Schneider and S. Granick, *Langmuir*, 11 (1995) 953.
- [71] G. Vigil, Z. Xu, S. Steinberg and J. Israelachvili, *J. Colloid Interface Sci.*, 165 (1994) 367–385.
- [72] J. L. Parker, D. L. Cho and P. M. Claesson, *J. Phys. Chem.*, 93 (1989) 6121.
- [73] J. L. Parker, P. M. Claesson, D. L. Cho, A. Ahlberg, J. Tidblad and E. Blomberg, *J. Colloid Interface Sci.*, 134 (1990) 449.
- [74] N. A. Alcantar, T. L. Kuhl and J. Israelachvili, *Langmuir*, 16 (2000) 6955.
- [75] A. Mukhopadhyay, J. Zhao, S. C. Bae and S. Granick, *Rev. Sci. Instrum.*, 74 (2003) 3067–3072.
- [76] A. M. Stewart, *Meas. Sci. Technol.*, 11 (2000) 298.
- [77] V. V. Yaminski and A. M. Stewart, *Langmuir*, 19 (2003) 4037.
- [78] J. Marra and J. Israelachvili, *Biochemistry*, 24 (17), (1985) 4608.
- [79] J. Marra, *J. Colloid Interface Sci.*, 109 (1), (1986) 11.
- [80] J. N. Israelachvili and R. M. Pashley, *Nature*, 300 (5890), (1982) 341.
- [81] J. N. Israelachvili and R. M. Pashley, *J. Colloid Interface Sci.*, 98 (2), (1984) 500.
- [82] H. K. Christenson and P. M. Claesson, *Science*, 239 (1988) 390.
- [83] Y. H. Tsao, S. X. Yang, D. F. Evans and H. Wennerström, *Langmuir*, 7 (1991) 3154–3159.
- [84] H. K. Christenson, J. L. Parker and V. V. Yaminski, *Langmuir*, 8 (1992) 2080.
- [85] Y. H. Tsao, D. F. Evans and H. Wennerström, *Langmuir*, 8 (1993) 779.
- [86] J. L. Parker, P. M. Claesson and P. Attard, *J. Phys. Chem.*, 98 (1994) 8468.
- [87] H. K. Christenson, P. M. Claesson and J. L. Parker, *J. Phys. Chem.*, 96 (1992) 6725.
- [88] P. M. Claesson and H. K. Christenson, *J. Phys. Chem.*, 92 (1988) 1650.
- [89] Q. Lin, E. E. Meyer, M. Tadmor, J. N. Israelachvili and T. L. Kuhl, *Langmuir*, 21 (2005) 251–255.
- [90] A. Ulman, *An Introduction to Ultrathin Organic Films*, Academic Press, San Diego, 1991.
- [91] T. Ederth, P. Claesson and B. Liedberg, *Langmuir*, 14 (1998) 4782.
- [92] J. Wood and R. Sharma, *J. Adhesion Sci. Technol.*, 8 (1995) 1075.
- [93] J. Wood and R. Sharma, *Langmuir*, 11 (1995) 4797.
- [94] H. K. Christenson and P. M. Claesson, *Adv. Colloid Interface Sci.*, 91 (2001) 391.
- [95] P. Claesson, A. M. Carmona-Ribeiro and K. Kurihara, *J. Phys. Chem.*, 93 (1989) 917.
- [96] R. M. Pashley, *J. Colloid Interface Sci.*, 83 (1981) 531.
- [97] J. N. Israelachvili and H. Wennerström, *Langmuir*, 6 (1990) 873.
- [98] J. Israelachvili and H. Wennerström, *Nature*, 379 (1996) 219.
- [99] R. M. Pashley, P. M. McGuiggan, B. W. Ninham, J. Brady and D. F. Evans, *J. Phys. Chem.*, 90 (1986) 1637.
- [100] I. Pezron, E. Pezron, P. M. Claesson and B. Bergenståhl, *J. Colloid Interface Sci.*, 144 (1991) 449–457.
- [101] L. J. Lis, V. A. Parsegian and R. P. Rand, *Biochemistry*, 20 (1981) 1761.
- [102] T. J. McIntosh and S. A. Simon, *Biochemistry*, 25 (1986) 4058.

- [103] T. J. McIntosh, A. D. Magid and S. A. Simon, *Biochemistry*, 26 (1987) 7325.
- [104] R. P. Rand, N. Fuller, V. A. Parsegian and D. C. Rau, *Biochemistry*, 28 (1988) 7711.
- [105] S. A. Simon, T. J. McIntosh and A. D. Magid, *J. Colloid Interface Sci.*, 126 (1), (1988) 74.
- [106] T. J. McIntosh, A. D. Magid and S. A. Simon, *Biochemistry*, 28 (1989) 7904.
- [107] I. Pezron, E. Pezron, B. Begenstahl and P. M. Claesson, *J. Phys. Chem.*, 94 (1990) 8255–8261.
- [108] T. J. McIntosh, A. D. Magid and S. A. Simon, *Biophys. J.*, 55 (1989) 897.
- [109] D. E. Leckband, F.-J. Schmitt, J. Israelachvili and W. Knoll, *Biochemistry*, 33 (1994) 4611–4624.
- [110] D. E. Leckband and J. Israelachvili, *Enzyme Microb. Technol.*, 15 (1993) 450.
- [111] S. R. Sheth and D. Leckband, *Proc. Natl. Acad. Sci.*, 94 (1997) 8399.
- [112] R. M. Pashley, *J. Colloid Interface Sci.*, 80 (1981) 153.
- [113] J. Klein, *Nature*, 288 (20), (1980) 248.
- [114] P. F. Luckham, *Curr. Opin. Colloid Interface Sci.*, 1 (1), (1996) 39.
- [115] P. M. Claesson, E. Poptoshev, E. Blomberg and A. Dedinaite, *Advances in Colloid and Interface Science*, 114–115 (2005) 173–187.
- [116] A. Broukhno, B. Jönsson, T. Åkesson and P. N. Vorontsov-Velyaminov, *J. Chem. Phys.*, 113 (2000) 5493–5501.
- [117] P. M. Claesson, A. Dedinaite and O. J. Rojas, *Adv. Colloid Interface Sci.*, 104 (2003) 53.
- [118] O. J. Rojas, M. Ernstsson, R. D. Neuman and P. M. Claesson, *Langmuir*, 18 (2002) 1604.
- [119] U. R. M. Kjellin, P. M. Claesson and R. Audebert, *J. Colloid Interface Sci.*, 190 (1997) 476.
- [120] O. J. Rojas, P. M. Claesson, D. Muller and R. D. Neuman, *J. Colloid Interface Sci.*, 205 (1998) 77–88.
- [121] M. A. G. Dahlgren, Å. Waltermo, E. Blomberg, P. M. Claesson, L. Sjöström, T. Åkesson and B. Jönsson, *J. Phys. Chem.*, 97 (1993) 11769–11775.
- [122] M. A. G. Dahlgren, *Langmuir*, 10 (1994) 1580.
- [123] A. Dedinaite and M. Ernstsson, *J. Phys. Chem. B.*, 107 (2003) 8181.
- [124] M. A. G. Dahlgren, H. C. M. Hollenberg and P. M. Claesson, *Langmuir*, 11 (11), (1995) 4480.
- [125] M. A. G. Dahlgren, P. M. Claesson and R. Audebert, *J. Colloid Interface Sci.*, 166 (2), (1994) 343.
- [126] P. M. Claesson, M. L. Fielden and A. Dedinaite, *J. Phys. Chem. B*, 102 (1998) 1270.
- [127] A. Dedinaite, P. M. Claesson, J. Nygren and I. Iliopoulos, *Progr. Colloid Polym. Sci.*, 116 (2000) 84–94.
- [128] D. Knorr, *Food Technology*, 38 (1984) 85–97.
- [129] V. Coma, A. Martial-Gros, S. Garreau, A. Copinet, F. Salin and A. Deschamps, *Journal of Food Science*, 67 (2002) 1162–1169.
- [130] M. N. V. Ravi Kumar, *React. Funct. Polym.*, 46 (2000) 1.
- [131] R. Tarsi, R. A. A. Muzzarelli, C. A. Guzman and C. Pruzzo, *J. Dent. Res.*, 76 (1997) 665–672.
- [132] P. M. Claesson and B. W. Ninham, *Langmuir*, 8 (5), (1992) 1406.

- [133] P. Pincus, *Macromolecules*, 24 (1991) 2912.
- [134] F. S. Casajka, R. R. Netz, C. Seidel and J.-F. Joanny, *J. Eur. Phys.*, E4 (2001) 505–513.
- [135] R. Israels, F. A. M. Leermakers, G. J. Fleer, E. B. Zhulina and T. M. Birshtein, *Macromolecules*, 27 (1994) 3249–3261.
- [136] Y. V. Lyatskaya, F. A. M. Leermakers, G. J. Fleer, E. B. Zhulina and T. M. Birshtein, *Macromolecules*, 28 (1995) 3562–3569.
- [137] E. B. Zhulina, J. K. Wolterink and O. V. Borisov, *Macromolecules*, 33 (2000) 4945.
- [138] E. B. Zhulina, O. V. Borisov and T. M. Birshtein, *Macromolecules*, 32 (1999) 8189.
- [139] E. B. Zhulina, T. M. Birshtein and O. V. Borisov, *Macromolecules*, 28 (1995) 1491.
- [140] R. S. Ross and P. Pincus, *Macromolecules*, 25 (1992) 2177.
- [141] V. A. Pryamitsyn, F. A. M. Leermakers, G. J. Fleer and E. B. Zhulina, *Macromolecules*, 29 (1996) 8260–8270.
- [142] Y. V. Lyatskaya and A. C. Balazs, *Macromolecules*, 29 (1996) 5469.
- [143] E. B. Zhulina and O. V. Borisov, *Macromolecules*, 29 (1996) 2618.
- [144] Y. Mir, P. Auroy and L. Auvray, *Phys. Rev. Lett.*, 75 (1995) 2863.
- [145] E. B. Zhulina, O. V. Borisov and T. M. Birshtein, *Macromolecules*, 33 (2000) 3488.
- [146] D. Dean, J. Seog, C. Ortiz and A. J. Grodzinsky, *Langmuir*, 19 (2003) 5526–5539.
- [147] S. J. Miklavic and S. J. Marcelja, *J. Phys. Chem.*, 92 (1988) 6718.
- [148] L. Sjöström, T. Åkesson and B. Jönsson, *J. Chem. Phys.*, 99 (1993) 4739.
- [149] K. Kurihara and T. Kunitake, *Langmuir*, 8 (1992) 2087.
- [150] K. Kurihara and Y. Murase, *Polyelectrolyte Brushes* (S. K. Tripathy, J. Kumarr and H. S. Nalwa, eds.), *Handbook of Polyelectrolytes and their Applications*, American Scientific Publishers, 2002, p. 207.
- [151] T. W. Kelley, P. A. Shorr, D. J. Kristin, M. Tirrell and C. D. Frisbie, *Macromolecules*, 31 (1998) 4297.
- [152] O. Prucker and J. Rühle, *Macromolecules*, 31 (1998) 592.
- [153] O. Prucker and J. Rühle, *Macromolecules*, 31 (1998) 602.
- [154] T. Abe, K. Kurihara, N. Higashi and M. Niwa, *J. Phys. Chem.*, 99 (1995) 1820–1823.
- [155] S. Hayashi, T. Abe, N. Higashi, M. Niwa and K. Kurihara, *Langmuir*, 18 (2002) 3932–3944.
- [156] K. Kurihara, T. Abe, N. Higashi and M. Niwa, *Colloids and Surfaces*, 103 (1995) 265–272.
- [157] T. Abraham, S. Giasson, J. F. Gohy and R. Jérôme, *Langmuir*, 16 (2000) 4286–4292.
- [158] M. Balastre, F. Li, P. Scorr, J. Yang, J. W. Mays and M. V. Tirrell, *Macromolecules*, 35 (2002) 9480–9486.
- [159] M. Heuberger, T. Drobek and J. Vörös, *Langmuir*, 20 (2004) 9445.
- [160] M. Heuberger, T. Drobek and N. D. Spencer, *Biophys. J.*, 88 (2005) 495.
- [161] T. Drobek, N. D. Spencer and M. Heuberger, *Macromolecules*, 38 (2005) 5254.

This page intentionally left blank

## Chapter 3

# Surface Plasmon Optics for the Characterization of Biofunctional Architectures

Fang Yu<sup>a</sup>, Danfeng Yao<sup>a</sup>, Jing Liu<sup>a</sup>, Danica Christensen<sup>a</sup>,  
Rolf Lauterbach<sup>b</sup>, Harald Paulsen<sup>b</sup>, Wolfgang Knoll<sup>a,\*</sup>

<sup>a</sup>Max-Planck-Institute for Polymer Research, Ackermannweg 10, 55128 Mainz, Germany

<sup>b</sup>Institute of General Botany, Johannes Gutenberg Universität Mainz, Müllerweg 6, 55099 Mainz, Germany

## 1. INTRODUCTION

A surface plasmon polariton (SPP) is a bound transverse magnetic (TM) electromagnetic field/charge-density oscillation, which may propagate along an interface between two optically dissimilar media, a metal and a dielectric. Earlier works from Kretschmann and Raether [1,2], Otto [3], Agarwal [4], Swalen [5] have generated a deep understanding of this phenomenon. Theoretically and experimentally, the following distinctive features of surface plasmon resonance (SPR) have been discovered and proven to be important:

- A. The electromagnetic field decays evanescently into the adjacent media, with a decay length of several hundreds of nanometers.
- B. The evanescent field is greatly enhanced at the interface in comparison with the field of the incoming plane wave.
- C. Its electromagnetic wave propagates at the interface with high attenuation.
- D. This wave is p-polarized, giving information about the spatial orientation of dipoles interacting with the SPP.

---

\*Corresponding author. E-mail: knoll@mpip-mainz.mpg.de

The versatility of the SPR technique has been shown by a vast amount of publications in the past decades; the method has matured into a well-accepted analytical tool for the characterization of interfaces and thin films as well as for the sensitive detection of interfacial biomolecular interaction. With a significant input from engineering, SPR has reached a decent signal-to-noise level with a lower limit for a reliable signal detection corresponding to an effective layer of about 0.3 Å [6], which is sufficient for most thin film studies. However, the intrinsic label-free characteristic of SPR detection technique still imposes limitation on further sensitivity improvement, especially if the analysis involves small molecules.

Alternatively, various analytical methods based on SPR phenomenon have been developed, including surface plasmon field-enhanced Raman scattering (SERS) [7], surface plasmon field-enhanced fluorescence spectroscopy (SPFS) [8–11], surface enhanced second harmonic generation (SHG) [12], surface enhanced infrared absorption (SEIRA) [13], surface plasmon field-enhanced diffraction spectroscopy (SPDS) [14–18]. Most of these methods take advantage of the greatly enhanced electromagnetic field of surface plasmon waves, in order to excite a chromophoric molecule, e.g., a Raman molecule or a fluorescent dye. Therefore, a better sensitivity is expected.

## 2. THEORETICAL BACKGROUND

### 2.1. Excitation of Surface Plasmon Modes

A surface plasmon is a light wave that is bound to the interface of a metal in contact to a dielectric medium. The free electrons of the metal respond collectively by oscillating in resonance with the light wave. The interaction occurs only if the momentum of the incoming photon matches with that of the surface plasmon mode.

Solving Maxwell's equations at the metal/dielectric interface at the appropriate boundary conditions yields the surface plasmon dispersion relation, that is, the relation of the angular frequency  $\omega$  and the  $x$ -component of the surface plasmon wave vector  $k_{\text{SP}}$ ,

$$k_{\text{sp},x} = \frac{\omega}{c} \left( \frac{\varepsilon_d \varepsilon_m}{\varepsilon_d + \varepsilon_m} \right)^{1/2} \quad (1)$$

where  $\varepsilon_d$  and  $\varepsilon_m$  are the dielectric constants of the dielectric and the metal, respectively, and  $c$  is the light speed in vacuum. In the frequency (spectral) range of interest we have:

$$\left( \frac{\varepsilon_d \varepsilon_m}{\varepsilon_d + \varepsilon_m} \right)^{1/2} \geq (\varepsilon_d)^{1/2} \quad (2)$$

This leads to the consequence that the momentum of a free photon,  $k_{\text{ph}}$ , propagating in a dielectric medium

$$k_{\text{ph}} = \frac{\omega}{c} (\varepsilon_d)^{1/2} \quad (3)$$

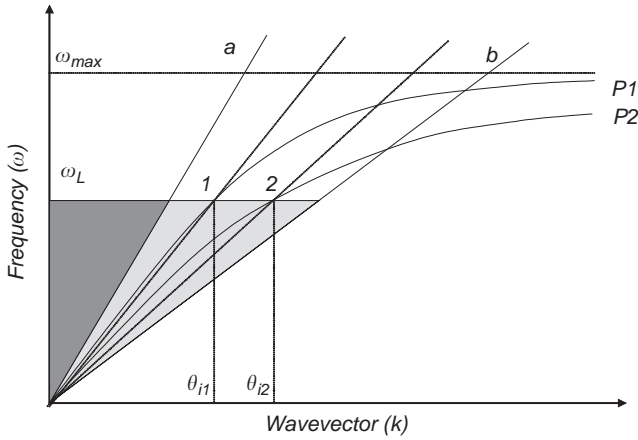


**Fig. 1.** Dispersion relation of (a) free photon in a dielectric, (b) free photon propagating in a coupling prism, and dispersion relations of surface plasmons at the interface between the metal and the dielectric before (P1) and after (P2) the deposition of a thin dielectric layer.

is always smaller than the momentum of a surface plasmon mode,  $k_{SP,x}$ . Fig. 1 presents these details graphically. The dark gray marked area represents the frequency/wave vector combinations that are accessible by light in vacuum. Although the dispersion of free photons (line a) approaches asymptotically that of the surface plasmons (P1), there is no intersection of both curves. It is therefore important to note that surface plasmons are not directly excitable by light in vacuum, unless the momentum of free photons is increased by appropriate experimental methods, e.g., by prism coupling, grating coupling, nonlinear coupling, or coupling by means of a rough surface.

By far, the prism coupling is the predominant coupling technique employed to increase the wave vector of the incident light. The coupling geometry is schematically shown in Fig. 2. Photons are not coupled directly to the metal/dielectric interface, but via the evanescent tail of the light totally internally reflected at the base of a high-index prism (with its dielectric constant  $\epsilon_p > \epsilon_d$ ). The corresponding dispersion curve of the incoming photons is shown as line b in Fig. 1. Given a laser wavelength  $\omega_L$ , coupling to a surface plasmon mode can be achieved at an appropriate angle of incidence,  $\theta_{i0}$  (cf. point 1). If a dielectric thin film (with dielectric constant  $\epsilon_f > \epsilon_d$ ) is deposited on the metal surface, the mean dielectric constant probed by the evanescent field increases. As a consequence, the dispersion relation is shifted towards larger wave vectors as depicted by P2. Therefore, coupling is achieved at an angle  $\theta_{i2}$  larger than  $\theta_{i1}$  (cf. point 2). This is the principle underlying thin film sensing by SPR.

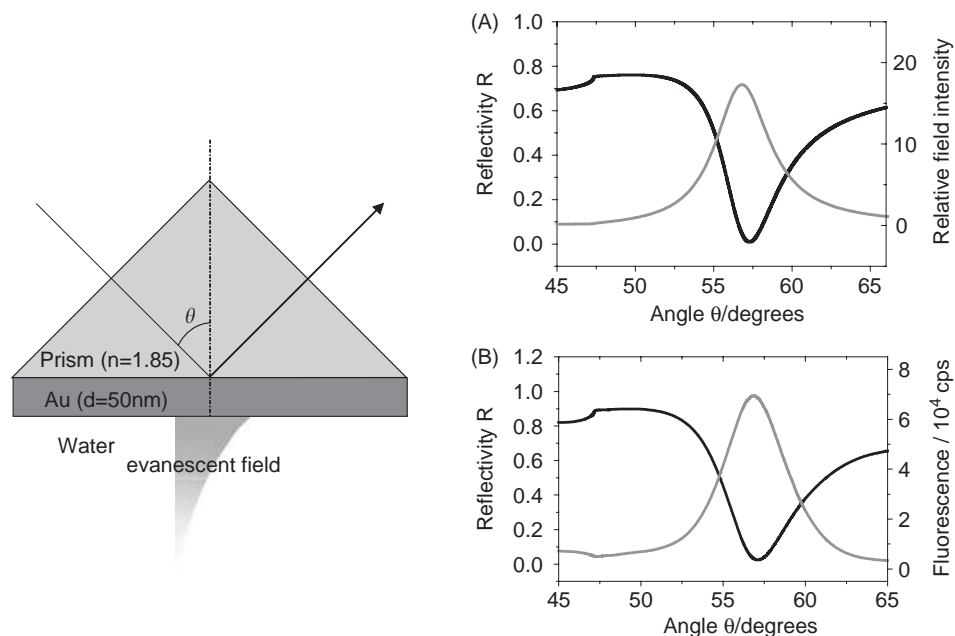


**Fig. 2.** (Left) Excitation of SPR via the Kretschmann geometry. (Right) (A) Fresnel simulation of angular dependence of reflected light intensity and the corresponding relative field intensity. (B) Experimental data of an angular scan of the reflected light intensity and the corresponding fluorescence emission from surface attached Cy5-DNA molecules.

## 2.2. Surface Plasmon Field-Enhanced Fluorescence Spectroscopy

If the incoming photons resonantly couple to the metal, enormously enhanced optical fields can be generated at the interface. This phenomenon is well-known and widely applied in SERS studies [7]. The field enhancement is also the most important feature of SPR used in combination with fluorescence spectroscopy development, which can be demonstrated by Fresnel simulations and experimental data (Fig. 2). The enhancement factor is given by the ratio of the electromagnetic field intensity on the metal surface at the dielectric side divided by the incoming electromagnetic field intensity for p-polarized light. Peak intensities scaled against the incoming intensity at a wavelength  $\lambda = 632.8\text{ nm}$  reach a factor of 16 for the prism/gold/water system. Generally, the smaller the imaginary part of the dielectric constant  $\varepsilon''$ , i.e., the lower the absorption and hence dissipation of the optical field intensity, the higher is the enhancement factor. This strong surface “light” can be used to excite a fluorescent dye placed within the evanescently decaying field, which is typically 100–200 nm for visible light wavelengths.

These features make SPFS to be surface sensitive and compatible to modern biosensor platforms. In the same category, total internal reflection fluorescence

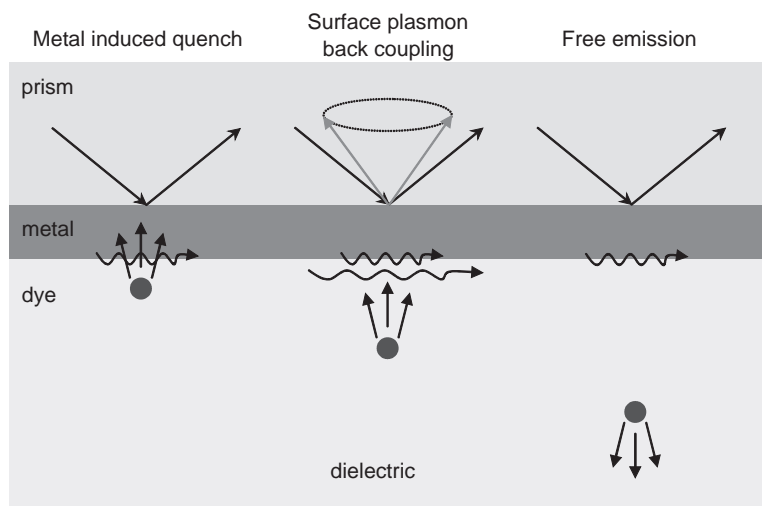


**Fig. 3.** Schematic drawing of a fluorophore positioned close to a metal/dielectric interface. Different fluorescence decay channels operate at different fluorophore/metal separation distances.

spectroscopy (TIRF) uses an evanescent field created by total internal reflection and has already been developed to be a mature basis for fluorosensors. Both SPFS and TIRF have shown remarkable sensitivity in bio-affinity sensing applications [11,19], and have been used to develop microscopic biosensors [20,21]. However, unlike in the pure dielectric case in TIRF, SPFS introduces a metal layer that significantly alters the way an excited fluorophore loses its excitation energy. Various additional decay channels contribute to the decrease of the radiative quantum yield of the fluorophores and are operational at different fluorophore/metal separations [22] (summarized in Fig. 3).

(A) If a dye is positioned at a distance within 10 nm to the metal surface, the non-radiative decay of fluorescence is the dominating process. It is assumed to be based on a dipole–dipole interaction process due to the mode coupling to an electron–hole pair (exciton) in the metal. For two molecular dipoles, the standard Förster model gives a  $R^{-6}$  dependence of the energy transfer efficiency on the separation distance of the donor molecule and the acceptor molecule. However, the distance dependence of energy transfers involving a dye and a surface (could be rough) can be greatly reduced to a  $R^{-3} \sim R^{-4}$  dependence. The transferred energy dissipated by the metal is mostly converted into heat. (B) At an intermediate-distance regime (a few nm up to  $\sim 20$  nm), a significant fraction of the excitation energy couples back to SPPs, by fulfilling the momentum match conditions, representing another loss channel for fluorescence. (C) At sufficient separation distances ( $> 20$  nm), the free fluorescence emission of the dyes dominates. However, the fluorescence intensity cannot be directly obtained unless two additional effects are considered. First, the fluorescence emission oscillates

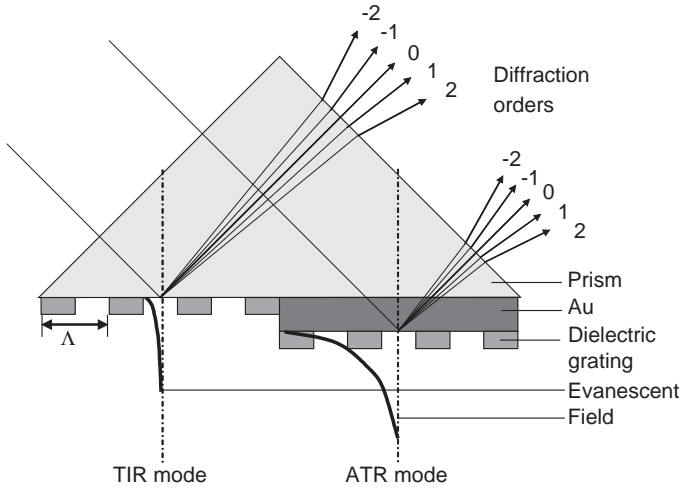


**Fig. 4.** Schematic representation of surface diffraction from dielectric pattern, based on total internal reflection (TIR) and attenuated total reflection (ATR) coupling geometries, respectively.

as the distance increases, since the metal reflects part of the fluorescence light which introduces an interference pattern. Second, the excitation source, i.e., the evanescent field weakens evanescently as the distance increases.

### 2.3. Surface Plasmon Field-Enhanced Diffraction

The local field generated by total internal reflection [23] or by the SPR [14–18] can be diffracted by gaining (or losing) discrete momenta  $\Delta k = mg$ , generated by the periodic surface structure of periodicity  $\Lambda$  (Fig. 4). The diffraction angle deviates in discrete increments from the specular-reflection angle (i.e., zeroth-order diffraction) in fulfillment of the corresponding momentum match condition:

$$k_{\text{diff}}^m = k_{\text{SP}} \pm mg \quad (4)$$

where  $k_{\text{diff}}^m$  is the wave vector of the  $m$ th diffraction order,  $k_{\text{SP}}$  the wave vector of the surface plasmon wave,  $g$  the grating constant with  $|g| = 2\pi/\Lambda$ , and  $m$  the diffraction order. In general, for a shallow sinusoidal grating composed of non-absorbing materials, the diffraction intensity  $I_d$  can be expressed by [24]

$$I_d \propto I_0 \left( \frac{\pi \Delta n d}{\lambda} \right)^2 \quad (5)$$

where  $I_0$  and  $\lambda$  are the intensity and wavelength of the source field respectively,  $\Delta n d$  represents the grating amplitude in an optical thickness format. This equation indicates: first, the diffraction intensity  $I_d$  is proportional to the intensity of the excitation source—the evanescent field, which emphasizes the importance of

the surface plasmon field enhancement; second,  $I_d$  is proportional to the square of the grating amplitude  $\Delta nd$ . Therefore, for a small additional optical contrast variation  $\partial nd$  above the initial contrast  $\Delta nd$

$$\frac{\partial I_d}{\partial nd} \propto \Delta nd \quad (6)$$

This implies that the diffraction signal modulated by a unit amount of optical contrast variation  $\partial nd$  increases linearly with the level of initial contrast  $\Delta nd$ .

### 3. INSTRUMENTAL

The SPR, as well as the SPFS and the SPDS set-ups are built in the Kretschmann–Raether configuration depicted in Fig. 5. A detailed description can be found in a more specific publication [25]. Briefly, the modulated and polarized beam of a laser is reflected off the base of the coupling prism and fed into a photo-diode detector. The prism/sample and the photo-detector are mounted on two co-axial goniometers, respectively, allowing for an independent tuning of the respective angular positions.

The fluorescence detection unit is mounted towards the base of the prism, rotating together with the prism (sample) at  $\theta$ , while the photo-diode detecting the reflected light rotates at  $2\theta$ . The fluorescence emission from the sample

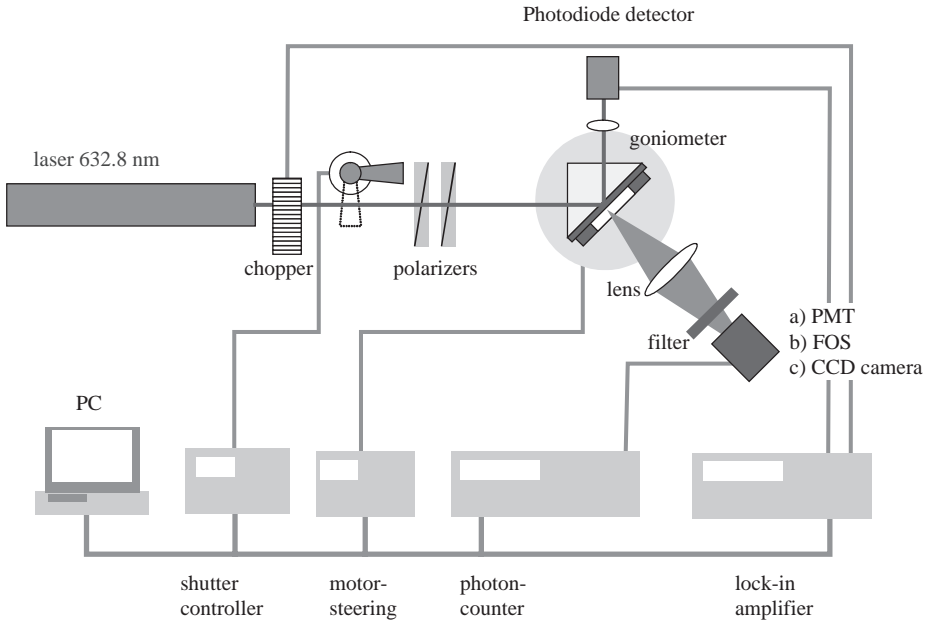


**Fig. 5.** Schematics of an SPR/SPFS set-up. Typically, an He–Ne laser with  $\lambda = 632.8$  nm is used. For the experiment in Section 4.7, an Nd:YAG diode pumped solid-state (DPSS) laser with  $\lambda = 473$  nm is used.

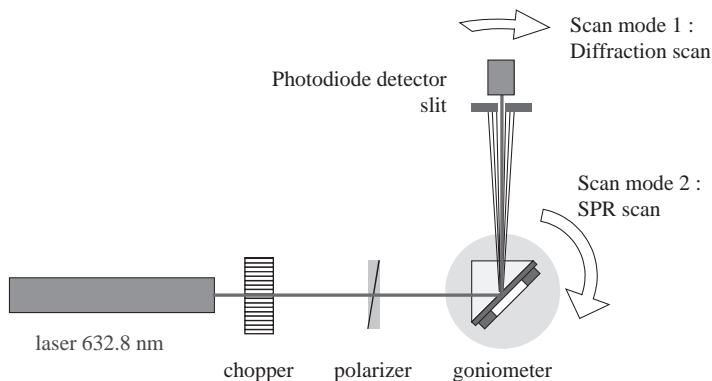


**Fig. 6.** Schematics of the diffraction mode of the SPR set-up.

surface is collected by a lens and passes through an interference filter into a photomultiplier tube (PMT). In order to get a full fluorescence spectrum, the fluorescence emission is fed into a fiber optic spectrometer (FOS) instead of the photomultiplier. Custom software is developed for the data acquisition and the controlling of the system electronics. Two measurement modes, i.e., angular scan mode (signal as a function of laser incident angle  $\theta$ ) and kinetic mode (signal as a function of time) are applicable.

The diffraction experiments can be performed on the same Kretschmann SPR set-up (cf. Fig. 6). To resolve the diffraction orders, the angular acceptance of the photo-diode detector is defined by a 1 mm slit to be  $\Delta\tau \approx 0.08^\circ$ . The coaxial goniometers enable an independent tuning of the incident angle of the laser and/or the detection angle. Both motors rotate in a  $\theta/2\theta$  fashion for the usual SPR angular scans, whereas only the detector motor rotates when performing diffraction scans.

#### 4. APPLICATION OF SPR AND SPFS IN BIO-AFFINITY ANALYSIS

As a novel surface characterization tool based on SPR technique, SPFS has shown great versatility and sensitivity in bio-interface studies (e.g., of proteins [11,25], oligonucleotides [9,10], PCR products [26], or enzymatic reaction [27]). Most of the intriguing properties of fluorescence techniques, in general, such as high-sensitivity [11], multiplexing formats [28], and energy transfer schemes [10], can be directly applied to SPFS. In particular, SPFS contributes a signal channel in addition to the SPR channel, which even enables obtaining conformational information of surface attached biomolecules [10,11]. In the following, the experimental examples start from basic, but fundamentally important property checks of the sensor matrices, such as nonspecific binding (NSB) and surface regeneration. Then, a variety of examples will follow to cover the aspects of biomolecular assembly, immuno-sensing, binding kinetics, affinity analysis, etc.

#### 4.1. Nonspecific Binding

As a prerequisite for the application of biomolecular interaction studies, the sensor surface should resist NSB of biomolecules. In the following, we will demonstrate that with the proper design of the sensor surface, NSB can be effectively eliminated.

Since the early 1980s, surface grafted poly (ethylene glycol) (PEG) has been used to prevent adsorption of proteins from analyte solution or biological media [29]. The resistance of these films is well explained by the “steric repulsion” theory, which associates the inertness of the polymer brushes with the high conformational freedom of the PEG chains in the near surface region. However, the ability to resist protein adsorption is also exhibited by conformationally restricted oligo (ethylene glycol) (OEG) terminated alkanethiolate self-assembled monolayers (SAMs). It thus appears that the protein resistance of these SAMs must be attributed to effects other than steric repulsion. In an effort to explain the protein adsorption characteristics on a molecular level, calculations on the interaction of water with OEG clusters as well as Monte Carlo simulations of the OEG-SAM/water interface have been performed [30]. It has been generally accepted that a tightly bound layer of interphase water, which prevents direct contact between the proteins and the surface, is responsible for the protein resistance of OEG-SAMs.

An SAM of an EG thiol was tested towards NSB of a labeled IgG, Alexa-Fluor 647 labeled rabbit anti-mouse IgG (AF-RaM). As Fig. 7 shows, the

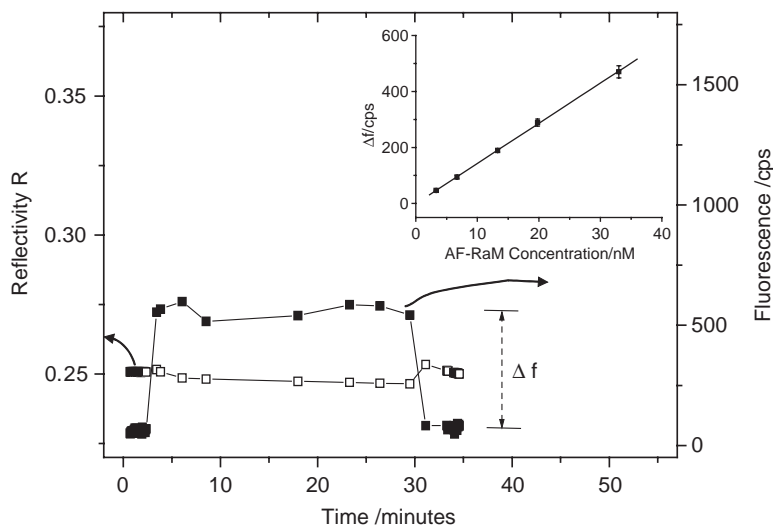


**Fig. 7.** Resistance of an EG SAM to nonspecific adsorption from a 33 nM solution of AF-RaM. The inset shows the relation between background fluorescence signal  $\Delta f$  and the bulk concentration of the AF-RaM solution.

AF-RaM solution injected into the cell at a working concentration of  $c_0 = 33$  nM caused an abrupt fluorescence signal ( $\Delta f = 470$  cps) increase. When pure buffer replaced the sample solution, the fluorescence signal instantaneously dropped back to the original baseline level. In the SPR signal channel, the reflectivity  $R$  showed only irregular noise caused by the sample solution exchange and no detectable minimum shift was found in the SPR scan curves. The fact that no further rise in the fluorescence signal after the initial jump and the quick drop back to the original value was observed, suggests that there was no observable NSB of labeled antibodies to the EG SAM. The  $\Delta f$  originates from two different contributions. First, there is a (small) fraction of labeled antibodies in the bulk solution, which can be excited by the evanescent tail of the surface plasmon mode that extends some 200 nm into the liquid phase. Second, the laser light randomly scattered by the roughness of sensor surface can also excite the fluorescent dyes in solution. Both contributions yielded a linear relation between  $\Delta f$  and sample concentration, as shown in the inset of Fig. 7.

The well-known surfactant Tween-20 was added routinely into the buffer for further minimizing protein NSB and avoiding sample depletion. It is a polyoxyethylene sorbitan ester of fatty acids, known as a model non-ionic detergent to preserve the native protein structure and has a relatively high critical micelle concentration (CMC = 0.05% (v/v)). Tween-20 is a vital reagent in clinical immuno-assays with extremely primitive sensor surface engineering [31], where the detergent is highly effective in preventing protein adsorptions and in even displacing adsorbed proteins. It was also determined that both, the minimum amount of adsorbed albumin and the minimum sessile water contact angle correlated closely with the CMC level of Tween-20, where a monolayer of Tween molecules forms with their hydrophilic heads oriented toward the exterior, i.e., the bulk phase [32].

Since an EG (or OEG, alike) SAM is the base layer of the supramolecular architectures of almost all the protein interaction studies presented here, the absence of NSB on such a matrix enables a good start for the observation of specific protein interactions.

## 4.2. Surface Regeneration

The robustness of the SAM allows for the repetitive removal of the bound antibodies by offensive reagents, including sodium dodecyl sulfate (SDS), guanidine hydrochloride (GdnHCl), etc. Although mild non-ionic detergents (such as beta-octyl glucoside) can also be used to competitively desorb proteins, it is generally demanded that the regeneration reagents denature the proteins for the fast disruption of the relatively stable interfacial immuno-complex. SDS is known as an anionic detergent with a high CMC level (1 mM) and also as a denaturing reagent. Reports have shown that SDS solutions below their CMC were much less effective at removing proteins from surfaces [33], which then suggests also the requirement of micelle formation. Therefore, 5 mM SDS

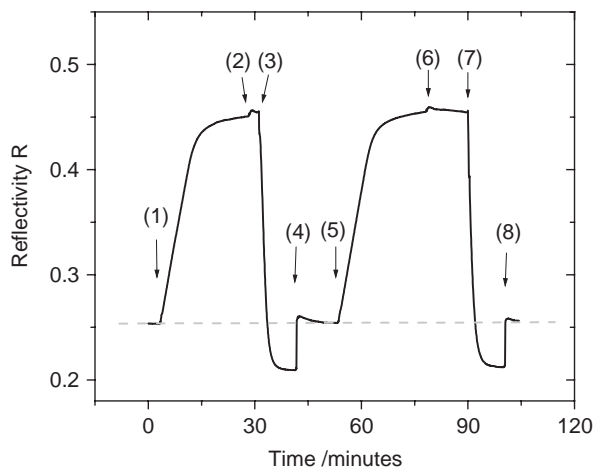


**Fig. 8.** Example of repetitive regenerations of bound anti-biotin antibody 2F5 by SDS solution: (1) 20 nM 2F5, (2) buffer rinse, (3) 0.5% SDS, (4) buffer, (5) 20 nM 2F5, (6) buffer rinse, (7) 0.5% SDS, and (8) buffer. The dashed line represents the baseline level.

solution was applied in the experiments. GdnHCl is a chaotropic reagent [34], which is also an effective protein denaturant. Efficient working concentration is at high concentration, e.g., 4–8 M.

As a demonstration of the regeneration (cf. Fig. 8), a SAM surface composed of 10% biotin thiol and 90% EG thiol was used, on which an anti-biotin antibody (2F5) was bound (cf. (1)) followed by a rinsing step (cf. (2)). Then, a pulse injection of a 5 mM SDS solution (cf. (3)) for ~10 min totally removed all the bound 2F5. The biotin functionality was completely preserved, shown by a subsequent identical binding of 2F5. Another regeneration could be performed equally well afterwards. The surface could be regenerated at least 20 times without any depletion of its functionality. The regeneration of the biotin SAM surface by a 4 M GdnHCl solution was equally applicable (data not shown).

Generally, having a repetitively renewable sensing matrix is of great importance to a successful biosensor. In fact, most of the matrices presented in this contribution can be easily regenerated by harsh or mild regeneration conditions [11,16,18,25,26].

### 4.3. Avidity of IgG Binding

The example of protein interactions presented in this paper will start from the recognition and binding between a surface bound ligand and its antibody approaching from solution. Study of such a model system will help to understand the binding kinetics and mechanisms of signal transduction on cell membranes [35], which are generally initiated by the interaction between a multivalent

molecule and membrane-restricted binding partners. Also this will help to optimize the ligand density for determining binding constants of ligand–ligand interactions in drug screening applications.

Our mixed SAM system is very well suited for our studies, since the surface biotin density (epitope to the 2F5 IgG) can be systematically varied. IgG is a bivalent molecule (with two recognition sites per molecule). Its binding constant to the surface attached ligands is a function of ligand density due to the accessibility of the antigenic epitopes, which is usually termed as the “avidity” phenomenon. A series of surfaces functionalized by SAMs of different molar ratios of biotin/EG thiols,  $\chi$  ( $\chi = 0.1, 0.04, 0.02, 0.01, 0.004, 0.002, 0.001, 0.0004, 0.0002, 0.0001$  respectively), were used for this demonstration. The 2F5 antibody solution (20 nM) was introduced into the flow cell, followed by a rinsing step with pure buffer. In order to rule out the influence of interfacial rebinding [36], a competitive rinse with a 1 mM biotin solution was subsequently conducted. For the surfaces with  $\chi < 0.002$ , the label-free detection by SPR was unable to give any convincing signal for kinetic evaluations. Therefore, an Alexa Fluor labeled 2F5 (L2F5) was applied and the fluorescent signal monitored. The SPR curves for the surfaces with  $\chi \geq 0.002$  are plotted in Fig. 9(A), normalized to the amount bound at equilibrium, in order to allow for a better comparison of the adsorption/desorption rates of the antibody to various biotin surfaces.

The mass-transport kinetics firmly controlled the adsorption kinetics for surfaces with  $\chi \geq 0.002$ , resulting in identical binding slopes. Normalized adsorption curves showed that the higher the surface biotin density was, the later the binding could reach equilibrium, because the equilibrium time was limited by the mass-transport rate of antibodies diffusing from the bulk to the interface. Mass-transport was so dominating that the adsorption phase contained no useful information on the interaction kinetics. However, the desorption phase lasted much longer so that mass-transport limitation could be ruled out. Therefore, the desorption rate reflected the affinity between the bound antibody and the biotin moieties of the SAM surfaces. As shown in Fig. 9(A), apparently, the desorption rate increased with decreasing biotin density, for both the normal and the competitive desorbing processes. The trend clearly indicates a transition from a 1:2 to a 1:1 interaction stoichiometry between the antibodies and the surface antigens, because statistically less antibodies were able to access two biotins for more diluted biotin SAM surfaces.

Taking advantage of the sensitivity of the fluorescent monitoring mode, the binding signal on the surfaces with  $\chi = 0.0004, 0.0002, 0.0001$ , respectively, could be resolved, which are shown in a normalized form in Fig. 9(B). At such low surface ligand densities, the adsorption phase was controlled by interaction kinetics, as indicated by the absence of a linear slope in the binding curves. Also, statistically, the IgG was unable to bridge two biotins at these low biotin densities. Therefore, the adsorption/desorption behavior in all three measurements represented the interaction between one Fab fragment with biotin.

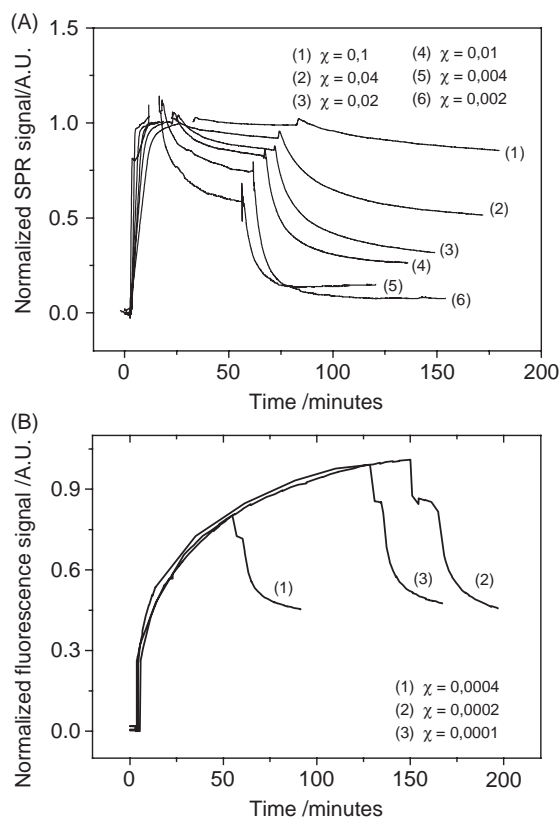


**Fig. 9.** Avidity controlled interaction kinetics between the anti-biotin antibody 2F5 and the surface-confined biotin moieties. (A) Normalized SPR curves of the 2F5 association/dissociation process on surfaces with relatively high biotin densities. (B) Fluorescence kinetic curves of the 2F5 association/dissociation on surfaces with lower biotin densities.

#### 4.4. SPFS Detection of Extremely Diluted Antigen Densities

As shown in the previous chapter, SPFS takes over the sensing task where SPR fails to monitor. The sensitivity advantage can be more pronounced if small (but labeled) molecules are involved, e.g., DNA oligonucleotides. For the system studied here, it is meaningful to demonstrate the suitability of the SPFS technique for probing SAM surfaces with extremely laterally diluted ligands. Fig. 10 shows the comparison of the fluorescence kinetic curves obtained for  $\chi = 0.0004$ ,  $0.0001$ , and  $0$  surfaces, respectively, obtained by the direct and the indirect detection scheme (see figure caption for details). Upon increasing the mole fraction of the biotin thiol in the SAM, a corresponding increase in the protein binding was observed, which also indicates specific bindings. In the indirect detection case, the fluorescence signals were much stronger than that of

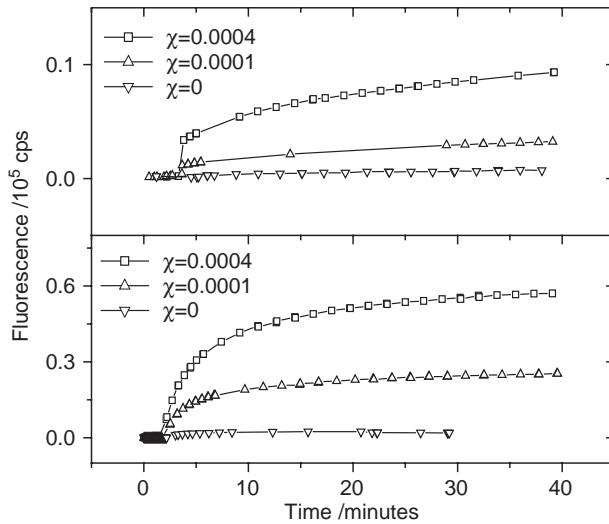


**Fig. 10.** Sensitivity evaluation of SPFS on planar surfaces. (1), (2), (3) are fluorescence kinetic curves of the binding of L2F5 to surfaces of different biotin densities of  $\chi = 0.0004$ ,  $0.0001$ ,  $0$ , respectively. (4), (5), (6) are fluorescence kinetic curves of the binding of AF-RaM to 2F5 (mouse IgG) bound surfaces of different  $\chi = 0.0004$ ,  $0.0001$ ,  $0$ , respectively.

the direct detection case, due to the signal amplification by the AF-RaM and the reduced fluorescence quenching [25].

Assuming a value for the cross-sectional area of a thiolate of  $A = 0.26 \text{ nm}^2$  and using the same biotin ratio as in the preparation solution, we can calculate that statistically a biotinylated thiolate occupies an area of  $2.6 \times 10^3 \text{ nm}^2$  on the  $\chi = 0.0001$  surface, meaning on average the next neighbor of each biotin is  $\sim 50 \text{ nm}$  away. If each of the binding sites holds one antibody, we can claim that the fluorescence measurements can easily detect surface concentrations as low as 1 molecule per  $2.6 \times 10^3 \text{ nm}^2$  that corresponds to a surface concentration of approx.  $10 \text{ ng cm}^{-2}$  or a coverage of 1.8% (assuming the cross-section of a Fab  $A = 6.5 \times 3.5 \text{ nm}^2$ ). For smaller analytes, e.g., a polypeptide with a molar mass of only 1000 Da, the mass detection limit would be  $\sim 70 \text{ pg cm}^{-2}$ .

The current model system is by no means optimized for exploiting the limit of detection (LOD) of SPFS. For example, by using a three-dimensionally extended matrix, SPFS has shown more extraordinary performance in detecting the flux of 10 antibody molecules binding to a sensing area of  $1 \text{ mm}^2$  in every minute [11].

#### 4.5. Layer-By-Layer Assembly of Proteins

Reports have shown that multi-layer thin films can be fabricated by an alternating deposition of two kinds of molecules with affinity to each other. This

technique is called layer-by-layer (LbL) deposition. Apart from the electrostatic interaction, a widely used strategy for the LbL technique, biological affinity can also be used to deposit proteins by means of, e.g., antigen–antibody interactions, biotin–avidin interactions, and sugar–lectin interactions. A merit of this protocol is that all-protein thin films can be prepared. On the other hand, the LbL technique offers a way to control the separation distance between the molecules of interest to the base surface, which is of particular interest for investigating the distance dependence of the fluorescence yield by SPFS [37]. In the experiments described in the following, we chose streptavidin and biotinylated IgG as the couple that forms alternating layers, which can be selectively fluorescently decorated by applying labeled molecules (Fig. 11).

A surface coated with a SAM of 3-mercaptopropionic-acid, was used for the covalent attachment of Alexa-Fluor 647 labeled streptavidin (AF-SA) by means of NHS-active ester chemistry [38]. This reaction yielded an SPR minimum shift of  $\Delta\theta \approx 0.27^\circ$  and contributed a fluorescence intensity of  $\Delta f \approx 350$  cps (layer b\*). Subsequently, the alternate binding of biotinylated IgG and streptavidin from  $20 \mu\text{g ml}^{-1}$  solutions was monitored.

A linear correlation between the thickness and the layer number with a slope of  $\sim 2$  nm per layer was obtained. On top of the eighth layer (a biotin-IgG layer) or the fourth double layer, i.e., at a distance of  $\sim 16$  nm to the Au surface, another AF-SA layer was built (j\*). It resulted in a much stronger fluorescence signal of  $\Delta f \approx 12,000$  cps, which was 33 times higher than the signal from the first AF-SA layer (b\*). This gives the intensity difference between quenched and unquenched fluorescence molecules, which points to the need of a spacer layer for the fluorescence molecules in real sensing applications.

#### 4.6. Affinity Determination Between hIL8 and Its Antibody Fragments

As an example of SPFS immuno-assay for clinically relevant samples, the affinity determination of hIL8 (human interleukin 8) with its antibody fragments (Fab13A and Fab6x, with different affinities to hIL8) were performed. Due to the small size of the hIL8 molecule ( $\sim 18$  kDa), a label-free SPR analysis is quite challenging. Therefore, Cy5 labeled hIL8 was used to allow for a fluorescence analysis. The study was based on a multi-layer functional architecture, composed of a biotin SAM (with 10% biotin functionality), a streptavidin layer, and a biotinylated Fab layer (cf. Fig. 12(A)). The use of this multi-layer structure is designed to alleviate fluorescence quenching and to control the lateral spacing of the ligand density.

First, streptavidin was bound to the biotin SAM. Typically, the density of the SAM was  $\sim 2$ – $2.5$  ng  $\text{mm}^{-2}$ . Next, the biotin–Fab was attached. The saturation density of biotin–Fab was  $\sim 2.7$ – $2.9$  ng  $\text{mm}^{-2}$ . In order to reduce the influence of steric hindrance/mass-transport/rebinding, a moderately reduced Fab density level was used, i.e.,  $\sim 2.1$  ng  $\text{mm}^{-2}$  for Fab13A and  $\sim 1.7$  ng

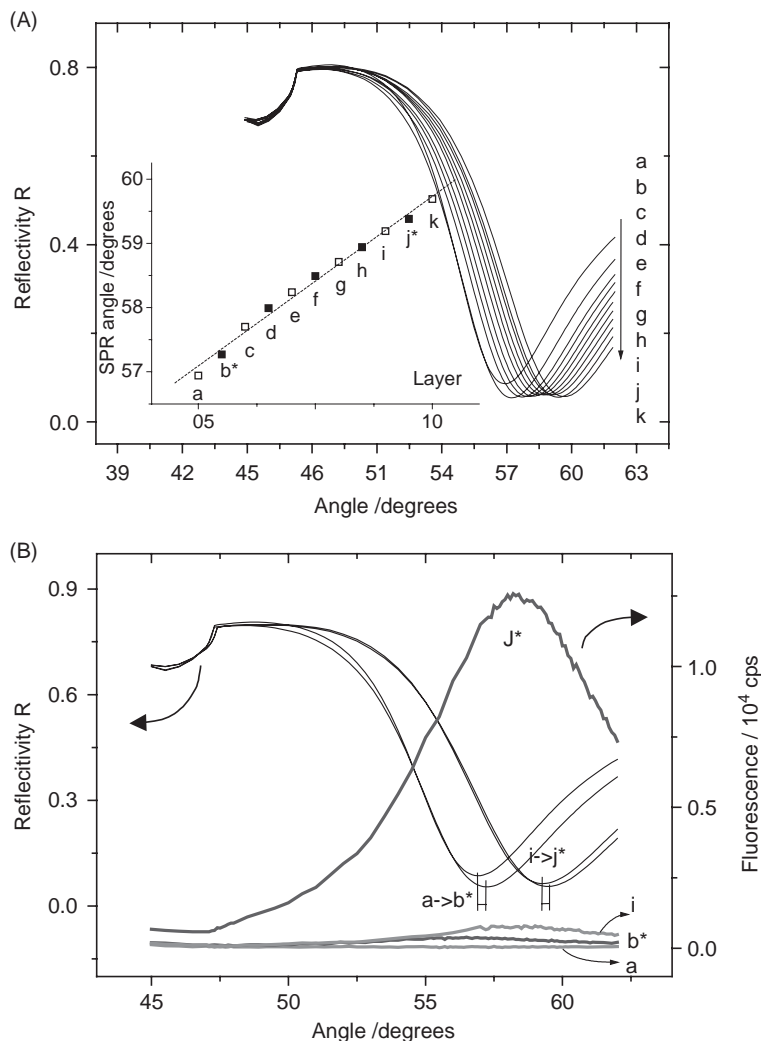


**Fig. 11.** A layer-by-layer model built by biotin–streptavidin interaction. (A) Angular SPR curves of each layer. The inset shows the SPR minimum position as a function of layer number. (B) SPR, fluorescence angular scans for layers “a”, “b\*”, “i”, and “j\*”.

$\text{mm}^{-2}$  for Fab6x, respectively. A 100 nM hIL8 solution containing  $500 \mu\text{g ml}^{-1}$  BSA was used for the binding study. Upon binding equilibrium, buffer (with  $500 \mu\text{g ml}^{-1}$  BSA) rinsing was performed and the dissociation process was recorded.

The association/dissociation curves are shown in Fig. 12(B). A common pseudo first-order kinetic model was applied to yield the kinetic constants ( $k_{\text{on}}$  and  $k_{\text{off}}$ ) and the affinity constants ( $K_A$  and  $K_D$ ). The association curves could

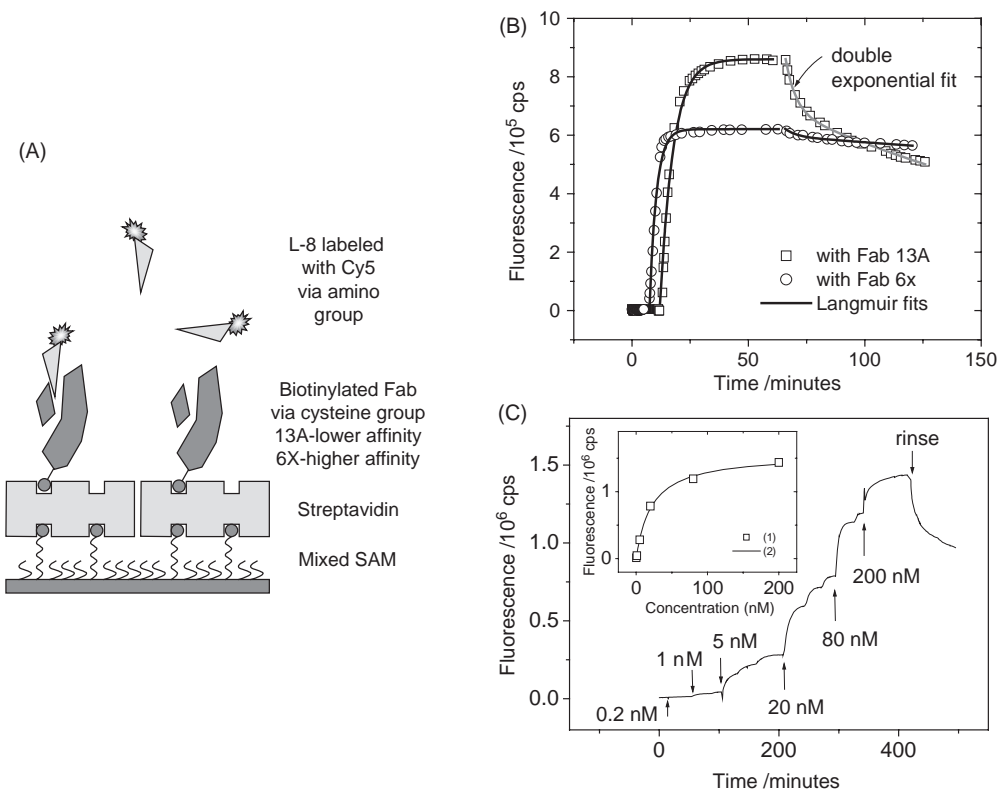


**Fig. 12.** (Left) (A) Schematic drawing of the hIL-8 kinetic assay experiments performed on a multi-layer architecture built by biotin-streptavidin interaction. (right) (B) Binding curves of hIL8-Cy5 on moderately diluted Fab surfaces. (C) Equilibrium titration of hIL8-Cy5 on Fab13A surface. The inset shows the titration results follow Langmuir adsorption isotherm, yielding the dissociation constant  $K_D = 21$  nM. Multiple injections were performed for each concentration, in order to overcome the sample depletion effect.

be fitted by

$$R = R_{\text{eq}}\{1 - \exp[-(k_{\text{on}}c_0 + k_{\text{off}})t]\} \quad (7)$$

where  $R$  is the fluorescence response,  $R_{\text{eq}}$  the equilibrium response at the bulk analyte concentration  $c_0$ .  $k_{\text{on}}$ , and  $k_{\text{off}}$  are the association and dissociation rate constants, respectively. For  $c_0 = 0$ , the dissociation (rinsing) kinetics is described by

$$R = R_{\text{eq}} \exp(-k_{\text{off}}t) \quad (8)$$

The affinity constant  $K_A$  and dissociation constant  $K_D$  can then be calculated according to

$$K_A = k_{\text{on}}/k_{\text{off}} \quad (9)$$

$$K_D = 1/K_A \quad (10)$$

However, the apparently bi-exponential dissociation behavior of the hIL8/Fab13A complex made it difficult to yield convincing kinetic constants within this simple Langmuir model [39]. Therefore, an upstream concentration titration method [40] was applied in order to determine the affinity constant of hIL8/Fab13A, shown in Fig. 12(C). A nonlinear steady-state fit, based on the Langmuir adsorption isotherm model, allows for the determination of  $K_D$ , according to (cf. Fig. 12(D))

$$R = \frac{c_0 R_{\text{max}}}{K_D + c_0} \quad (11)$$

where  $R_{\text{max}}$  is the fluorescence response of the highest (saturation) concentration applied.

The end-point fluorescence signals and the affinity results ( $K_D$ ) are listed in Table 1. Two features are noteworthy. First, although the end-point fluorescence signals for the Fab13A and the Fab6x surfaces are different, similar “binding stoichiometries” between hIL8 and Fabs are found, by normalizing the fluorescence signal to the corresponding Fab density derived from SPR. This reflects

**Table 1**

A comparison of binding stoichiometry, dissociation constants of Cy5-hIL8/Fab interactions for different Fabs. The  $K_D$  values are compared with the results from a commercial SPR instrument

	SA (SPR) (deg)	Fab (SPR) (deg)	hIL8-Cy5 (Fluorescence) (cps)	Binding Stoichiometry of hIL8/Fab* (cps/deg)	$K_D$ (SPFS) (nM)	$K_D$ (Biacore) (nM)
Lower affinity Fab (13A)	0.49	0.40	$8.5 \times 10^5$	$2.1 \times 10^6$	21	50–100
Higher affinity Fab (6x)	0.50	0.31	$6.2 \times 10^5$	$2.0 \times 10^6$	0.3	0.2

\*Fluorescence of hIL8/SPR of Fab

the fact that the working concentration of the hIL8 solution was high enough to saturate all binding sites on both Fab surfaces, since this concentration was already significantly larger than both  $K_D$  values. Second, the dissociation constants obtained via the fluorescence channel were comparable to the results determined by a commercial SPR instrument (Biacore 3000, Biacore AB) with the same molecules, confirming the applicability of SPFS in bio-affinity assays. However, there are still a considerable amount of factors that will influence the affinity determination, such as the binding matrix effect, the artificial labels on catcher and analyte molecules, the improper modeling of the kinetics. All these factors could contribute to the discrepancy between these results.

#### 4.7. Anchoring of Light-Harvesting Complex II Via a His-Tag

Next, we show an example of a multi-protein complex immobilization on a solid support while maintaining its functional integrity and long term stability, in order to mimic the energy transfer mechanism in plant photosynthesis. The light-harvesting complex II (LHCII) [41] is a major peripheral antenna complex accounting for 50–65% of the pigments in plant photosynthesis. An LHCII monomer is composed of a peptide backbone of 232 amino acids and at least 12 chlorophylls and 3 carotenoids. Here we use a recombinant LHCII [42], which contains (per monomer) 7 chlorophyll a and 5 chlorophyll b molecules as well as 2 luteins and 1 neoxanthin. In the natural supramolecular assembly of LHCII, the chlorophyll molecules are arranged such that virtually 100% energy transfer occurs from chlorophyll b to chlorophyll a. Thus, upon excitation of chlorophyll b, only the emission of chlorophyll a is observed. This in turn is used to judge the structural integrity of surface-anchored LHCII.

Here, the specific and strong chelating interaction between  $6 \times$  Histidine and the tetradentate nitrilotriacetic acid (NTA) mediated by  $\text{Ni}^{2+}$  [43] was used for the immobilization of a reconstituted LHCII mutant, whose c-terminus was extended by  $6 \times$  Histidine residues via genetic engineering (cf. Fig. 13(A)). NTA terminated thiols and OEG (spacer) thiols were used to build up a mixed SAM ( $\chi = 0.4$ ) on a substrate coated by 23 nm silver and 5 nm Au (the gold layer was used to protect the silver film from being oxidized).

The immobilization of trimeric LHCII is demonstrated in Fig. 13(B). After the nickel ion activation (5), a  $1 \mu\text{M}$  solution of trimeric recombinant LHCII prepared in NaP + DM buffer (20 mM sodium phosphate, pH 7.4, 0.1% (w/v) *n*-dodecyl- $\beta$ -D-maltoside) was introduced into the flow cell (1). For each cycle, the protein solution was incubated in the loop for 30 min, followed by buffer rinse (2), EDTA (3), and SDS (4) regeneration. EDTA was used to competitively chelate the nickel ions and break the linkage between NTA and Histidine. SDS, as mentioned in Section 4.2, was used to detach any remaining physically adsorbed proteins. As shown in Fig. 13(B), the immobilization/regeneration cycles from (1) to (5) can be well reproduced and the baseline after every cycle stabilized at a response close to the starting level. This indicates that the

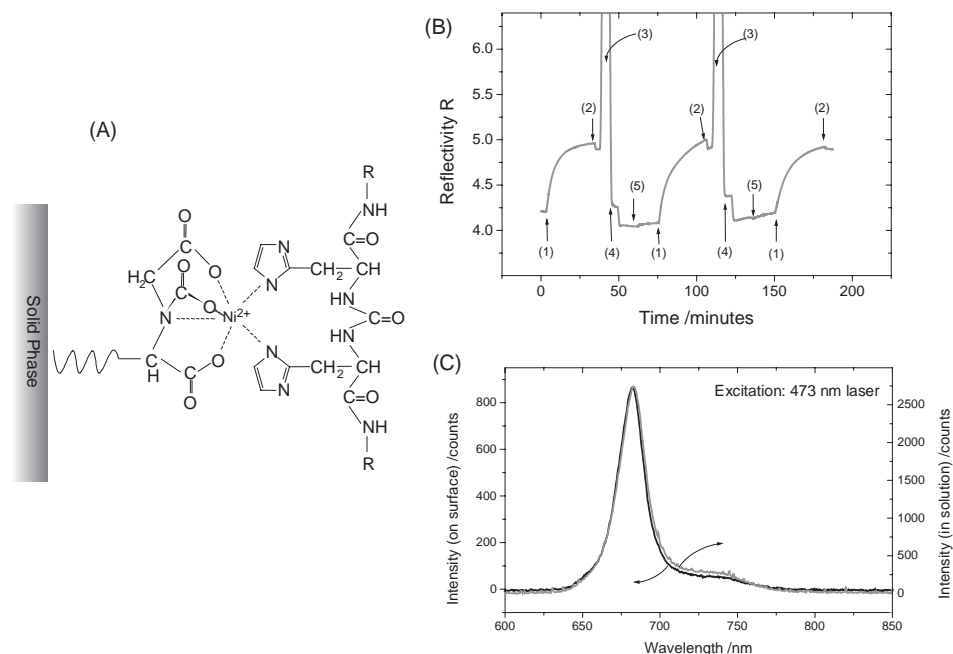


**Fig. 13.** (A) Schematic representation of the interaction between neighboring residues of the His-tag (6 consecutive Histidine residues) and an NTA-complexed Ni<sup>2+</sup> ion. (B) The performance of LHCII immobilization via chelating interaction. SPR kinetic curve of LHCII immobilization and regeneration cycles, monitored with an Nd:YAG DPSS laser ( $\lambda = 473$  nm). (C) Surface plasmon field-enhanced fluorescence emission spectrum of surface attached LHCII compared with the fluorescence emission from free LHCII in solution, excited by an Nd:YAG DPSS laser ( $\lambda = 473$  nm).

attachment/detachment of LHCII was specifically from NTA–Histidine interaction and the surface NTA functionality was not influenced. The structure of LHCII on the surface still kept the native structure as if it was in the solution, as can be seen by the identical fluorescence emission spectra in solution and on the surface, showing 100% efficient energy transfer from chlorophyll b to chlorophyll a (cf. Fig. 13(C)). Upon excitation of chlorophyll b by the  $\lambda = 473$  nm laser, LHCII both on the surface and in solution shows only chlorophyll a emission at about  $\lambda = 680$  nm. No chlorophyll b contribution at about  $\lambda = 660$  nm is seen which would be indicative of partial disintegration or structural distortion of the complex.

#### 4.8. Ionic Strength Dependence of PNA/DNA Hybridization

SPFS has been extensively used in characterizing DNA hybridization on surfaces. Due to the small molecular weight of DNA oligonucleotide molecules, it

is quite difficult to detect their binding signal with mere SPR, especially when using diluted catcher probe matrices. In contrast, SPFS has shown extraordinary femtomolar sensitivity in DNA studies, which also allows for investigations on substantially ( $>40$  times) diluted probe surfaces [44]. This sensitivity has greatly enabled a vast amount of in-depth conformational and functional DNA investigations on surfaces.

Here, we provide an example of the ionic strength dependence of PNA/DNA hybridization. The binding matrix was fabricated with biotinylated PNA probes (biotin-5'-ethylene glycol<sub>(9)</sub>-TGACATCACAATA-3') binding on the extensively used streptavidin matrix [9,10,16,20,26]. The DNA target length was varied from 15 bases to 75 bases, called T15\* (Cy5-5'-TAGTTGTGATGTACA-3'), T45\* (Cy5-5'-T<sub>(15)</sub>TAGTTGTGATGTACAT<sub>(15)</sub>-3'), and T75\* (Cy5-5'-T<sub>(30)</sub>TAGTTGTGATGTACAT<sub>(30)</sub>-3'), respectively. As shown in Fig. 14(A), a series of concentrations of T15\* ranging from 10 to 250 nM were used to titrate the PNA probe surface at 10 mM or 1 M Na<sup>+</sup> concentrations. It can be seen that the variation of the ionic strength did not make a difference in the responses of PNA P2 hybridizing with the 15-base oligonucleotides. However, the ionic strength significantly influenced the hybridization of the longer DNA targets. For T45\* (Fig. 14(B)) and T75\* (Fig. 14(C)), the fluorescence upon saturation ([T45\*] = [T75\*] = 250 nM) at 1 M Na<sup>+</sup> was enhanced by a factor of 2.35 and 2.8, respectively, with respect to the fluorescence level found at 10 mM. The corresponding surface coverage are expected to be even higher, because the surface plasmon field excited fluorescence arising from DNA binding is underestimated in a medium with higher salt concentration, which randomizes the DNA conformation and shortens the dye to metal distance [44]. We infer that although PNA is electrostatically neutral [45], the binding of DNA target strands upon hybridization still charges the surface resulting in a PNA/DNA hybridization that is highly sensitive to the ionic strength in the solution. With the higher axial charge of longer target DNA strands, the increase of the target length greatly enhances the corresponding electrostatic field, which induces severe electrostatic crosstalk and hinders the surface hybridization in low salt condition. Higher concentrations of cations in higher ionic strength buffers help to reduce the duplex–duplex crosstalk by shielding the charges on the DNA.

We can expect that in addition to adding more cations, increasing the spacing between probes on the surface will help to reduce the overlap between the electrostatic fields of and hence the crosstalk between two neighboring bound DNA molecules. The effective density of PNA probe can be reduced by the co-assembly of a completely non-complementary sequence to the streptavidin matrix. Three probe surfaces (1:0, 1:1, and 1:3) were prepared accordingly by tuning the ratio of non-complementary probes in the mixture to be 0%, 50%, and 75%, respectively. T75\* was tested for the hybridization since it possesses the highest charge. Fig. 15 presents the hybridization of T75\* on three probe surfaces at 10 mM and 1 M Na<sup>+</sup> buffer solution, respectively. Apparently, the kinetic curves obtained at low ionic strength approach those obtained

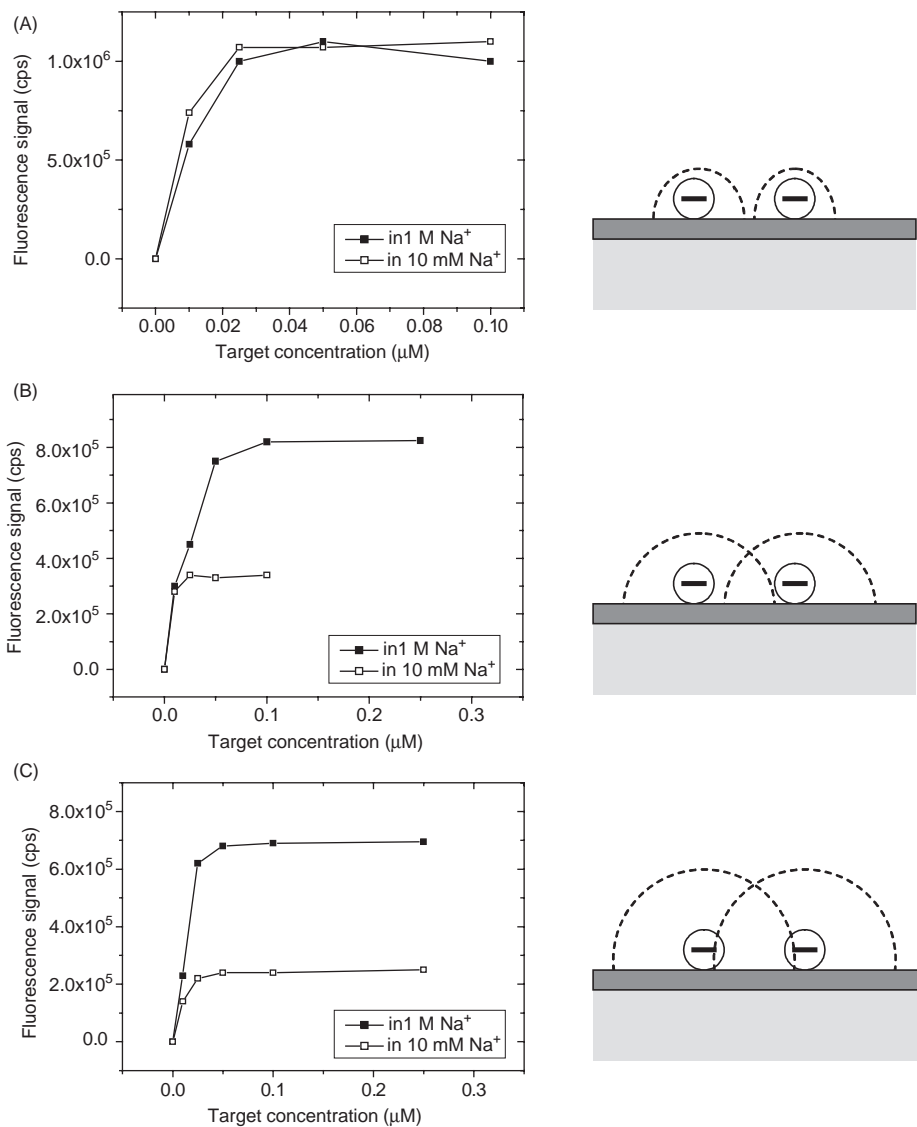


**Fig. 14.** Concentration titrations of T15\* (A), T45\* (B), and T75\* (C) target oligonucleotides on PNA probe surfaces at 10 mM or 1 M  $\text{Na}^+$  concentration, respectively. On the right side, schematic drawings represent the overlapping of the electrostatic fields between neighboring DNA strands.

at high ionic strength with the higher dilution of specific probes in the mixture, which indicates the efficient spacing of the specific probe and, hence, the subsequently bound DNA targets. The tendency implies that the electrostatic interaction among the bound targets will eventually vanish at low ionic strength

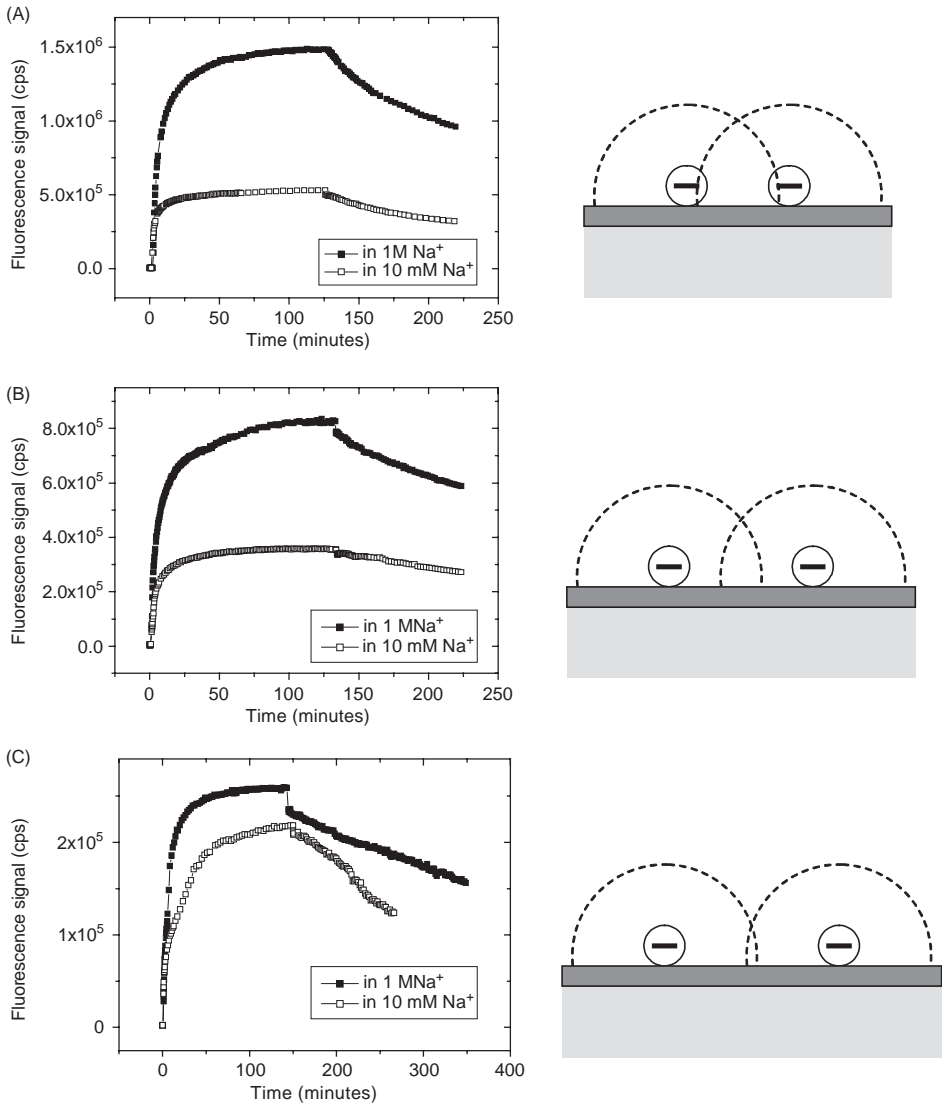


**Fig. 15.** Kinetic investigation of T75\* (250 nM) on 1:0 (A), 1:1 (B), 1:3 (C) diluted PNA probe surface at 10 mM or 1 M Na<sup>+</sup> concentration. On the right side, schematic drawings represent the overlapping of electrostatic field between neighboring DNA strands.

conditions with the further dilution of the probe density. This probe dilution strategy is highly beneficial in obtaining a Langmuir type binding of PCR products at low ionic strength [26], a condition necessary to separate the double strands of PCR products.

## 5. SURFACE PLASMON DIFFRACTION SENSOR

In contrast to SPFS, SPR, and SPDS are tools that can study biomolecular interactions without external labels. They share the same category of “label-free biosensors” with the reflectometry interference spectroscopy (RIfS) [46], waveguide spectroscopy [47], quartz crystal microbalance (QCM) [48], micro-cantilever sensors [49], etc. Although the label-free sensors cannot compete with SPFS in terms of sensitivity [11], they are however advantageous in avoiding any additional cost/time in labeling the molecules. In particular, the label-free detection concept eliminates undue detrimental effects originating from the labels that may interfere with the fundamental interaction. In this sense, it is worthwhile to develop and improve such sensors as instruments complementary to those ultra-sensitive sensors that require labels.

In 1987, our group has proposed that the diffraction efficiency of dielectric gratings can be greatly amplified by employing surface plasmon fields [14,15]. In this approach, a surface plasmon wave is excited and diffracted by a dielectric grating structure and back converted into light radiation. The application of this diffraction phenomenon for biological sensing involves the use of micro-patterning technique, e.g., micro-contact print ( $\mu$ CP) [50], in order to generate a surface grating structure composed of functional and non-functional zones. Generally, receptor molecules are immobilized on the functional area. The grating amplitude is subsequently modulated by the association/dissociation events of the analyte to the receptor molecules and is monitored by recording the variation in the diffraction intensity of one of the diffraction orders.

### 5.1. Diffraction Enhancement by Surface Plasmon Fields

According to the theory (cf. Chapter 2), the surface plasmon field enhancement greatly boosts the diffraction intensity. This is experimentally demonstrated by an identical polystyrene (PS) pattern on Au and glass surfaces respectively, generated by UV-ablation (254 nm) through a copper grid mask. Well-defined PS patterns could be clearly seen in surface plasmon microscopy images or depicted by a surface profiler. These PS patterns induced strong diffraction patterns visible to the naked eyes (cf. Fig. 16), in accordance with their Fourier transform patterns.

A glass prism was used to couple the light in and generate an evanescent field on both the glass and the Au samples. The prism attached to the glass sample defined a total internal reflection (TIR) scenario. In contrast, surface plasmon mode could be excited on the Au sample (cf. Fig. 4). As shown in Fig. 17, by setting the laser incident angle at the resonance angle, a series of diffraction peaks could be recorded in the vicinity of the specularly reflected laser beam in a nearly symmetrical distribution with a small, uniform angular spacing. The intensities of these orders were significantly higher than those found for the diffraction by the PS pattern in the TIR diffraction mode. An

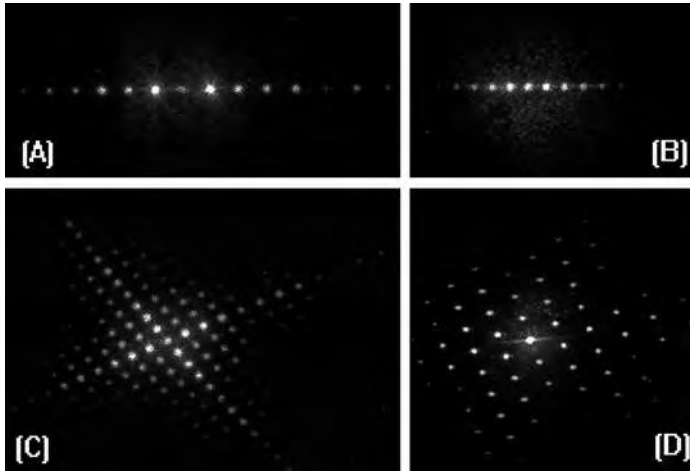


**Fig. 16.** Photographs of the surface plasmon field-enhanced diffraction patterns generated by various PS patterns on Au surfaces (A) parallel lines 40  $\mu\text{m}$  wide, separated by 62.5  $\mu\text{m}$ ; (B) parallel lines 28  $\mu\text{m}$  wide, separated by 83  $\mu\text{m}$ ; (C) square grid pattern, bar width 28  $\mu\text{m}$ , grid width 83  $\mu\text{m}$ , [D] hexagonal grid pattern, bar width 8  $\mu\text{m}$ , hexagonal grid width 48  $\mu\text{m}$ .

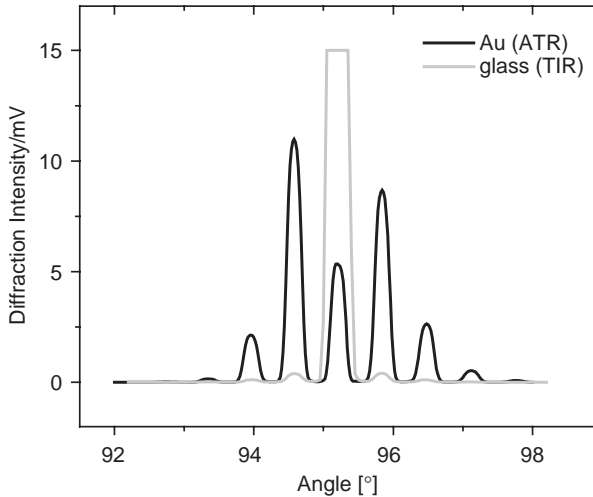


**Fig. 17.** The diffraction signal obtained from an identical PS pattern on Au and a glass surface, respectively. For the surface plasmon diffraction on Au and TIR diffraction on glass, the laser incident angle in both cases was set at  $\sim 47^\circ$  where the laser energy could be resonantly coupled into the surface plasmon mode.

enhancement factor of  $\sim 18\text{--}20$  was obtained by comparing the corresponding diffraction intensities in the attenuated total reflection (ATR) and TIR configuration, respectively. The gain in diffraction efficiency represents a sensitivity enhancement for sensing applications.

## 5.2. Quadratic Effect of Diffraction Intensity

Next, we demonstrate that strong diffraction signals can be generated by a monolayer of antibodies. Furthermore, the quadratic dependence of the diffraction intensity on the grating amplitude (cf. Eq. (5)) can be shown by this antibody binding system. Experimentally, the Au surface was patterned by a 1:9 mixed biotin SAM by the  $\mu\text{CP}$  technique [17,50], followed by passivating the remaining Au area by an OEG SAM. Next, an anti-biotin antibody 2F5 solution was injected and strong diffraction signal was observed as a result of the antibody monolayer formation (cf. Fig. 18(B)). The monolayer could be completely removed by a regeneration solution, and consequently the diffraction

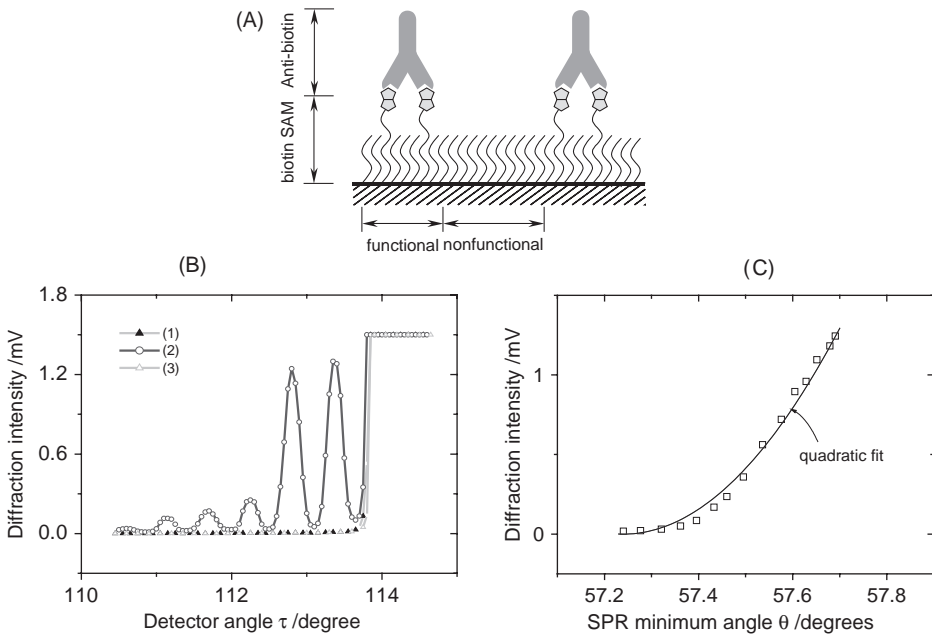


**Fig. 18.** (A) Schematic drawing of an antibody binding onto a patterned biotin SAM surface. (B) Diffraction scans obtained on the patterned surface (functional strip width =  $42\ \mu\text{m}$ ,  $\Lambda = 100\ \mu\text{m}$ , with functional lines containing 10% biotin, non-functional lines exposing 100%  $-\text{OH}$  groups) before (1), after (2) the anti-biotin antibody binding and after (3) the regeneration of the sensor surface by treatment with 4 M GdnHCl. (C) Diffraction intensities of the 1st diffraction order versus the corresponding SPR minimum angles.

peaks disappeared. Using a low concentration of antibody, the relation between the SPR signal (minimum angle shift upon antibody binding) and the diffraction signal can be depicted. As presented in Fig. 18(C), one finds a clear quadratic relationship between the SPR and the diffraction signal. Considering that the SPR minimum shift is a linear measure of the surface grating amplitude  $\Delta nd$ , the relationship is in agreement with the theoretical expectation (Eq. (5)).

### 5.3. SPDS for Oligonucleotide Hybridization

With the features of field-enhanced, quadratic signal amplification and its self-referencing property [16–18], SPDS has shown improved sensitivity compared to the normal SPR in biosensing applications. Especially, it generates a significantly improved signal-to-noise ratio in the study of oligonucleotide hybridization, where a classical SPR sensor is usually poorly qualified.

Therefore, we use the oligonucleotide hybridization as an example to demonstrate the applicability of SPDS biosensing. To the end we titrate two label-free DNA oligonucleotide targets T15-0 (5'-TAGTTGTGATGTACA-3') and T15-1 (5'-TAGTTGTGACGTACA-3') with surface-tethered DNA oligonucleotide probe (biotin-5'-T<sub>(15)</sub>TGTACATCACTA-3'). The T15-0 was fully complementary to the probe; while one base mismatch was designed in the sequence of T15-1.

A multi-layer surface architecture composed of SAM/streptavidin/probe was employed for the hybridization study (Fig. 19). Since the streptavidin density on the functional stripes was identical to that on a homogenous surface [9], i.e.,  $2.2 \times 10^{12}$  molecules  $\text{cm}^{-2}$ , the probe density was estimated to be  $\sim 2.9 \times 10^{12}$  molecules  $\text{cm}^{-2}$  by knowing from the diffraction signal the binding stoichiometry between streptavidin and the probe (ca. 0.75) [16].

Next, the target DNA solutions were sequentially injected and thus surface hybridization initiated. By recording the equilibrium hybridization signal of the target to the probe derivatized surface at different bulk target concentrations  $c_0$  (with the total span of the target concentrations ranging from 1 nM to 3  $\mu\text{M}$ ), the affinity constants  $K_A$  of target/probe could be determined (cf. Fig. 19(B) and (C)). The normalized equilibrium response is plotted against the corresponding target concentrations  $c_0$  in Fig. 20.

The data are fitted by a Langmuir adsorption isotherm based on a 1:1 interaction model (cf. Eqs. (10), and (11)). From the fit, the affinity constants for T15-0 and T15-1 are found to be  $K_A = 4.2 \times 10^8$  and  $1.9 \times 10^7 \text{ M}^{-1}$ , respectively. The affinity of the T15-1 target, is lower by more than one order of magnitude due to a single A–C mismatch, which is in agreement with earlier fluorescence investigations [9]. A Langmuirian behavior of the 15-mers hybridization processes is also implied by the fitting.

The saturation response of the T15-1 target at 3  $\mu\text{M}$  is estimated to be  $\sim 1.8 \times 10^{12}$  molecules  $\text{cm}^{-2}$  by comparing the diffraction signal between probe and target and determining their binding stoichiometry. The response from the 5 nM

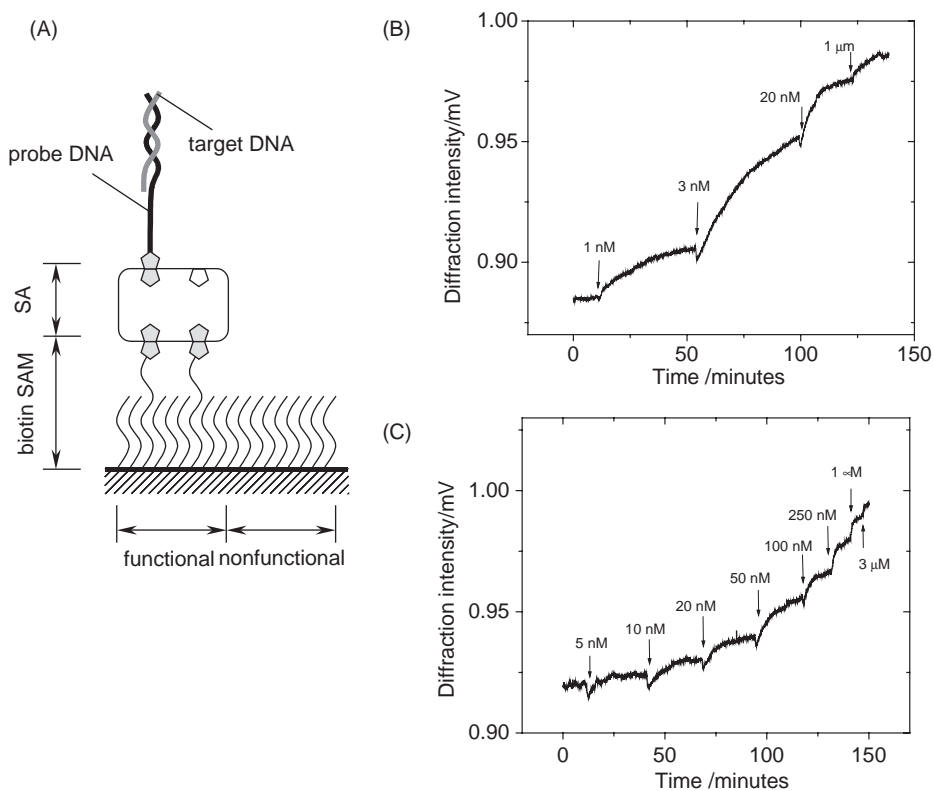


**Fig. 19.** (A) Schematic drawing of the multi-layer architecture built on the functional pattern surface (functional strip width =  $42\ \mu\text{m}$ ,  $\Lambda = 100\ \mu\text{m}$ , with functional lines containing 10% biotin, non-functional lines exposing 100%  $-\text{OH}$  groups). Kinetic curves of the titration of T15-0 (B) and T15-1 (C), respectively, with increasing concentrations.

T15-1 solution is considered to be the preliminary LOD of the diffraction DNA sensor, producing  $\sim 6\%$  of its saturation response and being easily resolvable above the baseline fluctuation. By this, SPDS was claimed to be able to detect at least  $1.1 \times 10^{11}$  molecules  $\text{cm}^{-2}$  of the 15-mer oligonucleotide, equivalent to a mass concentration of  $\sim 800\ \text{pg cm}^{-2}$ . This preliminary LOD level is already comparable to one of the best performance of label-free SPR sensing using near-infrared imaging by reported Corn's group [51], with an LOD of 10 nM for 18-mer oligonucleotide, corresponding to  $\sim 10^{11}$  molecules  $\text{cm}^{-2}$ .

## 6. CONCLUSION

This contribution has attempted to summarize a wide variety of work from our group employing SPR, SPFS, and SPDS analysis, specifically for investigations

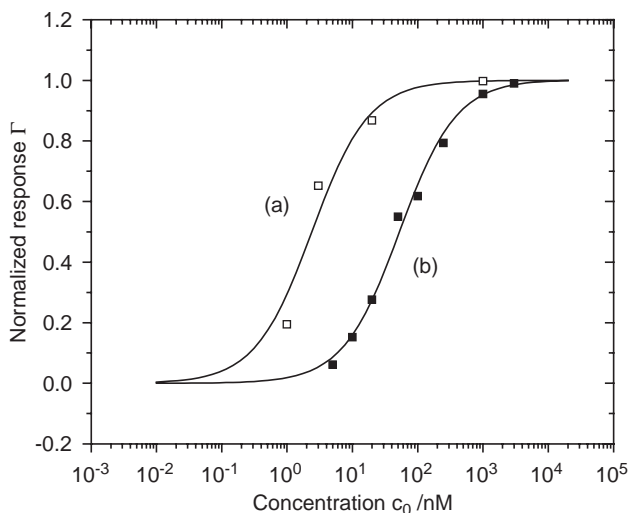


**Fig. 20.** The equilibrium signals of the titration of surface bound probe oligonucleotide with T15-0 (a) and T15-1 (b), respectively. The values are normalized to the saturation responses of the corresponding target at its maximum concentration.

relevant to biofunctional, bio-affinity aspects. The SPR has shown already its big impact on interfacial analysis. As newly developed tools based on the principle of SPR, SPFS, and SPDS have also proven to be valuable tools, concerning their improved sensitivity compared to SPR. In particular, the powerful combination of these three methods has the potential to generate more information and reveal details of biofunctional interfaces.

## REFERENCES

- [1] E. Kretschmann and H. Raether, *Z. Naturforsch A*, 23 (1968) 2135.
- [2] G. Höhler (ed.), *Surface Plasmons on Smooth and Rough Surfaces and on Gratings*, Springer-Verlag, Berlin, 1988.
- [3] A. Otto, *Z. Physik.*, 216 (1968) 398.
- [4] G. S. Agarwal, *Phys. Rev. B*, 8 (1973) 4768.
- [5] J. D. Swalen, *J. Mol. Electron.*, 2 (1986) 155.
- [6] A. G. Frutos, S. C. Weibel and R. M. Corn, *Anal. Chem.*, 71 (1999) 3935.
- [7] H. Knobloch, H. Brunner, A. Leitner, F. Aussenegg and W. Knoll, *J. Chem. Phys.*, 98 (1993) 10093.
- [8] T. Liebermann and W. Knoll, *Colloid Surf. A*, 171 (2000) 115.
- [9] T. Liebermann, W. Knoll, P. Sluka and R. Herrmann, *Colloid Surf. A*, 169 (2000) 337.
- [10] T. Neumann, M.-L. Johansson, D. Kambhampati and W. Knoll, *Adv. Func. Mate.*, 12 (2002) 575.

- [11] F. Yu, B. Persson, S. Löfås and W. Knoll, *J. Am. Chem. Soc.*, 126 (2004) 8902.
- [12] R. Naraoka, H. Okawa, K. Hashimoto and K. Kajikawa, *Opt. Commun.*, 248 (2005) 249.
- [13] M. Osawa, *Top. Appl. Phys.*, 81 (2001) 163.
- [14] B. Rothenhäusler and W. Knoll, *Opt. Commun.*, 63 (1987) 301.
- [15] B. Rothenhäusler and W. Knoll, *Appl. Phys. Lett.*, 51 (1987) 783.
- [16] F. Yu, D. Yao and W. Knoll, *Nucleic Acids Res.*, 32 (2004) e75.
- [17] F. Yu, S. Tian, D. Yao and W. Knoll, *Anal. Chem.*, 76 (2004) 3530.
- [18] F. Yu and W. Knoll, *Anal. Chem.*, 76 (2004) 1971.
- [19] T. E. Plowman, W. M. Reichert, C. R. Peters, H. K. Wang, D. A. Christensen and J. N. Herron, *Biosens. Bioelectron.*, 11 (1996) 149.
- [20] T. Liebermann and W. Knoll, *Langmuir*, 19 (2003) 1567.
- [21] B. Herman and J. J. Lemasters, *Optical Microscopy: Emerging Methods and Applications*, Academic Press, New York, 1993.
- [22] W. L. Barnes, *J. Mod. Optic.*, 45 (1998) 661.
- [23] J. B. Goh, P. L. Tam, R. W. Loo and M. C. Goh, *Anal. Biochem.*, 313 (2003) 262.
- [24] K. A. Nelson, R. Casalegno, R. J. D. Miller and M. D. Fayer, *J. Chem. Phys.*, 77 (1982) 1144.
- [25] F. Yu, D. Yao and W. Knoll, *Anal. Chem.*, 75 (2003) 2610.
- [26] D. Yao, F. Yu, J. Kim, J. Scholz, P. E. Nielsen, E.-K. Sinner and W. Knoll, *Nucleic Acids Res.*, 32 (2004) e177.
- [27] G. Stengel and W. Knoll, *Nucleic Acids Res.*, 33 (2005) e69.
- [28] R. Robelek, L. Niu, E. L. Schmid and W. Knoll, *Anal. Chem.*, 76 (2004) 6160.
- [29] J. M. Harris (ed.), *Poly(ethylene glycol) Chemistry*, Plenum Press, New York, 1992.
- [30] A. J. Pertsin and M. Grunze, *Langmuir*, 16 (2000) 8829.
- [31] E. Engvall and P. Perlmann, *J. Immunol.*, 109 (1972) 129.
- [32] M. Zhang and M. Ferrari, *Biotechnol. Bioeng.*, 56 (1997) 618.
- [33] G. B. Sigal, M. Mrksich and G. M. Whitesides, *J. Am. Chem. Soc.*, 120 (1998) 3464.
- [34] T. Arakawa and S. N. Timasheff, *Biochemistry*, 23 (1984) 5924.
- [35] C. Duschl, A. F. Sevin-Landais and H. Vogel, *Biophys. J.*, 70 (1996) 1985.
- [36] L. Nieba, A. Krebber and A. Pluckthun, *Anal. Biochem.*, 234 (1996) 155.
- [37] K. Vasilev, W. Knoll and M. Kreiter, *J. Chem. Phys.*, 120 (2004) 3439.
- [38] S. Löfås and B. Johnsson, *J. Chem. Soc., Chem. Commun.*, 21 (1990) 1526.
- [39] P. R. Edwards, A. Gill and D. V. Pollardknight, *Anal. Biochem.*, 231 (1995) 210.
- [40] P. Schuck, *Annu. Rev. Biophys. Biomol. Struct.*, 26 (1997) 541.
- [41] W. Kuhlbrandt, D. N. Wang and Y. Fujiyoshi, *Nature*, 367 (1994) 614.
- [42] P. J. Booth and H. Paulsen, *Biochemistry*, 35 (1996) 5103.
- [43] J. Porath, J. Carlsson, I. Olsson and G. Belfrage, *Nature*, 258 (1975) 598.
- [44] D. Yao, J. Kim, F. Yu, P. E. Nielsen, E.-K. Sinner and W. Knoll, *Biophys. J.*, 88 (2005) 2745.
- [45] M. Egholm, O. Buchardt, L. Christensen, C. Behrens, S. M. Freier, D. A. Driver, R. H. Berg, S. K. Kim, B. Norden and P. E. Nielsen, *Nature*, 365 (1993) 566.
- [46] A. Brecht, J. Piehler, G. Lang and G. Gauglitz, *Anal. Chim. Acta*, 311 (1995) 289.

- [47] R. Cush, J. M. Cronin, W. J. Stewart, C. H. Maule, J. Molloy and N. J. Goddard, *Biosens. Bioelectron.*, 8 (1993) 347.
- [48] K. Yun, E. Kobatake, T. Haruyama, M. L. Laukkanen, K. Keinanen and M. Aizawa, *Anal. Chem.*, 70 (1998) 260.
- [49] G. Wu, R. H. Datar, K. M. Hansen, T. Thundat, R. J. Cote and A. Majumdar, *Nat. Biotechnol.*, 19 (2001) 856.
- [50] Y. N. Xia and G. M. Whitesides, *Angew. Chem. Int. Ed.*, 37 (1998) 551.
- [51] B. P. Nelson, T. E. Grimsrud, M. R. Liles, R. M. Goodman and R. M. Corn, *Anal. Chem.*, 73 (2001) 1.

This page intentionally left blank

## Chapter 4

# Probing Surfactant Adsorption at the Solid–Solution Interface by Neutron Reflectometry

J. Penfold<sup>a,\*</sup>, R.K. Thomas<sup>b</sup>

<sup>a</sup>*Rutherford Appleton Laboratory, ISIS Facility, Chilton, Didcot, OXON, OX11 0QX, UK*

<sup>b</sup>*Physical and Theoretical Chemistry Laboratory, Oxford University, South Parks Road, Oxford, OXON, OX1 2JD, UK*

## 1. INTRODUCTION

Surfactant adsorption at the solid–solution interface plays an important role in many industrial and technological applications, such as detergency, fabric and hair conditioners, dyeing, mineral flotation, colloidal dispersion, corrosion inhibition, lubrication, and oil recovery. The nature of the adsorbed layer and the way in which it modifies surface properties depends upon the nature of the surfactant and its interaction with the surface. This can include electrostatic attraction, hydrogen or covalent bonding, and hydrophobic or solvation forces. Depending upon the amount adsorbed and the structure of the adsorbed layer (orientation of the surfactant at the interface), the surface can become more hydrophilic or more hydrophobic. In general terms, ionic surfactants adsorb to hydrophilic surfaces of opposite charge by electrostatic attraction, and the nonionic polyoxyethylene-based surfactants by hydrogen bonding between surface hydroxyl groups and the ether oxygens of the ethoxy groups. Such adsorption is cooperative and is initiated at the critical micellar concentration, cmc, to form a ‘fragmented bilayer’ or ‘flattened aggregated’ (micellar) structure at the interface. Depending upon the strength of the interaction, the outer layer is relatively easily removed, and the surface is left strongly hydrophobic. In contrast, the adsorption to hydrophobic surfaces is generally of the form of a monolayer, similar to that observed at the air–solution interface, and in this case, the surface will become hydrophilic.

---

\*Corresponding author. E-mail: j.penfold@rl.ac.uk

To characterize and understand the nature of surfactant adsorption at the solid–solution interface, it is not sufficient to just measure the amount adsorbed, but information on the kinetics of adsorption and on the structure of the adsorbed layer is required. A variety of ‘classical’ techniques, such as ‘solution depletion’ [1], measurement of the differential enthalpy of adsorption [2], fluorescence spectroscopy [3], and light scattering [4], have traditionally provided information about adsorbed amounts. These techniques are in general applied to dispersed or colloidal solid phases, such as polystyrene latex, colloidal silica, and clay particles, and any structural information is only indirectly implied. Light scattering [4], small angle X-ray scattering (SAXS) [5], and small angle neutron scattering (SANS) [6], however, provide some structural information on surfactant adsorption onto colloidal particles; but the scope of such measurements is limited by sensitivity and the requirement to maintain colloidal stability. More recently, the development of techniques such as optical reflectometry [7], ellipsometry [8], spectroscopic methods such as sum frequency spectroscopy (SFS) [9], second harmonic generation (SHG) [10], surface plasmon resonance (SPR) [11], and surface sensitive FTIR [12], neutron [13] and X-ray [14] reflectivity, and atomic force microscopy [15] has provided the opportunity to study the kinetics of adsorption and to obtain detailed structural information about the adsorbed layer. In recent years, these techniques have started to provide a wealth of new and complementary information on surfactant adsorption.

In the last 10–15 years, neutron reflectometry has been developed into a powerful technique for the study of surface and interfacial structure, and has been extensively applied to the study of surfactant and polymer adsorption and to determine the structure of a variety of thin films [14, 16]. Neutron reflectivity is particularly powerful in the study of organic systems, in that hydrogen/deuterium isotopic substitution can be used to manipulate the refractive index distribution without substantially altering the chemistry. Hence, specific components can be made visible or invisible by refractive index matching. This has, for example, been extensively exploited in studying surfactant adsorption at the air–solution interface [17]. In this chapter, we focus on the application of neutron reflectometry to probe surfactant adsorption at the solid–solution interface.

The scope of the chapter will include an introduction to the technique of neutron reflectometry, and how it is applied to the study of surfactant adsorption at the planar solid–solution interface, to obtain adsorbed amounts and details of the structure of the adsorbed layer. The advantages and limitations of the technique will be put in the context of other complementary surface techniques. Recent results on the adsorption of a range of anionic, cationic and nonionic surfactants, and surfactant mixtures onto hydrophilic, hydrophobic surfaces, and surfaces with specifically tailored functionality will be described. Where applicable, direct comparison with the results from complementary techniques will be made and discussed.

## 2. NEUTRON REFLECTIVITY

### 2.1. Basic Principles and Equations

The specular reflectivity of neutrons, like the analogous light or X-ray reflectivity, from a surface or interface provides information about the neutron refractive index gradient or distribution in the surface region and in a direction orthogonal to the plane. This can often be simply related to a composition or concentration profile in the direction orthogonal to the surface, to provide directly information about adsorption and the structure of the adsorbed layer.

In the simplest case of the interface between two bulk media, the reflectivity is related to the refractive index difference across the interface, and is described by Fresnel's Law [18]. The refractive index,  $n$ , is related to the neutron scattering length density, such that

$$n^2 = 1 - \frac{\lambda^2}{\pi} \rho \quad (1)$$

where  $\lambda$  is the neutron wavelength and  $\rho$  the scattering length density given by

$$\rho = \sum_i b_i n_i \quad (2)$$

where  $b_i$  is the scattering length and  $n_i$  the number density of species  $i$ . The refractive index is not a convenient term to use in neutron reflectivity as it is  $\sim 1.0$  (in contrast to light), and the scattering length density is a more relevant term. For most materials, the neutron scattering length,  $b$ , is positive (hydrogen is one of the exceptions), and so  $n$  is generally  $< 1.0$ . This highlights another difference compared with light; in general, total external reflection occurs as most materials have a refractive index less than air. Therefore, for example, at the air–D<sub>2</sub>O interface, there will be total reflection from the interface below the critical glancing angle of incidence. However, the information about the surface/interface structure occurs at grazing angles beyond the critical angle.

In the simple case of a monolayer (thin layer) of uniform composition and density at the interface between two bulk media (say air and a substrate), the neutron reflectivity can be given exactly as [19]

$$R = |\mathbf{R}|^2 = \frac{r_{01}^2 + r_{12}^2 + 2r_{01}r_{12} \cos(2\beta_1)}{1 + r_{01}^2 r_{12}^2 + 2r_{01}r_{12} \cos(2\beta_1)} \quad (3)$$

where the subscripts 0, 1, 2 refer to the air phase, the monolayer, and the substrate,  $\beta$  the optical path length,  $\beta_1 = q_1 \tau_1$ ,  $\tau_1$  the monolayer thickness, and  $q_1$  the neutron wave vector in the monolayer and normal to the interface. The reflectivity is usually expressed in terms of the wave vector transfer,  $\kappa$ , where

$$\kappa = \frac{4\pi \sin \theta_0}{\lambda} = 2q_0 \quad (4)$$

and  $\theta_0$  is the grazing angle of incidence. The Fresnel coefficients,  $r_{ij}$ , are then

$$r_{ij} = \frac{r_j - r_i}{r_j + r_i} \quad (5)$$

The critical wave-vector transfer (below which total reflection takes place) is

$$\kappa_{ci}^2 = 4q_{ci}^2 = 16\pi(\rho_j - \rho_i) \quad (6)$$

such that the Fresnel coefficients can be expressed in terms of  $\kappa$  and  $\kappa_{ci}$

$$r_{ij} = \frac{(\kappa^2 - \kappa_{ci}^2)^{1/2} - \kappa}{(\kappa^2 - \kappa_{ci}^2)^{1/2} + \kappa} \quad (7)$$

For a simple sharp interface between air and the substrate (Fresnel's law), Eq. (3) becomes

$$R = |r_{01}|^2 = \frac{16\pi^2}{\kappa^4} (\Delta\rho)^2 \quad (8)$$

and for a simple monolayer at the interface

$$R = \frac{16\pi^2}{\kappa^4} [(\rho_1 - \rho_0)^2 + (\rho_2 - \rho_1)^2 + 2(\rho_1 - \rho_0)(\rho_2 - \rho_1) \cos \kappa\tau] \quad (9)$$

Although only approximate, it is sufficient to describe the thin monolayer observed in surfactant absorption, and this is the essence of the measurement of surfactant adsorption.

So far, what has been described is applicable to any interface. However, the air-solution interface is the simplest to consider; and in the context of surfactant and mixed surfactant adsorption, we discuss that interface initially. The particular feature that makes the technique so powerful and particularly surface sensitive is the different scattering powers of hydrogen and deuterium (hydrogen has a negative scattering length of  $-0.374 \times 10^{-12}$  cm and deuterium a larger positive value of  $0.6764 \times 10^{-12}$  cm). Hence, D/H isotopic substitution can be used in organic systems to label particular components or fragments by refractive index matching, whilst leaving the chemistry essentially unaltered. For a 0.088 mole fraction  $D_2O/H_2O$  mixture, null reflecting water (nrw), the scattering length density is zero (a refractive index of unity), and there will be no specular reflectivity at the interface between that and air (in Eq. (8)  $\Delta\rho$  is zero). Specular reflection will occur if there is a monolayer of deuterated material at the interface, and Eq. (9) will become

$$\frac{\kappa^4}{16\pi^2} R = 2\rho^2(1 - \cos \kappa\tau) = 4b^2n^2 \sin \frac{\kappa\tau}{2} \quad (10)$$

Hence, treating the adsorbed layer as a thin film of uniform density the adsorbed amount,  $\Gamma$ , can be determined from the thickness,  $\tau$ , and the scattering

length density,  $\rho$ , such that [17]

$$\Gamma = \frac{\rho\tau}{N_a b} = \frac{1}{N_a A} \quad (11)$$

where  $A$  is the area/molecule, and  $N_a$  the Avogadro's number.

A similar expression to Eq. (10) can be obtained if it is assumed that the monolayer has a Gaussian distribution rather than a uniform form, to give [17]

$$\frac{\kappa^4}{16\pi^2} R = \frac{\pi\sigma^2 \rho_m^2 \kappa^2}{4} (\exp -\kappa^2 \sigma^2) \quad (12)$$

and  $\Gamma = (\pi\sigma\rho_m)^{1/2}/2N_a$ , where  $\sigma$  is the  $1/e$  width and  $\rho_m$  the scattering length density at the maximum of the distribution. In practice, either functional form can be used.

It is straightforward to extend Eq. (11) to take into account the adsorption of a multi-component mixture [17], such that for a binary mixture, Eq. (11) becomes

$$\rho = \frac{1}{\tau} \left( \frac{b_1}{A_1} + \frac{b_2}{A_2} \right) \quad (13)$$

where the subscripts now refer to the two different components. Measurements with an aqueous phase with a refractive index  $< 1.0$ , for example  $D_2O$ , then provides a reflectivity profile from the interface, which provides information not just about the adsorbed layer, but about the adsorbed layer in relationship to the subphase, the extent of overlap between the solvent and surface layer.

It is then straightforward to extend this approach to the solid–solution interface. For this interface Eqs. (3)–(9) are identical, but replacing the initial air phase (subscript 0) by the solid phase with a refractive index that is different from unity. In this case, the neutron beam is then incident at the solid–solution interface, by transmission through the solid upper phase (see later for more details on the experimental arrangement). By analogy with the air–solution interface, an appropriate mixture of  $D_2O/H_2O$  can be used to index match the solvent to the solid phase, or a specific ‘contrast’, such as solid– $D_2O$ , can be engineered; and this is often used to maximize the reflectivity signal. Alternatively, a range of different solute and solvent ‘contrast’ are used to maximize sensitivity. For the solid– $D_2O$  case, the expression equivalent to Eq. (11) becomes

$$\Gamma = \frac{d(\rho_s - \rho_2)}{N_a V(\rho_s - \rho_a)} \quad (14)$$

where  $d$  is the layer thickness,  $\rho_s$ ,  $\rho_a$ , and  $\rho_2$  the solvent, adsorbate, and layer scattering length densities, and  $V$  the adsorbate volume. This is equally applicable to a single component or a multi-component mixture, on the assumption that the components of the mixture can be index matched to the solvent.

Beyond the simple thin surfactant monolayer, the reflectivity can be interpreted in terms of the internal structure of the layer, and can be used to determine thicker layers and more complex surface structures, and this can be done in two different ways. The first of these uses the optical matrix method [18, 19] developed for thin optical films, and relies on a model of the surface structure being described by a series or stack of thin layers. This assumes that in optical terms, an application of Maxwell's equations and the relationship between the electric vectors in successive layer leads to a characteristic matrix per layer, such that

$$C_j = \begin{bmatrix} e^{i\beta_{j-1}} & r e^{i\beta_{j-1}} \\ r e^{-i\beta_{j-1}} & e^{-i\beta_{j-1}} \end{bmatrix} \quad (15)$$

For  $n$  layers, the matrices for each layer are multiplied together,  $[C] = [C_1][C_2] \dots [C_{n+1}]$ , to give the resultant reflectivity from the elements of the final  $2 \times 2$  matrix such that,  $R = cc^*/aa^*$ . In practice, recurrence relationships between the Fresnel coefficients in the successive layers can be used to provide an efficient calculation. Furthermore, following the approach of Nevot and Croce [20], a Gaussian roughness or diffuse profile can be included at each interface in the stack, such that

$$r'_j = r_j \exp -0.5\kappa_j\kappa_{j-1}\sigma^2 \quad (16)$$

The second method uses the kinematic approximation in which the reflectivity is given as [21]

$$R = \frac{16\pi^2}{\kappa^2} |\hat{\rho}(\kappa)|^2 = \frac{16\pi^2}{\kappa^4} |\hat{\rho}'(\kappa)|^2 \quad (17)$$

where  $\hat{\rho}(\kappa)$  is the one-dimensional Fourier transform of the scattering length density profile normal to that interface,  $\rho(z)$

$$\hat{\rho}(\kappa) = \int_{-\infty}^{\infty} \rho(z) \exp(i\kappa z) dz \quad (18)$$

and  $\hat{\rho}'(\kappa)$  is the corresponding Fourier transform of the derivative,  $\rho'(z)$ .

To date, the matrix method has been the preferred method applied for the analysis of neutron reflectivity data from the solid–solution interface, but in many cases, the kinematic approximation offers more flexibility. This has been exploited in studies at the air–solution interface, where both approaches are extensively used.

## 2.2. Application to the Solid–Solution Interface

The transmissions of thermal/cold neutrons through single crystal materials such as silicon and quartz (providing the orientation and the neutron wavelength combinations do not give rise to Bragg scattering) is sufficiently high ( $\sim 80\%$  for a 100 mm path length) that neutron reflectivity at the solid–solution

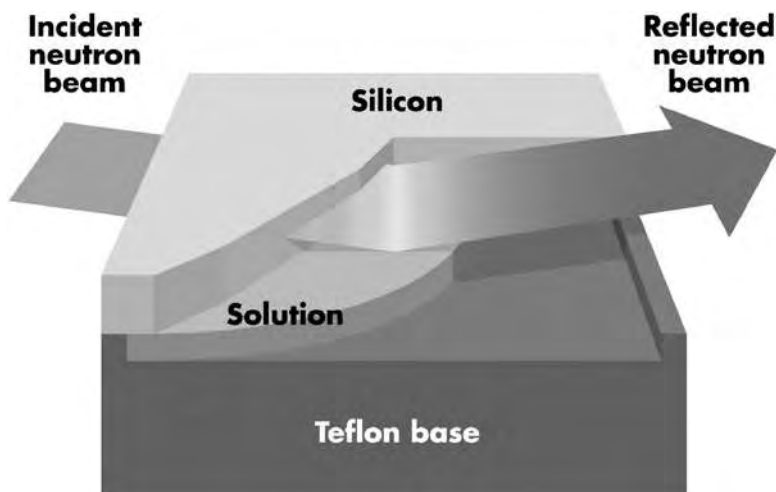


**Fig. 1.** Schematic representation of the scattering geometry for the neutron reflectivity measurements at the solid–solution interface.

**Table 1**

Scattering length density of commonly used solid substrates

	Scattering Length Density ( $\times 10^{-6} \text{ \AA}^{-2}$ )
D <sub>2</sub> O	6.35
Silicon	2.08
Quartz	4.2
Sapphire	5.4

interface is easily tractable. Measurements are made by transmitting the neutron beam (at normal incidence) through the crystalline solid upper phase to grazing incidence at the solid–solution interface [21] (see Fig 1).

In practice, a convenient range of solid crystalline materials, which can be polished to optical flatness over manageable areas, exists and includes silicon, quartz, and sapphire. The equivalent transmission through a block of amorphous quartz or silicon is  $\sim 10\text{--}15\%$ . This has so far precluded them from use, and limited the application to crystalline substrates. In aqueous solution, the most commonly use ‘contrasts’ are D<sub>2</sub>O, H<sub>2</sub>O, and water (H<sub>2</sub>O/D<sub>2</sub>O mixture) index matched to the solid phase. In D<sub>2</sub>O, the refractive index (or scattering length density) difference between that and the solid phase is significantly different for silicon, quartz, and sapphire (see Table 1).

From silicon to sapphire, the difference in scattering length density or refractive index compared with D<sub>2</sub>O is progressively smaller, which makes the region of total reflection more difficult to access, but enhances the sensitivity of

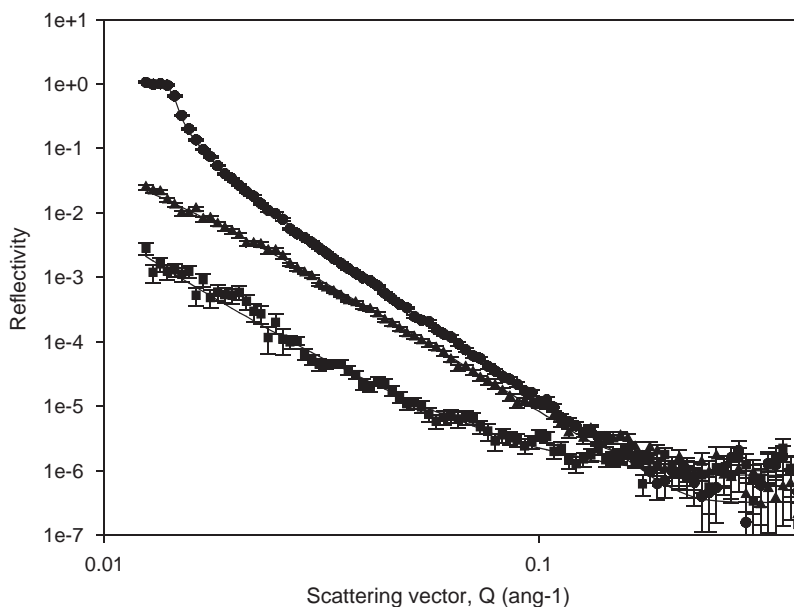


**Fig. 2.** Specular reflectivity for bare hydrophilic silica surface, (●) Si/D<sub>2</sub>O, (▲) Si/H<sub>2</sub>O, and (■) Si/cmSi. The solid lines are calculated curves for a thin oxide layer of 15 Å and a scattering length density of  $3.5 \times 10^{-6} \text{ \AA}^{-2}$ .

the reflectivity to a dilute hydrogenous layer at the interface. The solid surface, even if optically flat, is never perfect and there always exists a thin oxide or gel layer. It is necessary to measure this (to obtain its thickness and scattering length density) and to include it in any subsequent modelling of the data. The data in Fig. 2 below are typical of the data for the surface of silicon (measured at three different water ‘contrasts’) [23], and are consistent with a thin oxide layer  $\sim 15 \text{ \AA}$  and a scattering length density  $\sim 3.5 \times 10^{-6} \text{ \AA}^{-2}$  (silicon oxide, SiO<sub>2</sub>).

This is an important step as the surfaces are not always as well defined as the example shown in Fig. 2. Quartz is particularly troublesome, and thick gel layers often exist. For example, McDermott et al. [24] obtained a 85-Å thick layer of inhomogeneous material, with a scattering length density intermediate between crystalline quartz and amorphous silicon, on the surface of crystalline quartz. On silicon  $\langle 111 \rangle$  a more reproducible oxide layer, in thickness and density, is generally achieved. However, in the past some variability in the hydrophilic nature and hence reproducibility of adsorption has been experienced. This was discussed in detail by Penfold et al. [25], who found that the ‘mild piranha’ treatment produced a reproducible hydrophilic surface. Other treatments have also been found to be reliable and are discussed in more detail elsewhere [26]. Another important aspect that was discussed by Penfold et al. [25] and that is evident from a number of related studies is that the history of the surface and hence the experimental route can be of vital importance.

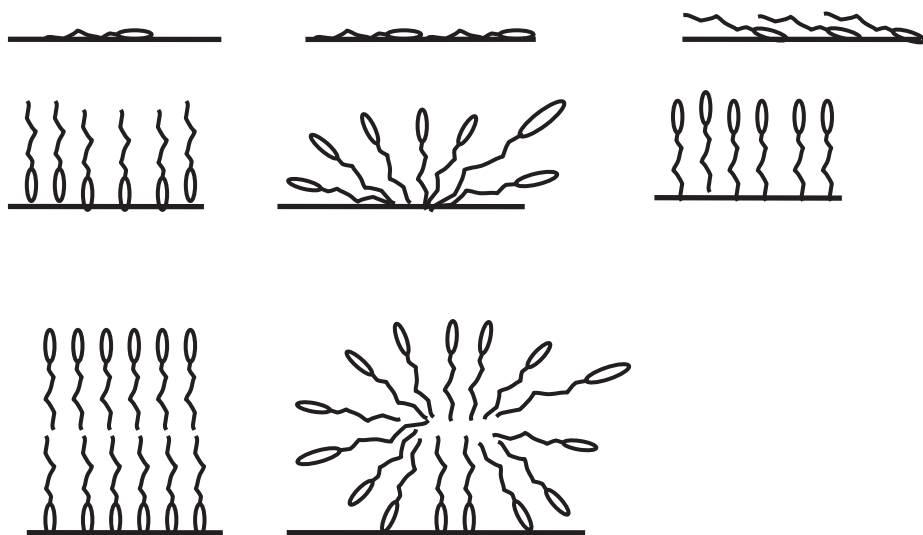


**Fig. 3.** Schematic representation of the structure of adsorbed surfactants layers deduced from different forms of the adsorption isotherm.

The nature of the adsorption of surfactants at both the hydrophilic and hydrophobic solid surfaces has been subject to extensive studies, and a number of excellent recent reviews exist [27–29]. The structure of the adsorbed layer, at both the hydrophilic and hydrophobic surfaces, has been the subject of much conjecture. From the form of the adsorption isotherm at the hydrophilic surface, the cooperative nature of the adsorption was established, and the evolution of the structure with concentration was inferred [30] (see Fig 3).

The more recent neutron reflectivity studies have established that flattened surface micelle or fragmented bilayer structure in more detail and with more certainty, using ‘contrast variation’ in the surfactant and the solvent [24, 31]. However, the extent of the lateral dimension (in the plane of the surface) and the detailed structure in that direction is less certain. From those neutron reflectivity measurements [24, 31] and related SANS data on the adsorption of surfactants onto colloidal particles [5], it is known that the lateral dimension is small compared with the neutron coherence length, such that averaging in the plane is adequate to describe the data. The advent of the AFM technique and its application to surfactant adsorption [15] has provided data that suggest that there is more structure and ordering in the lateral direction than implied from other measurements. This will be discussed in more detail in a later section of the chapter. At the hydrophobic interface, although the thickness of the adsorbed layer is now consistent with a monolayer, the same uncertainties about lateral structure exist.

In the treatment of the neutron reflectivity data for surfactants adsorbed at the hydrophilic solid–solution interface, we will assume that the flattened

surface micelle or fragmented bilayer structure is applicable. Variations in this basic model have been used to describe much of the data presented here, and is justified in the later discussion. This is the simplest model that is consistent with most of the data and is described in detail elsewhere [22, 31]. However, the main features of the model are a layer of thickness  $d_1$ , adjacent to the solid surface containing surfactant headgroups and associated hydration, a layer of thickness  $d_2$  containing the alkyl chains interpenetrating or overlapping from both sides, and a layer of thickness  $d_3$  adjacent to the fluid phase containing surfactant headgroups and hydration. To account for disorder and some degree of imperfection (due to intermixing), an additional parameter,  $f_c$ , which is the fraction of alkyl chains in the headgroup regions, is included. The model can then be described by three thicknesses,  $d_1$ ,  $d_2$ , and  $d_3$ , the area per molecule of each surfactant,  $A_1$ ,  $A_2$ , in the layer, a fractional coverage,  $f$ , to allow for incomplete coverage of the micelles or ‘patches’, and  $f_c$ . From known molecular volumes and scattering lengths, the scattering length density of each layer can be estimated.

## 2.3. Relationship to Other Techniques

### 2.3.1. Classical techniques

Much of the early studies of surfactant adsorption at the solid–solution interface were based on classical experimental techniques, such as solution depletion [1, 32], fluorescence spectroscopy [2], and measurements of the differential enthalpy of adsorption [2]. Such methods have provided much of the basic initial understanding. However, they provide no direct structural information and are difficult to apply to mixtures [23, 34]. However, when combined with other techniques, such as NMR and flow microcalorimetry, they provide some insight into the behaviour of mixtures. This was demonstrated by Thibaut et al. [33] on SDS/C<sub>10</sub>E<sub>5</sub> mixtures adsorbed onto silica and by Colombie et al. [34] on the adsorption of SLS/Triton X-405 mixtures onto polystyrene particles.

### 2.3.2. Scattering techniques

Similar measurements have been made on a range of colloidal particles, silica, polystyrene latexes, and clay particles. Using well-defined colloidal particles as the solid substrate makes scattering techniques a viable method for measuring surfactant adsorption. Through measurements of the hydrodynamic radius, light scattering provides access to the thickness of the adsorbed layer [7], but is difficult to interpret in terms of absolute adsorbed amounts. SAXS and SANS, however, provide access to both the thickness and density of the adsorbed layer. Seelenmeyer and Ballauff [5] have used SAXS to study the adsorption of C<sub>18</sub>E<sub>112</sub> onto polystyrene latex particles. Cummins et al. [6] have used SANS to study the adsorption of a range of nonionic surfactants onto Ludox silica, to

provide information on adsorbed amounts and on the structure of the adsorbed layer; and the effects of concentration, temperature, and surfactant type have been explored. Such studies provided the first direct evidence of the structure of the adsorbed layer, inferred from the accurate determination of the layer thickness. Because the average density was sufficient to describe the adsorbed layer, this was interpreted as an indication that any lateral dimensions within the layer were relatively small. More recently, Despert and Oberdisse [6], using the same approach, have provided direct SANS evidence for the discrete micellar nature of the adsorption onto silica at partial coverage.

### 2.3.3. Surface force probes

The advent of the AFM technique [15] and related surface force apparatus [35], and their application to soft surfaces raised the appealing possibility of direct imaging of the surface structures. The early work [36–38] focused on characterizing the nature of the surface forces, modified by the adsorption of  $C_{12}E_5$  onto silica [36], and  $C_{16}TAB$  onto glass [37, 39]. Nevertheless, the changes in the surface force profiles indicated bilayer-like surface structures that were consistent with the early scattering data [5] and the early neutron reflectivity measurements [22, 24, 31]. However, the application of the technique rapidly expanded following the pioneering work of Manne and Gaub [15], who were able to image the surface surfactant aggregates. They demonstrated the formation of a range of structures with the cationic surfactant  $C_{16}TAB$  on graphite, mica, and amorphous silica [15, 39]. Above the surfactant cmc, the images were interpreted as regular hemi-cylinders on graphite, full cylinders on mica, and full spheres on silica. Indeed, a surprising feature was the regularity and registration of the lateral structure. Similar structures were derived for SDS and SDS/dodecanol mixtures on graphite [40]. A further feature is that the surface structures seem to mirror the preferred bulk structures, with some perturbation to account for the frustration caused by the proximity of the surface. This was the case for the observation of different nonionic surfactant adsorption onto graphite [41], and for zwitterionic and nonionic surfactants adsorbed onto silicon nitride, mica, and graphite, where the role of the hydrophobicity of the substrate was specifically explored [42].

One of the difficulties of the technique is the specific nature of the surfaces that are used, predominantly mica and graphite. Hence, the ability to compare directly with the results from other techniques, such as ellipsometry and neutron reflectivity, is not straightforward. Furthermore, the degree to which the crystalline nature of those surfaces influences the observed structures is not established. This has been partially addressed in recent studies by Ducker and Wanless [43] on the adsorption of  $C_{16}TAB$  onto modified mica surfaces and by Wolgemuth et al. [44] with a range of surfactants adsorbed onto a TMCS-coated hydrophobic silica surface. In these studies, changes in the surface properties appear to have a dramatic effect upon the surface structures that are

produced. A major criticism and concern of the use of the AFM technique for the study of soft surfaces is whether it is truly non-evasive, and this has stimulated much discussion. However, the recent work of Shah et al. [45] is extremely relevant here. They have made specific molecular dynamics simulations of C<sub>12</sub>TAB adsorbed onto hydrophilic silica, and have simulated the relevant force conditions associated with the AFM tip. They observe that on hydrophilic silica, the experimentally observed flattened micellar structure is predicted, but that an indentation force  $\sim 1$  nN breaks up the surface aggregates to form a simple surfactant monolayer. These observations would imply that although the direct imaging methods have much to recommend them, their results require careful and critical evaluation and are probably not suitable for reliable quantitative data.

#### 2.3.4. Optical techniques

A range of different optical techniques have been applied to the study of surfactant adsorption at the solid–solution interfaces. Levitz and Van Damme [46] extended fluorescence decay spectroscopy, an established technique for measuring micelle aggregation number, to the solid–solution interface to provide some early indication of the micellar nature of the surface aggregates. Atkin et al. [7] have shown that simple optical reflectometry, providing the refractive index increment of the adsorbing material is known, provides a convenient way of measuring surface excess at the solid–solution interface. The particular attribute of the technique is the ability to follow rapid the kinetics of adsorption/desorption. However, it is difficult to extract structural information that is not highly model dependent.

However, ellipsometry, where the changes of the polarization state of the light before and after reflection are measured and related to the nature of the surface layer, is potentially more sensitive and provides the opportunity to measure adsorbed amounts and obtain some structural information. The difficulty is that the refractive index of the adsorbed layer is similar to the bulk solution, but by choosing a substrate with suitable optical properties, the optical contrast can be maximized such that separate determinations of thickness and refractive index can often be made. Null ellipsometry, where one looks for the condition that the elliptically polarized light becomes linear after reflection, is usually employed. This approach has been extensively used by Tiberg and co-workers [8], who have demonstrated how adsorbed amounts and adsorbed layer thicknesses of a range of nonionic surfactants absorbed onto silica can be determined. They have demonstrated in particular how the kinetics of adsorption/desorption can be followed, and have used such data to develop a theoretical model for the kinetics [Brinck, Jonsson, Tiberg]. They have also demonstrated how some limited information on the adsorption of binary mixtures can be obtained, and investigated the role of co-surfactants, such as long chain alcohols [Brinck, Tiberg]. In studying the effects of different alkyl and ethylene

oxide chain lengths on nonionic surfactant adsorption [Tiberg, Landgren; Tiberg, Jonsson, Tang, Lindman], they have discussed in detail the modelling assumptions that are made in the analysis of the data, and in the extraction of layer thicknesses. The application of ellipsometry to study interfacial dynamics and structure of adsorbed surfactant layers has been recently reviewed by Zhmud and Tiberg [47], with the emphasis on the kinetics and critical comparison with other techniques.

Other optical probes also provide access to the adsorption/desorption kinetics of surfactants at the solid–solution interface. Clark and Ducker [48] used ATR-IR to measure the rate of adsorption/desorption and exchange of C<sub>14</sub>TAB at the silica–D<sub>2</sub>O interface. They were able to show that the results were consistent with transport limited desorption for hydrophobic association with the surface and activation-limited diffusion for electrostatic association. Tulpar and Ducker [49] used SPR to determine the amounts of SDS adsorbed onto a SAM, in a study of the role of surface charge density and surface charge regulation. From this, they concluded that lateral ion mobility is an important factor in the formation of surface micelles. SFS, at the solid–solution interfaces, was recently reviewed [50]. It is a form of vibrational spectroscopy, which is surface specific. It provides structural information, through changes relating to conformation and orientational ordering at the interface. This was exploited by Briggs et al. [51] to study the structure of a dichain sugar surfactant at the hydrophobic solid–solution interface. As with neutron scattering, deuterium labelling can be used to manipulate different vibrational modes, and this was used by Ward et al. [52] to study the coadsorption of SDS and dodecanol at the hydrophobic surface. Becraft et al. [53] also used SFS to demonstrate bilayer formation and charge reversal at the CaF<sub>2</sub>–H<sub>2</sub>O–SDS interface.

### 3. SURFACTANT SYSTEMS

#### 3.1. Adsorption of Nonionic Surfactants onto Hydrophilic Surfaces

The earliest study of nonionic surfactant adsorption at the solid–solution interface by Lee et al. [22] using neutron reflectivity was on the adsorption of C<sub>12</sub>E<sub>6</sub> at the quartz–solution interface, and established many of the main features. Although with a limited  $q$  range ( $q_{\max} \sim 0.12 \text{ \AA}^{-1}$ ) measurements in D<sub>2</sub>O and water index matched to quartz were sufficient to interpret the data in terms of a fragmented bilayer structure, and show the variation with surfactant concentration. The results were consistent with those measured by SANS [5] at about the same time. Particularly valuable was the demonstration of the variation in the adsorption with pH, with a rapid reduction in the adsorbed amount over a narrow pH range at high pH. A more extensive study of nonionic adsorption onto a hydrophilic silica surface by neutron reflectivity was made by Bohmer et al. [54]. Adsorption isotherms and the structure of the adsorbed layer were measured for C<sub>12</sub>E<sub>6</sub> and C<sub>12</sub>E<sub>25</sub>, and consistent comparisons were made

with depletion measurements, and dynamic light scattering using Ludox silica sols. The cooperative nature of the adsorption isotherm and a structure consistent with a fragmented bilayer were established. An extended self consistent field (SCF) lattice theory was used to predict the main adsorption features of both surfactants, and the inclusion of lateral inhomogeneities consistent with the formation of small surface aggregates was predicted.

A characteristic of the early neutron reflectivity studies of nonionic surfactant adsorption was some variability in the pattern of adsorption. This was investigated in more detail and more systematically by McDermott et al. [55], who compared the adsorption of  $C_{12}E_6$  onto a range of different substrates, amorphous silica, crystalline quartz, and the oxide layer on a silicon single crystal. The adsorbed surfactant was found to form a bilayer with an overall thickness  $\sim 49 \pm 4 \text{ \AA}$ , with a structure similar to that determined in the previous studies (see Fig. 4).

Although the same model was applicable for each of the different substrates, the adsorbed amount or fractional coverage varied between 40 and 75%. There was an implication in the data that this correlated with the surface roughness of the substrates, but the evidence is not conclusive. Subsequently, Penfold et al. [25] have considered the consequences of the different surface treatments on the adsorption of nonionic surfactants at the hydrophilic silicon–solution interface. The delicate nature of the cooperativity of the adsorption results in variations in the adsorbed amount, which depend strongly upon

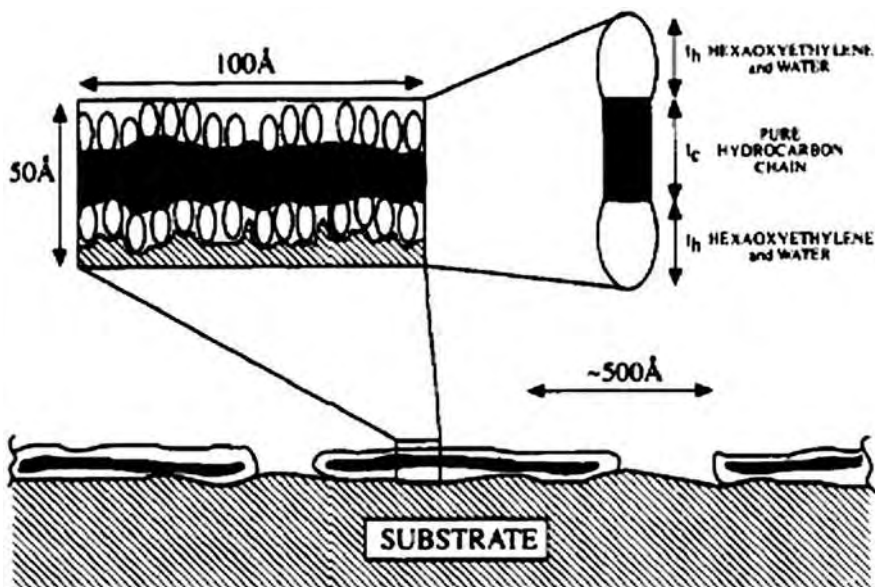
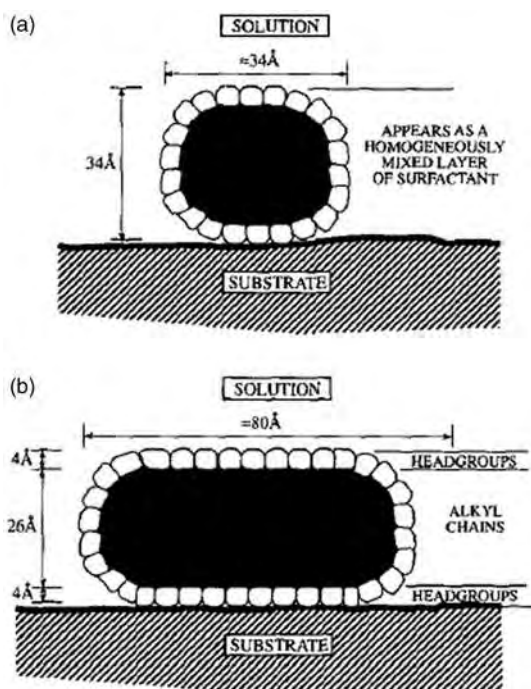


Fig. 4. Schematic representation of the adsorbed layer of  $C_{12}E_6$  at the silica–aqueous solution interface.

surface treatment, solution pH, and the exposure history of the surface (even at immeasurably low levels of adsorbate). However, that caveat notwithstanding, the general features observed are qualitatively and quantitatively consistent with the ellipsometry measurements of Tiberg and co-workers [8]; and the two methods combine to provide a detailed picture of nonionic adsorption at the hydrophilic solid–solution interface.

### 3.2. Adsorption of Ionic Surfactants onto Hydrophilic Surfaces

The electrostatic interaction between the cationic alkyl trimethyl ammonium bromide surfactants and the anionic surface of silica results in strong cooperative adsorption. This was demonstrated using neutron reflectivity for  $C_{16}TAB$  adsorbed onto amorphous silica by Rennie et al. [56]. The adsorption was measured at the cmc and below; and an overall thickness, equivalent to that expected of a bilayer, was obtained. A more detailed study was made by McDermott et al. [24] at the quartz–solution interface. By partial labelling of the  $C_{16}TAB$  and solvent (measurements were made in  $D_2O$ ,  $H_2O$ , and water index matched to quartz, and for  $d-C_{16}TAB$ ,  $h-C_{16}TAB$ ), it was possible to resolve the structure of the bilayer into headgroup and alkyl chain regions (see Fig 5).



**Fig. 5.** Schematic representation of the  $C_{16}TAB$  structure at the hydrophilic solid–solution at (a) low and (b) high coverage.

This was only possible at the higher coverage measured (at  $\sim$ cmc). At the lower concentration ( $\sim$ 50% coverage), it was not possible to make that distinction, and this suggests that at the lower coverage, the surface consists of small islands (bilayer patches) of surfactant on the surface (as depicted in Fig. 5). Estimates of those lateral dimensions are consistent with that expected for surface micelles of  $C_{16}$ TAB.

At the air–solution interface neutron reflectivity studies using more detailed isotopic labelling of the  $C_{16}$ TAB surfactant, deuterium-labelling groups of two or four methylenes at different positions on the  $C_{16}$  alkyl chain has provided a relatively high-resolution structural determined. In particular, the mean conformation of the molecule at the interface was determined. Fragneto et al. [31] applied the same approach to the adsorption of  $C_{16}$ TAB at the hydrophilic silica surface. Deuterium labelling of groups of four methylenes enabled the structure of the layer to be determined at a higher resolution than was previously possible. The measurements were made on smooth and rough surfaces, where the rms roughness was 6 and 14 Å, respectively. The roughness of the surface was found to have a significant effect on the structure of the surface layer. Fig. 6 shows a schematic representation of the model used to analyze the reflectivity data for the different isotopic combinations measured, on both the rough and smooth silica surfaces.

Constraining a model to simultaneously fit the different contrasts (11 different combinations were measured for the smooth surface and 16 for the rough surface) reduces substantially the uncertainties of the model. It provided relatively high-resolution structural information, where thicknesses and compositions can be determined with some accuracy. Furthermore, it provides an unambiguous interpretation of the surface structure as an interpenetrating bilayer at relatively high coverages. The effect of increased surface roughness is a lower surface coverage and a bilayer that is thicker and asymmetrical in the direction of the surface normal.

Atkin et al. [57] have recently produced a comprehensive review of the mechanisms of cationic adsorption at the solid–solution interface, and made a detailed comparison between AFM, neutron reflectivity, fluorescence quenching,

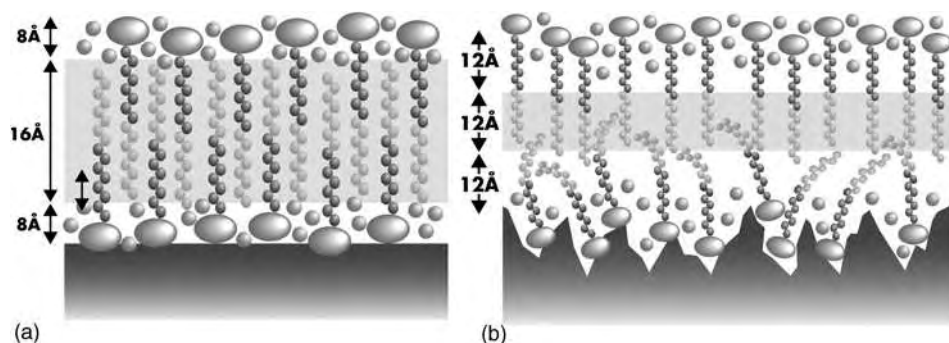


**Fig. 6.** Surface structure for  $C_{16}$ TAB bilayers adsorbed on (a) smooth and (b) rough hydrophilic silica.

ellipsometry, and optical reflectometry. In the broadest terms, the different techniques do provide a more or less consistent picture of the adsorption of cationic surfactants onto hydrophilic surfaces. However, some of the structural inferences have been dominated by the AFM data and its interpretation, and the apparent difficulties associated with that techniques have already been discussed here. The neutron reflection studies, using detailed labelling, by Fragneto et al. [31] provides structural information, in the direction normal to the surface, at a level of detail which is simply not available from any of the other techniques. Although its information on the lateral structure is relatively weak, it does firmly establish the bilayer nature of the adsorbed layer. If the adsorbed surfactant is in the form of micelles then they must be strongly flattened. The issue of lateral structure was addressed by Steitz et al. [64] in a study using grazing incidence SANS (GISANS) to investigate the adsorption of the nonionic surfactant  $C_8E_4$  onto hydrophilic silica. At partial coverage, they observed no preferred well-defined lateral structure, and the in-plane correlation length associated with the data was similar to micellar dimensions. They concluded that the well-defined surface aggregates observed in AFM may not generally apply. Any more detailed comparison between techniques is difficult due to differences/uncertainties associated with different surfaces and surface treatments (see earlier discussion).

### 3.3. Mixed Surfactant Adsorption

The ability to manipulate the neutron refractive index, through D/H isotopic substitution, makes neutron reflectivity and small angle scattering powerful techniques for the study of surfactant mixtures, and this has been extensively exploited in the study of adsorption at the air–water interface [17] and in micelles.

McDermott et al. [58] applied this approach in an initial study of the adsorption of  $C_{12}E_6/C_{16}TAB$  mixtures at the crystalline quartz–solution interface using neutron reflectivity. The adsorbed layer thickness was consistent with a mixed surfactant bilayer, and the surface composition (measured at two solution compositions) were in reasonable agreement with the predictions of Regular Solution Theory derived from surface tension measurements. A more extensive study was carried out by Hines et al. [59] on the adsorption of mixtures of SDS and dodecyl betaine at the hydrophobic solid–solution interface. The adsorption of the single surfactants was similar to that measured at the air–solution interface. The structure and composition of the mixed surfactant layer were also similar to those obtained at the air–water interface, and consistent with highly non-ideal mixing.

In contrast to the measurements by McDermott et al [58], neutron reflectivity measurements for the  $C_{12}E_6/C_{16}TAB$  mixture in 0.1 M NaBr at the air–water interface and SANS measurements of the mixed micelles show close to ideal mixing. Penfold et al. [60] has used neutron reflectivity to investigate this mixture at the solid–solution interface. For the hydrophilic silicon surface, the surface composition of the mixed surfactant bilayer adsorbed at the interface depended strongly upon the solution pH. At pH 2.4, the surface composition

was close to ideal, whereas at pH 7 the surface layer was relatively rich in  $C_{16}TAB$ . Changing the pH has dramatically changed the affinity of the two surfactants for the surface, and provided direct evidence for the role of a specific interaction with the surface in determining the surface composition. At low pH, the  $C_{12}E_6$  has a greater adsorption; and at high pH, the  $C_{16}TAB$  is more strongly adsorbing. Penfold et al. [61] extended this study at pH 2.4 to investigate in more detail the effects of solution composition and concentration on the surface mixing. Consistent with the previous studies, measurements using different isotopically labelled surfactants and solvent, provided evidence of a surface layer that is best described as a defective or fragmented bilayer or flattened micelle. The composition of the adsorbed layer was consistent with ideal mixing, except for solutions richer in  $C_{12}E_6$ , where the surface is then richer in  $C_{16}TAB$ . With solution composition, the adsorbed amount is a maximum for an equimolar solution, which indicates that synergistically this is the most favoured composition.

Penfold et al. [62] have also used neutron reflectivity to study the adsorption (structure and composition) of the mixed anionic/nonionic surfactants of SDS and  $C_{12}E_6$  at the hydrophilic silica–solution interface. This is rather different case to the cationic/nonionic mixtures, as the anionic SDS has no affinity for the anionic silica surface in the absence of the  $C_{12}E_6$ . The neutron reflectivity measurements, made by changing the isotopic labelling of the two surfactants and the solvent, show that SDS is coadsorbed at the interface in the presence of the  $C_{12}E_6$  nonionic surfactant. The variations in the adsorbed amount, composition, and the structure of the adsorbed bilayer reflect the very different affinities of the two surfactants for the surface. This is shown in Fig. 7, where the adsorbed amount and composition is plotted as a function of the solution composition.

At a solution concentration above the mixed cmc, the adsorbed amount decreases for solutions increasingly rich in SDS, such that for solutions richer than 50 mol% SDS, there is no measurable adsorption. The surface composition is also not consistent with the predictions of the pseudo phase approximation. The inherent lack of affinity of the SDS for the surface is also reflected in the structure of the adsorbed layer, as the SDS distribution within the bilayer is not uniform.

Nonionic surfactant adsorption at the hydrophilic solid–solution interface has been extensively studied by ellipsometry [8] and neutron reflectivity [22, 54, 55]. It was demonstrated that the adsorption depended upon the ethylene oxide chain length, and from studies on  $C_{12}E_5/C_{12}E_8$  and  $C_{10}E_6/C_{14}E_6$  mixtures [8] ideal mixing at the solid–solution interface was inferred. Penfold et al. [63] have extended their study of the nonionic mixture of  $C_{12}E_3/C_{12}E_8$  at the air–solution interface to the hydrophilic solid–solution interface. From surface tension data and micelle mixing, ideal behaviour is expected. At the air–solution interface, this did not seem to be the case; as at concentrations  $\sim 100$  times the mixed cmc, the surface was dominated by the  $C_{12}E_3$  and did not as normally expected reflect the solution composition. However, the results for the solid–solution interface show a marked difference to those for the air–solution interface, as shown in Fig. 8.

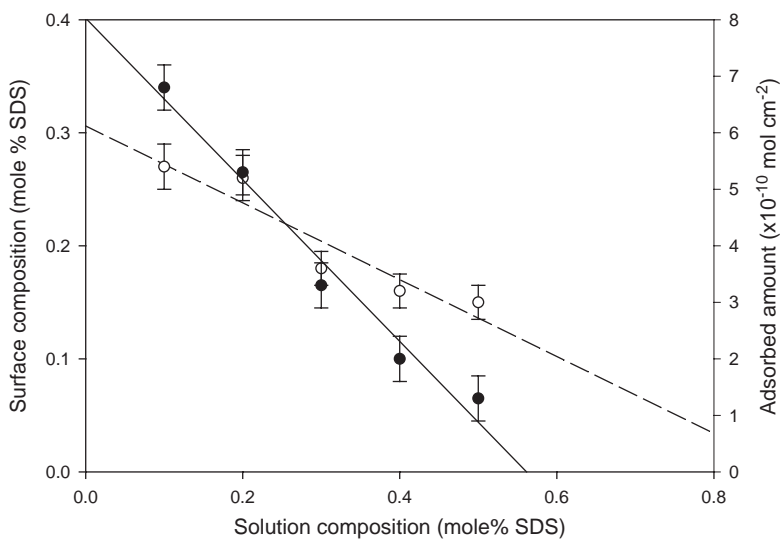


**Fig. 7.** Adsorbed amount and surface composition (mole fraction SDS) for  $10^{-3}$  M SDS/ $C_{12}E_6$  at the hydrophilic silica–solution interface (o) composition and (●) adsorbed amount.

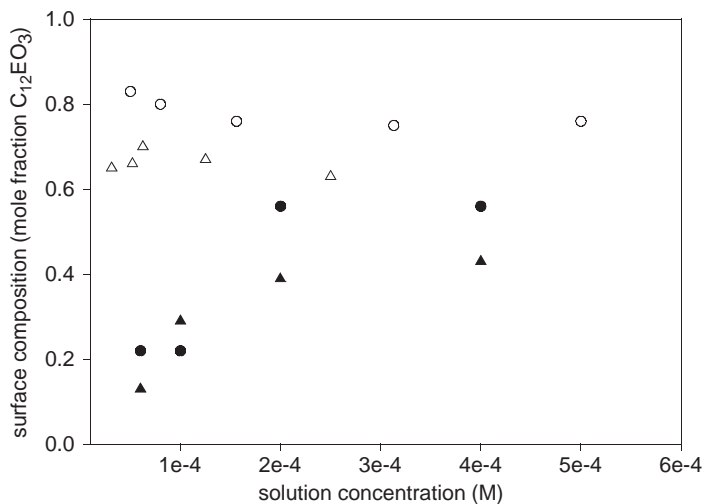


**Fig. 8.** Variation in surface composition (mole fraction  $C_{12}E_3$ ) with solution concentration: (o) 50/50, ( $\Delta$ ) 30/70, (open symbols) air–solution interface, and (closed symbols) solid–solution interface.

The variation in composition with cmc at the solid–solution interface now more closely resembles that expected for ideal mixing. The air–solution behaviour, where a monolayer is adsorbed, is associated with the different preferred

curvature of the  $E_3$  and  $E_8$  headgroups, and hence the packing constraints imposed by those differences. The  $C_{12}E_3$  favours a planar interface, whereas the  $C_{12}E_8$  a curved interface. Hence, the  $C_{12}E_3$  is more strongly adsorbed at the air–solution interface. This can be accounted for in the Regular Solution approach, by incorporating the differences in the packing constraints in terms of the surface pressure contributions. For the compositions studied (50/50 and 30/70  $C_{12}E_3/C_{12}E_8$ ), there is sufficient  $C_{12}E_8$  to ensure globular micelles are formed and hence ideal mixing is observed. This also implies that as a similar behaviour is observed at the solid–solution interface, the surface structure is in the form of ‘flattened’ micellar aggregates, and this is consistent with the model used to describe the neutron reflectivity data.

### 3.4. Adsorption onto Hydrophobic Surfaces

Although adsorption studies have been predominantly on hydrophilic surfaces, much of the work using probes such as AFM have been on hydrophobic surfaces, such as graphite. There is considerable interest, however, in the adsorption at the hydrophobic solid surface, and how that adsorption compares with the air–solution interface. A well-established method for making reproducible hydrophobic surfaces is to graft a layer of hydrocarbon by self-assembly. This was done by Fragneto et al. [65], by reacting octadecyl trichlorosilane (OTS) with a silicon surface. Neutron reflectivity measurements of the anionic surfactant, AOT, adsorbed at that hydrophobic surface were then made; where deuterium labelling of the alkyl chains of the OTS provided enhanced sensitivity to the adsorbed layer. The adsorption was of the form of a monolayer, with some penetration into the OTS layer, and the adsorption was similar to that observed at the air–solution interface (see Fig 9).

In comparison, the adsorption of the AOT was found to persist to lower surfactant concentrations than was the case for the nonionic surfactant  $C_{12}E_4$ .

Fragneto et al. [66] made a more complete study of the adsorption of  $C_{12}E_4$  onto an OTS hydrophobic surface. Two different isotopically labelled OTS surfaces (h-OTS, d-OTS) were used to establish the structure of the OTS layer in more detail. Subsequent measurements using differently labelled  $C_{12}E_4$  and solvent established that the adsorbed amount and structure of the adsorbed layer was similar to that obtained at the air–water interface. Furthermore, they were able to quantify the extent of penetration of the alkyl chains into the OTS layer.

### 3.5. Adsorption onto Functionalized Surfaces

Similar methods to the formation of hydrophobic self-assembled monolayers (SAMs), as described in the previous section, were used with chemical modification to prepare surfaces with different functionality, such as alkenes or hydroxylated surfaces. This approach was used by Thirtle et al. [67], where the adsorption of a series of nonionic surfactants from  $C_{12}E_5$  to  $C_{16}E_6$  onto surfaces

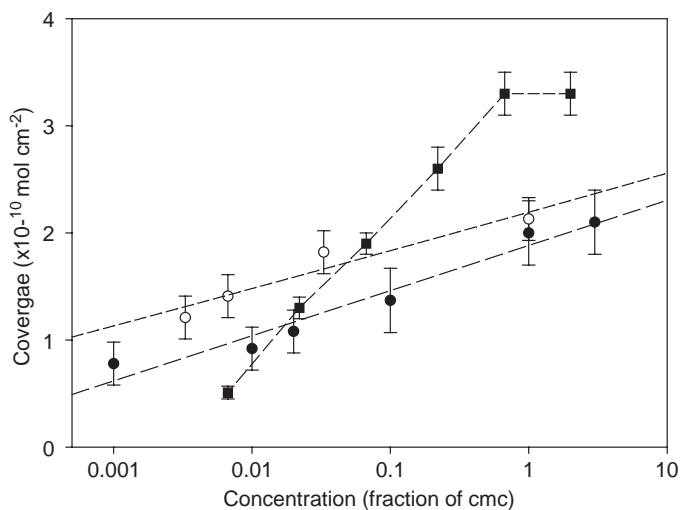


**Fig. 9.** Comparison of the adsorption isotherms of (■) nonionic surfactant  $C_{12}E_4$ , (●) AOT on OTS self-assembled monolayers (SAMs) on silicon, and (○) AOT adsorbed at the air–liquid interface.

with different functionality and onto bare silica was compared. On silica, all the surfactants adsorbed as a defective bilayer, but on the SAMs, distinctly different patterns of adsorption were observed. On an undecenyl trichlorosilane SAM layer, modified to include ethylenic groups on the ends of the alkyl chains, the nonionic surfactants adsorbed as a monolayer with a thickness and an adsorbed amount comparable to that obtained at the air–water interface. Some penetration of the alkyl chains into the SAM layer was observed. When the SAM was hydroxylated, the pattern of adsorption was found to be quite different, and a thin layer,  $\sim 4$  Å thick, was obtained. This was attributed to the strong hydrogen bonding between the surface OH groups and the ethylene glycol groups.

An alternative approach to producing a differently functional surface is to use spin coating techniques. This was done by Turner et al. [68], who spun cast layers of polystyrene onto a silica surface. They investigated the nature of the surface and of SDS adsorbed to that surface by neutron reflectivity and IR-ATR. A thin layer of polystyrene,  $\sim 275$  Å, was established. The subsequent SDS adsorption was consistent with a monolayer  $\sim 15$  Å thick and an adsorbed amount similar to that observed at the air–solution interface. Measurements above the cmc of SDS showed clearly the effects on the adsorption pattern of dodecanol impurities in the SDS.

### 3.6. More Complex Surface Structures

The adsorption of concentrated solution of AOT at the hydrophilic solid–solution and air–solution interfaces produced a rather different pattern of behaviour [69].

At 2 and 5 wt.%, a series of sharp diffraction peaks, characteristic of an adsorbed lamellar structure, were observed (see Fig 10).

The lamellar spacing observed is extremely sensitive to temperature, and remarkably decreases with increasing temperature. In contrast to the bulk solution behaviour, the surface structure is extremely sensitive to electrolyte; 1 mM NaBr causes the adsorbed lamellar phase to disappear. The adsorbed structure, in addition to the pronounced specular scattering, exhibits strong off-specular scattering (see Fig. 11) [70]. The specular reflectivity is consistent with a highly ordered layered structure at the interface consisting of 20–30 repeats and extending some 0.5  $\mu\text{m}$  from the interface into the solution. The off-specular scattering is attributed to conformal roughness in this long-range lamellar structure at the interface, and is also strongly temperature dependent. The specular and off-specular scattering show consistently increased order with increasing temperature, where normally the opposite would be expected from increased thermal fluctuations. The results are interpreted as due to a reduction in the preferred curvature for the AOT due to dehydration, and a consequent shift from an  $L_1$  to an  $L_\alpha$  phase in solution.

McGillivray et al. [71] have also observed stable layered structures adsorbed at the silicon–solution (and air–solution) interface for didodecyl dimethylammonium bromide (DDAB) and the corresponding diundecyl (DUDAB) cationic surfactants, in the concentration range 0.2–2 wt.%. Similar to AOT, the surface structures that are found are highly sensitive to temperature, with the repeat distance decreasing with increasing temperature. A notable difference between these systems and AOT [69] is that for the DDAB and DUDAB, the repeat distances are much larger,  $\sim 600$ – $1500$   $\text{\AA}$ . Furthermore, the observed structures

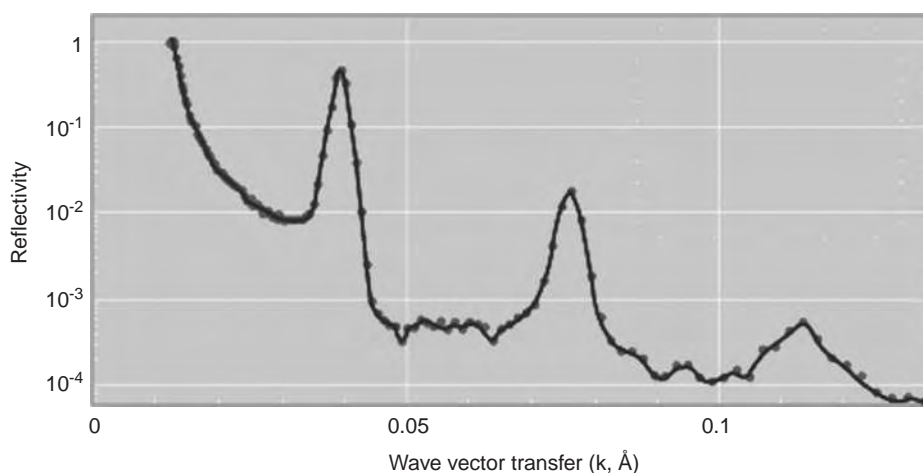


**Fig. 10.** Specular reflectivity for 2% h-AOT/D<sub>2</sub>O at hydrophilic silica–solution interface at 35 °C.

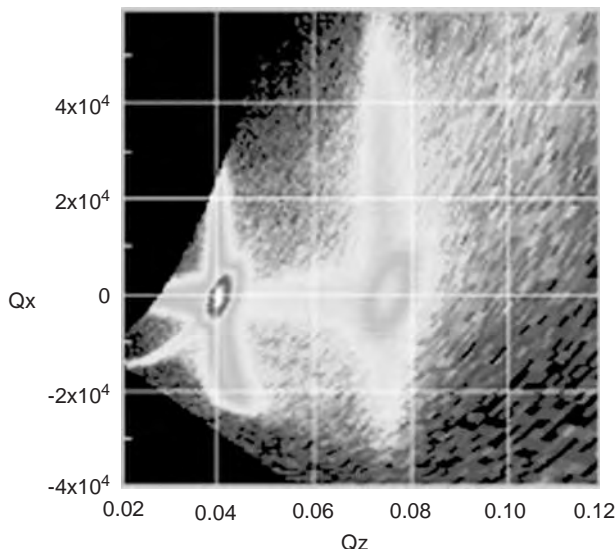


**Fig. 11.** Off-specular scattering ( $Q_x$ – $Q_z$  map) for 2% h-AOT/D<sub>2</sub>O at hydrophilic silica–solution interface at 25 °C and  $\theta = 0.8^\circ$ .

are consistent with only two to four correlated layers. This could arise for the adsorption of monodisperse unilamellar vesicles, a lamellar phase or a structured bicontinuous phase. Bulk scattering studies and cryo-TEM measurements show coexistence of unilamellar vesicles and lamellar phase.

Hamilton et al. [72] have used GISANS to study the shear-induced surface ordering in a viscoelastic surfactant solution. In a specially designed cell, they combined specular reflectivity and GISANS measurements with shear flow alignment. Close to the solid quartz–solution interface, they observed that the highly extended threadlike micelles of cetyltrimethyl ammonium 3,5-dichlorobenzoate (CTA 3,5 Cl-Bz) aligned in the flow direction. Furthermore, the GISANS data showed that within a few tens of microns of the surface, these micelles also form well-ordered hexagonal arrays, separated by  $\sim 370$  Å. The combination of the proximity of the surface and the application of shear flow has resulted in crystalline ordering, which is not observed in the bulk solution under similar concentration and shear conditions. Holt et al. [73] reported the formation of layered and subsequently hexagonal mesophase structures in the C<sub>18</sub>TAB-templated growth of silicate structures at the air–solution interface; and similar structures would be expected at the solid–solution interface.

### 3.7. Polymer/Surfactant Adsorption

The manipulation of the adsorption of surfactants at the air–solution interface by polymers and polyelectrolytes has been extensively studied [17], and has

revealed some striking and interesting phenomena. At the solid–solution interface, specific interactions, of either the surfactant or polymer with the solid surface, offers the potential for an even richer range of phenomena. A range of techniques have been used to study such phenomena, and include SFS, ellipsometry, IR-ATR, and AFM. In contrast, to date, relatively few neutron reflectivity studies have been made at the solid–solution interface.

Penfold et al. [74] have used neutron reflectivity to show that the cationic polyelectrolyte, polyDMAAC, adsorbed strongly and irreversibly onto hydrophilic silica to form a robust thin layer at the interface. A notable feature of this adsorbed layer was that the relative affinity of  $C_{16}TAB$  for the surface was substantially reduced (it normally adsorb strongly to the anionic surface of silica) and SDS adsorbed strongly to the surface (SDS has little or no affinity for the silica surface). This implies that the surface is now strongly cationic; that is, charge reversal has taken place. This is clearly illustrated in Fig. 12 for the 60/40 SDS/ $C_{12}E_6$  surfactant mixture at  $10^{-3}$  M, where the adsorption onto silica and the polyDMAAC-coated silica surface is compared. On silica, the reflectivity for the two isotopic combinations h-SDS/h- $C_{12}E_6$  and h-SDS/d- $C_{12}E_6$  in  $D_2O$  is identical and close to that for the bare surface, consistent with no SDS adsorption. Whereas on the polyDMAAC-coated surface there is a clear difference, which can be attributed to the increased SDS adsorption.

Further evidence of the charge reversal is demonstrated in that PSS can be adsorbed into the polyDMAAC-coated surface, and that surface now becomes

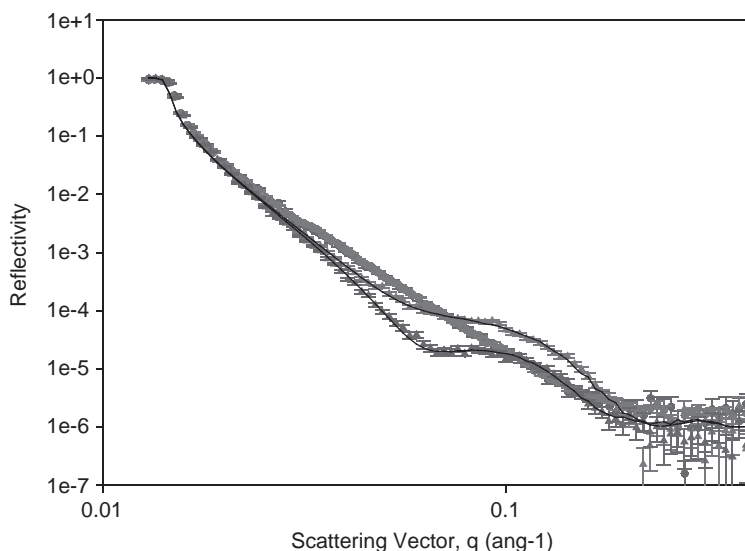


**Fig. 12.** Specular reflectivity for  $10^{-3}$  M 60/40 SDS/ $C_{12}E_6$ / $D_2O$  onto bare silica ( $\bullet$ ) and polyDMAAC coated silica ( $\blacktriangle$ ), and (red) for the isotopic combination h-SDS/h- $C_{12}E_6$ , and (blue) h-SDS/d- $C_{12}E_6$ . The solid lines are model calculations.

anionic again. This has been extensively exploited elsewhere to build up poly-electrolyte multilayer coatings. Liu et al. [75] in contrast observed from an AFM study that  $C_{16}$ TAC hindered polyDMDAAC adsorption onto silica. In the absence of surfactant, the polymer was found to form a neutral featureless layer on the surface, such that  $C_{16}$ TAC adsorbed in a manner similar to its adsorption onto silica. This implies that the adsorption conditions are crucial, and that in this case, only partial coverage of the polyDMDAAC was achieved. Penfold et al. [74] also observed similar effects with the deposition of Polystyrene sulfonate (PSS) onto polyDMDAAC, where it was possible to produce a surface where both SDS and  $C_{16}$ TAB adsorbed equally strongly. Fielden et al. [76], using AFM to study the adsorption of SDS and the cationic polyelectrolyte, AM-MAPTC onto mica, also observed that the adsorption of the AM-MAPTC left the surface slightly charged.

In those cases, there was no reported evidence of pronounced lateral structure or separation. This is in marked contrast to the study by Fleming et al. [77], who reported micron-sized domains of surfactant rich ordered aggregates inter-dispersed by disordered ill-defined polymer rich domains. Whether this is a feature of a hydrophobic surface or a highly non-equilibrium condition is not clear.

Using SFS, Davies and co-workers [77–79] reported enhanced adsorption and competitive adsorption at the hydrophobic surface, reminiscent of that seen at the air–solution interface. For the SDS/PEO mixture [79], competitive adsorption was observed at low concentrations, whereas at higher SDS concentrations, PEO was depleted from the surface. Similar observations were made from IR-ATR measurements by Poirier et al. [80] on  $C_{16}$ TAB/PSS mixtures at the silica–solution interface. However, the technique could not distinguish between depletion or surface complex formation. Similar trends were also reported by Fielden et al. [76] for SDS/AM-MAPTC mixtures on mica. For the PEI/SDS mixture at the hydrophobic interface [76], the SFS measurements indicated a higher degree of order and hence adsorption due to complexation at the interface. This was also shown to be strongly pH dependent [81].

A feature of the neutron reflectivity study on polyDMDAAC and surfactant adsorption by Penfold et al. [74] was that the adsorbed layer of polyDMDAAC was remarkably robust and unaffected by the subsequent surfactant adsorption. This is not always the case, and Fielden et al. [76] reported a large increase in the thickness of the surface layer of AM-MAPTC on mica due to complex formation with SDS. Thickness increases with electrolyte and pH were reported for high molecular weight polyacrylamide adsorbed onto silica, measured by null ellipsometry by Samoshina et al. [82] in the absence of surfactant. Complex formation at the interface, resulting in layer thickening, was also reported by Dedinaite et al. [83] for PCMA/SDS mixtures on mica from AFM measurements.

Another feature of the study by Penfold et al. [74] was that the polyDMDAAC layer is robust, and not removed by surfactant. However, in contrast, in other cases [76, 78, 80], desorption of the polymer is observed at higher surfactant concentrations.

#### 4. SUMMARY AND FUTURE PROSPECTS

Clearly, neutron reflectivity has contributed much to our understanding of the nature of surfactant adsorption at the solid–solution interface. It has already been successfully applied to an extensive range of systems, as illustrated in this chapter.

The ability to manipulate the neutron refractive index, through D/H isotopic substitution, makes it a powerful technique for the study of mixtures, and for more detailed structural investigations. This is an aspect of the technique that will clearly be important in the future as more complex multi-component systems are investigated.

The solid phase that can be used is currently limited to crystalline materials such as silicon, quartz and sapphire, and to relative large sample areas,  $> 10 \text{ cm}^2$ . The next generation (within the next 5 years) of neutron reflectometers will provide intensity increases of at least an order of magnitude. This will enable smaller sample areas to be used and allow a greater range of solid materials to be envisaged. This will open up a much greater range of interfaces and systems that can be explored. It makes electrochemical interfaces, bio-related surfaces, and a range of other functionalized surfaces more accessible, and offers the prospect of combining reflectivity measurements with SFA to simultaneously measure the surface force profile.

Although in the direction normal to the surface, relatively high-resolution structural information is already accessible; in the plane, there is relatively little direct information on a relevant length scale available. Current developments in the technique associated with off-specular scattering will address this over the next 2–3 years, and this will transform our ability to obtain the relevant structural information in the plane of the surface. Hence, the degree of surface ordering and the extent of the ‘bilayer or micellar patches’ will be accessible.

The associated and paralleled developments in GISANS will provide access to not only the surface, but also to the near surface structure, and this will enhance considerably our ability to study ordered and relatively more concentrated systems.

#### REFERENCES

- [1] Q. Xu, T. V. Vasudevan and P. Somersundaran, *J. Colloid Interf. Sci.*, 142 (1991) 528.
- [2] Z. Kiraly, R. H. K. Borner and G. H. Findenegg, *Langmuir*, 13 (1997) 3308.
- [3] P. Levitz and H. Van Damme, *J. Phys. Chem.*, 90 (1986) 1302.
- [4] M. Cohen Stuart and H. Tamai, *Macromolecules*, 21 (1988) 1863.
- [5] S. Seelenmeyer and M. Ballauff, *Langmuir*, 16 (2000) 4094.
- [6] P. G. Cummins, E. Staples and J. Penfold, *J. Phys. Chem.*, 94 (1990) 3740; P. G. Cummins, E. Staples and J. Penfold, *J. Phys. Chem.*, 95 (1991) 5902; P. G. Cummins, E. Staples and J. Penfold, *J. Phys. Chem.*, 96 (1992) 8092; J. Penfold, E.

- Staples, I. Tucker and P. G. Cummins, *J. Phys. Chem.*, 100 (1996) 18133; G. Despert and J. Oberdisse, *Langmuir*, 19 (2003) 7604; P. G. Cummins, E. Staples and J. Penfold, *PCCP*, 6 (2004) 1557.
- [7] R. Atkin, V. S. J. Craig and S. Biggs, *Langmuir*, 16 (2000) 9374.
- [8] P. Wangnevud and G. Olofsson, *J. Colloid Interf. Sci.*, 153 (1992) 392; F. Tiberg and M. Landgren, *Langmuir*, 9 (1993) 927; F. Tiberg, B. Jonsson, J. Tang and B. Lindman, *Langmuir*, 10 (1994) 2294; J. Brinck and F. Tiberg, *Langmuir*, 12 (1996) 5042; J. Brinck and F. Tiberg, *Langmuir*, 14 (1998) 1058.
- [9] R. M. Corn and D. A. Higgins, *Chem. Rev.*, 94 (1994) 107.
- [10] G. R. Bell, C. D. Bain and R. N. Ward, *J. Chem. Soc., Faraday Trans.*, 92 (1996) 215.
- [11] B. Schoeber, E. Poptoshev and F. Casuso, *Macromolecules*, 36 (2003) 5258.
- [12] R. A. Dluhy and D. G. Cornell, in *Fourier Transform Infrared Spectroscopy in Colloid and Interface Science* (D. R. Scheung, ed.), ACS Symp. Ser., 447 (1991) 192.
- [13] J. Penfold and R. K. Thomas, *J. Phys. Condens. Matter*, 2 (1990) 1369.
- [14] T. Russell, *Mater. Sci. Rep.*, 5 (1996) 171.
- [15] S. Manne and H. E. Gaub, *Science*, 220 (1995) 14550.
- [16] R. A. L. Jones and R. W. Richards, *Polymers at Surfaces and Interfaces*, Cambridge University Press, Cambridge, UK, 1999.
- [17] J. R. Lu, R. K. Thomas and J. Penfold, *Adv. Colloid Interf. Sci.*, 84 (2000) 143.
- [18] M. Born and E. Wolf, *Principles of Optics*, Pergamon Press, London, UK, 1990.
- [19] O. S. Heavens, *Optical Properties of Thin Films*, Dover, London, UK, 1955.
- [20] L. Nevot and P. Croce, *Phys. Appl.*, 15 (1980) 761.
- [21] T. L. Crowley, E. M. Lee, E. A. Simister, R. K. Thomas, J. Penfold and A. R. Rennie, *Colloid Surf.*, 52 (1990) 85.
- [22] E. M. Lee, R. K. Thomas, P. G. Cummins, E. J. Staples, J. Penfold and A. R. Rennie, *Chem. Phys. Lett.*, 162 (1989) 196.
- [23] J. Penfold, E. J. Staples, I. Tucker and L. J. Thompson, *Langmuir*, 13 (1997) 6635.
- [24] D. C. McDermott, J. McCarney, R. K. Thomas and A. R. Rennie, *J. Colloid Interf. Sci.*, 162 (1994) 344.
- [25] J. Penfold, E. Staples and I. Tucker, *Langmuir*, 18 (2002) 2967.
- [26] G. Fragneto, D.Phil. thesis, Oxford, 1996.
- [27] S. Paria and K. C. Khilar, *Adv. Colloid Interf. Sci.*, 110 (2004) 75.
- [28] C. Treiner, *Encyclopedia of Surface and Colloid Science*, Marcel Dekker, 2002, 5154 pp.
- [29] P. E. Levitz, *Colloid Surf. A*, 205 (2002) 31.
- [30] S. J. Clunie, B. T. Ingram, G. D. Parfitt and C. H. Rochester (eds.), *Adsorption from Solution at the Solid/Liquid Interface*, Academic Press, New York, 1983105 Chapter 3.
- [31] G. Fragneto, R. K. Thomas, A. R. Rennie and J. Penfold, *Langmuir*, 12 (1996) 6036.
- [32] A. Gellan and C. H. Rochester, *J. Chem. Soc., Faraday Trans.*, 1 (81), (1985) 2235.
- [33] A. Thibaut, A. M. Misselyn-Bauduin, J. Grandjean, G. Broze and R. Jerome, *Langmuir*, 16 (2000) 9192.

- [34] D. Colombie, K. Landfester, E. D. Sudol and M. S. El-Aasser, *Langmuir*, 16 (2000) 7095.
- [35] J. Klein, D. Perahia, S. Warburg and L. J. Fetters, *Nature*, 352 (1991) 143.
- [36] M. W. Rutland and T. J. Senden, *Langmuir*, 9 (1993) 412.
- [37] J. L. Parker, V. V. Vamimsky and P. M. Claesson, *J. Phys. Chem.*, 97 (1993) 7706.
- [38] R. Podgornik and V. A. Parsegian, *J. Phys. Chem.*, 99 (1995) 9491.
- [39] S. Manne, J. P. Cleveland, H. E. Gaub, G. D. Stucky and P. K. Hausma, *Langmuir*, 10 (1994) 4405.
- [40] E. J. Wanless, T. W. Davey and W. A. Ducker, *Langmuir*, 13 (1997) 4223.
- [41] H. N. Patrick, G. G. Warr, S. Manne and I. A. Aksay, *Langmuir*, 13 (1997) 4345.
- [42] L. M. Grant and W. A. Ducker, *J. Phys. Chem. B*, 101 (1997) 5337.
- [43] W. A. Ducker and E. J. Wanless, *Langmuir*, 15 (1999) 160.
- [44] J. L. Wolgemuth, R. K. Workmann and S. Manne, *Langmuir*, 16 (2000) 3077.
- [45] H. Shah, P. Chiu, M. Jain, J. Fortes, B. Moudgil and S. Sinnott, *Langmuir*, 21 (2005) 5337.
- [46] P. Levitz and H. Van Damme, *J. Phys. Chem.*, 90 (1986) 1307.
- [47] B. Zhmud and F. Tiberg, *Adv. Colloid Interf. Sci.*, 113 (2005) 21.
- [48] S. C. Clark and W. A. Ducker, *J. Phys. Chem. B*, 107 (2003) 9011.
- [49] A. Tulpar and W. A. Ducker, *J. Phys. Chem. B*, 108 (2004) 1667.
- [50] C. D. Bain, *J. Chem. Soc., Faraday Trans.*, 91 (1995) 1281.
- [51] A. M. Briggs, M. S. Johal, P. B. Davies and D. J. Cooke, *Langmuir*, 15 (1999) 1817.
- [52] R. N. Ward, P. B. Davies and C. D. Bain, *J. Phys. Chem. B*, 101 (1999) 1594.
- [53] K. A. Becraft, F. G. Moore and G. L. Richmond, *J. Phys. Chem. B*, 107 (2003) 3675.
- [54] M. R. Bohmer, L. K. Koopal, R. Janssen, E. M. Lee, R. K. Thomas and A. R. Rennie, *Langmuir*, 8 (1992) 2228.
- [55] D. C. McDermott, J. R. Lu, E. M. Lee, R. K. Thomas and A. R. Rennie, *Langmuir*, 8 (1992) 1204.
- [56] A. R. Rennie, E. M. Lee, E. A. Simister and R. K. Thomas, *Langmuir*, 6 (1990) 1031.
- [57] R. Atkin, V. S. J. Craig, E. J. Wanless and S. Biggs, *Adv. Colloid Interf. Sci.*, 103 (2003) 219.
- [58] D. C. McDermott, D. Kanelleas, R. K. Thomas, A. R. Rennie, S. K. Satija and C. F. Majkrzak, *Langmuir*, 9 (1993) 2404.
- [59] J. D. Hines, G. Fragneto, R. K. Thomas, P. R. Garrett, G. K. Rennie and A. R. Rennie, *J. Colloid Interf. Sci.*, 189 (1997) 259.
- [60] J. Penfold, E. J. Staples, I. Tucker and L. J. Thompson, *Langmuir*, 13 (1997) 6638.
- [61] J. Penfold, E. J. Staples, I. Tucker and R. K. Thomas, *Langmuir*, 16 (2000) 8879.
- [62] J. Penfold, E. Staples, I. Tucker and R. K. Thomas, *Langmuir*, 18 (2002) 5755.
- [63] J. Penfold, I. Tucker and R. K. Thomas, *Langmuir*, 21 (2005) 6330.
- [64] R. Steitz, P. Muller-Buschbaum, S. Schemmel, R. Cubitt and G. H. Findenegg, *Europhys. Lett.*, 67 (2004) 962.
- [65] G. Fragneto, Z. X. Li, R. K. Thomas, A. R. Rennie and J. Penfold, *J. Colloid Interf. Sci.*, 178 (1996) 531.

- [66] G. Fragneto, J. R. Lu, D. C. McDermott, R. K. Thomas, A. R. Rennie, P. D. Gallagher and S. K. Satija, *Langmuir*, 12 (1996) 477.
- [67] P. N. Thirtle, Z. X. Li, R. K. Thomas, A. R. Rennie, S. K. Satija and L. P. Sung, *Langmuir*, 17 (1997) 5451.
- [68] S. F. Turner, S. M. Clarke, A. R. Rennie, P. N. Thirtle, D. J. Cooke, Z. X. Li and R. K. Thomas, *Langmuir*, 15 (1999) 1017.
- [69] Z. X. Li, A. Weller, R. K. Thomas, A. R. Rennie, J. R. P. Webster, J. Penfold, R. K. Heenan and R. Cubitt, *J. Phys. Chem. B*, 103 (1999) 10800.
- [70] Z. X. Li, J. R. Lu, R. K. Thomas, A. Weller, J. Penfold, J. R. P. Webster, D. S. Sivia and A. R. Rennie, *Langmuir*, 17 (2001) 5858.
- [71] D. J. McGillivray, R. K. Thomas, A. R. Rennie, J. Penfold and D. S. Sivia, *Langmuir*, 19 (2003) 7719.
- [72] W. A. Hamilton, P. D. Butler, S. M. Baker, G. S. Smith, J. B. Hayter, L. J. Magid and R. Pynn, *Phys. Rev. Lett.*, 72 (1994) 2219.
- [73] S. A. Holt, J. L. Ruggles, J. W. White and R. F. Garrett, *J. Phys. Chem. B*, 106 (2002) 2330.
- [74] J. Penfold, I. Tucker, E. Staples and R. K. Thomas, *Langmuir*, 20 (2004) 7177.
- [75] J. F. Liu, G. Mui and W. A. Ducker, *Langmuir*, 17 (2001) 4895.
- [76] M. L. Fielden, P. M. Claesson and K. Schillen, *Langmuir*, 14 (1998) 5366.
- [77] B. D. Fleming, E. J. Wanless and S. Biggs, *Langmuir*, 15 (1999) 8719.
- [78] M. T. L. Casford, P. B. Davies and D. J. Neivandt, *Langmuir*, 19 (2003) 7386.
- [79] R. Windsor, D. J. Neivandt and P. B. Davies, *Langmuir*, 17 (2001) 7306.
- [80] J. S. Poirier, C. P. Tripp and D. J. Neivandt, *Langmuir*, 21 (2005) 2876.
- [81] R. Windsor, D. J. Neivandt and P. B. Davies, *Langmuir*, 18 (2002) 2199.
- [82] Y. Samoshina, T. Nylander, V. Shubin, P. Bauer and K. Eskilsson, *Langmuir*, 21 (2005) 5872.
- [83] A. Dedinaite, P. M. Claesson and M. Bergstrom, *Langmuir*, 16 (2000) 5257.

This page intentionally left blank

## Chapter 5

# Near-Field Scanning Optical Microscopy of Lipid Membranes

Bret N. Flanders<sup>a,\*</sup>, Robert C. Dunn<sup>b</sup>

<sup>a</sup>*Department of Physics, Oklahoma State University, 145 Physical Sciences II, Stillwater, OK 74078, USA*

<sup>b</sup>*Department of Chemistry, University of Kansas, 1251 Wescoe Dr., Lawrence, KS 66045, USA*

### 1. INTRODUCTION

Lipid membranes are one of the defining structural features of cells as they contribute both to the overall morphology of the cell, and organize and segregate the various internal organelles [1]. Lipids organize in a number of biologically relevant structures from simple lipid monolayers, such as those lining the lung [2], to bilayers, like the cellular membrane and the vesicles that play important roles in cellular signaling and trafficking. Increasingly, the role of lipids in these structures is proving more complex and important than first appreciated.

The introduction of the fluid mosaic model of cellular membranes in 1972 represented a pivotal moment, establishing the framework under which biological membranes are viewed today [3]. In this model, lipid bilayers form homogeneous membranes in which integral proteins freely diffuse. Since its introduction, this model has undergone continual evolution as experimental observations have provided an increasingly detailed view of membrane architecture. Far from being a homogeneous sea in which proteins freely diffuse, natural biomembranes are complex structures with intricate and dynamic domains. There is a rich assortment of lipids that are used to fine-tune membrane properties and an overall compositional asymmetry in the two leaflets of the plasma membrane, which is actively controlled by the cell.

---

\*Corresponding author. E-mail: [bret.flanders@okstate.edu](mailto:bret.flanders@okstate.edu)

Recently, much attention has focused on small lipid domains known as lipid rafts [4,5]. These domains, rich in cholesterol and gangliosides, are insoluble in cold detergents and hence are also known as detergent resistant fractions [4,6]. Studies find specific G-type proteins associated with these domains, suggesting that a partitioning mechanism causes the proteins to be sequestered in these microdomains to influence their activity [6]. These interesting structures have, therefore, profoundly affected the way lipid membranes are viewed. Far from simply being building blocks used to create static frameworks to support proteins, it now appears that lipids can form dynamic domains which influence both the spatial and temporal organization of proteins and modify their activity. Lipid rafts, however, have proven elusive to direct study. Because they are thought to exist on the nanometric scale, they are beyond the resolving power of conventional optical microscopy. However, the introduction of near-field scanning optical microscopy (NSOM) has enabled measurements with sub-diffraction limited spatial resolution. These developments have facilitated the study of small domains in models of the lipid membrane and more recently in living cells. While the technique continues to evolve, initial studies on model monolayers and bilayers suggest these capabilities will provide new insights into the structure and the physiological roles of lipid rafts.

## 2. NEAR-FIELD SCANNING OPTICAL MICROSCOPY

Near-field scanning optical microscopy is a scanning probe technique that enables optical measurements to be conducted with very high spatial resolution [7–9]. NSOM overcomes the diffraction barrier that restricts the spatial resolution in conventional optical measurements and provides both optical and topographical information on samples with nanometric spatial resolution.

In conventional light microscopy, which uses a lens to focus light, the ultimate spatial resolution is limited by diffraction from the limiting aperture in the optical path. This limiting aperture is usually determined by the diameter of the focusing element. Light waves passing through the focusing element interfere with each other around the focus to generate a three-dimensional diffraction pattern. The two-dimensional section of this pattern in the focal plane leads to the well-known Airy disk pattern that exhibits a bright central spot surrounded by concentric interference rings [10]. The size of the central spot in the Airy disk pattern dictates the maximal resolution achievable with the optical system. Assuming collimated, coherent light is directed through an aberration-free microscope objective, the spot size is given by

$$\text{spot size} = \frac{0.77\lambda_{\text{vac}}}{n \sin \theta} \quad (1)$$

where  $\lambda_{\text{vac}}$  is the vacuum wavelength,  $n$  is the refractive index of the medium that the light travels through, and  $\theta$  is the half angle through which the light is focused by the objective. In this equation, the spot size is defined as the distance from the

center of the Airy disk to the first node in the surrounding concentric rings. The collection of terms in the denominator of Eq. (1) determines the minimal spot size and is collectively known as the numerical aperture (NA) of the objective. Increasing resolution by reducing this spot size has led to the development of very high-quality objectives with NA values reaching as high as 1.65.

While the spot size can be directly quantified, resolution is a more subjective quantity and is usually discussed in terms of the Rayleigh criterion. Under this rubric, two features are resolvable if they are separated by a distance greater than or equal to that given by Eq. (1). Using this criterion, an image of two-point sources separated by this distance results in an intensity profile whose amplitude decreases by 20% between the two peaks. Obviously, with good signal-to-noise ratio, finer separations can be resolved, while imperfections in the optics, poor signal-to-noise ratio, or sample limitations conspire to lower the maximal resolution. Eq. (1) is often approximated to state that the resolving power using conventional optics is equal to  $\lambda/2$ . When working in the visible region of the spectrum, therefore, spatial resolution is limited to approximately 250–300 nm.

Overcoming the diffraction barrier motivated the development of NSOM. This method evolved out of the explosion in scanning probe technologies and their associated advances that were initiated in the early 1980s [11,12]. Of particular importance was the development of scanning tunneling microscopy (STM) and atomic force microscopy (AFM). Like these techniques, aperture NSOM is a scanning probe technique. Instead of using a lens to image a sample, NSOM overcomes the diffraction limit by using light passing through a sub-wavelength size aperture to deliver light down to the nanometric dimension. Light passes through the aperture and begins to diffract as shown schematically in Fig. 1. By positioning and maintaining the aperture near the sample surface, light exiting the

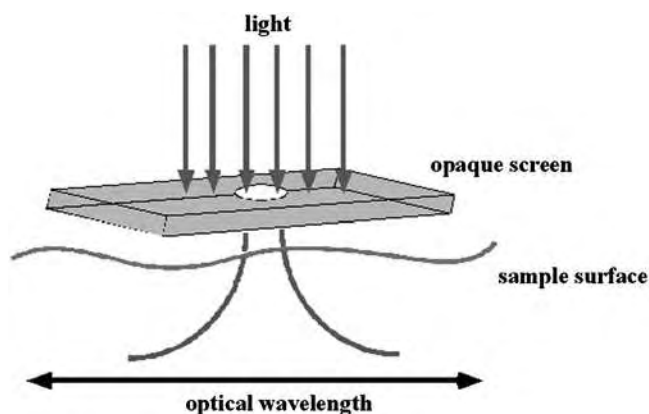


**Fig. 1.** Schematic of radiation passing through a sub-wavelength aperture in an opaque screen.

aperture is forced to interact with the sample before diffracting out. The spatial resolution is therefore determined only by the size of the aperture and its proximity to the sample surface and not the wavelength of the light as it is in conventional microscopy. This concept was originally proposed by Syge in the early 20th century [13–15], but was not experimentally realized until 1972 [16].

While the experimental details involved in implementing NSOM can be found elsewhere [7,8], it is instructive to briefly discuss the two main obstacles that must be overcome in order to conduct NSOM measurements. These revolve around aperture formation and implementing a feedback system for tip–sample distance control. For the former, as in all scanning probe techniques, the quality of the measurements is in large part dictated by the quality of the probe. For the latter, as the schematic in Fig. 1 suggests, high resolution requires that the NSOM probe be maintained within nanometers of the sample surface.

There are many aperture-formation methods, but those based on fiber optics have been the most widely adopted. In this approach, a single mode optical fiber is heated and pulled or etched to form a taper terminating in a small point. To confine the light inside the tapered region of the fiber and form an aperture at the distal end, the sides of the taper are coated with a reflective metal coating. When working in the visible region of the spectrum, aluminum is the most reflective metal with a skin depth of  $\sim 13$  nm at a wavelength of 500 nm. This small skin depth enables the light to be confined within the NSOM probe with an aluminum coating only 50–100 nm thick. Keeping the metal coating thin is important for keeping the probe aperture close to the sample surface. Fig. 2 shows magnified views of a typical fiber optic NSOM probe. In the electron microscopy image shown in Fig. 2, the granules from the aluminum coating are visible as is the aperture at the very end of the probe where the light emerges. In the optical image shown in Fig. 2, light emerging from the nanometric aperture is visible.

Once the NSOM probe is formed, high-resolution NSOM measurements rely on the ability to position and maintain the probe within nanometers of the sample surface during the experiment. There have been a myriad of different approaches that have been developed to control the tip–sample gap during measurements. These include approaches based on shear-force feedback, tapping-mode, such as that developed for AFM, and tuning fork feedback. All these methods enable nanometer control over the tip–sample gap and not only keep the NSOM probe close enough for high-resolution optical measurements, but also enable force mapping of the sample topography. NSOM measurements, therefore, provide simultaneous optical and topographical information about sample properties. Recent efforts have exploited these unique capabilities in order to gain insight into the spectroscopic, diffusive, and orientational properties of single molecules, as well as to characterize the submicron optical behavior of light-emitting polymers, J-aggregates, and liquid crystals. Here we summarize the insights that the NSOM technique has established in Langmuir–Blodgett films, with an emphasis on samples that are of biological importance.

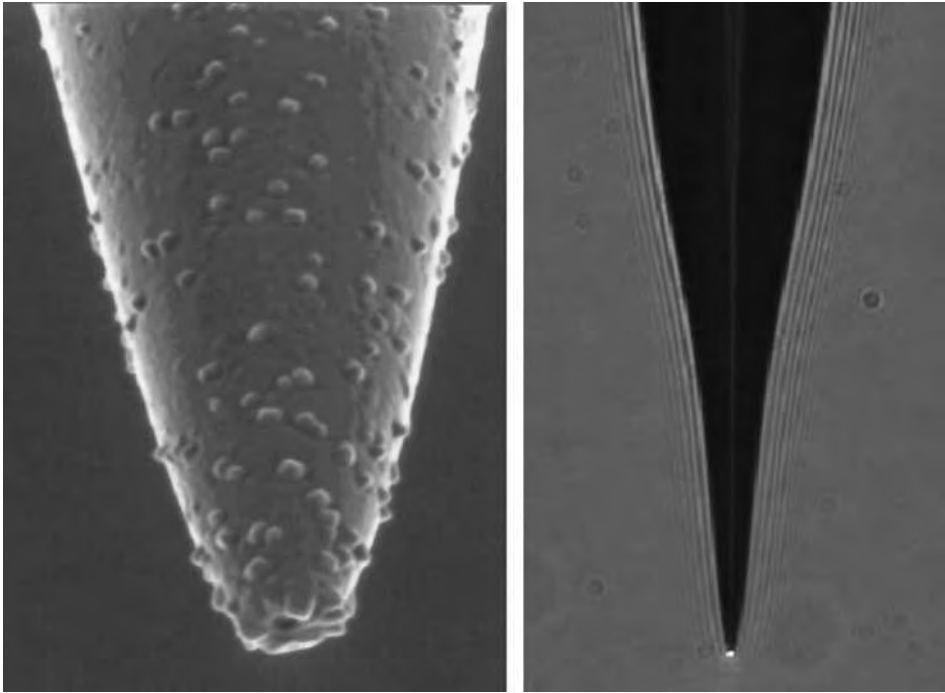


**Fig. 2.** (Left) Scanning electron micrograph of an Al-coated near-field probe, fabricated from a tapered optical fiber. (Right) Optical micrograph of a typical NSOM probe with light exiting the aperture at the end.

### 3. NEAR-FIELD STUDIES OF SUBMICRON MEMBRANE DOMAINS

#### 3.1. Monolayers

The manner in which cellular membranes organize in order to facilitate the coordination and regulation of trafficking and signal transduction are areas of intense, current research. The basis for our understanding of membrane organization is the fluid mosaic model [3]. This model describes the cellular membranes as a two-dimensional solution of integral proteins in a viscous bilayer solvent. Underlying this view is the implication that the proteins move via Brownian motion, so that their interactions occur only by chance. However, it is hard to reconcile this view that the proteins diffuse freely across the entire membrane with the facile assembly of the integral protein subunits into intricately structured channels. Rather, the substructure of the membrane must facilitate the assembly of such structures [17]. Hence, the notion that small domains like lipid rafts in the membrane compartmentalize the key subunits of such assemblies is gaining acceptance.

Lipid rafts are believed to be transient microdomains, perhaps 100 nm in size, that are composed chiefly of sphingolipids, cholesterol, and gangliosides. The aggregation of these components would facilitate their trafficking about the membrane. Additionally, their mobility facilitates their association with receptor subunits and, thereby, signal transduction. The original evidence underlying the lipid raft hypothesis is that a significant fraction of epithelial cellular membrane resists dissolution in cold, non-ionic detergents, such as Triton X-100 [4,5]. Because sphingolipids and cholesterol are detergent-resistant lipids that are present in these membranes and because they have been observed to form microdomains in model membranes, the detergent-resistant fraction of natural membranes has been associated with lipid rafts [4,6].

Substantial effort has been devoted to directly detecting these structures via conventional microscopic techniques. However, because their expected size is less than 100 nm, smaller than the optical diffraction limit, direct imaging of these structures is not possible with conventional optical microscopy. Therefore, near-field microscopic techniques, which are not diffraction-limited, provide a promising avenue to accurately characterizing lipid rafts, especially in combination with Langmuir–Blodgett techniques. Langmuir–Blodgett films provide largely static samples of lipid films, suppressing difficulties associated with the study of dynamical structures. Using such samples, several groups have made substantial headway in applying near-field microscopy to the study of lipid rafts.

Hollars and Dunn have shown that nanoscopic domains, with the dimensions of lipid rafts, form in *L*- $\alpha$ -dipalmitoyl phosphatidyl choline (DPPC) monolayers and bilayers transferred onto mica using the LB technique [18]. Fig. 3 shows a confocal fluorescence image of a DPPC monolayer deposited on mica at a surface pressure of 8 mN/m and containing 0.25 mol% of the fluorescent lipid analog diIC18. The membrane marker, diIC18, preferentially partitions into the less-ordered phase and, therefore, marks the liquid expanded (LE) phase in these films. The dark domains from which the dye is excluded represent the liquid condensed (LC) phase. Many studies of this system have been reported, but this work reveals an interesting new detail of the film's phase coexistence. No structure is evident within the LE phase in Fig. 3(A). Fig. 3(B) depicts a high-resolution topographical image of this film, obtained via AFM. The taller semi-circular regions in Fig. 3(B) are the LC domains evident in Fig. 3(A). However, Fig. 3(B) shows that the surrounding LE region is composed of coexisting domains with a height differential of 5–8 Å. These smaller domains could reflect coexisting lipid phases or simply defects in the monolayer, which are difficult to discern based on topography measurements alone. Fig. 3(C), however, shows an NSOM fluorescence image of this system. The bright regions denote the LE domains in which diIC18 is localized. With the high resolution provided by the NSOM technique, the substructure of the LE phase is apparent in this fluorescence image, whereas it is not evident in the far-field image of Fig. 3(A). Fig. 3(D) shows the simultaneously captured NSOM topography image of the same region shown in Fig. 3(C). The dark (i.e. low) regions in this image directly correlate with

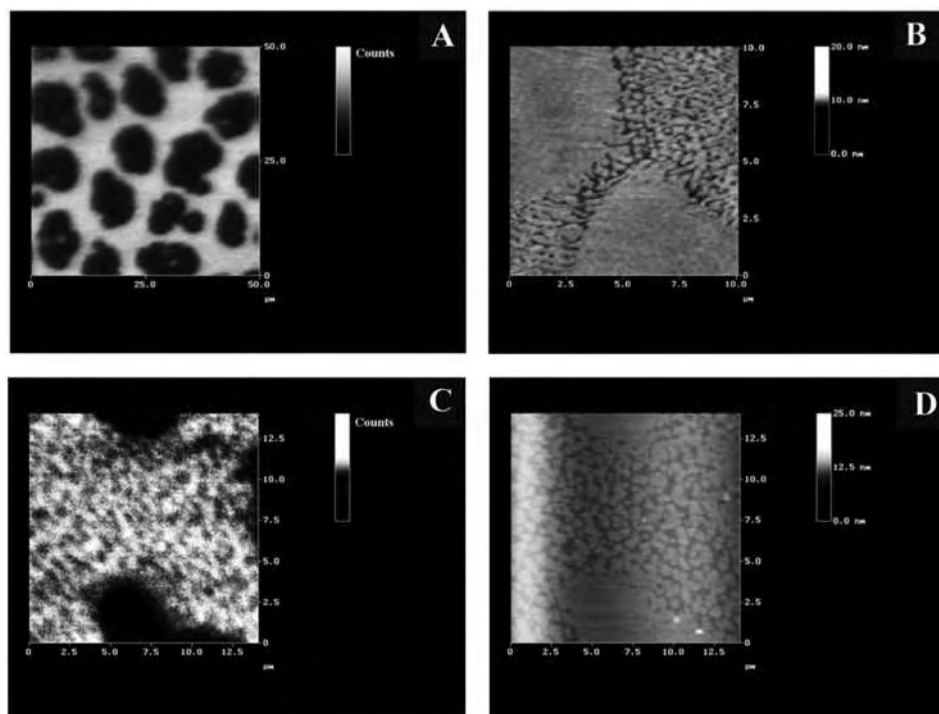


**Fig. 3.** (A) Far-field confocal micrograph ( $35\ \mu\text{m} \times 35\ \mu\text{m}$ ) of a mica-supported DPPC monolayer showing LE–LC phase coexistence, deposited at a surface pressure of  $9\ \text{mN/m}$ . (B) Atomic force micrograph of the film depicted in (A). Bright features denote topographically higher substructure of the film. (C) Near-field fluorescence image of the film shown in (A). (D) Near-field topology image collected simultaneously with the image depicted in (C). Reproduced with permission from Ref. [18]. Copyright 1998 Biophysical Society.

the regions of intense fluorescence in Fig. 3(C). This direct comparison indicates that the small domains are coexisting LE and LC domains.

Biological studies that employ model systems such as supported monolayers face the issue of demonstrating the physiological relevance of the model system. To address this issue, Shiku and Dunn extended the NSOM study of DPPC monolayers to the air–liquid interface, more closely approximating the biological environment of a cellular membrane [19]. NSOM studies of liquid-supported monolayers are challenging because attractive tip–film interactions cause the film to move with the tip as it scans over the surface. To overcome this problem, Shiku and Dunn used a 2% sucrose solution for the subphase. The large shear viscosity of this liquid provides sufficient drag to prevent tip-induced lateral motion of the sample.

Fig. 4(A) and (B) depict near-field fluorescence images of these films at low and high surface pressures, respectively. The LE–LC phase coexistence is clearly

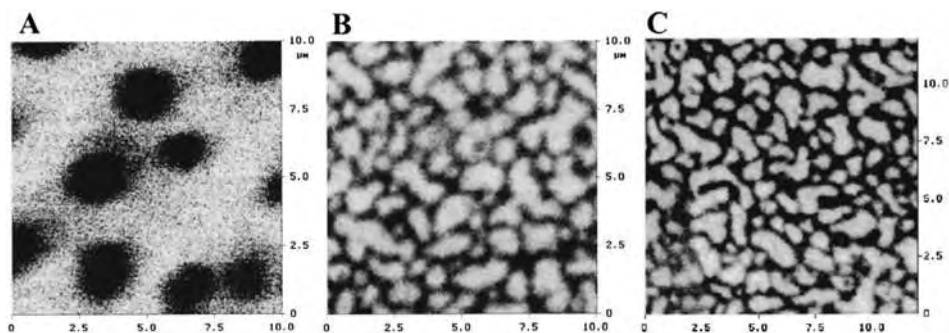


**Fig. 4.** (A) Near-field fluorescence image of a DPPC monolayer at the air–sucrose solution interface under low surface pressure. (B) Near-field fluorescence image of a DPPC monolayer at the air–sucrose solution interface under high surface pressure. (C) Near-field fluorescence image of a DPPC monolayer at the air–sucrose solution interface under high surface pressure, collected using the optical feedback approach. Reproduced with permission from Ref. [19]. Copyright 1999 Blackwell Publishing.

seen in these images. A further difficulty for these measurements lies in attaining strong feedback signal from Langmuir monolayers. That is, conventional tip positioning in scanning force microscopy is performed by force feedback methods that can damage the fragile, liquid-supported films. Therefore, this group developed an optical feedback method for positioning the near-field tip. This approach is gentler than force feedback because it can sense the film while the tip is several hundred nanometers from the surface. Fig. 4(C) shows a near-field fluorescence image of a DPPC film attained via this optical feedback method at high pressure on the air–sucrose interface. The imaging quality is superior to that of Fig. 4(B), which depicts a similar film attained via the conventional force feedback approach. The coexistence of small LC and LE domains, similar to those observed in the mica-supported monolayers (Fig. 3(C)), is evident. This finding suggests that the intermixing of submicron-sized domains is a general property of DPPC films, and not specific to Langmuir–Blodgett films.

These studies have demonstrated that microdomains in phospholipid membranes can be detected with NSOM and have, thereby, laid the groundwork for determining the composition of the submicron domains in more complex films. Recently, Johnston and co-workers employed a two-color NSOM approach to show that ganglioside-rich domains of  $\sim 100$  nm dimension form in model membranes composed of dioleoyl phosphatidyl choline (DOPC), sphingomyelin, and cholesterol in a 1:1:1 molar percentage, and 1 mol% GM1 [20]. In this study, the phospholipid was labeled with Texas Red, absorbing at 568 nm, and ganglioside was labeled with BODIPY, absorbing at 488 nm. The overlap between the absorbance spectra of these dyes is small, so 488 nm radiation causes both to fluoresce, while 568 nm excitation gives rise to fluorescence mainly from

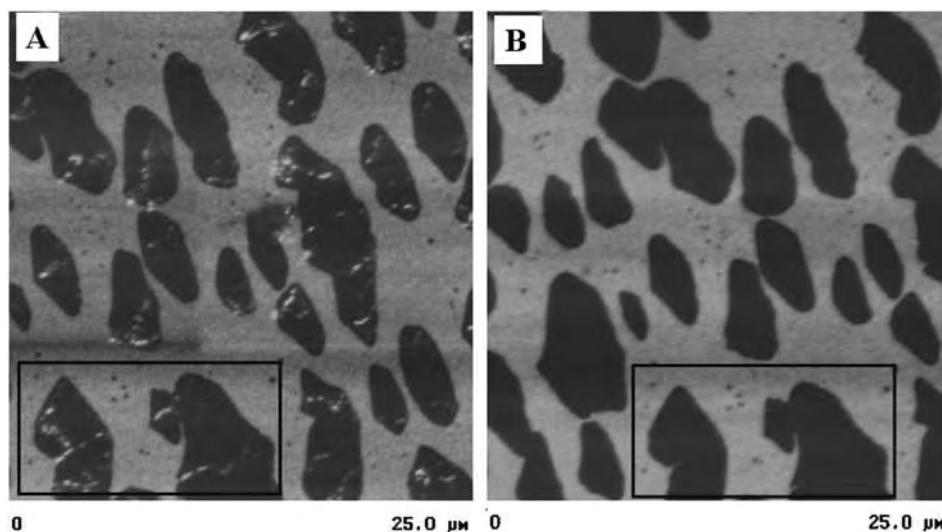


**Fig. 5.** (A) Near-field fluorescence image of a 1:1:1 sphingomyelin/cholesterol/DOPC monolayer containing 1% ganglioside (GM1), 0.005% GM1-BODIPY, and 1% Texas Red-DPPE. The excitation wavelength is resonant with both GM1-BODIPY and Texas Red-DPPE. (B) Near-field fluorescent image of the same film shown in (A), except that the excitation wavelength is 568 nm and is resonant with only Texas Red-DPPE. The rectangles denote film region common to both images. Reprinted in part with permission from Ref. [20]. Copyright 2003 The American Chemical Society.

Texas Red. Fig. 5(A) depicts an NSOM fluorescence image of this film obtained with 488 nm excitation. In addition to the bright fluid phase, this image depicts bright patches of fluorescence in the condensed domains. Fig. 5(B) depicts an image of the same area obtained with 568 nm excitation. Here, only the fluid phase is bright, while the condensed domains remain dark. A 568 nm radiation excites Texas Red and fails to excite BODIPY, the ganglioside label. Hence, this combination of images indicates that ganglioside is not homogeneously distributed in the film, but rather forms microdomains that are  $\sim 150$  nm wide, in agreement with dye-free AFM-based studies [21]. This finding provides support for the lipid raft hypothesis because such rafts are believed to be composed of ganglioside clusters in condensed lipid domains, and this study shows that the ganglioside readily partitions into nanoscopic regions within the condensed phase domains.

Complementing the above work on model membranes, Edidin and co-workers have performed an NSOM study of the nanoscale structure of lipid and protein patches in human skin fibroblasts [22]. As with the work of Dunn and co-workers [18,19], this work reveals lipid-rich regions with dimensions of 200 nm and smaller. Fig. 6(A) depicts an NSOM fluorescence image of a cellular

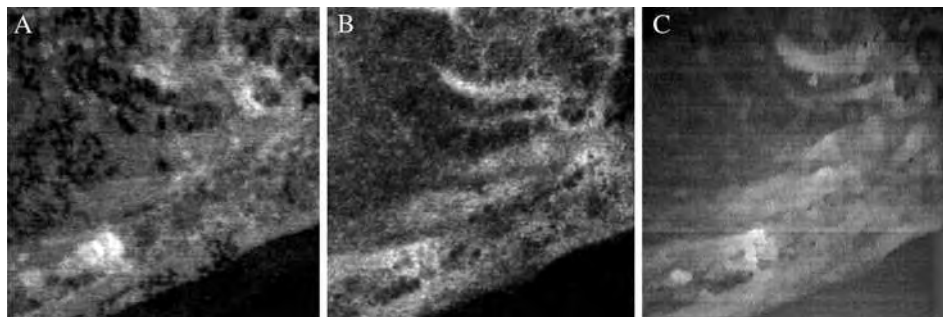


**Fig. 6.** (A) Near-field fluorescence image of a fibroblast containing the lipid analog BODIPY-PC and a tetramethylrhodamine-conjugated monoclonal antibody. In this image, the excitation wavelength is resonant with the BODIPY-PC tag. (B) In this image, the excitation wavelength is resonant with the antibody labeling the MHC complexes. (C) Shear force topographic image of the film of the cell shown in (A). Reproduced with permission from Ref. [22]. Copyright 1998 The Biophysical Society.

membrane that has been labeled with BODIPY-tagged phosphocholine molecules, which preferentially partition into the phosphocholine-rich regions of the film. In the left portion of this image, a highly branched dark pattern disrupts the otherwise uniform fluorescence in this region. These dark branches, roughly 200 nm wide, are not spatially correlated with any features in the topography image in Fig. 6(C), showing that they do not correspond to tears in the membrane. Rather, these features designate nanoscopic regions of the membrane from which phosphocholine is excluded.

Fig. 6(B) depicts a near-field fluorescence image of the same cell except that here, fluorescence from the antibody-labeled HLA class I protein molecules was collected. (HLA I fluoresces in a spectrally distinct region of the spectrum than does BODIPY-PC.) Comparison of this image with the topography image shows that the HLA I molecules tend to populate the ridges of the membrane. Moreover, in the left region of Fig. 6(B), the fluorescence from the HLA I protein molecules does not exhibit the same fractal-like pattern as the lipid-rich regions in Fig. 6(A). Corroborating the spatial resolution of Fig. 6(B), further analysis, based on quantification of the spatial extent of intensity fluctuations by calculating intensity auto-correlation functions, revealed that the HLA molecules tend to cluster into patches of  $\sim 70$  and  $\sim 600$  nm. The fractal regions in Fig. 6(A) represent film regions containing the protein but little phosphocholine. These results demonstrate that  $\sim 200$  nm proteinaceous domains, similar to those observed in the model membranes studies by Johnston and co-workers [20], occur in biological cells as well.

Other NSOM studies have revealed evidence for structural features that promote interaction between different membrane proteins. By exploiting the high spatial resolution of NSOM, Ianoul and co-workers have performed

colocalization investigations of caveolin-3 and  $\beta$ -adrenergic receptors in cardiac myocytes. A topographical image of the myocytes is shown in Fig. 7(A). In this study, the caveolin-3 has been labeled to fluoresce green and the  $\beta$ -adrenergic receptors to fluoresce red [23]. Fig. 7(B) and (C) are NSOM fluorescence images that show the distribution of caveolin-3 and  $\beta$ -adrenergic receptors in this cell, respectively. Analysis of these images reveals spatial overlap between a sub-population of caveolin-3 and  $\beta$ -adrenergic receptors. This property is seen most clearly in Fig. 7(D), which is an overlay of Fig. 7(B) on (C). The yellow features in this image denote the colocalization of caveolin-3 and  $\beta$ -adrenergic receptors. Roughly 20% of the  $\beta$ -adrenergic receptors are associated with caveolin-3. This finding suggests that the  $\beta$ -adrenergic receptors are compartmentalized by the caveolae, significant because this compartmentalization may facilitate the signaling processes that the  $\beta$ -adrenergic receptors induce. As similar structural organization has been observed in rhodopsin complexes, another G-protein-coupled receptor, this feature may be a general feature of cellular signaling [24,25] and requires further study.

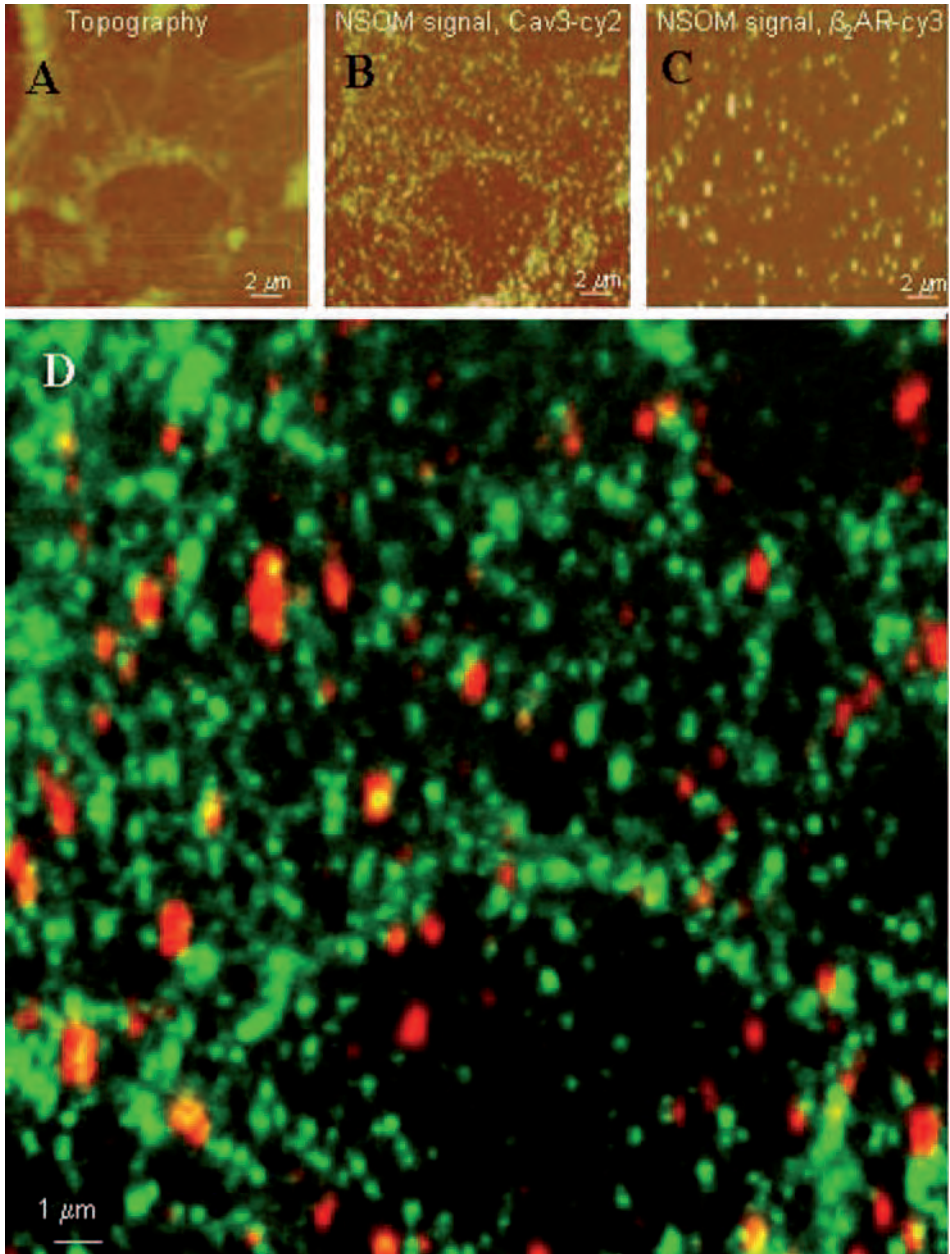
### 3.2. Bilayers and Multi-Layer Lipid Films

As shown in the previous section, the high resolution of NSOM enables the detection of small domains in lipid monolayers that are beyond the resolving power of techniques such as confocal fluorescence microscopy. Moreover, the simultaneous topography measurements reveal the angstrom-level height difference associated with coexisting lipid phases that can be directly correlated with the fluorescence signal. As model films become more complex to better mimic biomembranes, the simultaneous NSOM fluorescence and topography measurements become especially informative.

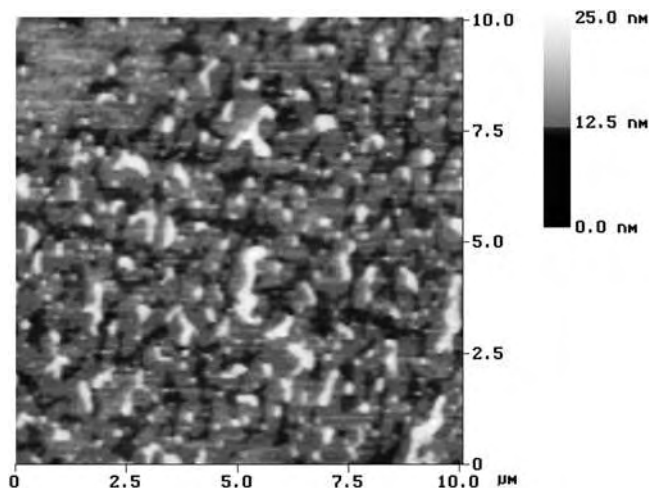
Model lipid bilayers have long been the focus of research and a vast literature exists discussing various approaches to fabricating bilayer films, measuring their physical properties, and understanding the influence of various constituents on those properties. These structures, ubiquitous in nature, can be formed on substrates where they are amenable for study with surface techniques such as AFM and NSOM.

Fig. 8 shows an AFM image of a DPPC bilayer formed using a combination of the LB technique and the Langmuir–Schaefer (LS) method [18]. In this approach, the first monolayer is deposited onto the substrate using the LB dipping technique. The second monolayer is deposited on the first using the LS approach where the substrate is positioned parallel with the air–water interface and transferred through the interface. This results in a Y-type lipid bilayer supported on a substrate.

For bilayers in which each monolayer is transferred in a phase coexistence region of the pressure isotherm, the phase structure in each leaflet of the bilayer is preserved. For example, each leaflet of the bilayer shown in Fig. 8 was transferred in the LE–LC phase coexistence region of the pressure isotherm.



**Fig. 7.** (A) NSOM topographical image of a cardiac myocyte. NSOM fluorescence images of the myocyte immunostained for (B) caveolin-3 and (C)  $\beta$ -adrenergic receptors. (D) An overlay image composed of the NSM fluorescence images shown in (B) and (C). Reproduced with permission from Ref. [23]. Copyright resides with the authors.



**Fig. 8.** An AFM image of a DPPC bilayer formed using a combination of the LB and LS film transfer techniques. Three distinct height levels are seen that correspond to the layering of LE on LE, LE on LC (or LC on LE), and LC on LC. Reproduced with permission from Ref. [18]. Copyright 1998 The Biophysical Society.

Unlike the AFM image for a simple monolayer where the 5–8 Å height difference between the LE and LC phases can easily map the phase structure of the film, for bilayers the convolution of the two leaflets complicates this assignment. In Fig. 9, the AFM image of the DPPC bilayer reveals three distinct height levels [18]. This corresponds to stacking of LE on LE, LE on LC (or LC on LE), and LC on LC, in order of increasing height. While images such as these suggest that phase coexistence remains present in each monolayer of the bilayer, assignment of the phase structure from each leaflet cannot be extracted from AFM measurements alone. However, with the high-resolution fluorescence measurements of NSOM, this information can be uncovered.

Fig. 9 shows NSOM fluorescence (top panel) and topography (bottom panel) measurements, respectively, on a Y-type DPPC bilayer similar to that shown in Fig. 8 [18]. As in the AFM measurements, the NSOM topography provides little information about the phase structure present on either side of the membrane leaflet. However, by adding a fluorescent lipid analog to only one side of the bilayer, the NSOM fluorescence image reveals the phase structure in either leaflet. As an example, Fig. 9(top) shows the NSOM fluorescence image of a DPPC bilayer in which the bottom monolayer contains the fluorescent lipid analog diIC18. Large circular dark regions excluding the lipid dye mark LC regions, while the surrounding bright regions mark areas of LE phase. As seen previously, the LE regions actually contain small coexisting domains of LE and LC phases that require the resolution of NSOM to be resolved. Similar measurements on bilayers in which the upper leaflet is doped with the fluorescent lipid analog reveal similar structures.

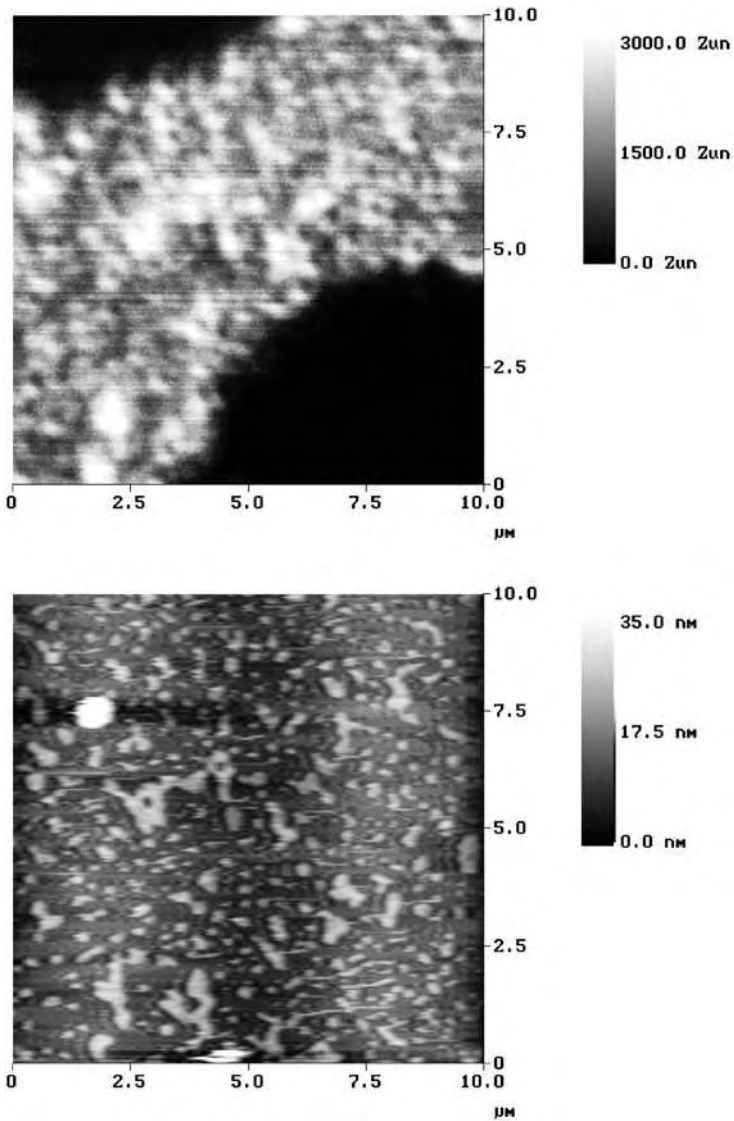


**Fig. 9.** (Top) NSOM fluorescence image of a DPPC bilayer in which the bottom monolayer contains the fluorescent lipid analog diIC<sub>18</sub>. (Bottom) NSOM force image of the same bilayer. Reproduced with permission from Ref. [18]. Copyright 1998 The Biophysical Society.

The ability to measure the distribution of lipids across natural biomembranes is a potentially powerful capability. Natural biomembranes maintain an asymmetric distribution of lipid components across the membrane with the inner leaflet rich in anionic lipids and both leaflets containing proteins and species specific to each

side. Maintaining this asymmetry is important for proper cellular function and the loss of this asymmetry is often used as an indicator of apoptosis. Probing this asymmetry and changes in these components directly, however, has proven difficult. Preferentially labeling species on either side of the membrane can be used to probe these differences, but this is often difficult and not always practical. Since the width of a bilayer is only a few nanometers thick, normal optical sectioning methods do not have the resolution necessary to probe these differences.

One optical technique that does operate on this length scale, however, is fluorescence resonance energy transfer (FRET). FRET takes advantage of energy transfer from an excited donor dye molecule to an acceptor dye molecule to probe distance relationships on the nanometer length scale. The distance dependence of the FRET technique was combined with NSOM to create a new method for optical sectioning with nanometer resolution [26,27]. In this approach, an acceptor dye of a FRET pair is attached to the distal end of an uncoated NSOM probe. The acceptor dye was dispersed in a lipid matrix and transferred onto the NSOM probe using the LB technique. This results in a controlled coating of a single monolayer onto the surface of the fiber optic NSOM probe. The sample used to demonstrate the sectioning capabilities of the combined NSOM/FRET technique consisted of a multi-layer LB film. The bottom and top layers of the multi-layer film were doped with the donor dye of the FRET pair. These layers were separated by three spacer layers of arachidic acid that did not contain the donor dye. The film is shown schematically in Fig. 10.

Light from the NSOM probe is resonant with the donor dye in the sample but not the tip-bound acceptor dye. The fluorescence from the donor dye, therefore, maps the location of domains that contain the donor dye in both the bottom and top layers of the multi-layer film, but cannot distinguish between the two. However, as the NSOM probe nears the film, energy transfer from the excited donor dye in the sample to the tip-bound acceptor dye can occur, leading to fluorescence from the acceptor. Because of the strong distance dependence of this process, energy transfer is dominated by donor dye in the upper layer of the film closest to the NSOM probe. To demonstrate this technique, a multi-layer film was deposited onto a glass substrate using the LB method. The first monolayer transferred was composed of DPPC doped with 0.5 mol% of the donor dye fluorescein. Three spacer layers of arachidic acid were then transferred followed by a top layer composed again of DPPC/0.5 mol% fluorescein. The LB technique was also used to attach the acceptor dye, rhodamine, to an NSOM probe that had not been coated with aluminum. A monolayer of DPPC/0.5 mol% rhodamine was transferred onto the pulled fiber optic to provide a well-defined monolayer coating around the apex of the probe [26,27].

As shown in Fig. 10, this experimental arrangement reveals significant differences in the NSOM fluorescence images following excitation of the donor dye in the multi-layer film and monitoring either the donor dye fluorescence or the fluorescence from the tip-bound acceptor dye. Fluorescence from the donor dye (left) reveals domains in the multi-layer film that contain the donor dye but is

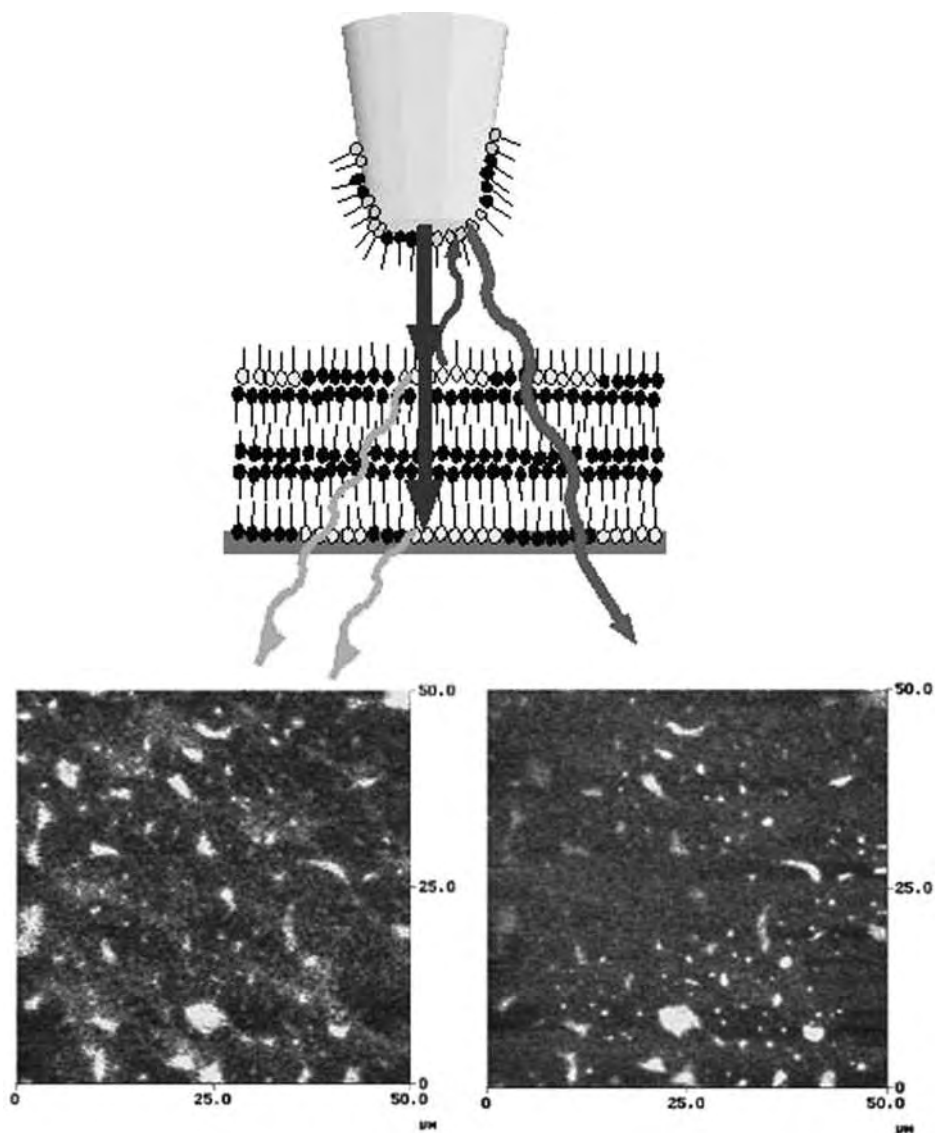


**Fig. 10.** (Top) Schematic of the experimental arrangement for carrying out NSOM/FRET measurements. An acceptor dye of a FRET pair is attached to the NSOM probe while the sample contains the donor dye in the bottom and top layers of a multi-layer film. The left fluorescence image shows the donor fluorescence and the right the fluorescence from the tip-bound acceptor dye. Reproduced with permission from Ref. [26]. Copyright 1999 The Biophysical Society.

unable to discriminate between domains located in the top and bottom layers of the film. However, when acceptor emission, arising from energy transfer from excited donors in the sample to the tip-bound acceptors, is monitored (right), new features are observed. Some regions that appeared bright in the donor emission image almost completely disappear when acceptor emission is monitored. These areas mark regions in the film where the donor dye is in the bottom layer of the film and energy transfer to the tip is small. Other regions in the acceptor image become brighter and the resolution in these areas sharpens. These regions reveal areas where the donor dye is located in the top layer of the film where energy transfer to the acceptor on the tip is maximized. Therefore, the combination of these images can be used to delineate between donor dye located on either side of the film. Combining NSOM with FRET therefore provides an optical sectioning tool with nanometric sectioning capabilities. Probing membrane asymmetry in living cells is obviously a very important area that can potentially take advantage of these unique capabilities. While progress in applying NSOM to living, viable biological samples has been slow, recent advances are starting to open this important area.

### **3.3. Live Cell Measurements**

Extending NSOM measurements from model lipid films to biomembranes in viable cells has proven difficult. Initial problems revolved around difficulties in implementing the force feedback, necessary for maintaining the tip-sample gap, in the aqueous environments necessary for viable tissues. This, however, has been circumvented using a number of approaches. The more daunting challenge has been to reduce the forces involved in the feedback such that fragile samples, such as living cells, are not destroyed in the imaging process. Approaches to reduce these forces have largely revolved around the development of new feedback schemes or through modifications in the NSOM probe aimed at reducing its spring constant. The fiber optic probes used in NSOM normally have spring constants on the order of hundreds of nanonewtons per meter. This can be compared with conventional AFM probes, which are compatible with living cells, that have spring constants less than a nanonewton per meter. An obvious direction, therefore, has involved coupling the low spring constant of conventional AFM probes with the light delivery capabilities of NSOM to create hybrid probes capable of live cell imaging.

One such approach has recently been developed and shown to enable high-resolution NSOM fluorescence and force measurements on viable cultured human arterial smooth muscle (HASM) cells under buffered conditions [28,29]. This approach takes advantage of the nanofabrication capabilities of focused ion beam (FIB) milling to sculpt a light delivery structure into the end of a conventional AFM probe. The FIB technique, which utilizes a focused beam of gallium ions to mill samples with nanometer resolution, was first used by van Hulst and co-workers to modify conventional NSOM probes [30]. They demonstrated an improvement in single molecule fluorescence measurements using

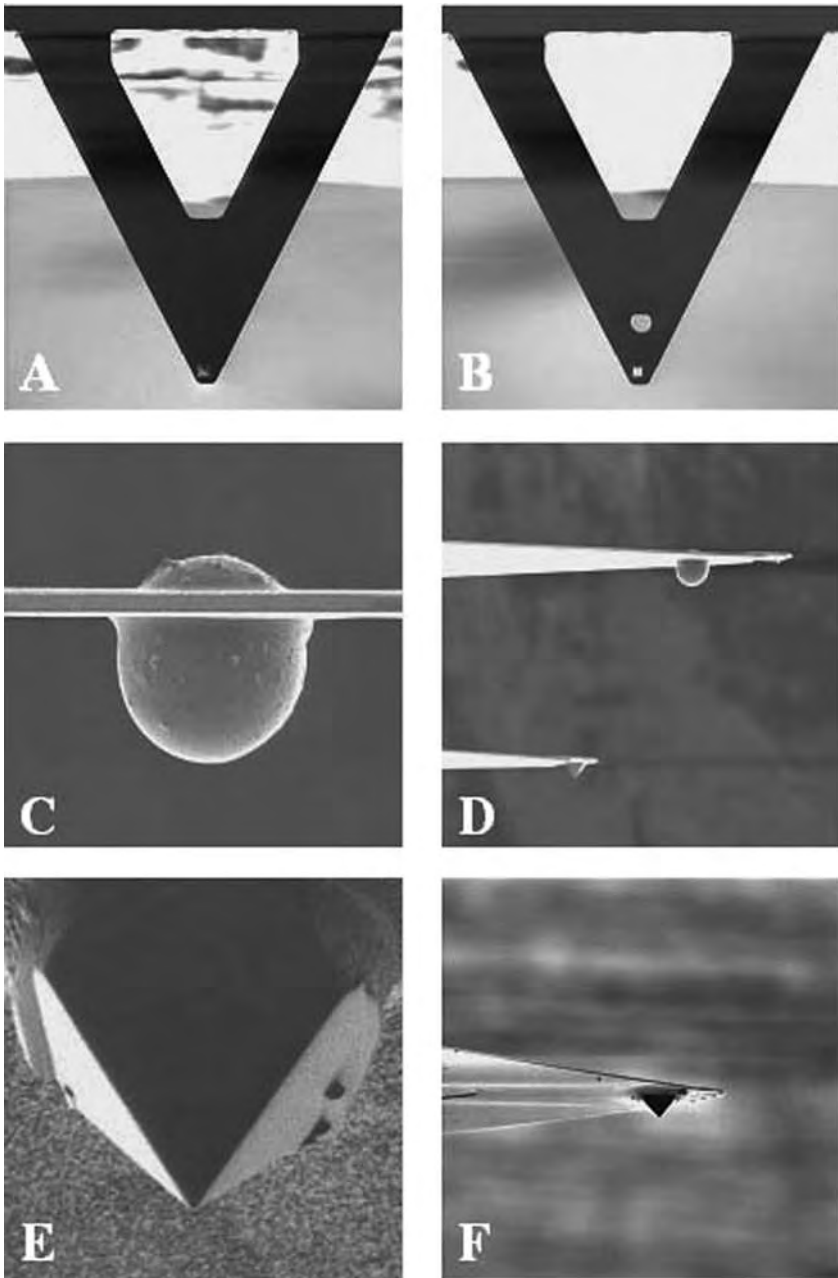


**Fig. 11.** Series of steps used to fabricate a small light source onto the end of a commercial AFM cantilever (A). (B) A small hole is cut into the cantilever and (C) an 8  $\mu\text{m}$  high-index glass sphere is glued in place. (D) The glass sphere is then shaped into a pyramid (E), coated with aluminum and an aperture formed to produce small light source on the end of the cantilever (F). Reproduced with permission from Ref. [29]. Copyright 2001 American Institute of Physics.

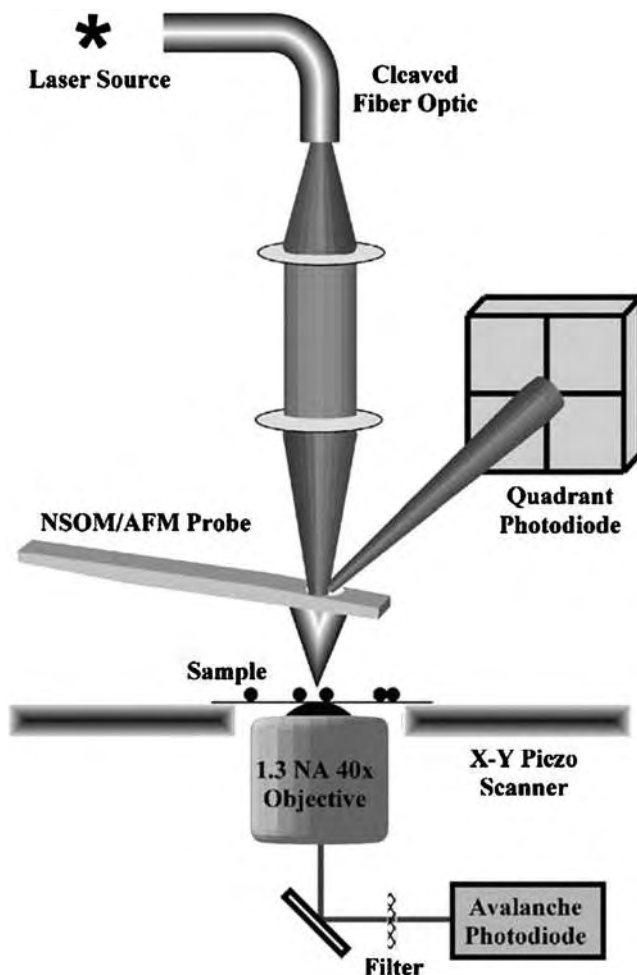


**Fig. 12.** Schematic showing the hybrid NSOM/AFM probes used in a commercially available scan head. Light focused on the backside of the cantilever is used as both the excitation source and the feedback signal for the force feedback. Reproduced with permission from Ref. [29]. Copyright 2001 American Institute of Physics.

NSOM probes in which the aperture had been milled flat using the FIB technique.

In another approach, FIB milling was used to incorporate a light delivery structure into a conventional AFM probe. In one report, a  $7\ \mu\text{m}$  hole was cut into the end of an AFM probe and an  $8\ \mu\text{m}$ , high-refractive index glass sphere was glued in the hole. The series of steps is shown in Fig. 11 [29]. The FIB was then used to flatten the backside of the sphere and sculpt the rest into a pyramid shape that terminated at an apex that would form the aperture for light delivery. The

sides of the pyramid were evaporatively coated with 50–100 nm of aluminum to confine the light within the taper region, and an aperture was opened at the very end of the probe with the FIB approach. The result is a hybrid NSOM/AFM probe that has the small spring constant of conventional AFM probes, amenable to imaging soft and fragile samples, and an aperture for optical measurements.

Fig. 12 schematically shows how these hybrid NSOM/AFM probes are used in commercially available scan heads. Light is focused on the backside of the probe where a small amount is transmitted to the aperture at the apex of the pyramid. Most of the light is reflected from the backside of the cantilever and onto a quadrant detector, where it is used to generate the feedback signal for tip-sample distance control. The light transmitted from the aperture excites fluorescence in the sample, which is collected from below using a high-numerical aperture objective. The collected light is filtered to remove residual excitation light and the fluorescence is imaged onto a high-quantum efficiency avalanche photodiode detector. Fig. 13 shows the NSOM fluorescence and force images of a test sample consisting of 50 nm fluorescent latex spheres embedded in an acetate matrix [29]. The NSOM fluorescence image reveals small fluorescence spots that indicate the location of the beads in the sample. The force image, taken in contact mode, tracks the topography of the sample.

A similar design that coupled fiber optic NSOM probes with AFM cantilevers was also reported [28]. In this approach, shown in Fig. 14, a standard fiber optic NSOM probe was carefully inserted through the 7  $\mu\text{m}$  hole that was cut into the end of an AFM probe. Once glued into place, the excess fiber on the backside of the AFM cantilever was removed using FIB milling. This approach

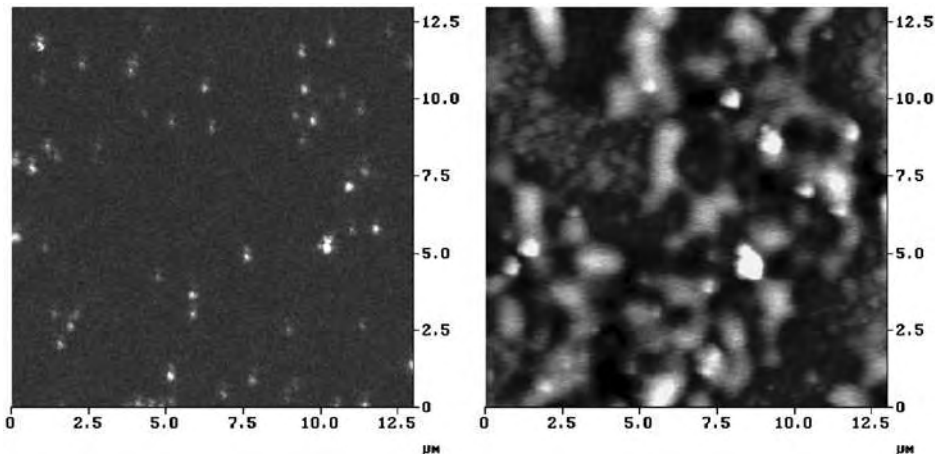


**Fig. 13.** NSOM fluorescence (left) and force (right) images of 50 nm fluorescent latex spheres in a thin film. The fluorescence image exhibits high resolution while the small spring constant of the probe allowed the force image to be taken in contact mode without damaging the NSOM aperture.

had the advantage of incorporating the well-known properties of fiber optic NSOM probes into the design along with a fabrication process that required fewer steps. The former approach using sculpted spheres offers more flexibility in choice of material and, therefore, refractive index and more control over the taper geometry in the probe which strongly influences light throughput. Because of the small spring constant of the AFM cantilever, both tip designs can be operated in contact mode without damaging the aperture, are easily operated in aqueous environments, and are amenable to live cell imaging.

Fig. 15 shows the simultaneously measured NSOM fluorescence, topography, and deflection of a viable HASM cell under buffered conditions [28]. These images were collected in contact mode using a hybrid NSOM/AFM probe. The fluorescence signal maps the location of adrenergic receptors in the cellular membrane, which have been fluorescently labeled with prazosin BODIPY-FL. These measurements show that the hybrid NSOM/AFM probes are capable of

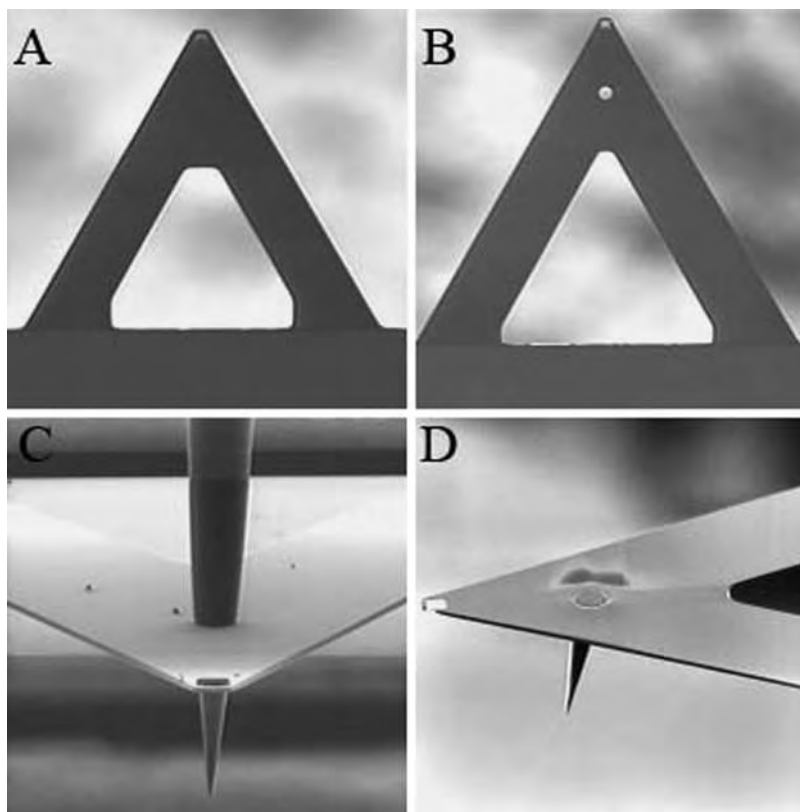


**Fig. 14.** (A) Magnified view of an AFM cantilever and (B) the same cantilever with a  $7\ \mu\text{m}$  hole drilled with a FIB. (C) A fiber optic NSOM probe is positioned and glued in the hole and (D) the excess fiber removed with a FIB. Reproduced with permission from Ref. [28]. Copyright 2004 American Institute of Physics.

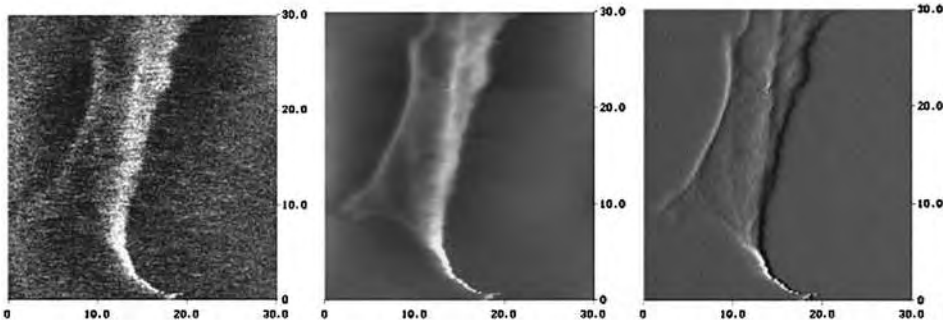


**Fig. 15.** NSOM fluorescence (left), force (middle), and deflection (right) images of a living HASM cell under buffered conditions. The cell has not been fixed and the adrenergic receptors in the membrane have been fluorescently labeled with prazosin BODIPY-FL. Reproduced with permission from Ref. [28]. Copyright 2004 American Institute of Physics.

live cell measurements and repeated scans on the same cell revealed no evidence of evolution in cellular morphology that might indicate damage. Besides mapping the adrenergic receptors through the fluorescence signal, the deflection and force images reveal the overall morphology of the cell and the location of structural fibers in the cell.

#### 4. CONCLUSIONS AND FUTURE DIRECTIONS

While NSOM offers unique capabilities that should prove informative in future biological applications. The method continues to prove difficult to implement on living biological samples due to technical aspects associated with this challenging technique. Perhaps the most critical limitation on the near-field technique is the difficulty associated with fabricating probes that have reproducible properties. Reducing the probe-to-probe variation in the aperture size, taper, and metallic coating of these probes as well as scaling up the quantity that may be produced at one time would make possible the systematic data-processing and analysis routines that are exploited to great advantage in the more conventional microscopies. For example, there has been relatively little work on the development and implementation of the deconvolution protocols for near-field imaging that are widely used in optical microscopies where Gaussian optics is well obeyed. To progress in this direction, techniques must be developed that will enable the point-spread function of the near-field probes to be measured. In most cases, this would be a prohibitively laborious undertaking to perform on a sample-by-sample basis, but if large numbers of tips could be produced with precisely controlled optical characteristics, then a single point-spread function could be applied to all of them.

## REFERENCES

- [1] B. Alberts, D. Bray, J. Lewis, M. Raff, K. Roberts and J. D. Watson, *Molecular Biology of the Cell*, Garland Publishing, New York, 1994.
- [2] J. R. Bourbon, *Pulmonary Surfactant*, CRC Press, Boca Raton, FL, 1991.
- [3] S. J. Singer and G. L. Nicolson, The fluid mosaic model of the structure of cell membranes, *Science*, 175 (1972) 730–731.
- [4] D. A. Brown and J. K. Rose, Sorting of GPI-anchored proteins to glycolipid-enriched membrane subdomains during transport to the apical cell surface, *Cell*, 68 (1992) 533–544.
- [5] R. G. Parton and K. Simons, Digging into caveolae, *Science*, 169 (1995) 1398–1399.
- [6] D. A. Brown and E. London, Structure of detergent-resistant membrane domains: does phase separation occur in biological membranes, *Biochem. Biophys. Res. Commun.*, 240 (1997) 1–7.
- [7] E. Betzig, M. Isaacson, H. Barshatzky, A. Lewis and K. Lin, Near-field scanning optical microscopy (NSOM), *Proc. SPIE*, 897 (1988) 91–99.
- [8] R. C. Dunn, Near-field scanning optical microscopy, *Chem. Rev.*, 99 (1999) 2891–2927.
- [9] M. Edidin, Near-field scanning optical microscopy, a siren call to biology, *Traffic*, 2 (2001) 797–803.
- [10] E. Abbe, *Mikrosk. Anat.*, 9 (1873) 413–468.
- [11] G. Binning, H. Rohrer, Scanning apparatus for surface investigation using vacuum-tunnel effect at cryogenic temperatures, *Eur. Pat. Appl. IBM, USA*, 1981, p. 37.
- [12] G. Binning, H. Rohrer, C. Gerber and E. Weibel, Surface studies by scanning tunneling microscopy, *Phys. Rev. Lett.*, 49 (1982) 57–61.
- [13] E. H. Syge, *Philos. Mag.*, 6 (1928) 356–362.
- [14] E. H. Syge, *Philos. Mag.*, 11 (1931) 65–80.
- [15] E. H. Syge, *Philos. Mag.*, 13 (1932) 297.
- [16] E. A. Ash and G. Nicholls, *Nature*, 237 (1972) 510–512.
- [17] P. S. H. Park and K. Palczewski, Imaging G protein-coupled receptor islands, *Nat. Chem. Biol.*, 1 (2005) 184–185.
- [18] C. W. Hollars and R. C. Dunn, Submicron structure in 1-*a*-dipalmitoylphosphatidylcholine monolayers and bilayers probed with confocal, atomic force, and near-field microscopy, *Biophys. J.*, 75 (1998) 342–353.
- [19] H. Shiku and R. C. Dunn, Domain formation in thin lipid films probed with near-field scanning optical microscopy, *J. Microscopy*, 194 (1998) 455–460.
- [20] P. Burgos, C. Yuan, M. Viriot and L. J. Johnston, Two-color near-field fluorescence microscopy studies of microdomains (“rafts”) in model membranes, *Langmuir*, 19 (2003) 8002–8009.
- [21] C. Yuan, J. Furlong, P. Burgos and L. J. Johnston, The size of lipid rafts: an atomic force microscopy study of ganglioside GM1 domains in sphingomyelin/DOPC/cholesterol membranes, *Biophys. J.*, 82 (2002) 2526–2535.
- [22] J. Hwang, L. A. Gheber, L. Margolis and M. Edidin, Domains in cell plasma membranes investigated by near-field scanning optical microscopy, *Biophys. J.*, 74 (1998) 2184–2190.

- [23] A. Ianoul, D. D. Grant, Y. Rouleau, M. Bani-Yaghoub, L. J. Johnston and J. P. Pezacki, Imaging nanometer domains of  $\beta$ -adrenergic receptor complexes on the surface of cardiac myocytes, *Nat. Chem. Biol.*, 1 (2005) 196–202.
- [24] D. Fotiadis, Y. Liang, S. Filipek, D. A. Saperstein, A. Engel and K. Palczewski, Atomic-force microscopy: rhodopsin dimers in native disc membranes, *Nature*, 421 (2003) 127–128.
- [25] Y. Liang, D. Fotiadis, S. Filipek, D. A. Saperstein, K. Palczewski and A. Engel, Organization of G protein-coupled receptors rhodopsin and opsin in native membranes, *J. Biol. Chem.*, 278 (2003) 21655–21662.
- [26] S. A. Vickery and R. C. Dunn, Scanning near-field fluorescence resonance energy transfer microscopy, *Biophys. J.*, 76 (1999) 1812–1818.
- [27] S. A. Vickery and R. C. Dunn, Combining AFM and FRET for high resolution fluorescence microscopy, *J. Microscopy*, 202 (2001) 408–412.
- [28] L. K. Kapkiai, D. Moore-Nichols, J. Carnell, J. R. Krogmeier and R. C. Dunn, Hybrid near-field scanning optical microscopy tips for live cell measurements, *Appl. Phys. Lett.*, 84 (2004) 3750–3752.
- [29] J. R. Krogmeier and R. C. Dunn, Focused ion beam modification of atomic force microscopy tips for near-field scanning optical microscopy, *Appl. Phys. Lett.*, 79 (2001) 4494–4496.
- [30] J. A. Veerman, A. M. Otter, L. Kuipers and N. F. van Hulst, High definition aperture probes for near-field optical microscopy fabricated by focused ion beam milling, *Appl. Phys. Lett.*, 72 (1998) 3115–3117.

## Chapter 6

# Micro/Nanolithography Using Self-Assembled Monolayers (SAMs)

O. Takai\*, K. Hayashi

*EcoTopia Science Institute and Department of Materials, Physics and Energy Engineering, Graduate School of Engineering, Nagoya University, Nagoya 464-8603, Japan*

### 1. SELF-ASSEMBLED MONOLAYERS (SAMs)

#### 1.1. What is SAM?

Self-assembled monolayer (SAM) is a single layer of organic molecules formed on a substrate in a liquid or gas phase. When a suitable combination of a substrate material and organic molecules is selected, and the substrate is located into a solution or vapor which contains the organic molecules, the molecules are chemically adsorbed onto the substrate surface through the chemical reaction of the molecules with the substrate material. As shown in Fig. 1, the adsorbed molecules gather closely due to interactions among molecules under a certain condition during the chemisorption process, and a monolayer with highly oriented molecules is formed on the substrate surface. As the monolayer formation is completed, the growth of the layer is stopped automatically, because the molecule-covered surface runs out of reaction site and the adsorption reaction does not continue. Such an ultrathin organic film is called SAM due to spontaneous assembling of organic molecules [1,2].

Two-dimensional arrangement in SAMs is formed in a process where the whole system is approaching equilibrium. This means that SAMs are close to a

---

\*Corresponding author. E-mail: takai@plasma.numse.nagoya-u.ac.jp

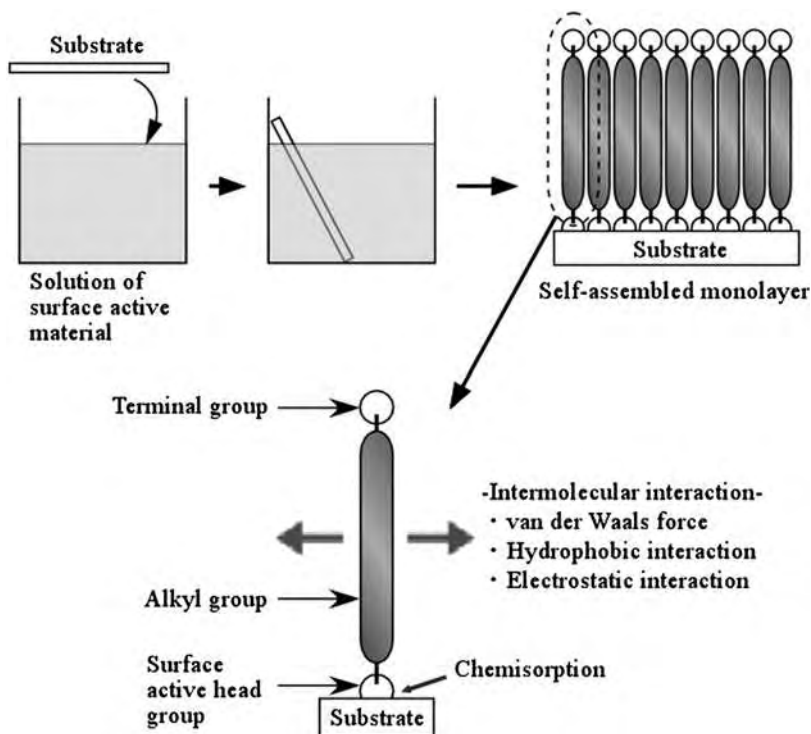


**Fig. 1.** Illustration of the SAM.

thermodynamically stable state. Examples of typical combinations of substrate materials and organic molecules for the formation of SAMs are as follows: aluminum oxide, silver oxide or glass and carboxylic acid [3–9], gold, silver, copper or GaAs and organic sulfur compounds, such as thiol [10–17], and silicon oxide, titanium oxide or other oxides and organosilane compounds [18–31].

Terminated functional groups located at the tops of organic molecules chemisorbed onto a substrate surface cover over the surface. It is, therefore, possible to design and control physical and chemical properties of the surface by the selection of terminated functional groups. For example, it is possible to add surface reactivity by choosing amino, epoxy or vinyl group, or to reduce surface energy by selecting alkyl or fluoroalkyl group.

Especially, organosilane SAMs have high stability because they are immobilized at substrates through siloxane bonding, a kind of covalent bonding, and neighboring molecules are bonded together through siloxane network. Therefore, organosilane SAMs are much superior to other SAMs in mechanical strength and chemical stability with the largest possibility of the practical uses for surface modification and surface functionalization. We have used the organosilane SAMs as resists and applied them to micro/nanolithography.

## 1.2. Usefulness of SAMs in Lithography

Lithography is indispensable technology in micro/nanofabrication processes for semiconductor integrated circuits, sensors, displays, macro/nanomachines, etc. In photolithography, a photosensitive organic polymer thin film called photoresist is coated onto a substrate, and a photomask pattern is transferred to the resist by exposure through the photomask. As the degree of integration in integrated circuits increases from year to year, development of lithography technology, in which more precise patterning and transferring are possible, is required.

For this reason, the study on the application of organic ultrathin films of several nanometers thickness to resist materials has been advanced as one of the technologies which makes much finer lithography possible [32–36]. Moreover, the trials to fabricate molecular devices have begun to unfold by immobilizing functional molecules, such as DNA and proteins, selectively at fine-structured SAMs which have reactive terminated groups like  $\text{NH}_3^-$ ,  $\text{COOH}^-$  and  $\text{Cl}^-$  [37–42].

Thick organic polymer resist films are used for the conventional lithography. Their thicknesses are dozens to hundreds of nanometers. When a processing size becomes small and enters nanometer order in electron beam lithography, scattering of electrons in a resist causes various problems, such as the proximity effect. The variation in molecular mass of each molecule which forms the resist also reduces the resolution. If the ultrathin resist film of several nanometers thickness will be realized, the lithography of higher resolution will become possible.

The thicknesses of SAMs are 1–2 nm, depending on the length of molecules comprising the monolayer. Moreover, the SAMs consist of molecules of the same kind, and there is no variation in molecular mass in SAMs, which is in contrast to the polymer films. Therefore, SAMs are highly promising as high-resolution resists. The uniform coating of SAMs is also possible onto substrates with three-dimensional complex shapes, fine-structured substrates and inner surfaces of tubes.

From the viewpoint of environmental issues, conventional lithographic processes discharge liquid wastes, such as developing solutions and resist removal ones; however, the SAM lithographic process does not discharge liquid waste. The consumption of raw materials used in the process is extremely small because of the thickness of 1–2 nm. The raw material of 2  $\mu\text{l}$  is enough to coat an area of 1  $\text{m}^2$ . The use of SAMs is superior to the conventional resist process in solving environmental and resources problems. In addition, the use of SAMs leads to better productivity due to the self-stopping process from a standpoint of industrial applications.

We are investigating lithographic techniques using SAMs by employing vacuum ultra-violet (VUV) light, electron and ion beams, and scanning probe microscope (SPM) as shown in Fig. 2. Notably the methods using VUV light and SPM are carried out under atmospheric pressure or in low vacuum, which makes their industrial applications advantageous on the cost front. The wide

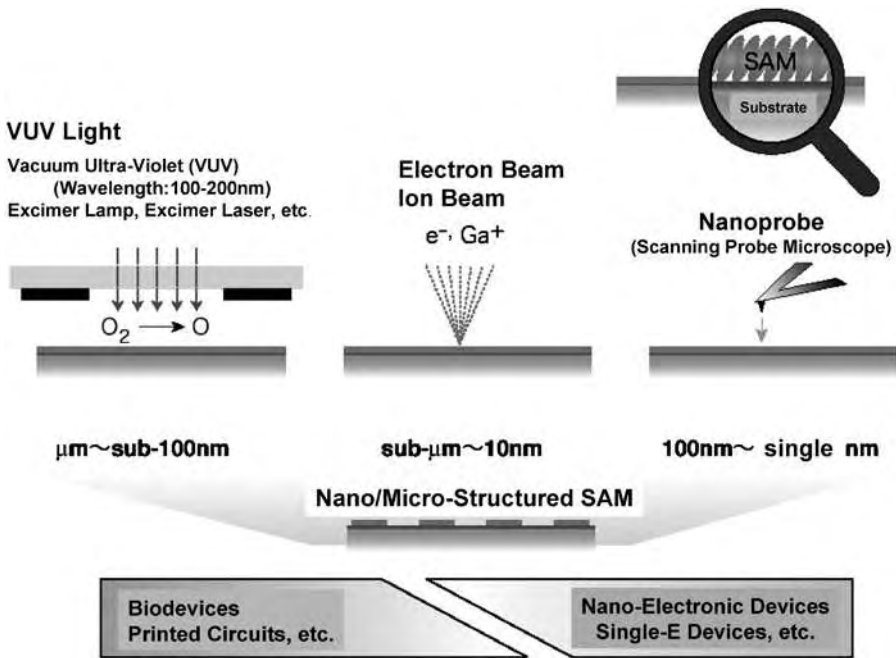


Fig. 2. Micro/nanolithography of SAMs.

range of patterning from single nanometer to several hundreds micrometers becomes possible by the combination of VUV lithography and SPM. In conclusion, the usefulness of SAMs is extremely high.

## 2. PREPARATION OF SAMs BY CHEMICAL VAPOR DEPOSITION (CVD)

### 2.1. Structure and Formation Mechanism of Organosilane SAMs

The molecule  $\text{SiR}_n\text{X}_{4-n}$ , where at least one of the functional groups X of a silane molecule  $\text{SiX}_4$  is replaced by an organic group (R), is called organosilane. An organic film is formed on an oxide surface by chemical reaction of hydroxyl groups on the oxide surface with organosilane molecules. This reaction is widely used practically for organic coatings on inorganic substrates as silane-coupling processing [18]. By adjusting preparation conditions, such an organic coating can become a monolayer, or SAM [19]. Various oxide materials, such as silicon oxide, titanium oxide, aluminum oxide, indium-tin oxide (ITO), tin oxide, germanium oxide, glass, mica, etc., are used for substrates [20–31].

Trichloroalkylsilane with one alkyl group and three chloro groups and trialkoxyalkylsilane with one alkyl group and three alkoxy groups (methoxy or ethoxy groups) are often used as the raw materials of SAMs. The formation

mechanisms of organosilane SAMs are rather complex compared to those of other SAMs because these organosilane molecules contain three reactive functional groups. Fig. 3 shows the molecular structure of organosilane molecules and the illustration of reactions. A small amount of water is necessary for the formation of organosilane SAMs. At first  $-\text{Cl}$  or  $-\text{OR}$  groups in organosilane molecules change to silanol groups by hydrolysis. Next these silanol groups make siloxane network with hydroxyl groups on a substrate surface by the dehydration/condensation reaction. Then organosilane molecules are chemically immobilized onto the surface. Since there are multiple reactive functional

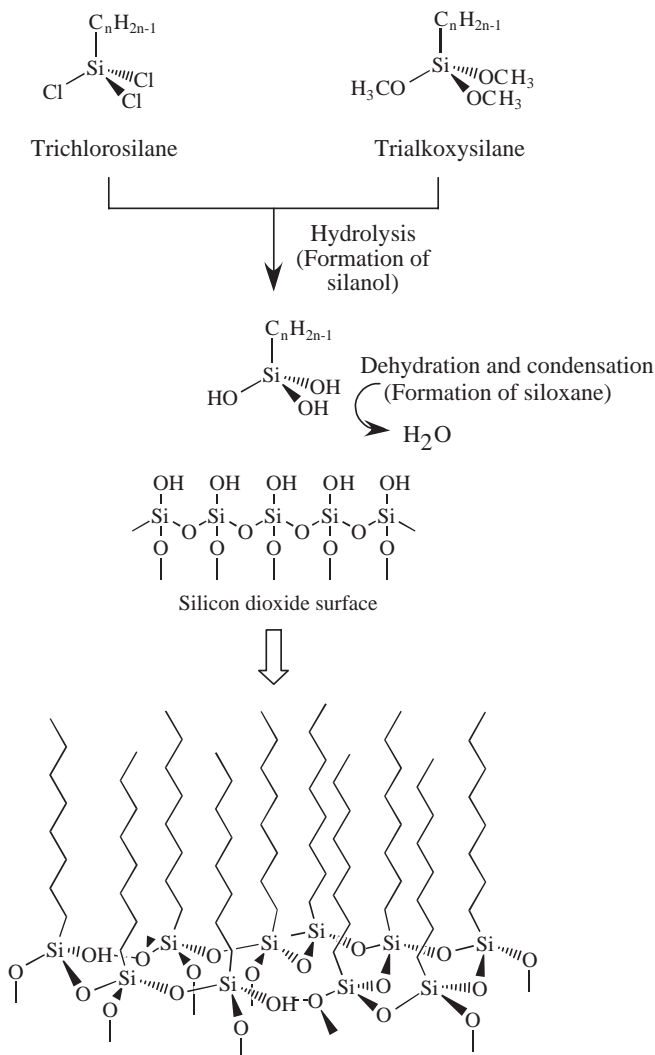


**Fig. 3.** Illustration of organosilane SAM.

groups in one molecule, the siloxane bonding is formed not only between the hydroxyl group on the surface and the organosilane molecule but also between adjacent organosilane molecules. This horizontal polymerization plays an important role in the two-dimensional organization of organosilane SAMs, in addition to the interactions between alkyl groups (van der Waals force, hydrophobic interaction and electrostatic interaction).

## 2.2. Preparation Method of SAMs by CVD

We have prepared organosilane SAMs both by wet processing and by dry processing. The preparation method of SAMs by CVD, dry processing, is described in this chapter because CVD has such advantages over wet processing as easy large-area preparation, high productivity and no discharge of liquid waste. This method uses the chemical reaction of organosilane molecules in a gas phase with a substrate surface.

### 2.2.1. Substrates and raw materials

We used n-type Si (100) plates (10 mm × 10 mm × 0.4 mm) as substrates. The raw materials used are the following four types of organosilane compounds, whose molecular structures are shown in Fig. 4.

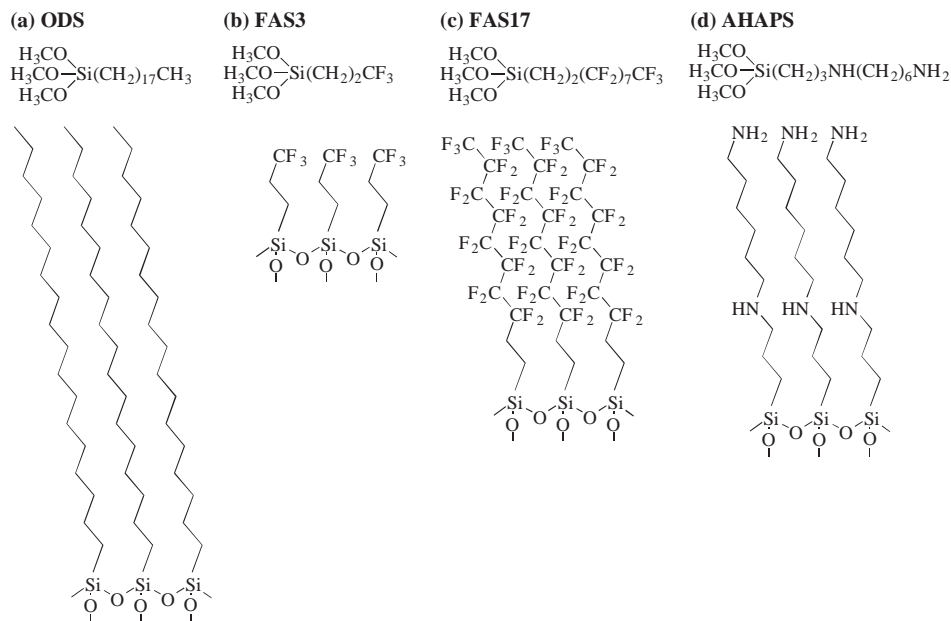


Fig. 4. Four types of organosilane molecules used and their molecular structure.

- (a) *n*-Octadecyltrimethoxysilane [ODS:  $\text{CH}_3(\text{CH}_2)_{17}\text{Si}(\text{OCH}_3)_3$ , 95%, Tokyo Kasei Kogyo Co., Ltd]
- (b) 3,3,3-Trifluoropropyltrimethoxysilane [FAS3:  $\text{CF}_3(\text{CH}_2)_2\text{Si}(\text{OCH}_3)_3$ , Shin-Etsu Chemical Co., Ltd]
- (c) Heptadecafluoro-1,1,2,2-tetrahydro-decyl-1-trimethoxysilane [FAS17:  $\text{CF}_3(\text{CF}_2)_7(\text{CH}_2)_2\text{Si}(\text{OCH}_3)_3$ , Shin-Etsu Chemical Co., Ltd]
- (d) *n*-(6-Aminohexyl)aminopropyltrimethoxysilane [AHAPS:  $\text{H}_2\text{N}(\text{CH}_2)_6\text{NH}(\text{CH}_2)_3\text{Si}(\text{OCH}_3)_3$ , 95%, Gelest Inc.]

We denote the SAMs prepared from these compounds as ODS-, FAS3-, FAS17- and AHAPS-SAMs hereafter.

### 2.2.2. Cleaning of substrates by UV/ozone cleaning method

We used the UV/ozone cleaning method for the cleaning of substrates [43]. An Xe excimer lamp with the wavelength 172 nm (UER 20-172, Ushio Inc.) was used for the UV light source. The principle and method of the UV/ozone cleaning are described below.

An excimer lamp has dual quartz-tube structure, where a metal electrode is set at the inner side of the inner tube, and a mesh-type metal electrode is placed at the outside of the outer tube as shown in Fig. 5. When we apply ac high voltage between two electrodes, the dielectric barrier discharge ignites between two dielectric materials, and reaches an excimer state instantaneously by the excitation of atoms of a filling gas. Then the excimer light is emitted by the

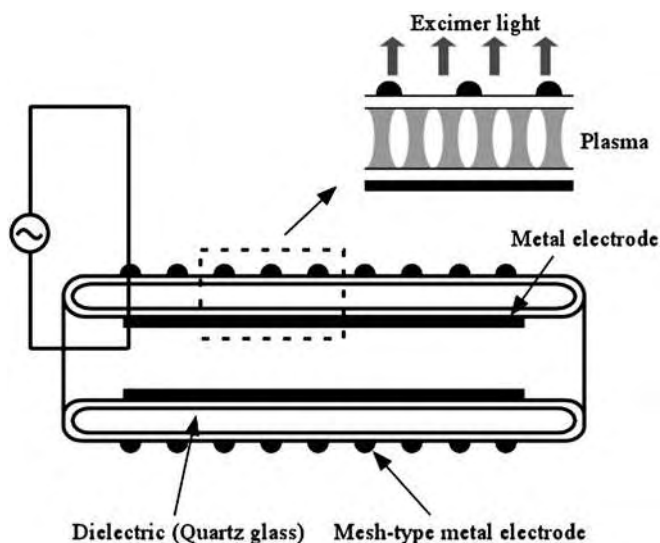


Fig. 5. Schematic diagram of the barrier-discharge excimer lamp.

**Table 1**

Bond energies of six bonds present in the structure of SAMs used

	Bond					
	C-F	C-H	N-H	C-C	Si-C	C-N
Bond energy (kcal/mol)	115.2	98.5	92.7	83.2	75.5	72.9

transition from the excited state to the ground state. The most important feature of the excimer light is to obtain the single-wavelength emission unlike the conventional low-pressure mercury lamp. The central wavelength depends on the type of the filling gas in the lamp. Now five types of excimer lamps come onto the market; central wavelength: 126 nm (Ar), 146 nm (Kr), 172 nm (Xe), 222 nm (KrCl) and 308 nm (XeCl). The light whose wavelength is below 200 nm is called the VUV light which has very high photon energy according to the equation  $E = hv$  ( $h$ : Planck constant,  $v$ : velocity of light/wavelength). For example, the photon energy of the Xe excimer light (172 nm) is 166.7 kcal/mol which is higher than the bond energy of a C-F bond (115.2 kcal/mol). Therefore, this light easily cuts the C-F bond. Table 1 shows the bond energies of six bonds present in the structure of SAMs used in this study. The VUV light can also dissociate directly oxygen molecules in atmosphere and generate oxygen radicals [44]. These oxygen radicals have strong oxidation power against organic materials. Therefore, organic materials are removed as volatile molecules, such as CO, CO<sub>2</sub> and H<sub>2</sub>O, by the reaction of free radicals produced by the photocutting reaction of organic bonds with the oxygen radicals. As these two different photochemical reactions advance simultaneously, it is possible to remove organic materials efficiently for a short time.

The schematic diagram of the UV/ozone cleaning used is shown in Fig. 6. The VUV irradiation was carried out for silicon substrates under atmospheric pressure and at room temperature during 20 min (illumination intensity: 10 mW/cm<sup>2</sup>). The contact angle of a water droplet was measured with a contact angle meter (CA-D, Kyowa Interface Science) by the sessile drop method. The water contact angle for the silicon substrate became less than 5° after irradiation, whereas it was 30–60° before irradiation. This means that contaminants were removed and hydroxyl groups were introduced on the silicon surface with native oxide. The thickness of the native oxide was ca. 2 nm determined with an ellipsometer (PZ2000, Philips Japan, Ltd.).

### 2.2.3. Preparation of SAMs by CVD

The preparation method of organosilane SAMs is described below [31, 45]. A simple CVD apparatus shown in Fig. 7 was used. Although the precise preparation conditions for substrates is as follows: First, the silicon substrate cleaned

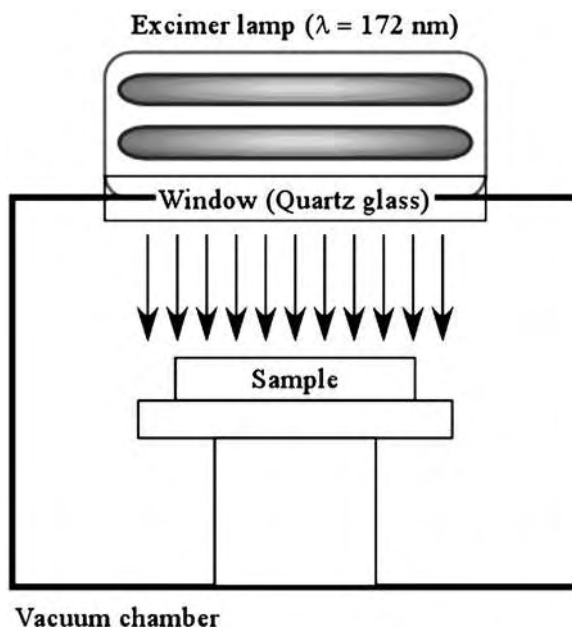


Fig. 6. Schematic diagram of the UV/ozone cleaning apparatus.

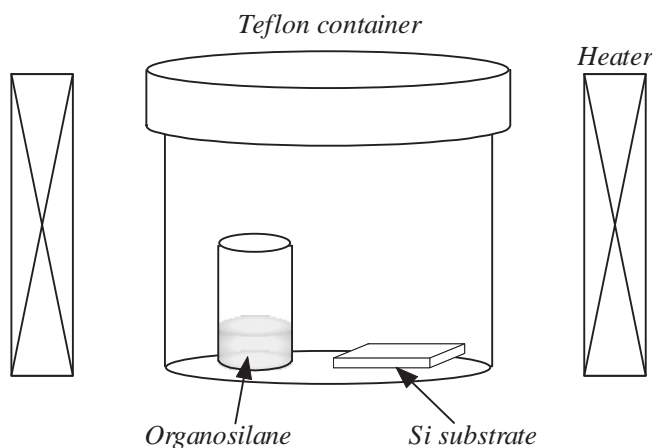


Fig. 7. Schematic diagram of the CVD apparatus.

by the UV/ozone cleaning was encapsulated into a closed vessel (volume: 65 ml) made of polytetrafluoroethylene (PTFE; commercial name: Teflon) with a raw material put in a small glass vessel. Second, the PTFE vessel was set in an electric furnace after closing a lid and maintained at preset temperature for several hours. Third, the silicon substrate with SAM was taken out from the

**Table 2**

Preparation conditions of SAMs by CVD

	Raw material			
	ODS	FAS3	FAS17	AHAPS
Dose (cm <sup>3</sup> )	0.2	0.2	0.2	0.1*
Temperature (°C)	150	100	150	100
CVD time (min)	180	60	180	60

\*Diluted with 0.7 cm<sup>3</sup> toluene.

vessel after cooling. The typical preparation conditions for each SAM are given in Table 2.

These conditions are determined by our studies as shown in Figs. 8 and 9. Fig. 8 shows the variation in thicknesses and water contact angles of SAMs against preparation time. The formation of SAMs is completed at the time when these values are saturated, and the self-assembling is stopped.

For the AHAPS-SAM, the cleaning by organic solvents, an acid solution and an alkaline solution was carried out after preparation [46]. In this case the thickness and the contact angle continued to increase with the preparation time as shown in Fig. 9. This phenomenon comes from the electrostatic physisorption of silanol-terminated molecules at unshared electron pairs of the amino groups of the AHAPS-SAM. To remove such admolecules, the ultrasonic cleaning was performed in ethanol, toluene, sodium hydrate (1 mM) and nitric acid solutions (1 mM) sequentially. Finally, the substrate was cleaned in ultrapure water (Milli-Q water) and dried in dry nitrogen. By using these processes the thickness and the contact angle measured after cleaning became saturated at 1 h.

Table 3 summarizes the thicknesses and water contact angles obtained. The thickness was determined by ellipsometry. The refractive indexes of SAMs were assumed to be the same as that of the thermally oxidized film of silicon, 1.465. The obtained thicknesses are a little shorter than the molecular chain lengths calculated by using *ab initio* molecular orbital theory as shown in Fig. 10 [47]. Hence the molecules in the SAMs are supposed to be immobilized on the angle [1]. On the other hand, the water contact angles of the SAMs almost correspond to those of the SAMs with similar terminated functional groups prepared by wet processing [1, 48–50]. The contact angle of FAS3-SAM is, however, smaller than that of FAS17-SAM, although these SAMs are terminated by same trifluoromethyl groups. This comes from the difference in surface density of molecules.

In conclusion, the SAMs of ODS, FAS3, FAS17 and AHAPS were successfully prepared by CVD. However the size of the substrates used here was 10 mm<sup>2</sup>. The uniform deposition of SAMs is possible onto larger size substrates like silicon wafers with a diameter of 300 mm by using a large-scale CVD apparatus shown in Fig. 11.

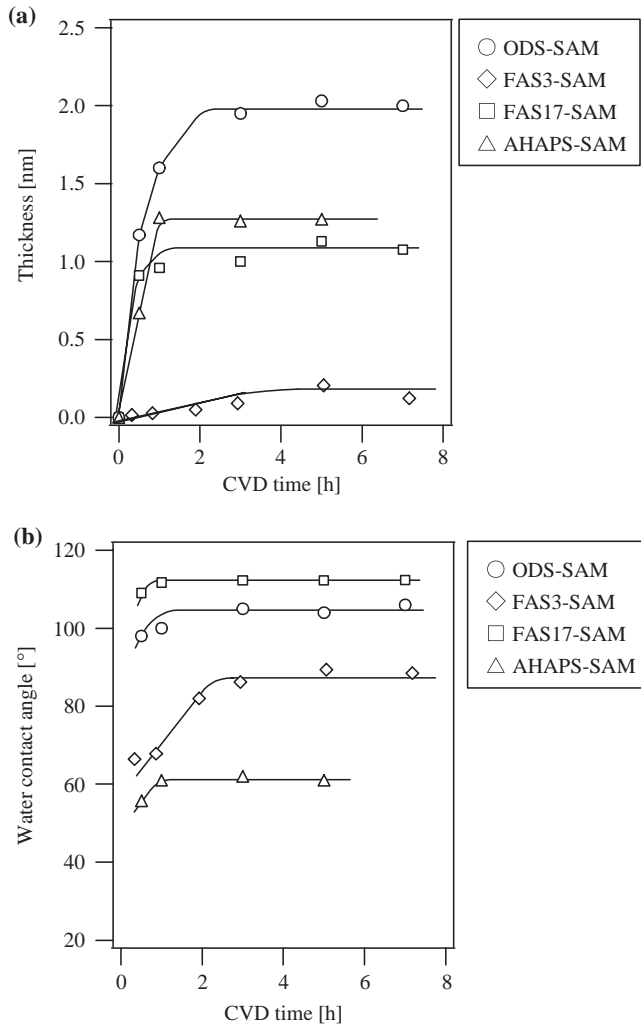


**Fig. 8.** Variation in thickness and water contact angle with CVD time for SAMs used.

### 3. MICROLITHOGRAPHY USING SAMs

Microlithography of organosilane SAMs is carried out by using VUV light. The minimum line width of 300 nm is obtained by this method at present.

#### 3.1. Photodegradation of Organosilane SAMs by VUV Light

##### 3.1.1. Experimental method

The schematic diagram of the VUV irradiation apparatus is shown in Fig. 12. We used ODS-SAM as a sample. First, the sample was set in a vacuum chamber

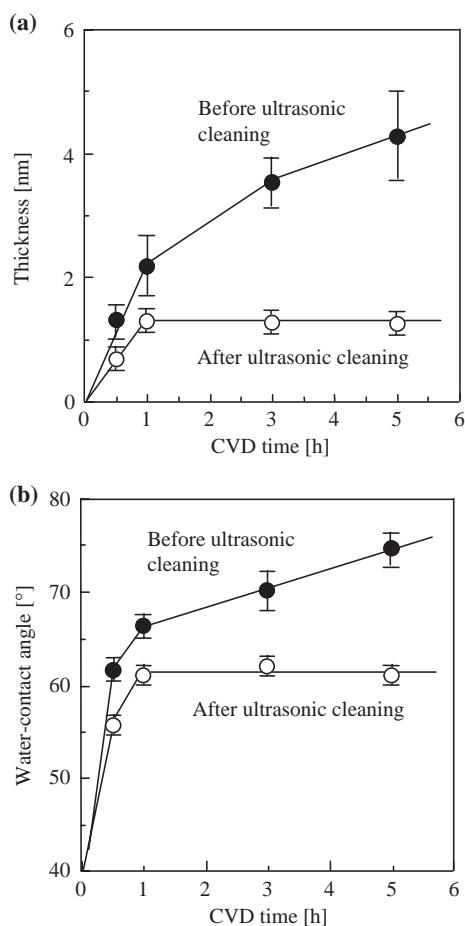


**Fig. 9.** Variation in thickness and water contact angle with CVD time for AHAPS-SAM before and after ultrasonic cleaning.

**Table 3**

Thicknesses and water contact angles of SAMs

	Raw material			
	ODS	FAS3	FAS17	AHAPS
Thickness (nm)	1.8	0.3	1.2	1.7
Water contact angle (°)	108	86	116	58

which was evacuated by a rotary pump. The pressure in the chamber was controlled by adjusting the leak valve. Next, the sample was irradiated by the excimer lamp through a quartz plate (thickness: 10 mm) and a patterned chromium-plated spacer of a quartz plate (thickness: 2 mm) on the sample. The

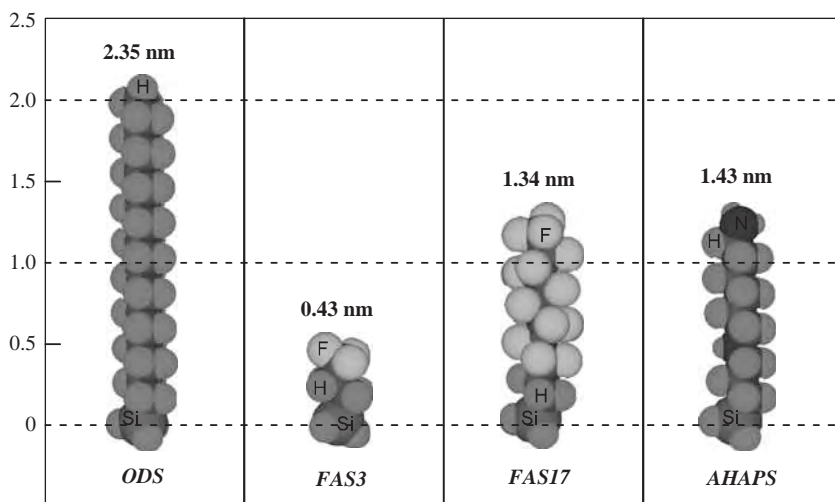


**Fig. 10.** Molecular chain lengths of four types of organosilane molecules calculated by using *ab initio* molecular orbital theory. The  $-\text{Si}(\text{OCH}_3)_3$  was converted to the  $-\text{SiH}_3$  for the model molecules used in the calculation using GAUSSIAN 98.



**Fig. 11.** Photo of the CVD apparatus for the large size substrates.

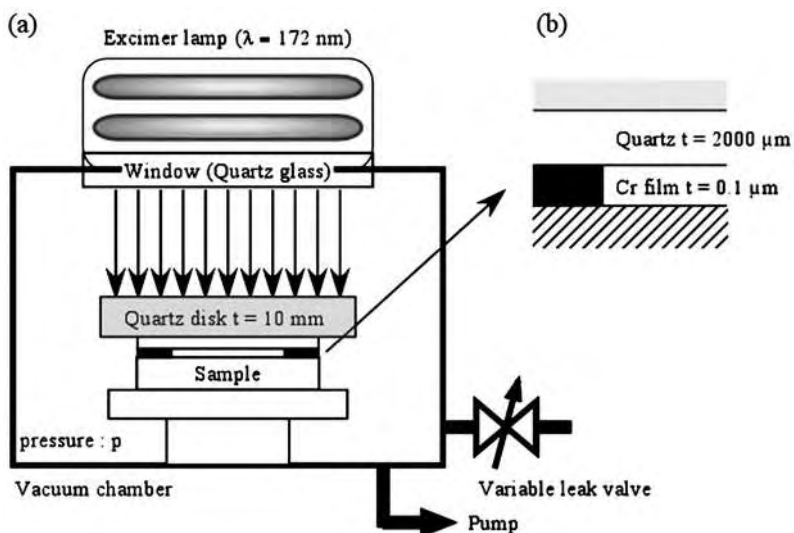


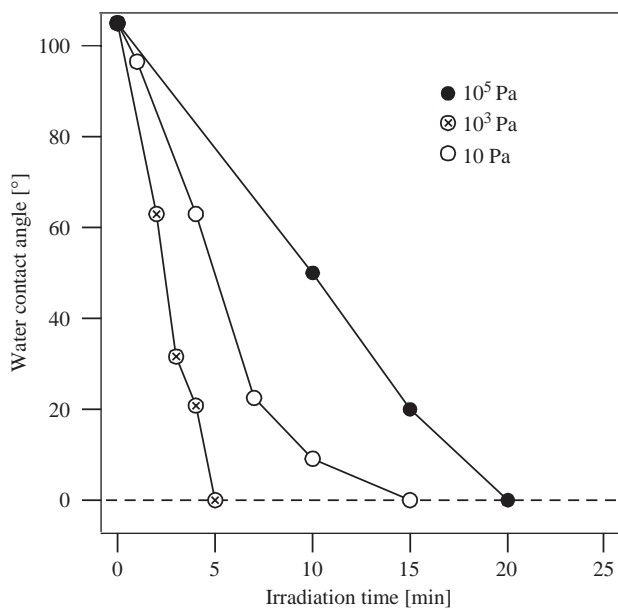
**Fig. 12.** Schematic diagram of the VUV irradiation apparatus.

transmittance of the plate 10 and 2 mm thick was ca. 70% and 93%, respectively, at 172 nm. The thickness of the chromium film was 0.1  $\mu\text{m}$ , which made 0.1  $\mu\text{m}$  gap between the quartz plate and the sample. This situation simulates a micropatterning process using a conventional photomask. After irradiation the contact angle was measured and the surface was analyzed by X-ray photoelectron spectroscopy (XPS; ESCA3400, Shimadzu).

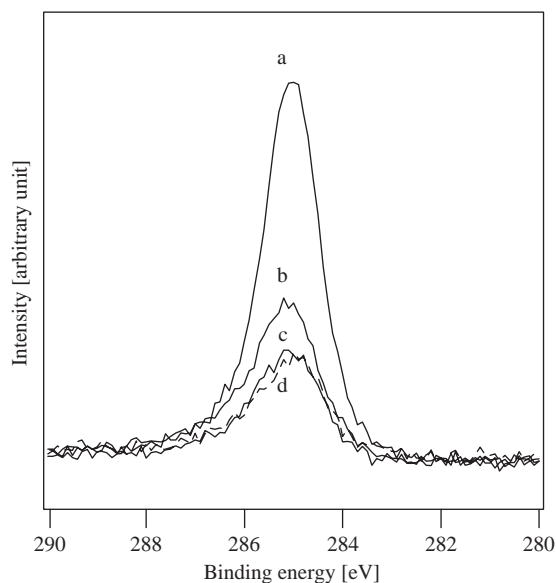
### 3.1.2. Effect of ambient pressure on photodegradation of SAMs

Fig. 13 shows the variation in contact angle with irradiation time of the VUV light at various ambient pressures (10,  $10^3$  and  $10^5$  Pa). The angle decreased and finally became less than  $5^\circ$  with increasing irradiation time under any pressure. Fig. 14 indicates the XPS C1s spectra for the unirradiated ODS-SAM and the irradiated ODS-SAM at  $10^5$  Pa. The spectrum for a cleaned silicon substrate is also shown for comparison. The peak height of the C1s spectra decreased with increasing irradiation time. The height of the spectrum for the sample irradiated for 20 min (spectrum c) was almost same as that for the cleaned silicon (spectrum d). The origin of the C1s peak for the cleaned silicon was some organic contamination adsorbed in the air before setting the sample into the XPS chamber. This contamination was also adsorbed on the irradiated samples. Therefore, the ODS-SAM was removed completely by the VUV irradiation for 20 min.

The photodegradation rate at  $10^3$  Pa is much bigger than that at 10 Pa as shown in Fig. 13. This expresses the important role of oxygen played in photodegradation, and also draws a proof of the existence of oxygen at the



**Fig. 13.** Relationships between water contact angle and irradiation time at various ambient pressures (10, 10<sup>3</sup> and 10<sup>5</sup> Pa).



**Fig. 14.** XPS C1s spectra for ODS-SAM under the following conditions: (a) un-irradiated, (b) 10 min irradiation, (c) 20 min irradiation and (d) UV-cleaned Si substrate.

small gap between the photomask and the sample (gap length: 0.1  $\mu\text{m}$ ). The rate, however, decreased at higher pressure  $10^5$  Pa because the light intensity at the sample surface dropped at this pressure due to the absorption by rich oxygen in the air. (The intensity of light at 172 nm decreases to 10% at the transmitted distance 8 mm in the air.)

### 3.1.3. Photodegradation mechanism of SAMs

The photodegradation mechanism of SAMs is discussed here. When the VUV light irradiates organic molecules in the atmosphere containing oxygen, the light is simultaneously absorbed by the organic molecules and oxygen. The Xe excimer light at 172 nm has high photon energy, and directly cuts chemical bonds in the molecules and produces radicals. This light also produces oxygen radicals by the direct dissociation given in the following equations [44]:



These oxygen radicals have high oxidation power to organic materials and react immediately with free radicals generated by the photocutting reaction. By these reactions the SAM is removed from the substrate as volatile molecules, such as CO, CO<sub>2</sub> and H<sub>2</sub>O.

## 3.2. Photopatterning of SAMs

The photopatterning apparatus used is the same as shown in Fig. 12 [45, 51]. First, a photomask was set on a SAM sample in the vacuum chamber. Second, a quartz plate (thickness: 10 mm) was put on the photomask, the chamber was evacuated to 10 Pa and the VUV light irradiated the sample for 20 min. The photomask consisted of quartz glass of 2 mm thick (transmittance at 172 nm: 93%) with rectangular patterns of chromium as shown in Fig. 15(a). By using these patterns, the micropatterns were formed on the SAM sample by removing part of the SAM by the VUV irradiation as shown in Fig. 15(b).

Fig. 16 demonstrates the lateral force microscope (LFM) image of the micropatterned ODS-SAM sample. The LFM is one type of atomic force microscope (AFM) (SPA-300 HV + SP13800, Seiko Instruments Inc.) to measure lateral force. The frictional force is high at bright regions and low at dark regions. The rectangular regions indicate the photodegraded areas by the VUV irradiation, or the revealed bare silicon substrate. Their surrounding regions correspond to the ODS-SAM area. In general, the native oxide surface of silicon is hydrophilic and has large frictional force compared to the ODS-SAM surface due to the chemical and physical interactions between the probe and the sample

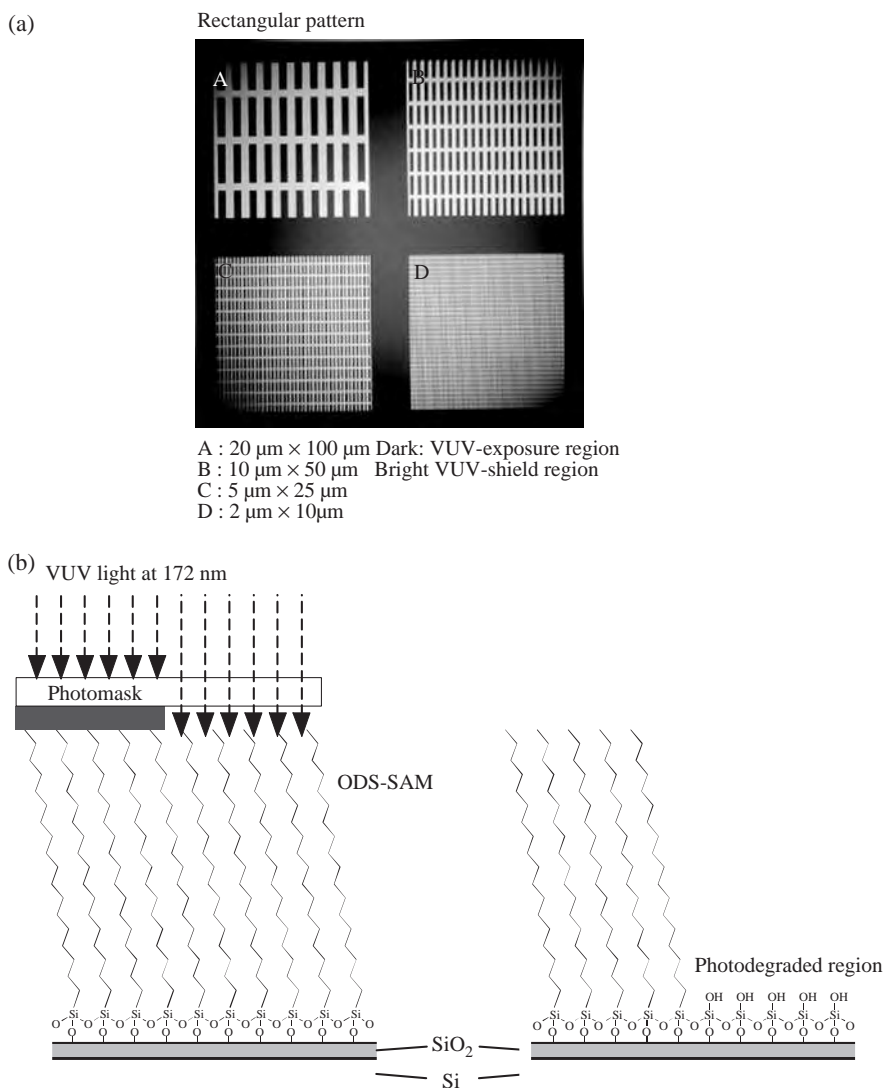


**Fig. 15.** VUV patterning of the alkylsilane SAM: (a) optical microscope image of photomasks used and (b) illustration for VUV patterning.

surface. This figure proves the possibility of the micropatterning of organosilane SAMs with high resolution by VUV irradiation.

#### 4. NANOLITHOGRAPHY USING SAMs

Nanolithography of organosilane SAMs is performed with SPM [52, 53]. The minimum line width of 10 nm is obtained by this method at present.

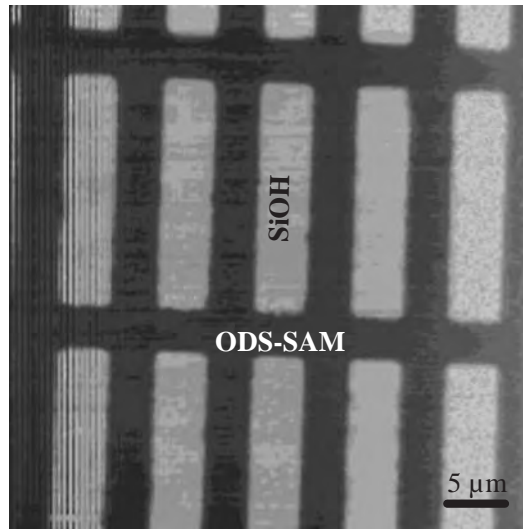


**Fig. 16.** LFM image of ODS-SAM after VUV patterning.

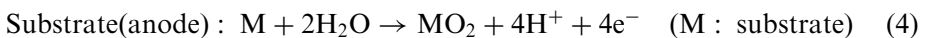
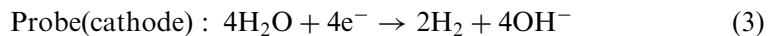
#### 4.1. Principle of Nanolithography with SPM

SPM is widely used as research tool and industrial measuring instrument, and has drawn attraction as nanoscale processing tool at nanometer order from the initial stage of development. The atomic operation became possible by SPM [54], and scanning probe nanolithography (SPNL) was developed at ca. 10 nm level [55].

There are three major categories for SPNL as follows:

- (1) Electron irradiation by using field emission [56–66],
- (2) Mechanical scratch [67–73],
- (3) Electrochemical reaction (anodic oxidation) [74–83].

The method nearest to electronic device fabrication is the nanoscale processing based on the anodic oxidation of semiconductors and metals. The following electrochemical reactions proceed after applying voltage between the probe and the substrate in the column of adsorbed water generated at the region between them in the air as shown in Fig. 17.



The oxide film of the substrate is formed at the front of the probe. It is, therefore, possible to form patterns to scan the probe.

Other processing techniques, such as etching and metal plating, are also necessary to be developed when the nanopattern drawing by SPM is advanced

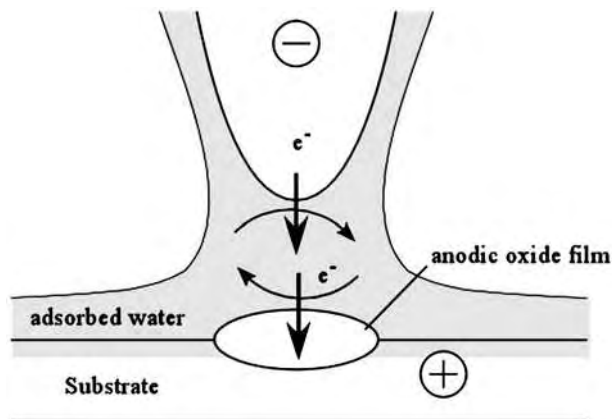


**Fig. 17.** Illustration of the anodic oxidation using AFM probe.

to the overall nanolithography. The SPM pattern drawing was reported to be carried out by the oxidation process with metal or semiconductor films as resists [84–88]. Organic resists are, however, much better than the inorganic resists because many pattern transfer techniques like etching and lift-off developed until now are available not only for photolithography and electron beam lithography but also SPNL. The SAMs have, therefore, the potential to develop the consistent flexible nanolithographic process.

## 4.2. SPNL of SAMs

The organic thin films used in lithography are polymer casting films, Langmuir–Blodgett (LB) films, SAMs and plasma-polymerized films. The molecular designs and syntheses of organic monolayer materials are studied for SPNL resists [89].

We have carried out the SPNL of organosilane SAMs [90, 91]. The outline is described below.

### 4.2.1. Lithography using contact-mode AFM (CM-AFM)

The substrate and SAM sample used are silicon and ODS-SAM. Fig. 18 shows the LFM images for the surfaces after SPNL in the air and in vacuum. The square-shaped area with high friction corresponds to the current-injected region from the probe scanned at  $0.1 \mu\text{m/s}$  in the air (Fig. 18(a)). The scanned area had upheaved several nanometers compared to the unscanned area. On the contrary, there is no difference between the current-injected area and the non-injected one although the similar probe scan was carried out at the same load and voltage in vacuum ( $3.2 \times 10^{-4} \text{ Pa}$ ) (Fig. 18(b)). Since the ODS-SAM has no damage by the scanning at the load of  $600 \text{ nN}$  [92], this frictional change, or surface modification, is not caused by the mechanical scratch. The surface modification proceeded

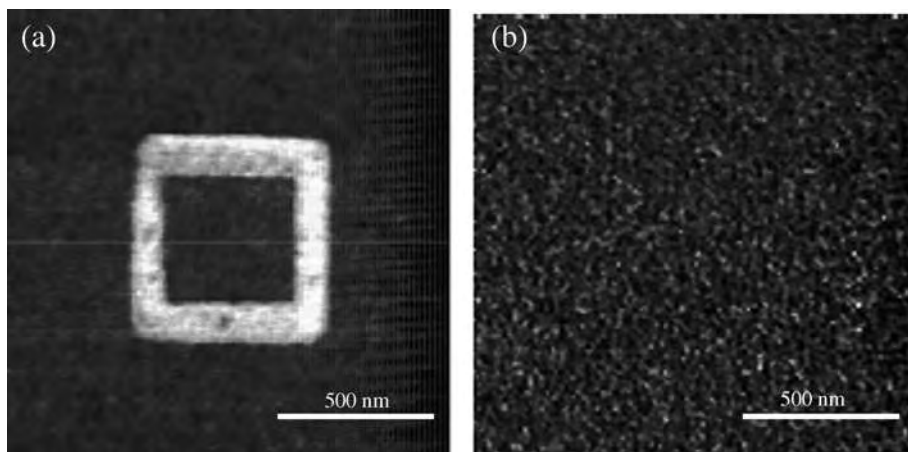


**Fig. 18.** CM-AFM lithography: LFM images of the sample surfaces with the current injection in (a) the air and (b) in vacuum.

only at the current injection time in the air as shown in Fig. 18(a). Therefore, the ODS-SAM on the silicon substrate is modified and decomposed by the electrochemical reactions in the water column formed between the probe and the sample like the anodic oxidation reaction for metals [93, 94] and semiconductors [95–98].

#### 4.2.2. Lithography using dynamic force mode AFM (DFM-AFM)

Subsequently, the nanolithography of organosilane SAMs was performed by using DFM-AFM where a probe touched a sample intermittently. The damage for the probe is mitigated by using DFM-AFM. Moreover, since the contact time with the sample is short and the amount of current injected to the sample decreases, a different chemical reaction is expected from SPNL using CM-AFM. The ODS-SAM on the silicon substrate was also used. The surfaces after lithography were evaluated from the surface potential measurement with Kelvin force microscope (KFM), and were compared with the lithography using CM-AFM.

Fig. 19(b) shows the schematic diagram of SPNL using DFM-AFM. In order to inject current to ODS-SAMs, dc bias voltage 10 V was applied between a conductive probe as anode and a silicon substrate as cathode. The silicon probe used had the spring constant 20–40 N/m and the resonance frequency 260 kHz (NANOSENSOR, resistivity: 0.1–0.2  $\Omega$  cm). Fig. 19(a) indicates the schematic diagram of SPNL using CM-AFM. The silicon probe was also used (Ultralever, high-doped Si probe, Park Scientific Instruments; resistivity: 0.1  $\Omega$  cm). For comparison, the lithography using non-contact AFM (NC-AFM) was conducted additionally. The same probe for DFM-AFM was used in this case. After lithography, the surface topography and surface potential were measured with a gold-coated silicon probe in dry nitrogen atmosphere. This probe had the

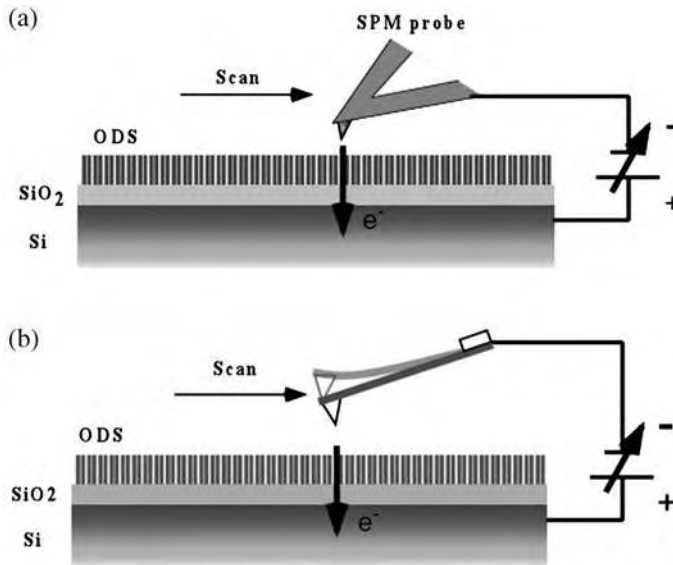


**Fig. 19.** Illustration of SPM lithography: (a) CM-AFM lithography and (b) DFM-AFM lithography.

spring constant  $1.8 \text{ N/m}$ , the resonance frequency  $27.53 \text{ kHz}$  and the  $Q$  value 180. The working conditions for KFM were as follows: ac bias voltage:  $2 \text{ V}$ , ac frequency:  $25 \text{ kHz}$  and scan rate:  $9.1 \text{ Hz}$  [99]. The experimental results obtained are described below.

- (1) Comparison between DFM-AFM and CM-AFM lithographies: The topographic images and surface potential ones are shown in Fig. 20(a) and (b) for CM-AFM lithography, Fig. 20(c) and (d) for NC-AFM lithography and Fig. 20(e) and (f) for DFM-AFM lithography. The swirl-like portions in Fig. 20 are the areas where lithography was performed. Any lithography was conducted at the bias voltage  $10 \text{ V}$  and the scan rate  $0.5 \text{ Hz}$  in the air (relative humidity:  $40\%$ , temperature:  $24^\circ \text{C}$ ). The oxide film was formed on the ODS-SAM-coated silicon substrate by anodic oxidation for CM-AFM lithography as clearly shown in Fig. 20(a). Its thickness is ca.  $3 \text{ nm}$ . This anodized region has lower surface potential than the surrounding, as shown in Fig. 20(b). This result corresponds to the result obtained for the photo-degraded surface of the ODS-SAM-coated silicon substrate. There is no change in topography and surface potential for NC-AFM lithography because of the non-contact of the probe with the sample. On the other hand, the change in surface potential and no change in topography are observed for DFM-AFM lithography (Fig. 20(e) and (f)). The surface potential image shows, however, opposite contrast from the potential image obtained for CM-AFM lithography. Moreover, the topographic image showed no

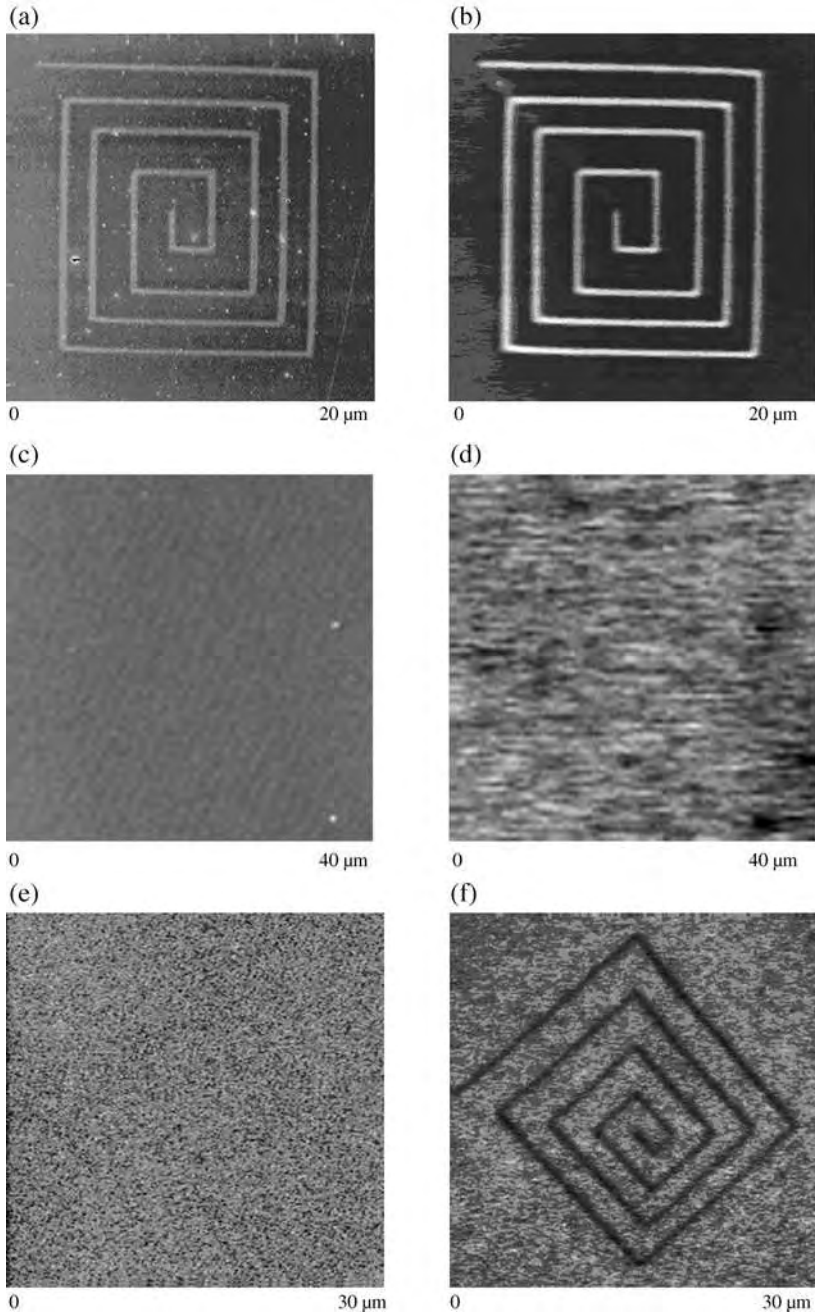


**Fig. 20.** Comparison among CM-AFM, NC-AFM and DFM-AFM lithographies: (a) the topographic image and (b) the surface potential one after CM-AFM lithography; (c) the topographic image and (d) the surface potential one after NC-AFM lithography; and (e) the topographic image and (f) the surface potential one after DFM-AFM lithography.

change in Fig. 21 when the pulse bias voltage of 10 V was applied for 50 s for DFM-AFM lithography. We discuss this topographic change and the contrast in surface potential images in the following sections in detail.

- (2) Topographic change in DFM-AFM lithography: No change in the topographic image was observed after DFM-AFM lithography. This is probably due to no formation of an oxide film by anodic oxidation. In order to investigate in more detail about this point, lithography was performed on an oxide-free silicon substrate (hydrogen-terminated silicon substrate).

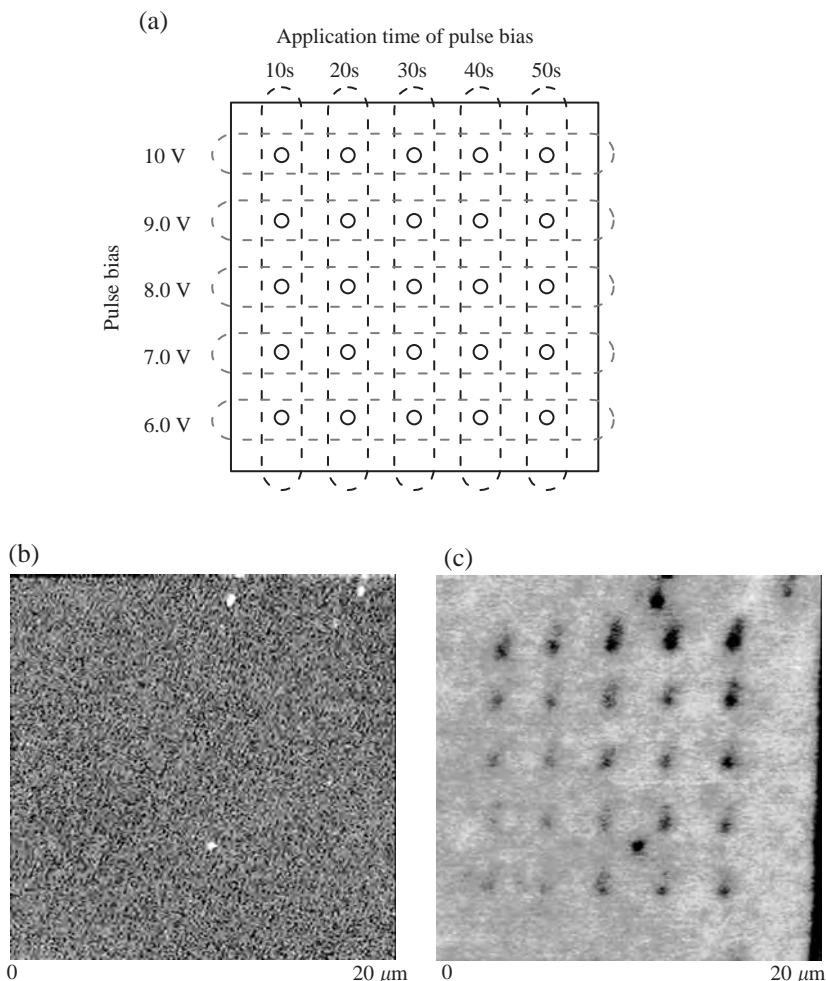


**Fig. 21.** Dependence of DFM-AFM lithography on the pulse bias voltage and the application time of pulse bias: (a) illustration of the pulse bias voltage and application time of pulse bias used, (b) topographic image and (c) surface potential image.

This substrate was prepared by wet etching in a 5% hydrofluoric acid solution for 20 min. The XPS Si1s spectra for the silicon substrate before and after etching are shown in Fig. 22. The peak attributed to SiO<sub>2</sub> disappeared completely after etching. Fig. 23(a) and (b) show the two-dimensional and three-dimensional topographic images of the hydrogen-terminated substrate after CM-AFM lithography. On the other hand, Fig. 23(c) indicates the topographic image of the hydrogen-terminated substrate after DFM-AFM lithography. In the case of CM-AFM lithography, the oxide film of the line width 100 nm and the height 2.5 nm was formed. On the contrary, no change in topography was observed for DFM-AFM lithography. This means that the current injection is insufficient to form the oxide film in DFM-AFM lithography.

- (3) Surface potential contrast in DFM-AFM lithography: The reversal phenomenon of the surface potential contrast in Fig. 20(b) and (f) obtained with CM-AFM and DFM-AFM lithography is considered. The surface potential contrast of ODS-SAM observed after CM-AFM lithography is in agreement with that of the sample photodegraded by VUV light. In the VUV lithography, the bare silicon substrate appeared by the decomposition of SAM. Furthermore, the decomposition of SAM and formation of oxide proceed in CM-AFM lithography. Therefore, conformity of both surface potential contrasts is an appropriate result.

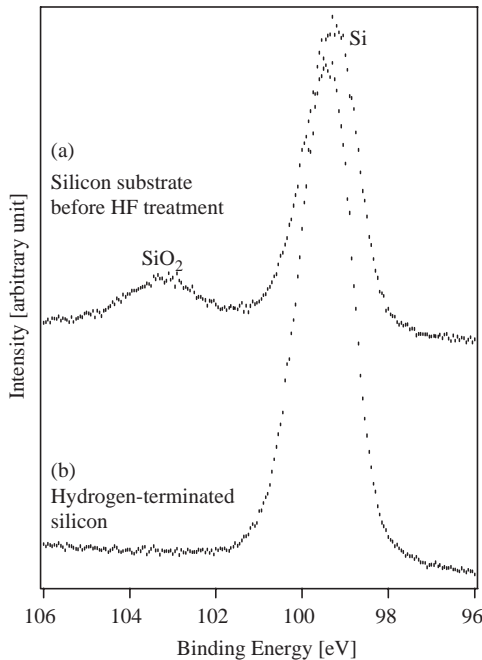


**Fig. 22.** XPS Si2p spectra (a) before and (b) after hydrofluoric acid etching.

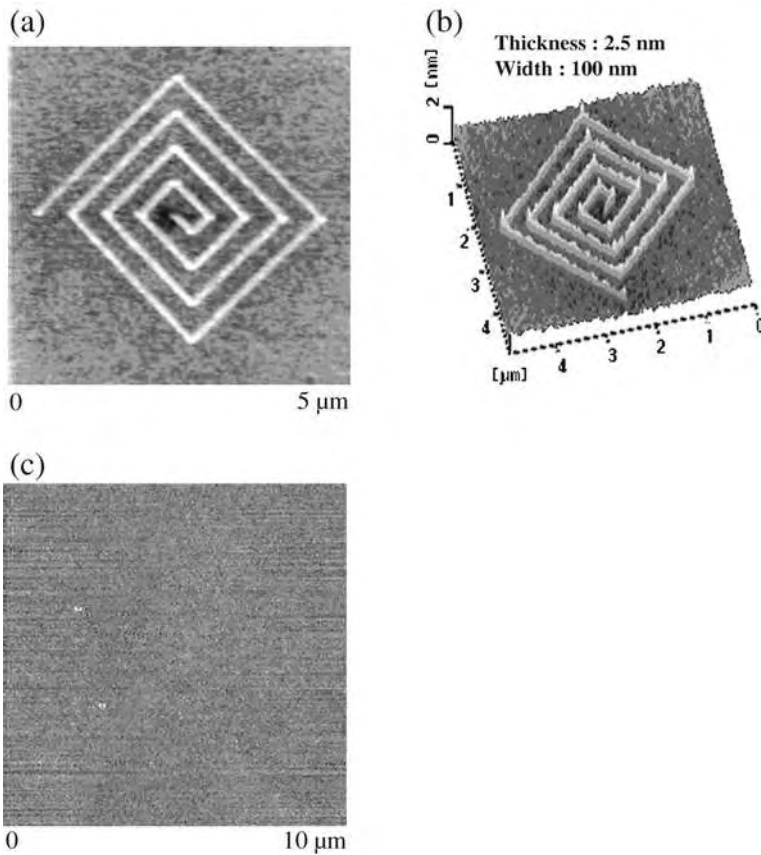


**Fig. 23.** AFM lithography of the hydrogen-terminated silicon substrate: (a) the topographic image and (b) the three-dimensional one after CM-AFM lithography, and (c) the topographic image after DFM-AFM lithography.

On the other hand, the different result was obtained for DFM-AFM lithography. The anodic oxidation does not occur in this lithography because the sufficient current is not injected, which is proved in the lithography using the hydrogen-terminated silicon substrate. That is, SAM is not removed from the substrate surface and a different chemical reaction occurs on the SAM surface.

In order to confirm this reaction, the similar lithography was performed both in vacuum ( $3.5 \times 10^{-4}$  Pa, 24 °C) and in dry nitrogen (relative humidity: <1%, 24 °C). Fig. 24(a) and (b) show the surface potential images for the ODS-SAM surfaces after lithography in vacuum and in dry nitrogen, respectively. No pattern formation is confirmed in these figures. Hence DFM-AFM lithography is possible only in the air. That is, the oxidation reaction related to both oxygen and water proceeds in DFM-AFM lithography just like CM-AFM

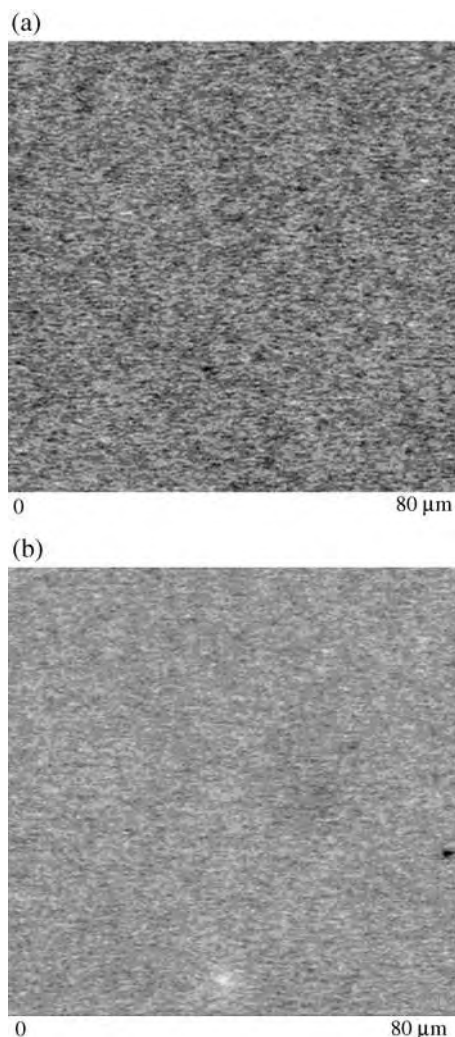


**Fig. 24.** Surface potential images for the ODS-SAM surfaces after DFM-AFM lithography (a) in vacuum ( $3.5 \times 10^{-4}$  Pa,  $24^\circ\text{C}$ ) and (b) in dry nitrogen (relative humidity:  $<1\%$ ,  $24^\circ\text{C}$ ).

lithography. However, since an oxide film is not formed, this oxidation reaction occurs only on the SAM surface unlike the case of CM-AFM lithography. It is thought that the aldehyde group ( $-\text{CHO}$ ) or the carboxyl group ( $-\text{COOH}$ ) is formed on the SAM surface by the oxidation reaction as an oxidation product. The group of Sagiv et al. confirmed the production of carboxylic acid in a macroscopic scale [100]. They prepared the trichlorosilane SAM, which had the similar structure as ODS-SAM, by wet processing, put a copper plate on it, and applied bias voltage. From the result of the infrared spectroscopic analysis of

the sample, it was proved that the peak of terminated methyl group ( $-\text{CH}_3$ ) decreased ca. 16%, and the peak of carbonyl group ( $-\text{C}=\text{O}$ ) appeared further. Moreover, the peak of central methylene group ( $-\text{CH}_2-$ ) showed no change after biasing. From these results they came to a conclusion that only terminated methyl groups were oxidized to change into carboxylic acid.

When the terminated group of SAM changes into carboxylic acid, the whole molecule polarizes to minus in the direction towards the SAM surface and to plus in the direction towards the substrate because the carbonyl group has polarization of  $\delta^-$  and  $\delta^+$  between oxygen and carbon. This corresponds well to our surface potential result obtained by the KFM measurement.

## 5. APPLICATIONS OF MICRO/NANOPATTERNED SAMs

The wide range of patterning from nanometer level to micrometer one becomes possible by using SAMs. Various materials, such as semiconductors, metals, glass, ceramics, organic polymers and other materials, can be used for substrates. Fig. 25 shows the applications of micro/nanostructured SAM; the resist for etching, the site-selective growth of metals, semiconductors, dielectric materials, mesoscopic materials, etc., the site-selective growth and array

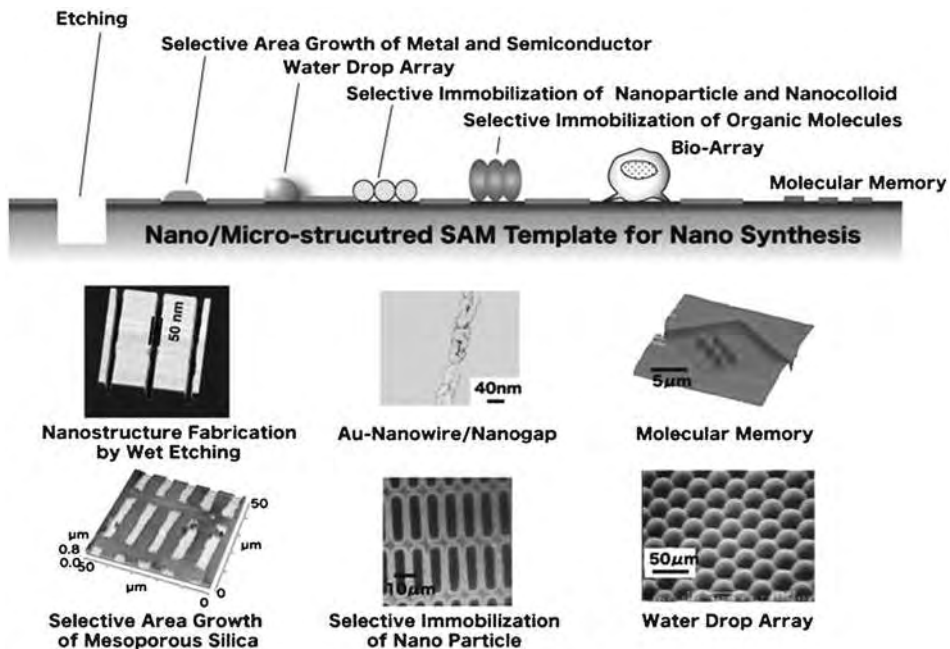


**Fig. 25.** Applications of micro/nanostructured SAM templates to micro/nano-processing.

formation of water droplets, the integration of fine particles and colloids, the assembling of functional organic molecules, the array formation of cells, DNA, proteins, etc., and the formation of molecular memories. There are too many potential applications of the patterned SAMs. Here three examples are described below.

### 5.1. Application of Organosilane SAMs to Transferring of Nanopatterns

Since ODS-SAM is chemically stable, it can be used as a resist. We investigated the possibility of ODS-SAM as a resist for transferring of nanopatterns. The line pattern of the minimum line width 30 nm was successfully prepared by optimizing the bias voltage, the application time of bias voltage, the scanning rate, etc. in SPNL as shown in Fig. 26(a). Using this nanopatterned ODS-SAM substrate, the etching of silicon was carried out in an aqueous ammonium fluoride solution ( $\text{NH}_4\text{F}:\text{H}_2\text{O}_2:\text{H}_2\text{O} = 10:3:100$ , 1 min, room temperature) after removing the oxide film by etching in a hydrofluoric acid (0.1% HF, 10 min, room temperature). The transferring of a pattern of 50 nm width and 30 nm depth was successfully achieved on the silicon substrate as shown in Fig. 26(b).

### 5.2. Application of Nanopatterned Substrates to Immobilization Surfaces of Molecules

Since the region where lithography is carried out on the ODS-SAM silicon substrate reveals the bare silicon surface again, the different type of organosilane molecule can be immobilized at this region. Fig. 27 shows the immobilization processes for two types of organosilane molecules. Fig. 27(a) indicates the nanopatterned ODS-SAM surface, whereas Fig. 27(d) the ODS-SAM/FAS17-SAM surface where the FAS17-SAM as the second SAM is immobilized at the removal areas of the ODS-SAM. In Fig. 27(d), the contrast at the FAS17-SAM area is reversed compared to the surface potential image before the FAS17 deposition. This means that the surface potential at the line-patterned area is lower than that at its surrounding area. This result gives the similar contrast to the micropatterned ODS-SAM/FAS17-SAM sample by the VUV lithography. This results from the negative dipole moment (from the SAM surface to the direction of the substrate) of the FAS17 molecule due to high electronegativity of fluorine atoms. Moreover, the line-patterned area upheaved 2–3 nm compared to its surrounding ODS-SAM area as shown Fig. 27(e). That is, the height of the line-patterned area increased 1.0–1.5 nm after the FAS17-SAM deposition. This increased height is almost same as the thickness of FAS17-SAM ca. 1.4 nm. In conclusion, FAS17 molecules are immobilized selectively only on the line pattern from the surface potential and topographic

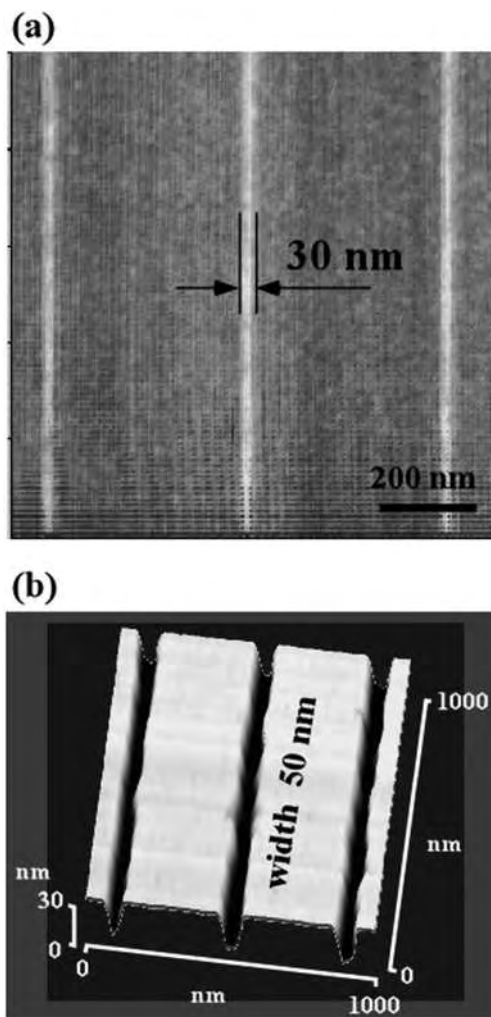


**Fig. 26.** Pattern transfer by etching: (a) LFM image of the patterned ODS-SAM surface and (b) three-dimensional topographic image of the silicon surface after wet etching.

images. Nanoscale immobilization templates of functional molecules can be fabricated by using this technique.

### 5.3. Application of Patterned SAMs to Circuit Formation

Fine metal wiring can be fabricated by the selective deposition of gold, copper, nickel, etc. onto patterned SAMs on substrates of silicon or plastics like polyimide. The nickel and copper patterns on silicon substrates are shown in

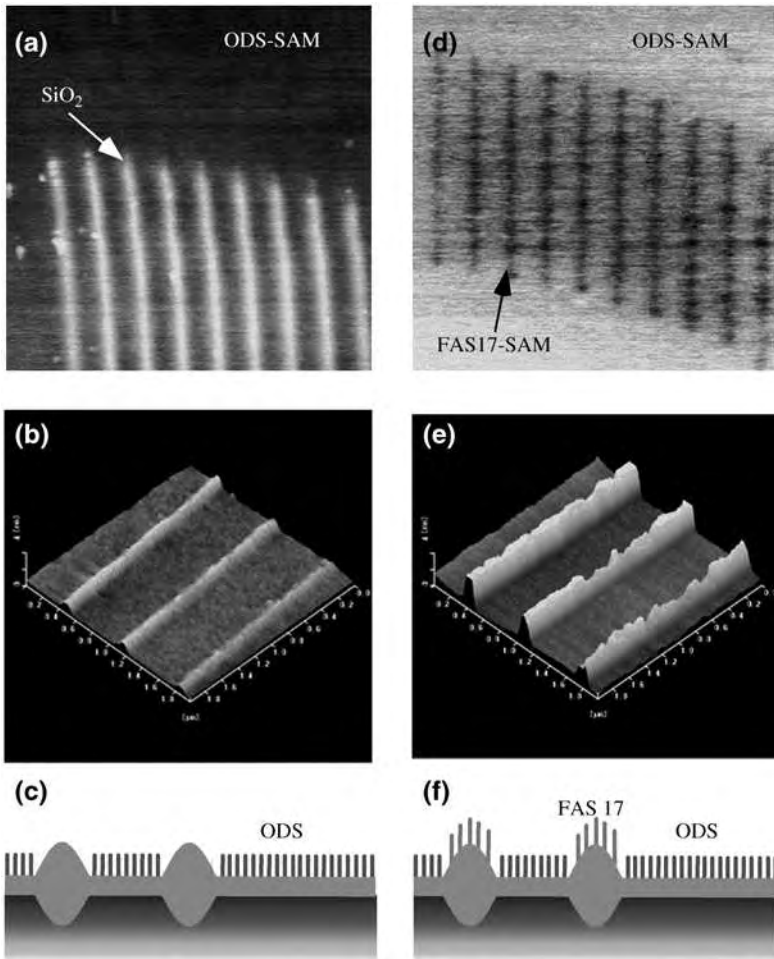


**Fig. 27.** Selective immobilization of the FAS17-SAM on the nanopatterned ODS-SAM substrate: (a) surface potential image, (b) topographic one and (c) illustration of the nanopatterned ODS-SAM, and (d) surface potential image, (e) topographic one and (f) illustration of the ODS-SAM/FAS17 SAM.

**Figs. 28 and 29.** The circuit of the minimum line width of 300 nm was fabricated by using VUV lithography of SAMs and electroless plating, and that of the minimum line width of 10 nm was done by SPNL of SAMs and electroless plating under atmospheric pressure.

In conclusion, the nano/microstructured SAMs are possible to apply to electric circuits, nano/micromoulds, nano/microsurface modification, semiconductor devices, molecular devices, sensors, bio chips, etc. and are expected to be developed in various industrial fields.

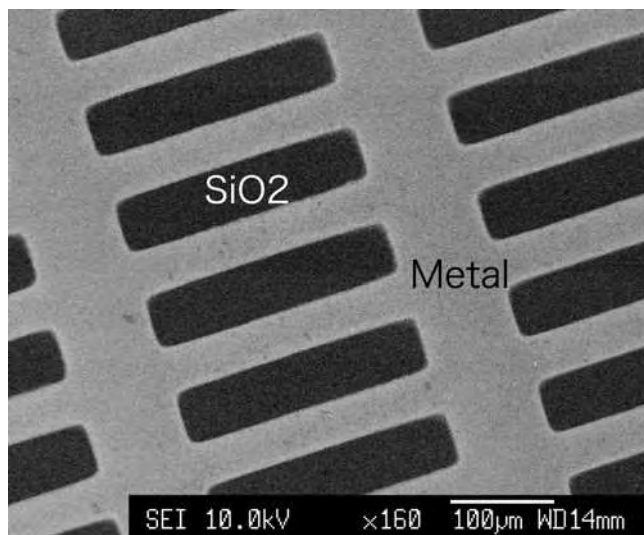


**Fig. 28.** Nickel pattern on the silicon substrate fabricated by the electroless plating (line width: 50  $\mu\text{m}$ ).

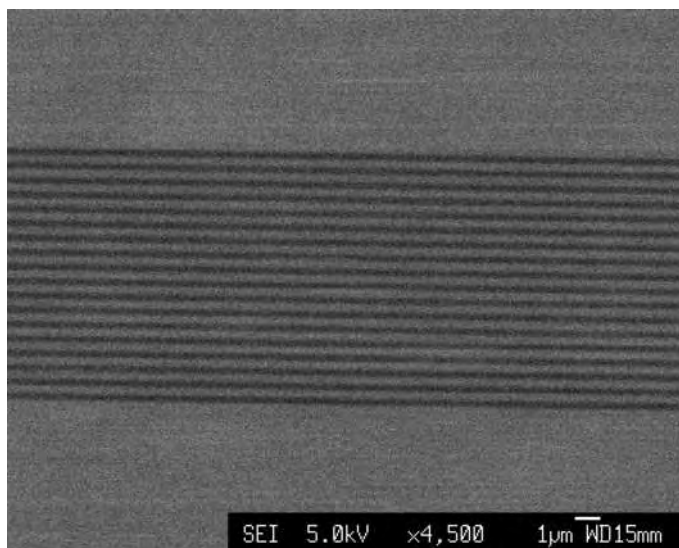


**Fig. 29.** Copper pattern on the silicon substrate fabricated by the electroless plating (line width: 1  $\mu\text{m}$ ).

#### Acknowledgements

We would like to thank Professor H. Sugimura and Professor N. Saito for their valuable help in this study. This work is supported in part by the Research

Project “Biomimetic Materials Processing” (No. JSPS-RFTF 99R13101), Research for the Future (RFTF) Program, Japan Society for the Promotion of Science, and the Aichi/Nagoya Knowledge Cluster of Environment-friendly Manufacturing Using Nano-Technology, Aichi Science and Technology Foundation sponsored by Ministry of Education, Culture, Sports, Science, and Technology.

## REFERENCES

- [1] A. Ulman, *An Introduction to Ultrathin Organic Films from Langmuir–Blodgett to Self-Assembly*, Academic Press, Boston, 1991.
- [2] A. Ulman, *Chem. Rev.*, 96 (1996) 1533.
- [3] D. L. Allara and R. G. Nuzzo, *Langmuir*, 1 (1985) 45.
- [4] D. L. Allara and R. G. Nuzzo, *Langmuir*, 1 (1985) 52.
- [5] H. Ogawa, T. Chihera and K. Taya, *J. Am. Chem. Soc.*, 107 (1985) 1365.
- [6] N. E. Scholotter, M. D. Porter, T. B. Bright and D. L. Allara, *Chem. Phys. Lett.*, 132 (1986) 93.
- [7] M. S. Smart, C. A. Brown and J. G. Gordon, *Langmuir*, 9 (1993) 1082.
- [8] Y.-T. Tao, *J. Am. Chem. Soc.*, 115 (1995) 4350.
- [9] W. R. Thompson and J. E. Pemberton, *Langmuir*, 11 (1995) 1720.
- [10] C. D. Bain, E. B. Troughton, Y.-T. Tao, J. Evall, G. M. Whitesides and R. G. Nuzzo, *J. Am. Chem. Soc.*, 111 (1989) 321.
- [11] J. P. Folkers, J. A. Zerkowski, P. E. Laibinis, C. T. Steo and G. M. Whitesides, (T. Bein, ed.), *Supramolecular Architecture*, American Chemical Society, Washington, DC, 1992, p. 10.
- [12] P. E. Laibinis, G. M. Whitesides, D. L. Allara, Y.-T. Tao, A. N. Parikh and R. G. Nuzzo, *J. Am. Chem. Soc.*, 113 (1991) 7152.
- [13] M. W. Walczak, C. Chung, S. M. Stole, C. A. Widrig and M. D. Prter, *J. Am. Chem. Soc.*, 113 (1991) 2370.
- [14] A. Domez and D. J. Harrison, *Langmuir*, 9 (1993) 1046.
- [15] M. Startmann, *Adv. Mater.*, 2 (1990) 191.
- [16] C. W. Sheen, J. X. Shi, J. Martensson, A. N. Parikh and D. L. Allara, *J. Am. Chem. Soc.*, 114 (1992) 1514.
- [17] Y. Gu, B. Lin, V. S. Smentkowski and D. H. Waldeck, *Langmuir*, 11 (1989) 321.
- [18] E. P. Plueddemann, *Silane Coupling Agents*, Second Edition, Plenum Press, New York, London, 1991.
- [19] J. Sagiv, *J. Am. Chem. Soc.*, 102 (1980) 92.
- [20] P. Silberzan, L. Leger, D. Susserre and J. J. Bentattar, *Langmuir*, 7 (1991) 1647.
- [21] S. R. Wasserman, Y.-T. Tao and G. M. Whitesides, *Langmuir*, 5 (1989) 1074.
- [22] J. D. Le Grange, J. L. Markham and C. R. Kurjian, *Langmuir*, 9 (1993) 1749.
- [23] R. Maoz and J. Sagiv, *J. Colloid Interface Sci.*, 100 (1984) 465.
- [24] N. Tillman, A. Ulman, J. S. Schikraut and T. L. Penner, *J. Am. Chem. Soc.*, 110 (1988) 6136.
- [25] S. Brandriss and S. Margel, *Langmuir*, 9 (1993) 1232.

- [26] K. Mathauser and C. W. Frank, *Langmuir*, 9 (1993) 3002.
- [27] C. R. Kessek and S. Granick, *Langmuir*, 7 (1991) 532.
- [28] H. Tada, *J. Electrochem. Soc.*, 142 (1995) L11.
- [29] R. Vaidya, R. J. Simonson, J. Cesarano, III., D. Dimons and G. P. Lopez, *Langmuir*, 12 (1996) 2830.
- [30] H. Hillebrandt, G. Wiegand, M. Tanaka and E. Sackmann, *Langmuir*, 15 (1999) 8451.
- [31] A. Hozumi, K. Ushiyama, H. Sugimura and O. Takai, *Langmuir*, 15 (1999) 7600.
- [32] C. R. K. Marrian, F. K. Perkins, S. L. Brandow, T. S. Koloski, E. A. Dobisz and J. M. Calvert, *Appl. Phys. Lett.*, 64 (1994) 390.
- [33] H. Sugimura and O. Takai, *Langmuir*, 11 (1995) 3623.
- [34] S. C. Minne, Ph. Flueckiger, H. T. Soh and C. F. Quate, *J. Vac. Sci. Technol. B*, 13 (1995) 1380.
- [35] H. Sugimura and N. Nakagiri, *Jpn. J. Appl. Phys.*, 36 (1997) L968.
- [36] A. Kumar, H. A. Biebuyck and G. M. Whitesides, *Langmuir*, 10 (1994) 1498.
- [37] D. G. Kurth and T. Bein, *Langmuir*, 9 (1993) 2965.
- [38] S. L. Clark, M. Montague and P. T. Hammond, *Macromolecules*, 30 (1997) 7237.
- [39] H. Sugimura and N. Nakagiri, *J. Am. Chem. Soc.*, 119 (1997) 9226.
- [40] D. S. Petri, G. Wenz, P. Schunk and T. Schimmel, *Langmuir*, 15 (1999) 4520.
- [41] C. K. Harnett, K. M. Satyalakshmi and H. G. Craighead, *Langmuir*, 17 (2001) 178.
- [42] S. J. Oh, J. C. Cho, C. O. Kim and J. W. Park, *Langmuir*, 18 (2002) 1764.
- [43] H. Sugimura and N. Nakagiri, *J. Photopolym. Sci. Technol.*, 10 (1997) 661.
- [44] A. Holländer, J. E. Klemberg-Sapieha and M. R. Wertheimer, *Macromolecule*, 27 (1994) 2893.
- [45] H. Sugimura, K. Ushiyama, A. Hozumi and O. Takai, *Langmuir*, 16 (2000) 885.
- [46] A. Hozumi, H. Sugimura, H. Shiroyama, Y. Yokogawa, T. Kameyama and O. Takai, *J. Vac. Sci. Technol. A*, 19 (2001) 1812.
- [47] H. Sugimura, K. Hayashi, N. Saito, O. Takai and N. Nakagiri, *Ultramicroscopy*, 188 (2002) 403.
- [48] V. DePalma and N. Tillman, *Langmuir*, 5 (1989) 868.
- [49] N. Balachander and C. N. Sukenik, *Langmuir*, 6 (1990) 1621.
- [50] A. L. Vinson, L. M. Lander, M. D. Foster, W. J. Brittain, E. A. Vogler, C. F. Majkrzak and S. Stija, *Langmuir*, 12 (1996) 2256.
- [51] H. Sugimura, T. Shimizu and O. Takai, *J. Photopolym. Sci. Technol.*, 13 (2000) 69.
- [52] G. Binnig, H. Rohrer, Ch. Gerber and E. Weibel, *Phys. Rev. Lett.*, 49 (1982) 57.
- [53] G. Binnig, C. F. Quate and Ch. Gerber, *Phys. Rev. Lett.*, 56 (1986) 930.
- [54] P. Avouris, *Acc. Chem. Res.*, 28 (1995) 95.
- [55] R. M. Nyffebegger and R. M. Penner, *Chem. Rev.*, 97 (1997) 1195.
- [56] M. A. McCord and R. F. W. Pease, *J. Vac. Sci. Technol. B*, 4 (1986) 86.
- [57] M. A. McCord and R. F. W. Pease, *J. Vac. Sci. Technol. B*, 6 (1988) 86.
- [58] C. R. K. Marrian and R. J. Colton, *Appl. Phys. Lett.*, 56 (1990) 755.
- [59] A. Dobisz and C. R. K. Marrian, *Appl. Phys. Lett.*, 58 (1991) 2526.
- [60] C. R. K. Marrian and E. A. Dobisz, *Ultramicroscopy*, 42 (1992) 1309.

- [61] L. Stockman, G. Neuttiens, C. V. Haesendonck and Y. Bruynseraede, *Appl. Phys. Lett.*, 62 (1993) 2935.
- [62] F. K. Perkins, E. A. Dobisz and C. R. K. Marrian, *J. Vac. Sci. Technol. B*, 11 (1993) 2596.
- [63] M. Wendel, S. Kuhn, J. P. Kohaus and M. Holland, *Appl. Phys. Lett.*, 65 (1994) 1775.
- [64] G. K. Vinogradov, S. Growadkas, K. Senda and S. Morita, *Jpn. J. Appl. Phys.*, 33 (1994) 6412.
- [65] K. Wilde, C. F. Quate, B. Singh and D. F. Kyser, *J. Vac. Sci. Technol. B*, 16 (1998) 3864.
- [66] K. Wilde, C. F. Quate, D. Adderton, R. Bernstein and V. Elings, *Appl. Phys. Lett.*, 73 (1998) 2527.
- [67] E. Boschung, M. Heuberger and G. Dietler, *Appl. Phys. Lett.*, 64 (1994) 3566.
- [68] J. Garnæs, T. Bjornholm and J. A. N. Zasadzinski, *J. Vac. Sci. Technol. B*, 12 (1994) 1839.
- [69] S. Yamamoto, H. Yamada and H. Tokumoto, *Jpn. J. Appl. Phys.*, 34 (1995) 3396.
- [70] V. Bouchiat and D. Esteve, *Appl. Phys. Lett.*, 69 (1996) 3098.
- [71] S. Hu, S. Altmeyer, A. Hamidi, B. Spangenberg and H. Kurz, *J. Vac. Sci. Technol. B*, 16 (1998) 1983.
- [72] B. Klehn and U. Kunze, *J. Appl. Phys.*, 85 (1999) 8170.
- [73] K. Wieasure and G. Springholz, *J. Appl. Phys.*, 88 (2000) 7289.
- [74] H. C. Day, D. R. Allee, R. George and V. A. Burrows, *Appl. Phys. Lett.*, 62 (1993) 1629.
- [75] C. B. Ross, L. Sum and R. M. Crooks, *Langmuir*, 9 (1993) 632.
- [76] M. J. Lercel, G. F. Redinbo, H. G. Craighead, C. W. Sjeen and D. L. Allara, *Appl. Phys. Lett.*, 65 (1995) 974.
- [77] J. K. Schoer, C. B. Ross, R. M. Crooks, T. S. Corbit and M. J. Hampden-Smith, *Langmuir*, 10 (1994) 615.
- [78] H. Sugimura and N. Nakagiri, *Langmuir*, 11 (1995) 3623.
- [79] J. K. Schoer, F. P. Zamborini and R. M. Crooks, *J. Phys. Chem.*, 100 (1996) 11086.
- [80] H. Sugimura and N. Nakagiri, *J. Vac. Sci. Technol. A*, 14 (1996) 1223.
- [81] H. Sugimura, K. Okiguchi, N. Nakagiri and M. Miyashita, *J. Vac. Sci. Technol. B*, 14 (1996) 4140.
- [82] S. L. Brandow, J. M. Calvert, E. S. Snow and P. M. Campbell, *J. Vac. Sci. Technol. A*, 15 (1997) 1445.
- [83] A. Avramescu, A. Ueta, K. Uesugi and I. Suemune, *Appl. Phys. Lett.*, 72 (1998) 716.
- [84] J. A. Dagata, J. Schneir, H. H. Haray, J. Bennet and W. Tseng, *J. Vac. Sci. Technol. B*, 9 (1991) 1384.
- [85] E. S. Snow, P. M. Campbell and B. V. Shanabrook, *Appl. Phys. Lett.*, 63 (1993) 749.
- [86] H. Sugimura, T. Uchida, N. Kitamura and H. Masuhara, *J. Vac. Sci. Technol. B*, 11 (1994) 12884.
- [87] H. J. Song, M. J. Rack, K. Abugharbieh, S. Y. Lee, V. Khan, D. K. Ferry and D. R. Allee, *J. Vac. Sci. Technol. B*, 12 (1994) 3720.
- [88] N. Kramer, H. Brik, J. Jorritsma and C. Schonberger, *Appl. Phys. Lett.*, 66 (1995) 1325.

- [89] D. C. Tully, K. Wilder, J. M. J. Frechet, A. R. Trimble and C. F. Quate, *Adv. Mater.*, 11 (1999) 314.
- [90] H. Sugimura, T. Hanji, K. Hayashi and O. Takai, *Ultramicroscopy*, 91 (2002) 221.
- [91] H. Sugimura, T. Hanji, K. Hayashi and O. Takai, *Adv. Mater.*, 14 (2002) 524.
- [92] K. Hayashi, H. Sugimura and O. Takai, *Jpn. J. Appl. Phys.*, 40 (2001) 4344.
- [93] H. Sugimura, T. Uchida, N. Kitamura and H. Masuhara, *Jpn. J. Appl. Phys.*, 32 (1993) L553.
- [94] H. Sugimura, T. Uchida, N. Kitamura and H. Masuhara, *J. Phys. Chem.*, 98 (1994) 4352.
- [95] M. Yasutake, Y. Ejiri and T. Hattori, *Jpn. J. Appl. Phys.*, 32 (1993) L1021.
- [96] H. Sugimura, N. Kitamura and H. Masuhara, *Jpn. J. Appl. Phys.*, 33 (1994) L143.
- [97] T. Hattori, Y. Ejiri, K. Saito and M. Yasutake, *J. Vac. Sci. Technol. A*, 12 (1994) 2590.
- [98] E. S. Snow and P. M. Campbell, *Appl. Phys. Lett.*, 64 (1994) 1932.
- [99] H. Sugimura, K. Hayashi, N. Saito, O. Takai and N. Nakagiri, *Jpn. J. Appl. Phys.*, 40 (2001) 4373.
- [100] R. Maoz, E. Frydman, S. R. Cohen and J. Sagiv, *Adv. Mater.*, 12 (2000) 725.

This page intentionally left blank

## Chapter 7

# Highly Fluorinated Langmuir, Langmuir–Blodgett and Gibbs Monolayers

Marie Pierre Krafft\*

*Systèmes Organisés Fluorés à Finalités Thérapeutiques (SOFFT), Institut Charles Sadron (UPR 22 CNRS), 6 rue Boussingault, 67083 Strasbourg Cedex, France*

### 1. INTRODUCTION

Fluorocarbons and fluorinated amphiphiles have found a variety of applications in materials science and medicine [1–5]. As many of these applications involve colloidal systems stabilized by a monolayer of fluorinated amphiphiles, it is essential to understand the structure and properties of these interfacial films. Such knowledge can provide improved control over the engineering and properties of highly fluorinated colloids and interfaces [6].

This chapter reviews the efforts recently devoted to understanding the structure and properties of monolayers made of fluorinated surfactants, including the less conventional type of fluorinated amphiphiles represented by semifluorinated alkanes  $C_nF_{2n+1}C_mH_{2m+1}$ . After a brief description of the specific physico-chemical characteristics of fluorinated chains, the article focuses on Langmuir monolayers, either spread at the air/water interface or transferred onto solid substrates (Langmuir–Blodgett monolayers), and on Gibbs films (adsorbed films). Recent results have shown that fluorinated amphiphiles are useful tools for investigating certain properties, such as phase transitions, that Gibbs and Langmuir monolayers have in common. The lateral phase separation into micron-size domains that occurs within mixed monolayers of fluorinated and hydrogenated surfactants is also discussed, as well as a recently reported

---

\*Corresponding author E-mail: krafft@ics.u-strasbg.fr

case of vertical phase segregation. Finally, some examples of potential uses of fluorinated monolayers in biological sciences and in materials sciences are given.

## 2. SPECIFIC PHYSICO-CHEMICAL CHARACTERISTICS OF FLUORINATED CHAINS

Perfluoroalkyl chains (*F*-chains) strongly differ from hydrogenated chains (*H*-chains) by their bulkiness (cross-sections of  $\sim 28$  and  $20 \text{ \AA}^2$ , respectively), helical conformation (rather than planar “zigzag” structure) and stiffness [2,4]. *F*-chains are considerably more hydrophobic than *H*-chains [2,7]. This is illustrated by the formation of a stable Langmuir monolayer from a non-ampiphilic fluoroalkane,  $\text{C}_{20}\text{F}_{42}$ , at room temperature [8], while such behavior was subsequently only seen for alkanes one and a half times longer [9]. The low polarizability of the fluorine atom results in very weak van der Waals interactions among *F*-chains [10]. On the other hand, the low tendency for *F*-chains to form gauche defects facilitates close packing and ordering of monolayers [11]. In addition to extreme hydrophobicity, *F*-chains have a pronounced lipophobic effect, estimated at about one-third in magnitude of the hydrophobic effect [12]. The unusual combination of these two characters promotes phase separation and compartmentalization at meso-, micro- and nano-scales in molecular systems made from mixtures of fluorinated and hydrogenated surfactants. Examples of such behavior include segregated micelles [13,14], liposomes [15] and Langmuir monolayers with laterally phase-separated zones within their bilayers and films, respectively [16].

## 3. MONOLAYERS OF FLUORINATED SURFACTANTS

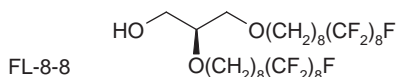
### 3.1. Langmuir Monolayers

Owing to the small size of their polar heads, fluorinated fatty acids and alcohols have been widely used to probe the effect of *F*-chain/*F*-chain interactions on the physical state and stability of monolayers. Highly stable monolayers have been obtained at room temperature from compounds with short *F*-chains such as  $\text{C}_8\text{F}_{17}\text{COOH}$  (*F*-nonanoic acid) [17],  $\text{C}_{10}\text{F}_{21}\text{COOH}$  (*F*-undecanoic acid) [7] or  $\text{C}_{10}\text{F}_{21}(\text{CH}_2)_2\text{OH}$  (1,1,2,2-tetrahydrohenicosaperfluorododecanol) [18]. By contrast, a minimum of 13  $\text{CH}_2$  groups are needed to obtain a stable monolayer from standard hydrocarbon acids or alcohols, which further confirms the higher hydrophobicity of *F*-chains. A specific feature of monolayers of perfluorinated acids (*F*-acids) and alcohols (*F*-alcohols), or acids and alcohols with a short, one or two  $\text{CH}_2$  groups hydrocarbon spacer (*H*-spacer), is that they undergo a direct transition from the gas (G) phase to an untilted liquid condensed (LC) phase during compression, without occurrence of a liquid expanded (LE) phase [11,17,18]. The LE phase formation is prevented by *F*-chain stiffness. No tilted, organized phase has ever been observed for *F*-acids and *F*-alcohols. This was

explained by the weakness of the interactions among *F*-chains, associated to the large *F*-chain cross-section as compared to the polar head size [19], as well as by a theory based on amphiphile–amphiphile and amphiphile–water interactions [20]. The phase diagram of fluorinated surfactants is thus simplified as compared to that of hydrogenated surfactants [21]. The first-order character of the G/LC transition was evidenced by grazing incidence X-ray diffraction (GIXD) [11] and surface potential measurements [22]. The LC phase structure of *F*-acids and *F*-alcohols, identified as the LS phase [21], is identical to that found for C<sub>20</sub>F<sub>42</sub> [8]. The molecules are vertically oriented and packed in a well-organized 2D hexagonal lattice with a unit cell area of  $\sim 29 \text{ \AA}^2$ , as observed by GIXD [18]. Considering the stiffness of *F*-chains and their helical conformation, this 2D lattice would be identical for molecules in a rotator phase or presenting azimuthal ordering [23]. Simulations, however, indicated that azimuthal order should appear around 150 K [24]. Moreover, the weak intermolecular interactions correlated to the absence of LE phase lead to stabilization of the G phase at the expense of the LC phase, resulting in an increase of the surface pressure and a shorter G/LC coexistence plateau [25].

The introduction of an *H*-spacer in carboxylic *F*-acids substantially modifies their compression isotherm. A decrease of monolayer order is generally observed due to the combined effects of *F*-chain and *H*-spacer cross-sections mismatch, and of repulsive interactions of the dipoles associated to the CF<sub>2</sub>–CH<sub>2</sub> linkage. As a result, the isotherms of the partially fluorinated carboxylic acids C<sub>*n*</sub>F<sub>2*n*+1</sub>(CH<sub>2</sub>)<sub>*m*</sub>COOH (*n* = 8, *m* = 4) [11] and (*n* = 4, 6, 8 and *m* = 10) [26] exhibited an LE phase in addition to G and LC phases. This indicates that gauche defects are enabled by a four-carbon *H*-spacer. However, for *n* = 8 and *m* = 10, only an LC phase, with a limiting molecular area of 29 Å<sup>2</sup>, was observed at room temperature (Goldmann et al., unpublished). The LE phase reappeared, however, at 32 °C [26]. When *n* increased from 4 to 8, the limiting molecular area decreased from  $\sim 40$  to 35 Å<sup>2</sup>, i.e. is always larger than the *F*-chains' close packing area. This indicates that increasing the length of *F*-chain decreases the density of gauche defects in the *H*-spacer. Monolayers of carboxylic acids with longer *H*-spacers (*n* = 8; *m* = 10, 16, 22) spread on a cadmium acetate subphase have also been investigated [7]. The minimum compressibility values of these monolayers were significantly higher than that of C<sub>19</sub>H<sub>39</sub>COOH (arachidic acid) monolayers in the same conditions. The ability to form monolayers of a series of long-chain fatty acids with alternating *F*- and *H*-blocks has recently been explored [27].

A partially fluorinated lipid (FL-8-8) was found to form stripe-like microdomains at the gas–liquid phase coexistence region, when spread on water as a Langmuir monolayer [28].



The formation of microdomains was assessed by fluorescence microscopy (FM). Their shape (elongated or spherical) can be understood in terms of competitive effect between long-range dipole–dipole repulsions between terminal groups that tend to elongate the domains, and line tension that tends to minimize the length of the domain boundary. In the case of FL-8-8, stripe-like domains exist because the dipole–dipole repulsions are particularly strong, as compared with non-fluorinated lipids, due to the low dielectric constant of the surrounding medium (air). By contrast, the hydrogenated analog of FL-8-8 forms spherical microdomains (bubbles) at the gas–liquid phase coexistence. The domain periodicity ranged from 2 to 8  $\mu\text{m}$ , in agreement with theoretical modeling.

### 3.2. Langmuir–Blodgett Monolayers

Two-dimensional monodisperse surface micelles have been visualized by atomic force microscopy (AFM) in monolayers of partially fluorinated carboxylic acids ( $n = 4, 6, 8$  and  $m = 10, 16, 22$ ) spread on a cadmium acetate subphase and transferred on cover glass [2,7]. Micelle diameter (a few tens of nanometers) was found to depend on the structure of the amphiphile. The reduction in electrostatic energy of such ionic surfactants, resulting from their segregation in micelles, was deemed as being a driving force for their formation [29]. Polarization modulation infrared reflection absorption spectroscopy (PM-IRRAS), performed on the aqueous subphase and on solid substrate, showed that micelles pre-existed on the water surface and allowed determination of molecular orientations [30]. It was proposed that micelle formation arises from the interplay between the steric hindrance of the *F*-chain and the van der Waals interactions between the *H*-spacers. On both aqueous subphase and solid substrate, the *H*-spacers and *F*-chains of  $\text{C}_8\text{F}_{17}(\text{CH}_2)_{10}\text{COOH}$  were tilted at similar angles ( $\sim 25^\circ$ ) [30]. The *H*-spacers adopted a zigzag trans conformation and displayed a hexagonal subcell packing. For  $m = 22$ , the trans zigzag *H*-spacers were strongly tilted ( $43\text{--}40^\circ$ ) and twisted ( $66\text{--}61^\circ$ ) on the subphase surface, and formed a pseudotriclinic subcell packing [31]. However, after transfer onto the solid substrate, the inclination and twisting of the *H*-spacers diminished and their conformational order decreased, while the *F*-chains' orientation did not change significantly.

### 3.3. Gibbs Monolayers

*F*-chains being efficient probes for X-ray scattering techniques, fluorinated surfactants provide effective tools for studying phase transitions in Gibbs monolayers. Gibbs films of the partially fluorinated alcohol  $\text{C}_8\text{F}_{17}(\text{CH}_2)_2\text{OH}$  (1,1,2,2-tetrahydroheptadecaperfluorodecanol) and  $\text{C}_{10}\text{F}_{21}(\text{CH}_2)_2\text{OH}$  formed at an hexane/water interface have been investigated by surface tension measurements, Brewster angle microscopy (BAM) and X-ray surface scattering [32–34]. Although phase transitions are influenced by molecular interactions, only two phases, a gaseous and a condensed phase, were observed. BAM experiments

gave evidence for small circular condensed-phase domains ( $\sim 10\ \mu\text{m}$ ) coexisting with the gaseous phase, as encountered in a first-order transition in Langmuir films [34]. Investigations by X-ray reflectivity and diffuse scattering of the domains' presence and phase structure, and of their interfacial coverage as a function of temperature, confirmed the first-order character of the transition [33]. X-ray reflectivity data indicated that the *F*-chains were perpendicular to the interface in the condensed phase, in agreement with BAM imaging. It appears reasonable to consider that the microscopic structure of this condensed phase is similar to the LC phase observed at the air/water interface. Comparison between Langmuir and Gibbs monolayers for a series of hydrogenated and fluorinated amphiphiles derived from mannitol confirmed the structural analogies between these two types of films, in spite of their different formation mechanisms [35]. Comparison of Gibbs and Langmuir monolayers made from non-ionic surfactants bearing two polyethoxylated chains and two *F*-chains (or two *H*-chains) was also recently reported [36].

## 4. MONOLAYERS OF SEMIFLUORINATED ALKANES

### 4.1. Langmuir Monolayers

Semifluorinated alkanes  $C_nF_{2n+1}C_mH_{2m+1}$  (*F<sub>n</sub>H<sub>m</sub>* diblocks) consist of a lipophobic fluorocarbon block (*F*-block) and a hydrocarbon block (*H*-block). The mutual antipathy of these blocks results in a tendency for them to demix, which can lead to self-organization of *F<sub>n</sub>H<sub>m</sub>* both in the pure state and in solutions. Since the first published report [37], the structure of *F<sub>n</sub>H<sub>m</sub>* monolayers has remained controversial. A legitimate question concerns which block is in contact with the water surface in the absence of a true polar head. In addition, the presence of *F*- and *H*-blocks within the same molecule helps in the investigation of the interplay between molecular conformation and packing structures. GIXD and/or grazing incidence X-ray reflectivity (GIXR) studies were conducted on perfluorooctyldecane (F8H12), perfluorodecyldecane (F10H12) and perfluorododecyldecane (F12H18) [38]. Although monolayer stability improved as the length of *F*-block increased, relaxation times may reach several days [38]. The limiting areas were similar to those of vertical close-packed *F*-chains. In-plane diffraction evidenced a close packing of the *F*-blocks and a weak organization for the *H*-blocks. Other GIXD studies, including out-of-plane measurements, showed that F8H16 formed organized phases, but the structure of these phases remains undetermined [39]. The peaks, partially out-of-plane, were broad, revealing a low positional correlation length. *F*-blocks may either pack in a tilted structure or in several differently tilted coexisting pseudo-hexagonal phases. No indication of organization of the *H*-blocks was observed. GIXR data suggested an *H*-block-down, *F*-block-up orientation for F8H18 [38]. An alternative configuration has, however, been proposed in which F8H18 would adopt an antiparallel structure, with the *F*-blocks pointing outwards and the *H*-blocks

interleaved inwards [40]. In this configuration, F8H18 would form a stable smectic bilayer phase. Molecular dynamics simulations of the F8H18 monolayer indicated that the structure consisted of mixed orientations, with a slightly larger fraction for an *H*-block-down, *F*-block-up configuration [41].

The effect of introducing a sulfur atom in *F<sub>n</sub>H<sub>m</sub>* diblocks has been investigated, for example with the fluorinated thioalkane C<sub>8</sub>F<sub>17</sub>(CH<sub>2</sub>)<sub>2</sub>SC<sub>16</sub>H<sub>33</sub> [42]. Despite the observation of a single G/LC transition in the isotherm, two-phase transitions were proposed based on FM and surface potential experiments. In a first low-density condensed phase, *F*-blocks would be vertical and *H*-blocks would lie on the subphase. In a second condensed phase, F8H18 molecules would be totally vertical with *F*-blocks up. Monolayers of the related branched amphiphile C<sub>6</sub>F<sub>13</sub>(CH<sub>2</sub>)<sub>2</sub>SCH<sub>2</sub>CHOHCH<sub>2</sub>OCH<sub>2</sub>CH(C<sub>2</sub>H<sub>5</sub>)(C<sub>4</sub>H<sub>9</sub>) (FEP) have been investigated by BAM and GIXD [43,44]. FEP presented a fluid LE phase, whose limiting area is compatible with a folded conformation where the hydrophilic part is lying on the water. However, when transferred on a hydrophilic substrate, FEP adopted a stretched conformation inducing a weakly ordered hexagonal packing of  $\sim 30 \text{ \AA}^2$  of the *F*-blocks [45].

## 4.2. Langmuir–Blodgett Monolayers

It has been established that the presence of surface hemimicelles in monolayers of semifluorinated alkanes C<sub>*n*</sub>F<sub>2*n*+1</sub>C<sub>*m*</sub>H<sub>2*m*+1</sub> (*F<sub>n</sub>H<sub>m</sub>*, *n* = 6, 8, 10, *m* = 14, 16, 18, 20) transferred onto silicon wafers is a general phenomenon [46,47]. The influence of the molecular structure of the *F<sub>n</sub>H<sub>m</sub>* compounds of this series on the morphology and size of the micelles has been determined. F6H16, F8H14 and F8H16 exclusively form monodisperse circular hemimicelles, which are organized as a hexagonal array when the monolayers are transferred at high surface pressure. The X-ray reflectivity spectra could be fitted with a two-layer model. The variation of the electron density as a function of the height of the micelle showed that the *H*-blocks were in contact with the wafer and the *F*-blocks were pointing outwards. In the case of F8H16, the height of the micelle (29.3 Å), as measured by X-ray reflectivity, was close to that of a fully extended F8H16 molecule (33.2 Å). Independently of surface density, the diameter of the micelles (from  $\sim 20$  to  $\sim 50$  nm) depended mainly on the length of the *H*-block while, unexpectedly, the length of the *F*-block did not have any significant effect on micelle diameter [48]. A disk-like shape was proposed for the surface micelles on the basis of electron density calculations. The other semifluorinated alkanes investigated form both circular and elongated hemimicelles. The longer the *F<sub>n</sub>H<sub>m</sub>* molecule, the larger the area fraction of elongated micelles in the mixture. The length of the elongated micelles also increases with the length of the *F<sub>n</sub>H<sub>m</sub>* diblocks. A detailed examination of the surface morphology of the circular micelles showed that these micelles generally present a pit or a tip at their center. It was further determined that the width of the elongated micelles was comparable to the radius of the circular pit-centered micelles. This suggests that

the formation of the circular micelles arises from a partition of the elongated micelles, followed by the coalescence of the edges of the resulting segments. It is noteworthy that well-defined nanoscopic ribbon, spiral and toroidal superstructures were also observed in monomolecular cast films of F14H20 [49]. The shape of the aggregates was found to depend on the solvent from which the film was cast. The well-ordered, highly stable, hexagonally packed lattice of  $F_nH_m$  hemimicelles may prove useful as nanomasks in the elaboration of metallic or polymeric nanostructures.

### 4.3. Surface Freezing

An ordered monolayer was found to form at the free surface of F12H $m$  ( $m = 8, 14, 19$ ) melts, a few degrees above the freezing points of the bulk material [50]. X-ray and surface tension measurements showed that the structure is fully crystalline for  $m = 8, 14$ , while it has only short-range in-plane order for  $m = 19$ , which was assigned to packing frustration of the  $F$ - and  $H$ -blocks. The structure and thermal expansion of surface-frozen monolayers of F8H8, F10H8 and F10H6 have been investigated using surface-sensitive X-ray techniques, demonstrating an unexpectedly strong dependence on the  $H$ -block's length [51]. The molecule was totally stretched, and the  $H$ -blocks appeared to be organized on the 2D lattice formed by the  $F$ -blocks. It should be noticed that the measured nearest-neighbor distance was smaller ( $\sim 5.5 \text{ \AA}$ ) than that typically observed for  $F$ -blocks 2D packing ( $\sim 5.8 \text{ \AA}$ ) in Langmuir monolayers.

Gibbs films of F12H $m$  ( $m = 12, 14, 16, 18$ ) at the free surface of their solutions in dodecane, bicyclohexyl and hexadecane have been studied by surface tension measurements and surface-sensitive X-ray techniques [52]. The monolayers at the surface of dodecane and bicyclohexyl exhibited sharp first-order transitions from a gas-like state at high temperatures to a condensed state at lower temperatures. In the condensed film, the  $F$ -blocks were close-packed in a 2D hexagonal array (cross-sectional area  $\sim 28 \text{ \AA}^2$ ) with an in-plane order limited to  $20 \text{ \AA}$ . Moreover, the  $F$ -blocks appeared to be vertically distributed over  $\sim 20$ – $30 \text{ \AA}$ . The short-range order was attributed again to the packing frustration induced by the mismatch between  $F$ - and  $H$ -blocks. In the case of the F12H16 monolayer on hexadecane, the sharp transition was replaced by a gradual surface concentration increase below  $25^\circ\text{C}$ , which was attributed to solvation of the  $H$ -blocks by the alkane, thus preventing close packing of the  $F$ -blocks.

## 5. MIXTURES OF FLUORINATED AND HYDROGENATED AMPHIPHILES

### 5.1. Lateral Phase Separation

The mutual antipathy between  $F$ - and  $H$ -chains can be exploited to create patterned surfaces. Control of the shape, size and molecular organization is

necessary to achieve mastered construction of 2D supramolecular architectures. An efficient way to induce micro phase separation is to mix a hydrogenated and a fluorinated surfactant that form LC and LE monolayers, respectively. The mixture of  $C_{17}H_{35}COOH$  (stearic acid), which forms an L2 mesophase at 5 mN/m and LS mesophase at 30 mN/m, with the fluorinated surfactant FEP, which forms an LE phase, presented complete phase separation over the entire range of molar fractions and surface pressures investigated, as assessed by FM, BAM and GIXD [45]. 2D circular domains, exclusively occupied by  $C_{17}H_{35}COOH$  molecules, displayed an optical anisotropy that was related to the tilt of the molecules. Lateral micro phase separation has also been achieved in mixed monolayers of cadmium salts of *n*-alkyl fatty acids  $C_nH_{2n+1}COOH$  ( $n = 17, 19, 21, 23$ ) and the *F*-polyether surfactant  $F(CF(CF_3)CH_2O)_3CF(CF_3)COOH$  (PFPE), as demonstrated by BAM at various temperatures [53]. The  $C_nH_{2n+1}COOH$  monolayers underwent direct transition from the gas state to the solid state during compression. PFPE was in the expanded state due to the affinity of the *F*-polyether groups for water. The two-step collapse and the additivity rule showed that the two components were immiscible in the water-supported monolayers. Monolayers have then been transferred on silicon wafers and studied by AFM at various temperatures [53]. The mixed monolayers were found to separate into microscopic domains of condensed phase of  $C_nH_{2n+1}COOH$  in a surrounding matrix in an expanded phase of PFPE. Circular-shaped condensed-phase microdomains were formed when mixed monolayers were prepared using short alkyl chain fatty acids and/or at a high temperature, whereas branched narrow domains were observed when longer chain fatty acids were used at lower temperatures. Mixed Langmuir monolayers of  $C_8F_{17}COOH$  and  $C_{18}H_{37}SO_3Na$  (sodium octadecanesulfonate) have been transferred on mica and investigated by AFM and friction force microscopy (FFM), providing evidence for 2D phase separation and crystallization [17]. The mixing behavior of fluorinated and hydrogenated cationic gemini surfactant was studied at the air/water interface by BAM [54]. When the monolayer was formed by separate deposition of the two spreading solutions, the gemini surfactants formed separate domains, which was not the case when the two spreading solutions were mixed before deposition.

It has also been shown, experimentally and through simulation, that segregation also occurred in monolayers made from hydrocarbon and fluorocarbon surfactants in the condensed state, because of their mutual phobicity. Mixed monolayers of  $C_{10}F_{21}(CH_2)_2OH$  and  $C_{14}H_{29}OH$  (1-tetradecanol) at the air/water surface were investigated by BAM and GIXD at 25 °C, showing that these molecules are practically immiscible in the condensed phase [18]. The miscibility of hydrogenated alcohols and semifluorinated alkanes has also been investigated [55].

AFM observations have been carried out on transferred monolayers of binary mixtures of  $C_{19}H_{39}COOH$ ,  $C_{17}F_{35}COOH$  (*F*-octadecanoic acid),  $C_{13}F_{27}COOH$  (*F*-tetradecanoic acid) and [2-(*F*-decyl)ethyl]dimorpholinophosphate (F10C2DMP) [56]. In  $C_{17}F_{35}COOH/C_{19}H_{39}COOH$  and  $C_{13}F_{27}COOH/C_{19}H_{39}COOH$  monolayers, two types of domains with different heights were

visualized, indicating phase separation. At low surface pressures,  $C_{19}H_{39}COOH$ -rich (or  $C_{17}F_{35}COOH$ -rich) domains coexisted in a continuous  $C_{13}F_{27}COOH$ -rich region. Phase separation was also observed in  $C_{17}F_{35}COOH/C_{13}F_{27}COOH$  mixed monolayers.  $C_{13}F_{27}COOH$  was miscible with F10C2DMP, and the hybrid film displayed a fractal texture.

The phase separation and molecular orientation in mixed films of  $C_{21}H_{43}COOH$  (behenic acid) and  $C_{13}F_{27}COOH$  have been investigated using scanning surface potential microscopy (SSPM) and FFM [57]. The structure of the monolayers formed on a  $CaCl_2$ -aqueous subphase and transferred onto an oxidized doped *n*-type Si(100) substrate was a “side-by-side” structure, different from that of monolayers complexed with polymer cations (“on-top” structure). However, the small differences in surface potentials between the two separated phases, and the low contrast in friction, revealed that the excess concentration of one component in one phase was only slightly higher than that in the other phase. Scanning near-field fluorescence microscopy (a combination of scanning near-field optical microscopy and AFM that allows fluorescence imaging and spectroscopy of a localized nanoarea) has shown that a small amount of a cationic cyanine dye with two long alkyl chains was preferentially solubilized in islands of  $C_{19}H_{39}COOH$  in phase-separated monolayers of  $C_{19}H_{39}COOH$  and of the partially fluorinated surfactant  $C_9F_{19}C_2H_4OC_2H_4COOH$  [58].

## 5.2. Vertical Phase Separation

Compression of mixed Langmuir monolayers made from combinations of dipalmitoyl phosphatidylethanolamine (DPPE) and the semifluorinated F8H16 diblock resulted in expulsion of the diblock molecule at high pressure [39]. Depending on the DPPE/F8H16 molar ratio, either a monolayer or a bilayer of F8H16 was formed on top of a DPPE-only monolayer. The structure of these vertically separated bi- or trilayer was determined using GIXD. The phenomenon was found to be reversible and represents a unique case of vertical, pressure-induced phase separation. AFM and X-ray reflectivity studies on DPPE/F8H16 mixed monolayers transferred on silicon wafers indicated that the F8H16 molecules formed surface micelles coexisting with DPPE molecules, within the mixed monolayer [59]. When surface pressure increased, the F8H16 surface micelle network progressively glided on top of the DPPE monolayer until total coverage was achieved.

A similar behavior has been observed, based on isotherms and BAM experiments, for mixed monolayers of 10,12-pentacosadiynoic acid (PDA) and F8H16 that form a miscible film at low surface pressures [60]. When surface pressure was increased, the F8H16 molecules were ejected on top of the PDA monolayer. A bilayer structure was then obtained, with the PDA molecules anchored on the water surface and the F8H16 on top, with their *H*-blocks intercalated with the PDA chains. This process has been monitored by UV-visible spectroscopy, as the *H*-blocks of F8H16 prevented PDA polymerization

when they were intercalated. Mixtures of F8H18 and a poly(styrene)/poly(ethylene oxide) copolymer have been investigated by isotherms and AFM experiments [61]. As observed in the above cases, F8H18 segregated on top of the copolymer for all copolymer densities. When transferred on a glass substrate, the film exhibited a surface structure described as honeycombs (periodicity of  $\sim 40$  nm) with a hump (diameter of  $\sim 30$  nm) at the center.

## 6. POTENTIAL USE OF FLUORINATED MONOLAYERS IN BIOLOGICAL SCIENCES

The examples given here involve lung surfactant replacement compositions and surfactant systems used for 2D protein crystallization. Other potential systems include direct, reverse and multiple emulsions for drug and gene delivery, as well as micro- and nano-sized gas bubbles for O<sub>2</sub> delivery and diagnosis [3, 4]

### 6.1. Lung Surfactant

With the objective of designing new compositions of synthetic substitutes for the native lung surfactant, it is desirable to control the physical state and properties of dipalmitoylphosphatidylcholine (DPPC) spread at the air/water interface. DPPC is the main component of the native lung surfactant, which also comprises a complex mixture of lipids and specific proteins [62]. Langmuir monolayers provide a model of the air/alveolar interface that is widely used for assessing the properties of lung surfactant replacement compositions.

Many studies have been conducted on the influence of perfluorinated or partially fluorinated acids or alcohols on monolayers of DPPC or of other hydrocarbon surfactants, in order to provide a rationale for their mixing behavior. A series of partially fluorinated acids, C<sub>n</sub>F<sub>2n+1</sub>(CH<sub>2</sub>)<sub>11</sub>COOH ( $n = 4, 6, 8$ ), was found to be miscible (between 3 and 25 mN/m) with DPPC (pH 1.9, 32 °C) [63]. The same series of compounds was partially miscible in mixed Langmuir monolayers with hydrocarbon carboxylic acids of similar length, at 37 °C [64]. The mixing behavior of a series of perfluorinated carboxylic acids with DPPC has recently been reported [65]. The results show that only the shortest compounds, with a chain length of 12 or 14 carbon atoms, were perfectly miscible; limited miscibility or immiscibility were observed for compounds bearing longer chains. Mixtures of partially fluorinated amphiphiles with various polar heads (i.e. C<sub>8</sub>F<sub>17</sub>(CH<sub>2</sub>)<sub>5</sub>OH/C<sub>8</sub>F<sub>17</sub>(CH<sub>2</sub>)<sub>5</sub>OP(O<sub>2</sub>)<sup>-</sup>(CH<sub>2</sub>)<sub>2</sub>N<sup>+</sup>(CH<sub>3</sub>)<sub>3</sub> [66] and C<sub>12</sub>F<sub>25</sub>COOH/C<sub>11</sub>F<sub>23</sub>CH<sub>2</sub>N<sup>+</sup>(CH<sub>3</sub>)<sub>3</sub>Cl<sup>-</sup> [22]) were found to be miscible in mixed monolayers.

The mixing behavior of 10-(perfluorohexyl)-decanol and DPPC in Langmuir monolayers has recently been reported, showing partial miscibility, especially at low surface pressure [67]. 10-(perfluorohexyl)-Decanol was studied because it is a fluorinated analog of hexadecanol, which has been used in synthetic lung surfactant compositions.

However, it is known that carboxylic perfluorinated acids, in particular perfluorooctanoic acid, accumulate in the living organisms and are environmentally persistent [68].

Recently, fluorocarbon gases (gFCs) were found to have a highly effective fluidizing effect on DPPC monolayers by inhibiting their LE/LC phase transition [69, 70]. Upon compression, the FC molecules are inserted into the DPPC monolayer, which remains in the LE phase until high surface pressures are reached ( $\sim 40$  mN/m), as assessed by FM and GIXD. Moreover, gFCs can induce the dissolution of pre-existing LC phase domains and facilitate the re-spreading of the DPPC molecules on the water surface. The candidate FCs were chosen among those already investigated for biomedical applications, and in particular for intravascular oxygen transport, i.e. perfluorooctyl bromide, perfluorooctylethane, bis(perfluorobutyl)ethane and perfluorodecalin. The biocompatibility of these FCs is well documented [71]. Moreover, gFCs were found to reduce the delipiding effect induced by serum protein, such as albumin, that is frequently observed with commercial lung surfactant substitutes extracted from animal lungs [72]. These studies suggest that FCs may be useful in the design of new synthetic lung surfactant substitute compositions.

The mixed monolayer behavior of a fluorinated surfactant derived of dimorpholinophosphate,  $C_8F_{17}(CH_2)_{11}OP(O)[N(CH_2CH_2)_2O]_2$  (F8H11DMP), with DPPC has been investigated [73]. F8H11DMP is the emulsifier involved in the preparation of water-in-fluorocarbon microemulsions destined for pulmonary delivery of bioactive materials, in particular for local administration using pressurized metered-dose inhalers. F8H11DMP/DPPC mixtures form miscible, mixed monolayers in the LE state, both at the air/water and water/fluorocarbon interfaces. Furthermore, spreading an F8H11DMP-based water-in-PFOB microemulsion on a DPPC monolayer led to the quantitative adsorption of F8H11DMP at the interface, and formation of a mixed DPPC/F8H11DMP monolayer, which favorably augurs the delivery capacity of these microemulsions to the lungs.

## 6.2. Two-Dimensional Protein Crystallization

Langmuir monolayers of partially fluorinated lipids have been used to induce 2D crystallization of soluble proteins and membrane proteins, thus allowing access to a powerful tool for structure determination. Lipids with an *F*-spacer were synthesized in order to separate a lipophilic retinoid ligand from the lipidic tails [74]. The fluorocarbon film that forms by aggregation of the *F*-spacers keeps the ligand exposed on the aqueous side of the monolayer, preventing it from being buried in the lipidic region of the monolayer. More recently, lipids containing one *F*-chain and one *H*-chain have been synthesized in order to increase monolayer fluidity [75]. Such fluid monolayers, containing fluorinated  $Ni^{2+}$ -chelating lipids, have been investigated for 2D crystallization of a histidin-tagged protein. 2D crystals of the proton ATPase, a membrane protein, have also been obtained using a detergent-resistant monolayer of such fluorinated lipids [76].

## 7. POTENTIAL USE OF FLUORINATED MONOLAYERS IN MATERIALS SCIENCE

Porphyrin derivatives, substituted with donor and acceptor groups, have focused attention because such compounds exhibit large molecular hyperpolarizability, suggesting that they may be valuable for their nonlinear properties. Langmuir monolayers of tetraphenylporphyrins grafted with four fluorocarbon chains have been investigated by BAM and polarized UV-visible spectroscopy after transfer [77]. The porphyrin rings were tilted on average, but, as the *F*-chains' length increased, tended to adopt an orientation more parallel to the water surface. The third-order nonlinear optical susceptibilities of these monolayers were evaluated.

Another potential application for fluorinated monolayers is their use as lubricants for microelectronics. Such a lubricant needs to be ultra-thin, ideally a monolayer, strongly adsorbed on the substrate surface, and should have lateral fluidity. Fluorinated amphiphiles are particularly suited for such uses because of their chemical, thermal and photolytic stability, their low surface tension and extreme hydrophobicity. Langmuir monolayers of hexakis(tetrahydrofluorododecanoxyl) cyclotriphosphazene transferred on mica or on a gold-coated glass plate have been shown to adsorb strongly onto substrates and produce significant friction reduction [78]. Temperature-dependent friction measurements indicated that monolayers of partially fluorinated carboxylic acids, transferred from an aqueous  $\text{Cd}^{2+}$  subphase onto aluminum-evaporated glass substrates, exhibited good thermal stability and could be used as molecular lubricants in the range of 25–140 °C [79]. Langmuir monolayers of a series of long-chain esters of acrylic and methacrylic acids containing *F*-chains or partially fluorinated chains, transferred using various methods, have also been investigated [80].

Surface micelles of fluorinated amphiphiles have potential as templates for the elaboration of metallic nanodot arrays. Hexagonal arrays of gold and silver nanodots, a few nM in size, have been observed by AFM to form when a thin layer of metal was deposited through vacuum evaporation on a silicon wafer covered with hemimicelles of the F8H16 diblock (E. Charrault, P. Muller, M. Maaloum, M.P. Krafft, C. Petit, P. Petit, unpublished).

### Acknowledgement

I am indebted to Prof. Dr. B. Aerele (Harangoutte University, Digital Management and Stone Building Department) for secretarial help.

## REFERENCES

- [1] E. Kissa, *Fluorinated Surfactants and Repellents*, Marcel Dekker, New York, 2001.
- [2] J. G. Riess, *Tetrahedron*, 58 (2002) 4113.

- [3] M. P. Krafft, *Adv. Drug Deliv. Rev.*, 47 (2001) 209.
- [4] J. G. Riess, (J. A. Gladysz, I. Horváth and D. P. Curran, eds.), *Handbook of Fluorous Chemistry*, Wiley-VCH, Weinheim, 2004, p. 521.
- [5] E. G. Schutt, D. H. Klein, R. M. Mattrey and J. G. Riess, *Angew. Chem. Int. Ed.*, 42 (2003) 3218.
- [6] M. Krafft (ed.), *Fluorinated Colloids and Interfaces*, *Curr. Opin. Colloid Interf. Sci.*, 8 (2003) 213.
- [7] T. Kato, M. Kameyama, M. Ehara and K.-I. Iimura, *Langmuir*, 14 (1998) 1786.
- [8] M. Li, A. A. Acero, Z. Huang and S. A. Rice, *Nature*, 367 (1994) 151.
- [9] I. Kuzmenko, H. Rapaport, K. Kjaer, J. Als-Nielsen, I. Weissbuch, M. Lahav and L. Leiserowitz, *Chem. Rev.*, 101 (2001) 1659.
- [10] P. Mukerjee and T. Handa, *J. Phys. Chem.*, 85 (1981) 1659.
- [11] S. W. Barton, A. Goudot, O. Bouloussa, F. Rondelez, B. Lin, F. Novak, A. Acero and S. A. Rice, *J. Chem. Phys.*, 96 (1992) 1343.
- [12] B. Binks, P. Fletcher, S. Kotsev and R. Thompson, *Langmuir*, 13 (1997) 6669.
- [13] P. Mukerjee and A. Y. S. Yang, *J. Phys. Chem.*, 80 (1976) 1388.
- [14] K. Staehler, J. Selb and F. Candau, *Langmuir*, 15 (1999) 7565.
- [15] M. Schmutz, B. Michels, P. Marie and M. P. Krafft, *Langmuir*, 19 (2003) 4889.
- [16] R. Elbert, T. Folda and H. Ringsdorf, *J. Am. Chem. Soc.*, 106 (1984) 7687.
- [17] B.-Y. Zhu, P. Zhang, R.-X. Wang, Z.-F. Liu and L. Lai, *Colloids Surf.*, 157 (1999) 63.
- [18] T. Takiue and D. Vollhardt, *Colloids Surf.*, 198–200 (2002) 797.
- [19] V. Kaganer, M. Osipov and I. Petersen, *J. Phys. Chem.*, 98 (1993) 3512.
- [20] S. Shin and S. Rice, *J. Chem. Phys.*, 101 (1994) 2508.
- [21] A. Bibo, C. Knobler and I. Peterson, *J. Phys. Chem.*, 95 (1991) 5591.
- [22] M. Rusdi, Y. Moroi, S. Nakamura, O. Shibata, Y. Abe and T. Takahashi, *J. Colloid Interf. Sci.*, 243 (2001) 370.
- [23] M. Goldmann, P. Nassoy, F. Rondelez, A. Renault, S. Shin and S. Rice, *J. Phys. II (France)*, 4 (1994) 773.
- [24] M. Schmidt, S. Shin and S. Rice, *J. Chem. Phys.*, 104 (1996) 2101.
- [25] A. Acero, M. Li, B. Lin, S. Rice, M. Goldmann, I. Azouz, A. Goudot and F. Rondelez, *J. Chem. Phys.*, 99 (1993) 7214.
- [26] H. Lehmler, M. Oyewumi, M. Jay and P. Bummer, *J. Fluorine Chem.*, 107 (2001) 141.
- [27] P. Beier, D. O'Hagan, C. Pearson, M. C. Petty and A. M. Slawin, *J. Fluorine Chem.*, 126 (2005) 673.
- [28] M. F. Schneider, D. Andelman and M. Tanaka, *J. Chem. Phys.*, 122 (2005) 94717.
- [29] H. Ichinose, T. Kato, M. Takefu and Y. Suezaki, *Langmuir*, 15 (1999) 4705.
- [30] Y. Ren, K.-I. Iimura, A. Ogawa and T. Kato, *J. Phys. Chem.*, 105 (2001) 4305.
- [31] Y. Ren, K.-I. Iimura and T. Kato, *J. Phys. Chem.*, 106 (2002) 1327.
- [32] T. Takiue, A. Yanata, N. Ikeda, K. Motomura and M. Aratano, *J. Phys. Chem.*, 100 (1996) 13743.
- [33] A. M. Tikhonov, M. Li and M. Schlossman, *J. Phys. Chem.*, 105 (2001) 8065.
- [34] S. Uredat and G. Findenegg, *Langmuir*, 15 (1999) 1108.
- [35] E. Rogalska, R. Bilewicz, T. Brigaud, C. Moujahid El, G. Foulard, C. Portella and M.-J. Stébé, *Chem. Phys. Lipids*, 105 (2000) 71.

- [36] M.-J. Stébé, V. Istratov, A. Langenfeld, V. A. Vasnev and V. G. Babak, *J. Fluorine Chem.*, 119 (2003) 191.
- [37] G. L. Gaines, *Langmuir*, 7 (1991) 3054.
- [38] Z. Huang, A. A. Acero, N. Lei, S. A. Rice, Z. Zhang and M. L. Schlossman, *J. Chem. Soc. Faraday Trans.*, 92 (1996) 545.
- [39] M. P. Krafft, F. Giulieri, P. Fontaine and M. Goldmann, *Langmuir*, 17 (2001) 6577.
- [40] A. El-Abed, E. Pouzet, M.-C. Fauré, M. Sanière and O. Abillon, *Phys. Rev. E*, 62 (2000) R5895.
- [41] N. Kim and S. Shin, *J. Chem. Phys.*, 110 (1999) 10239.
- [42] A. El Abed, M. Fauré, M. Hamdani, F. Guittard, J. Billard and P. Peretti, *Mol. Cryst. Liq. Cryst.*, 329 (1999) 283.
- [43] V. Duprès, S. Cantin, F. Benhabib and F. Perrot, *Europhys. Lett.*, 48 (1999) 86.
- [44] V. Duprès, S. Cantin, F. Benhabib, F. Perrot, P. Fontaine and M. Goldmann, *Langmuir*, 16 (2000) 10189.
- [45] V. Duprès, S. Cantin, F. Perrot, J. Michel, E. Lacaze, P. Fontaine and M. Goldmann, *Thin Solid Films*, 457 (2004) 381.
- [46] M. Maaloum, P. Muller and M. P. Krafft, *Angew. Chem. Int. Ed.*, 41 (2002) 4331.
- [47] G. Zhang, P. Marie, M. Maaloum, P. Muller, N. Benoit and M. Krafft, *J. Am. Chem. Soc.*, 127 (2005) 10412.
- [48] G.-F. Zhang, M. Maaloum, P. Muller, N. Benoit and M. P. Krafft, *Phys. Chem. Chem. Phys.*, 6 (2004) 1566.
- [49] A. Mourran, B. Tartsch, M. Gallyamov, S. Magonov, D. Lambeva, B. I. Ostrovskii, I. P. Dolbnya and M. Moeller, *Langmuir*, 21 (2005) 2308.
- [50] O. Gang, J. Ellmann, M. Möller, H. Kraak, E. Sirota, B. Ocko and M. Deutsch, *Europhys. Lett.*, 49 (2000) 761.
- [51] E. Sloutskin, H. Kraak, B. Ocko, J. Ellmann, M. Möller, P. LoNostro and M. Deutsch, *Langmuir*, 18 (2002) 1963.
- [52] P. Marczuk, P. M. Lang, G. Findenegg, S. Mehta and M. Möller, *Langmuir*, 18 (2002) 6830.
- [53] K. Iimura, T. Shiraku and T. Kato, *Langmuir*, 18 (2002) 10183.
- [54] J. Nishida, A. Brizard, B. Desbat and R. Oda, *J. Colloid Interf. Sci.*, 284 (2005) 298.
- [55] M. Broniatowski, M. Nieto-Suarez, N. Vila-Romeu, K. Halc-Wydro and P. Dynarowicz-Latka, *Colloids Surf.*, 249 (2004) 3.
- [56] T. Imae, T. Takeshita and M. Kato, *Langmuir*, 16 (2000) 612.
- [57] K. Yagi and M. Fujihara, *Appl. Surf. Sci.*, 157 (2000) 405.
- [58] H. Monobe, A. Koike, H. Muramatsu, N. Chiba, N. Yamamoto, T. Akata and M. Fujihara, *Ultramicroscopy*, 71 (1998) 287.
- [59] M. Maaloum, P. Muller and M. P. Krafft, *Langmuir*, 20 (2003) 2261.
- [60] S. Wang, R. Lunn, M. Krafft and R. Leblanc, *Langmuir*, 16 (2000) 2882.
- [61] A. L. Simoes Gamboa, E. Filipe and P. Brogueira, *Nano Lett.*, 2 (2002) 1083.
- [62] J. A. Zasadzinski, J. Ding, H. E. Warriner, F. Bringezu and A. J. Waring, *Curr. Opin. Colloid Interf. Sci.*, 6 (2001) 506.
- [63] H. Lehmler, M. Jay and P. Bummer, *Langmuir*, 16 (2000) 10161.
- [64] H. Lehmler and P. Bummer, *J. Colloid Interf. Sci.*, 249 (2002) 381.

- [65] H. Nakahara, S. Nakamura, H. Kawasaki and O. Shibata, *Colloids Surf.*, 41 (2005) 285.
- [66] O. Shibata and M. Krafft, *Langmuir*, 16 (2000) 10281.
- [67] H. J. Lehmler and P. M. Bummer, *Colloids Surf.*, 44 (2005) 74.
- [68] F. A. Ubel, S. C. Sorenson and D. E. Roach, *Am. Ind. Hyg. Assoc.*, 41 (1980) 584.
- [69] F. Gerber, M. P. Krafft, T. F. Vandamme, M. Goldmann and P. Fontaine, *Angew. Chem. Int. Ed.*, 44 (2005) 2749.
- [70] F. Gerber, M. P. Krafft, T. F. Vandamme, M. Goldmann and P. Fontaine, *Biophys. J.*, 90 (2006) 3184.
- [71] J. G. Riess, *Chem. Rev.*, 101 (2001) 2797.
- [72] F. Gerber, M. P. Krafft and T. F. Vandamme, *Biomaterials*, (2006) DOI: 10.1016/j.bbame.2006.09.022.
- [73] H. M. Courrier, T. F. Vandamme, M. P. Krafft, S. Nakamura and O. Shibata, *Colloids Surf.*, 215 (2003) 33.
- [74] P. Held, F. Lach, L. Lebeau and C. Mioskowski, *Tetrahedron Lett.*, 38 (1997) 1937.
- [75] S. Nuss, C. Mioskowski and L. Lebeau, *Chem. Phys. Lipids*, 103 (1999) 21.
- [76] L. Lebeau, F. Lach, C. Vénien-Bryan, A. Renault, J. Dietrich, T. Jahn, M. Palmgren, W. Kühlbrandt and C. Mioskowski, *J. Mol. Biol.*, 308 (2001) 639.
- [77] H. Nakahara, W. Liang, K. Fukuda, L. Wang, T. Wada and H. Sasabe, *J. Colloid Interf. Sci.*, 208 (1998) 14.
- [78] Y. Tian, Q. Ng and J. H. Fendler, *Langmuir*, 14 (1998) 3067.
- [79] Y. Ren, M. Asanuma, K.-I. Imura and T. Kato, *J. Chem. Phys.*, 114 (2001) 923.
- [80] A. Fujimori, T. Araki and H. Nakahara, *J. Colloid Interf. Sci.*, 247 (2002) 351.

This page intentionally left blank

## Chapter 8

# Structure and Physicochemical Properties of Polyalkylsiloxane Monolayers Prepared onto the Solid Substrate

T. Koga, A. Takahara\*

*Institute for Materials Chemistry and Engineering, Kyushu University, Higashi-ku, Fukuoka 812-8581, Japan*

### 1. INTRODUCTION

Ultrathin films of organosilane have been identified as promising nanocoating for micro- and nanoscale technologies such as electronic devices and micromachines [1–3]. As the silanol groups of organosilane monolayer prepared from organotrichlorosilane or organotrialkoxysilane strongly interact with the substrate surface by covalent bond and multiple hydrogen bonds, the monolayer is thermally and chemically robust compared with conventional amphiphilic monolayers. Since the chain length of organosilane is approximately 1–3 nm, the organosilane forms a uniform ultrathin film on the substrate surface. Furthermore, the organosilane molecules formed two-dimensionally polymerized monolayers between their silanol groups.

Two methods have been proposed for the preparation of organosilane monolayers. One is chemisorption from organosilane solution [4–6], and the other one is Langmuir–Blodgett (LB) method or water-cast method [7–23]. Fig. 1 shows the film formation mechanism of the organosilane by LB method (a) and chemisorption method (b). In the case of LB method (Fig. 1(a)), the toluene solution of organotrichlorosilane was spread on the water surface (pH 5.8) at a controlled subphase temperature. To attain quasi-equilibrium state of the monolayer, the monolayer was kept on the water subphase under a given

---

\*Corresponding author. E-mail: takahara@cstf.kyushu-u.ac.jp

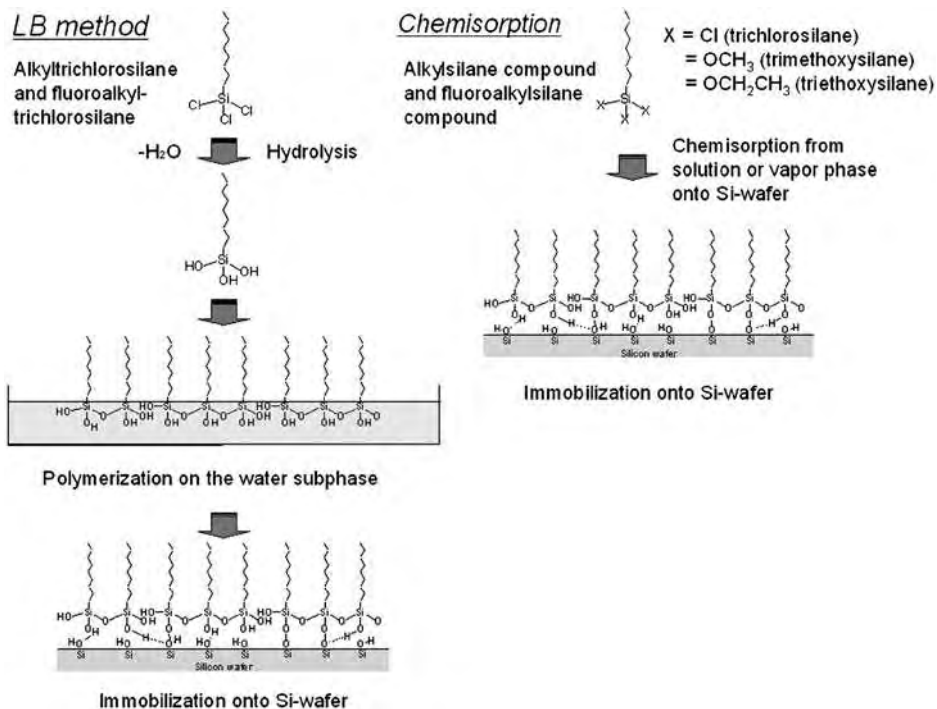


**Fig. 1.** Film formation mechanism of the organosilane by (a) LB method and (b) chemisorption method.

constant surface pressure for 15 min. The monolayer was transferred and immobilized onto the Si-wafer substrate surface by the LB method. In the case of chemisorption (Fig. 1(b)), the organosilane molecule was deposited from the solution at room temperature. It has been clarified that the aggregation state of the organosilane monolayers prepared by the LB method showed higher packing density compared with the chemisorbed monolayers [14, 21]. In recent years, the chemical vapor adsorption (CVA) method has attracted much attention as a simple technique for the preparation of organosilane monolayers (Fig. 1(b)) [24–36]. Sugimura et al. reported that the organosilane monolayers prepared by the CVA method possess remarkable uniform surfaces without defects or aggregates [34], and these uniform surfaces are suitable for a microfabrication process based on the photolithography of nanofilms [26–36].

Organosilane monolayers, which have surfaces terminated by various functional groups, are useful for the manipulation of physicochemical properties of solid surfaces such as wettability, nanotribology, and protein adsorption behavior. A key to fabricating functional organosilane monolayers is controlling the distribution of surface functional groups. Fabricating micro- and nanodevices using a bottom-up approach requires building blocks with a precisely controlled

and tunable chemical composition, morphology, and size that can be fabricated virtually at will. Organosilane monolayer is a candidate for such building blocks because of its robustness and ease of fabrication. Patterned microfeatures of organosilane monolayers can be fabricated on the substrate, allowing surface physicochemical properties to be area-selectively controlled. Two methods will be discussed in this chapter. One of them utilizes the crystallization of organosilane of binary component monolayer at air/water interface [7–10]. Since the diffusion of organosilane molecule at air/water interface is slow, the macroscopic phase separation is inhibited even through the alkylsilane and fluoroalkylsilane mixed monolayers. The phase-separated monolayer is transferred to the Si-wafer substrate by the LB method. Another method utilizes the photolithography by vacuum ultra-violet (VUV)-ray source [26–36]. In the case of a VUV source with  $\lambda = 172$  nm, photodecomposition of the organic moiety occurs due to the higher photon energy of the VUV light compared with the bond energy of a typical C–C linkage. Using photolithography, one can prepare a micropatterned surface with various organosilane monolayers by repeating the photodecomposition and chemisorption processes. By changing the shape and area-ratio of the patterns of the photomask, this technique enables one to control the area ratio and surface energy gap of different organosilane monolayers.

## 2. FABRICATION OF MICROPATTERNED ORGANOSILANE MONOLAYERS

### 2.1. Formation of Organosilane Monolayers at the Air/Water Interface

Fig. 2 shows the chemical structure of organosilanes used for monolayer preparation. Organotrichlorosilane is mainly used for monolayer preparation at the air/water interface. The chlorine groups of organosilane on the water surface were substituted by hydroxyl groups. At surface pressure of 10–30 mN m<sup>-1</sup>, the hydroxyl groups in an organosilane molecule reacted with those in the adjacent molecules in the case of the highly condensed monolayer, resulting in the formation of a polymerized monolayer. The polymerized monolayer was easily transferred onto a Si-wafer by an LB method and the residual hydroxyl groups could be covalently bonded with silanol groups on the silicon wafer surface [7–10]. In the case of the water-cast method, the organosilane monolayer was also immobilized onto a Si-wafer through the evaporation process of water [22, 23].

Fig. 3 shows the surface pressure ( $\pi$ )-area per molecule ( $A$ ) ( $\pi$ - $A$ ) isotherms for the OTS, DDTS, FDOPTES, and FOETS monolayers on the water surface at a subphase temperature of 293 K, as well as electron diffraction (ED) patterns of the monolayers transferred onto the hydrophilic SiO<sub>2</sub> substrate on the EM grid at the surface pressure of around 20 mN m<sup>-1</sup>. The  $\pi$ - $A$  isotherms of the OTS and the FDOPTES monolayers showed a steep increase in surface pressure with a decrease in the surface area. The molecular occupied areas were determined to be 0.24 and 0.29 nm<sup>2</sup> per molecule for the OTS and the FDOPTES

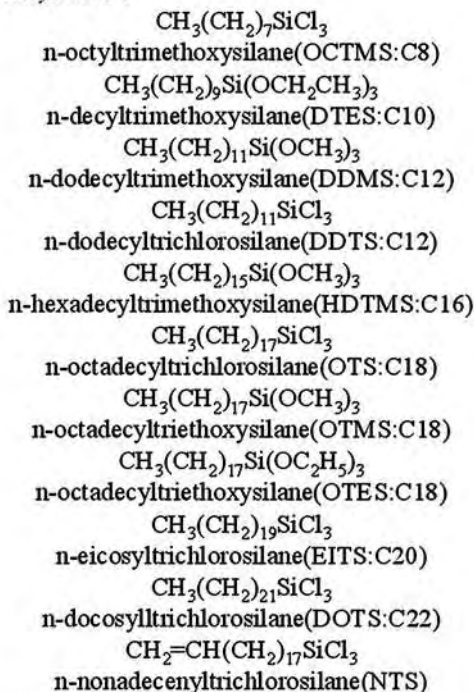
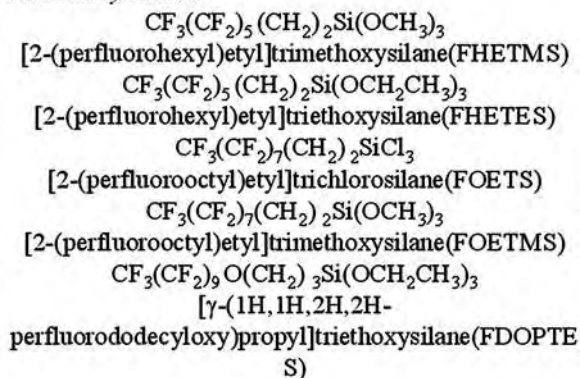
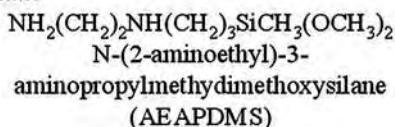
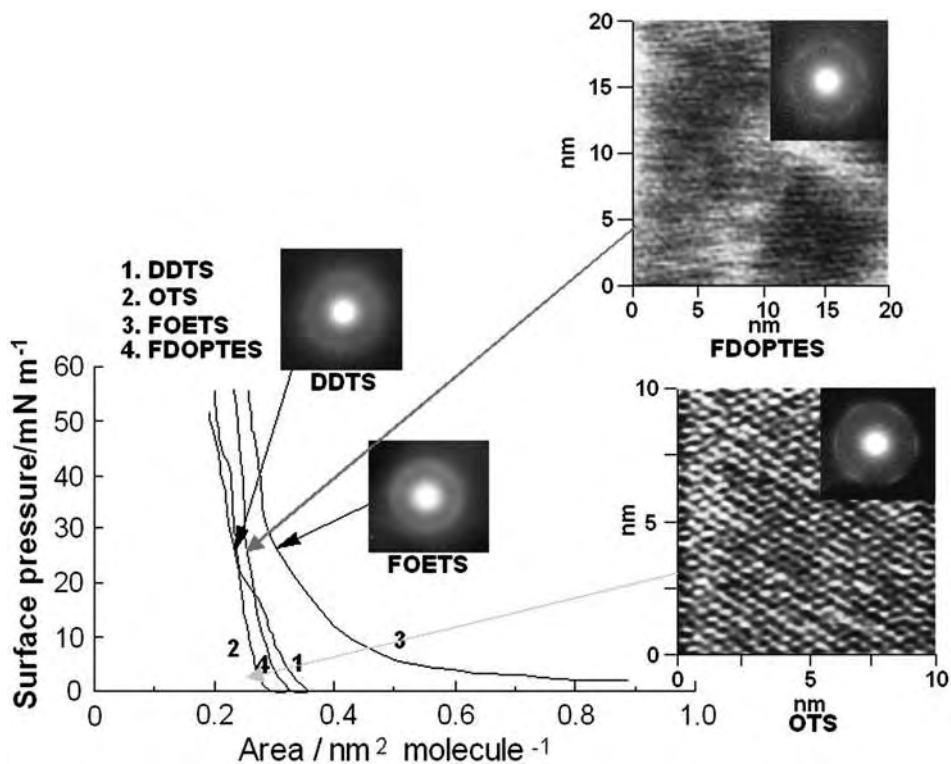
*Alkylsilanes**Fluoroalkylsilanes**Aminosilane*

Fig. 2. Chemical structures of organosilanes.



**Fig. 3.** The  $\pi$ -A isotherms for the OTS, DDTS, FDOPTES, and FOETS monolayers on the water surface at a subphase temperature of 293 K, as well as the AFM images and ED patterns of the monolayers transferred onto the substrate at the surface pressure of around 20 mN m<sup>-1</sup>.

monolayers, respectively. Both ED patterns of the OTS and the FDOPTES monolayers showed hexagonal crystalline arcs at 293 K. The (10) spacings of the OTS and the FDOPTES monolayers were calculated to be ca. 0.42 and 0.50 nm based on ED patterns, respectively [17]. Therefore, the ED results make it clear that the hydrophobic alkyl and fluoroalkyl chains in the crystalline OTS and FDOPTES monolayers were closely packed in the hexagonal crystal lattice at 293 K. High-resolution AFM was applied to observe the molecular arrangement for the crystalline OTS monolayer as well as the crystalline FDOPTES one. Fig. 3 also displays AFM images on molecular scale for the crystalline OTS and the FDOPTES monolayers transferred onto the silicon wafer at the surface pressure of 15 mN m<sup>-1</sup> at 293 K [18]. The (10) spacing was evaluated to be ca. 0.42 and 0.50 nm on the basis of the two-dimensional fast Fourier transform (2D-FFT) [11]. These values are in good agreement with the (10) spacings determined from the ED patterns for the crystalline OTS and the FDOPTES monolayers. Thus, it is conceivable that the higher portions (the brighter dots)

in the AFM images of Fig. 3 correspond to the individual methyl group of the OTS molecule and the fluoromethyl group of the FDOPTES one in the monolayers, respectively. On the contrary, the  $\pi$ - $A$  isotherms for the DDTs and the FOETS monolayers with shorter alkyl chain showed a gradual increase in surface pressure with the decreasing surface area. In general, this can be the signature that the monolayer is in the liquid-condensed or the liquid-expanded state. In addition, the ED patterns of the DDTs and the FOETS monolayers showed amorphous halo at 293 K. Hence, it can be envisaged that the chain length of hydrophobic groups of the DDTs and the FOETS molecules were not long enough to crystallize on the water subphase at 293 K.

## 2.2. Phase Separation of Mixed Monolayers at Air/Water Interface

Binary components monolayer of crystalline OTS and amorphous FOETS is expected to form phase separation because of the incompatibility of OTS and FOETS [9]. Fig. 4 shows the surface pressure–area isotherm and AFM image of the scanned area  $10 \times 10 \mu\text{m}^2$  for the OTS/FOETS (50/50, mol/mol) mixed monolayer, which was transferred onto the silicon wafer substrate by the LB method at the surface pressure of  $25 \text{ mN m}^{-1}$ . The height profile along the line shown in AFM image revealed that the brighter and the darker portions in AFM image correspond to the higher and the lower regions of the monolayer surface, respectively. The molecular occupied area (the limiting area) of  $0.28 \text{ nm}^2$  per molecule for the OTS/FOETS (50/50) mixed monolayer is almost equal to the average of the molecular occupied area for the OTS ( $0.24 \text{ nm}^2$  per molecule) and the FOETS ( $0.31 \text{ nm}^2$  per molecule) monolayer in consideration of the molar fraction of OTS and FOETS. The OTS/FOETS mixed monolayer can be transferred onto the silicon wafer substrate over a wide surface pressure range. The transfer ratio of the OTS/FOETS mixed monolayer was ca. 1.0 at the surface pressure of  $25 \text{ mN m}^{-1}$ . This indicates that the substrate surface is almost completely covered with the immobilized mixed monolayer. Also, the transfer of the OTS/FOETS mixed monolayer on the silicon substrate was confirmed by using an attenuated total reflection Fourier transform infrared (ATR-FT-IR) spectroscopy and an X-ray photoelectron spectroscopy (XPS). Since the area occupied by the circular flat-topped domains increases with an increase in the OTS content, it is expected that the circular domains correspond to the OTS domain. AFM line profile revealed that the circular domains were 1.1–1.3 nm higher than the surrounding area. Since the difference in molecular lengths between OTS and FOETS is ca. 1.3 nm, it can be concluded that the higher, circular domains and the surrounding flat matrix regions were composed of OTS and FOETS molecules, respectively. OTS molecules formed circular domains even if the molar percent of OTS molecules was 75%. It is apparent from the ED pattern of the OTS/FOETS (75/25) mixed monolayer that the OTS domain is in a crystalline state, since ED pattern showed Debye ring and the magnitude of spacing corresponds to the (10) spacing of the OTS monolayer. In

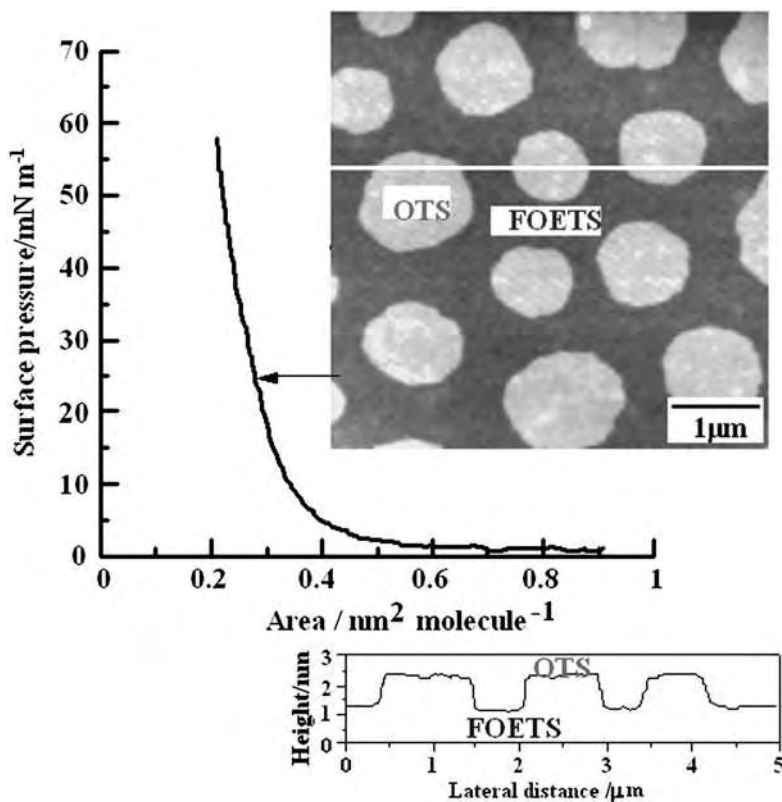


**Fig. 4.** The  $\pi$ - $A$  isotherm and AFM image of the scanned area  $10 \times 10 \mu\text{m}^2$  for the OTS/FOETS (50/50) mixed monolayer, which was transferred onto the silicon wafer substrate by the LB method at the surface pressure of  $25 \text{ mN m}^{-1}$ .

the case of the mixture of fluoroalkane and alkane, the macroscopic phase separation is observed. However, in the case of organosilanes at the air/water interface, the macroscopic phase separation such as coalescence of crystalline domain is inhibited due to the limited diffusion at the air/water interface.

Similar phase separated structure was also expected for mixed monolayer of the crystalline NTS and amorphous FOETS. Crystallization of NTS phase was confirmed by ED [16]. Fig. 5 shows the AFM images of the mixed NTS/FOETS and carboxylated NTS(NTS<sub>COOH</sub>)/FOETS monolayers. It was clarified that the NTS/FOETS mixed monolayers were in a phase-separated state, and circular flat-topped domains with ca. 1–2 μm in diameter were surrounded by a sea-like flat region. The phase separation in the mixed NTS/FOETS is also arisen from the crystallization of the NTS component. The NTS<sub>COOH</sub>/FOETS mixed monolayer was prepared through an oxidation of vinyl end-group of the NTS molecule in the NTS/FOETS mixed monolayer [17]. The NTS<sub>COOH</sub> monolayer showed high surface free energy, where the magnitude was comparable to that

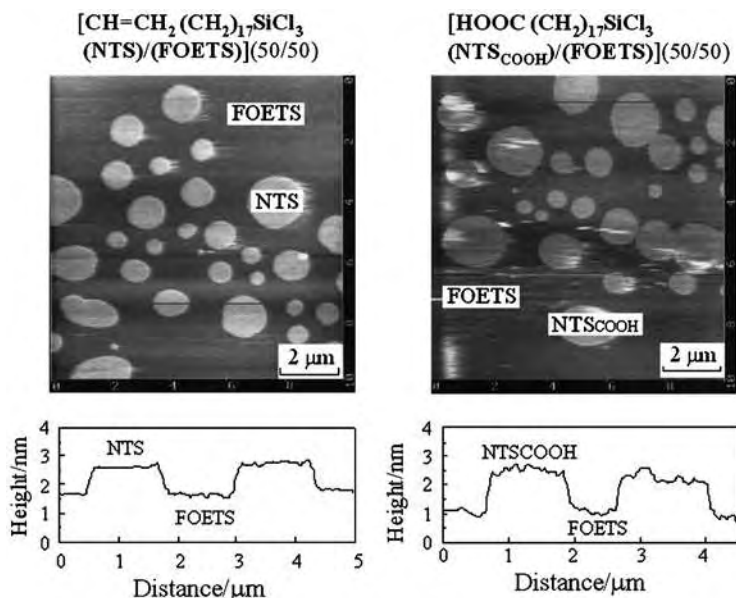


**Fig. 5.** The AFM images of the mixed NTS/FOETS and carboxylated NTS( $\text{NTS}_{\text{COOH}}$ )/FOETS monolayers.

of water. The surface morphology of the NTS/FOETS mixed monolayer was not changed even after oxidation, because of the presence of strong interaction between silanol groups of NTS and silicon wafer. The height difference between the  $\text{NTS}_{\text{COOH}}$  domain and FOETS matrix phase in the  $\text{NTS}_{\text{COOH}}$ /FOETS mixed monolayer was almost the same as that for the NTS/FOETS mixed monolayer. Also, XPS measurement was performed for the NTS/FOETS and the  $\text{NTS}_{\text{COOH}}$ /FOETS mixed monolayers to confirm the oxidation of the NTS phase. Since the ratio of oxygen/carbon atoms for the  $\text{NTS}_{\text{COOH}}$ /FOETS mixed monolayer was larger than that for the NTS/FOETS one, it was suggested that the vinyl end-groups of the NTS molecules were oxidized to carboxyl groups. The magnitude of lateral force of the  $\text{NTS}_{\text{COOH}}$  phase was higher than that of the FOETS phase in the case of the  $\text{NTS}_{\text{COOH}}$ /FOETS mixed monolayer in contrast to the case of the NTS/FOETS mixed monolayer. As the  $\text{NTS}_{\text{COOH}}$  phase had hydrophilic carboxyl end-groups at the surface, presumably these end-groups can form intermolecular hydrogen bonds with neighboring  $\text{NTS}_{\text{COOH}}$  molecules. Therefore, the surface of the outermost  $\text{NTS}_{\text{COOH}}$  phase is expected to show higher shear strength than the case of the NTS one due to difficulty in surface deformation. Also, there is a significant contribution of adhesion force between the sample surface and  $\text{Si}_3\text{N}_4$  tip on lateral force. Since the surface free energy of  $\text{NTS}_{\text{COOH}}$  phase is comparable to that of the water, the water capillary force interacting between  $\text{NTS}_{\text{COOH}}$  monolayer surface and hydrophilic  $\text{Si}_3\text{N}_4$  tip could strongly contribute to the adhesion force of the

NTS<sub>COOH</sub> phase. Therefore, it is conceivable that the NTS<sub>COOH</sub> phase exhibited higher lateral force than the FOETS one due to the formation of intermolecular hydrogen bonding and thicker absorbed water layer as discussed above. LFM and XPS measurements revealed that the phase-separated monolayer with a large surface energy gap was successfully prepared. The state of phase separation was also investigated for the mixed monolayer with crystalline alkylsilane (OTS) and amorphous alkylsilane (DDTS). Even though the alkyl chain is compatible, the phase separation similar to OTS/FOETS was clearly observed by AFM and LFM. These results suggest that the phase separation of mixed monolayer is governed by crystallization kinetics [16].

### 2.3. Fabrication of Multi-Phase Organosilane Monolayers through Chemisorption and Photolithography Process

Since the phase separation mentioned above is controlled by crystallization kinetics, more sophisticated method for the fabrication of multiphase monolayer was proposed [27–36]. A structural surface that exhibits patterns of varying wettability can be produced by chemisorption and local photodecomposition of organosilanes. Using such patterns as templates for three-dimensional structures with various topographic and surface properties appears very promising. Site-specific adsorption of microparticles can be achieved by specific interaction between microparticles and a monolayer surface. The immobilization of a polymerization initiator on a functional monolayer enables site-specific polymerization, which can result in a large topography change. Fig. 6 summarizes the

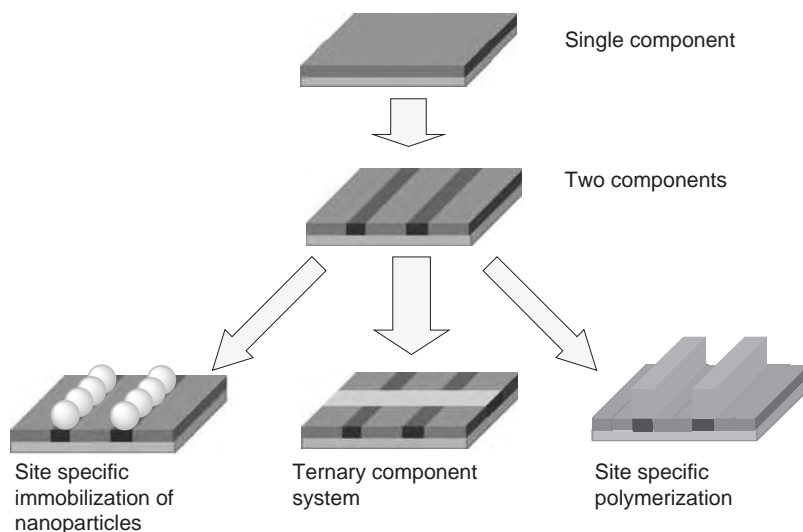


**Fig. 6.** The schematic representation of surface patterning, site-specific polymerization, and site-specific immobilization of microparticles.

scheme of fabrication of micropatterned organosilane monolayers, site-specific polymerization, and immobilization of microparticles on patterned organosilane monolayers. Micropatterning method will be described in this section. Other applications such as immobilization of nanoparticles and site-specific polymerization will be discussed in Section 4.

Fig. 7 outlines the essential steps for fabrication of micropatterned organosilane monolayers. The first step was the preparation of organosilane-grafted Si-wafer substrates. The CVA method was used to fabricate the monolayers from organotrialkoxysilane. A uniform monolayer formation was confirmed by AFM observation. Removal of the monolayer in selected areas by photodecomposition was the next step in the process. In photolithography, irradiation with VUV light ( $\lambda = 172$  nm) leads to excitation cleavage of covalent bonds, such as C–C, C–H, and Si–C bonds, and formation of surface Si–OH residues [26]. Fig. 8 shows the variation of water contact angle on OTES and FHETES monolayers with the irradiation time of VUV light generated from an excimer lamp ( $\lambda = 172$  nm). VUV irradiation was carried out under 0.8 mmHg of pressure. Initially, OTES

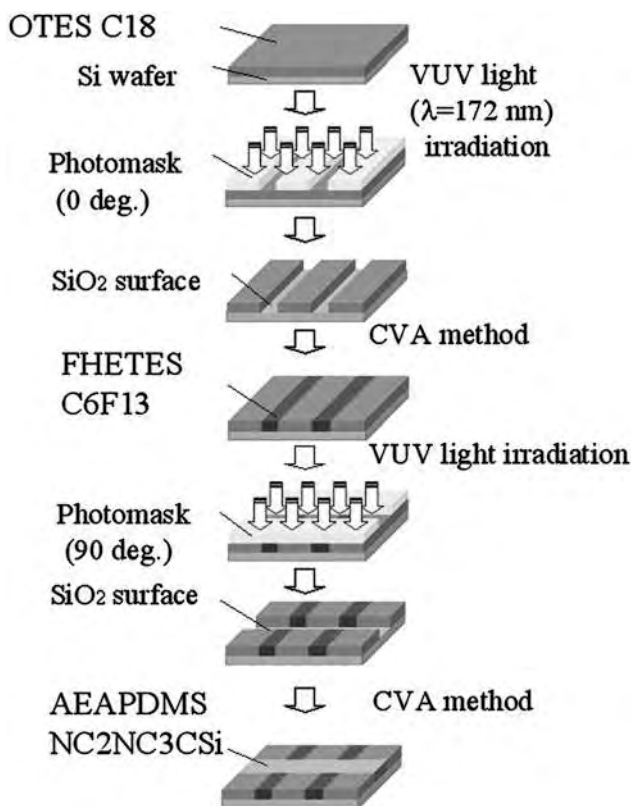


**Fig. 7.** The schematic representation of site-specific photodecomposition by irradiation with VUV light and chemisorption.

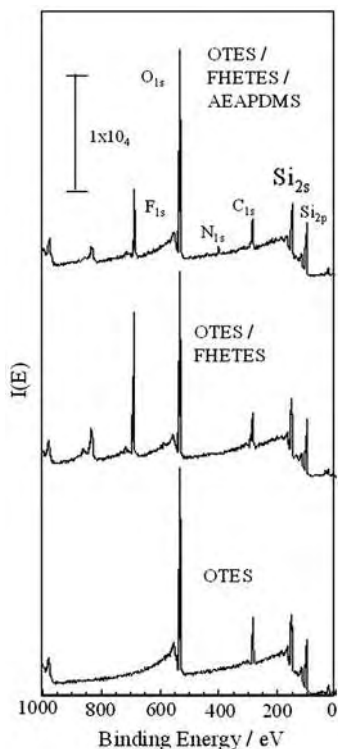


**Fig. 8.** The XPS survey scan spectra of the changes in the surface chemical compositions through the micropatterning process.

and FHETES monolayers gave water contact angles larger than  $100^\circ$ . However, within 15 min, the angles approached  $0^\circ$ , which indicates that almost complete removal of a monolayer can be achieved with 15-min irradiation of VUV light [33]. The monolayer removal was also confirmed by XPS measurement. Using a photomask, one can prepare a pattern with the desired shape and precisely controlled arrangement of surface functional groups. As an example, the preparation and characterization of OTES/FHETES/AEAPDMS patterned surface is discussed in this section. The OTES-grafted Si-wafer was irradiated for 15 min with VUV light. Then, the second organosilane monolayer, FHETES (molecular length is ca. 1.0 nm), was then introduced into the first patterned surfaces by a similar method with alkylsilane. The formation of a ternary component monolayer requires another photodecomposition and chemisorption process, with the photomask rotated  $90^\circ$  from its position in the first patterning step. The OTES/FHETES sample was then irradiated with VUV, resulting in cross-line micropatterns on the substrate surfaces. The third organosilane monolayer, AEAPDMS (molecular length is ca. 0.9 nm), was finally introduced into the second-patterned substrate surfaces, again by the CVA method.

The XPS and the contact angle measurements have been employed in order to characterize the changes in the surface chemical compositions of the micro-patterned organosilane monolayers [31, 32]. Fig. 8 shows the XPS survey scan spectra of the changes in the surface chemical compositions through the micro-patterning process. The OTES monolayer showed  $C_{1s}$ ,  $O_{1s}$ ,  $Si_{2s}$ , and  $Si_{2p}$  peaks at 285, 533, 151, and 100 eV, respectively. The OTES/FHETES patterned Si substrate clearly showed an additional  $F_{1s}$  peak at 690 eV, while the OTES/FHETES/AEAPDMS-grafted Si substrates showed another  $N_{1s}$  peak at 400 eV. The decomposition of the FHETES monolayer was revealed from the decreased intensity of the  $F_{1s}$  peak. The grafting of organosilane monolayers was also confirmed from  $C_{1s}$  and  $N_{1s}$  XPS narrow scan spectra. These results indicated that the three kinds of organosilane molecules were subsequently grafted on the substrate surfaces.

The local photodecomposition of the organosilane monolayer was also confirmed by time-of-flight secondary ion mass spectroscopy (ToF-SIMS) [33]. The (2-perfluorohexyl)ethyltrimethoxysilane (FHETMS) monolayer was irradiated with VUV light through a photomask, and the secondary ion image was measured. A Physical Electronics TRIFT-II ToF SIMS instrument was used to make the SIMS imaging. Negative ion images were obtained with a 15 kV primary pulsed  $Ga^+$  ion beam (pulse width of 13 ns) with a 2 nA beam current. The scan area was  $100 \mu m \times 100 \mu m$ . Fig. 9 shows  $F^-$  ( $m/z = 18.987-18.99$ ) and  $SiO^-$  ( $59.84-59.88$ ) in a secondary ion image FHETMS monolayer irradiated with VUV light under a photomask.  $F^-$  originated from the fluorine group of the fluoroalkyl chain, and  $SiO^-$  originated from the native oxide layer of the Si-wafer substrate corresponding to the photodecomposed area. In spite of the large diameter (ca. 300 nm) of the  $Ga^+$  ion beam, a line pattern was clearly observed. Since  $F^-$  was not observed from the region where  $SiO^-$  showed strong intensity, the removal of the monolayer by irradiation with VUV light was confirmed.

Fabrication of a micropattern with three kinds of surface functional groups was confirmed by SFM observation. Fig. 10 shows (a) AFM and (b) LFM

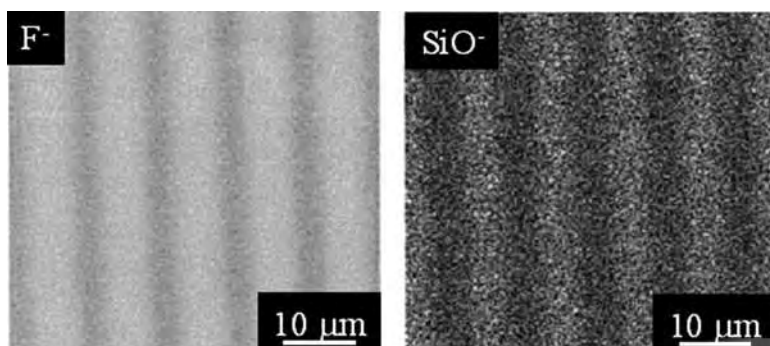


**Fig. 9.** ToF-SIMS  $F^-$  ( $m/z = 18.987-18.99$ ) and  $SiO^-$  ( $m/z = 59.84-59.88$ ) in a secondary ion image FHETMS monolayer.

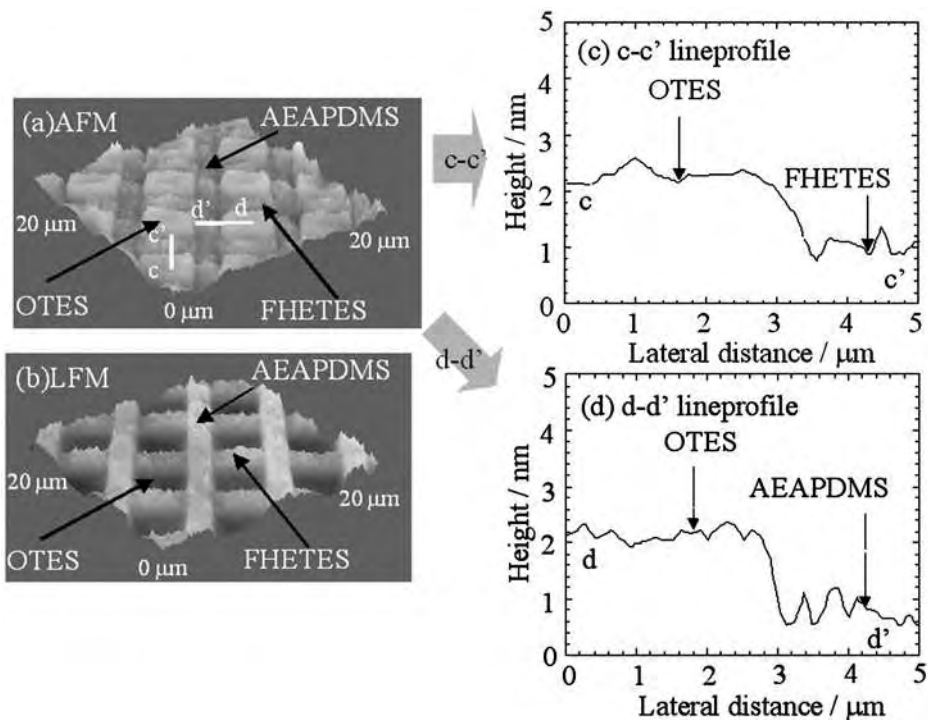


**Fig. 10.** AFM and LFM images of three-component micropatterned organosilane monolayers. (a) The AFM and LFM images of an OTES/FHETES/AEAPDMS micropatterned surface; (c) and (d) the line profiles of white line parts in (a).

images of a (OTES/FHETES/AEAPDMS) three-component micropatterned organosilane monolayer, respectively. Fig. 10(c) and (d) show the line profiles of the white lines in Fig. 10(a). These figures show cross-line microstructures fabricated on Si-wafer substrates. The widths of the fabricated FHETES and AEAPDMS lines were consistent with the widths of slits in the photomask. In the line profile of the AFM image as shown in Fig. 10(c), the height difference between the OTES and FHETES surfaces was ca. 1.4 nm. The height difference corresponds to the difference in the molecular length (ca. 1.3 nm) between OTES and FHETES. On the other hand, the height difference between the OTES and AEAPDMS surfaces was ca. 1.5 nm (Fig. 10(d)), corresponding to the difference in the molecular length (ca. 1.4 nm) between OTES and AEAPDMS. The origin of the contrast in the LFM image is explained by the difference in surface properties of three components, i.e., the chain rigidity, crystallinity, and chemistry of terminal functional groups of the organosilane molecules [31]. AEAPDMS-grafted areas are the brightest of the three components, because the terminal amino groups exerted high lateral force due to the strong interaction between the hydrophilic amino group and the Si-OH group of the cantilever tip

**Table 1**

Surface free energy of micropatterned organosilane monolayers

Organosilanes	$\gamma_{sv}$ (mJ m <sup>-2</sup> )	$\gamma_s^d$ (mJ m <sup>-2</sup> )	$\gamma_s^h$ (mJ m <sup>-2</sup> )
AEAPDMS	48.5	34.3	14.2
OTES	20.1	18.1	2.0
FHETES	14.7	13.1	1.6
OTES/FHETES	17.1	15.5	1.6
OTES/FHETES/AEAPDMS	23.8	19.7	4.1

[31]. The area ratio of the prepared micropatterned monolayer is in accord with that of the target value, i.e., the estimated area ratio of OTES/FHETES/AEAPDMS was 4/2/3.

The introduction of different organosilane component was also confirmed by the measurement of surface free energy. Table 1 shows the surface free energies of uniform or micropatterned organosilane monolayers. The surface free energy was calculated from the contact angles of water and methylene iodide based on Owens and Wendt's method [37]. In Table 1,  $\gamma_s^d$  and  $\gamma_s^p$  denote the dispersion and polar components of surface free energy, respectively. The surface free energy of the OTES/FHETES micropatterned surface is smaller than that of the OTES monolayer surface; the decrease can be attributed to the fluoroalkyl groups of FHETES, which are known to decrease surface free energy. On the other hand, the surface free energy, especially the hydrogen-bonding component  $\gamma_s^h$ , extensively increased after the grafting of AEAPDMS; this increase was attributed to the relatively high polarity of amino groups introduced in the grafted AEAPDMS monolayers [31]. Taken together with the SFM observation, this stepwise change of surface free energy confirmed that the three-component organosilane surfaces had been micropatterned with highly hydrophobic, hydrophobic, and hydrophilic areas. Our patterning of three-component organosilane monolayers is expected to be a useful template for immobilizing various organic or inorganic materials on Si surfaces.

A laterally structured surface with different wetting properties may be produced by various techniques such as microcontact printing [38], micromachining [39], photolithography [40], and vapor deposition [41]. If one phase of a micropatterned surface has an affinity towards a certain liquid, the surface can be utilized as a template for local liquid condensation. A line-patterned high-wettability contrast surface was prepared via the local photodecomposition of an FHETMS monolayer. Fig. 11(a) shows FE-SEM image of FHETMS/Si-OH patterned monolayer. Bright part corresponded to the bare Si-OH, which was formed after VUV decomposition. The advantage of this method for anisotropic wetting study is that the height difference of the two phases is less than 2 nm and topographic effect on wettability can be ignored. The water droplet formation on the micropatterned surface was directly observed with an environmental scanning electron microscope (ESEM) [33]. At first, the ESEM

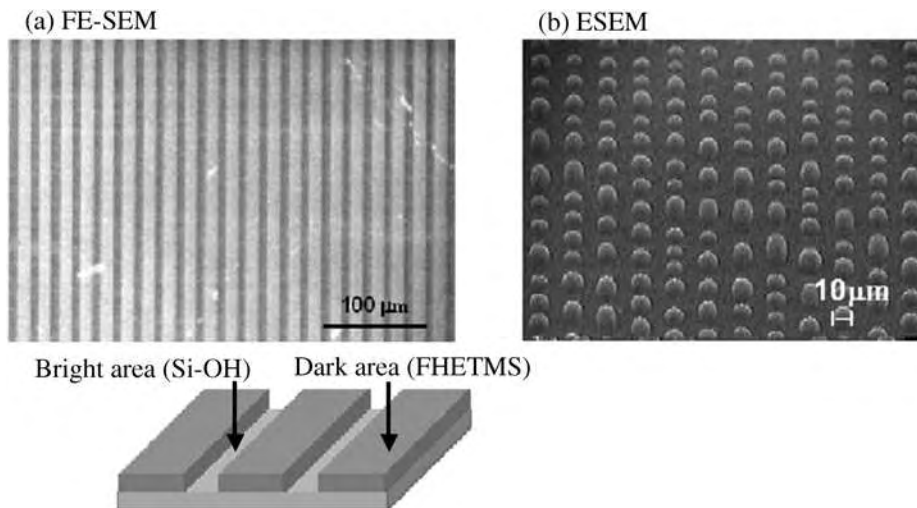


**Fig. 11.** (a) FE-SEM image of FHetMS/Si-OH patterned monolayer and (b) ESEM image of a water droplet on an FHetMS/Si-OH patterned monolayer after exposure in water vapor at 273 K.

sample chamber was evacuated below the saturated vapor pressure (612 Pa) of water at 273 K. Then, the sample surface was cooled to 273 K and the vapor pressure of the ESEM sample chamber was increased to 700 Pa. Fig. 11(b) shows the ESEM image of the water droplet on the surface of the FHetMS/Si-OH patterned monolayer during the initial condensation process. The water started to condense on the Si-OH part of the patterned surface. The size of the water droplet and the number of water droplets increased until the droplets coalesced in a line. Since water has large surface free energy compared with the FHetMS phase, the water is more likely to condensate on the higher surface free energy region. After the vapor pressure of the ESEM sample chamber was raised to 1050 Pa, the water droplet started to bridge with droplets on the adjacent line. Since the micropatterning surface can confine liquid in distinct micropatterned regions, the surface can be used for the local growth of a solution of functional molecules [42] or as a substrate for inkjet printing with functional molecules [36, 43].

### 3. DEPENDENCE OF THE MOLECULAR AGGREGATION STATE OF ORGANOSILANE MONOLAYERS ON PREPARATION METHODS

The surface morphology of organosilane monolayer is strongly dependent on their fabrication processes [34]. The surface morphology and thickness of the organosilane monolayers were evaluated by AFM measurement. Fig. 12 shows

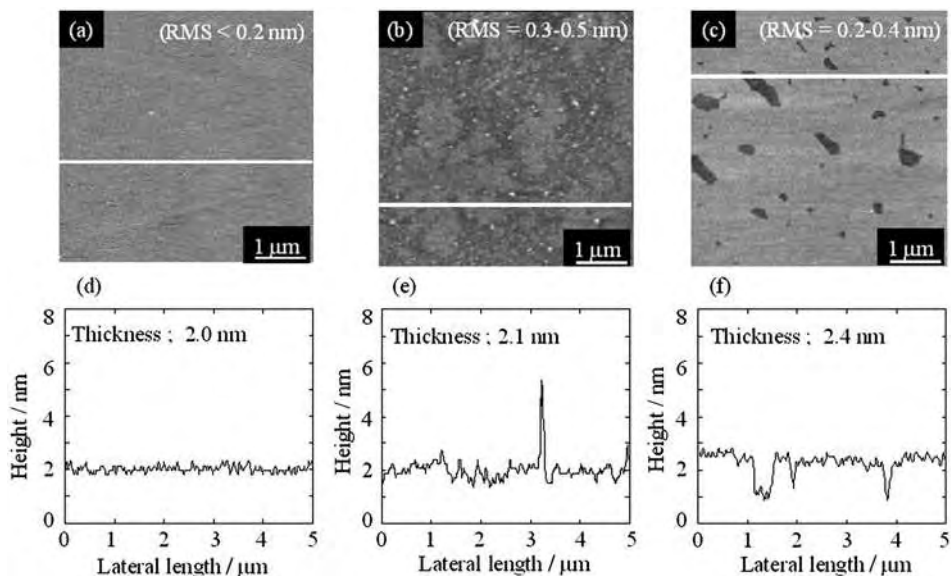


**Fig. 12.** The AFM images of (a) the OTMS-CVA monolayer surface, (b) the OTS-S monolayer surface, (c) the OTS-W monolayer surface, and the line profiles of the white line part in the AFM images ((d) OTMS-CVA, (e) OTS-S, and (f) OTS-W).

the AFM images of (a) the OTMS monolayer surface prepared by the CVA method (OTMS-CVA), (b) the OTS monolayer surface prepared by chemisorption method from solution phase (OTS-S), (c) OTS monolayer surface prepared by water-cast method (OTS-W), and line profiles of the white line part in the AFM images ((d) OTMS-CVA, (e) OTS-S, and (f) OTS-W). The AFM images revealed that the OTMS monolayer possessed highly uniform surfaces ( $\text{RMS} < 0.2 \text{ nm}$ ), and that there were no domains and defects on the OTMS monolayer. On the other hand, some crystalline domains of OTS molecules and defects were observed on the OTS-S and OTS-W monolayer surfaces (OTS-S,  $\text{RMS} = 0.3\text{--}0.5 \text{ nm}$ ; OTS-W,  $\text{RMS} = 0.2\text{--}0.4 \text{ nm}$ ). The thicknesses of the monolayers estimated by the AFM observation of the micropatterned samples were ca. 2.0, 2.1, and 2.3 nm for OTMS, OTS-S, and OTS-W, respectively.

The molecular aggregation state of the organosilane monolayers also depends on the difference of fabrication process [23, 34]. Fig. 13 shows the grazing incident X-ray diffraction (GIXD) profiles of the organosilane monolayers: (a) the OTMS-CVA, (b) the OTS-S, and (c) the OTS-W. In Fig. 13(a), no crystalline diffraction peak was observed, indicating that the octadecyl groups in the OTMS monolayer were immobilized on the Si-wafer substrate in a disordered state. On the other hand, crystalline diffraction peaks were observed at  $q_{xy,\text{max}} = 14.9\text{--}15.2 \text{ nm}^{-1}$  in Figs. 13(b) and 14(c). In our previous reports [21], ED of the OTS monolayer prepared by the LB method gave a (10) diffraction of the hexagonal crystalline lattice with a 0.42 nm spacing. Furthermore, the (10)

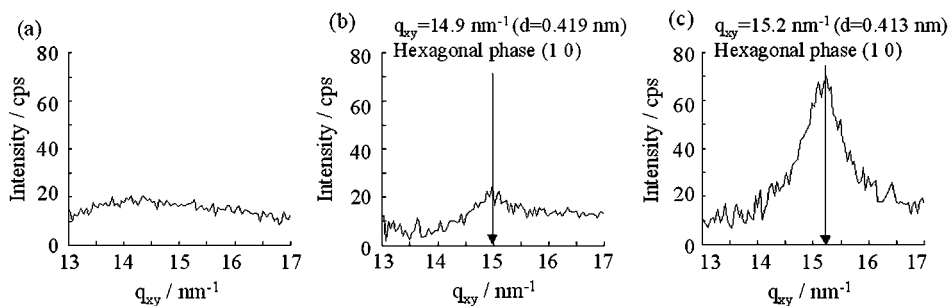


**Fig. 13.** Synchrotron GIXD profiles of the organosilane monolayers: (a) OTMS-CVA, (b) OTS-S, and (c) OTS-W.

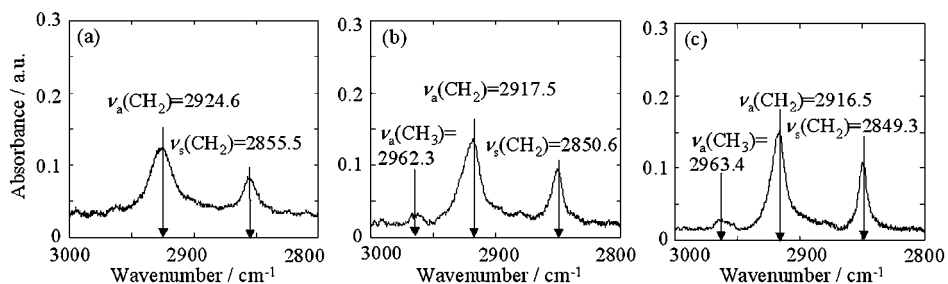


**Fig. 14.** The FT-IR spectra for the organosilane monolayers: (a) OTMS-CVA, (b) OTS-S, and (c) OTS-W.

spacing of the OTS-W monolayer was smaller than that of OTS-S monolayer. These results apparently indicate that the OTS molecules in the monolayer prepared by the water-cast method are tightly packed in comparison with those prepared by the chemisorption method.

The conformation of octadecyl groups in the organosilane monolayers was investigated using FT-IR spectroscopy [34]. Fig. 14 illustrates the FT-IR spectra for the organosilane monolayers: (a) the OTMS-CVA monolayer, (b) the OTS-S monolayer, and (c) the OTS-W monolayer. The peaks observed at 2916.5–2924.6, 2849.3–2855.5, and 2962.3–2963.4  $\text{cm}^{-1}$  were, respectively, assigned to antisymmetric [ $\nu_a(\text{CH}_2)$ ], symmetric [ $\nu_s(\text{CH}_2)$ ], and antisymmetric [ $\nu_a(\text{CH}_3)$ ] bands for the alkylene chains and terminal methyl groups of OTS and OTMS molecules [15, 21]. It has been reported that the peak positions of the  $\nu_a(\text{CH}_2)$  and  $\nu_s(\text{CH}_2)$  bands of the octadecyl groups in the hexagonal crystalline lattice are observed at 2915–2918 and 2846–2850  $\text{cm}^{-1}$ . They are also observed at greater than 2921 and 2852  $\text{cm}^{-1}$  in the case of the amorphous alkylsilane monolayer, which has molecular chains with *gauche*-rich conformation [9]. This suggested that the *gauche*-rich conformation of octadecyl assembles in the OTMS-CVA monolayer. On the other hand, Fig. 14(b) and (c) revealed that the OTS

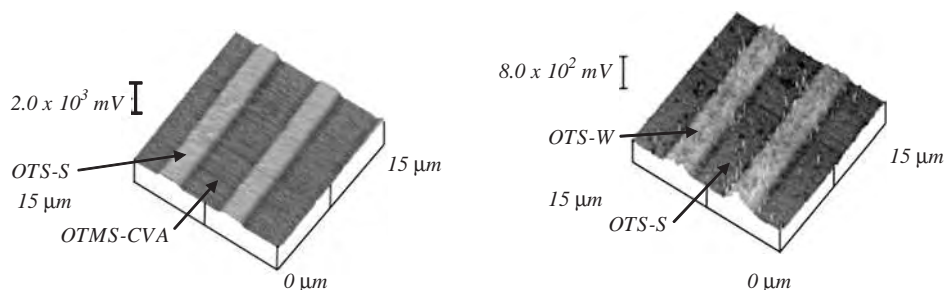


**Fig. 15.** The LFM images of (a) OTMS-CVA/OTS-S and (b) OTS-S/OTS-W micropatterned monolayer surfaces in air at room temperature.

monolayers prepared by the chemisorption and the water-cast methods were in a hexagonal crystalline state.

The relationship between the molecular aggregation state and the molecular motion of the organosilane monolayers was investigated using LFM measurements [34]. Fig. 15 illustrates the LFM images of (a) the OTMS-CVA/OTS-S and (b) the OTS-S/OTS-W micropatterned monolayer surfaces in the air at room temperature. The LFM results indicate that the magnitude of the lateral force corresponds to the packing density of the organosilane molecules. In one of our previous studies, we revealed that the lateral force of the crystalline alkylsilane domain in the crystalline/amorphous mixed alkylsilane monolayer was larger than that of the amorphous alkylsilane matrix [15]. Since the alkylsilane monolayer was in an amorphous state at room temperature, its molecular motion was activated in comparison with crystalline monolayers. This means that a smaller sheer force can cause molecular bending and/or a conformational change of alkyl chains in the amorphous monolayer. Thus, it is considered that the lateral force of the OTMS-CVA monolayer with an amorphous state showed the smallest value.

## 4. APPLICATIONS OF ORGANOSILANE MONOLAYERS

### 4.1. Site-Specific Polymerization of Methacrylate Monomers

The patterned organosilane monolayers introducing organosilane molecule with a polymerization initiating unit are useful as template surfaces for site-specific polymerization. Atom transfer radical polymerization (ATRP) unit was immobilized as a monolayer component. Since ATRP is one of the most successful methods for polymerizing a variety of monomers in a controlled fashion [44, 45], tailor-made surface topography is possible. Several reports have described the formation of polymer thin film by the radical polymerization from the immobilized ATRP initiator [46, 47].

Fig. 16 shows a schematic representation of a site-specific ATRP from a micropatterned monolayer surface [47]. Prior to introducing the initiator for

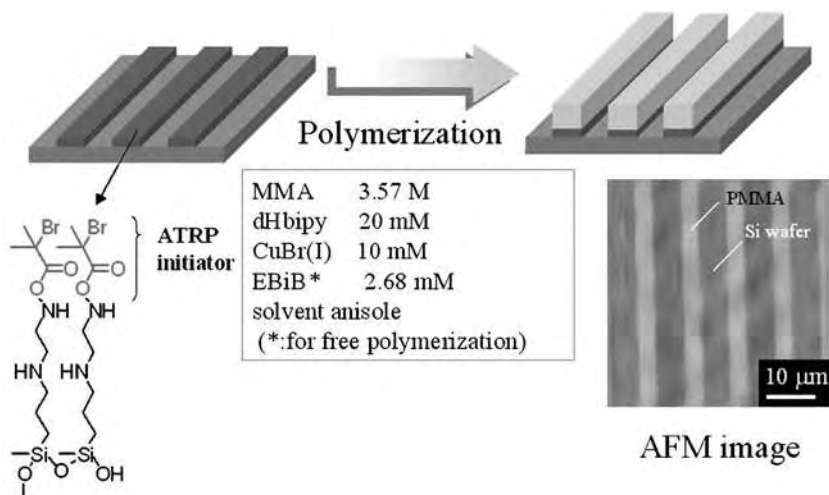


**Fig. 16.** The schematic representation of the site-specific ATRP from a micropatterned monolayer surface and AFM image of line-patterned PMMA ultrathin film.

ATRP into the organosilane monolayer system, an AEAPDMS monolayer was prepared on a Si-wafer substrate surface. The prepared surface terminated by amino groups was treated with 2-bromoisobutyric acid in the presence of a condensation agent. After the modification, the water contact angle of the obtained surface increased from  $63^\circ$  to  $69^\circ$  due to the change of the surface functional groups. The introduction of the initiating unit was further confirmed by XPS measurement, in which the peaks attributed to Br and carbonyl carbon were observed at 68 and 287.9 eV, respectively. The resulting surface was irradiated by VUV light through a photomask. The LFM image of the patterned surface shows the presence of a pattern corresponding to the line width of the photomask used.

Surface-initiated radical polymerization of methyl methacrylate (MMA) was carried out in the presence of CuBr(I) and 4,4'-di-*n*-heptyl-2,2'-bipyridine in anisole. In order to control the polymerization process, the corresponding initiator, ethyl 2-bromoisobutyrate, was also added for bulk polymerization. The mixture was degassed, and argon was bubbled through the mixture for 20 min to ensure that oxygen was removed completely. The mixture was heated at 363 K. After several hours, the polymerization solution was cooled to room temperature to terminate the polymerization. The Si-wafer was immersed in THF and rinsed with toluene to remove the adsorbed free poly(methyl methacrylate) (PMMA). The PMMA micropattern was observed by AFM. Fig. 16 also shows the AFM image of the line-patterned PMMA ultrathin film. An AFM image revealed that the site-specific polymerization of methacrylate monomer occurred on the micropatterned surface of the ATRP initiator. The height and width of the PMMA layer is ca. 6–10 nm and ca. 5 μm, respectively.

The width estimated from the AFM image is in good agreement with the line width of surface initiator micropatterns. The formation of a PMMA layer was further confirmed by XPS measurement, in which the characteristic peaks attributed to aliphatic carbon, the ether carbon, and carbonyl carbon were observed at 285, 286.5, and 288.8 eV, respectively.

## 4.2. Site-Specific Immobilization of Charged Microparticles

Two-dimensional alignment of micro- and nanoparticles on a substrate surface might be a promising method for fabricating functional materials, since properties of micro- and nanoparticles can be tuned by controlling the size and surface chemistry. Various attempts have been made at the site-specific immobilization of micro- and nanoparticles [48–50]. In this study, the micropatterned organosilane monolayer with an aminosilane/fluoroalkylsilane line pattern was applied for a template surface for site-specific immobilization of negatively charged microparticles.

FHETMS and AEAPDMS were used as surface modifiers for a Si-wafer substrate. The AEAPDMS/FHETMS micropattern (line width, AEAPDMS/FHETMS = 2/4 ( $\mu\text{m}/\mu\text{m}$ )) was fabricated by a similar method as that used to yield the multi-component organosilane monolayer. The Si-wafer substrate with a micropatterned surface was then exposed to the  $0.1 \text{ g L}^{-1}$  aqueous dispersed solution of sulfonated polystyrene (PS) microparticles (diameter is ca. 200 nm, Polyscience Co. Ltd.) at pH ca. 6.0 for 30 min. As shown in Fig. 19, the site-specific immobilization of PS particles was successfully achieved on the micropatterned substrate surface. An AFM image shows that the layers consisting of adsorbed PS microparticles are ca. 200 nm high and ca.  $2 \mu\text{m}$  wide (Fig. 17). The height and width estimated from the AFM image is in good agreement with the diameter of PS microparticles and the line width of AEAPDMS micropatterns, respectively. This result suggested that the sulfonated PS particles were adsorbed on the surface as a monolayer. The site-specific adsorption of PS particles onto the AEAPDMS-grafted surfaces was ascribed to the electrostatic interaction between negatively charged sulfonic acid groups of PS particles and positively charged amino groups of AEAPDMS-grafted surfaces.

## 4.3. Tribological Control

Recently, ultrathin organic thin films attract attention as new film lubricant [51]. Organosilane monolayer, which is one of the ultrathin films, has been identified as promising boundary lubricants. This is because organosilane molecules interact strongly with substrates and they are robust against solvent and temperature increase. Friction and wear tests of monolayers were carried out with a conventional ball-on-disk type friction tester (SHINTO Scientific Co. Ltd.) in air and tetradecane at 298 K. A 5.0 mm radius ball made of stainless steel was slid on a disk. The friction coefficient was determined by the distortion of a

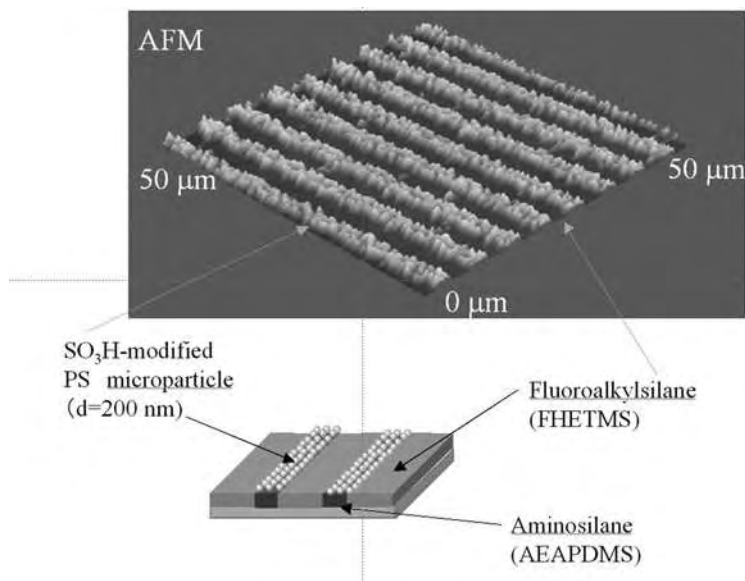
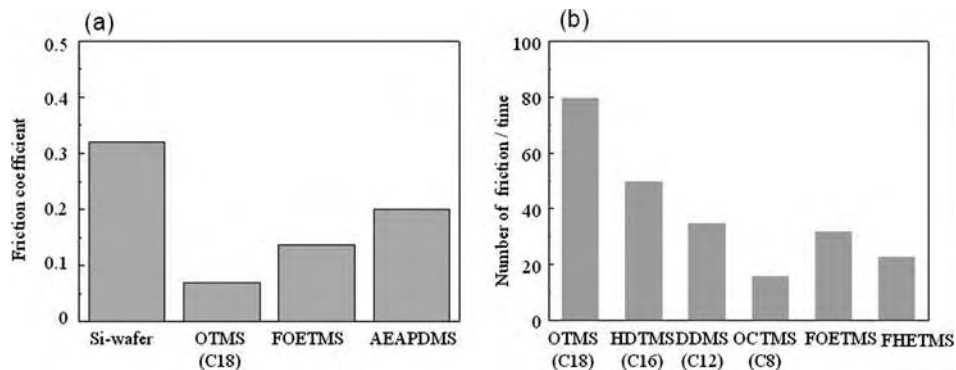


**Fig. 17.** The AFM image of the AEAPDMS/FHETMS monolayer after exposure to the aqueous dispersion of sulfonated PS microparticles.

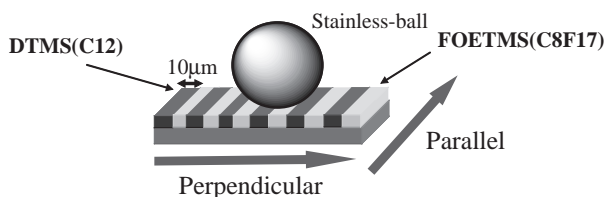
strain gauge attached to the arm of the tester and was recorded as a function of time. The friction test was performed under the conditions of normal load 20 g and scan rate  $80 \text{ mm min}^{-1}$  at room temperature in air.

Fig. 18(a) shows the dynamic friction coefficients of various organosilane monolayers prepared by CVA method investigated by friction tester. All organosilane monolayers showed lower friction coefficient than the unmodified Si-wafer surface. The friction coefficient had no distinct chain-length dependence among the alkylsilane and fluoroalkylsilane monolayers. Furthermore, alkylsilane monolayer with non-polar methyl group had the smallest friction coefficient and aminosilane monolayer with polar amino group exhibited the highest among all. This is because interaction between the stainless ball and monolayer with amino group was stronger than those with other monolayers. It is considered that the nature of the terminal functional group has a strong influence on friction coefficient.

The bar graph in Fig. 18(b) shows the wear resistance of the alkylsilane and fluoroalkylsilane monolayers in air [51]. The vertical axis exhibits sliding cycles when the friction coefficient exceeds 0.3 (Si-wafer substrate's friction coefficient). The organosilane monolayers with longer alkyl chains showed higher wear resistance than those with shorter chains. Since the intramolecular interaction among alkyl chains increased with a chain length, the organosilane monolayers with long alkyl chains showed strong wear resistance. The same experiment was performed in tetradecane as a lubricant. Compared with the friction tests in air, the friction coefficient was slightly lower in the tetradecane lubricant, and the



**Fig. 18.** (a) Friction coefficient and (b) wear resistance of organosilane monolayers prepared by CVA method.



**Fig. 19.** Frictional direction of two-component micropatterned organosilane monolayer.

frictional wear was much less than that in air. From these results, it can be concluded that organosilane monolayers can exhibit excellent tribological performance.

In order to obtain further insight into the tribological properties of organosilane monolayers, the authors prepared two-component, microscopically line-patterned organosilane monolayer of DTMS and FOETMS by a photolithographic process [51]. The difference in height between the DTMS and FOETMS monolayers was less than 1 nm. The friction coefficients of DTMS and FOETMS monolayers were 0.09 and 0.15, respectively. The spherical stainless steel probe was slid either parallel with or perpendicular to the direction of the line pattern of the two-component monolayer, as shown in Fig. 19. The normal load and scan rate were 20 g and  $80 \text{ mm s}^{-1}$ , respectively. The magnitude of the friction coefficient ( $0.14 \pm 0.02$ ) in perpendicular scanning was higher than that ( $0.104 \pm 0.005$ ) in parallel scanning. In the case of parallel scanning, the contact component of the stainless steel probe and monolayer surfaces was always the same, hence there was no change in frictional behavior along the line. With perpendicular scanning, on the other hand, the contact component periodically changed as the friction probe advanced. Therefore, it was speculated that

resistance arose by the difference in surface free energy at the interface between the DTMS and FOETMS monolayers. This was the first observation of friction force anisotropy originating from the surface chemical composition of a flat surface.

## 5. CONCLUSION

The organosilane monolayers prepared by the chemisorption and water-cast methods were in hexagonal crystalline states. By contrast, the monolayer prepared by the CVA method was in an amorphous state. Patterned microfeatures of organosilane monolayers were fabricated on the substrate by two different methods. One of them utilizes the crystallization of binary component organosilane monolayer at the air/water interface. Another method utilizes the local photodecomposition by VUV light and backfilling of the decomposed area by chemisorption of organosilane monolayers. It was also revealed that micropatterned organosilane monolayers can be used as model surfaces with controlled, area-selective surface natures, such as free energy, nanostructure, and chemical composition.

### Acknowledgements

The authors acknowledge Professor T. Kajiyama, Dr H. Otuska, Dr K. Kojio, Dr S. Sasaki, Dr O. Sakata, Mr H. Ishida, and Dr M. Morita for their helpful comments and discussion. This research was partially supported by a Grant-in-Aids for Scientific Research, No. 12480264, No. 1200875189, the COE Research “Design and Control of Advanced Molecular Assembly Systems” (08CE2005), and the 21st Century COE Program, “Functional Innovation of Molecular Informatics” from the Ministry of Education, Culture, Sports, Science and Technology, Japan. The authors would like to acknowledge Ulvac. Phi Co. for the ToF-SIMS measurement. The synchrotron radiation X-ray diffraction experiments were performed at SPring-8 with the approval of the Japan Synchrotron Radiation Research Institute (JASRI) as Nanotechnology Support Project of the Ministry of Education, Culture, Sports, Science, and Technology, Japan (Proposal 2002B0227-ND1-np/BL-13XU). The FE-SEM observation was performed using S-4300SE (Hitachi Co. Ltd.) at the Collabo-station II, Kyushu University.

## REFERENCES

- [1] A. Ulmann, *An Introduction to Ultrathin Organic Films: From Langmuir-Blodgett to Self-Assembly*, Academic Press, San Diego, USA, 1991.

- [2] R. H. Tredgold, *Order in Thin Organic Films*, Cambridge University Press, Cambridge, UK, 1994.
- [3] G. Timp (ed.), *Nanotechnology*, Springer, New York, USA, 1999.
- [4] J. Sagiv, *J. Am. Chem. Soc.*, 102 (1980) 92.
- [5] S. R. Wasserman, Y. T. Tao and G. M. Whitesides, *Langmuir*, 5 (1989) 1074.
- [6] A. N. Parikh, D. L. Allara, I. Ben Azouz and F. Rondelez, *J. Phys. Chem.*, 98 (1994) 7577.
- [7] S.-R. Ge, A. Takahara and T. Kajiyama, *J. Vac. Sci. Technol. A*, 12 (1994) 2530.
- [8] S.-R. Ge, A. Takahara and T. Kajiyama, *Langmuir*, 11 (1995) 1341.
- [9] A. Takahara, K. Kojio, S. R. Ge and T. Kajiyama, *J. Vac. Sci. Technol. A*, 14 (1996) 1747.
- [10] T. Kajiyama, S. R. K. Kojio and A. Takahara, *Supramol. Sci.*, 3 (1996) 123.
- [11] K. Kojio, S. R. Ge, A. Takahara and T. Kajiyama, *Langmuir*, 14 (1998) 971.
- [12] A. Takahara, K. Kojio, S. R. Ge and T. Kajiyama, *ACS Symp. Ser. Scanning Probe Microscopy of Polymers*, American Chemical Society, Vol. 694 (B. D. Ratner and V. V. Tsukruk, eds.), 1998, p. 204.
- [13] K. Kojio, A. Takahara and T. Kajiyama, *Colloids Surf. A*, 180 (2000) 294.
- [14] K. Kojio, A. Takahara, K. Omote and T. Kajiyama, *Langmuir*, 16 (2000) 3932.
- [15] K. Kojio, A. Takahara and T. Kajiyama, *Langmuir*, 16 (2000) 9314.
- [16] K. Kojio, A. Takahara and T. Kajiyama, *ACS Symp. Ser. Silicones and Silicon-Modified Materials*, American Chemical Society, Vol. 729, 2000, p. 332.
- [17] K. Kojio, A. Takahara and T. Kajiyama, *ACS Symp. Ser. Fluorinated Surfaces, Coatings, and Films*, American Chemical Society, Vol. 787, 2001, p. 31.
- [18] A. Takahara, S. R. Ge, K. Kojio and T. Kajiyama, *J. Biomater. Sci. Polym. Edn.*, 11 (2000) 111.
- [19] A. Takahara, Y. Hara, K. Kojio and T. Kajiyama, *Macromol. Symp.*, 167 (2001) 271.
- [20] A. Takahara, Y. Hara, K. Kojio and T. Kajiyama, *Colloids Surf. B*, 23 (2002) 141.
- [21] A. Takahara, K. Kojio and T. Kajiyama, *Ultramicroscopy*, 91 (2002) 203.
- [22] K. Kojio, K. Tanaka, A. Takahara and T. Kajiyama, *Bull. Chem. Soc. Jpn.*, 74 (2001) 1.
- [23] T. Koga, M. Morita, H. Ishida, H. Yakabe, S. Sasaki, O. Sakata, H. Otsuka and A. Takahara, *Trans. Mater. Res. Soc. Jpn.*, 28 (2003) 85.
- [24] H. Tada, *J. Electrochem. Soc.*, 142 (1995) L11.
- [25] H. Tada, K. Shimoda and K. Goto, *J. Electrochem. Soc.*, 12 (1995) L230.
- [26] H. Sugimura, K. Ushiyama, A. Hozumi and O. Takai, *Langmuir*, 16 (2000) 885.
- [27] T. Koga, H. Otsuka and A. Takahara, *Trans. Mater. Res. Soc. Jpn.*, 26 (2001) 889.
- [28] T. Koga, H. Otsuka and A. Takahara, *Trans. Mater. Res. Soc. Jpn.*, 27 (2002) 497.
- [29] T. Koga, M. Morita, H. Otsuka and A. Takahara, *Trans. Mater. Res. Soc. Jpn.*, 28 (2004) 153.
- [30] H. Otsuka, T. Arima, T. Koga and A. Takahara, *J. Phys. Org. Chem.*, 18 (2005) 957.
- [31] T. Koga, H. Otsuka and A. Takahara, *Chem. Lett.*, 31 (2002) 1196.

- [32] T. Koga, M. Morita, H. Sakata, H. Otsuka and A. Takahara, *Intern. J. Nanosci.*, 1 (2002) 419.
- [33] A. Takahara, H. Sakata, M. Morita, T. Koga and H. Otsuka, *Compos. Interfaces*, 10 (2003) 489.
- [34] T. Koga, M. Morita, H. Ishida, H. Yakabe, S. Sasaki, O. Sakata, H. Otsuka and A. Takahara, *Langmuir*, 21 (2005) 905.
- [35] M. Morita, T. Koga, H. Otsuka and A. Takahara, *Langmuir*, 21 (2005) 911.
- [36] M. Morita, S. Yasutake, H. Ishizuka, Y. Sakai, J. Fukai and A. Takahara, *Chem. Lett.*, 34 (2005) 916.
- [37] D. K. Owens and R. C. Wendt, *J. Appl. Polym. Sci.*, 13 (1969) 1741.
- [38] A. Kumar, H. A. Biebuyk and G. M. Whitesides, *Langmuir*, 10 (1994) 1498.
- [39] N. L. Abbott, J. P. Folkers and G. M. Whitesides, *Science*, 257 (1992) 1380.
- [40] J. M. Calvert, *J. Vac. Sci. Technol. B*, 11 (1993) 2155.
- [41] H. Gau, S. Herminghaus, P. Lenz and R. Lipowsky, *Science*, 283 (1999) 46.
- [42] C. R. Kagan, T. L. Breen and L. L. Kosbar, *Appl. Phys. Lett.*, 79 (2001) 3536.
- [43] P. Calvert, *Chem. Mater.*, 13 (2001) 3299.
- [44] J. S. Wang and K. Matyjaszewski, *J. Am. Chem. Soc.*, 117 (1995) 5614.
- [45] K. Matyjaszewski and J. Xia, *Chem. Rev.*, 101 (2001) 2921.
- [46] M. Ejaz, K. Ohno, Y. Tsujii and T. Fukuda, *Macromolecules*, 33 (2000) 2870.
- [47] X. Kong, T. Kawai, J. Abe and T. Iyoda, *Macromolecules*, 34 (2001) 1837.
- [48] T. Koga, M. Morita, H. Otsuka and A. Takahara, *Trans. Mater. Res. Soc. Jpn.*, 29 (2004) 153.
- [49] Y. Masuda, M. Itoh, T. Yonezawa and K. Koumoto, *Langmuir*, 18 (2002) 4155.
- [50] H. Fudouzi, M. Kobayashi and N. Shinya, *Langmuir*, 18 (2002) 7648.
- [51] H. Ishida, T. Koga, M. Morita, H. Otsuka and A. Takahara, *Tribol. Lett.*, 19 (2005) 3.

This page intentionally left blank

## Chapter 9

# Homo- and Hybrid-Monolayers of Dendritic Polymers

Toyoko Imae<sup>a,b,\*</sup>, Masaki Ujihara<sup>b</sup>, Mariko Hayashi<sup>b</sup>

<sup>a</sup>*Research Center for Materials Science, Nagoya University, Chikusa, Nagoya 464-8602, Japan*

<sup>b</sup>*Graduate School of Science and Technology, Keio University, Hiyoshi, Yokohama 223-8522, Japan*

### 1. INTRODUCTION

“Nano-technology”, that is, a technique handling materials at nano-meter scale is a trendy scientific field and remarked as one of key sciences in the 21st century [1,2]. Fabrication and characterization of the “nano-scaled materials” have been investigated by many scientists, since this concept was proposed [3]. To fabricate such materials, two classes of methods are available. The first method is the “top-down” approach, where bulk materials are fragmented. Second, in the “bottom-up” approach, characteristics of spontaneous organization of atoms and molecules are utilized. The latter method is called “self-assembly” and advantageous to the construction of both small materials and large products [4]. One of the typical self-assemblies is colloidal metal, which is used since 17th century [5]. Micelles of amphiphilic compounds in solutions, monolayers (Gibbs adsorption and Langmuir monolayers) at air/water interface, and adsorbed or transferred (Langmuir–Blodgett (LB)) films on solid substrates have also been extensively studied [6–8]. Monolayers of thiols on metal substrates are known as typical “self-assembled monolayers (SAMs)” since 1980s [9]. Since the SAMs are easy fabricated, thiol SAMs functionalized have been developed for many applications in the fields of electronics, optics, and catalysis [10]. Along with

---

\*Corresponding author. E-mail: imae@nano.chem.nagoya-u.ac.jp

SAM, conventional LB films are also useful for some applications in the nanotechnology field [11]. In this way, “self-assembling” can be defined as not only simple spontaneous aggregation but also functionalized organization.

Novel polymers, “dendrimers”, were introduced as prospective materials in 1980s [12–15]. Unlike traditional polymers, dendrimers are monodisperse in molecular mass, precisely designed in chemical structure and highly branched in symmetric globular shape. That is, dendrimers are molecules organized in themselves and have been widely investigated not only from the interest as the basic science but also from the viewpoint of the application: Since the dendrimers are thermodynamically stable, they could be functionalized and utilized as nano-capsules and nano-reactors [16,17]. Although dendrimers are useful by themselves as isolated nanomaterials, they are also indispensable as building blocks in self-assembling of higher order [18]. The self-assembled architectures of dendrimers have been prepared in solutions [19], at air/water interfaces [20], and on solid substrates [21]. On the preparation of dendrimer-based nanostructures through self-assembling approach, adsorption films and SAMs of dendrimers can be easily and preferably produced, since dendrimers have many adsorption sites, that is, terminal groups in the periphery of their spherical structure [22–24]. When terminals of dendrimers are substituted by hydrophobic moieties, dendrimer films can be fabricated by LB technique [25]. The self-assembled functional dendrimers on solid substrates are also valuable, because they work on surface modification [26, 27]. Among dendritic polymers denoted by “dendrimers” or “dendrons”, poly(amido amine) (PAMAM) and poly(propyleneimine) (PPI) dendrimers and dendrons are applicable to biochemical and medical objects [28]. Such dendritic polymers function as aggregates in solutions and films at interfaces. Especially, thin films of biocompatible dendritic polymers may be built in nanodevices and nanosensors for medical therapy [29]. Moreover, the functions of films of dendritic polymers are enhanced and extended, when the dendritic polymers are hybridized. The hybridization is possible with not only organic platforms such as liquid crystals [30] and macromolecular layers [31] but also inorganic scaffolds like clays [32] and metal nanoparticles [33].

In the present chapter, the fabrication of monolayers of dendritic polymers at air/water interfaces and on solid substrates is reviewed in Section 2. In Section 3, the hybrids of dendritic polymers with linear polymers at interfaces are focused, and the hybrids with inorganic materials are introduced in Section 4.

## 2. HOMO-MONOLAYERS OF DENDRITIC POLYMERS

In respect to thin films of dendritic polymers, many investigators have fabricated different types of films such as multilayers of amine-terminated PAMAM dendrimers on a silicon wafer [34], covalent attachment of amine-terminated PAMAM dendrimers [35] and poly(iminopropane-1,3-diyl) dendrimers [36] on thiol SAMs, self-assembled composite multilayer films from amine- and

carboxyl-terminated PAMAM dendrimers [21], mixed monolayers of amine-terminated PAMAM dendrimers with alkylthiols on gold [37, 38], chemisorbed adlayers of dendron-thiols on gold [39–41], spread films of carbosilane dendrimers at air/water interface [42], monolayer films of poly(benzyl ether) monodendrons with oligo(ethylene glycol) tails [43], and ordered array of metal-initiated self-assembly from terpyridyl-pendant dendrimers and bridging ligands [44].

The adsorption at air/water interface is remarkable for amphiphilic dendritic polymers, as demonstrated by the decrease in surface tension [45]. Most typical amphiphilic dendritic polymers consist of a dendritic head and a linear polymer chain tail [43, 46–54]. Dendritic head may behave as hydrophilic or hydrophobic moiety depending on the combination with linear polymer tail. Spherical dendrimers, where terminal groups of one half moiety of a dendrimer are hydrophilic and those of another half moiety are hydrophobic, are also amphiphilic at air/water interface [16, 45, 46, 55–60]. These kinds of dendrimers can form amphiphilic bilayer accumulation on solid substrates [18, 45, 59, 60]. Then the bilayers are composed of hydrophilic and hydrophobic halves of dendrimers, while symmetric dendrimers cannot prepare the self-assembled ordered array on solid substrate. Another variation of amphiphiles is a core-shell block dendrimer, where internal and peripheral moieties have different solvophilicity [25, 61–65]. Amphiphilic PAMAM dendrimers, which have their terminal groups modified with 12-hydroxydodecanoic acid, take the “edge-on” configuration in Langmuir films and the column-like structure in LB films [66]. PAMAM dendrimers attach 10,12-pentacosadiynoic acid to their terminal groups to form a stable monolayer at air/water interface, where the compressed monolayer is polymerized upon UV irradiation [67]. The perfluorinated dendritic polymers self-assemble on water subphase through the different mechanism from conventional amphiphiles, owing to the additional interaction of the perfluorinated tails [68].

Adsorption of target molecules on solid substrates depends on the interaction of molecules with substrates. It is well known that molecules with siloxy groups chemically interact with silicone or glass substrate and form uniform SAMs. Correspondingly, thiol molecules preferably react with gold substrate. Recently, SAM formation of carboxyl-terminated PAMAM dendrimer on gold substrate was reported (Fig. 1) [69]. A 2.5th generation dendrimer displays multilayers on adsorption processing, different from alkyl thiol SAM. Adlayer thickness is highest at neutral pH and increases with dendrimer concentration in solution. However, the adlayers are rinsed with solvent down to monolayer thickness. This indicates that carboxyl-terminated derivatives of PAMAM dendrimers can form SAMs on metal substrates. Since the stable SAMs are resulted at whole pH region from acid to alkaline and at every dendrimer concentration, these self-assembled dendrimer monolayers prepared by one-pot method should be expected the utilization as functional films. In this case, the chemical species of carboxyl groups and the interactions between dendrimers or

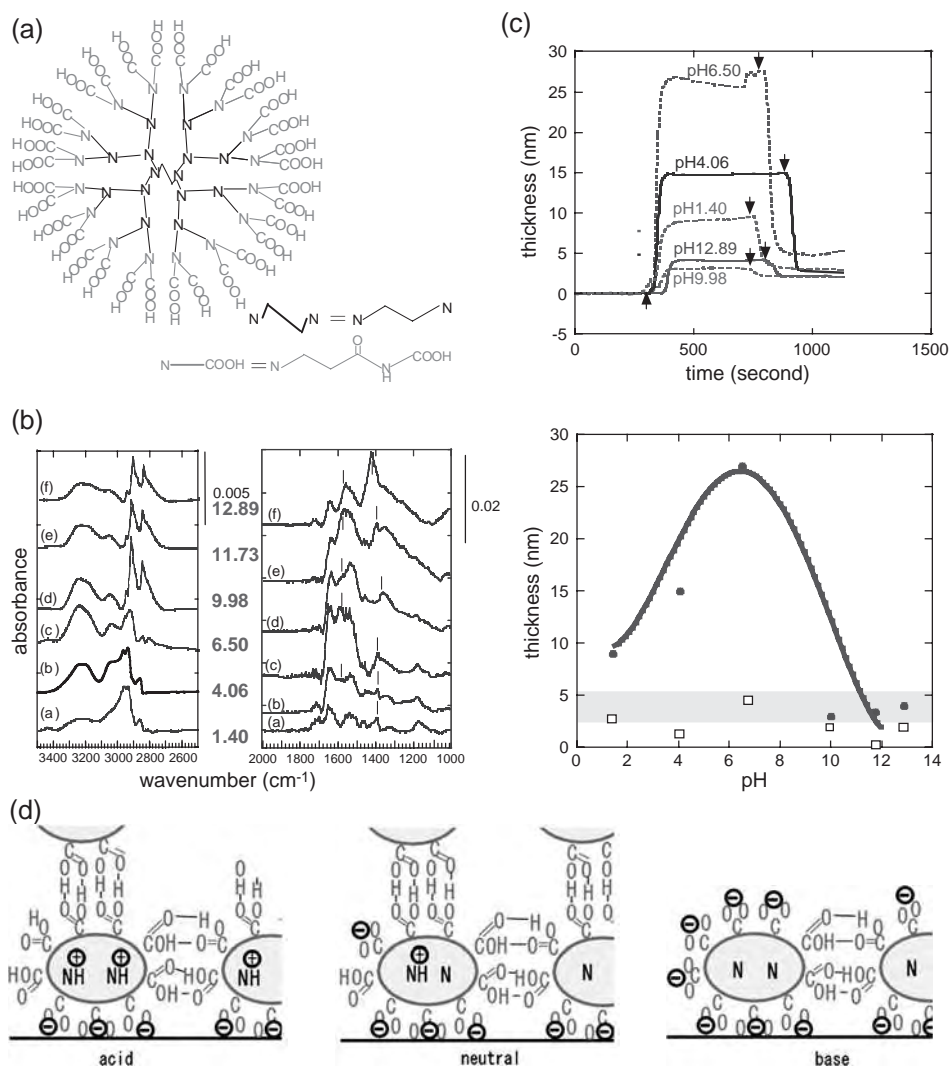


**Fig. 1.** (a) A chemical structure of a 2.5th generation carboxylic acid-terminated poly(amido amine) (PAMAM) dendrimer. (b) Transmission surface enhanced infrared absorption spectra (SEIRAS) of dendrimer adlayers prepared at 30 min adsorption from aqueous solutions (0.01 wt.%) of a dendrimer at different pHs. Numerical values are pHs of the solutions. (c) Adsorption-desorption profiles as a function of time at different pHs and adlayer thicknesses at adsorption and desorption equilibrium as a function of pH for aqueous solutions (0.1 wt.%) of the dendrimer. The symbols,  $\uparrow$  and  $\downarrow$ , in the top figure denote start of adsorption and desorption, respectively. In the bottom figure, filled circle and opened square denote adlayer thicknesses at adsorption and desorption equilibrium, respectively. The dark tie denotes the calculated dendrimer size width. A solid curve is drawn to be visual. (d) Schematic illustration of dendrimers adsorbed at different pHs. Reprinted with permission from Ref. [69], © 2006, American Scientific Publishers.

between dendrimer and substrate in SAMs can be elucidated from infrared absorption spectra.

Self-assemblies of carboxyl-terminated dendrons through multiple ionic interaction were reported [70]: Dendrons form a compact and smooth molecular layer on the aminosilylated surface on fused silica or silicon wafer. Monolayer survives for 1–2 h in water at 100 °C or for 3 h at pH 4–10, indicating the strong interaction of dendrons with substrate surface. The stability of adsorbate on substrate was investigated for monolayer of dendrons with thiol terminals [71]: The films of dendrons with three and nine thiol groups were characterized on gold surfaces. Although about 20 and 28%, respectively, of sulfur atoms terminated are free, the films exhibit higher stability than octadecanethiolate monolayers on gold upon heating in mediums. Similar characterization was carried out with allyl-terminated carbosilane dendrons [72]. For the films prepared by thermally induced hydrosilation on hydrogen-terminated silicon surfaces, the analytical results indicate the presence of roughly 20, 27, and 46% of unreacted allyl groups for 3, 9, and 27 allyl groups, respectively, in dendrons. In order to create stable reactive surface platforms on gold substrates, disulfide-cored poly(propionic acid)-based dendrimers with acetamide-terminal groups were synthesized [73]. Acetamide groups of dendrimers in SAM on gold substrates are hydrolyzed with subsequent formation of hydroxyl-terminated dendron SAM. This modification provides an easy and fast way to control the wettability of the surfaces.

Monolayers of dendritic polymers can be formed on SAM of functional molecules: The protonated amine-terminated groups of PAMAM dendrimers bind to carboxylate groups of 3-mercaptopropionic acid (MPA) SAM by the electrostatic interaction [74, 75]. In this case, hydrogen bonding of amide groups in PAMAM dendrimers with carboxyl groups in MPA SAM is also a motive force of adsorption. Aggregation of carboxyl- and amine-terminated PAMAM dendrimers was compared on naked and thiol-modified gold substrates [76]. Surface coverages of both dendrimers on the naked surface are almost half of those on the thiol-modified surfaces, where the electrostatic interaction promotes the large coverage values, although the latter adsorption process is influenced by the solution pH. It may be noted that the main effect of thiol SAM is a favorable lateral interaction between the adsorbed dendrimer molecules but not an overall adsorption energy.

Langmuir films prepared at air/water interface are transferred on solid substrates and LB films are constructed. The morphologies of the LB films and their molecular arrangements depend on the characters of hydrophilic and hydrophobic moieties of amphiphiles and the affinity of the moieties to the substrates. Transition of molecular arrangement in LB films of third generation amphiphilic PAMAM dendrimers with dodecyl terminal groups was elucidated [77]. The LB films were transferred by horizontal lifting onto hydrophobic silicon wafers and were devoted to their structural characterization. Since silicon wafers are ahead treated (that is, oxidized) by an aqueous solution of

ammonium bifluoride, their surfaces are hydrophilic, resulting in turning upside down of dendrimers during the drying process. Then dendrimers on the substrate take an oblate shape, where hydrophilic core is preferably toward the substrate and alkyl terminals trend selectively to air side.

The fullerene having unique structure is one of the most focused materials, since it is applicable as electron acceptor, antioxidant, singlet oxygen sensitizer, and so on. Primarily solvo-insoluble fullerene can be improved to be more available, when it is hybridized with solvophilic moiety [78, 79]. However, the monolayer of fullerene derivatives with dendritic moiety is rarely investigated. The fullerodendrons were synthesized by reacting fullerenes to anthracenyl focal points of methyl ester-terminated PAMAM dendrons, and their films were fabricated (Fig. 2) [80]. Although dendrons of 0.5th, 1.5th, and 2.5th generations are randomly oriented in the adsorbed films, the LB films of 0.5th and 1.5th generation dendrons take a well-ordered four-layer structure, which consists of a bilayer of fullerodendrons and allows fullerene moieties to exist in the interior of the LB films. By contrast, the LB film of 2.5th generation molecule is in a two-layer structure, where the fullerene moieties are at air side and the dendron moieties are at substrate side. This is a result of the competition between the amphiphilicity of fullerodendron and the fullerene–fullerene attractive interaction. These effects bring monolayer or bilayer formation of fullerodendrons, that is, two-dimensional arrays of fullerene moieties: One is sandwiched by layers of dendron moieties and other is exposed on a layer of dendron moieties. Such difference in two-dimensional arrays of fullerodendrons may play a key role in bringing about changes on the electrochemical and photoelectrochemical properties of the arrays and their availabilities as micro-sensors and optoelectronic devices.

The difference between LB films and adsorption films in morphology and molecular arrangement was revealed in a case of poly(phenylene sulfide) dendrimers and dendrons [81]. Unlike PAMAM dendrimers, since poly(phenylene sulfide) dendrimers have a rigid skeleton, the face-to-face stacking between them is assumed. In fact, multilayers exist in the LB films of poly(phenylene sulfide) dendrimers as a result of accumulation and aggregation of molecular layers, where molecules are oriented perpendicular to the substrate, that is, with “edge on” configuration. Carboxyl-focal dendrons take a domain (or aggregate) structure in the LB films, owing to the face-to-face interaction of dendron moieties and the amphiphilicity of the dendron. By contrast, adsorption films of these dendritic polymers are fundamentally monolayer, where the dendrimer molecules are tilted and the self-assembled in-plane ordering of the dendrons is promoted by thermo-annealing, as seen in Fig. 3(a).

The films consisting of poly(benzylether) dendrons are comparably different from those of poly(phenylene sulfide) dendrons. Second generation poly(benzylether) dendrons with an amine-focal point form uniform films after adsorption at room temperature, and the thermo-annealing results only in the increased roughness of the surface (Fig. 3(b)) [82]. SAMs were also

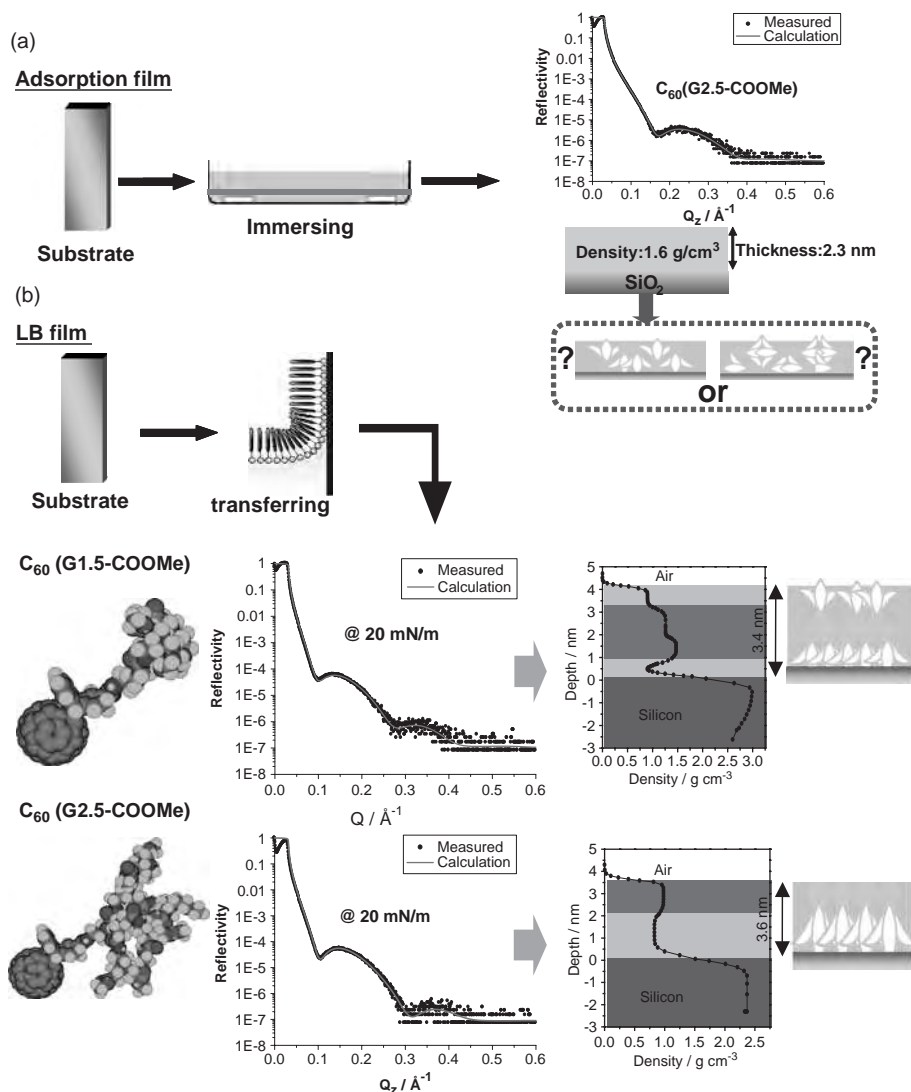


**Fig. 2.** Preparation schemes, X-ray reflectivity curves, and depth profiles of  $n$  generation methylether-terminated fullerodendron ( $C_{60}(G_n\text{-COOME})$ ) films, and schematic illustrations of molecular arrangements in the films. (a) Adsorption film of  $C_{60}(G_{2.5}\text{-COOMe})$ ; (b) LB films of  $C_{60}(G_{1.5}\text{-COOMe})$  and  $C_{60}(G_{2.5}\text{-COOMe})$ . Reprinted with permission from Ref. [80], © 2005, American Chemical Society.

fabricated by thiol-focal poly(benzylether) dendrons at room temperature [41]. The size of ordered region of monolayer increases after annealing for about 4 h at  $70^\circ\text{C}$ . The LB films of second generation poly(benzyl) dendrons with a carboxylic acid focal point display discotic monolayer domains, and the

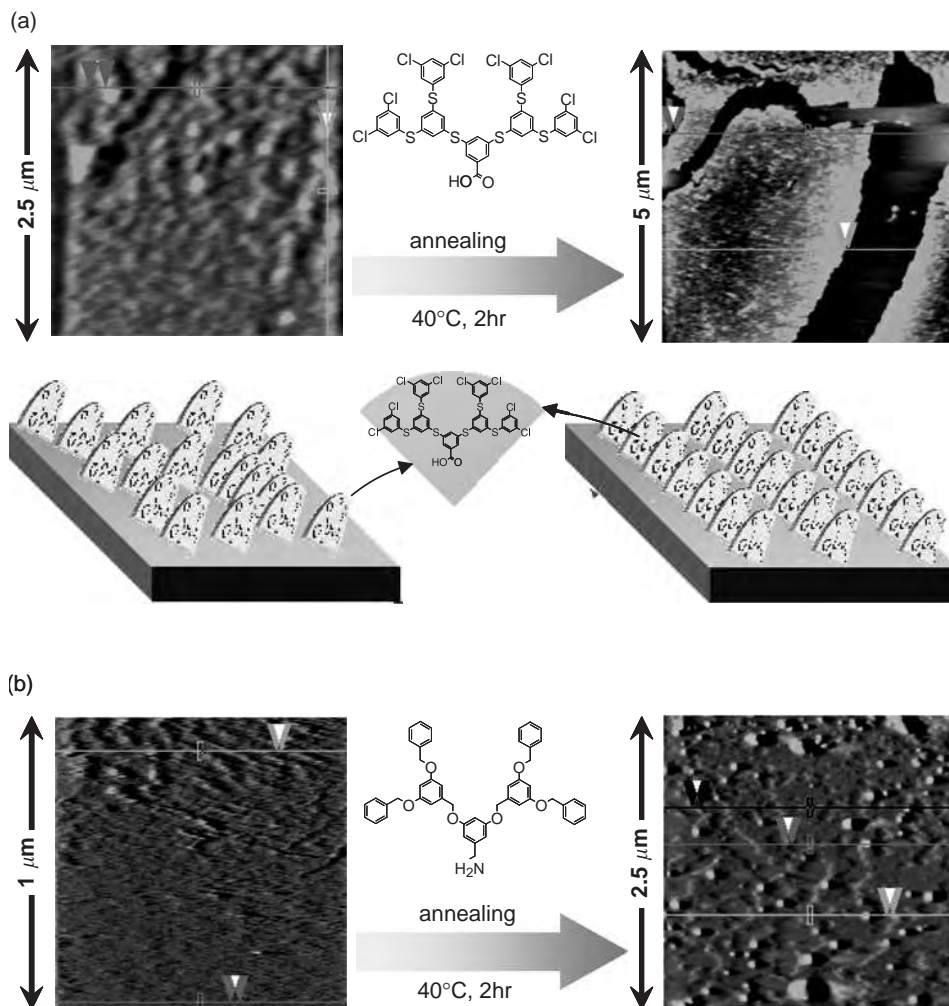


**Fig. 3.** Atomic force microscopic images of adsorption films of second generation dendrons before and after annealing for 2 h at 40 °C. (a) Carboxylic acid-focal poly(phenylene sulfide) dendron. Reprinted with permission from Ref. [81], © 2005, The Society of Polymer Science, Japan. (b) Amine-focal poly(benzylether) dendron. Reprinted from Ref. [82]. Schematic illustration of molecular arrangements on substrates is included in (a).

homogeneity and flattening increase with increasing generation, depending on the increase in surface coverage [83], although the stability and reversibility of the Langmuir monolayers at air/water interface decrease with generation [84]. Anyhow, the formation of multilayer aggregation or accumulation in the films of poly(benzylether) dendrons is not found, different from a case of poly(phenylene sulfide) dendrons as described above. It can be assumed that this

difference comes from the strong  $\pi$ - $\pi$  stacking interaction between poly(phenylene sulfide) dendrons because of the restricted configuration of the dendron [81]. The difference in the  $\pi$ - $\pi$  stacking interaction may be relative to the crystallinity of two dendrons.

Dendrons attached as side chains on linear polymer chains behave different from free dendrimers and dendrons. Block copolymers, poly(3,5-bis(3,5-bis(benzyloxy)benzyloxy)-benzyl methacrylate-random-methacrylic acid)-block-poly(2-perfluorooctylethyl acrylate), possess poly(benzylether) dendrons and perfluorinated alkyl chains in their side chains (Fig. 4) [85]. While an LB film of a copolymer with a medium substitution fraction of poly(benzylether) dendron side chain in poly(methacrylic acid) displays flat surface, a copolymer with high fraction of poly(benzylether) dendron side chains produces the zone texture. Dendron rich blocks are hydrophobic and oleophilic but perfluorinated blocks are solvophobic. Therefore, in this case, the "solvophobicity-to-solvophilicity balance" must be considered. As a result, copolymers with medium fraction of dendron are laid on solid substrate, but dendron blocks of copolymers with high fraction prefer to arrange at air side of air/water interface and the fluorocarbon blocks are enforced to exist close to water subphase, resulting in the zone texture [86]. These situations of molecular arrangements at air/water interface are kept even after transfer on solid substrate. By contrast, when perfluorooctadecanoic acids are mixed with block copolymers with high dendron fraction, the flat monolayers are visualized as terrace [87]. The monolayers are hierarchized into carboxyl, perfluoroalkyl, and dendron layers, that is, hydrophilic, solvophobic, and oleophilic layers. In this case, perfluorooctadecanoic acids play a role for ordering of block copolymers.

### 3. HYBRID-MONOLAYERS OF DENDRITIC POLYMERS WITH LINEAR POLYMERS

The interaction of biomacromolecules with surfactant micelles and dendrimers is focused with the aim of clarification of vital functions and as the mimetic processing of native organisms. Especially, the mimetic processing is developed with backing from the recent breakthrough nano-technology. The complexation of biomacromolecule, DNA, with dendrimers is energetically carried out because of the applicability to the producible intravenous gene delivery [88–100]. Biocompatible complexation of sodium hyaluronate (NaHA) and PAMAM dendrimer has also been performed [101]. One of the driving forces on complexation of anionic polyelectrolytes and cationic dendrimers at alkaline condition is the electrostatic interaction. Such interaction is possible between anions of linear polymers and protonated amine groups of PAMAM dendrimers. The electrostatic complexation of linear polyelectrolytes with dendrimers in solutions is also investigated between anionic sodium poly-L-glutamates

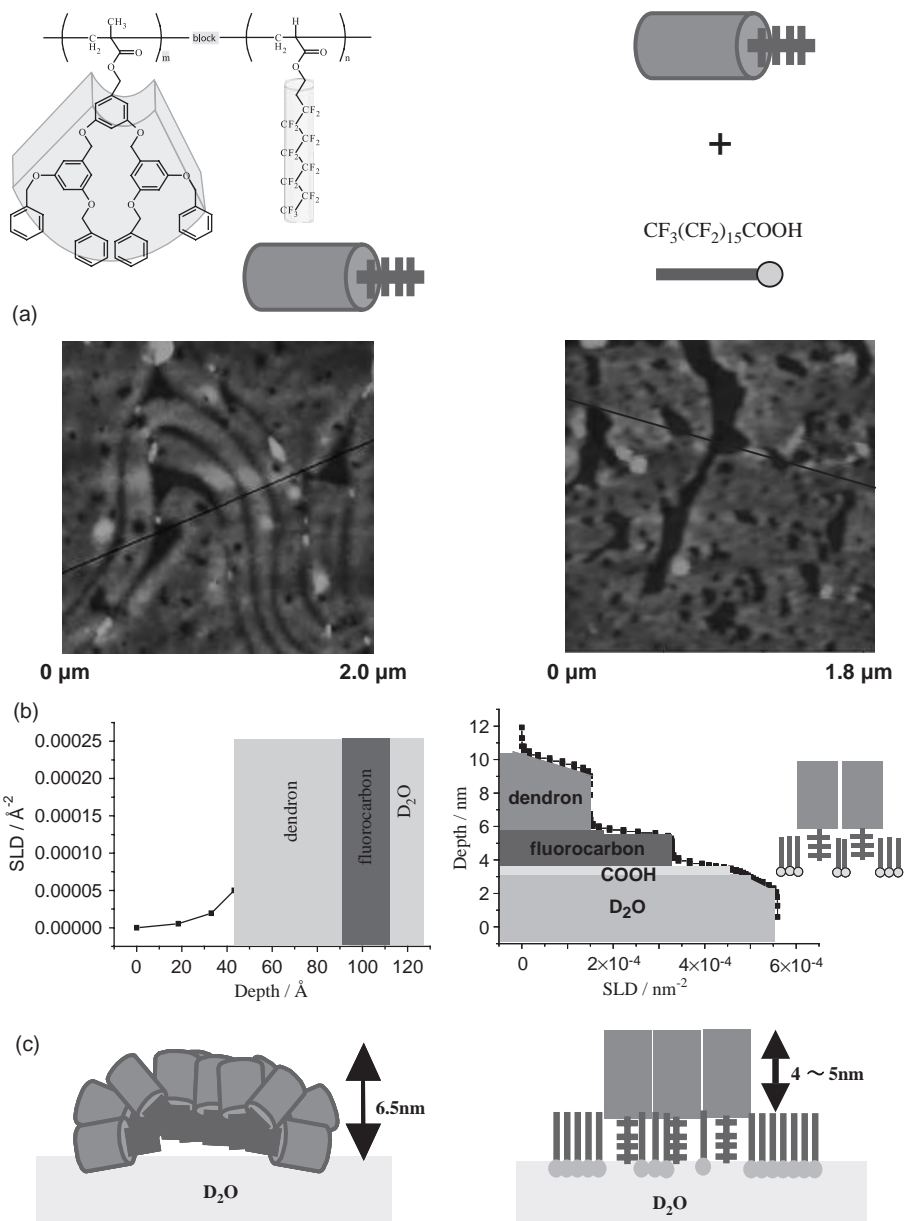


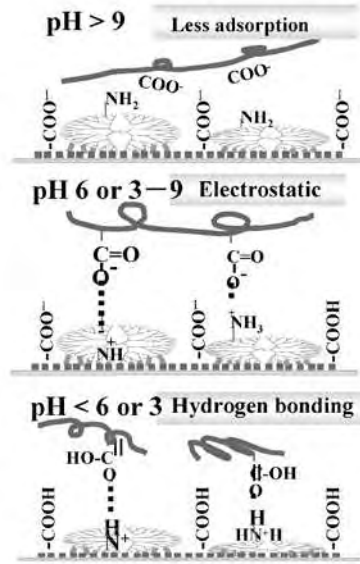
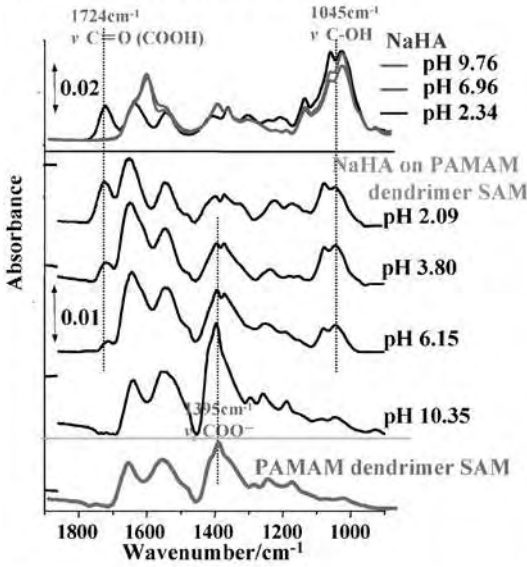
**Fig. 4.** Monolayers of poly(3,5-bis(3,5-bis(benzyloxy)benzyloxy)benzyl methacrylate)-block-poly-(2-perfluorooctylethyl acrylate) (left) and its hybrid with perfluorooctadecanoic acid at [polymer]:[C<sub>17</sub>F<sub>35</sub>COOH] = 1:4 (right). (a) Atomic force microscopic (AFM) images of LB films; (b) depth vs. scattering length density (SLD) profiles of Langmuir films; (c) schematic illustration of molecular arrangements on water subphase. Reprinted with permission from Ref. [86], © 2004, The Materials Research Society of Japan; Ref. [87], © 2006, American Scientific Publishers.

(NaPGA) and amine-terminated PAMAM dendrimers [102–105]. The flexible NaPGAs are possible to interact not only with protonated primary amines in the periphery of a dendrimer but also with tertiary amines in its interior. Opposite combination of the complex, which is stimulated by the electrostatic interaction, was formed between cationic synthetic polyelectrolyte, poly(diallyldimethylammonium chloride), and anionic carboxyl-terminated PAMAM dendrimers [106–109].

By contrast, there are fewer reports for the complexation of linear polymers and dendrimers at interface, despite demands of technology on molecular recognition devices and sensing. Adsorption reactions on dendrimer SAMs were carried out by immersing PAMAM dendrimer SAMs into aqueous solutions of polyelectrolytes [24, 110]. With lowering pH, C=O(COOH) and C–OH stretching absorption bands of NaPGA and NaHA are intensified differently from characteristic infrared absorption bands of PAMAM dendrimers, indicating the increase in amount of adsorbed polymers (see surface enhanced infrared absorption spectra (SEIRAS) in Fig. 5). Additionally, characteristic amide I and II bands of NaPGA and NaHA are also observed at acidic condition. At pHs higher than  $pK_a$  (9.20 and 6.65, respectively [105]) of primary and tertiary amines of a PAMAM dendrimer, almost of NaPGAs and NaHAs prefer to be free in solution rather than to be localized near the surface of dendrimer SAMs because of the high solubility of polyelectrolytes. If pHs are lowered below  $pK_a$  of amines of a dendrimer, negatively charged moieties of linear polyelectrolytes electrostatically interact with protonated amines on dendrimer SAMs. However, at pHs lower than  $pK_a$  [105] of linear polymers, COOH moieties of linear polymers must interact through the hydrogen bonding with protonated amines of dendrimer SAMs. Adsorption of NaHAs at acidic condition (pH 2.5) increases with increasing concentrations of NaHA from 0.02 to 0.04 wt.%, but there is no increase of adsorption at concentrations above 0.04 wt.%, suggesting the saturation in the adsorption of NaHA on dendrimer SAM.

In adsorption reactions of DNA from aqueous solutions on PAMAM dendrimer SAMs, less amount of DNA are adsorbed on dendrimer SAMs at pH higher than 7, and the amount of adsorbed DNA increases with lowering pH, as seen from detectable intensity of characteristic SEIRA bands (for example, P=O and C=O(base) stretching bands) of DNA (Fig. 5) [110]. At pH region of 7–9, only primary amines of a dendrimer are protonated, and DNA is adsorbed electrostatically on the surface of dendrimer SAMs. By contrast, since tertiary amines of a dendrimer are also protonated at lower pH, electrostatic binding of DNA is possible even with tertiary amines in the interior of a dendrimer, besides with primary amines at the periphery of a dendrimer, indicating the increased adsorption of DNA on dendrimer SAMs with decreasing pH. Such penetration of DNA into a dendrimer is possible, when DNA is denaturated. It is known that an UV–vis absorption band of DNA at 258.8 nm becomes stronger, without band shift, with increasing denaturation

(a) Sodium hyaluronate (NaHA)



(b) DNA

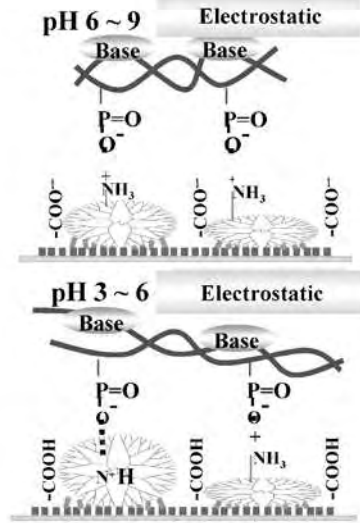
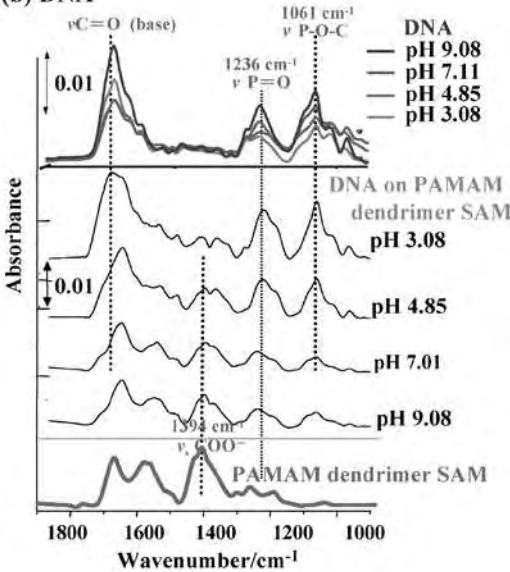


**Fig. 5.** (Left) SEIRAS of NaHA and DNA on PAMAM dendrimer SAMs after adsorption for 30 min from aqueous solutions. Dendrimer SAMs were prepared by the amide bond formation of dendrimers with active ester groups of 3-mercaptopropionic acid (MPA) SAMs on CaF<sub>2</sub> substrates. Infrared absorption spectra of NaHA, DNA, and PAMAM dendrimer are also included. (Right) Schematic illustration of the interactions between polyelectrolytes and dendrimer SAMs. Reprinted from Ref. [110].

degree of DNA. Then the denaturation degree of DNA (0.0023 wt.%) in an aqueous solution evaluated from the decrease of band intensity is 60% at pH 3 and 47% at pH 4–9 [110]. This indicates that about half of DNA strands become single stranded or slackened in water due to the break of base-pair hydrogen bonds. Single-stranded portions of DNA chains are easily penetrated into dendrimer interior. The saturation of adsorption is reached at 0.02 wt.% for DNA at two pHs ( $\sim 7$  and  $\sim 4.8$ ), different from the case of adsorption of NaHA.

The quantitative difference in adsorption behavior of linear polymers between alkaline and acidic conditions can be verified from surface plasmon resonance (SPR) results [111]. As seen in Fig. 6, the adsorption kinetics change along any profile of rapid saturation, gradual increase after rapid increase or gradual increase, depending on the type of linear polymers. The equilibrium of adsorption is reached faster for NaPGA and NaHA than for DNA. However, the film at equilibrium is thicker at acidic condition than at alkaline condition. The quantitative estimation of adsorption of DNA on dendrimer SAMs can be also carried out from the intensity increase of a UV–vis absorption band at 258.8 nm [110].

Desorption reaction in water at different pHs on polyelectrolyte-adsorbed PAMAM dendrimer SAM substrates was followed up with SEIRAS (Fig. 7) [24, 110]. The characteristic amide I and II bands of NaPGA, a C–OH band of NaHA and DNA, and a P=O band of DNA decrease with increasing pH of immersion water. The desorption is almost done within initial 30 min but proceeds slowly with time till overnight and, in all cases, the desorption reaction runs down, when the adsorbed molecules decrease down to the amount adsorbed at each pH. Namely, it can be remarked that the adsorption/desorption processes are reversible. Moreover, the present dendrimer SAMs have an advantage to be reusable for the adsorption/desorption reactions. In the case of the desorption reaction at pH 9.08 on a DNA-adsorbed PAMAM dendrimer SAM substrates, DNA on a substrate prepared at pH 3.04 does not achieve the adsorption amount at the adsorption reaction at the same pH, owing to the

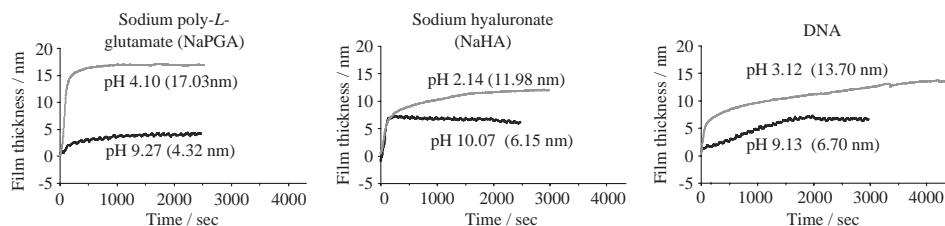


**Fig. 6.** Time dependence of film thicknesses of polyelectrolytes adsorbed on dendrimer SAMs. Concentrations of polyelectrolytes are 0.04 wt.% for NaPGA and NaHA and 0.02 wt.% for DNA. Numerical values in blankets after pH values denote the film thicknesses at absorption equilibrium. Reprinted from Ref. [111].

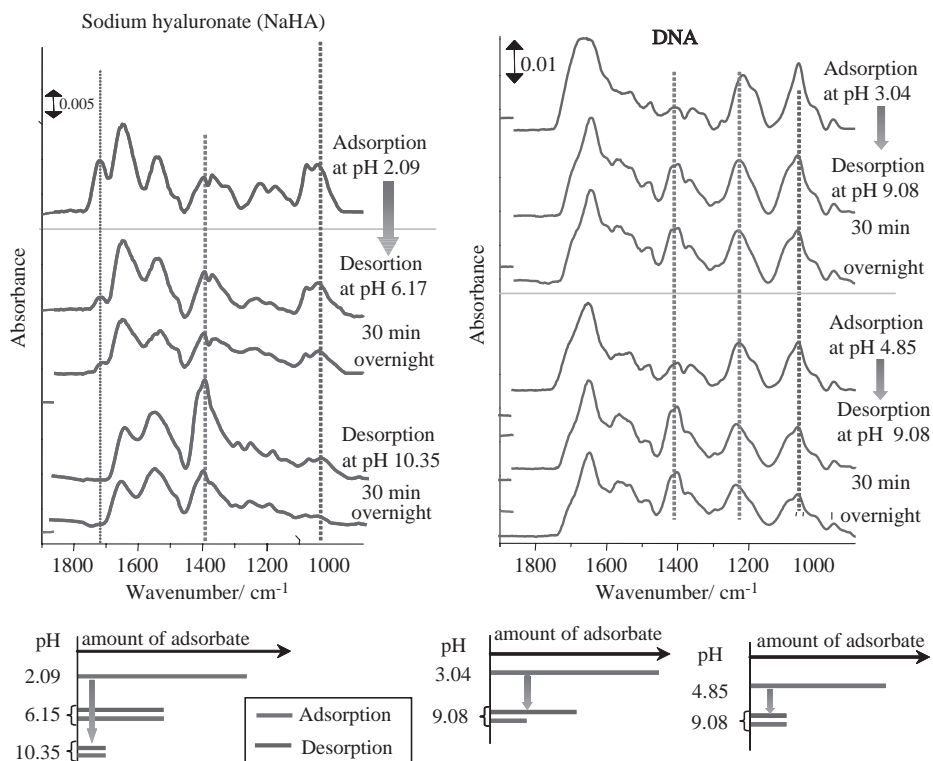


**Fig. 7.** (Top) SEIRAS after desorption process of NaHA and DNA adsorbed on PAMAM dendrimer SAMs. (Bottom) Schematic illustration of the amounts of adsorbate on the adsorption and desorption processes. Reprinted from Ref. [110].

unreproducible denaturation of DNA. In other words, denatured DNA is tightly bound to PAMAM dendrimer, and thus the desorption reaction is irreversibly accomplished.

The selective interaction of polyelectrolytes and dendrimers can be intelligibly examined using patterned substrates. On SAM of *n*-octadecyltrimethoxysilane (ODS) prepared on a silicon substrate, alkyl groups are oxidized to carboxyl groups by partial irradiation of vacuum ultra-violet light under the photo mask, producing the COOH/ODS line pattern (Fig. 8(a)) [112]. After the active esterification of carboxyl groups by using coupling reagents, 1-ethyl-3-(3-dimethylaminopropyl)-carbodiimide hydrochloride (EDC) and *N*-hydroxy succinimide (NHS), NH<sub>2</sub>-terminated dendrimers are immobilized on a COOH pattern through amide bond. The fabrication process of photolithographic PAMAM dendrimer/ODS pattern can be certified by an atomic force microscopy (AFM), as seen in Fig. 8(a). Irradiated lines are lower than the original ODS surface and the same situation is maintained even after the

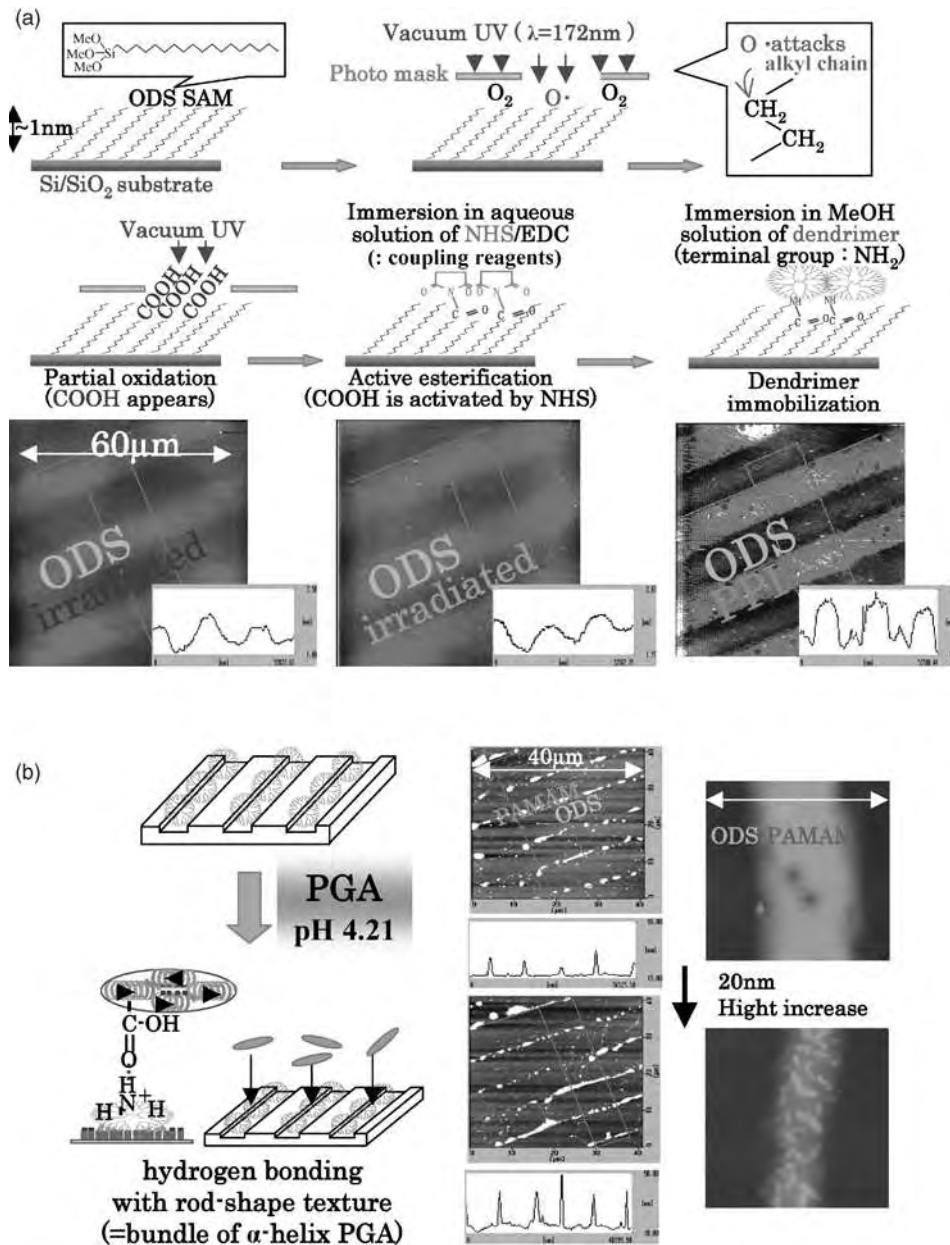


**Fig. 8.** (a) Schematic illustration of photolithographic formation of poly(propyleneimine) (PPI) dendrimer/*n*-octadecyltrimethoxysilane (ODS) patterns and AFM images with section analyses at reaction steps. (b) Schematic illustration of adsorption process and AFM images before and after adsorption of NaPGA on PAMAM dendrimer/ODS patterns. Reprinted with permission from Ref. [112], © 2005, American Scientific Publishers.

esterification. However, after the fabrication of dendrimers, the irradiated lines are heightened more than the ODS lines because of the increased thickness by immobilized dendrimers.

The prepared patterns were used for the selective adsorption of polyelectrolytes (Fig. 8(b)) [112]. At acidic condition, anionic polyelectrolytes described above interact with cationic PAMAM dendrimers through hydrogen bonding (for NaPGA at pH 4.21) or electrostatic interaction (for NaHA at pH 3.82 and DNA at 4.15). Then the heights of dendrimer lines increase 3–20 nm, indicating the selective adsorption of polyelectrolytes on dendrimer SAM lines. Focusing is that the rod-shape texture is observed on an AFM image of the dendrimer lines in a PGA-adsorbed dendrimer/ODS pattern. This texture is an aggregate of  $\alpha$ -helical PGA, because the adsorption of PGA was carried out at a pH below  $\alpha$ -helix random-coil transition. Similar characteristic textures are not observed on the adsorption of HA and DNA.

There are some reports of hierarchically patterned monolayer structures, where dendrimers are one of the building blocks or units. Dendrimers were interacted with gold ions and chemically bonded on a plasma-treated substrate [113]. Then, the photo-masked substrate was irradiated by UV light, resulting in dendrimer + gold nanoparticle patterns. The pattern of amine-terminated PAMAM dendrimer (fourth generation) was also prepared by the microcontact printing method where the patterned stamp was utilized [114]. The stable multilayered pattern structure was prepared at a high concentration of dendrimer ink. The guest, palladium ion, was adsorbed on the host, dendrimer on pattern, which was prepared by the contact printing method [115]. The pattern was used as the nucleation core on the formation of metal cobalt pattern. Dendrimers encapsulating gold nanoparticles were selectively accumulated on hydrophilic stripe of amphiphilic SAM patterns on the printed substrate [116]. Amine-terminated PAMAM dendrimers were immobilized via amide linkage on a carboxyl-terminated thiol SAM on gold surfaces [117]. Patterning was achieved by microcontact printing and dip pen nanolithography. The patterns possess high degree of order and stability.

#### **4. HYBRID-MONOLAYERS OF DENDRITIC POLYMERS WITH INORGANIC NANOPARTICLES**

Metal nanoparticles have been used for many applications because of their unique characteristics, even before they were visualized as small particles of nano-meter order by using a transmission electron microscope [118]. For example, colored glasses, which gained in popularity in medieval times, contain nanoparticles of noble metals. These colors originate from the SPR of metal nanoparticles, which is the resonance phenomenon of surface electron density wave with incident light wave at the metal surface [119]. Since this resonance is sensitive to the dielectric constant of surrounding media, the phenomenon has

an advantage as sensors [120]. Furthermore, this phenomenon is also effective to enhance photoreactions, since nanoparticles accumulate the energy of photons [121–124]. Nanoparticles are valuable not only in photonics but also in many fields of science. In electronics, nanoparticles can be used as “quantum dots”, which behave quantum theoretically: Memory effects using nanoparticles (quantum dots) have been reported [125]. In chemistry, nanoparticles are activated and used as catalysts, even though they are made of inactive materials like gold [126].

For these applications, nanoparticles and their aggregates should be designed in preferable structures and arrangements. Up to date, some shape-control methods [127, 128] and organization techniques [129–133] of nanoparticles have been reported. For organizing nanoparticles to the desirable arrangements, scaffold materials are widely utilized. The scaffolds are divided into two types. The first one is a protector, which prevents the undesired aggregation of nanoparticles and maintains a constant interparticle distance. It follows that nanoparticles and protectors take spontaneously crystalline arrays [134–137]. Alkyl thiols, fatty acids, and alkyl amines are typically used as protectors [138, 139]. The other is a template. Binding sites in the template for nanoparticles are patterned on a substrate and nanoparticles are adsorbed along the pattern [140]. The patterning at sub-micrometer order is generally carried out by lithography [141]. To obtain smaller patterned arrangements, the templates should be prepared by self-assembly. Dendrimers are stable and have possible binding sites in the molecules, and their sizes (nm order) are convenient. Thus they could be ideal templates. The combination of characteristic materials, dendrimers and nanoparticles, should be useful in terms of practicality. Therefore, the investigation of dendrimer/nanoparticle hybrids with ordered arrangements is still in progress.

Concerning the investigation on the hybridization of dendrimers with nanoparticles and on the structures of the prepared bifunctional hybrid films, dendrimers possessing an azacrown core and long alkyl chain (hexylene) spacers were newly designed for the fabrication of the hybrid films [142]. Amine-terminated (second and third generations (G2, G3)) homologs of this dendrimer in a methanol solution are adsorbed onto the gold surface and MPA SAM [143]. Especially, the MPA SAM strongly interacts with the dendrimers via electrostatic interaction between carboxyl groups of MPA and amine groups of dendrimer. While G3 dendrimer has perpendicular molecular axis to the substrate, G2 dendrimer changes its globule conformation to oblate one and rearranges to the prolately oriented one during the adsorption onto MPA SAM. Such conformational change of dendrimer adsorbed has not been discussed deeply in prior reports. By contrast, methyl ester-terminated dendrimers (1.5th and 2.5th generations (G1.5, G2.5)) are hardly adsorbed onto MPA SAMs. Although minor amount of G1.5 dendrimers can interact with the substrate via the electrostatic interaction of azacrown in the dendrimer with horizontal molecular axis to the substrate, G2.5 dendrimer is scarcely detected on the substrate. The

terminal ester groups hide the interior binding sites of the dendrimer, and the dendrimer of higher generation has disadvantage for adsorption. Thus, the different efficiencies between terminal and interior groups of dendrimers were clarified for adsorption on the metal surface or SAM. Now, it is required that the conformation of dendrimers should be controlled in order to hybridize effectively at interface.

An adsorption behavior of nanoparticles to the Langmuir films of dendrimers was examined at air/water interface, by using water-insoluble dendrimers with azacrown core and hydrophobic terminal groups, with expectation of interaction with nanoparticles dispersed in water subphase [144]. First, to control the conformation of methyl ester-terminated dendrimers, G1.5 and G2.5 dendrimers were spread on water subphase. The dendrimers take the “face-on” configuration and form small circular domains at air/water interface. When the aqueous subphase contains silver nanoparticles protected with MPA, the Langmuir film of G1.5 dendrimer is reinforced by hybridization with silver nanoparticles. By contrast, the film of G2.5 dendrimer is not strengthened in the presence of silver nanoparticles. From the plasmon band variation and electron microscopic image, it is clarified that the silver nanoparticles are adsorbed onto both G1.5 and G2.5 dendrimer films. After film-collapsing by compression, the hybrid film of G1.5 dendrimer arises cracks at the interface, while G2.5 dendrimers in the film produces water-dispersible aggregates with nanoparticles. This difference suggests that the structures of hybrid films are not the same. The adsorption property of G1.5 dendrimer is weaker than that of G2.5 dendrimer because of the less number of binding sites per dendrimer molecule. Therefore, the structure of dendrimers could be controlled to preferable one for hybridization with nanoparticles at air/water interface.

Fabrication of monolayer of metal nanoparticles was carried out at air/water interface with aid of Langmuir films of octyl-terminated amphiphilic PAMAM dendrimers, and the effect of terminal groups of dendrimer for the structures of hybrid films was discussed (Figs. 9 and 10) [145]. The gold nanoparticles in the subphase are adsorbed to dendrimers in the Langmuir film to form a monolayer with hexagonal lattice ordering. Several dendrimers are bound only on the upper-half surface of a gold nanoparticle at air/water interface. The dendrimer used is characterized by azacrown core, hexylene spacers, and terminal octyl groups. In the interaction of dendrimers with gold nanoparticles, the azacrown core is an effective binding site, the flexible hexylene spacers allow dendrimers to take favorable conformation, and the terminal octyl groups stimulate two-dimensional ordering of dendrimer/gold nanoparticle composites through their hydrophobic interaction. This method using dendrimer template is valuable to obtain new type of hybrid films of metal nanoparticles, and this is a unique case of dendrimer template technique. In the obtained film, the half surface of a nanoparticle is lapped by functional dendrimers, and the other half is bare active metal. Such bifunctional surfaces could be independently used on some purposes.

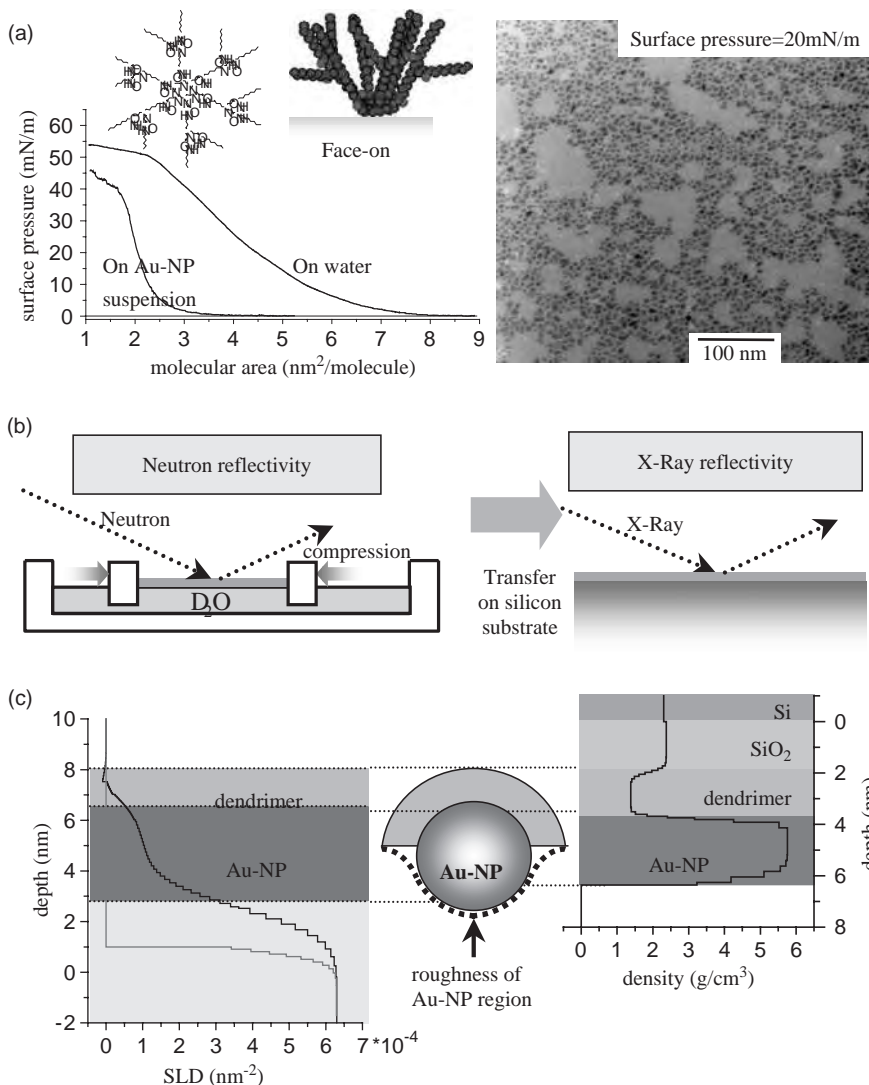


**Fig. 9.** (a) A chemical structure and a “face-on” configuration of a 1.5th generation azacrown-core PAMAM dendrimer with hexyl spacers, surface pressure–molecular area isothermal curves of the dendrimer on water and gold-nanoparticle (Au-NP) suspension subphases, and a TEM image of Au-NP-adsorbed LB film. (b) Schematic illustration of neutron and X-ray reflectivity measurement systems at air/subphase interface and on silicon substrate, respectively. (c) (Left) Depth vs. scattering length density (SLD) profiles of dendrimer/Au-NP hybrid Langmuir film (black) and D<sub>2</sub>O and Au-NP suspension subphases (red); (right) depth vs. density profile of its LB film. Dendrimer and Au-NP regions are illustrated with a corresponding model. Reprinted with permission from Ref. [145], © 2006, American Chemical Society.

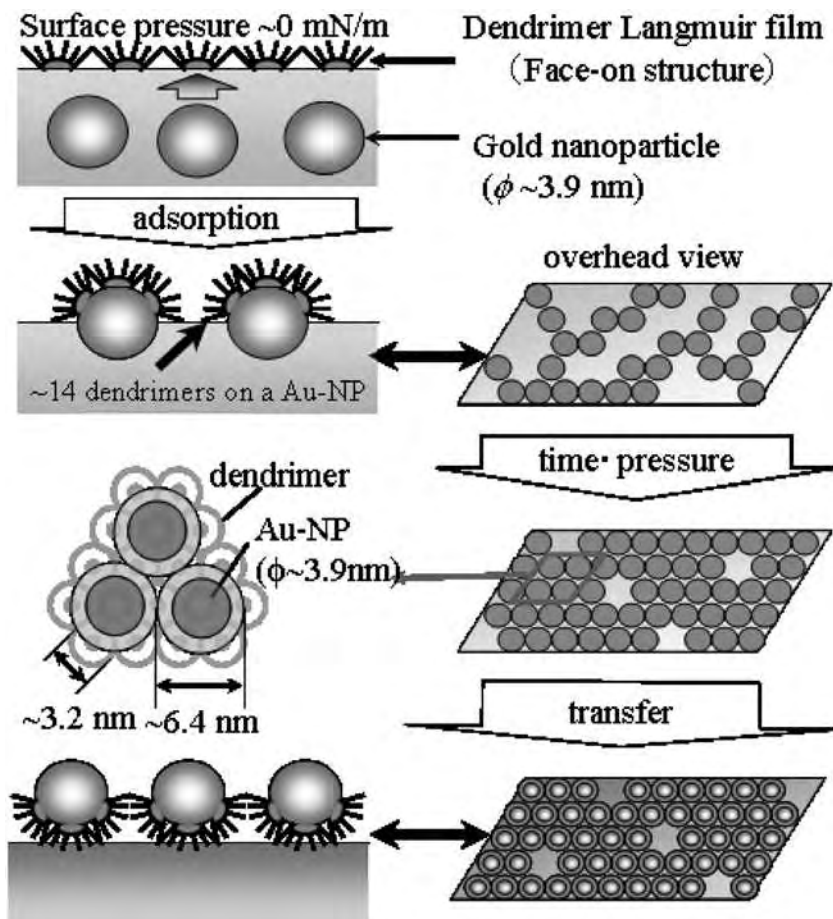


**Fig. 10.** Schematic illustration of the formation of dendrimer/Au-NP hybrid films via hybridization at air/suspension interface and transfer to the solid substrate. Reprinted with permission from Ref. [145], © 2006, American Chemical Society.

## 5. CONCLUSION

Dendrimers consist of dendritic branches, and high generation homologs have dense peripheral functional groups and inner voids. These structural characters give advantages over the uptake of the volatile organic compounds (VOCs) and the size selectivity of guest molecules. Moreover, peripheral functional groups stimulate the strong (multiple) interaction and affinity with the substrates. This indicates the advantage of dendritic polymers as building blocks. Even if parts of functional terminal groups are used for anchoring on substrates, the residual terminal groups are active as functional sites. Then internal voids are operative as reservoirs of guest molecules. How dendritic polymers are suitable for usage

to chemical sensing systems is reviewed [146]. It is possible to apply dendrimers for making different types of surface acoustic waves (SAWs). On PAMAM dendrimer-modified SAW devices, the response for dosing of VOCs depends on the chemical structure and character of VOCs, indicating the molecular recognition by dendrimers.

As one of applications of dendrimer SAMs, the deposition of nanostructures was carried out [147]. On the dendron thiol SAM as an underlying surface, gold nanostructures were electrodeposited. Then the size and shape of nanostructures can be controlled by the deposition time and potential. By the surface modification of gold nanostructures with *n*-dodecanethiol or 11-mercaptoundecanol, the surfaces with the superhydrophobic (water contact angle: about 155°) or superhydrophilic (water contact angle: about 0°) properties, respectively, are created. Moreover, pH-responsive surface can be prepared by reacting 2-(11-mercaptoundecanamido)benzoic acid on the surface of gold nanostructures. It is expected that this series of researches offer the route for fabrication of nanostructured functional materials with the use of dendrimer SAMs.

Surface of gold electrodes was modified with thiol SAM and further reacted with PAMAM dendrimers by electrostatic interaction [148]. Then, Prussian Blue (PB) was anchored on the surface of electrodes. The surface coverage of PB at acidic condition is improved on the dendrimer-modified electrodes as compared with that on naked electrodes. Moreover, the stability of electrodes at neutral pH increases on dendrimer-modified electrodes, while PB film is not formed on naked electrodes at the condition of neutral pH. It is suggested that, in the stable PB-dendrimer composite films prepared on thiolated gold electrode surfaces, the uptake of PB takes place inside the dendrimer and PB molecules retain their electrocatalytic properties for the electro-oxidation due to the permeability and hosting properties of dendrimer.

Many scientists, who go for the application of dendrimer architectures, pay attention to the biological purposes like antigen–antibody reaction, biomacromolecule-detection sensing (or chips), and so on. The investigation of protein–ligand (avidin–biotin) interactions was carried out on SAMs of fourth generation PAMAM dendrimer fabricated on 11-mercaptoundecanoic acid SAM [149]. The specific binding of avidin to the fully biotinylated dendrimer monolayers is about 80% of the maximum binding. It is implied that the efficient avidin–biotin interaction on dendrimer monolayers originates from surface exposure of biotin ligands and corrugation of surface. The chemical (covalent) immobilization of DNA and protein on dendrimer-functionalized SAM was carried out [150]. Amine-terminated PAMAM dendrimers supported by aminoundecanethiol SAMs on gold substrates were used as intermediate layers, and biomolecular sensing layers were fabricated. It is found that sensor surfaces containing dendrimer layers display an increased capacity of protein immobilization in comparison with those without dendrimer. This dendrimer-based surfaces are sensitive specific detectors of DNA–DNA interaction and display

high stability for repeated reuses. The fabrication of dendrimer-mediated sensors will contribute to the development of biosensing devices.

The application of dendrimer-activated surface as a protein chip was carried out [151]. Amine-terminated PPI dendrimers are immobilized onto silicon and glass surfaces using coupling procedure. The amine content on dendrimer-coated surfaces increases with increasing dendrimer generation higher than the third generation. Simultaneously, the concentration of immobilized proteins and the activity of immobilized alkaline phosphatase also rise. The high activity of immobilized proteins is indispensable in the application of functional surface as a protein chip. Stable and uniform SAM of hydroxyl-terminated dendron thiol was prepared on gold substrate, and the subsequent derivation of activated monolayer was performed via bridging reactions with amine-terminated dendrimers [152]. Then the stability, reactivity, and versatility of the prepared surface are enhanced. This biosensitive surface is useful in the immobilization of biological macromolecules for the fabrication of DNA microarrays and protein chips.

With a view of applying to biomolecular recognition and biosensing array technologies, the patterned platforms consisting of functional groups with high density and the hierarchical structures distinctly controlled are strongly demanded in late years. The dendrimer-mediated surfaces are on a way to them. The further development of monolayer surfaces including dendrimer SAMs is expected and in progress.

## REFERENCES

- [1] A. Hullmann and M. Meyer, *Sciencetometrics*, 58 (2003) 507.
- [2] K. Havancsak, *Mater. Sci.*, 414 (2003) 85.
- [3] A. Franks, *J. Phys. E*, 20 (1987) 1442.
- [4] N. Kimizuka, *Curr. Opin. Chem. Biol.*, 7 (2003) 702.
- [5] H. Siedentopf and R. Zsigmondy, *Ann. Physik.*, 10 (1903) 1.
- [6] J. W. McBain, *Trans. Faraday Soc.*, 9 (1913) 99.
- [7] K. B. Blodgett, *J. Am. Chem. Soc.*, 56 (1934) 495.
- [8] D. K. Schwartz, *Surf. Sci. Rep.*, 27 (1997) 245.
- [9] C. D. Bain and G. W. Whitesides, *Science*, 240 (1988) 62.
- [10] J. J. Gooding, F. Mearns, W. Yang and J. Liu, *Electroanalysis*, 15 (2003) 81.
- [11] O. Albrecht, K. Sakai, K. Takimoto, H. Matsuda, K. Eguchi and T. Nakagiri, *Adv. Chem. Ser.*, 240 (1994) 341.
- [12] J. M. J. Fréchet and C. J. Hawker, in *Comprehensive Polymer Science*, 2nd Suppl. (G. Allen, ed.), Elsevier, Pergamon, Oxford, 1996.
- [13] C. R. Newkome, C. N. Moorefield and F. Vögtle, *Dendritic Molecules: Concepts, Synthesis, Perspectives*, VCH, Weinheim, 1996.
- [14] J. M. J. Fréchet and D. A. Tomalia, *Dendrimers and Other Dendritic Polymers*, Wiley, Chichester/New York, 2001.

- [15] F. Vögtle, *Dendrimers III Design, Dimension, Function*, 212 Topics in Current Chemistry, Springer, Berlin, 2001.
- [16] J. M. J. Fréchet, *J. Polym. Sci. A*, 41 (2003) 3713.
- [17] D. A. Tomalia, *Prog. Polym. Sci.*, 30 (2005) 294.
- [18] T. Imae, K. Funayama, Y. Nakanishi and K. Yoshii, *Functionalities of dendrimers in Encyclopedia of Nanoscience and Nanotechnology*, Vol. 3 (H. S. Nalwa, ed.), American Scientific Publishers, 2004, p. 685.
- [19] D. K. Smith, A. R. Hirst, C. S. Love, J. G. Hardy, S. V. Brignell and B. Huang, *Prog. Polym. Sci.*, 30 (2005) 220.
- [20] T. Kajiyama, K. Kojio and K. Tanaka, *Adv. Colloid Interface Sci.*, 111 (2004) 159.
- [21] V. V. Tsukruk, F. Rinderspacher and V. N. Bliznyuk, *Langmuir*, 13 (1997) 2171.
- [22] H. Tokuhisa, M. Zhao, L. A. Baker, V. T. Phan, D. L. Dermody, M. E. Garcia, R. F. Peez, R. M. Crooks and T. M. Mayer, *J. Am. Chem. Soc.*, 120 (1998) 4492.
- [23] V. Chechik and R. M. Crooks, *Langmuir*, 15 (1999) 6364.
- [24] T. Yamazaki and T. Imae, *J. Nanosci. Nanotechnol.*, 5 (2005) 1066.
- [25] K. Aoi, T. Hatanaka, K. Tsutsumiuchi, M. Okada and T. Imae, *Macromol. Rapid Commun.*, 20 (1999) 378.
- [26] R. M. Crooks, M. Q. Zhao, L. Sun, V. Chechik and L. K. Yeung, *Acc. Chem. Res.*, 34 (2001) 181.
- [27] T. Imae, K. Funayama, K. Aoi, K. Tsutsumiuchi, M. Okada and M. Furusaka, *Langmuir*, 15 (1999) 4076.
- [28] R. Esfand and D. A. Tomalia, *DDT*, 6 (2001) 427.
- [29] C. C. Lee, J. A. MacKay, J. M. J. Fréchet and F. C. Szoka, *Nat. Biotechnol.*, 23 (2005) 1517.
- [30] X. Li, T. Imae, D. Leisner and M. A. López-Quintela, *J. Phys. Chem. B*, 106 (2002) 12170.
- [31] C. Li, K. Mitamura and T. Imae, *Macromolecules*, 36 (2003) 9957.
- [32] A. S. Costa, T. Imae, K. Takagi and K. Kikuta, *Prog. Colloid Polym. Sci.*, 128 (2004) 113.
- [33] A. Manna, T. Imae, K. Aoi, M. Okada and T. Yogo, *Chem. Mater.*, 13 (2001) 1674.
- [34] S. Watanabe and S. L. Regen, *J. Am. Chem. Soc.*, 116 (1994) 8855.
- [35] M. Wells and R. M. Crooks, *J. Am. Chem. Soc.*, 118 (1996) 3988.
- [36] H. Tokuhisa and R. M. Crooks, *Langmuir*, 13 (1997) 5608.
- [37] M. Zhao, H. Tokuhisa and R. M. Crooks, *Angew. Chem. Int. Ed. Engl.*, 36 (1997) 2596.
- [38] W. M. Lackowski, J. K. Campbell, G. Edwards, V. Chechik and R. M. Crooks, *Langmuir*, 15 (1999) 7632.
- [39] C. B. Gorman, R. L. Miller, K.-Y. Chen, A. R. Bishop, R. T. Haasch and R. G. Nuzzo, *Langmuir*, 14 (1998) 3312.
- [40] Z. Bo, L. Zhang, B. Zhao, X. Zhang, J. Shen, S. Höppener, L. Chi and H. Fuchs, *Chem. Lett.*, 27 (1998) 1197.
- [41] L. Zhang, F. Huo, Z. Wang, L. Wu, X. Zhang, S. Höppener, L. Chi, H. Fuchs, J. Zhao, L. Niu and S. Dong, *Langmuir*, 16 (2000) 3813.

- [42] S. S. Sheiko, A. I. Buzin, A. M. Muzafarov, E. A. Rebrov and E. V. Getmanova, *Langmuir*, 14 (1998) 7468.
- [43] J. P. Kampf, C. W. Frank, E. E. Malmström and C. J. Hawker, *Langmuir*, 15 (1999) 227.
- [44] D. J. Díaz, G. D. Storrer, S. Bernhard, K. Takada and H. D. Abruña, *Langmuir*, 15 (1999) 7351.
- [45] T. Imae, in *Structure-Performance Relationships in Surfactants*, Second Edition, Revised and Expanded, Surfactant Science Series Vol. 112 (K. Esumi and M. Ueno, eds.), Marcel Dekker, New York, 2003, p. 525.
- [46] J. M. J. Fréchet, *Science*, 263 (1994) 1710.
- [47] T. M. Chapman, G. L. Hillyer, E. J. Mahan and K. A. Shaffer, *J. Am. Chem. Soc.*, 116 (1994) 11195.
- [48] J. C. M. van Hest, D. A. P. Delnoye, M. W. P. L. Baars, M. H. P. van Genderen and E. W. Meijer, *Science*, 268 (1995) 1592.
- [49] J. C. M. van Hest, M. W. P. L. Baars, C. Elissen-Román, M. H. P. van Genderen and E. W. Meijer, *Macromolecules*, 28 (1995) 6689.
- [50] K. Aoi, A. Motoda, M. Okada and T. Imae, *Macromol. Rapid Commun.*, 18 (1997) 945.
- [51] J. Iyer, K. Fleming and P. T. Hammond, *Macromolecules*, 31 (1998) 8757.
- [52] D. Yu, N. Vladimirov and J. M. J. Fréchet, *Macromolecules*, 32 (1999) 5186.
- [53] C. Román, H. R. Fischer and M. Meijer, *Macromolecules*, 32 (1999) 5525.
- [54] K. Aoi, A. Motoda, M. Ohno, K. Tsutsumiuchi, M. Okada and T. Imae, *Polym. J.*, 31 (1999) 1071.
- [55] C. J. Hawker, K. L. Wooley and J. M. J. Fréchet, *J. Chem. Soc. Perkin Trans.*, 1 (1993) 1287.
- [56] K. Aoi, K. Itoh and M. Okada, *Macromolecules*, 30 (1997) 8072.
- [57] K. Aoi, H. Noda, K. Tsutsumiuchi and M. Okada, *IUPAC 37th International Symposium on Macromolecules*, Preprints, 1998, p. 765.
- [58] T. Imae, K. Funayama, K. Aoi, K. Tsutsumiuchi and M. Okada, in *Yamada Conference L, Polyelectrolytes* (I. Noda and E. Kokufuta, eds.), 1999, p. 439.
- [59] T. Imae, M. Ito, K. Aoi, K. Tsutsumiuchi, H. Noda and M. Okada, *Colloids Surf. A Phys. Eng. Aspects*, 175 (2000) 225.
- [60] M. Ito, T. Imae, K. Aoi, K. Tsutsumiuchi, H. Noda and M. Okada, *Langmuir*, 18 (2002) 9757.
- [61] K. Aoi, K. Itoh and M. Okada, *Macromolecules*, 28 (1995) 5391.
- [62] K. Aoi, K. Tsutsumiuchi, E. Aoki and M. Okada, *Macromolecules*, 29 (1996) 4456.
- [63] M. C. Coen, K. Lorentz, J. Kressler, H. Frey and R. Mülhaupt, *Macromolecules*, 29 (1996) 8069.
- [64] S. Stevelmans, J. C. M. van Hest, J. F. G. A. Jansen, D. A. F. J. van Boxel, E. M. M. de Brabander-van der Berg and E. W. Meijer, *J. Am. Chem. Soc.*, 118 (1996) 7398.
- [65] A. P. H. J. Schenning, C. Elissen-Román, J.-W. Weener, M. W. P. L. Baars, S. J. van der Gaast and E. W. Meijer, *J. Am. Chem. Soc.*, 120 (1998) 8199.
- [66] G. Sui, M. Mabrouki, Y. Ma, M. Micic and R. M. Leblanc, *J. Colloid Interface Sci.*, 250 (2002) 364.

- [67] G. Sui, M. Micic, Q. Huo and R. M. Leblanc, *Colloids Surf. A Physicochem. Eng. Aspects*, 171 (2000) 185.
- [68] S. R. Lee, D. K. Yoon, S.-H. Park, E. H. Lee, Y. H. Kim, P. Stenger, J. A. Zasadzinski and H.-T. Jung, *Langmuir*, 21 (2005) 4989.
- [69] M. Ito and T. Imae, *J. Nanosci. Nanotechnol.*, 6 (2006) 1667.
- [70] B. J. Hong, J. Y. Shim, S. J. Oh and J. W. Park, *Langmuir*, 19 (2003) 2357.
- [71] C. M. Yam, J. Cho and C. Cai, *Langmuir*, 19 (2003) 6862.
- [72] C. M. Yam, J. Cho and C. Cai, *Langmuir*, 20 (2004) 1228.
- [73] E. Östmark, L. Macakova, T. Auletta, M. Malkoch, E. Malmström and E. Blomberg, *Langmuir*, 21 (2005) 4512.
- [74] H. Nagaoka and T. Imae, *Trans. Mater. Res. Soc. Jpn.*, 26 (2001) 945.
- [75] H. Nagaoka and T. Imae, *Int. J. Nonlinear Sci. Numer. Simul.*, 3 (2002) 223.
- [76] J. Manríquez, E. Juaristi, O. Muñoz-Muñiz and L. A. Godínez, *Langmuir*, 19 (2003) 7315.
- [77] K. Tanaka, S. Dai, T. Kajiyama, K. Aoi and M. Okada, *Langmuir*, 19 (2003) 1196.
- [78] Y. Rio, G. Accorsi, H. Nierengarten, C. Bourgogne, J.-M. Strub, A. V. Dorselaer, N. Armadori and J.-F. Nierengarten, *Tetrahedron*, 59 (2003) 3833.
- [79] Y. Takaguchi, Y. Sako, Y. Yanagimoto, S. Tsuboi, J. Motoyoshiya, H. Aoyama, T. Wakahara and T. Akasaka, *Tetrahedron Lett.*, 44 (2003) 5777.
- [80] C. Hirano, T. Imae, S. Fujima, Y. Yanagimoto and Y. Takaguchi, *Langmuir*, 21 (2005) 272.
- [81] O. Yemul, M. Ujihara, N. Maki and T. Imae, *Polym. J.*, 37 (2005) 82.
- [82] N. Maki and T. Imae, unpublished data.
- [83] S. Xu, S. Kang, G. Deng, P. Wu, Q. Fan, C. Wang, C. Wan and C. Bai, *Chem. Lett.*, 32 (2003) 290.
- [84] S. Kang, S. Xu, G. Deng, P. Wu, Q. Fan, C. Wang, L. Wanand and C. Bai, *Chem. Phys. Lett.*, 370 (2003) 542.
- [85] M. Takahashi, S. Hamaguchi, H. Ito, T. Imae and T. Nakamura, *Prog. Colloid Polym. Sci.*, 128 (2004) 68.
- [86] K. Mitamura, M. Takahashi, S. Hamaguchi, T. Imae and T. Nakamura, *Trans. Mater. Res. Soc. Jpn.*, 29 (2004) 255.
- [87] K. Mitamura, T. Imae, E. Mouri, N. Torikai, H. Matsuoka and T. Nakamura, *J. Nanosci. Nanotechnol.*, 6 (2006) 36.
- [88] M. F. Ottaviani, B. Sacchi, N. J. Turro, W. Chen, S. Jockusch and D. A. Tomalia, *Macromolecules*, 32 (1992) 2275.
- [89] C. Plank, K. Mechtler, F. C. Szoka, Jr. and E. Wagner, *Hum. Gene Ther.*, 7 (1996) 1437.
- [90] M. X. Tang, C. T. Redemann and F. C. Szoka, Jr., *Bioconjug. Chem.*, 7 (1996) 703.
- [91] A. U. Bielinska, J. Johnson, R. Spindler, D. A. Tomalia and J. R. Baker, Jr., *Proc. Natl. Acad. Sci. USA*, 93 (1996) 4897.
- [92] A. U. Bielinska, J. F. Kukowska-Latallo, J. Johnson, D. A. Tomalia and J. R. Baker, Jr., *Nucleic Acids Res.*, 24 (1996) 2176.
- [93] A. U. Bielinska, J. F. Kukowska-Latallo and J. R. Baker, Jr., *Biochim. Biophys. Acta*, 1353 (1997) 180.

- [94] V. A. Kabanov, A. B. Zezin, V. B. Rogacheva, Zh. G. Gulyaeva, M. F. Zansochova, J. G. H. Joosten and J. Brackman, *Macromolecules*, 32 (1999) 1904.
- [95] V. A. Kabanov, V. G. Sergeev, O. A. Pyshkina, A. A. Zinchenko, A. B. Zezin, J. G. H. Joosten, J. Brackman and K. Yoshikawa, *Macromolecules*, 33 (2000) 9587.
- [96] W. Chen, N. J. Turro and D. A. Tomalia, *Langmuir*, 16 (2000) 15.
- [97] C. L. Gebhart and V. A. Kabanov, *J. Control. Release*, 73 (2001) 401.
- [98] M. D. Brown, A. G. Schätzlein and I. F. Uchegebu, *Int. J. Pharm.*, 229 (2001) 1.
- [99] D. Luo, K. Haverstick, N. Belcheva, E. Han and W. M. Saltman, *Macromolecules*, 35 (2002) 3456.
- [100] A. Mitra and T. Imae, *Biomacromolecules*, 5 (2004) 69.
- [101] T. Imae, T. Hirota, K. Funayama, K. Aoi and M. Okada, *J. Colloid Interface Sci.*, 263 (2003) 306.
- [102] D. Leisner and T. Imae, *J. Phys. Chem. B*, 107 (2003) 8078.
- [103] T. Imae and A. Miura, *J. Phys. Chem. B*, 107 (2003) 8088.
- [104] D. Leisner and T. Imae, *J. Phys. Chem. B*, 107 (2003) 13158.
- [105] D. Leisner and T. Imae, *J. Phys. Chem. B*, 108 (2004) 1798.
- [106] Y. Li, P. L. Dubin, R. Spindler and D. A. Tomalia, *Macromolecules*, 28 (1995) 8426.
- [107] H. Zhang, P. L. Dubin, R. Spindler and D. A. Tomalia, *Ber. Bunsenges. Phys. Chem.*, 100 (1996) 923.
- [108] H. Zhang, P. L. Dubin, J. Ray, G. S. Manning, C. N. Moorefield and G. R. Newkome, *J. Phys. Chem. B*, 103 (1999) 2347.
- [109] N. Miura, P. L. Dubin, C. N. Moorefield and G. R. Newkome, *Langmuir*, 15 (1999) 4245.
- [110] M. Hayashi, Bachelor report, Nagoya University, 2005.
- [111] K. Ishikawa, Bachelor report, Nagoya University, 2004.
- [112] T. Yamazaki, T. Imae, H. Sugimura, N. Saito, K. Hayashi and O. Takai, *J. Nanosci. Nanotechnol.*, 5 (2005) 1792.
- [113] J. Won, K. J. Ihn and Y. S. Kang, *Langmuir*, 18 (2002) 8246.
- [114] D. Arrington, M. Curry and S. C. Street, *Langmuir*, 18 (2002) 7788.
- [115] X. C. Wu, A. M. Bittner and K. Kern, *Langmuir*, 18 (2002) 4984.
- [116] F. Gröhn, X. Gu, H. Gröll, J. C. Meredith, G. Nisato, B. J. Bauer, A. Karim and E. J. Amis, *Macromolecules*, 35 (2002) 4852.
- [117] G. H. Degenhart, B. Dordi, H. Schönherr and G. J. Vancso, *Langmuir*, 20 (2004) 6216.
- [118] R. H. O. Franklin, *J. Inst.*, 227 (1939) 398.
- [119] P. Mulvaney, *Langmuir*, 12 (1996) 788.
- [120] A. N. Shipway, E. Katz and I. Willner, *ChemPhysChem*, 1 (2000) 18.
- [121] X. L. Zhou, X. Y. Zhu and J. M. White, *Surf. Sci. Rep.*, 13 (1991) 73.
- [122] R. T. Kidd, D. Lennon and S. R. Meech, *J. Chem. Phys.*, 113 (2000) 8276.
- [123] E. S-Bárdos, H. Czili and A. Horváth, *J. Photochem. Photobiol. A*, 154 (2003) 195.
- [124] T. Imae, in *Encyclopedia of Surface and Colloid Science* (A. T. Hubbard, ed.), Marcel Dekker, New York, 2002, p. 3547.
- [125] F. Rosei, *J. Phys. Condens. Matter*, 16 (2004) 1373.
- [126] M. C. Daniel and D. Astruc, *Chem. Rev.*, 104 (2004) 293.

- [127] M. J. Yacaman, J. A. Ascencio and H. B. Liu, *J. Vac. Sci. Technol. B*, 19 (2001) 1091.
- [128] J. J-P'erez, I. S-Pastoriza, L. M. L-Marz'an and P. Mulvaney, *Coord. Chem. Rev.*, 249 (2005) 1870.
- [129] G. L. Hornyak, M. Kröll, R. Pugin, T. Sawitowski, G. Schmid, J. O. Bovin, G. Karrson, H. Hofmeister and S. Hopfe, *Chem. Eur. J.*, 3 (1997) 1951.
- [130] Y. M. Lo and R. R. Price, *Colloids Surf. B*, 23 (2002) 251.
- [131] M. G. Warner and J. E. Hutchison, *Nat. Mater.*, 2 (2003) 272.
- [132] T. Teranishi, *Comptes Rendus Chimie*, 6 (2003) 979.
- [133] A. S. Costa and T. Imae, *Trans. Mater. Res. Soc. Jpn.*, 29 (2004) 3211.
- [134] C. J. Kiely, J. Fink, M. Brust, D. Bethell and D. J. Schiffrin, *Nature*, 396 (1998) 444.
- [135] A. Manna, T. Imae, M. Iida and N. Hisamatsu, *Langmuir*, 17 (2001) 6000.
- [136] A. Manna, T. Imae, T. Yogo, K. Aoi and M. Okazaki, *J. Colloid Interface Sci.*, 256 (2002) 297.
- [137] S. Nakao, K. Torigoe and K. Kon-no, *J. Phys. Chem. B*, 106 (2002) 12097.
- [138] C. J. Kiely, J. Fink, J. G. Zheng, M. Brust, D. Bethell and D. Schiffrin, *J. Adv. Mater.*, 12 (2000) 640.
- [139] A. Manna, T. Imae, T. Yogo, K. Aoi and M. Okazaki, *Mol. Simul.*, 29 (2003) 661.
- [140] S. Maenosono, T. Okubo and Y. Yamaguchi, *J. Nanoparticle Res.*, 5 (2003) 5.
- [141] M. Giersig and M. Hilgendorff, *Eur. J. Inorg. Chem.*, 18 (2005) 3571.
- [142] O. Yemul, M. Ujihara and T. Imae, *Trans. Mater. Res. Soc. Jpn.*, 29 (2004) 165.
- [143] M. Ujihara, J. Orbulescu, T. Imae and R. M. Leblanc, *Langmuir*, 21 (2005) 6846.
- [144] M. Ujihara and T. Imae, *J. Colloid Interface Sci.*, 293 (2006) 333.
- [145] M. Ujihara, K. Mitamura, N. Torikai and T. Imae, *Langmuir*, 22 (2006) 3656.
- [146] R. M. Crooks and A. Ricco, *Acc. Chem. Res.*, 31 (1998) 219.
- [147] Y. Jiang, Z. Wang, X. Yu, F. Shi, H. Xu and X. Zhang, *Langmuir*, 21 (2005) 1986.
- [148] E. Bustos, J. Manríquez, G. Orozco and L. A. Godínez, *Langmuir*, 21 (2005) 3013.
- [149] M.-Y. Hong, H. C. Yoon and H.-S. Kim, *Langmuir*, 19 (2003) 416.
- [150] S. S. Mark, N. Sandhyarani, C. Zhu, C. Campagnolo and C. A. Batt, *Langmuir*, 20 (2004) 6808.
- [151] S. Pathak, A. K. Singh, J. R. McElhanon and P. M. Dentinger, *Langmuir*, 20 (2004) 6075.
- [152] M. Yang, E. M. W. Tsang, Y. A. Wang, X. Peng and H.-Z. Yu, *Langmuir*, 21 (2005) 1858.

This page intentionally left blank

## Chapter 10

# Infrared Reflection Absorption Spectroscopy of Monolayers at the Air–Water Interface

Jiayin Zheng, Roger M. Leblanc\*

*Department of Chemistry, University of Miami, 1301 Memorial Drive, Coral Gables, FL 33124-0431, USA*

### 1. INTRODUCTION

There has been considerable interest in the characterization of the conformation and orientation of amphiphilic molecules in Langmuir monolayers in the past few decades [1–5]. Monolayers at the air–water interface are widely employed as convenient experimental paradigms that mimic many vital biological processes. The advantages realized when using monolayers as models for biological interfaces arise primarily from the ease with which experimental variables may be manipulated. These include parameters that are not readily controlled in bulk phases or in films prepared on solid substrates, such as lateral pressure, surface area, and domain size and shape [6].

The acquisition of structural information from Langmuir films began in the mid-1980s, with the application of epifluorescence microscopy to study domain formation and the application of X-ray reflection and diffraction to study molecular orientation [7–11]. Since then, a variety of methods have been employed to evaluate the physical state of monolayer films. For example, Brewster angle microscopy was applied to study the topography of molecules at the air–water interface [12–15]. Techniques used for the characterization of Langmuir films also include surface pressure–area isotherms from which phase transitions, limiting molecular area and packing densities, can be obtained [3,16–18]. Moreover, surface potential–area isotherms contain information about film homogeneity and data about orientation of the molecules and molecular groups [16,19].

---

\*Corresponding author. E-mail: rml@miami.edu

Ellipsometry and nonlinear optics have proven their sensitivity in studying monolayer thickness and molecular orientation, but generally the anisotropic nature of the interface makes results rather difficult to interpret [20–22]. In many cases, these methods were limited in their potential to supply information about biophysical issues such as head group structure, enzyme secondary structure, and the orientation of ordered regions.

Infrared reflection absorption spectroscopy (IRRAS) was first applied in the mid-1980s by Dluhy and co-workers, who demonstrated the feasibility of acquiring infrared (IR) spectra from aqueous Langmuir films of fatty acids and phospholipids *in situ* at the air–water interface [23–29]. IRRAS provides several well-known advantages for the conformation and orientation characterization of Langmuir films. The technique monitors molecular vibrations that produce dipole moment oscillations. IR absorptions are sensitive to displacements of the permanent bond dipole moment, which in turn depend upon changes in conformation and configuration of the bonds making up the normal mode of vibration [30,31]. Thus, IRRAS has been shown to be one of the leading structural analysis for monolayers at the air–water interface over the past decade [32–35].

However, the IRRAS method presents some difficulties for the study of Langmuir film because the strong absorption of the water vapor hides the spectral region where the most interesting molecular information is. Besides, even though the interferometers are now very stable and the detectors very sensitive, conventional IRRAS requires long acquisition times and accurate control of vapor pressure during sample (covered water) and reference (uncovered water) spectrum recordings. To overcome these problems, a differential IR reflectivity technique by polarization modulation of the incidence light (PM-IRRAS) was developed [20,30]. This technique has been proven to be almost insensitive to the strong IR absorption of water vapor, and only important bands arising from the Langmuir film were observed [20]. PM-IRRAS also allows the extraction of information about conformation and orientation of the Langmuir film.

This review includes the structural information that has been carried out to date from films of single chain amphiphiles, enzymes, and proteins using both IRRAS and PM-IRRAS methods.

## 2. IN SITU INFRARED REFLECTION ABSORPTION SPECTROSCOPY (IRRAS) OF LANGMUIR FILMS

### 2.1. Background

For many years, IRRAS has been successfully applied to the study of thin films adsorbates on metal surfaces [36]. In the case of monolayers deposited on metal surfaces, an IR external reflection spectrum is obtained by reflecting the incoming radiation from the three-phase ambient–adsorbate–substrate system, measuring the reflected intensity as a function of wavelength, and then ratioing

this spectrum against the reflected intensity from a bare substrate. The reflection spectrum obtained by this process is a function of the wavelength, the state of polarization, the adsorbate thickness, the angle of incidence of the reflected light, and the optical constants of the three phases involved [30,37,38].

While there are many instances in which it is appropriate to study monomolecular films on metal surfaces, there exists a large group monolayer films whose native substrate is water and are best studied *in situ* to avoid the problems associated with transfer artifacts. Such molecules include surfactants, polymers, proteins, lipids, and other compounds of a biological nature [24]. In most optical setups for IRRAS, the incident IR beams is directed onto the surface of a Langmuir trough filled with pure H<sub>2</sub>O or with the model monolayer film on H<sub>2</sub>O at different angles of incidence. The IR beam has to be polarized to allow measurements of molecular orientation. However, most experiments are carried out with unpolarized IR radiation to improve the S/N ratio. The Langmuir troughs are often placed outside the spectrometer and are completely enclosed. The molecular area can be easily controlled and Wilhelmy plate is used to monitor surface tension [39].

There is a large difference in the reflectance of the two substrates as a function of the angle of incidence of the incoming radiation. While the reflectivity of metals is always very high, the reflectance of IR radiation from a water subphase is considerably weaker, and approaches zero at the pseudo-Brewster angle [24]. An additional difference between the two types of external reflection experiments is the polarization dependence of the spectra. When recording external reflectance spectra of thin films on metal substrates, the best experimental conditions of obtaining IRRAS spectra are governed by the selectivity of metal surfaces and the spectra have to be recorded at grazing incidence (around 80°) with the radiation polarized parallel to the plane of incidence (p-polarized), because the electric field perpendicular to the plane of incidence (s-polarized) is almost zero. Under such conditions, the surface electric field of the resulting stationary wave is normal to the metal plane and presents an enhanced intensity due to constructive interferences. This is the origin of the “surface selection” rule, which states that only vibrational dipole moments oriented perpendicular to the surface will be observed, since this is the only orientation that p-polarized radiation will excite [30,40]. This is not the case when using water as the reflective substrate, as finite values of the mean square electric fields for both p- and s-polarized radiation are present at the air–water interface [24]. In the case of s-polarization, the bands have the same sign throughout the entire range of incidence angles. In the case of p-polarization, the sign of the IRRAS bands changes by crossing the Brewster angle and their intensity varies with the angle of incidence. This polarization provides information on film anisotropy because the electric field is spread both in and out of the plane of the film. IRRAS of thin films at the air–water interface is thus a convenient technique for studying vibrations with transition moments in the plane of the film as opposed to IRRAS on metal surfaces [1,41,42].

## 2.2. Application

### 2.2.1. Single-chain fatty acids

The IRRAS experiments consist of recording the reflectance spectrum of the monolayer at the air–water interface  $R(d)$  and then normalizing it with respect to the reflectance of the water subphase  $R(0)$ . Thus, detailed information about the structure and the interactions of head groups such as carboxylic acids, carboxylic esters, carboxylates, and amides becomes accessible. The first IRRAS spectrum from an oleic acid (9-*cis*-octadecenoic acid) monolayer at the air–water interface was reported by Dluhy and co-workers [23]. The most obvious feature of the spectrum is the negative absorbance bands of the oleic acid due to the properties of the complex refractive index of the water substrate [43]. The symmetric and asymmetric  $\text{CH}_2$  stretching bands of the saturated hydrocarbon chain were observed, together with an intense alkenic C–H stretching vibration. The C = O stretching vibration of the carboxylic acid was also detected.

Several other saturated long-chain fatty acids were investigated at the air–water interface using IRRAS at different pH values (from pH 2 to 10) and at temperatures 288 and 294 K by Gericke and Hühnerfuss [44]. The chain order decreases with decreasing chain length ( $\text{C}_{18} > \text{C}_{16} > \text{C}_{15}$ ), although this effect is not so pronounced for pH 2 as for pH 6. For pH 9 the order increases greatly and the molecules are oriented almost vertically with respect to the water surface. They also reported the head group structure of the fatty acid monolayers at the air–water interface for the first time. The stretching vibrations of unprotonated, monoprotonated, and doubly protonated functional groups were observed.

They also studied the interaction of stearic acid ( $\text{C}_{18}$ ) monolayers at the air–water interface with bivalent cations ( $\text{Cd}^{2+}$ ,  $\text{Pb}^{2+}$ ,  $\text{Ca}^{2+}$ ,  $\text{Ba}^{2+}$ ,  $\text{Cu}^{2+}$ ,  $\text{Ni}^{2+}$ , and  $\text{Zn}^{2+}$ ) in aqueous subphase using the IRRAS technique [45–47]. However, the information on molecular orientation was limited due to the use of unpolarized IR radiation. Recently, the headgroup interaction and chain orientation in the monolayers of stearic acid on pure water and ion ( $\text{Ag}^+$ ,  $\text{Co}^+$ ,  $\text{Zn}^{2+}$ , and  $\text{Pb}^{2+}$ )-containing subphases have been investigated using the IRRAS technique [48].

Fig. 1 shows the surface pressure–area ( $\pi$ – $A$ ) isotherms of stearic acid monolayers on pure water and ion-containing subphases, respectively. The presence of bivalent cations in the subphase gives rise to condensation of the monolayers. On the  $\text{Ag}^+$ -containing subphase, the isotherm shows extremely compressed characteristics with a limiting area of  $0.12 \text{ nm}^2/\text{molecule}$ , much smaller than the cross-sectional area of  $0.20 \text{ nm}^2$  of a saturated hydrocarbon chain, which suggests the formation of a three-dimensional structure of the compressed monolayer [48].

Fig. 2 shows the IRRAS spectra of stearic acid monolayers on pure water and ion-containing subphases at the angle of incidence of  $30^\circ$  for p-polarization. On pure water surface, the monoprotonated and double protonated carbonyl groups in the stearic acid monolayer were observed ( $1724, 1705 \text{ cm}^{-1}$ ). On the

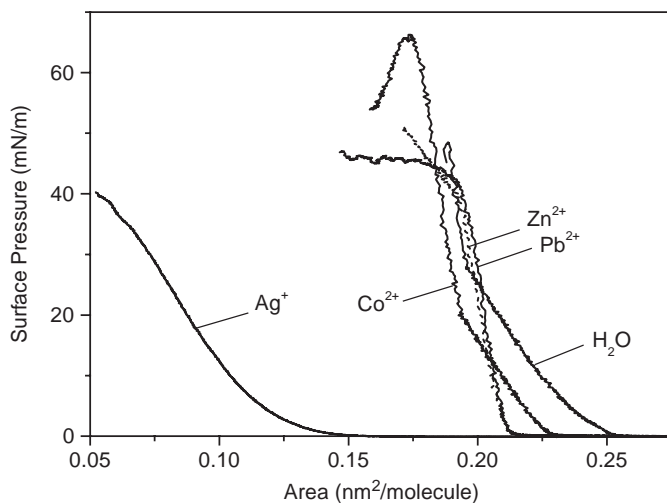


**Fig. 1.**  $\pi$ - $A$  isotherms of stearic acid monolayers on pure water and ion-containing subphases (1 mmol/L,  $\text{Ag}^+$ ,  $\text{Co}^{2+}$ ,  $\text{Zn}^{2+}$ , and  $\text{Pb}^{2+}$ ), respectively: compression rate, 5 mm/min; 22 °C. Reprinted with permission from Ref. [48]. Copyright 2006, American Institute of Physics.

ion-containing subphase, carboxylate groups were formed (between 1600–1500 and 1430–1400  $\text{cm}^{-1}$ ) at the expense of carbonyl ones. Based on the separation between the  $\nu_a(\text{COO})$  and  $\nu_s(\text{COO})$  vibrational frequencies, it is known that for  $\text{Co}^{2+}$  and  $\text{Zn}^{2+}$ , the H-bonded monodentate and unsymmetric bidentate chelating structure within the headgroups were formed [48–50]. For  $\text{Pb}^{2+}$ , three types of structures, bidentate chelating, unsymmetric chelating, and bidentate bridging coordinations, were formed [45,48]. Moreover, the hydrocarbon chains in the monolayers are uniaxially oriented at a tilt angle of  $\sim 0^\circ$  with respect to the surface normal in contrast to a tilt angle of  $\sim 20^\circ$  on pure water surface at 20 mN/m by the computer simulation. In the presence of  $\text{Ag}^+$ , all the bands were considerably enhanced, multilayers were formed with the highly ordered hydrocarbon chains in a triclinic subcell structure and a bidentate bridging structure within the headgroups. The multilayers were composed of three monolayers, and the hydrocarbon chains in each monolayer were oriented at a tilt angle of  $\sim 30^\circ$  away from the surface normal.

### 2.2.2. Phospholipids

In addition to the long-chain fatty acid molecules described above, a large number of studies have appeared that use IRRAS to study phospholipid monolayers as models of biomembrane interfaces. Mitchell and Dluhy [26] reported the first IRRAS spectra of 1,2-distearoyl-*sn*-glycero-3-phosphocholine (DSPC), 1,2-dimyristoyl-*sn*-glycero-3-phosphocholine (DMPC), and 1,2-dipalmitoyl-*sn*-glycero-3-phosphocholine (DPPC) monolayers at the air–water

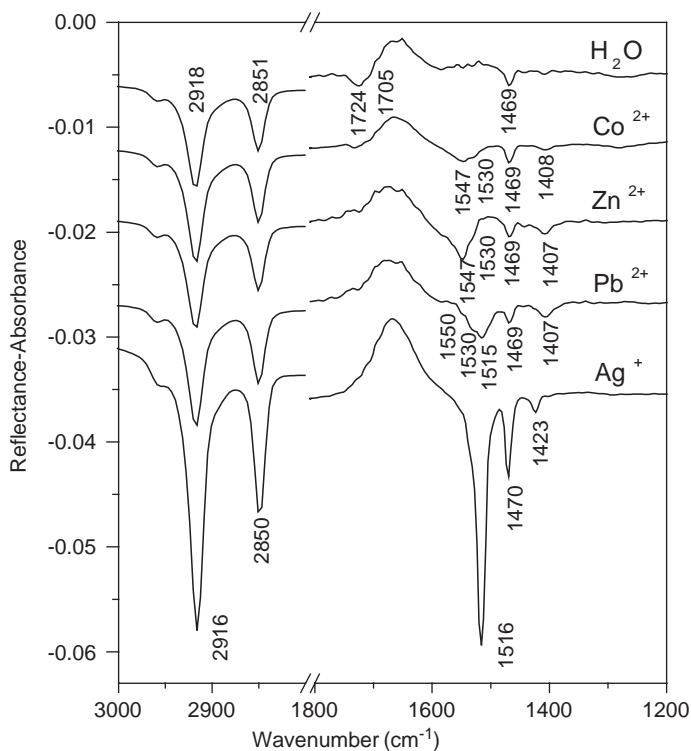


**Fig. 2.** IRRAS spectra of stearic acid monolayers on pure water and ion-containing subphases (1 mmol/L,  $\text{Ag}^+$ ,  $\text{Co}^{2+}$ ,  $\text{Zn}^{2+}$ , and  $\text{Pb}^{2+}$ ) at the surface pressure of 20 mN/m: angle of incidence,  $30^\circ$ ; p-polarization;  $22^\circ\text{C}$ . Reprinted with permission from Ref. [48]. Copyright 2006, American Institute of Physics.

interface. The results demonstrated that the liquid-expanded (LE) to liquid-condensed (LC) phase transition of DPPC monolayer is heterogeneous and biphasic in character, with coexistence of fluid and solid phase and involves a conformational change in the hydrocarbon chains of the monolayer as the average molecular area is decreased in the transition region. These trends are supported by the data for the other two monolayer films.

The study of the interaction of divalent cations with liposomes is of great interest, because a number of biological processes, such as membrane fusion, enzyme regulation, and signal transduction, are induced by the association of cations with negatively charged lipids of natural membranes [51–56].

The interaction of soluble cations with the phospholipid phosphate groups has been investigated on a mixture of DPPC and 1,2-dipalmitoyl-sn-glycero-3-phosphoserine DPPS as a function of surface pressure and  $\text{Ca}^{2+}$  ion presence [51]. The presence of  $\text{Ca}^{2+}$  in the subphase induce an acyl chain ordering at all surface pressures in both components of the binary mixture that was not observed in the case of pure DPPC alone. Unlike the bulk phase mixture of

DPPC–DPPS, the binary lipids in this mixed monolayer film appear to retain their miscibility in the presence of  $\text{Ca}^{2+}$ . Finally,  $\text{Ca}^{2+}$ -induced dehydration of the phosphate group was observed through characteristic frequency shifts in the asymmetric  $\text{PO}_2^-$  stretching mode.

The interaction of aqueous phospholipid dispersions of negatively charged 1,2-dimyristoyl-*sn*-glycero-3-phosphoglycerol, sodium salt (DMPG) with the divalent cations  $\text{Ca}^{2+}$ ,  $\text{Mg}^{2+}$ , and  $\text{Sr}^{2+}$  was investigated by IRRAS [56]. Fig. 3 shows the frequency of the maximum of the symmetric  $\text{CH}_2$  stretching bands  $\nu_s(\text{CH}_2)$  of DMPG and DMPG:divalent cation complexes as a function of temperature. The phase transition from the gel to the liquid crystalline phase is marked by an abrupt change in the frequencies of the  $\nu_s(\text{CH}_2)$  mode. The

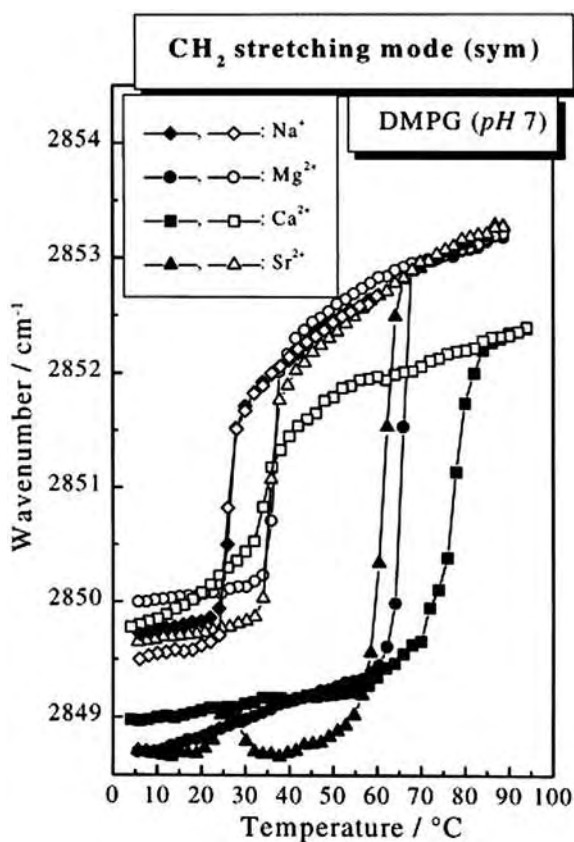


**Fig. 3.** Temperature dependence of the symmetric  $\text{CH}_2$  stretching mode frequency of DMPG: $\text{Na}^+$  (diamonds) and of the equimolar complexes DMPG: $\text{Mg}^{2+}$  (circles), DMPG: $\text{Ca}^{2+}$  (squares) and DMPG: $\text{Sr}^{2+}$  (triangles) in 100 mM NaCl at pH 7. Solid symbols represent the heating and open symbols the cooling scan. The samples were stored for 24 h at 4 °C prior to the first cycle. Reprinted with permission from Ref. [56]. Copyright (2000), Elsevier.

addition of divalent cations shifts the phase transition to higher temperatures. From Fig. 3 it can also be concluded that the binding of the cations to the lipid bilayer leads to an increase in conformational order of the hydrocarbon chains. Compared to free, uncomplexed DMPG, the frequencies of the  $\nu_s(\text{CH}_2)$  shifted to lower values, an indication for a tight packing of immobilized all-*trans* acyl chains.

The IRRAS results also suggest a deep penetration of the divalent cations into the polar head group region of DMPG bilayers, whereby the ester carbonyl groups, located in the interfacial region of the bilayers, are indirectly affected by strong hydrogen bonding of immobilized water molecules.

IRRAS was also used to provide straightforward information about structure and ionization state of the L-1,2-dipalmitoylphosphatidylglycerol (DPPG) monolayer [57]. Surface pressure–area isotherms of a DPPG monolayer on aqueous subphase with various pH values containing 0.01 M  $\text{K}^+$  are presented in Fig. 4. The shape of the isotherm depends strongly on the subphase pH. At pH 2, the DPPG monolayer is fully condensed and the molecules occupy the smallest area. Increasing pH shifts the isotherm to larger molecular areas and a plateau can be observed, which corresponds to the phase transition from the LE to an LC state.

Obviously, the ionization state of the phosphate group strongly influences the structure and phase state of the DPPG monolayer. The higher degree of ionization at higher pH values leads to increasing repulsion between lipid molecules and thus to a more expanded structure.

IRRAS in the region of phosphate stretching bands of the DPPG monolayer on subphase with various and constant ionic strength yield direct information about the protonation of the headgroup. The intensity of the negative

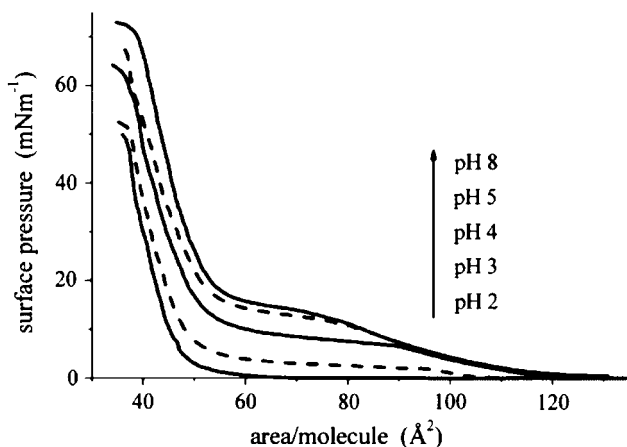


**Fig. 4.** Surface pressure–area isotherms of DPPG monolayers at 23 °C on subphases with various pH values in the presence of 0.01 M  $\text{K}^+$ . Taken from Ref. [57] with permission from American Chemical Society.

bands arising from  $\text{PO}_2^-$  stretching (asymmetrical  $1217\text{ cm}^{-1}$  and symmetrical  $1080\text{ cm}^{-1}$ ) and C–O–P–O–C stretching ( $1067\text{ cm}^{-1}$ ) increases with increasing pH. Moreover, the asymmetrical phosphate-stretching mode appears at smaller wavenumbers compared with other phospholipids. This can be explained by a better hydration or by involving the phosphate group of DPPG into hydrogen-bonding with the glycerol hydroxyl group of neighboring molecules [58].

### 2.2.3. Peptides and proteins

*The pulmonary surfactant system.* The next generation of IRRAS applications involved determination of peptide or protein secondary structure at the air–water interface [59,60]. IRRAS is currently the only physical method able to directly monitor peptide and protein secondary structure *in situ* in Langmuir films. Protein monolayers' study began in 1989 on the pulmonary surfactant system [29]. This lipid–protein mixture ( $\sim 90\%$  lipid and  $\sim 10\%$  protein by weight) exists *in vivo* as a monomolecular film that lowers surface tension, thus allowing normal breathing. A lot of attention has been paid on this system for the determination of the phospholipidic chain orientation and conformation and also for the determination of the secondary structure of its protein components (SP-B and SP-C) [61–63]. SP-B and SP-C are small hydrophobic proteins processed from large precursors that enhance the rate of adsorption of phospholipids from the subphase to the air–water interface and facilitate spreading across the interface [64]. The amide I and II regions for SP-C monolayer showed two peaks at  $1654$  and  $1542\text{ cm}^{-1}$ , respectively, and are characteristic of an  $\alpha$ -helical secondary structure [59]. Additional support of a helical structure of SP-C monolayer form comes from the relative sharpness of the amide I mode, which suggests a regular structure with minimal distortion from idealized geometry. The secondary structure of SP-B Langmuir film was also studied by IRRAS in the presence and absence of lipids under conditions of varying surface pressure [6,60]. The most striking behavior was a surface pressure induced conformational change in the peptide monolayer (from mixed helix/random to  $\beta$ -strands). This feature disappears when the film is re-expanded. Similar patterns are noted for the peptide in a mixed film with DPPC. Although the biological significance of this surface pressure induced reversible secondary structure change remains obscure, it is evident that IRRAS provided a unique means of studying this phenomenon.

In a recent research, effect of hydrophobic surfactant proteins SP-B and SP-C on binary phospholipid monolayers was studied by IRRAS [65]. The phospholipids examined were DPPC plus either DPPG or 1,2-dioleoyl-*sn*-glycero-3-phosphoglycerol (DOPG). IRRAS obtained at the air–water interface for a monolayer film of 7:1 DPPC-d62:DPPG plus 5 wt.% SP-B/C are shown in Fig. 5. Both C–H and C–D vibrational bands grow in intensity as the surface pressure increases and the surface density of the lipid molecules increases. As the average surface area per molecule is reduced, hydrophobic

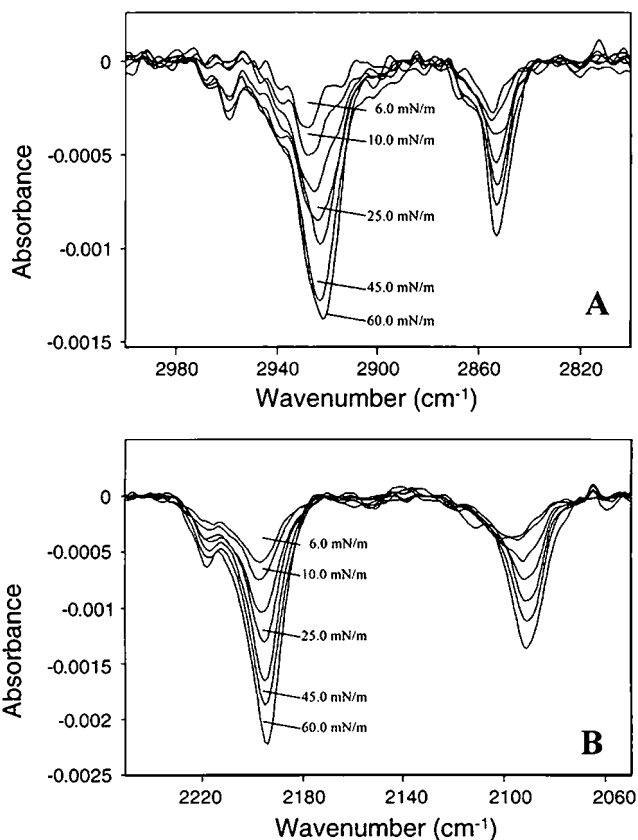


**Fig. 5.** IR external reflection absorption spectra of a 7:1 DPPC-d<sub>62</sub>:DPPG + 5 wt.% SP-B/C monolayer film collected at surface pressures from 6 to 60 mN/m. (A) CH<sub>2</sub> stretching region between 3000 and 2800 cm<sup>-1</sup>. (B) CD<sub>2</sub> stretching region between 2250 and 2050 cm<sup>-1</sup>. Taken from Ref. [65] with permission from Biophysical Society.

interactions predominate and the lipids begin to adopt a more ordered and condensed configuration because the CH<sub>2</sub> antisymmetric stretching band shifts to lower frequency. A close study of variations in wavenumber for the CH<sub>2</sub> antisymmetric stretching with different amount of SP-B/C reveals that the extent of this ordering depends on the amount of SP-B/C incorporated into the film, with the largest effect seen upon addition of the smallest amount of protein.

Deuteration of the DPPC acyl chains produces a shift in the vibrational bands to lower wavenumber values. The CD<sub>2</sub> vibrational modes exhibited similar behavior to the CH<sub>2</sub> modes: the wavenumber positions decreased as surface pressure increased. However, the addition of different amounts of SP-B/C had relatively little influence on the wavenumber or intensity of the CD<sub>2</sub> stretching bands.

Synthetic surfactant peptides based on patterns of structure or charge found in the human SP-B or SP-C appear to mimic some of the structural and functional properties of the native proteins and thus may offer a useful basis for the design of synthetic agents for therapeutic intervention [66]. Cochrane and Revak [67] suggested that the simple peptide KLLLLKLLLLKLLLLKLLLLK (KL<sub>4</sub>) with its pattern of five positively charged lysine residues interspaced with four leucines would be an effective therapeutic agent because it may mimic aspects of the positive charge and hydrophobic residue distribution in SP-B. As KL<sub>4</sub> has been used in clinical trials for pathological states of the lung in both animal models and in humans, it seemed of importance to determine the secondary structures of this peptide in monolayers at the air–water interface. Fig. 6 shows the IRRAS spectra in the region of 1550–1800 cm<sup>-1</sup> acquired from aqueous monolayers of DPPC containing KL<sub>4</sub> (20/1, lipid–peptide mol ratio) on D<sub>2</sub>O at several surface pressures ( $\pi$ ) [66].

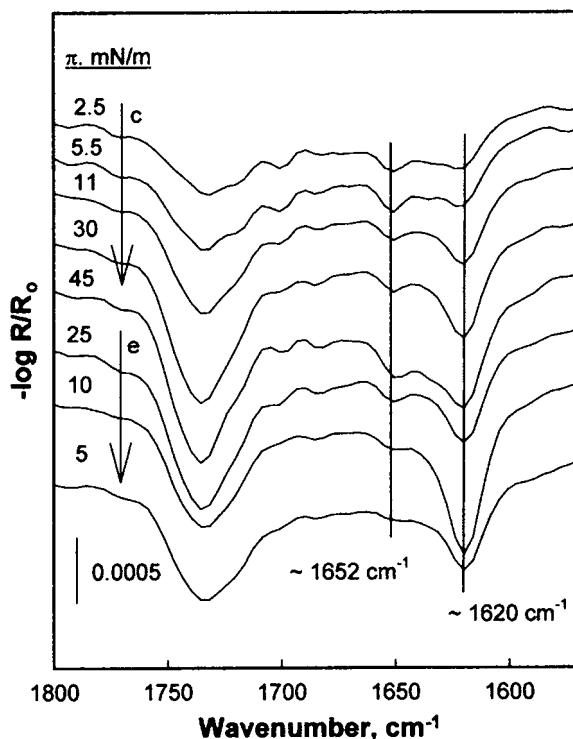


**Fig. 6.** IRRAS spectra of the lipid carbonyl and peptide amide I region (1550–1800 cm<sup>-1</sup>) for a mixed film of DPPC with 5 mol% KL<sub>4</sub> on a D<sub>2</sub>O subphase. Spectra were acquired using s-polarization, and surface pressure values are noted from top to bottom during compression (c) and expansion (e) of the film. The angle of incidence was 50°. Taken from Ref. [66] with permission from American Chemical Society.

The peak at  $1652\text{ cm}^{-1}$  was assigned to  $\alpha$ -helical secondary structure, while the major component near  $1620\text{ cm}^{-1}$  was assigned to antiparallel  $\beta$ -sheet. As the surface pressure is increased, the predominant secondary structure adopted by  $\text{KL}_4$  is that of an antiparallel  $\beta$ -sheet. This conformation is retained at physiologically relevant pressures ( $>40\text{ mN/m}$ ) [66].

The same authors also explore  $\text{KL}_4$  secondary structure in aqueous monolayers of DPPC/DPPG, and DPPG only. The secondary structure of the peptide is a function of lipid headgroup charge and surface pressure. Although in DPPC/DPPG mixtures, the peptide also adopted mainly antiparallel  $\beta$ -sheet structure, when DPPG/peptide film was spread at higher initial pressures, the  $\alpha$ -helical component was observed to be the most intense during the compression.

*Other IRRAS applications to peptides and proteins.* In addition to the pulmonary surfactant system, a variety of other applications employing IRRAS to study peptide and protein conformation and orientation have appeared. The secondary structure conversion of the amyloid (prion)-protein in the normal form into the abnormal form is the main cause of several human and animal diseases, such as Alzheimer's disease [68]. The secondary structure of the first 40 residues of the amyloid protein was detected by circular dichroism (CD) in aqueous solution and with IRRAS at the interface. A stable  $\beta$ -sheet-enriched state of the amyloid is formed at the air–water interface, in contrast to the initial bulk solution containing high  $\alpha$ -helix/random coil and low  $\beta$ -sheet parts. The change in the pH going from bulk (alkaline pH) to the interface (neutral or slightly acidic pH) can have effects on the conformation at the interface. Another alternative might be the intrinsic hydrophobicity of the air–water interface, which is a hydrophobic–hydrophilic system with air as the hydrophobic part.

IRRAS was also employed to determine the orientation of the peptide at the interface [69]. Spectra were acquired with p-polarized light at various angles of incidence (Fig. 7).  $\beta$ -Sheets split into two components: the transition dipole moment at  $1627\text{ cm}^{-1}$  is oriented along the plane of the interchain hydrogen bonds, perpendicular to the peptide chain, and the one at  $1690\text{ cm}^{-1}$  is oriented along the peptide chain [70]. The transition moment of amide II band is oriented along the peptide chain.

Simulations of amide bands for a  $\beta$ -sheet oriented parallel to the interface with different angles of incidence and use of p-polarized light are shown in Fig. 8. Comparison of measured and simulated spectra reveals that amyloid- $\beta$  ( $A\beta$ ) is lying almost flat at the air–water interface, although a slightly tilted conformation cannot be excluded.

Besides  $A\beta$ , other amphipathic model peptides are also studied using IRRAS. The linear sequence  $\text{KLAL}$  ( $\text{KLALKLALKALKLA-NH}_2$ ) is a model compound to form amphipathic helices, which is able to bind to membranes and to increase the membrane permeability in a structure and target-dependent manner [71,72]. Kerth et al. first studied the secondary structure of

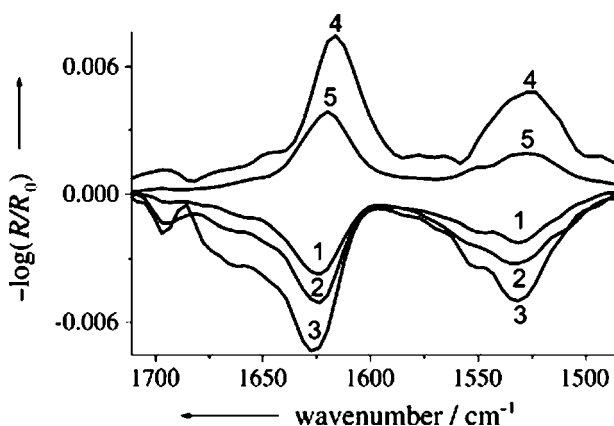


**Fig. 7.** IRRAS spectra of  $A\beta$  adsorbed at the air/buffer interface acquired with p-polarized light at various incident angles: (1)  $32^\circ$ , (2)  $40^\circ$ , (3)  $48^\circ$ , (4)  $56^\circ$ , (5)  $62^\circ$ . The surface pressure was 15 mN/m. Taken from Ref. [69] permission pending from Wiley Interscience Journals.

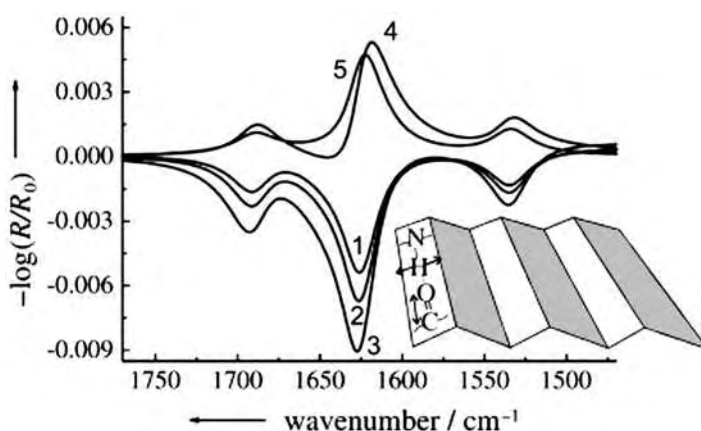


**Fig. 8.** Simulation of IRRAS spectra of a  $\beta$ -sheet lying flat at the air/buffer interface. The calculation was performed for p-polarized light and different incident angles: (1)  $32^\circ$ , (2)  $40^\circ$ , (3)  $48^\circ$ , (4)  $56^\circ$ , (5)  $62^\circ$  for the amide I bands at 1627 and 1690  $\text{cm}^{-1}$  and the amide II band at 1535  $\text{cm}^{-1}$ . Taken from Ref. [69] permission pending from Wiley Interscience Journals.

KLAL and its analogs bound to the air–water interface using IRRAS [72]. The  $\pi$ - $A$  isotherm of KLAL together with its IRRAS spectra are shown in Fig. 9. At large areas (position a) the surface pressure is nonzero, namely  $\sim 0.7$  mN/m. At this area, an  $\alpha$ -helical secondary structure of the peptide is observed because the amide I band is centered at  $\sim 1660$   $\text{cm}^{-1}$ . It is very interesting that a decrease

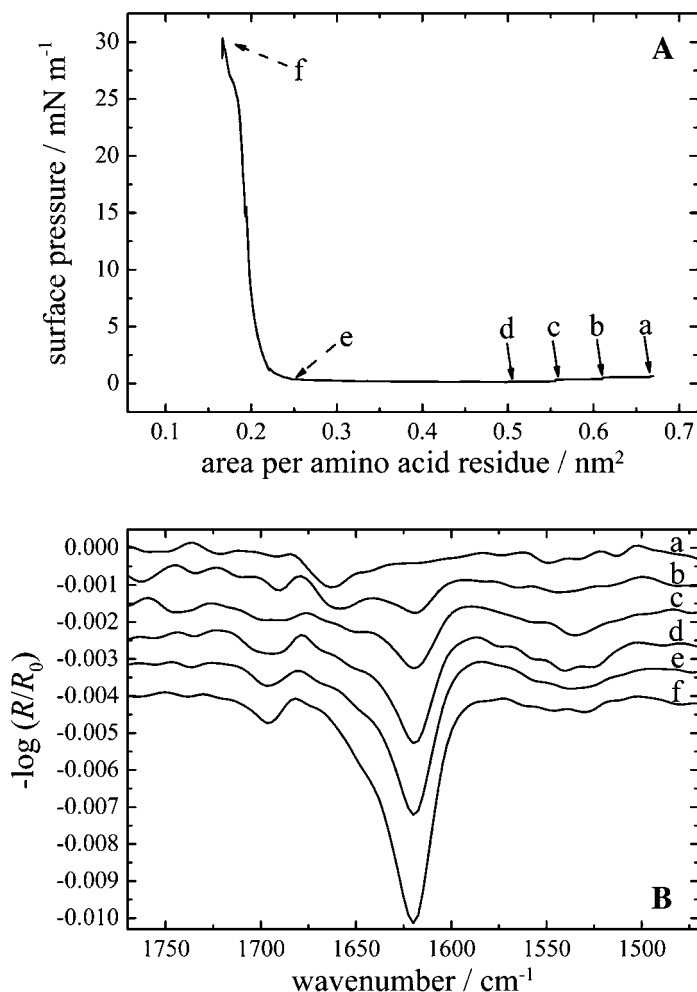


**Fig. 9.** (A) Surface pressure vs. area per amino acid residue of a KLAL film spread from an aqueous buffer solution. (B) IRRAS spectra of the KLAL film during the compression at the respective areas per amino acid residues at positions a–f of the surface pressure area curve in (A). The intensity of the spectra taken at positions e and f has been reduced by a factor of 2 for clarity. All spectra have been recorded at an angle of incidence of 40° and with p-polarized light. Taken from Ref. [72] with permission from Biophysical Society.

in surface pressure was observed when KLAL was compressed (from positions b to d). At the same time, the IRRAS spectra show the development of the amide I band at  $\sim 1620\text{ cm}^{-1}$ . The band at  $1660\text{ cm}^{-1}$  is reduced to a shoulder. Upon further compression, the intensity of the IRRAS bands at  $1695$  and  $1620\text{ cm}^{-1}$  associated to  $\beta$ -sheets increases, especially during the steep rise of the

surface pressure. Thus, the secondary structure of this peptide changes from random coil in solution to  $\alpha$ -helical after spreading at the air–water interface. The amphipathic  $\alpha$ -helical secondary structure is therefore energetically more favorable than the random coil when the peptide is located at the interface. However, this structure converts to intermolecular  $\beta$ -sheet with compression because of an energy gain [72].

IRRAS has also been used to probe protein–lipid interactions at the air–water interface [73–76]. The interaction of model proteins, lysozyme, and bovine and human serum albumins (BSA and HSA) with insoluble lipid layers has been investigated using both Langmuir trough arrangement and IRRAS [76]. Fig. 10(a) shows a series of spectra for the adsorption of lysozyme to a compressed stearic acid monolayer in its condensed phase ( $20 \text{ \AA}^2/\text{molecule}$ ). Fig. 10(b) reveals changes in intensity (peak area) of the major peaks as adsorption occurred. During adsorption the  $\text{CH}_2$  stretch peaks did not change, revealing that the presence of lysozyme did not significantly alter the stearic acid layer. The amide I peak at  $1650 \text{ cm}^{-1}$  increased in size during protein adsorption and shifted to slightly lower wavenumbers as the adsorption time increased. Such changes in peak shape appear to correspond to a reduction in  $\alpha$ -helix structure ( $1650 \text{ cm}^{-1}$ ) and a small increase in random coil structure ( $1640 \text{ cm}^{-1}$ ) [77]. However, the secondary structure of lysozyme will shift from  $\alpha$ -helix to predominantly  $\beta$ -sheet ( $1625 \text{ cm}^{-1}$ ) at the bare air–water interface [78]. This is a further evidence that adsorption of lysozyme to stearic acid monolayers is driven by a different interaction (electrostatic interactions between the negatively charged stearic acid head group and positively charged lysozyme) than adsorption to the bare air–water interface (hydrophobic interactions).

#### 2.2.4. Compensation of the water vapor vibration bands

The spectral region between  $1400$  and  $1800 \text{ cm}^{-1}$  is of importance for the investigation of biomolecules as it contains several conformation-sensitive bands, e.g., the amide I, amide II, carbonyl, and carboxylate vibrations [7]. Unfortunately, strong water vapor bands overlap the IRRAS in that region. An improvement in both S/N ratio and water vapor compensation has been obtained by Gericke et al. using fine regulation of the humidity in the sample compartment with a low flow of dry nitrogen in the chamber [79].

Mendelsohn and co-workers have proposed a new external reflection IR sampling accessory, which permits the acquisition of spectra from protein monolayers *in situ* at the air–water interface [59,80]. The accessory, a sample shuttle that permits its collection of spectra in alternating fashion from sample and background troughs, reduces interface from water vapor bands in the amide I and II regions of protein spectra by nearly an order of magnitude. The trough shown in Fig. 11 has the same feature, and permits subphase injection of aqueous solutions without disturbing a preexisting monolayer and inhibits the diffusion of

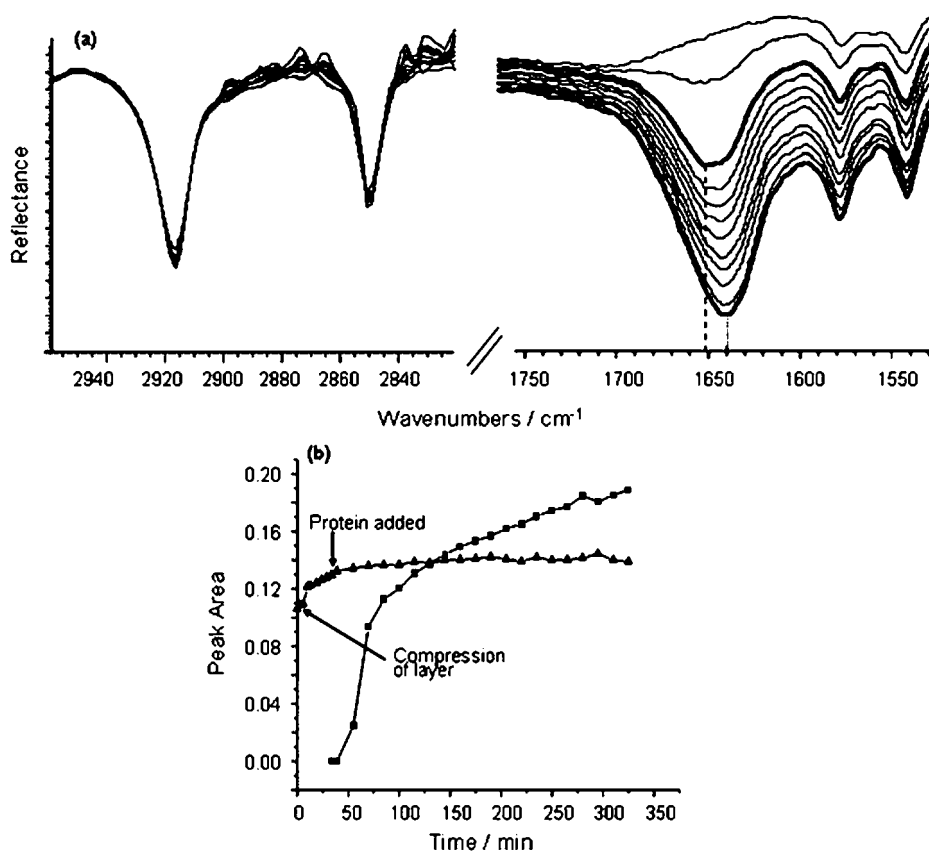


**Fig. 10.** External reflection FTIR spectra for lysozyme adsorption to stearic acid in its condensed phase state (at  $20 \text{ \AA}^2/\text{molecule}$ ). (a) The spectral regions corresponding to  $\text{CH}_2$  stretch vibrations ( $2820\text{--}2960 \text{ cm}^{-1}$ ) and the amide I vibration ( $1500\text{--}1750 \text{ cm}^{-1}$ ). (b) Peak area against time for  $\text{CH}_2$  asymmetric stretch (triangle) and the amide I stretch (square). Peak area was calculated between  $2940$  and  $2900 \text{ cm}^{-1}$  for the  $\text{CH}_2$  asymmetric stretch, and between  $1680$  and  $1600 \text{ cm}^{-1}$  for the amide I peak. Taken from Ref. [76] with permission from The Royal Society of Chemistry.

solutes to the background side of the trough [81,82]. The trough has two independently controlled barriers and a center divider, the top of which lies just beneath the water surface. Injections are made when the back barrier is positioned over the divider that leaves a small gap of  $\sim 0.25 \text{ mm}$ . This retards the rate of solute diffusion to the background side while maintaining an equal subphase height on either side of the barrier for acquisition of high-quality IRRAS spectra. In addition, to obtain more accurate spectra, these authors have used  $\text{D}_2\text{O}$  as the subphase [59]. However, this procedure is evidently risky due to the potential shift in the exchanged amide I mode of the  $\alpha$ -helix to a frequency overlapped with those of unordered structures.

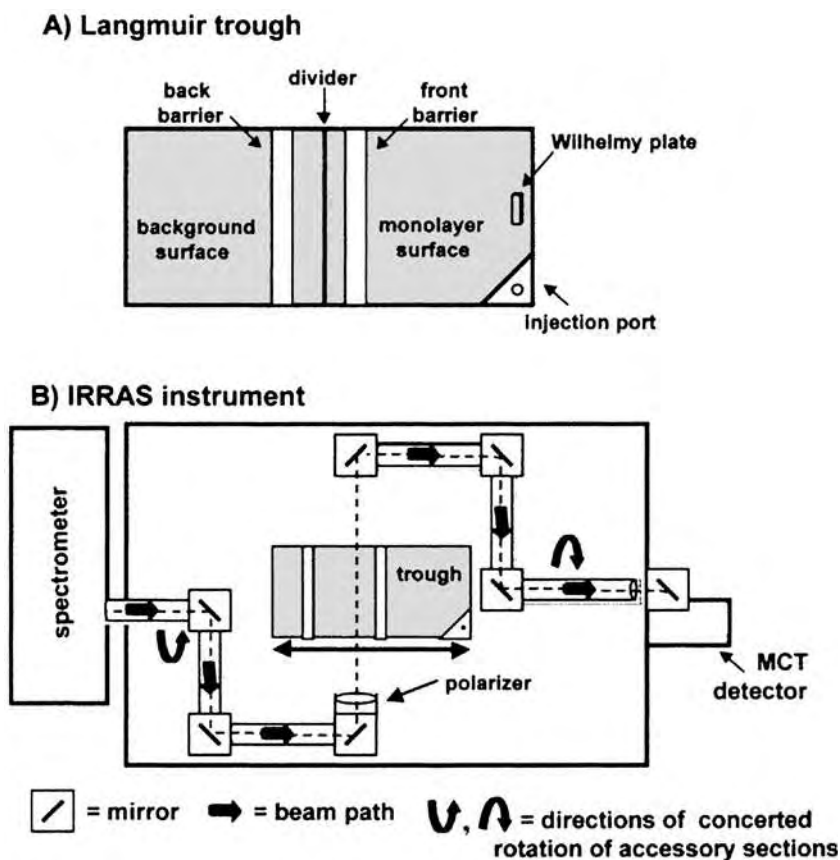


**Fig. 11.** (A) Design of the Langmuir trough used in the current studies. The trough is shuttled under computer control for IR illumination of the background surface and monolayer covered surface. (B) Schematic of the IRRAS instrument displaying the sections of the accessory that rotate in concert under computer control to provide the desired angle of incidence. Taken from Ref. [81] with permission from American Chemical Society.

### 3. POLARIZATION MODULATION REFLECTION ABSORPTION SPECTROSCOPY (PM-IRRAS) OF LANGMUIR FILMS

#### 3.1. Theory of PM-IRRAS on Dielectrics

As discussed above, the IRRAS method still lacks sensitivity for the study of a monolayer spread on water; it seems to necessitate running successive long-time accumulations of many interferograms with a covered and uncovered water surface. Moreover, the strong absorption of the water vapor hides the spectral region where the most interesting molecular information is. In order to

overcome most of the limitations of the IRRAS experiments, polarization modulation spectroscopy (PM-IRRAS) has been applied [83,84].

On a metallic substrate, PM increases the surface absorption detectivity of IRRAS by several orders of magnitude and provides high-quality monolayer spectra that can be quantitatively analyzed in terms of orientation and conformation of the surface molecules in a few minutes [85–88]. Moreover, due to the differential nature of the detected signal, these spectra are independent of the isotropic IR absorptions of the sample environment and water vapor interference is diminished. For these particular reasons, it appeared interesting to adapt PM-IRRAS method to the study of a monolayer spread at the air–water interface.

### 3.1.1. PM-IRRAS signal

Basically, in general PM-IRRAS experiment on any sample with polarized reflectances  $R_p$  and  $R_s$ , the signal at the detector output can be electronically split into a first part carrying only the intensity modulation induced by the moving mirror of the Fourier transform infrared (FTIR) spectrometer:

$$I_+ = C_+ \{ (R_p + R_s) + J_0(\phi_0)(R_p - R_s) \} I_0(\omega_i) \quad (1)$$

and a second

$$I_- = C_- \{ J_2(\phi_0)(R_p - R_s) \} I_0(\omega_i) \cos(2\omega_m t) \quad (2)$$

That in addition contains the PM induced by the photoelastic modulator [85,86].

After demodulation, the ratio of these two parts gives the so-called PM-IRRAS signal:

$$S = C \frac{J_2(\phi_0)(R_p - R_s)}{(R_p + R_s) + J_0(\phi_0)(R_p - R_s)} \quad (3)$$

where  $J_2$  and  $J_0$  are the second- and zero-order Bessel functions of the maximum dephasing  $\phi_0$  introduced by the photoelastic modulator, and  $C$  is a constant accounting for the different amplification of the two parts during the two-channel electronic processing [83,89].

To eliminate the Bessel function-type variations in the baseline, spectra data are plotted as  $(S - S_0)/S_0$ , where  $S$  and  $S_0$  are the polarization modulated reflectivities of the film-covered and film-free water surface.

### 3.1.2. Experimental setup

We already know that PM-IRRAS combines Fourier transform mid-IR reflection spectroscopy with fast PM of the incident beam (ideally between p- and s-linear states) and with two-channel electronic and mathematical processing of the detected signal in order to get a differential reflectivity spectrum:  $\Delta R/R = (R_p - R_s)/(R_p + R_s)$  [20].

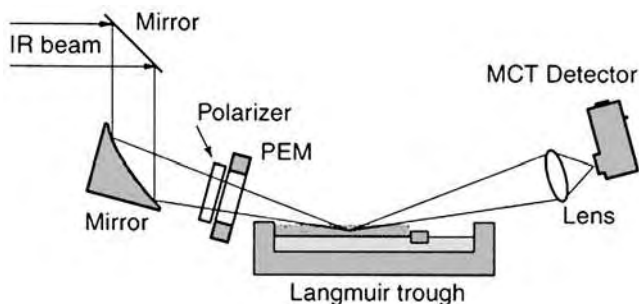


**Fig. 12.** Scheme of the PM-IRRAS setup at the air–water interface. Taken from Ref. [90] with permission from Biophysical Society.

The basic optical setup was shown in Fig. 12 [90]. The spectra were recorded on a commercially available spectrometer equipped with an external PM setup. The photoelastic modulator modulated the polarization of the IR light at a fixed frequency. Demodulation was performed with a lock-in amplifier and a low-pass filter. After the IR beam passes through the polarizer and modulator, it is focused on the sample, then focused on an mercury-cadmium-telluride (MCT) detector cooled by liquid nitrogen.

### 3.1.3. Optimization of the angle of incidence

Optimization of a PM-IRRAS experiment on a dielectric substrate covered with a monolayer having a thickness  $d$  can be made using the behavior of the difference PM-IRRAS signal vs. the angle of incidence:  $\Delta S = S(d) - S(0)$ .

Calculated behaviors of  $\Delta S$  vs. angle of incidence show that  $\Delta S$  values corresponding to ( $x$ ,  $y$ )- and ( $z$ )-oriented transition moments have opposite signs, which switch when the angle of incidence passes through the Brewster angle [20]. Consequently, ( $x$ ,  $y$ )- and ( $z$ )-oriented monolayer absorptions will always have opposite sign on the PM-IRRAS spectra relative to the uncovered substrate spectrum,  $S(0)$ . Additionally, as  $|\Delta S|$  is always larger for ( $x,y$ )-oriented moments than for ( $z$ )-oriented moments, detection of the in-plane monolayer absorption will be easier.

There are two angles of incidence ( $36^\circ$  and  $75^\circ$ ) that maximize the surface-absorption detection. Although these two maxima have theoretically almost the same absolute values, experimentally it was found that  $75^\circ$  is the more appropriate angle of incidence for both the S/N ratio and the sensitivity to the molecular anisotropy of the monolayer [20,83].

### 3.1.4. Surface selection rules of PM-IRRAS

Under the optimum incidence angle, the direction and the intensity of the bands on PM-IRRAS spectra are governed by a surface selection rule that depends on the orientation of the corresponding transition moment: a transition moment

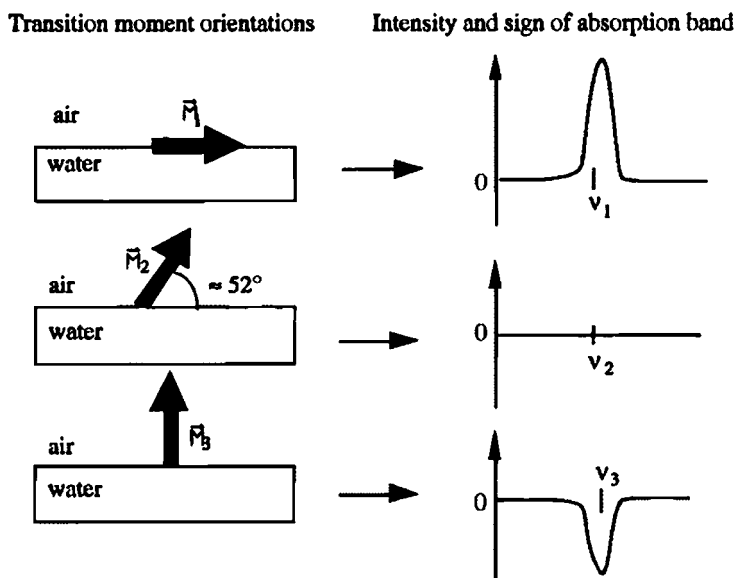


**Fig. 13.** Surface selection rules linking the transition moment orientation and the sign and intensity of the absorption band at the air–water interface. Taken from Ref. [91] with permission from American Chemical Society.

lying in the surface plane gives rise to an absorption band oriented positively with respect to the baseline while a transition moment perpendicular to the surface gives rise to an absorption band oriented negatively with respect to the baseline [91] (Fig. 13). Moreover, for an intermediate angle of about  $52^\circ$  between the transition moment and the surface, the band totally vanishes.

## 3.2. Applications

### 3.2.1. Fatty acids on subphase of different pH and cations

The applications of PM-IRRAS also include fatty acids, phospholipids, and protein conformations. Desbat and co-workers reported on the variation of the dissociation of a Langmuir monolayer of arachidic acid at the air–water interface as a function of the subphase pH and for several cations ( $\text{Cd}^{2+}$ ,  $\text{Ca}^{2+}$ ,  $\text{Mg}^{2+}$ , and  $\text{Na}^+$ ) with the help of the PM-IRRAS method [92]. Fig. 14 shows the PM-IRRAS spectra of Langmuir monolayer of deuterated arachidic acid in the presence of  $\text{CdCl}_2$  as a function of the subphase pH. At low subphase pH (pH = 3.5), the spectrum only presents absorption bands related to the acid form, i.e., the C = O stretching vibration ( $\nu(\text{C}=\text{O})$ ) and the OH bending ( $\delta(\text{O}-\text{H})$ ) located at  $1720$  and  $1270\text{ cm}^{-1}$ , respectively. The frequency position of the  $\nu(\text{C}=\text{O})$  is characteristic of a hydrogen-bonded carbonyl group. As the subphase pH is increased, the arachidic acid is progressively deprotonated to

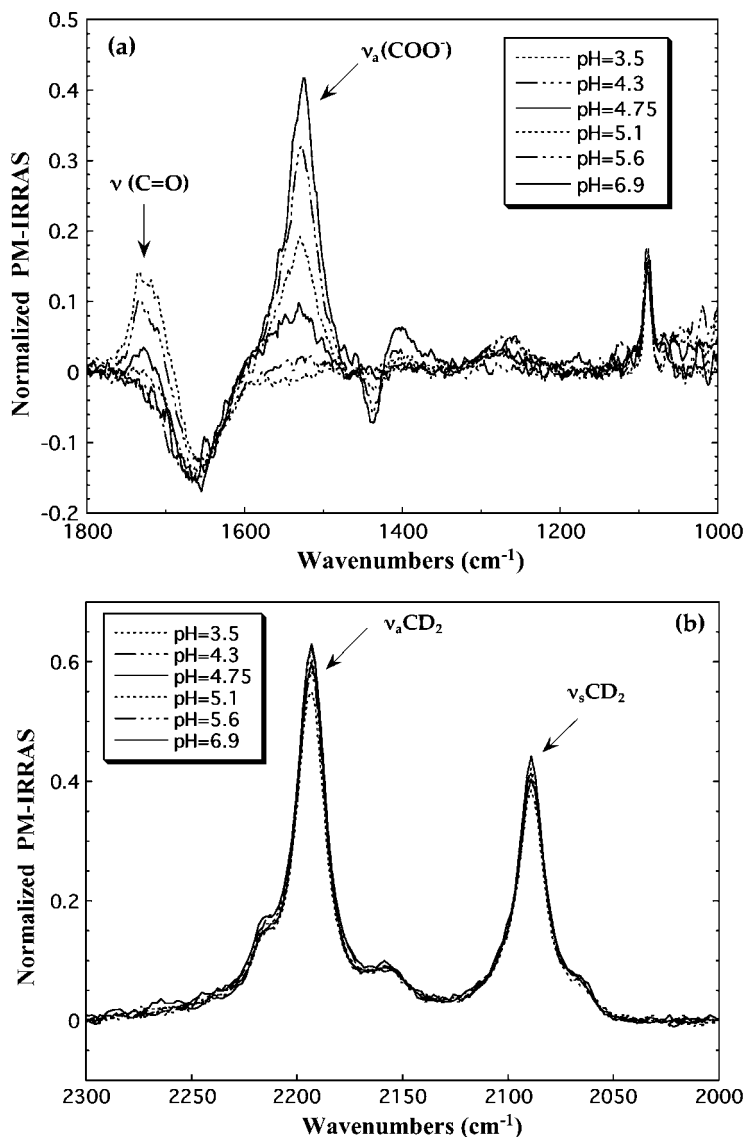


**Fig. 14.** Normalized PM-IRRAS spectra of a monolayer of deuterated arachidic acid spread onto a water subphase containing  $3.5 \times 10^{-3}$  M  $\text{CdCl}_2$  as a function of the subphase pH in the headgroups vibration range (a) and in the alkyl chains vibration range (b). Taken from Ref. [92] with permission from American Chemical Society.

give cadmium arachidate as indicated by the appearance and the increase in the carboxylate antisymmetric ( $\nu_a(\text{COO}^-)$ ) and symmetric ( $\nu_s(\text{COO}^-)$ ) bands, located at 1540 and 1415  $\text{cm}^{-1}$ , respectively. These bands are correlated with the decrease in the  $\nu(\text{C}=\text{O})$  and  $\delta(\text{O}-\text{H})$  bands. With the cadmium counterion,

a total deprotonation is achieved for a subphase pH of 6.9. The absorptions corresponding to the antisymmetric and symmetric stretching of the CD<sub>2</sub> groups, located at 2193 and 2089 cm<sup>-1</sup>, respectively, present intense and narrow bands that slightly decrease in intensity as the pH decreases (Fig. 14(B)). The observed frequencies are indicative of an almost all-*trans* conformation for the deuterated alkyl chains.

Möhwald and co-workers conducted similar research on arachidic acid monolayer on the subphase of different pHs in the presence of sodium ions [93]. The fitted peak intensities are related to surface concentrations of single and double hydrogen bonded and non-hydrogen bonded carbonyl and carboxylate. From the change of the concentrations with the pH, tentative conclusions are drawn on the bonding situation of fatty acids in monolayers on water and alkaline solution.

### 3.2.2. Hydrolysis reaction analysis of phospholipids

Phospholipase A<sub>2</sub> (PLA<sub>2</sub>) is a calcium-dependent enzyme, which exists extensively in organisms. It can stereoselectively hydrolyze the *sn*-2 ester linkage of enantiomeric L-phospholipids to release fatty acids and lysophospholipids [94]. The hydrolysis reaction of DPPC monolayers has been studied using PM-IRRAS [95,96]. Wang et al. used this technique to investigate the hydrolysis process of an L-DSPC monolayer at the air–water interface catalyzed by PLA<sub>2</sub> at different surface pressures [94]. Spectra changes of L-DSPC monolayers with reaction were recorded at different initial surface pressures and the results are presented in Fig. 15. At 40 mN/m (Fig. 15(a)), no change was observed, indicating that at such high surface pressure the hydrolysis reaction cannot occur. At 10 mN/m, the ester band intensity at 1734 cm<sup>-1</sup> decreases quickly within the first 30 min and the fatty acid bands increases correspondingly (Fig. 15(b)). It directly reflects the formation of hydrolysis products. Fig. 15(c) shows the obvious change of the spectra after the injection of enzyme into the subphase at 0.5 mN/m. Due to the fast reaction rate under this initial surface pressure, the monolayer can only be compressed to 10 mN/m for performing the PM-IRRAS measurements.

### 3.2.3. Enzymes and proteins

Since PM-IRRAS is insensitive to the strong IR absorption of water vapor, it has proved to be an efficient way to study the conformation and orientation of protein molecules because only important bands arising from the monolayer are observed [72,97–103]. The first *in situ* study of the protein conformation by PM-IRRAS technique was reported by Dziri et al. [97]. The vibrational spectrum of acetylcholinesterase (AChE) at the air–water interface in its free form and bound to either its substrate or organophosphorus (OP) inhibitor was measured. PM-IRRAS spectra collected during compression of the AChE

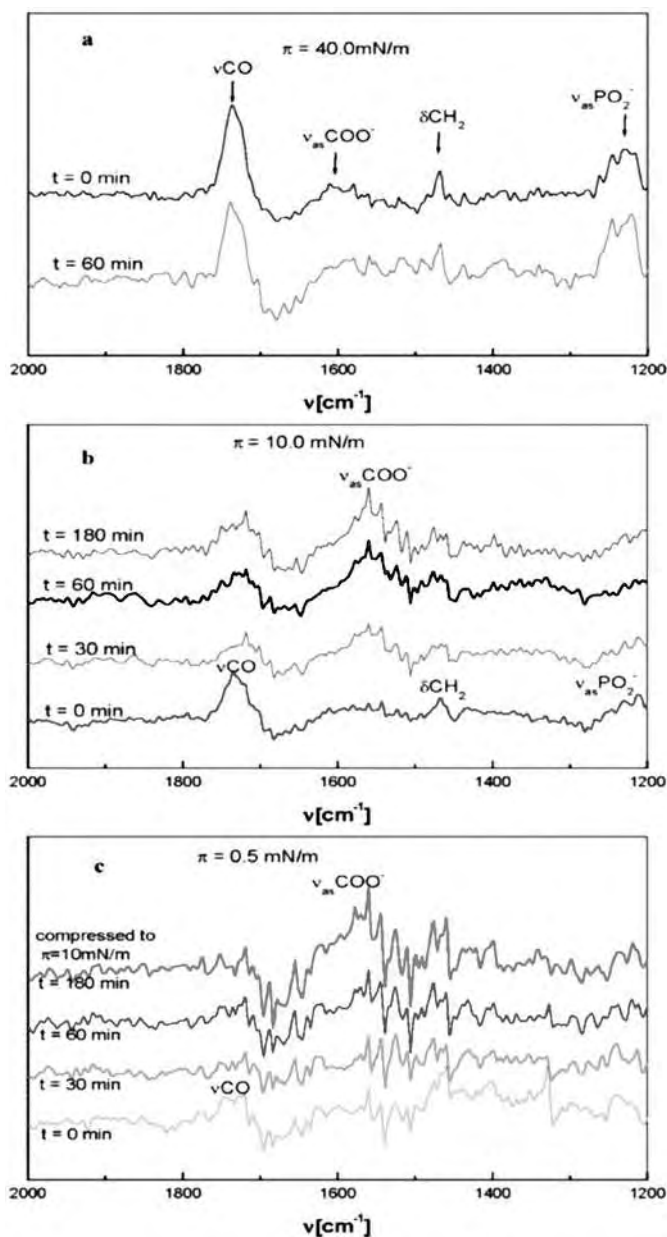


**Fig. 15.** PM-IRRAS spectra of L-DSPC monolayer hydrolysis by PLA<sub>2</sub> with the enzyme concentration in the subphase of 173 ng/mL. The surface pressures were kept at different initial surface pressure for the hydrolysis reaction. (a)  $\pi = 40 \text{ mN/m}$  and (b)  $\pi = 10 \text{ mN/m}$  for 180 min, respectively, and then the monolayer was compressed to  $\pi = 40 \text{ mN/m}$  for the PM-IRRAS measurements. (c)  $\pi = 0.5 \text{ mN/m}$  for the hydrolysis reaction of 180 min, and then the monolayer was compressed to  $\pi = 10 \text{ mN/m}$  for the PM-IRRAS measurements. Taken from Ref. [94] with permission from American Chemical Society.

monolayer are shown in Fig. 16. Careful examination of the amide I band revealed that AChE contained both  $\alpha$ -helix ( $1655, 1647\text{ cm}^{-1}$ ) and  $\beta$ -sheet ( $1630, 1696\text{ cm}^{-1}$ ). The measured secondary structure content indicated that the enzyme did not unfold for the surface pressure used. In all PM-IRRAS spectra, at low surface pressures ( $1\text{--}15\text{ mN/m}$ ), the  $\alpha$ -helix was dominant, whereas the  $\beta$ -sheet structure was less significant. At high surface pressure ( $20\text{--}35\text{ mN/m}$ ), the  $\beta$ -sheet became much more pronounced, whereas the  $\alpha$ -helix was shown only as a shoulder. A change in the orientation of the AChE secondary structure components occurred during the compression. In fact, at low surface pressure, the  $\alpha$ -helices were lying parallel to the water surface. Upon further compression, the tilt axis of the  $\alpha$ -helix relative to the water surface achieved a perpendicular orientation. Their PM-IRRAS results also show that the OP inhibitor, paraoxon, was observed to unfold the enzyme at the air–water

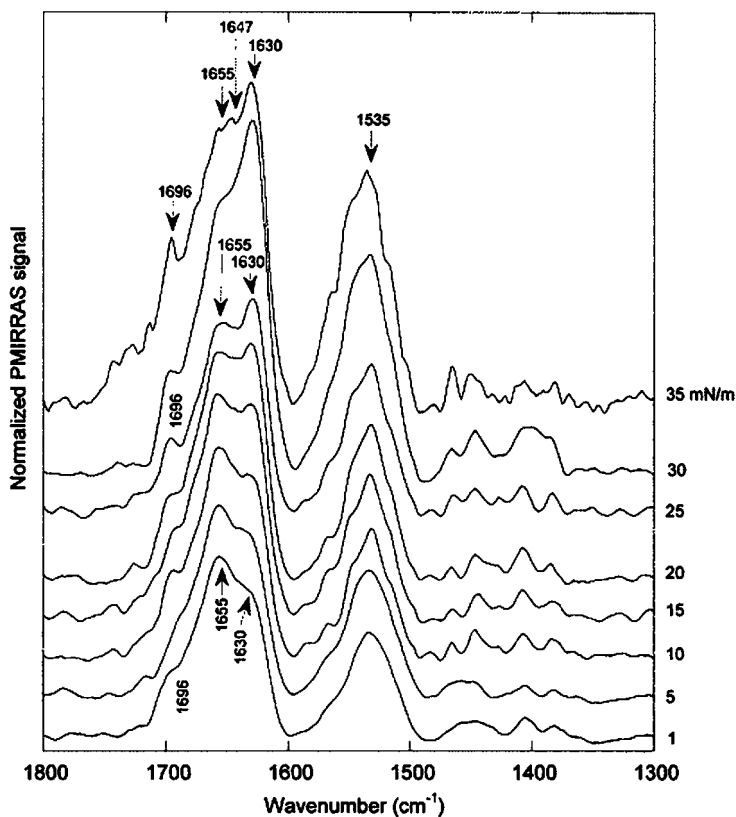


**Fig. 16.** Normalized PM-IRRAS spectra of AChE monolayer collected at the air–water interface at different surface pressures. The AChE solution was spread at zero surface pressure. Taken from Ref. [97] with permission from American Chemical Society.

interface because only high-frequency components associated with the extended conformation were observed upon compression.

Monomolecular films of the membrane protein rhodopsin have been investigated *in situ* at the air–water interface by PM-IRRAS and X-ray reflectivity in order to find conditions that retain the protein secondary structure [104]. The spreading of rhodopsin at 0 or 5 mN/m followed by a 30 min incubation time at 21 °C resulted in the unfolding of rhodopsin. In contrast, when spreading is performed at 5 or 10 mN/m followed by an immediate compression at, respectively, 4 or 21 °C, the secondary structure of the protein is retained.

### 3.2.4. Effect of $\alpha$ -helix orientation on amide I/II ratio and band position

To understand spectra in terms of  $\alpha$ -helix orientation relative to the water surface, the theoretical normalized PM-IRRAS signal was calculated for an anisotropic polypeptide monolayer, using a general software program [105]. The simulation was performed at different orientation angles of the  $\alpha$ -helix relative to the water surface [98,106]. When the helix axis is parallel to the interface these simulations give a strong positive amide I band and a weak positive amide

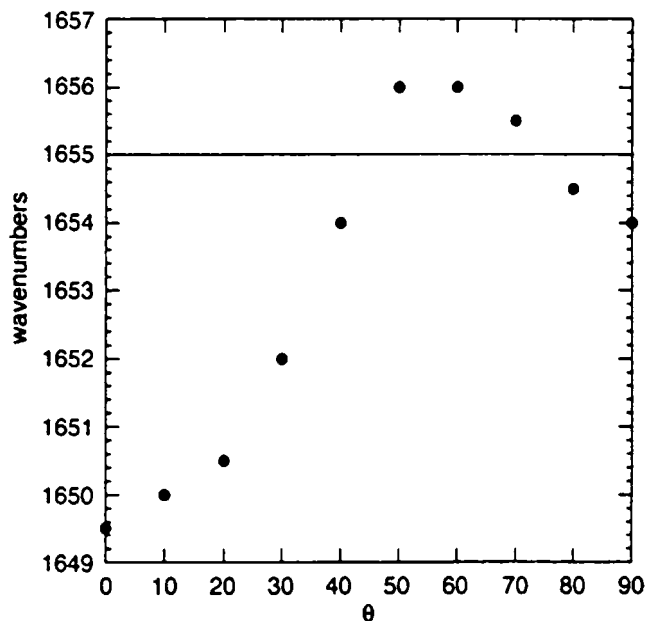


**Fig. 17.** Effect of the orientation of a helical structure on the position of the amide I band adapted from Cornut et al. [98]. Variation of the amide I band wavenumber maximum on the PM-IRRAS spectra as a function of the  $\theta$  tilt angle of the  $\alpha$ -helix is shown.  $\theta$  is the tilt angle between the helical axis and the normal to the interface. Taken from Ref. [107] with permission from American Chemical Society.

II band. Conversely, when the  $\alpha$ -helix is perpendicular to the interface, a negative strong amide I band and a strong positive amide II band are expected.

Fig. 17 shows the effects of the orientation of  $\alpha$ -helix structures on the position of the amide I band [107]. It is adapted from calculated spectra in the amide I and II regions for pure  $\alpha$ -helices when changing the tilt angle [98]. If the helix tilt angle is varied from  $0^\circ$  ( $\alpha$ -helix perpendicular to the interface) to  $90^\circ$  ( $\alpha$ -helix parallel to the interface), the amide I band position should shift from  $1656$  to  $1649\text{ cm}^{-1}$ . Therefore, changes in the orientation of  $\alpha$ -helix structure may cause the shift of the amide I band, as well as the intensity ratio of amide I and II.

The monolayer organization of intestinal alkaline phosphatase (AP), a glycosylphosphatidyl inositol (GPI) anchored dimeric protein (AP-GPI) was monitored using PM-IRRAS. Normalized PM-IRRAS spectra collected at different applied pressures are presented in Fig. 18. In this compression experiment, the  $\alpha$ -helix band is located at  $1655\text{ cm}^{-1}$  just after spreading and an overnight compression at  $20\text{ mN/m}$  (Fig. 18(a) and (e)); it is possible to suggest that the tilt angles of the helices are about  $45^\circ$  or about  $80^\circ$  [107].

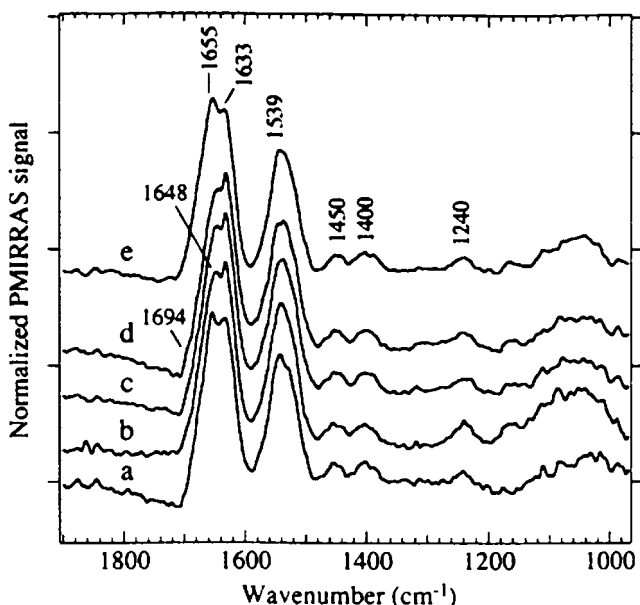


**Fig. 18.** Normalized PM-IRRAS spectra of native AP-GPI monolayers at the air/buffer interface. Initial surface pressure was at  $5\text{ mN/m}$ . Spectra were collected at a surface pressure of  $5$  (a),  $10$  (b),  $15$  (c), and  $20\text{ mN/m}$  (d), and after a standby period of one night at  $20\text{ mN/m}$  (e). Taken from Ref. [107] with permission from American Chemical Society.

## 4. CONCLUSION

IRRAS can provide information concerning conformation, tilt angle, and head group structure, as well as information about protein secondary structure and orientation. The technique in general can be extended by introducing the PM technique to the IRRAS experiment. It takes advantage of the great difference in the absorption of p- and s-polarized light at high angles of incidence. In particular, the sensitivity can be significantly increased. Both IRRAS and PM-IRRAS have proved to be a versatile and powerful technique for the spectroscopic characterization of biophysical monomolecular films at the air–water interface. Advances in instrumental design coupled with newly developed sampling methodology have enabled researchers to develop these techniques into methods with great sensitivity. This has allowed great insight into not only the study of monolayer structural and conformational analysis, but also the study of monolayer spatial and orientational analysis, which has led to increased insights into molecular organization in two dimensions.

### Acknowledgements

The preparation of this chapter was supported by the National Science Foundation (USA, CHE-0091390) and the U.S. Army Research Office (DAAD19-03-1-0131).

## REFERENCES

- [1] M. Milosevic, *Appl. Spectrosc. Rev.*, 39 (2004) 365.
- [2] R. A. Dluhy, *Appl. Spectrosc. Rev.*, 35 (2000) 315.
- [3] D. Blaudez, T. Buffeteau, B. Desbat, P. Fournier, A. M. Ritcey and M. Pezolet, *J. Phys. Chem. B*, 102 (1998) 99.
- [4] R. H. Tredgold, *Order in Thin Organic Films*, Cambridge University Press, Cambridge, 1994.
- [5] A. Ulman, *An Introduction to Ultrathin Organic Films*, Academic Press, San Diego, 1991.
- [6] R. Mendelsohn and C. R. Flach, *Curr. Top. Membr.*, 52 (2002) 57.
- [7] R. Mendelsohn, J. W. Brauner and A. Gericke, *Annu. Rev. Phys. Chem.*, 46 (1995) 305.
- [8] H. Mohwald, *Annu. Rev. Phys. Chem.*, 41 (1990) 441.
- [9] H. M. McConnell, *Annu. Rev. Phys. Chem.*, 42 (1991) 171.
- [10] X. J. Ji, C. S. Wang, J. M. Xu, J. Y. Zheng, K. M. Gattas-Asfura and R. M. Leblanc, *Langmuir*, 21 (2005) 5377.
- [11] K. M. Gattas-Asfura, C. A. Constantine, M. J. Lynn, D. A. Thimann and R. M. Leblanc, *J. Am. Chem. Soc.*, 127 (2005) 14640.
- [12] K. Hosoi, T. Ishikawa, A. Tomioka and K. Miyano, *Jpn. J. Appl. Phys.*, 32 (1993) L135.

- [13] D. K. Schwartz, R. Viswanathan, J. Garnæs and J. A. Zasadzinski, *J. Am. Chem. Soc.*, 115 (1993) 7374.
- [14] G. A. Overbeck, D. Honig and D. Mobius, *Thin Solid Films*, 242 (1994) 213.
- [15] X. H. Cao, S. V. Mello, G. D. Sui, M. Mabrouki and R. M. Leblanc, *Langmuir*, 18 (2002) 7616.
- [16] G. L. Gaines, Jr., *Insoluble Monolayers at Liquid-Gas Interfaces*, Wiley, New York, 1966.
- [17] C. S. Wang, C. Q. Li, X. J. Ji, J. Orbulescu, J. M. Xu and R. M. Leblanc, *Langmuir*, 22 (2006) 2200.
- [18] J. Y. Zheng, C. A. Constantine, L. Zhao, V. K. Rastogi, T. C. Cheng, J. J. DeFrank and R. M. Leblanc, *Biomacromolecules*, 6 (2005) 1555.
- [19] C. Q. Li, J. Orbulescu, G. D. Sui and R. M. Leblanc, *Langmuir*, 20 (2004) 8641.
- [20] D. Blaudez, J. M. Turllet, J. Dufourcq, D. Bard, T. Buffeteau and B. Desbat, *J. Chem. Soc., Faraday Trans.*, 92 (1996) 525.
- [21] D. Ducharme, J. J. Max, C. Salesse and R. M. Leblanc, *J. Phys. Chem.*, 94 (1990) 1925.
- [22] J. H. Hunt, P. Guyot-Sionnest and Y. R. Shen, *Chem. Phys. Lett.*, 133 (1987) 189.
- [23] R. A. Dluhy and D. G. Cornell, *J. Phys. Chem.*, 89 (1985) 3195.
- [24] R. A. Dluhy, *J. Phys. Chem.*, 90 (1986) 1373.
- [25] R. A. Dluhy, N. A. Wright and P. R. Griffiths, *Appl. Spectrosc.*, 42 (1988) 138.
- [26] M. L. Mitchell and R. A. Dluhy, *J. Am. Chem. Soc.*, 110 (1988) 712.
- [27] R. A. Dluhy, M. L. Mitchell, T. Pettenski and J. Beers, *Appl. Spectrosc.*, 42 (1988) 1289.
- [28] R. D. Hunt, M. L. Mitchell and R. A. Dluhy, *J. Mol. Struct.*, 214 (1989) 93.
- [29] R. A. Dluhy, K. E. Reilly, R. D. Hunt, M. L. Mitchell, A. J. Mautone and R. Mendelsohn, *Biophys. J.*, 56 (1989) 1173.
- [30] R. A. Dluhy, S. M. Stephens, S. Widayati and A. D. Williams, *Spectrochim. Acta, Part A*, 51 (1995) 1413.
- [31] J. A. Mann, *Langmuir*, 1 (1985) 10.
- [32] X. Du and Y. Liang, *J. Phys. Chem. B*, 108 (2004) 5666.
- [33] J. W. Brauner, C. R. Flach, Z. Xu, X. Bi, R. N. A. H. Lewis, R. N. McElhaney, A. Gericke and R. Mendelsohn, *J. Phys. Chem. B*, 107 (2003) 7202.
- [34] Y. Ren, K. I. Iimura and T. Kato, *Langmuir*, 17 (2001) 2688.
- [35] Y. Ren, K. I. Iimura and T. Kato, *Langmuir*, 18 (2002) 6699.
- [36] J. D. Swalen, J. F. Rabolt, J. R. Ferraro, L. J. Basile, (eds.), *Fourier Transform Infrared Spectroscopy. Application to Chemical Systems*, Vol. 4, Academic Press, New York, 1985.
- [37] D. L. Allara, A. Baca and C. A. Pryde, *Macromolecules*, 11 (1978) 1215.
- [38] D. L. Allara and R. G. Nuzzo, *Langmuir*, 1 (1985) 52.
- [39] D. Blaudez, T. Buffeteau, B. Desbat and J. M. Turllet, *Curr. Opin. Colloid Interface Sci.*, 4 (1999) 265.
- [40] H. A. Pearce and N. Sheppard, *Surface Sci.*, 59 (1976) 205.
- [41] T. Hasegawa, J. Umemura and T. Takenaka, *J. Phys. Chem.*, 97 (1993) 9009.
- [42] H. Brunner, U. Mayer and H. Hoffmann, *Appl. Spectrosc.*, 51 (1997) 209.
- [43] J. D. E. McIntyre, *Adv. Electrochem. Electrochem. Eng.*, 9 (1973) 61.
- [44] A. Gericke and H. Hühnerfuss, *J. Phys. Chem.*, 97 (1993) 12899.

- [45] J. Simon-Kutscher, A. Gericke and H. Hühnerfuss, *Langmuir*, 12 (1996) 1027.
- [46] A. Gericke and H. Hühnerfuss, *Thin Solid Films*, 245 (1994) 74.
- [47] V. Neumann, A. Gericke and H. Hühnerfuss, *Langmuir*, 11 (1995) 2206.
- [48] Y. C. Wang, X. Z. Du, L. Guo and H. J. Liu, *J. Chem. Phys.*, 124 (2006) 134706.
- [49] K. Nakamoto, *Infrared and Ramam Spectra of Inorganic and Coordination Compounds*, Wiley, New York, 1986.
- [50] J. E. Tackett, *Appl. Spectrosc.*, 43 (1989) 483.
- [51] C. R. Flach, J. W. Brauner and R. Mendelsohn, *Biophys. J.*, 65 (1993) 1994.
- [52] F. R. Poulain, S. Nir and S. Hawgood, *Biochim. Biophys. Acta*, 1278 (1996) 169.
- [53] V. Koppaka, J. F. Wang, M. Banerjee and B. R. Lentz, *Biochemistry*, 35 (1996) 7482.
- [54] D. Trommeshäuser and H. J. Galla, *Chem. Phys. Lipids*, 94 (1998) 81.
- [55] P. Mustonen, J. Y. A. Lehtonen and P. K. J. Kinnunen, *Biochemistry*, 37 (1998) 12051.
- [56] P. Garidel, A. Blume and W. Hübner, *Biochim. Biophys. Acta*, 1466 (2000) 245.
- [57] E. Maltseva, V. L. Shapovalov, H. Möhwald and G. Brezesinski, *J. Phys. Chem. B*, 110 (2006) 919.
- [58] Y. P. Zhang, R. Lewis and R. N. McElhaney, *Biophys. J.*, 72 (1997) 779.
- [59] C. R. Flach, J. W. Brauner, J. W. Taylor, R. C. Baldwin and R. Mendelsohn, *Biophys. J.*, 67 (1994) 402.
- [60] B. Pastrana-Rios, S. Taneva, K. M. W. Keough, A. J. Mautone and R. Mendelsohn, *Biophys. J.*, 69 (1995) 2531.
- [61] A. Gericke, C. R. Flach and R. Mendelsohn, *Biophys. J.*, 73 (1997) 492.
- [62] R. A. Dluhy, Z. Ping, K. Faucher and J. M. Brockman, *Thin Solid Films*, 327 (1998) 308.
- [63] B. Pastrana-Rios, A. J. Mautone and R. Mendelsohn, *Biochemistry*, 30 (1991) 10058.
- [64] X. H. Bi, C. R. Flach, J. Perez-Gil, I. Plasencia, D. Andreu, E. Oliveira and R. Mendelsohn, *Biochemistry*, 41 (2002) 8385.
- [65] J. M. Brockman, Z. D. Wang, R. H. Notter and R. A. Dluhy, *Biophys. J.*, 84 (2003) 326.
- [66] P. Cai, C. R. Flach and R. Mendelsohn, *Biochemistry*, 42 (2003) 9446.
- [67] C. G. Cochrane and S. D. Revak, *Science*, 254 (1991) 566.
- [68] St. B. Prusiner, *Science*, 278 (1997) 245.
- [69] E. Maltseva, A. Kerth, A. Blume, H. Möhwald and G. Brezesinski, *ChemBioChem*, 6 (2005) 1817.
- [70] Y. N. Chirgadze and N. A. Nevskaya, *Biopolymers*, 15 (1976) 607.
- [71] R. M. Epand and H. J. Vogel, *Biochim. Biophys. Acta*, 1462 (1999) 11.
- [72] A. Kerth, A. Erbe, M. Dtahe and A. Blume, *Biophys. J.*, 86 (2004) 3750.
- [73] J. Zhao, D. Vollhardt, G. Brezesinski, S. Siegel, J. Wu, J. B. Li and R. Miller, *Colloid Surf. A*, 171 (2000) 175.
- [74] J. B. Li, H. Chen, J. Wu, J. Zhao and J. Miller, *Colloid Surf. B*, 15 (1999) 289.
- [75] T. Lefevre and M. Subirade, *Int. J. Biol. Macromol.*, 28 (2000) 59.
- [76] M. D. Lad, F. Birembaut, R. A. Frazier and R. J. Green, *Phys. Chem. Chem. Phys.*, 7 (2005) 3478.
- [77] H. Z. Liu, W. J. Yang and J. Y. Chen, *Biochem. Eng. J.*, 2 (1998) 187.

- [78] C. Postel, O. Abillon and B. Desbat, *J. Colloid Interface Sci.*, 266 (2003) 74.
- [79] A. Gericke, A. V. Michailov and H. Hühnerfuss, *Vib. Spectrosc.*, 4 (1993) 335.
- [80] C. R. Flach, J. W. Brauner and R. Mendelsohn, *Appl. Spectrosc.*, 47 (1993) 982.
- [81] X. H. Bi, S. Taneva, K. M. W. Keough, R. Mendelsohn and C. R. Flach, *Biochemistry*, 40 (2001) 13659.
- [82] C. R. Flach, Z. Xu, X. Bi, J. W. Brauner and R. Mendelsohn, *Appl. Spectrosc.*, 55 (2001) 1060.
- [83] D. Blaudez, T. Buffeteau, J. C. Cornut, B. Desbat, N. Escafre, M. Pezolet and J. M. Turllet, *Appl. Spectrosc.*, 47 (1993) 869.
- [84] D. Blaudez, T. Buffeteau, J. C. Cornut, B. Desbat, N. Escafre and M. Pezolet, *Thin Solid Films*, 242 (1994) 146.
- [85] K. W. Hipps and G. A. Grosby, *J. Phys. Chem.*, 83 (1979) 555.
- [86] W. G. Golden, D. S. Dunn and J. J. Overend, *J. Catal.*, 71 (1981) 395.
- [87] W. G. Golden, *Fourier Transform Infrared Spectroscopy*, Academic Press, New York, 1985.
- [88] W. G. Golden, D. D. Saperstein, M. W. Severson and J. Overend, *J. Phys. Chem.*, 88 (1984) 574.
- [89] T. Buffeteau, B. Desbat and J. M. Turllet, *Appl. Spectrosc.*, 45 (1991) 380.
- [90] W. P. Ulrich and H. Vogel, *Biophys. J.*, 76 (1999) 1639.
- [91] S. Payan, B. Desbat, C. Destrade and H. T. Nguyen, *Langmuir*, 12 (1996) 6627.
- [92] E. L. Calvez, D. Blaudez, T. Buffeteau and B. Desbat, *Langmuir*, 17 (2001) 670.
- [93] R. Johann, D. Vollhardt and H. Möhwald, *Colloid Surf. A*, 182 (2001) 311.
- [94] X. L. Wang, S. P. Zheng, Q. He, G. Brezesinski, H. Möhwald and J. Li, *Langmuir*, 21 (2005) 1051.
- [95] U. Dahmen-Levison, G. Brezesinski, H. Möhwald, J. Jakob and P. Nuhn, *Angew. Chem. Int. Ed.*, 39 (2000) 2775.
- [96] U. Dahmen-Levison, G. Brezesinski and H. Möhwald, *Thin Solid Films*, 616 (1998) 327.
- [97] L. Dziri, B. Desbat and R. M. Leblanc, *J. Am. Chem. Soc.*, 121 (1999) 9618.
- [98] I. Cornut, B. Desbat, J. M. Turllet and J. Dufourcq, *Biophys. J.*, 70 (1996) 305.
- [99] S. Castano, B. Desbat, M. Laguerre and J. Dufourcq, *Biochim. Biophys. Acta*, 1416 (1999) 176.
- [100] O. Berdycheva, B. Desbat, M. Vaultier and M. Saint-Pierre-Chazalet, *Chem. Phys. Lipids*, 123 (2003) 1.
- [101] S. Shanmukh, N. Biswas, A. J. Waring, F. J. Walther, Z. D. Wang, Y. Chang, R. H. Notter and R. A. Dluhy, *Biophys. Chem.*, 113 (2005) 233.
- [102] S. Castano, D. Blaudez, B. Desbat, J. Dufourcq and H. Wróblewski, *Biochim. Biophys. Acta*, 1562 (2002) 45.
- [103] R. A. Dluhy, S. Shanmukh, J. B. Leopard, P. Krüger and J. E. Baatz, *Biophys. J.*, 85 (2003) 2417.
- [104] H. Lavoie, B. Desbat, D. Vakin and C. Salesse, *Biochemistry*, 41 (2002) 13424.
- [105] T. Buffeteau and B. Desbat, *Appl. Spectrosc.*, 43 (1989) 1027.
- [106] H. Lavoie, J. Gallant, M. Grandbois, D. Blaudez, B. Desbat, F. Boucher and C. Salesse, *Mater. Sci. Eng. C*, 10 (1999) 147.
- [107] F. Ronzon, B. Desbat, T. Buffeteau, C. Mingotaud, J. P. Chauvet and B. Roux, *J. Phys. Chem. B*, 106 (2002) 3307.

## Chapter 11

# Measurement of Complex Formation and Aggregation at the Liquid–Liquid Interface

Hitoshi Watarai\*

*Department of Chemistry, Graduate School of Science, Toyonaka 560-0043, Japan*

### 1. INTRODUCTION

The liquid–liquid interface formed between two immiscible liquids is an extremely thin mixed-liquid state with about one nanometer thickness, in which the properties such as cohesive energy density, electrical potential, dielectric constant, and viscosity are drastically changing from those of bulk phases. Solute molecules adsorbed at the interface can behave like a 2D gas, liquid, or solid depending on the interfacial pressure, or interfacial concentration. But microscopically, the interfacial molecules exhibit local inhomogeneity. Therefore, various specific chemical phenomena, which are rarely observed in bulk liquid phases, can be observed at liquid–liquid interfaces [1–3]. However, the nature of the liquid–liquid interface and its chemical function are still less understood. These situations are mainly due to the lack of experimental methods required for the determination of the chemical species adsorbed at the interface and for the measurement of chemical reaction rates at the interface [4,5]. Recently, some new methods were invented in our laboratory [6], which brought a breakthrough in the study of interfacial reactions.

Liquid–liquid systems have been most widely used in the solvent extraction of various compounds in chemical and hydrometallurgy industries. Kinetic process of solvent extraction of metal ions depends intrinsically on the mass transfer to or across the interface and the chemical reactions in both bulk phases and at the interface. Therefore, the study of the role of the interface is very

---

\*Corresponding author. E-mail: watarai@chem.sci.osaka-u.ac.jp

important to analyze the real extraction mechanism and to control the extraction kinetics. In the beginning of 1980s, the high-speed stirring (HSS) method was invented by Watarai and Freiser [7,8]. Thereafter, various new methods were made in our laboratory, which included the two-phase stopped flow method [9], the capillary plate method [10], the total internal reflection (TIR) spectrometry [11], the centrifugal liquid membrane (CLM) method [12], the two-phase sheath flow method [13], the CLM/Raman microscope spectrometry [14], the single molecule probing at the interface [15,16], the magnetophoretic velocimetry of microdroplets [17], the surface enhanced Raman scattering (SERS) of nanoparticles at the interface [18], the CLM/circular dichroism (CD) spectrometry [19], and the second harmonic generation/circular dichroism (SHG/CD) [20].

The most specific role of liquid–liquid interfaces in the solvent extraction kinetics of metal ions that we elucidated is a catalytic effect on the interfacial complexation kinetics [21]. Shaking or stirring of solvent extraction system generates a wide interfacial area or a high specific interfacial area defined as the interfacial area divided by a bulk phase volume. Almost all extractants, and an auxiliary ligand in some cases, are interfacially adsorbable more or less, since they have both hydrophilic and hydrophobic groups. Interfacial adsorption of the extractant or an intermediate complex at the liquid–liquid interface can facilitate the extraction rate extremely. Another specific role of the interfacial reaction is the formation of aggregates of various organic molecules or metal complexes, which results in characteristic spectral properties such as extremely large spectral shift and generation of optical chirality.

In this chapter, some useful measurement methods of the interfacial adsorption and interfacial reaction, which take place at the monolayer region of the liquid–liquid interface, are reviewed along with some essential examples.

## **2. MEASUREMENT OF LIQUID–LIQUID INTERFACE**

There are many classical methods to investigate the chemical reaction and kinetics at the liquid–liquid interface, which include a Lewis cell, a single drop method, and rotating disc method [22]. All of these methods however could not measure both the extraction rate and interfacial concentration of extractant, simultaneously. Modern experimental methods of interfacial reaction can determine the interfacial species, interfacial concentration, and interfacial chirality of an extractant or complex as a function of time.

### **2.1. High-Speed Stirring Method**

HSS method made it possible to measure both an interfacial concentration and an extraction rate for the first time by a simple principle. When a two-phase system is highly stirred or agitated in a vessel and the interfacial area is extremely extended, the interfacial amount of an adsorbed compound is increased

and then the bulk concentration in organic phase is decreased. The interfacial area can easily be increased as much as 500 times larger than that in a standing condition. The specific interfacial area in HSS condition can attain as high as  $400 \text{ cm}^{-1}$ . The saturated interfacial concentration of an ordinary compound is the order of  $10^{-10} \text{ mol/cm}^2$ . Therefore, when the agitated interface of 50 ml organic phase/50 ml aqueous phase is saturated by a compound, the total amount of the interfacial compound corresponds to 50 ml solution of  $10^{-4} \text{ M}$  concentration, which is ready to be detectable by a conventional spectrometry. In the original HSS method, the concentration decrease in the organic phase caused by an agitation was measured spectrophotometrically using a PTFE phase separator and a spectrophotometer. Furthermore, the extraction rate can also be measured by this method simultaneously [23]. A schematic drawing of the apparatus is shown in Fig. 1 with a schematic representation of a typical result. The measurements were carried out by employing 50 ml for each phase at the stirring speed of 5000 rpm in high-speed stirring condition and 200 rpm in a phase separation condition. The flow rate is 10–20 ml/min. The concentration change caused by the stirring speed change is attributable to the change of the total amount of the species adsorbed at the interface. The concentration change of the extracted complex or consumed ligand can be used for the kinetic analysis of the extraction or interfacial complexation. The HSS method is an indirect method; therefore direct spectroscopic observation is not possible. Nevertheless, this method is very useful for the determination of adsorptivity in a dilute concentration of weekly adsorbable molecules and the study of extraction kinetics, because of its high sensitivity [24].

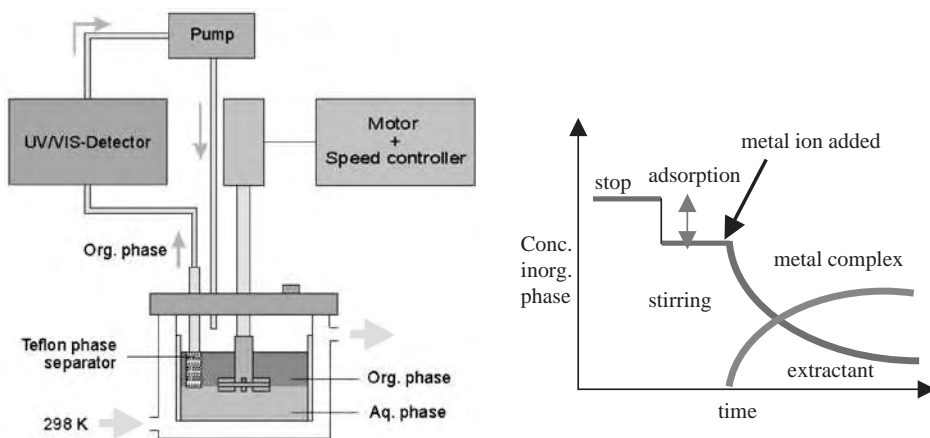


**Fig. 1.** Schematic drawing of the high-speed stirring (HSS) apparatus. The increase in the interfacial area by the stirring can increase the amount of the interfacial adsorbate, which results in the decrease in the organic phase concentration. The figure at the right is a schematic presentation of an observed result.

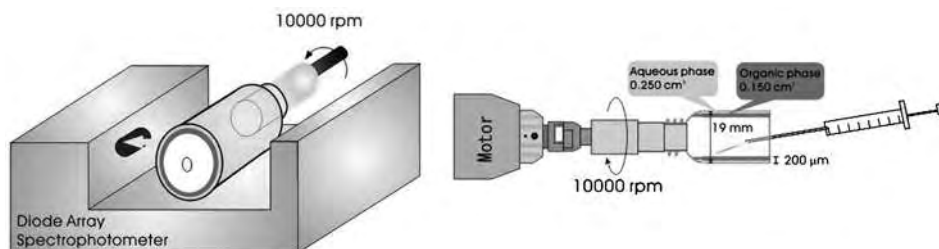


**Fig. 2.** Schematic diagram of the centrifugal liquid membrane (CLM) apparatus. The glass cylinder cell (i.d.: 19 mm) was rotated at a speed of 7000–10,000 rpm. Introduction of 50–200  $\mu\text{l}$  of the organic and the aqueous phase generated a two-liquid layer with a thickness of 50–100  $\mu\text{m}$  for each phase. Reagents can be injected from a small hole at the end side of the cell.

## 2.2. Centrifugal Liquid Membrane Method

Both requirements of a high specific interfacial area and a direct spectroscopic observation of the interface were attained by the CLM method shown in Fig. 2 [12]. Two-phase system containing about 100  $\mu\text{l}$  volumes of organic and aqueous phases is introduced into a cylindrical glass cell with a diameter of 19 mm. The cell is rotated at the speed of 7000–10,000 rpm. By this procedure, a stacked two-liquid membrane each with thickness of 50–100  $\mu\text{m}$  is produced inside the cell wall, which attains the specific interfacial area over  $100\text{ cm}^{-1}$ . UV-Vis spectrometry was used in the original work for the measurement of the interfacial species as well as those in the bulk phases. This method can be excellently applied for the measurement of interfacial reaction rate as fast as the order of seconds.

The study of interfacial aggregation also has been developed by this technique, since this method is very advantageous for measuring the formation of interfacial aggregates of dyes and metal complexes, which are formed only at the interface and usually exhibit unique spectral changes.

CLM method can also be combined with various kinds of spectroscopic methods. Fluorescence lifetime of an interfacially adsorbed zinc–tetraphenylporphyrin complex was observed by a nanosecond time-resolved laser induced fluorescence method [25]. Microscopic resonance Raman spectrometry was also combined with the CLM. This combination was highly advantageous to measure the concentration profile at the interface and a bulk phase [14]. Furthermore, circular dichroic spectra of the liquid–liquid interface in the CLM could be measured [19].

## 2.3. Two-Phase Stopped Flow Method

Analogous to the stopped flow method used in studies of solution kinetics, rapid stopped flow mixing of organic and aqueous phases is an effective way to produce dispersed condition within a few milliseconds. The specific interfacial

area of the dispersion attained as high as  $700 \text{ cm}^{-1}$  and the interfacial reaction in the dispersed system can be measured by photodiode array spectrophotometer during the period of ca. 200 ms up to the time when the dispersion system starts to separate. This method is applicable for rather fast interfacial reactions such as diffusion rate limiting reactions as observed in the protonation reaction of tetraphenylporphyrin (TPP) at dodecane–acid interface [9].

## 2.4. Interfacial Reflection Spectrometry

By the TIR condition at the liquid–liquid interface, one can observe interfacial reaction in the evanescent layer with a thickness of ca. 100 nm calculated by

$$d = \frac{\lambda}{4\pi\sqrt{(n_1^2\sin^2\theta_1 - n_2^2)}} \quad (1)$$

where  $d$  is the penetration depth,  $\lambda$  the wavelength of the beam irradiated to the interface from phase 1 to phase 2,  $n_1$  and  $n_2$  the refractive indexes of phase 1 and phase 2 ( $n_1 > n_2$ ) and  $\theta_1$  the incident angle, which is set larger than the critical angle  $\theta_c$  ( $= \sin^{-1}(n_2/n_1)$ ).

Fluorometry is the most sensitive method for detection of interfacial species and its dynamics [26]. Time-resolved laser spectrofluorometry is a powerful tool for the elucidation of rapid dynamic phenomena at the interface [27]. Time-resolved total reflection fluorometry can be used for the evaluation of rotational relaxation time of octadecylrhodamin B and thus the viscosity of the interface [28]. Laser excitation can produce excited states of the adsorbed compound at the interface. As an example, the decay of the triplet state of porphyrine was observed at the interface [29].

In the case that an organic phase contains light absorbing compounds, an external reflection (ER) absorption spectrometry is more useful than a TIR spectrometry [30,31]. Another advantage of the ER method is its higher sensitivity than the TIR method, especially as using s-polarized light. Therefore, it can be used as a universal absorption spectrometry of adsorbed species. Typical optical cells used for the TIR spectrometry and ER absorption spectrometry are shown in Fig. 3.

## 2.5. Micro-Two-Phase Sheath Flow Method

The measurement of fast chemical reactions at the liquid–liquid interface is very difficult, since the reaction which starts just after the contact of two phases has to be measured. The dead time of the HSS method was several seconds and that of the two-phase stopped flow method was from few tenth millisecond to several hundred milliseconds. The micro-two-phase sheath flow method is the only method that can measure such fast interfacial reactions, which finish within  $100 \mu\text{s}$ . An inner organic microflow was generated in an outer aqueous phase

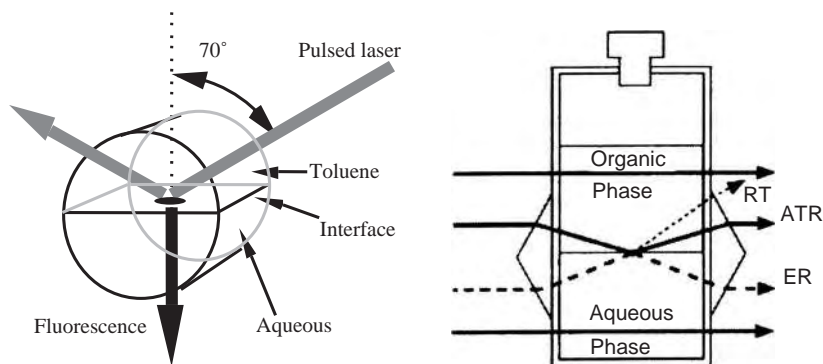


**Fig. 3.** Total internal reflection cell used for the interfacial fluorescence lifetime measurement (left) and the external reflection absorption spectrometry (right).

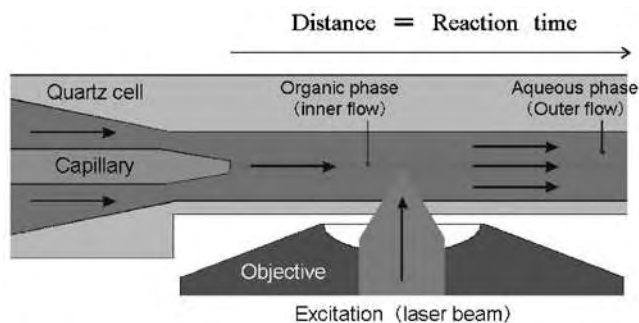


**Fig. 4.** Schematic drawing of the laser fluorescence microscopy method for the measurement of fast interfacial reactions in micro-two-phase sheath flow systems.

flow from the tip of a capillary (i.d.  $10\ \mu\text{m}$ ) with the same linear velocity (Fig. 4). The fluorescence spectrum at the interface was observed as a function of the distance from the tip of the inner capillary, which was the starting point of the reaction. The distance from the tip was converted to the reaction time. Thus, a very fast interfacial or diffusion reaction (less than 1 ms) could be measured. This technique enabled the detection of a fast interfacial reaction of the order of  $10\ \mu\text{s}$ . This technique is analogous to the continuous-flow method developed for a homogeneous fast reaction [32].

The schematic drawing of the microsheat flow system combined with a laser-induced fluorescence measurement is shown in Fig. 5. The fast complexation rate of Zn(II) ion with 8-quinolinol (Hqn) or 5-octyloxymethyl-8-quinolinol (Hocqn) at the 1-butanol–water interface was measured by the micro-two-phase sheath flow method [33]. The diffusion length of Hocqn in the 1-butanol phase for 2 ms was calculated as  $0.8\ \mu\text{m}$ , which is smaller than the experimental resolution depth of  $2\ \mu\text{m}$  in the microscopy used. Therefore, the observed rate

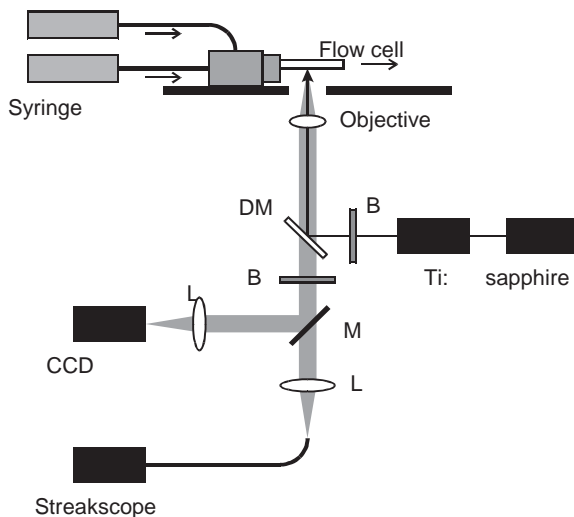


**Fig. 5.** Schematic drawing of the microsheath flow apparatus combined with two-photon excitation fluorescence microscopy. DM: dichroic mirror; BF: barrier filter; M: mirror changing light path; and L: lens for bearing images.

constant was analyzed by taking diffusion and reaction rates into account between Zn(II) and Hocqn at the interfacial region by a digital simulation method [34]. The rate of the lactone cleavage reaction of octadecylrhodamine B ( $C_{18}RB$ ) was investigated with the micro-two-phase sheath flow/two-photon excitation microscopy. The formation of the fluorescent forms of  $C_{18}RB$  was confirmed from the two-photon excitation fluorescence spectra at the toluene–water and heptane–water interface during  $80\ \mu\text{s}$  after the contact of two phases. The rate of the lactone cleavage was measured successfully and analyzed with the digital simulation of the time-dependent Langmuir adsorption model. The lactone cleavage rate constants were determined as  $(1.6 \pm 0.3) \times 10^7\ \text{mol}^{-1}\ \text{dm}^{-3}\ \text{s}^{-1}$  at toluene–water interface and  $(8.6 \pm 5.0) \times 10^7\ \text{mol}^{-1}\ \text{dm}^{-3}\ \text{s}^{-1}$  at heptane–water interface, respectively [35]. This method was applied for the measurement of luminescence lifetime of samarium(III) complex with 2-thenoyltrifluoroacetone and the synergic extraction rate at the interface [36].

## 2.6. Raman Spectroscopy of the Interface

Raman scattering spectrometry has some advantages over an infrared (IR) spectrometry in the sensitivity, the space resolution, and the applicability to aqueous solution. It can attain high sensitivity, when it is performed under the resonance Raman condition, or under the surface enhanced condition, where silver or gold nanoparticle is used as a source of plasmon. These techniques have been applied successfully for the measurement of extremely small amount of molecules adsorbed at the liquid–liquid interfacial region.

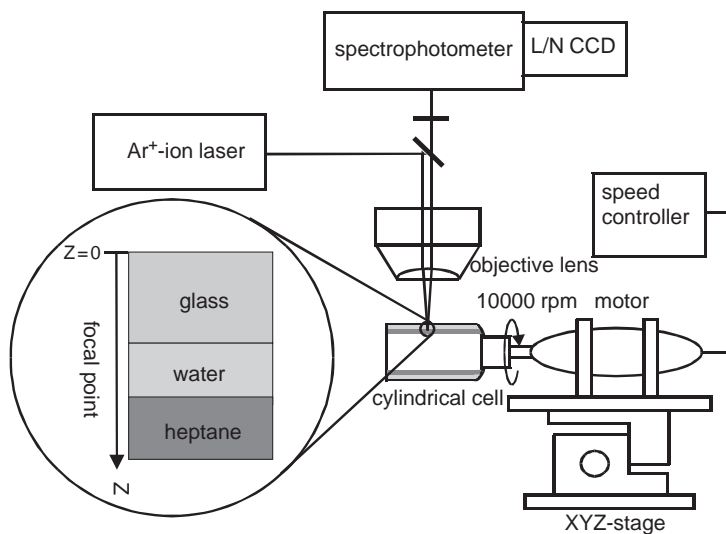


**Fig. 6.** Schematic drawing of the apparatus for the centrifugal liquid membrane-resonance Raman microprobe spectroscopy.

### 2.6.1. CLM/Raman microscope spectrometry

The combination of resonance Raman microscope spectrometry and the CLM method allowed us to directly observe the Raman spectra of the liquid–liquid interface and the bulk phases by shifting the focal point of an objective lens. A schematic diagram of the measurement system is shown in Fig. 6. CLM/Raman microscope spectrometry was applied in order to measure the rate of complex formation between Pd(II) and 5-Br-PADAP (HL) at the heptane–water interface and it was demonstrated that this method was highly useful for the kinetic measurement of the interfacial reaction [37].

Fig. 7 shows 3D spectra depicting the formation of interfacial complex of PdLCl. Raman intensities at 1599, 1408, and 1303  $\text{cm}^{-1}$  assigned to PdLCl clearly increased at the interface with increasing reaction time. The initial rate of complexation of Pd(II) with 5-Br-PADAP at the interface obtained from the Raman intensity change was in good agreement with that obtained from the absorbance change observed by CLM spectrophotometry. Furthermore, the resonance Raman spectra of the interfacial PdLCl provided the information on the nanoenvironment of the complex. The resonance Raman spectra of PdLCl adsorbed at the heptane–water and toluene–water interfaces were not in agreement with those in toluene and chloroform with the lower dielectric constants, but close to those in alcohol and aqueous alcohol-mixed solvents with the higher dielectric constants.

These results suggested that the PdLCl complex at the interface partially contacted water molecules. The solvent effect on the resonance Raman spectra

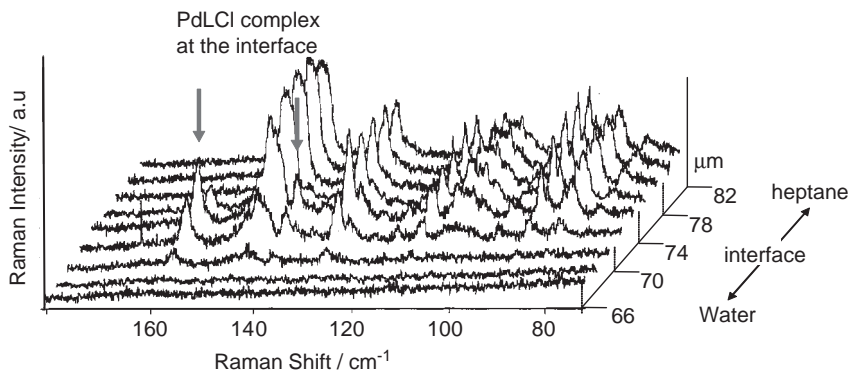


**Fig. 7.** 3D CLM/Raman spectra depicting the formation of interfacial complex of PdLCl.

of PdLCl reflected a change in the ratio of the azo and imine resonance structures. The bands at 1482, 1463, 1307, and 1284  $\text{cm}^{-1}$  were assigned to  $\nu(\text{C}=\text{C})$  of pyridine ring in the azo form, imine  $\nu(\text{CNNC})$ , azo  $\nu(\text{CNNC})$ , and imine  $\nu(\text{CNNC})$ , respectively. The azo–imine intensity ratios of  $I_{1482}/I_{1463}$  at 1482 and 1463  $\text{cm}^{-1}$  and  $I_{1307}/I_{1284}$  at 1307 and 1284  $\text{cm}^{-1}$  both increased with a decrease in the dielectric constant of the solvent. The values of  $I_{1482}/I_{1463}$  and  $I_{1307}/I_{1284}$  in the resonance Raman spectra of PdLCl adsorbed at the toluene–water interface were 0.63 and 1.47, respectively, and those of PdLCl complex formed at the heptane–water interface were 0.86 and 1.85, respectively [38].

### 2.6.2. SERS of nanoparticles at the interface

Nanosized silver colloids have been used as substrates of SERS, surface plasmon resonance (SPR), scanning near-field optical microscopy (SNOM), nanoelectrodes, photolithographic tools, and so on. In the SERS measurements, its high signal intensity compared to the ordinary Raman scattering by a factor of over  $10^5$  enables the characterization of the trace amount of molecules adsorbed to the silver surface. The resonance Raman condition, which can also attain a high signal enhancement, adds significant increase in the SERS measurement, provided that the plasmon peak wavelength is agreed with the excitation wavelength. Using this advantage, the Raman spectra of single molecule [39] or a monolayer of the nonresonant molecules [40] have been measured by SERS method. Another unique feature of SERS is to enhance the only molecules that are adsorbed at or are in contact with the silver surface. This results in the high spatial selectivity of SERS, which can overcome the optical resolution restricted by the light wavelength.

Applications of SERS for the detection of molecules at the liquid–liquid interface have not been carried out. The liquid–liquid interface has been studied

as a model of biomembrane and as an important reaction field in the solvent extraction of metal ions. For this importance, a detailed understanding of the molecular structure of the adsorbate and the solvent molecules is highly required. However, it is difficult to obtain the vibrational spectra of the adsorbate or solvent molecules at the liquid–liquid interface, because only small amounts of the molecules exist at the interface. Therefore, SERS method will make it possible to detect the interfacial molecules and to get valuable insight on the interfacial species

SERS from oleate-stabilized silver colloids, with 5 nm in diameter, adsorbed at the toluene–water interface was measured in TIR condition as depicted in Fig. 8 [41]. Based on the electromagnetic enhancement mechanism of SERS, it was concluded that the oleate molecules would be adsorbed to the silver surface through carboxylate group in the organic phase side and with ethylene group in the aqueous phase side at the liquid–liquid interfacial region. The SERS shifts of the adsorbed toluene were same with those in bulk toluene, but the relative intensities were reduced. This result suggested that the interaction between toluene molecules and silver surface was weak, though the adsorbed toluene was stimulated enough by the local electromagnetic field. The liquid–liquid interface is advantageous to make 2D assembly of metal nanoparticles, which is required for SERS method. Thus, it will be applicable to detect extremely small amount of molecules adsorbed at the liquid–liquid interface, though the molecules are adsorbed finally at the metal surface.

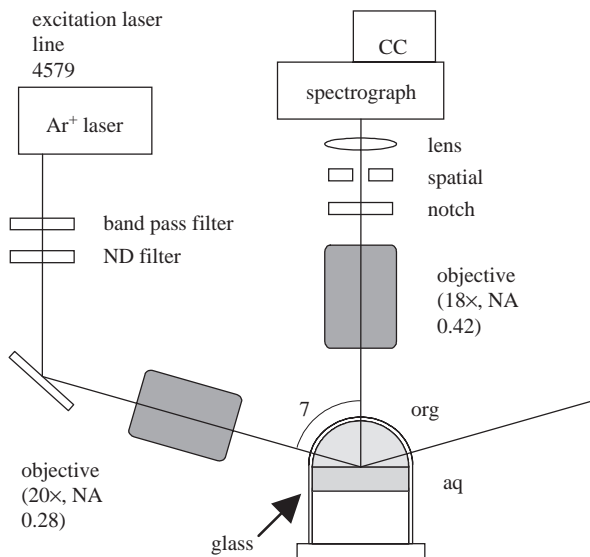


**Fig. 8.** Raman microscope for the measurement of SERS spectra of liquid–liquid interface; organic phase 250  $\mu$ l and aqueous phase 250  $\mu$ l.

## 2.7. Optical Chirality Measurement of the Interface

Optical chirality of molecules is a characteristic measure of stereo-chemical property of biological, pharmaceutical, and metal coordination compounds. Chiral structures of amino acids, proteins, DNAs, and various drugs in solutions have been determined from the measurement of circular dichroism (CD). However, small amount of molecules at the liquid–liquid interfaces has never been measured before CLM/CD method [19] and SHG/CD method have been reported [20].

### 2.7.1. CLM/circular dichroism (CD) spectrometry

The CLM cell was combined with the CD spectropolarimeter to measure the CD spectra of the liquid–liquid interface. The setup of the CLM cell in the cell compartment of a CD polarimeter is almost same with the CLM/UV-Vis spectrometry shown in Fig. 2. CLM cell whose height and outer diameter were 3.3 and 2.1 cm, respectively, was fixed horizontally in the sample room of CD spectropolarimeter. By this technique, the CD spectra of the aggregate of TPP diacid was observed; 4 M  $\text{H}_2\text{SO}_4$  0.500  $\text{cm}^3$  and toluene 0.300  $\text{cm}^3$  (blank) were put into the cylindrical cell through a sample inlet hole (2 mm in diameter) at the bottom of the cylindrical cell. Then the cylindrical cell was rotated at about 7000 rpm by the high-speed motor fixed on XZ-stage with a speed controller. After the blank was measured, TPP toluene solution (0.100  $\text{cm}^3$ ) was injected rapidly by a microsyringe from the hole at the bottom to initiate the aggregation of TPP. TPP monomer in toluene shows the Soret band at 419 nm and Q band at 515 nm. Two red shifted bands at 473 and 720 nm corresponding to the interfacial J-aggregate of diprotonated TPP ( $(\text{H}_4\text{TPP}^{2+})_n$ ) were observed. Diprotonated TPP ( $\text{H}_4\text{TPP}^{2+}$ ), whose absorption maximum is 438.0 nm, was not clearly observed, because it was ready to aggregate at the interface. The bisignate CD band centered at 473 nm was observed as shown in Fig. 9, which is a characteristic spectrum of the exciton coupling, corresponding to the J-band in the absorption spectrum. Bulk TPP monomer does not affect CD spectra [19]. By this study, it was demonstrated for the first time that the convenient CD spectroscopy with CLM method was effective for the measurement of the interfacial chiral species. From the CD spectrum, the diacid TPP J-aggregate was thought to have a helical structure. This method can be applied to any optical active species formed at the liquid–liquid interface. Applications of the CLM/CD for biomolecules such as proteins and DNA will be interesting subject.

### 2.7.2. Second harmonic generation-circular dichroism

Most selective technique to measure the optical chirality at the interface will be the SHG/CD spectroscopy, as demonstrated by a pioneering work of Hicks and

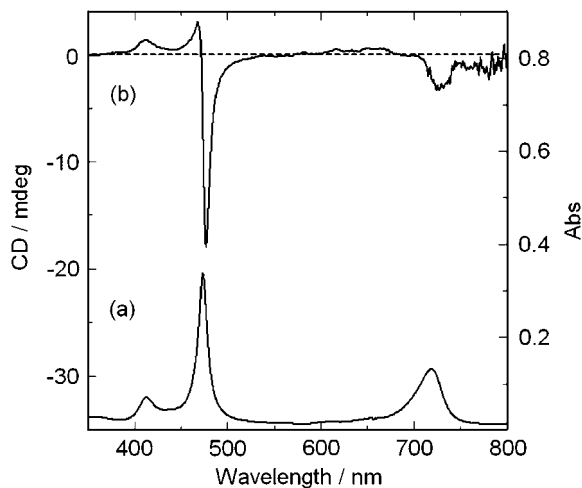


**Fig. 9.** (a) Absorption and (b) CD spectra of the diacid TPP species in the toluene/4 M sulfuric acid system measured with CLM method. Initial concentration of TPP is  $1.0 \times 10^{-5}$  mol/dm<sup>3</sup> in toluene.

co-workers [42,43]. SHG is advantageous to other spectroscopic techniques in its inherent high interfacial selectivity due to the second order nonlinear susceptibility and in its high sensitivity afforded by the resonance effect in an adsorbed dye molecule [44,45]. Therefore, SHG spectroscopy can provide specific information relating to the electronic state of dye molecules, which are present only at the interface. SHG spectroscopy has been utilized to study solvation [46] and aggregation [47] of dye molecules at the electrochemical liquid–liquid interfaces. Recently, the nonlinear optical activity of originally chiral molecules adsorbed at various interfaces has been observed by means of SHG/CD [48,49]. However, the nonlinear optical activity of the liquid–liquid interface adsorbed by an aggregate of achiral molecules was not investigated before our work.

The apparatus used in our SHG experiments included a Ti:sapphire laser (80 MHz, 100 fs, tuning range of 780–920 nm) and a photon counter as shown in Fig. 10. An angle of the linearly polarized fundamental beam was adjusted by an achromatic half waveplate and employing an achromatic quarter waveplate generated a circularly polarized fundamental beam. All SHG spectra were acquired in TIR condition with the incident angle of  $74.1^\circ$ , and the beam spot of the fundamental beam at the interface was ca. 2.0 mm. For the SHG measurements, the heptane–water interface was formed in a rectangular optical quartz cell with an area of  $2.0 \times 1.0$  cm<sup>2</sup>. The first measurement of the nonlinear chirality of J-aggregate formed from the achiral H<sub>4</sub>TPPS<sup>2-</sup> and cetyltrimethylammonium (CTA<sup>+</sup>) surfactant was observed at the heptane–water interface by the *in situ* SHG polarization spectroscopy (Fig. 11).

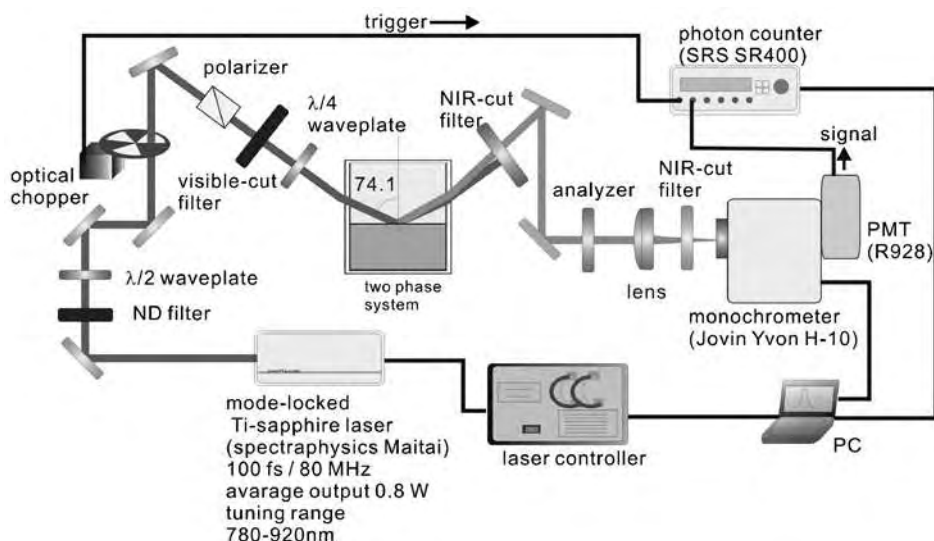
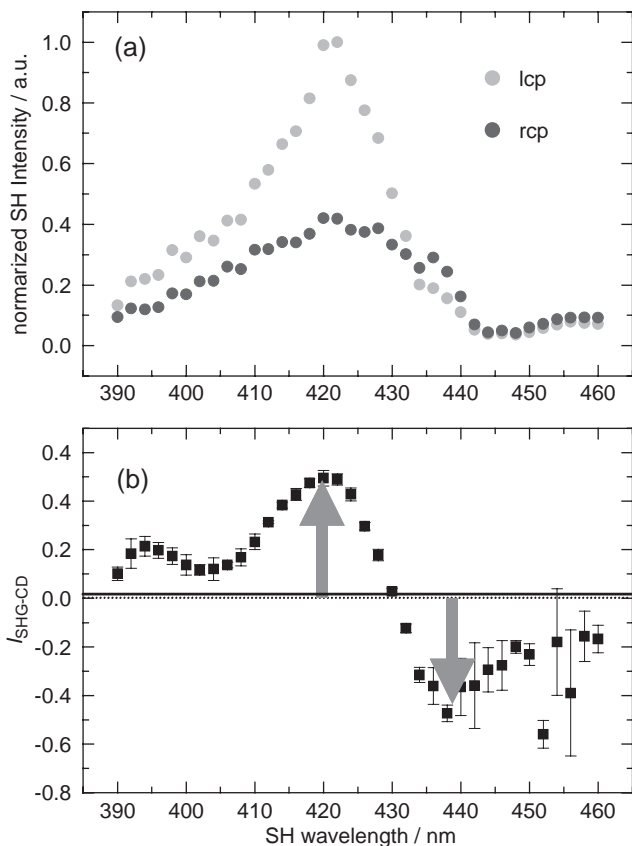


Fig. 10. Schematic representation of SHG/CD measurement system.

## 2.8. Single Molecule Probing at the Interface

A single molecule probing is an ultimate method for measuring the behavior of molecules and the properties of the nanoenvironment at the liquid–liquid interface. A number of studies on single molecule detection in solutions [50–52] and at the solid–liquid interface [53–55] were reported, but there were no studies on single molecule detection at the liquid–liquid interface. The first observation of the single molecule detection at the liquid interface has been accomplished by means of the TIR fluorescence microscopy [15,16]. Fig. 12 shows the optical arrangement of the measurement method and the microcell. The apparatus consisted of an inverted microscope, an oil immersion objective (PlanApo 60 $\times$ , NA 1.4, working distance 0.21 mm), a cw-Nd:YAG laser (532 nm), and an avalanche photodiode detector (APD), which provided a quantum efficiency of about 65–67% at 570–600 nm. A pinhole, 50  $\mu\text{m}$  in diameter, was attached just in front of the photodiode, restricting the observation area to a diameter of 830 nm ( $d_{\text{obs}}$ ). p-Polarized laser light was irradiated at an angle of incidence 73 $^\circ$  from the interface, which was larger than the critical angle. Fluorescence emitted by interfacial molecules was collected by the objective lens and focused on the pinhole after passing through a band pass filter (path range, 587.5–612.5 nm). Time-resolved photon counting was carried out using a multichannel scalar. The overall detection efficiency of fluorescence at the interface was calculated to be 3.3%.

A demonstration of the single molecule detection at the liquid–liquid interface was reported for the fluorescent probe of 1,1'-dioctadecyl-3,3,3',3'-tetramethylindocarbocyanine (DiI), which is a monovalent cation with two C<sub>18</sub> alkyl chains. Thus, it has high adsorptivity at the dodecane–water interface.



**Fig. 11.** (a) s-Polarization analyzed SHG spectrum of adsorbed TPPS at the heptane–water interface. lcp: left-circularly polarized fundamental beam. rcp: right-circularly polarized fundamental beam. (b) SHG/CD spectrum of adsorbed TPPS at the heptane–water interface. Aqueous phase was containing  $5.35 \times 10^{-7}$  M TPPS,  $3.36 \times 10^{-7}$  M CTAB, 0.001 M HCl (pH 3.0), and 0.009 M NaCl.

Aqueous phase ( $2.7 \text{ mm}^3$ ) was placed in the thin lower compartment of the microcell and the DiI dodecane solution ( $63 \text{ mm}^3$ ) was added on top of the aqueous layer. Fluorescence of the interfacial DiI was observed in the range of 571–575 nm. The influence of two kinds of surfactants, sodium dodecyl sulfate (SDS) and dimyristoyl phosphatidylcholine (DMPC), on the lateral diffusion dynamics of single molecules at the interface was investigated. DMPC was dissolved in chloroform, and the solution was mixed with pure diethyl ether at a ratio of 1:19 (chloroform:diethyl ether) by volume. Pure water was placed in the lower container, and the DMPC solution was subsequently ( $5 \text{ mm}^3$ ) spread carefully on the water. After evaporation of chloroform and diethyl ether, the DiI dodecane solution was added on the DMPC layer. Since DiI has a high

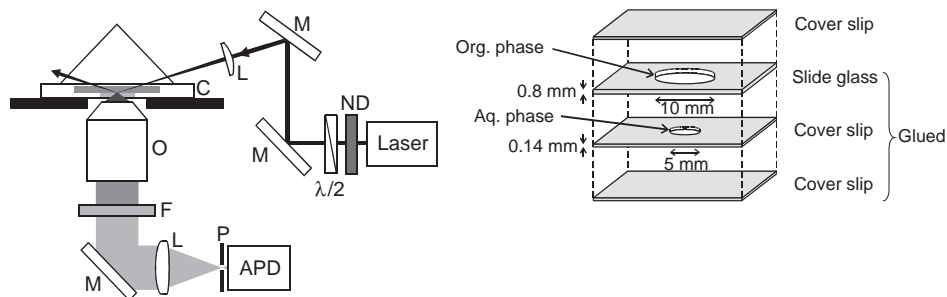


**Fig. 12.** The figure at the left is the schematic illustration of laser induced total internal reflection fluorescence microscopy for the single molecule detection at the liquid–liquid interface. Abbreviations: ND: ND filter,  $\lambda/2$ :  $\lambda/2$  plate, M: mirror, L: lens, C: microcell, O: objective ( $60\times$ ), F: band path filter, P: pinhole, APD: avalanche photodiode detector. The figure at the right shows the composition of the microcell.

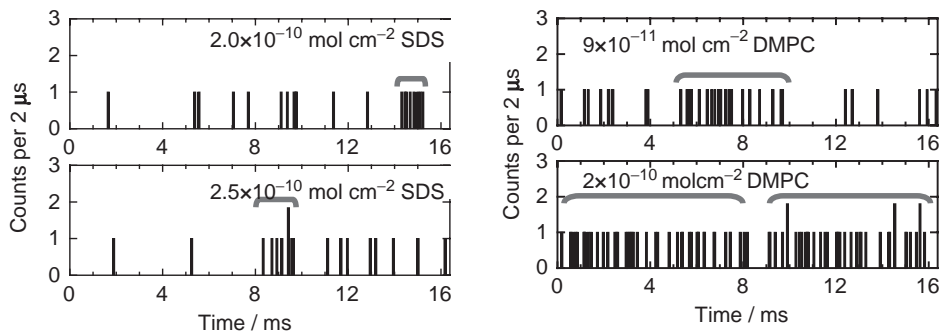


**Fig. 13.** Single molecule detection of DiI at the dodecane–water interface by fluorescence microscopy (left). Short photon burst in the SDS systems and (right) long burst in the DMPC systems.

adsorptivity at the interface, no DiI molecules remained in the dodecane phase, as an initial DiI concentration was lower than  $1 \times 10^{-7} \text{ M}$ .

In the presence of few of DiI molecules (0.02 molecules on an average) in the observation area, a clear intermittent photon bundle was observed (Fig. 13). Since DiI molecules are adsorbed at the interface, the diffusion of DiI is thought to be restricted in the lateral direction at the interface. Therefore, the maximum duration of the photon bundles ( $t_{\max}$ ) corresponds to the period in which the single DiI molecule is diffusing through the observation area. The  $t_{\max}$  is thought to be the time for a single molecule to move along the diameter of the round observation area.

The lateral diffusion coefficient ( $D_l$ ) of DiI was calculated using the equation:

$$D_l = \frac{d_{\text{obs}}^2}{2t_{\max}} \quad (2)$$

The radius ( $r$ ) and the diffusion coefficient ( $D$ ) of a spherical molecule are related to the viscosity ( $\eta$ ) of the medium surrounding the molecule by the Einstein–Stokes equation:

$$D = \frac{kT}{6\pi r\bar{\eta}_i} \quad (3)$$

where  $k$  is the Boltzmann constant,  $T$  the absolute temperature, and  $\bar{\eta}_i$  the apparent viscosity. The DiI molecule was estimated from the molecular volume of DiI to be a sphere with a radius of 0.70 nm. In the surfactant-free system, the calculated viscosity of 1.4 mPa s was close to the value for dodecane (1.4 mPa s) and was higher than that of water (0.89 mPa s). This result suggested that the two long alkyl groups of DiI were deeply immersed in the dodecane phase.

The  $D_1$  and  $\bar{\eta}_i$  values were only slightly affected by the coexistence of SDS, though the interfacial concentration of SDS was as high as the saturated interfacial concentration,  $2.5 \times 10^{-10}$  mol/cm<sup>2</sup> (Fig. 13). This suggested that the translational motion of interfacial SDS molecules is similar to that of dodecane molecules, because both are almost the same size having C<sub>12</sub> chain. On the other hand, DMPC had a remarkable effect. The maximum  $\bar{\eta}_i$  value in the DMPC system was 0.170 Pa s, which was 100 times larger than that at the surfactant-free interface. DMPC molecule has two alkyl chains fixed to the polar group. This will be the cause of the stiffness of the monolayer of DMPC molecules. These results demonstrated that single molecule probing method could successfully measure the hydrodynamic properties of the interfacial monolayer.

## 2.9. Magnetophoretic Velocimetry of Microdroplets

As for separation and characterization methods of microparticles in liquid, field flow fractionation (FFF) [56] and split-flow thin fractionation (SPLITT) [57], which utilized external fields, have been developed. Recently, a high magnetic field of 10 T has become available in laboratory, and some new applications of high magnetic field and some new findings have been reported. Beaugnon and Tournier demonstrated magnetic levitation of diamagnetic materials [58], Kitazawa et al. performed the levitation of paramagnetic aqueous solution [59], and Kimura et al. succeeded in fabricating large-size polymer spheres by using magnetic levitation [60]. These methods utilize a magnetic force that depends on not only magnetic flux density  $B$  but also on its gradient ( $dB/dx$ ).

Magnetophoretic velocimetry is a new analytical technique to measure the magnetic susceptibility and the amount of some composite in an individual microparticle using magnetic force [61]. In this technique, the size and the migration velocity of a microparticle are directly measured with a microscope, and then from their values the magnetic susceptibility is obtained. By using high magnetic field (10 T) generated with a superconducting magnet, this technique allowed us to measure a volume magnetic susceptibility of  $10^{-6}$  level for a single

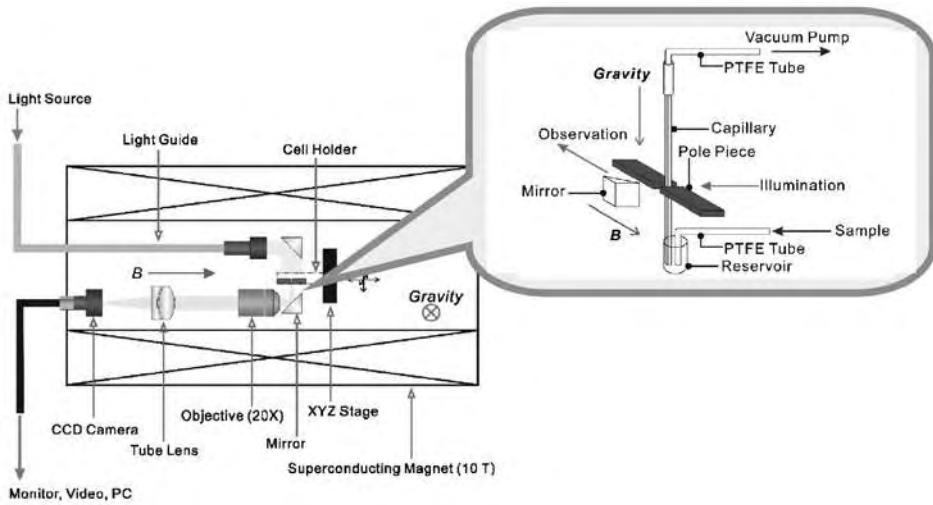


**Fig. 14.** Schematic drawing of the magnetophoretic velocimetry apparatus installed in the bore of a superconducting magnet.

microparticle [62] which is sensitive enough to detect the interfacial amount of paramagnetic ion on a single organic droplet in water.

A cryogen free superconducting magnet generated a high magnetic field of 10 T. The experimental setup is shown in Fig. 14. The gap of a pair of the pole pieces (iron pieces) that accommodated the capillary cell was  $400\ \mu\text{m}$  and the maximum value of  $B(\text{dB}/\text{dx})$  was  $4.7 \times 10^{4+}\ \text{T}^2/\text{m}$ . Soon after the introduction of the sample solution such as an oil-in-water dispersion into the reservoir, it was introduced spontaneously into the square capillary cell by its capillary force. After the capillary rise of the solution into the capillary stopped, the behavior of organic droplets in the aqueous solution near the edge of the pole pieces was observed by an objective, a tube lens, and a CCD camera.

The magnetophoretic velocity  $v_m$  of a droplet with radius  $r$  in a medium is represented by the equation:

$$v_{m,x} = \frac{2(\chi_p - \chi_m)}{9} \frac{r^2 B}{\mu_0 \eta} \left( \frac{\text{dB}}{\text{dx}} \right) \quad (4)$$

where  $\chi_p$  is the magnetic susceptibility of the droplet,  $\eta$  the viscosity of the medium,  $\mu_0$  the permeability of vacuum, and  $\chi_m$  the magnetic susceptibility of the medium.

Fig. 15 shows the magnetophoretic behavior of a single pure 2-fluorotoluene droplet in water. This image was made by superimposing microphotographs captured at  $1/5\ \text{s}$  intervals. The direction of migration was set as  $x$ -direction and the edge of the pole pieces as  $x = 0$ . The droplet was attracted toward the gap of the pole pieces, because the inside of the gap had higher

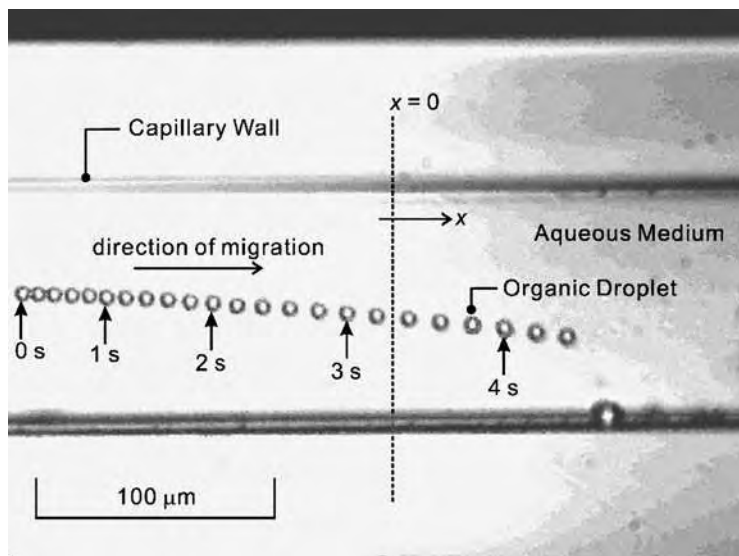


**Fig. 15.** The magnetophoretic behavior of a single microdroplet of 2-fluorotoluene in water. This microphotograph was made by superimposing the images captured at 1/5 s intervals. The dashed line indicates the position of the edge of pole pieces ( $x = 0$ ).

magnetic flux density. The migration velocity was maximized near the edge of the pole pieces, where the value of  $B(dB/dx)$  becomes largest. In the case of pure 2-fluorotoluene in water, the velocity was in agreement with the calculated one using  $(\chi_p - \chi_m) = 0.82 \times 10^{-6}$ . When the organic droplets contains lauric acid and dispersed in a dilute Dy(III) aqueous solution, the observed  $\chi_p$  of the single droplet depended on the radius by the next equation,

$$\chi_p = \frac{3\chi_{\text{Dy}}^{\text{M}} C_{\text{int}}}{r} + \chi_{2\text{FT}}^{\text{V}} \quad (5)$$

where  $C_{\text{int}}$  is the interfacial concentration of dysprosium(III) ( $\text{mol}/\text{m}^2$ ), the superscripts M and V refer to a molar and volume magnetic susceptibility ( $\text{m}^3/\text{mol}$ ), respectively, and the subscripts Dy and 2FT indicate dysprosium(III) and 2-fluorotoluene, respectively. For example, under the condition of  $1.0 \times 10^{-2} \text{ M}$  lauric acid in 2-fluorotoluene and dispersed in  $5.0 \times 10^{-4} \text{ M}$  Dy(III) aqueous solution, the interfacial concentration of Dy(III) as the 1:1 complex with laureate was determined as  $2.6 \times 10^{-10} \text{ mol}/\text{cm}^2$ . This technique is now the only method to be able to measure the interfacial magnetic susceptibility of a single droplet,  $\chi_{\text{Dy}}^{\text{M}} C_{\text{int}}$  in the above example, and to determine the interfacial concentration from the magnetophoretic velocity measurement. Magnetophoretic force is promising for making a new tool to manipulate a droplet in liquid.

### 3. INTERFACIAL COMPLEXATION AND AGGREGATION

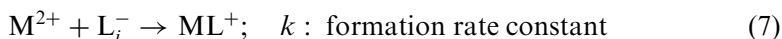
Most attractive features of the liquid–liquid interfacial reaction are the catalytic effect in the solvent extraction or interfacial complexation and the aggregation of hydrophobic dyes and metal complexes.

#### 3.1. Interfacial Catalysis in Metal Extraction Kinetics

The extraction kinetics of Ni(II) and Zn(II) with *n*-alkyl-substituted dithizone (HL) in chloroform has been studied by HSS method [7]. The observed extraction rate constants was linearly proportional to both metal ion concentration in the aqueous phase  $[M^{2+}]$  and ligand concentration in the organic phase  $[HL]_o$ , and inversely to the hydrogen ion concentration  $[H^+]$  in the aqueous phase. Thus, the rate law for the extraction was determined as

$$-\frac{d[M^{2+}]}{dt} = k' \frac{[M^{2+}][HL]_o}{[H^+]} \quad (6)$$

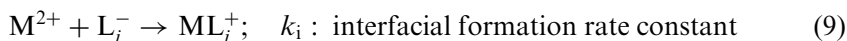
where  $k'$  is the extraction rate constant. If the rate-determining step of the extraction kinetic is the formation of 1:1 complex in bulk aqueous phase,



the extraction rate constant is represented by

$$k' = \frac{kK_a}{K_D} \quad (8)$$

where  $K_a$  is the dissociation constant and  $K_D$  the distribution constant of *n*-alkyl-substituted dithizone. However, the observed extraction rate constant  $k'$  did not decrease with the increase of  $K_D$ . Furthermore, the HSS method revealed that the dissociated form of the *n*-alkyl-dithizone adsorbed at the interface generated by the vigorous agitation [8]. From these experimental results, the contribution of the interfacial reaction was concluded:



Then, the observed extraction rate constant  $k'$  was rewritten as

$$k' = \left( k + k_i K_L' \frac{A_i}{V} \right) \frac{K_a}{K_D} \quad (10)$$

where  $A_i/V$  refers to the specific interfacial area, and  $K_L'$  the adsorption constant of  $L^-$  from the aqueous phase to the interface. Under the conditions of  $k \ll k_i K_L' A_i/V$ , the interfacial reaction will govern the overall extraction rate. The value of  $K_L' A_i$  could be determined by HSS method. Analysis of the extraction rate gave  $\log(k_i/M^{-1} \text{ s}^{-1}) = 8.08$  for  $Zn^{2+}$  system and  $\log(k_i/M^{-1} \text{ s}^{-1}) = 5.13$  for  $Ni^{2+}$  system, respectively [7].

From this study, one can understand that the liquid–liquid interface has a role of catalyst in the extraction rate through the adsorption of extractants like

a solid catalyst. A primary criterion of the interfacial adsorption of the ligand is whether the interfacial ligand concentration shows a Nernst isotherm or an adsorption isotherm. This was proved in the extraction of Ni(II) with 2-hydroxy oxime such as 5-nonylsalicylaldoxime (P50) [63], 2-hydroxy-5-nonylacetonone oxime (SME529 or LIX83) [23], and 2-hydroxy-5-nonylbenzophenone oxime (LIX65N) [64]. These extractants adsorbed at the interface in their neutral forms, obeying the Langmuir isotherm:

$$[\text{HL}]_i = \frac{aK'[\text{HL}]_o}{a + K'[\text{HL}]_o} \quad (11)$$

where  $[\text{HL}]_i$  and  $[\text{HL}]_o$  refer to the concentrations at the interface and organic phase, respectively,  $a$  the saturated interfacial concentration, and  $K'$  the interfacial adsorption constant defined by  $K' = [\text{HL}]_i/[\text{HL}]_o$  under the condition of  $[\text{HL}]_o \rightarrow 0$ . The interfacial adsorptivity was confirmed also by the interfacial tension measurement. The initial rate constant for the extraction of Ni(II) ion,  $r^0$ , was represented by

$$r^0 = k_i K'_a n_i \frac{[\text{Ni}^{2+}]}{[\text{H}^+]} \quad (12)$$

where  $K'_a$  is the dissociation constant at the interface and  $n_i$  the interfacial amount of the ligand in the present experimental conditions. As shown in Fig. 16, the linear relationship between  $r^0$  and  $n_i$  was experimentally confirmed. Then, it was concluded that the reaction between the dissociated form,  $\text{L}^-$ , and Ni(II) ion at the interface governed the overall extraction rate. The complex formed at the interface was not adsorbed at the interface, but extracted into the organic phase. We determined the adsorption constants of the three

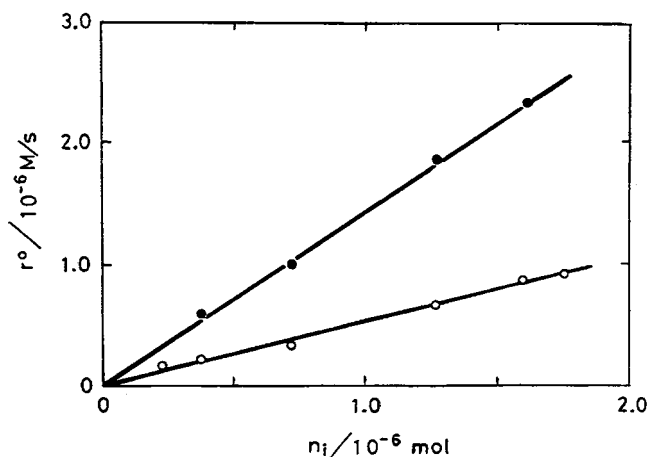
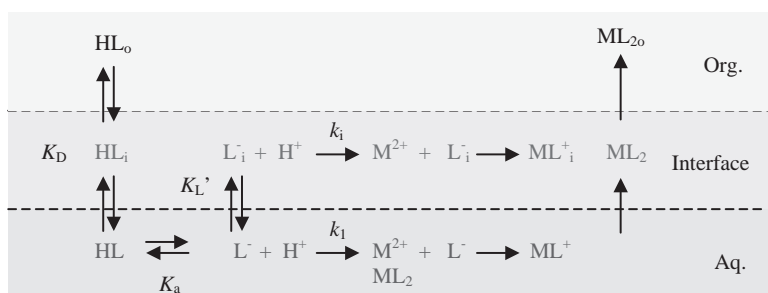


**Fig. 16.** Linear correlation between the initial extraction rate and the interfacial amount of P50: •  $[\text{Ni}^{2+}] = 8.0 \times 10^{-3} \text{ M}$ , ○  $[\text{Ni}^{2+}] = 1.0 \times 10^{-3} \text{ M}$ .

2-hydroxyoximes and the complexation rate constants with Ni(II) and Cu(II) ions at the interface by means of the HSS method. The adsorption constants ( $K'$ ) of the neutral forms were all in the order of  $10^{-3}$  cm and the complexation rate constants of the dissociated form with Ni(II) ion at the interface were in the order of  $10^5 \text{ M}^{-1} \text{ s}^{-1}$  for the three extractants, though the distribution constants ( $\log K_D$ ) were significantly different. The complex formation rate constants were not seriously affected by the interface of heptane–water in comparison with those in bulk aqueous solution. However, in the chloroform system, the magnitude of  $k_i$  was decreased about two orders. This can be thought as a specific solvent effect in the interface. The ligand might be solvated by chloroform molecules even when it was adsorbed at the interface. The whole scheme of the extraction mechanism including the interfacial reaction is shown in Scheme I. In conclusion, the catalytic effect of the interface is primarily governed by the value of  $A_i/V$ , which can be increased by agitation or stirring.

The adsorptivity and the orientation of the 2-hydroxyoxime molecule were well simulated by the MD simulations [65]. In Fig. 17, the polar groups of –OH



**Scheme I.** Interfacial mechanism of solvent extraction of metal ion ( $\text{M}^{2+}$ ).

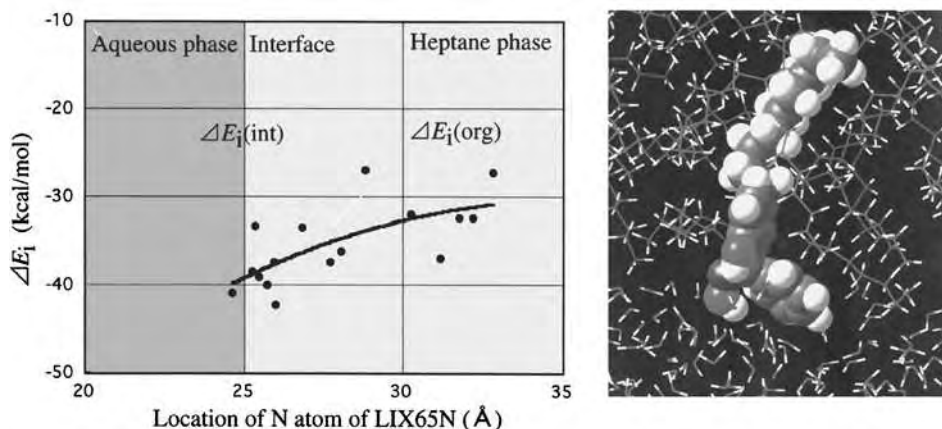


**Fig. 17.** Solvation energy of LIX65N around the heptane–water interface calculated by the molecular dynamics simulation.

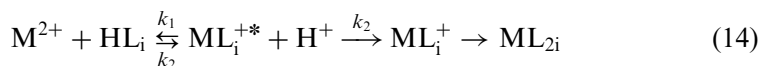
and =N–OH of the interfacially adsorbed P50 molecule is accommodated in the aqueous phase side of the interface so as to react with Ni(II) ion at the interfacial region [66]. The diffusive behavior of LIX65N around the interface was also simulated for 1 ns. Fig. 17 clearly shows that LIX65N is more stable at the interface than in heptane phase. This is thought to be the reason why the reaction rate constants of Ni(II) at the heptane–water interface have almost same magnitude with those in aqueous phase.

Pyridylazo ligands have been widely used in the extraction photometry of various metal ions. For example, 1-(2-pyridylazo)-2-naphthol (Hpan) is one of the most well-known reagents, but it shows slow extraction rate for some metal ions such as Ni(II) and Pd(II). 2-(5-Bromo-2-pyridylazo)-5-diethylaminophenol (5-Br-PADAP) is a relatively new reagent, which is more sensitive than Hpan for Cu(II), Ni(II), Co(II), and Zn(II), giving the metal complexes of molar absorptivities in the order of  $10^5 \text{ M}^{-1} \text{ cm}^{-1}$ .

5-Br-PADAP showed a significant adsorption at the interface of heptane–water under HSS conditions (5000 rpm). On the other hand, the adsorptivity at the toluene–water interface was very low. Hpan did not adsorb at the toluene–water interface at all. The adsorption constants of 5-Br-PADAP (HL) at the heptane–water and toluene–water interfaces were obtained as  $\log K'A_i (\text{cm}^3) = 1.64$  and  $\log K'A_i (\text{cm}^3) = -0.367$  [21]. The solvent effect on the adsorptivity of the ligand affected directly the interfacial reaction rate. In the heptane system, the Ni(II) complex was not extracted into the heptane phase. On the other hand, in toluene system, the complex was extracted very slowly. Recently, the extraction rates of Ni(II) and Zn(II) with 5-Br-PADAP were studied by means of CLM [67]. Based on the reaction mechanism shown in Scheme I, the initial formation rate was represented by

$$r^0 = \left\{ k[\text{HL}] \frac{V_a}{V_o} + \left( \frac{k_1 k_2 [\text{HL}]_i}{k_2 + k_{-1} [\text{H}^+]} \right) \frac{A_i}{V_o} \right\} [\text{M}^{2+}] \quad (13)$$

where  $V_a$  and  $V_o$  refer to the aqueous and organic phase volumes and the definitions of  $k_1$ ,  $k_2$ , and  $k_{-1}$  are shown in the next equation, respectively.



The complex formation proceeded almost completely at the interface. The rate constant of  $k = 5.3 \times 10^2 \text{ M}^{-1} \text{ s}^{-1}$  was determined by a stopped-flow spectrometry in the region where the formation rate was independent of pH. The conditional interfacial rate constants represented by  $k_i = k_1 k_2 [\text{HL}]_i / (k_2 + k_{-1} [\text{H}^+])$  were larger in the heptane–water interface than the toluene–water interface, regardless of metal ions. The molecular dynamics simulation of the adsorptivities of 5-Br-PADAP in heptane–water and toluene–water interfaces suggested that 5-Br-PADAP could be absorbed at the interfacial region more closely to the aqueous phase, but 5-Br-PADAP in the toluene–water

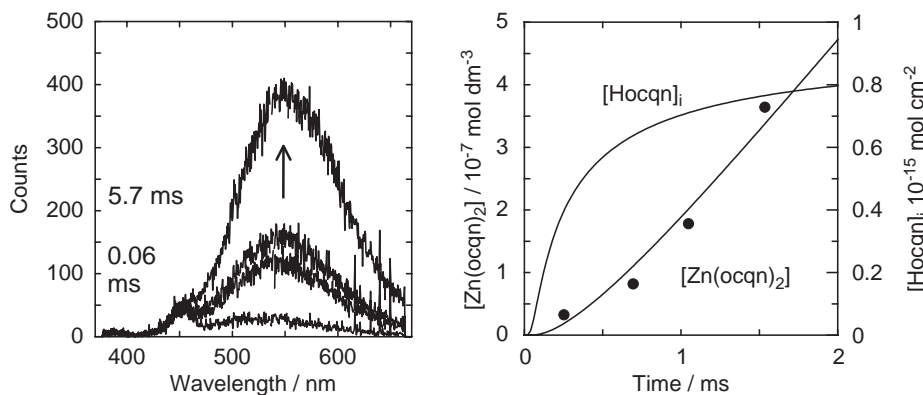


**Fig. 18.** (Left) Change in fluorescence spectra measured by streakscope at the different reaction times. The increasing count at 560 nm proved the formation of Zn(II)–ocqn complex at the interface of two-phase microsheat flow system. (Right) The result of the digital simulation of the Zn(II)–Hocqn complexation. The initial concentration of Hocqn was  $1.1 \times 10^{-4}$  M.

interface was still surrounded by toluene which might lower the probability to react with aqueous Ni(II) ions [21].

The fast reaction rate between Zn(II) ion with Hocqn at the 1-butanol–water interface was measured by two-phase sheath flow method [33]. The formation of a fluorescence complex at the interface was measured in the period less than 5 ms after the two-phase contact as shown in Fig. 18. By the help of digital simulation, the initial process of the interfacial reaction between Zn(II) and Hqn was analyzed (Fig. 18). This approach is promising for the measurement of rapid interfacial reactions such as protein folding and luminescence lifetime as well [36].

In the ion association extraction systems, hydrophobic and interfacially adsorbable complex ions are included very often. Cationic complexes of Fe(II), Cu(II), and Zn(II) with 1,10-phenanthroline (phen) and its hydrophobic derivatives exhibited remarkable interfacial adsorptivity, although the legends themselves can hardly adsorb at the interface, unless they were protonated [68–70]. The extraction rate profiles of Fe(II) with phen and its dimethyl (DMP) and diphenyl (DPP) derivatives into chloroform were investigated by HSS method. In the presence of 0.1 M NaClO<sub>4</sub>, both of the formation rates of phen complex and its interfacial adsorption were remarkably dependent on the counter anions of Cl<sup>−</sup> and ClO<sub>4</sub><sup>−</sup>. The initial extraction rate of Fe(II) was described by the equation

$$\left( \frac{d[\text{FeL}_3\text{X}_2]}{dt} \right)_{t=0} = k_1[\text{Fe}^{2+}][\text{L}] + k'_1[\text{Fe}^{2+}][\text{L}]_i \frac{A_i}{V_o} \quad (15)$$

where X is an anion, and  $k_1$  and  $k'_1$  stand for the 1:1 formation rate constant of  $\text{FeL}_2^+$  in the aqueous phase and at the interface, respectively. The apparent

extraction rate constant,  $k_{\text{obs}}$ , was written as

$$k_{\text{obs}} = \frac{1}{1 + K'_C A_i / V_o} \left( \frac{k_1}{K_D} + k_i K'_L \frac{A_i}{V_o} \right) \quad (16)$$

where  $K'_L$  and  $K'_C$  refer to the adsorption constants of L and  $\text{FeL}_3\text{X}_2$  from the organic phase to the interface, respectively. Experimental results showed that the rate-determining step was the 1:1 complex formation in both aqueous phase and interface. The adsorption of ligand accelerated the extraction (a positive catalytic effect), but the adsorption of the Fe(II) complex suppressed the extraction rate (a negative catalytic effect). The effects of anion and solvent on the extraction rate can be explained through the change of the adsorption constant of Fe(II) complex ion,  $K'_C$  [71].

A typical kinetic synergism has been observed for the catalytic effect of *N,N*-dimethyl-4-(2-pyridylazo)aniline (PADA) on the extraction of  $\text{Ni}(\text{pan})_2$  [72]. The extraction rate of  $\text{Ni}(\text{pan})_2$  into toluene is very slow even under an HSS condition. Whereas, the addition of PADA at the diluted concentration as  $10^{-5}$  M can accelerate the extraction rate about 10 times. The observed extracted species was only  $\text{Ni}(\text{pan})_2$  and no net consumption of PADA was observed after the extraction, while a significant interfacial adsorption of PADA was observed during the extraction under the HSS condition as shown in Fig. 19. These results were analyzed by the mechanism of the interfacial ligand-substitution reaction:

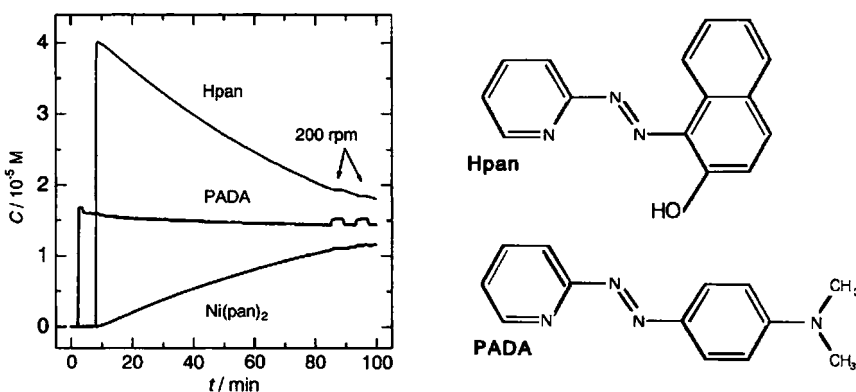
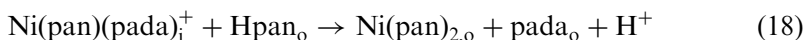
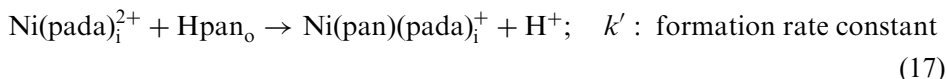


**Fig. 19.** Concentration changes of Hpan, PADA, and  $\text{Ni}(\text{pan})_2$  in the catalytic extraction of Ni(II) into the toluene phase. Initial concentrations are  $[\text{Ni}^{2+}] = 1.0 \times 10^{-5}$  M,  $[\text{Hpan}] = 4.0 \times 10^{-5}$  M, and  $[\text{PADA}] = 1.7 \times 10^{-5}$  M at pH = 5.6.

The value of  $k'$  was obtained as  $90 \text{ M}^{-1} \text{ s}^{-1}$  [72]. The key process of the catalytic extraction of Ni(II)–Hpan–PADA system is the fast aqueous phase formation of  $\text{Ni}(\text{pada})^{2+}$ , which adsorbed at the interface and increased the reaction probability with Hpan in the organic phase to produce  $\text{Ni}(\text{pan})_{2,\text{o}}$ .

Usually, acidic condition decreases the extraction rate of metal ions with acidic ligand, because of the suppression of the dissociation of extractant. However, in the extraction of Pd(II) with 5-Br-PADAP, the lowering of pH accelerated the extraction rate [73]. The protonation of 5-Br-PADAP increased its adsorptivity but did not decrease the reactivity with Pd(II), for the nitrogen atom of imine form was protonated. The rate constant is larger for the reaction with the protonated 5-Br-PADAP than with the neutral one, because Pd(II) is coordinated by chloride ion to be charged negatively as  $\text{PdCl}_3^-$  and  $\text{PdCl}_4^{2-}$ .

In summary, the catalytic role of the liquid–liquid interface is realized through the adsorption of the extractant or interfacial complex at the interface. Therefore, the enlargement of the specific interfacial area is necessary for the increase of the contribution of the interfacial reaction in the overall extraction rate.

### 3.2. Interfacial Aggregation at the Liquid–Liquid Interface

Another unique and specific feature of the interfacial reaction is the formation of aggregate of dye molecules, metal complexes, and other solvophobic molecules. As reported in many interfacial adsorption systems, the saturated interfacial concentration of usual molecules is of the order of  $10^{-10} \text{ mol/cm}^2$ , which can be attained even under an extremely low bulk phase concentration. This means that the liquid–liquid interface is ready to be saturated to form a two-dimensionally condensed state for the adsorbate. In solvent extraction process of metal ions, we used to find formation of some precipitate at the interface, which is called crud. The study of the interfacial aggregate is therefore important to know the real interfacial reaction as met in the industrial solvent extraction where rather concentrated solutes have to be treated.

A typical example of interfacial aggregation is that of the protonated TPP at the toluene or dodecane–aqueous acid solution interface. The maximum absorption wavelength of TPP is shifted from 419 to 473 nm due to the interfacial J-aggregation. The aggregation rate of  $\text{H}_2\text{TPP}^{2+}$  at the dodecane–sulfuric acid solution was measured by a two-phase stopped flow method [9] and a CLM method [12]. In the former method, it was found that the stagnant layer of  $1.4 \mu\text{m}$  still existed in the dodecane phase side of the droplet interface even under the highly dispersed system and the diffusion in the layer is the rate-determining step. In the CLM method, the liquid membrane phase of 50–100  $\mu\text{m}$  thickness behaved as a stagnant layer where the TPP molecule had to migrate according to its self-diffusion rate before the rapid protonation of TPP and the aggregation of the diprotonated species.

Recently, the formation of the dinuclear Eu(II) complex at the toluene–water interface was found out by a time-resolved total reflection fluorometry. When bathophenanthroline sulfate (bps) was added to the extraction system of Eu(III) with 2-thenoyltrifluoroacetone (Htta), a double component luminescence decay profile was observed and it showed the presence of dinuclear complex at the interface [27]. The observed life times  $\tau = 22$  and  $203 \mu\text{s}$  were attributed to the dinuclear complex  $\text{Eu}_2(\text{tta})_2(\text{bps})_2$  and the mononuclear complex  $\text{Eu}(\text{tta})_2\text{bps}^-$ . The shorter lifetime of the dinuclear complex than  $\tau = 98 \mu\text{s}$  for an aqua-Eu(III) ion suggested a charge transfer deactivation in the dinuclear complex.

The aggregate of Pd(II)–tetrapyrrolylporphine (tpyp) complex was formed at the toluene–water interface, when a tpyp toluene solution was contacted with a  $\text{PdCl}_2$  aqueous solution under an acidic condition. Pd(II) was bound to the nitrogen atoms of pyridyl group, not to the central pyrrole nitrogens. Depending on the concentration ratio of Pd(II)/tpyp, it formed two kinds of aggregates: an aggregate (AS1) observed in a lower tpyp concentration has a 3:1 composition in Pd/tpyp ratio with a shorter life time of 0.15 ns, and another one (AS2) observed higher tpyp concentration has a 1:1 composition with a longer life time of 1.1 ns. The 1:1 aggregate ( $\lambda_{\text{max}} = 668 \text{ nm}$ ) showed a red shift of 12 nm from the 3:1 aggregate ( $\lambda_{\text{max}} = 656 \text{ nm}$ ), and suggested a  $\pi$ -stacking interaction in the 1:1 aggregate [74].

The palladium(II) ion forms a 1:1 complex with 5-Br-PADAP, leaving one site for the coordination of another ligand. The Pd(II)–5-Br-PADAP (PdL) complex cation has specific properties such as an extremely high molar absorptivity ( $\epsilon_{564} = 4.33 \times 10^4 \text{ M}^{-1} \text{ cm}^{-1}$  in toluene), a high adsorptivity to the liquid–liquid interface, and a soft Lewis acid easy to be bound to a soft Lewis base. Therefore,  $\text{PdL}^+$  is expected to have a function as an interfacial molecular recognition reagent of Lewis bases.

The molecular recognition ability of Pd(II)–5-Br-PADAP for the isomers of diazine derivatives (abbreviated as Dzs or N) has been evaluated.  $\text{PdLCl}$  reacted with a neutral diazine with one or two nitrogen atoms, forming a  $\text{PdLN}^+$  complex at the toluene–water interface. The interfacial formation constant ( $\beta_i$ ) of the  $\text{PdLN}^+$  complex was determined as follows [38]:



$$\beta_i = \frac{[\text{PdLN}_i^+][\text{Cl}^-]}{[\text{PdLCl}_i][\text{N}]} \quad (20)$$

A linear relationship was obtained between the logarithmic interfacial formation constant ( $\log \beta_i$ ) for  $\text{PdL}^+$ -diazine derivative complexes and the logarithmic ratio of the distribution constant ( $K_D$ ) to the acid-dissociation constant ( $K_a$ ) for the two groups.  $\text{PdL}^+$ -pyridazine derivative complexes showed much higher stability at the interface than pyrimidine and pyrazine derivative complexes. This result suggests that pyridazine derivative complexes become more

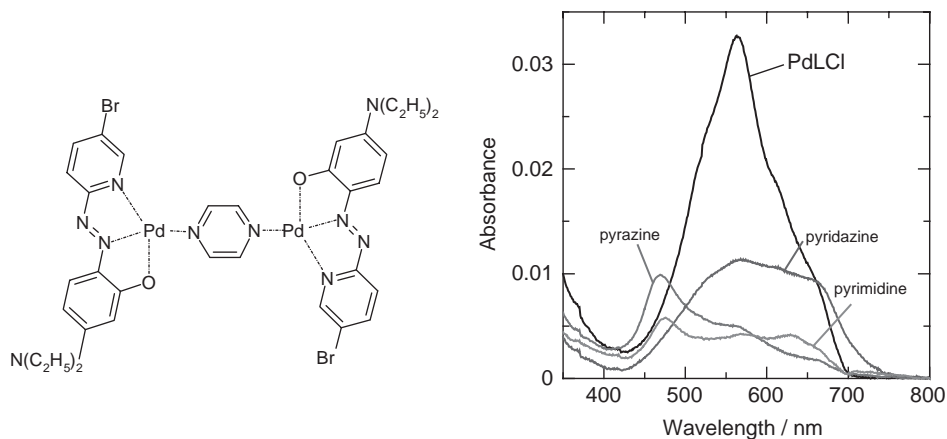


**Fig. 20.** Absorption spectra of PdLCl and the interfacial aggregates of ternary PdL–Dz complexes measured by the CLM method.  $[\text{PdLCl}]_{\text{init}} = 5.6 \times 10^{-5} \text{ M}$ ,  $[\text{pyridazine}] = 2.0 \times 10^{-4} \text{ M}$ ,  $[\text{pyrimidine}] = 8.0 \times 10^{-3} \text{ M}$ ,  $[\text{pyrazine}] = 8.0 \times 10^{-5} \text{ M}$ ,  $[\text{ClO}_4^-] = 0.1 \text{ M}$ ,  $[\text{Cl}^-] = 0 \text{ M}$ , pH 2.0. The left structure shows a probable unit of the membrane-like aggregate formed in pyrazine complexes.

liable to be adsorbed at the interface than pyrimidine and pyrazine derivative complexes, since the bonding of the pyridazine derivative to  $\text{PdL}^+$  increases its hydrophobicity by decreasing its dipole moment, which was evaluated by molecular orbital calculations.

At low concentrations of chloride ions, PdL–Dz complexes formed aggregates at the interface [75]. Fig. 20 shows the absorption spectra of PdLCl and the PdL–Dz complex aggregates. The formation of each interfacial aggregate of PdL–Dz was accompanied with a drastic absorbance decrease at 564 nm of PdLCl and the change in the spectral shape. Difference in the compositions of the interfacial aggregates of PdL–Dz was observed among the Dz isomers: the PdL–pyridazine aggregate formed blue domains at the interface and the composition ratio was pyridazine:PdL = 1:1, whereas the PdL–pyrazine aggregate was a thin membrane with the composition of pyrazine:PdL = 1:2 and the PdL–pyrimidine aggregate showed blue domains with the unknown composition.

The aggregation kinetics of nickel(II)–5-Br-PADAP complex at the heptane–water interface has been studied by using CLM spectrophotometry [76]. The interfacial aggregation between ligands in  $\text{NiL}_2$  complexes was observed as the growth of a remarkably intense and narrow absorption band (J-band) at 588 nm, showing a bathochromic shift from the absorption maximum of the monomer complex (569 nm), accompanied by a decrease of the absorbance of the free ligand at 452 nm as shown in Fig. 21. The formation of the aggregate was initiated at the time when the interfacial concentration of the monomer complex attained the critical aggregation concentration (cac) of  $2.4 \times 10^{-10} \text{ mol/cm}^2$ . The

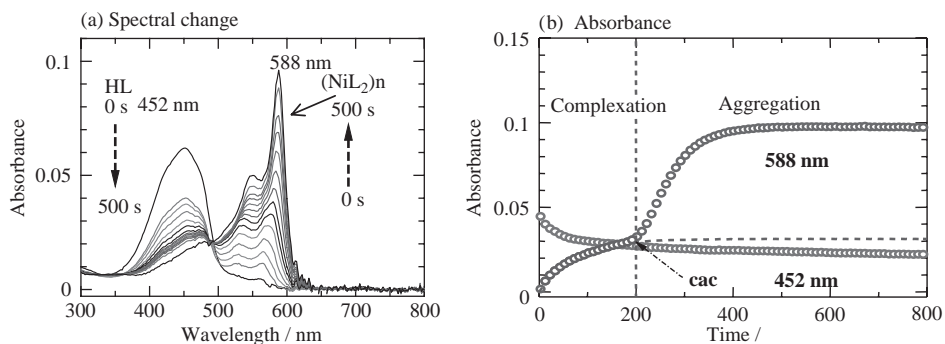


**Fig. 21.** Critical aggregation concentration in the interfacial aggregation of Ni(II)–5-Br-PADAP.

initial formation rate of the interfacial aggregate was proportional to concentrations of both free Ni(II) and free ligand after the attainment of cac. The observed rate constant for the aggregation,  $4.1 \times 10^1 \text{ M}^{-1} \text{ s}^{-1}$ , was smaller than the formation rate constant of  $\text{NiL}_2$  complex at the interface. A long period observation of the profile of absorbance change showed an oscillation of the interfacial aggregate concentration until all of the ligand was consumed, suggesting a subsequent flocculation of the aggregate in the rotating cell.

Very recently, the SHG/CD method has been applied, for the first time, to the measurement of the CD spectra of the interfacial complex [20]. Interfacial aggregation of tetra-*p*-sulfonatophenylporphyrin (TPPS) induced by the coexistence of a cationic surfactant was studied using the SHG/CD method. Cetyltrimethylammonium bromide (CTAB) was used as a cationic surfactant. The SHG signal increased with the increase in the concentration of CTAB. Under acidic conditions (pH 3.0), the absorption spectrum of the aqueous solution of TPPS showed a maximum at 435 nm, which was assigned to the diprotonated TPPS ( $\text{H}_4\text{TPPS}^{2-}$ ). On the other hand, the p-polarized interfacial SHG spectrum obtained from the irradiation of the p-polarized fundamental beam at pH 3.0 gave two maxima at 400 and 415 nm. The maxima in the SHG spectrum were assigned to the mixture of the H-aggregate of TPPS (405 nm) and the aqueous unprotonated TPPS (413 nm). It was, therefore, suggested that these two unprotonated species coexisted at the heptane–water interface. The present results also suggested that the formation of the H-aggregate was favored at the interface in contrast with the results in aqueous solutions. The chirality of the interfacial aggregate of TPPS has been investigated using SHG/CD spectroscopy for the first time. This study enabled the chirality measurements of the interfacial complex and the interfacial aggregates, which were very difficult to be measured using ordinary CD spectroscopy, due to the very low interfacial concentrations. In the near future, the chiral selectivity related to the molecular recognition ability of the interfacial aggregates will be investigated in detail.

#### 4. CONCLUDING REMARKS

Modern measurement methods of the liquid–liquid interfacial reaction were reviewed as well as specific features of the interfacial reactions, notably the complexation of metal ions and the aggregation of complexes. The prospect of interfacial analytical methods is summarized as follows:

- 1) Single molecular diffusion method enabled us to measure the nanoviscosity of the liquid–liquid interface. The single molecular probing technique will be extended to the measurement of single molecule reaction at the interface, which is useful to elucidate the polarity, acidity, and reactivity of ions adsorbed at the interface. The mechanism of cell membrane reaction also will be investigated by the single molecule probing method.
- 2) Various kinds of new spectroscopic methods will be applied to observe micro- and nanometer sized area in the liquid–liquid interface, and some inhomogeneity or localization of the interfacial compound will be observed. Especially, the optical chirality of the interfacial molecule and molecular aggregate will be very important and fundamental subject. The time-resolved chiral spectrometry, chiral microscope, and imaging technique of interfacial chirality will be developed in very near future. Nonlinear chiral spectrometry is developed and will become more popular, because its high spatial resolution ability.
- 3) Kinetic measurement of the interfacial reaction is still very important in relation to the biological reactions taking place at the cell membrane and the surface of biological organism. The catalytic mechanism of enzyme at the liquid–liquid interface is not well understood yet. The interaction between the enzyme and the substrate at the oil–water interface has to be investigated urgently.
- 4) Again, I would like to emphasize the interesting phenomena of the generation of optical chirality at the interface by the aggregation of achiral molecules. The flexible but shear forced liquid–liquid interface may generate nanochiral environment at the interface, which facilitates the chiral aggregation. Chiral generation or chiral selection is an essential subject not only in chemistry, but also in biology. Detailed investigation should be carried out by using new chiral measurement methods introduced in this chapter.
- 5) Finally, an exotic technique such as magnetophoresis has to be developed. A droplet or particle was moved by the magnetophoretic force, which was only femtonewton. Such tiny force is enough to migrate a microparticle in liquid, and the velocity gives the value of magnetic susceptibility of the single particle and further that of the interface. The magnetophoretic mobility method is predicting a further possibility of other innovative measurement methods of the interface by using external force, which utilizes electromagnetic force, dielectric force, and laser scattering force [77].

### Acknowledgements

The studies in this chapter were supported in part by a Grant-in-Aid for Scientific Research (S) (No. 16105002) from the Ministry of Education, Culture, Sports, Science and Technology of Japan.

### REFERENCES

- [1] H. Watarai, N. Sawada and T. Sawada (eds.), *Interfacial Nanochemistry*, Kluwer Academic/Plenum Publishers, New York, 2005.
- [2] A. G. Volkov and D. W. Deamer (eds.), *Liquid-Liquid Interfaces, Theory and Methods*, CRC Press, New York, 1996.
- [3] A. G. Volkov, D. W. Deamer, D. L. Tanelian and V. S. Markin (eds.), *Liquid Interfaces in Chemistry and Biology*, Wiley, New York, 1998.
- [4] J. Rydberg, C. Musikas and G. R. Choppin (eds.), *Principles and Practices of Solvent Extraction*, Marcel Dekker, New York, 1992.
- [5] H. Watarai, *Trends Anal. Chem.*, 12 (1993) 313.
- [6] H. Watarai, S. Tsukahara, H. Nagatani and A. Ohashi, *Bull. Chem. Soc. Jpn.*, 76 (2003) 1471.
- [7] H. Watarai and H. Freiser, *J. Am. Chem. Soc.*, 105 (1983) 189.
- [8] H. Watarai and H. Freiser, *J. Am. Chem. Soc.*, 105 (1983) 191.
- [9] H. Nagatani and H. Watarai, *Anal. Chem.*, 68 (1996) 1250.
- [10] H. Watarai and Y. Chida, *Anal. Sci.*, 10 (1994) 105.
- [11] H. Watarai and Y. Saitoh, *Chem. Lett.*, (1995) 283.
- [12] H. Nagatani and H. Watarai, *Anal. Chem.*, 70 (1998) 2860.
- [13] T. Tokimoto, S. Tsukahara and H. Watarai, *Chem. Lett.*, (2001) 204.
- [14] A. Ohashi and H. Watarai, *Chem. Lett.*, (2001) 1238.
- [15] F. Hashimoto, S. Tsukahara and H. Watarai, *Anal. Sci.*, 17 (2001) i81.
- [16] F. Hashimoto, S. Tsukahara and H. Watarai, *Langmuir*, 19 (2003) 4197.
- [17] M. Suwa and H. Watarai, *J. Chromatogr. A*, 1013 (2003) 3.
- [18] S. Yamamoto, K. Fujiwara and H. Watarai, *Anal. Sci.*, 20 (2004) 1347.
- [19] S. Wada, K. Fujiwara, H. Monjushiro and H. Watarai, *Anal. Sci.*, 20 (2004) 1489.
- [20] K. Fujiwara, H. Monjushiro and H. Watarai, *Chem. Phys. Lett.*, 349 (2004) 353.
- [21] H. Watarai, M. Gotoh and N. Gotoh, *Bull. Chem. Soc. Jpn.*, 70 (1997) 957.
- [22] G. J. Hanna and R. D. Noble, *Chem. Rev.*, 85 (1985) 583.
- [23] H. Watarai, M. Takahashi and K. Shibata, *Bull. Chem. Soc. Jpn.*, 59 (1986) 3469.
- [24] H. Watarai, K. Kamada and S. Yokoyama, *Solvent Extr. Ion Exch.*, 7 (1989) 361.
- [25] H. Nagatani and H. Watarai, *Chem. Lett.*, (1999) 701.
- [26] H. Watarai and F. Funaki, *Langmuir*, 12 (1996) 6717.
- [27] M. Fujiwara, S. Tsukahara and H. Watarai, *Phys. Chem. Chem. Phys.*, 1 (1999) 2949.
- [28] S. Tsukahara, Y. Yamada, T. Hinoue and H. Watarai, *Bunsekikagaku*, 47 (1998) 945.
- [29] S. Tsukahara and H. Watarai, *Chem. Lett.*, (1999) 89.

- [30] K. Fujiwara and H. Watarai, *Bull. Chem. Soc. Jpn.*, 74 (2001) 1885–1890.
- [31] Y. Moriya, S. Nakata, H. Morimoto and N. Ogawa, *Anal. Sci.*, 20 (2004) 1533.
- [32] G. D. Owens, R. W. Taylor, T. Y. Ridley and D. W. Margerum, *Anal. Chem.*, 52 (1980) 130.
- [33] T. Tokimoto, S. Tsukahara and H. Watarai, *Bull. Chem. Soc. Jpn.*, 76 (2003) 1569.
- [34] A. J. Bard and L. R. Faulkner, *Electrochemical Methods, Fundamentals and Applications*, Wiley, New York, 2001.
- [35] T. Tokimoto, S. Tsukahara and H. Watarai, *Langmuir*, 21 (2005) 1299.
- [36] T. Tokimoto, S. Tsukahara and H. Watarai, *Analyst*, 129 (2004) 1099.
- [37] A. Ohashi and H. Watarai, *Chem. Lett.*, 32 (2003) 218.
- [38] A. Ohashi and H. Watarai, *Langmuir*, 18 (2002) 10292.
- [39] A. Otto, *J. Raman Spectrosc.*, 33 (2002) 593.
- [40] V. V. Tarabara, I. R. Nabiev and A. V. Feofanov, *Langmuir*, 14 (1998) 1092.
- [41] K. Fujiwara, H. Monjushiro and H. Watarai, *Chem. Phys. Lett.*, 394 (2004) 349.
- [42] T. Petralli-Mallow, M. T. Wong, J. D. Byers, H. I. Yee and J. M. Hicks, *J. Phys. Chem.*, 97 (1993) 1383.
- [43] J. M. Hicks, T. Petralli-Mallow and J. D. Byers, *Faraday Discuss.*, 99 (1994) 341.
- [44] R. M. Corn and D. A. Higgins, *Chem. Rev.*, 94 (1994) 107.
- [45] P.-F. Brevet, *Surface Second Harmonic Generation*, Presses Polytechniques et Universitaires Romandes, Lausanne, 1997.
- [46] W. H. Steel and R. A. Walker, *J. Am. Chem. Soc.*, 125 (2003) 1132.
- [47] H. Nagatani, Z. Samec, P.-F. Brevet, D. J. Fermin and H. H. Girault, *J. Phys. Chem. B*, 107 (2003) 786.
- [48] T. Verbiest, M. Kauranen and A. Persoons, *J. Mater. Chem.*, 9 (1999) 2005.
- [49] M. J. Crawford, S. Haslam, J. M. Probert, Y. A. Gruzdkov and J. G. Frey, *Chem. Phys. Lett.*, 229 (1994) 260.
- [50] S. Nie, D. T. Chiu and R. N. Zare, *Anal. Chem.*, 67 (1995) 2849.
- [51] T. Funatsu, Y. Harada, M. Tokunaga, K. Saito and T. Yanagida, *Nature*, 374 (1995) 555.
- [52] D. C. Nguyen, R. A. Keller, J. H. Jett and J. C. Martin, *Anal. Chem.*, 59 (1987) 2158.
- [53] M. Ishikawa, K. Hirano, T. Hayakawa, S. Hosoi and S. Brenner, *Jpn. J. Appl. Phys.*, 33 (1994) 1571.
- [54] M. J. Wirth and D. J. Swinton, *Anal. Chem.*, 70 (1998) 5264.
- [55] S. Ho Kang, M. R. Shortreed and E. S. Yeung, *Anal. Chem.*, 73 (2001) 1091.
- [56] M. Schimpf, K. Caldwell and J. C. Giddings, *Field Flow Fractionation Handbook*, Wiley, New York, 2000.
- [57] C. B. Fuh, *Anal. Chem.*, 72 (2000) 266A.
- [58] E. Beaugnon and R. Tournier, *Nature*, 349 (1991) 470.
- [59] Y. Ikezoe, N. Hirota, J. Nakagawa and K. Kitazawa, *Nature*, 393 (1998) 749.
- [60] M. Yamato, H. Nakazawa and T. Kimura, *Langmuir*, 18 (2002) 9609.
- [61] M. Suwa and H. Watarai, *Anal. Chem.*, 73 (2001) 5214.
- [62] M. Suwa and H. Watarai, *Anal. Chem.*, 74 (2002) 5027.
- [63] H. Watarai and K. Satoh, *Langmuir*, 10 (1994) 3913.
- [64] H. Watarai and M. Endo, *Anal. Sci.*, 7 (1991) 137.

- [65] Y. Onoe and H. Watarai, *Anal. Sci.*, 14 (1998) 237.
- [66] H. Watarai and Y. Onoe, *Solvent Ext. Ion Exch.*, 19 (2001) 155.
- [67] Y. Yulizar, A. Ohashi and H. Watarai, *Anal. Chim. Acta*, 447 (2001) 247.
- [68] H. Watarai, *J. Phys. Chem.*, 89 (1985) 384.
- [69] H. Watarai, *Talanta*, 32 (1985) 817.
- [70] H. Watarai and Y. Shibuya, *Bull. Chem. Soc. Jpn.*, 62 (1989) 3446.
- [71] H. Watarai, K. Sasaki and N. Sasaki, *Bull. Chem. Soc. Jpn.*, 63 (1990) 2797.
- [72] Y. Onoe, S. Tsukahara and H. Watarai, *Bull. Chem. Soc. Jpn.*, 71 (1998) 603.
- [73] A. Ohashi, S. Tsukahara and H. Watarai, *Anal. Chim. Acta*, 364 (1998) 53.
- [74] N. Fujiwara, S. Tsukahara and H. Watarai, *Langmuir*, 17 (2001) 5337.
- [75] A. Ohashi, S. Tsukahara and H. Watarai, *Langmuir*, 19 (2003) 4645.
- [76] Y. Yulizar and H. Watarai, *Bull. Chem. Soc. Jpn.*, 76 (2003) 1379.
- [77] H. Watarai, H. Monjushiro, S. Tsukahara, M. Suwa and Y. Iiguni, *Anal. Sci.*, 20 (2004) 423.

## Chapter 12

# Monolayers on Air/Solid Interfaces: Vibrational Spectroscopy and Atomic Force Microscopy Studies

Yukihiro Ozaki<sup>a,\*</sup>, Shin-ichi Morita<sup>b</sup>, Yoshiaki Hirano<sup>a</sup>,  
Xiaoling Li<sup>c</sup>

<sup>a</sup>*Department of Chemistry, School of Science and Technology, Kwansai Gakuin University, 2-1 Gakuen, Sanda 669-1337, Japan*

<sup>b</sup>*Department of Chemistry, The University of Georgia, Athens, GA 30602-2556, USA*

<sup>c</sup>*Department of Physics, University of Guelph, Guelph, Ont., Canada N1G 2W1*

### 1. INTRODUCTION

The purpose of this chapter is to demonstrate the usefulness of vibrational spectroscopy [1–8] and atomic force microscopy (AFM) [9,10] in the studies of monolayers on air/solid interfaces. In this chapter, considerable attention is paid to the combined use of vibrational spectroscopy and AFM. These two techniques, widely used in the studies of monolayers on air/solid interfaces, have complementary advantages; vibrational spectroscopy is suitable to investigate structure and orientation of monolayers [2,3,6–9], while AFM is useful to observe the surface morphology and the thickness of the monolayers [9].

The utility of vibrational spectroscopy lies in the fact that the vibrational spectrum of a molecule is a sensitive indicator of chemical properties [1–5]. The vibrational spectrum reflects the disposition of atomic nuclei and chemical bonds within a molecule and the interactions between the molecule and its immediate environments. Thus, vibrational spectroscopy, infrared [1–3] and Raman spectroscopies [4,5], in the present case, allows one to investigate

---

\*Corresponding author. E-mail: ozaki@kwansai.ac.jp

structure, orientation, and interactions in monolayers on air/solid interfaces at the functional group level [2,3,6–8].

Vibrational spectroscopy has following advantages for investigations of monolayers [2,3,6–8]:

1. One can measure a spectrum non-destructively at room temperature under a normal pressure.
2. It is possible to measure a spectrum of even a one-layer film.
3. Since an infrared spectrum or a Raman spectrum can be obtained for monolayers, a solution, a solid, and a crystal, one can compare the structure of a sample in the monolayers with that in other states.
4. Operations for spectra measurements are relatively easy.
5. In the case of infrared spectroscopy, various types of infrared measurement methods (transmission method, attenuated total reflection (ATR) method, reflection–absorption (RA) method, surface-enhanced method, etc.) may be applied.
6. As for Raman spectroscopy one may expect resonance Raman effect and/or surface-enhanced Raman scattering (SERS). By using these effects, the Raman spectrum of a monolayer film may be enhanced by  $10^3$ – $10^6$ . Resonance Raman spectroscopy is useful for exploring the electronic structure of monolayers with a chromophore and SERS technique is applied to study structure, orientation, and interactions of monolayers on a silver or gold surface.

Information obtained from infrared and Raman spectra of monolayers are summarized as follows:

1. Orientation of molecules: it is possible to quantitatively estimate tilt angles of a hydrocarbon chain and a chromophore.
2. Conformations of hydrocarbon chains.
3. Conformations and electronic structures of chromophores.
4. Interactions between a substrate and the first layer and those between layers.
5. Subcell packing of hydrocarbon chains.

AFM can image both conductors and non-conductors with atomic resolution [9,10]. AFM is being used to solve materials and processing problems in a wide range of sciences and technologies including material, chemical, and biological sciences and technologies [9,10]. The materials investigated include thin and thick films, coatings, ceramics, composites, glasses, synthetic and biological membranes, metals, polymers, and semiconductors. AFM is being applied to studies of phenomena such as abrasion, adhesion, cleaning, corrosion, etching, friction, lubrication, plating, and polishing. By using AFM one can not only image a surface in atomic resolution but also measure the force at nano-Newton scale.

The following part of this review article consists of four sections. Section 2 is concerned with infrared and AFM studies of Langmuir–Blodgett (LB) films. This section contains introductory parts for infrared and AFM studies of monolayers. This section also emphasizes the importance of combined use of infrared spectroscopy and AFM. LB films of 2-alkyl-7,7,8,8-tetracyanoquinodimethane (alkyl-TCNQ) are taken up as examples. Section 3 outlines SERS studies of monolayers. This section describes the usefulness and uniqueness of SERS in the investigations of LB and self-assembled monolayer (SAM) films. Following this section, we present other AFM studies on monolayers in Section 4. In Section 5 infrared and visible spectroscopy studies on J- and H-aggregates in LB films of macrocyclic dye are reported.

## 2. INFRARED AND ATOMIC FORCE MICROSCOPY STUDIES OF LB FILMS

### 2.1. An Infrared Study of LB Films of Cadmium Stearate

Fig. 1 shows infrared RA and transmission spectra of seven-layer LB films of cadmium stearate on silver and ZnSe plates, respectively [11]. When one measures an infrared spectrum of a molecule with a long hydrocarbon chain such as cadmium stearate, one typically observes a number of infrared bands due to the

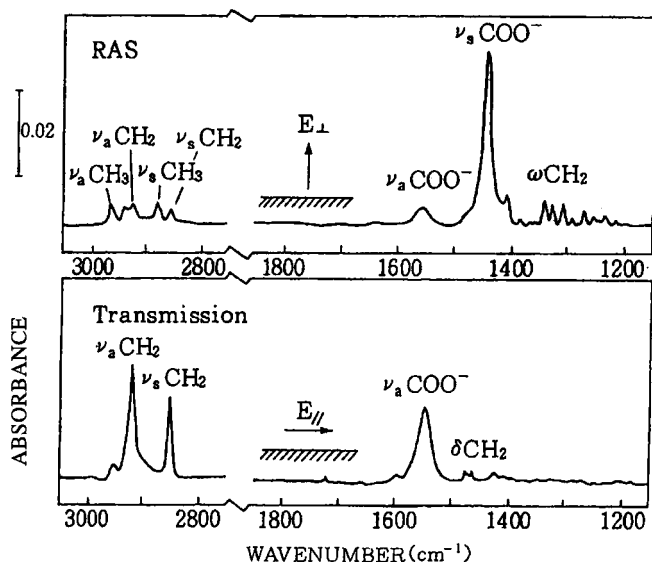


**Fig. 1.** Infrared RA and transmission spectra of seven-layer LB films of cadmium stearate on silver and ZnSe plates, respectively. (Reproduced with permission from Ref. [11]. Copyright (1990) American Chemical Society.)

hydrocarbon chain. One can expect bands due to CH<sub>3</sub> asymmetric stretching, CH<sub>3</sub> symmetric stretching, CH<sub>2</sub> antisymmetric stretching, CH<sub>2</sub> symmetric stretching, CH<sub>2</sub> scissoring, CH<sub>2</sub> wagging vibrations, and so on. The infrared spectra in Fig. 1 show bands at 2955, 2918, 2875, 2847, 1471, and 1462 cm<sup>-1</sup> assigned to CH<sub>3</sub> asymmetric stretching, CH<sub>2</sub> antisymmetric stretching, CH<sub>3</sub> symmetric stretching, CH<sub>2</sub> symmetric stretching, and CH<sub>2</sub> scissoring vibrations (the CH<sub>2</sub> scissoring vibrations appear as a doublet) [11]. The CH<sub>2</sub> wagging vibration yields a band progression in the 1350–1200 cm<sup>-1</sup> region. CH<sub>2</sub> antisymmetric and symmetric stretching bands are known to appear in the vicinity of 2918 and 2848 cm<sup>-1</sup>, respectively, when the hydrocarbon chain assumes *trans*-zigzag structure, but they shift to a higher wavenumber side if the hydrocarbon chain contains some *gauche* forms [12,13]. Hence, the result shown in Fig. 1 suggests that the hydrocarbon chain of cadmium stearate has *trans*-zigzag conformations in the LB films. The subcell packing of hydrocarbon chains can be investigated from bands due to CH<sub>2</sub> scissoring mode [14,15]. The CH<sub>2</sub> scissoring vibrations emerge as a doublet at 1471 and 1462 cm<sup>-1</sup> when the hydrocarbon chains take orthorhombic subcell packing, but as a single band at 1467 cm<sup>-1</sup> when the chains assume hexagonal subcell packing. Since bands due to a CH<sub>2</sub> scissoring vibration appear as a doublet in the transmission spectrum in Fig. 1, it is very likely that the hydrocarbon chains of cadmium stearate assume orthorhombic subcell packing in the LB film [11].

If one wishes to study the molecular orientation in an LB film, one must compare an infrared transmission spectrum with an infrared RA spectrum. We can readily notice the remarkable differences in the intensities of infrared bands between the two spectra in Fig. 1. It is these differences in the intensities that allow us to discuss the molecular orientation in an LB film. Now, let us consider which bands will appear strongly in the transmission spectrum on an assumption that the molecular axis of cadmium stearate is nearly perpendicular to a substrate (see Fig. 2) [11]. In the case of a transmission mode, since an electric vector of infrared light is parallel to the substrate, strong bands are those due to vibrations whose transition moments are perpendicular to the molecular axis, such as CH<sub>2</sub> antisymmetric and symmetric stretching vibrations, COO<sup>-</sup> antisymmetric stretching vibration (1543 cm<sup>-1</sup>) and CH<sub>2</sub> scissoring vibrations, whereas bands due to vibrations whose transition moments are parallel to the molecular axis, such as COO<sup>-</sup> symmetric stretching vibration (1433 cm<sup>-1</sup>) and CH<sub>2</sub> wagging vibrations, should be rarely observed. The transmission spectrum in Fig. 1 strongly supports the hypothesis described above. According to the surface selection rule in infrared RA spectroscopy [16,17], molecular vibrations whose transition moments are perpendicular to a substrate surface appear strongly in an RA spectrum. As we have assumed above, if the molecular axis of the hydrocarbon chain is perpendicular to the substrate, COO<sup>-</sup> symmetric stretching and CH<sub>2</sub> wagging vibrations (when a hydrocarbon chain has *trans*-zigzag conformation, as all CH<sub>2</sub> groups vibrate in the same plane and couple with each other, a series of bands (band progression) appears that

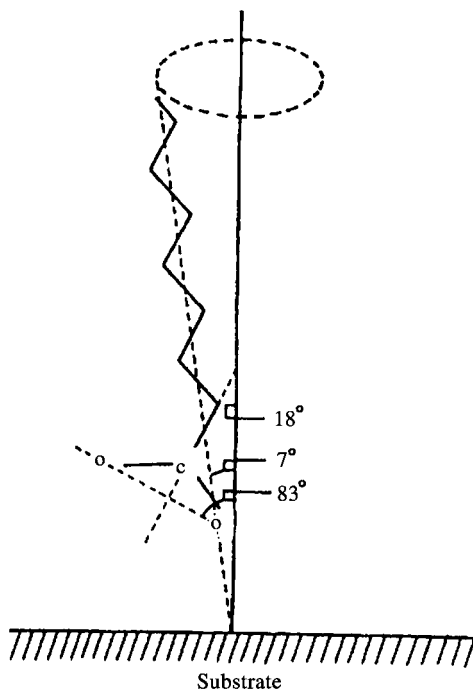


**Fig. 2.** Calculated tilt angles in an LB film of cadmium stearate. (Reproduced with permission from Ref. [11]. Copyright (1990) American Chemical Society.)

expresses phase differences of the vibrations) should appear as strong bands in the RA spectrum. Fig. 1 clearly shows that the above hypothesis is correct.

It is also possible to quantitatively discuss the molecular orientation based on comparison of the intensity of each band between the transmission spectrum and the RA spectrum. From the comparison of the two spectra shown in Fig. 1, Umemura et al. [11] calculated the molecular orientation in the LB film of cadmium stearate as shown in Fig. 2.

## 2.2. Infrared and AFM Studies of LB Films of 2-Alkyl-7,7,8,8-tetracyanoquinodimethane

LB films having a tetracyanoquinodimethane (TCNQ) chromophore have recently received keen interest because some of them have shown fairly high conductivity [18,19]. To understand the interesting properties that the conducting LB films with a TCNQ chromophore show, it is very important to investigate the relationship between the function and structure of the films. As the first step of the studies of the relationship, Ozaki et al. [20–36] have been investigating the structural characterization of LB films of alkyl-TCNQ (Fig. 3). Molecular aggregation, orientation, structure, morphology, and thermal behavior have

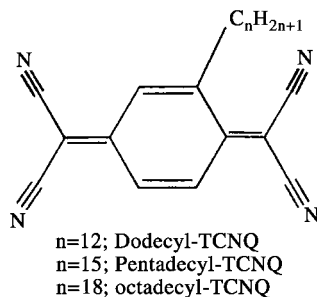


**Fig. 3.** Structure of 2-alkyl-7,7,8,8-tetracyanoquinodimethane.

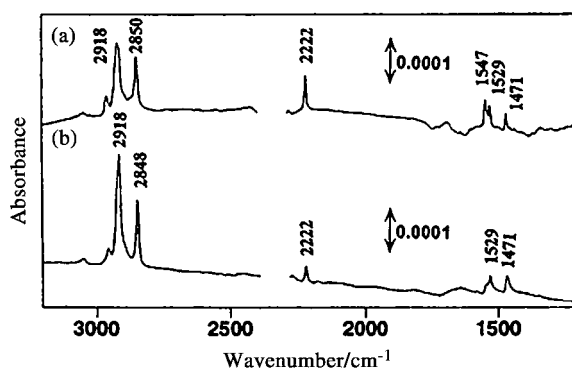


**Fig. 4.** (a) Infrared RA and (b) transmission spectra of one-layer LB films of pentadecyl-TCNQ prepared on a gold-evaporated glass slide and  $\text{CaF}_2$  plate, respectively. The spectra were measured at 6 and 5 min after the film deposition, respectively. An intense absorption band due to  $\text{CO}_2$  near  $2350\text{ cm}^{-1}$  was cut artificially. (Reproduced with permission from Ref. [34]. Copyright (2000) American Chemical Society.)

been explored for LB films of 2-dodecyl-7,7,8,8-tetracyanoquinodimethane (dodecyl-TCNQ; Fig. 3), 2-pentadecyl-7,7,8,8-tetracyanoquinodimethane (pentadecyl-TCNQ; Fig. 3), and 2-octadecyl-7,7,8,8-tetracyanoquinodimethane (octadecyl-TCNQ; Fig. 3) using visible and infrared spectroscopies and AFM.

Fig. 4(a) and (b) compare infrared RA and transmission spectra of one-layer LB films of pentadecyl-TCNQ prepared on a gold-evaporated glass slide and  $\text{CaF}_2$  plate, respectively [34]. Assignments for infrared bands of alkyl-TCNQ have been well established, and those for key bands in the infrared spectra of the LB films are as follows [20]:  $2918\text{ cm}^{-1}$ ,  $\text{CH}_2$  antisymmetric stretching;  $2850\text{ cm}^{-1}$ ,  $\text{CH}_2$  symmetric stretching;  $2222\text{ cm}^{-1}$ ,  $\text{C}\equiv\text{N}$  stretching;  $1547$  and  $1529\text{ cm}^{-1}$ ,  $\text{C}=\text{C}$  stretching;  $1471$  and  $1462\text{ cm}^{-1}$ , a doublet due to the  $\text{CH}_2$  scissoring. Bands due to the  $\text{CH}_2$  antisymmetric and symmetric stretching modes of alkyl-TCNQ are identified at  $2918$  and  $2849\text{ cm}^{-1}$ , respectively. These

frequencies suggest that the hydrocarbon chain of alkyl-TCNQ has *trans*-zigzag conformation in the LB films [20].

It is noted in Fig. 4 that the intensities of the bands at 2222, 1547, and 1529  $\text{cm}^{-1}$  due to in-plane TCNQ modes are much stronger in the RA spectrum than in the transmission spectrum. Therefore, it seems that the TCNQ plane is nearly perpendicular to the substrate surface. Transition moments of the two C=C stretching bands at 1547 and 1531  $\text{cm}^{-1}$  are perpendicular to the molecular axis of the TCNQ chromophore [20]). It should be noted that both have comparable intensities in the transmission and RA spectra (Fig. 4). Therefore, it may be concluded that the molecular axis of the TCNQ chromophore is neither parallel nor perpendicular to the surface, being in an intermediate direction. The intensities of CH<sub>2</sub> antisymmetric and symmetric stretching bands are also comparable between the two spectra, suggesting that the alkyl chain is tilted considerably with respect to the surface normal.

For the LB films of dodecyl-, pentadecyl-, and octadecyl-TCNQ, not only molecular orientation and structure but also molecular aggregation, morphology, and thermal behavior have been explored by infrared and visible spectroscopies and AFM.

The following conclusions could be reached about the molecular orientation, structure, morphology, and thermal behavior of the LB films of alkyl-TCNQ [20–25,32–35]: a one-layer LB film of octadecyl-TCNQ shows gradual thermally induced structural changes, while its multi-layer films show abrupt structural changes [21,24]. The order–disorder transition in a multi-layer LB film of octadecyl-TCNQ with the longer even-numbered hydrocarbon chain occurs at a higher temperature than that in the corresponding LB film of dodecyl-TCNQ with the shorter even-numbered hydrocarbon chain [21,24]. A multi-layer LB film of pentadecyl-TCNQ with the odd-numbered hydrocarbon chain shows a transition temperature similar to the corresponding film of dodecyl-TCNQ. The AFM studies verified that LB films of octadecyl-TCNQ consist of numerous plate-like microcrystal domains, which have the layered assembly formed by bimolecular layers with a thickness of 3.7 nm [25]. A periodic arrangement of octadecyl-TCNQ molecules with a period of 0.85 nm can be observed inside the domains. The domains in the first layer (4.3 nm) are thicker than those above the first layer (3.7 nm) [25].

### 2.3. Infrared and AFM Studies of Time-Dependent Changes in Molecular Orientation, Structure, and Morphology in One-Layer LB Films of Alkyl-TCNQ

Infrared spectroscopy and AFM were also used to explore time-dependent changes in molecular orientation, structure, and morphology in one-layer LB films of dodecyl-, pentadecyl-, and octadecyl-TCNQ [34]. Fig. 5(a)–(d) show time-dependent changes in the 3000–2800, 2250–2190, 1580–1500, and

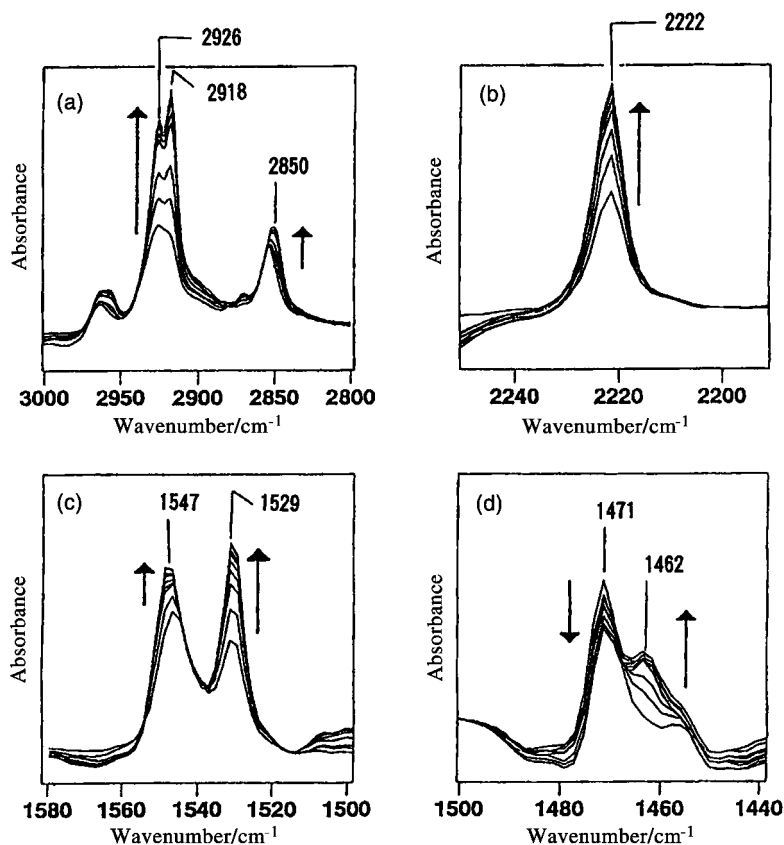


**Fig. 5.** Enlargement of time-dependent changes in the infrared RA spectrum of a one-layer LB film of pentadecyl-TCNQ on a gold-evaporated glass slides. (a) 3000–2800  $\text{cm}^{-1}$  region; (b) 2250–2190  $\text{cm}^{-1}$  region; (c) 1580–1500  $\text{cm}^{-1}$ ; (d) 1500–1440  $\text{cm}^{-1}$  region. The spectra were obtained from 6 to 131 min after the film deposition. (Reproduced with permission from Ref. [34]. Copyright (2000) American Chemical Society.)

1500–1440  $\text{cm}^{-1}$  regions of the infrared RA spectrum of a one-layer LB film of pentadecyl-TCNQ, respectively [34]. The spectra were measured between 6 and 131 min after the film deposition on a gold-evaporated glass slide. Of note in Fig. 5(a) is that the intensities of the bands due to the  $\text{CH}_2$  antisymmetric and symmetric stretching modes increase with time. This suggests that the alkyl chain is nearly perpendicular to the substrate surface in the LB film just after the film deposition, but that it becomes tilted gradually with time [34].

Fig. 5(d) reveals that the relative intensity of the two bands at 1471 and 1462  $\text{cm}^{-1}$ , assigned to  $\text{CH}_2$  scissoring modes of non-interdigitated and interdigitated parts of the alkyl chain, respectively, changes as a function of time. The observation in Fig. 5(d) suggests that the proportion of the interdigitated

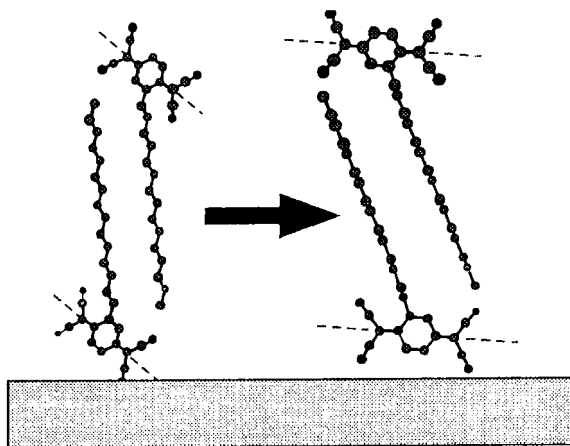


**Fig. 6.** Possible model for time-dependent (a) orientational and (b) morphological changes in a one-layer LB film of pentadecyl-TCNQ. (Reproduced with permission from Ref. [34]. Copyright (2000) American Chemical Society.)

part increases with time probably because of the evaporation of water molecules. It can be seen from Fig. 5(b) and (c) that the intensities of the  $C\equiv N$  and  $C=C$  stretching bands increase during the time course and that the relative intensity of the two bands at  $1547$  and  $1529\text{ cm}^{-1}$  varies. These observations lead to the conclusion that the TCNQ plane becomes more perpendicular with respect to the substrate surface and the molecular axis of the TCNQ chromophore becomes more tilted with respect to the surface normal with time. Based upon the results in Fig. 5, Morita et al. [34] proposed a possible model for time-dependent orientational changes in a one-layer LB film of pentadecyl-TCNQ. Fig. 6 depicts the model [34].

A one-layer LB film of dodecyl-TCNQ also undergoes similar time-dependent infrared spectral changes, although the changes are much smaller than those for the films of pentadecyl-TCNQ [34]. The corresponding LB film of octadecyl-TCNQ does not show appreciable time-dependent changes. The differences in the aging effects among the one-layer LB films of the three kinds of alkyl-TCNQ may be caused by the differences in the strength of the hydrophobic interaction between the interdigitated alkyl chains and in the degree of three-dimensional microcrystal growth in the one-layer LB films.

Morita et al. [34] also used AFM to monitor the aging of the one-layer LB films of alkyl-TCNQ. Fig. 7 depicts AFM images of a (a) fresh (15 min after the film deposition) and (b) aged (120 min after the deposition) one-layer LB films of pentadecyl-TCNQ on mica. It can clearly be seen from comparison between the images in Fig. 8(a) and (b) that flat and uniform domains in the LB film change into smaller and more condensed domains whose sizes are  $\sim 1\ \mu\text{m}$  in a few hours. Fig. 9(a) shows an AFM image of a one-layer LB film of dodecyl-TCNQ on mica measured 2 days after the film deposition. It is noted that the

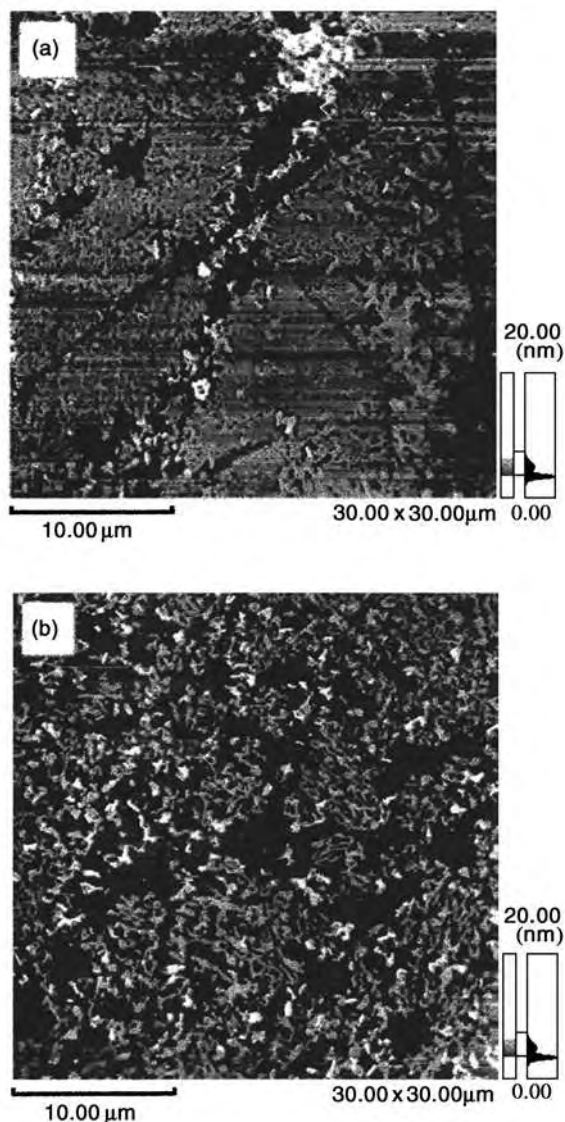


**Fig. 7.** AFM images of (a) fresh (15 min after the deposition) and (b) aged (120 min) one-layer LB films of pentadecyl-TCNQ on mica. (Reproduced with permission from Ref. [34]. Copyright (2000) American Chemical Society.)

morphology of the aged film of dodecyl-TCNQ is very similar to that of the aged LB film of pentadecyl-TCNQ (Fig. 7(b)). The domains of the aged one-layer LB films of dodecyl- and pentadecyl-TCNQ are located separate from one another with a certain distance, indicating that the condensation of the films occurs after the film deposition.

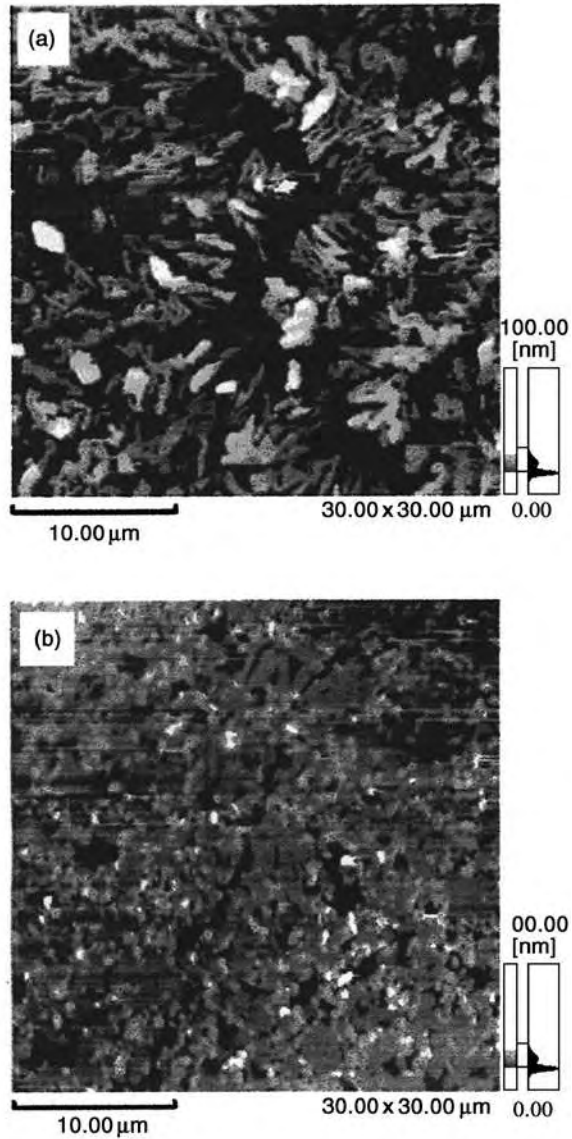


**Fig. 8.** (a) AFM images of an aged (2 days after the deposition) one-layer LB film of dodecyl-TCNQ on mica. (b) AFM image of an aged (2 days after the deposition) one-layer LB film of octadecyl-TCNQ on mica. (Reproduced with permission from Ref. [34]. Copyright (2000) American Chemical Society.)

An AFM image of a one-layer LB film of octadecyl-TCNQ on mica measured 2 days after the film deposition is shown in Fig. 9(b). In contrast to the morphology of aged one-layer LB films of dodecyl- and pentadecyl-TCNQ, the image of the aged one-layer LB film of octadecyl-TCNQ shows more flat and

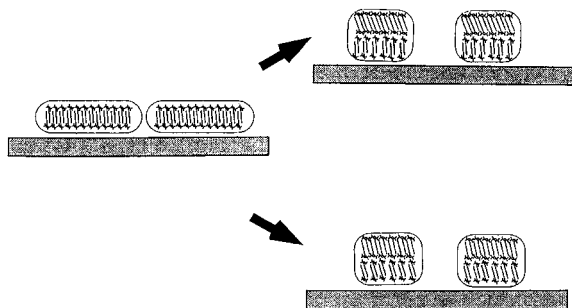


**Fig. 9.** Model for time-dependent morphological and structural changes in the one-layer LB film of pentadecyl-TCNQ. (Reproduced with permission from Ref. [34]. Copyright (2000) American Chemical Society.)

**Table 1**

Time-dependent change in the thickness of a one-layer LB film of pentadecyl-TCNQ on mica after the film deposition (from Ref. [34])

Time (min)	15	60	80	120	180
Thickness (nm)	4.6	7.7	8.3	7.9	8.2

uniformed morphology. This morphology is close to that of the fresh one-layer LB film of pentadecyl-TCNQ, suggesting that the morphology of the film of octadecyl-TCNQ varies little with aging. It is obvious that the one-layer LB film of octadecyl-TCNQ with the longer alkyl chain is more stable than those of dodecyl- and pentadecyl-TCNQ with the shorter alkyl chains, when the films are transferred onto the solid substrates from the air/water interface.

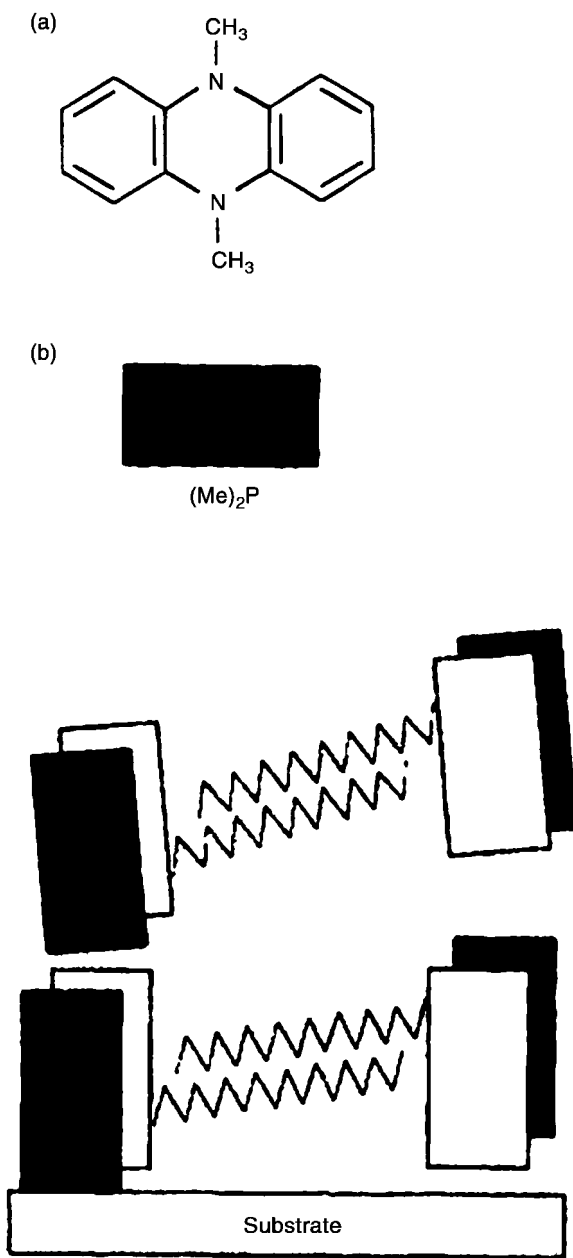
Table 1 shows the time-dependent variation in the thickness of a one-layer LB film of pentadecyl-TCNQ [34]. The thickness of the fresh LB film of pentadecyl-TCNQ is estimated to be 4.6 nm, while that of the aged film is  $\sim 8.0$  nm, which is almost double of the original thickness. The value 4.6 nm, the observed height of the fresh one-layer LB film of pentadecyl-TCNQ, is larger than the layer distance in upper layers (3.4 nm). As described above, it is very likely that in the fresh one-layer LB film of pentadecyl-TCNQ, the molecules direct more perpendicular to the substrate surface compared with those in the aged film. It is noted that the thickness of the aged one-layer LB film of pentadecyl-TCNQ is stabilized at  $\sim 8.0$  nm. This variation in the height value means that the one-layer LB film of pentadecyl-TCNQ changes its morphology from the unstable one-layer structure to the stable two-layer structure. The relative intensity of two bands at  $2926$  and  $2918\text{ cm}^{-1}$  changes largely with time. This observation suggests that the alkyl chain has more all-*trans* nature in the stable two-layer structure. It is likely that water molecules attaching to the alkyl chain evaporate with time, leading to the stable crystalline state where the alkyl chain tends to the all-*trans* conformation.

Fig. 8 illustrates two models for the aging effects on the structure and morphology of a one-layer LB film of pentadecyl-TCNQ proposed by Morita et al. [34]. The top model shows that the thickness of the bottom layer of the aged one-layer LB film is very close to that of the fresh film and that the top layer has a thinner thickness with tilted hydrocarbon chains. The bottom model depicts that both the bottom and the top layers have similar thickness with tilted hydrocarbon chains.

#### **2.4. Structural Characterization of Mixed-Stack Charge Transfer Films of Octadecyl-TCNQ and 5,10-Dimethyl-5,10-dihydrophenazine Prepared by the LB Technique and Donor Doping: Molecular Orientation and Structure and Morphology Investigated by Infrared Spectroscopy, X-ray Diffraction, and AFM**

Molecular orientation and structure and morphology in mixed-stack charge transfer (CT) films of octadecyl-TCNQ doped by 5,10 dimethyl-5,10-dihydrophenazine ((Me)<sub>2</sub>P) (Fig. 10) were investigated by using ultraviolet–visible–near-infrared and infrared spectroscopies, X-ray diffraction, and AFM [28–30]. Organic donor–acceptor CT complexes have been matters of keen interest because the segregated-stack CT complexes show metal electrical conductivity and even superconductivity [18,19]. Interest in the mixed-stack CT complexes, forming another class of donor (D)–acceptor (A) CT complexes, was awakened by a neutral-to-ionic phase transition induced by pressure or temperature. The mixed-stack CT complexes have been studied extensively because they show a variety of physical properties, such as nonlinear electrical and optional properties, and an anomalous dielectric response. The mixed-stack CT complexes, with the CT transition moments along the one-dimensional columns of D and A molecules, are further divided into quasi-neutral (N) and quasi-ionic (I) states by the magnitude of a partial electron transfer ( $\rho$ ) from the D to A molecules. When  $\rho$  is less than or greater than the value of the neutral–ionic (N-I) boundary, a CT complex is in the quasi-neutral or quasi-ionic state, respectively. In this section, the X-ray and infrared studies of the CT films are described briefly and their AFM study is introduced in some detail.

The X-ray diffraction pattern of an 11-layer film of the mixed-stack CT complex of octadecyl-TCNQ doped with (Me)<sub>2</sub>P revealed that the film has a well-ordered layered structure in which the D and A are highly oriented [28]. A  $d$  value of 3.3 nm indicates that each layer in the CT film contains biomolecular layers of alternately stacked D and A. A comparison of the IR transmission and RA spectra of the one-layer mixed-stack CT films suggested that both chromophoric planes of D and A and their long molecular axes are preferentially perpendicular to the substrate surface, while the hydrocarbon chains are parallel to it [28]. In the case of the multi-layer CT films, the D and A planes were found to be slightly tilted with respect to the surface normal and the



**Fig. 10.** Schematic models for the molecular orientation and stacking pattern of D and A molecules: (a) the LB films of octadecyl-TCNQ; (b and c) the mixed-stack CT films of octadecyl-TCNQ doped by TMB and (Me)<sub>2</sub>P, respectively. (Reproduced with permission from Ref. [28]. Copyright (1997) American Chemical Society.)

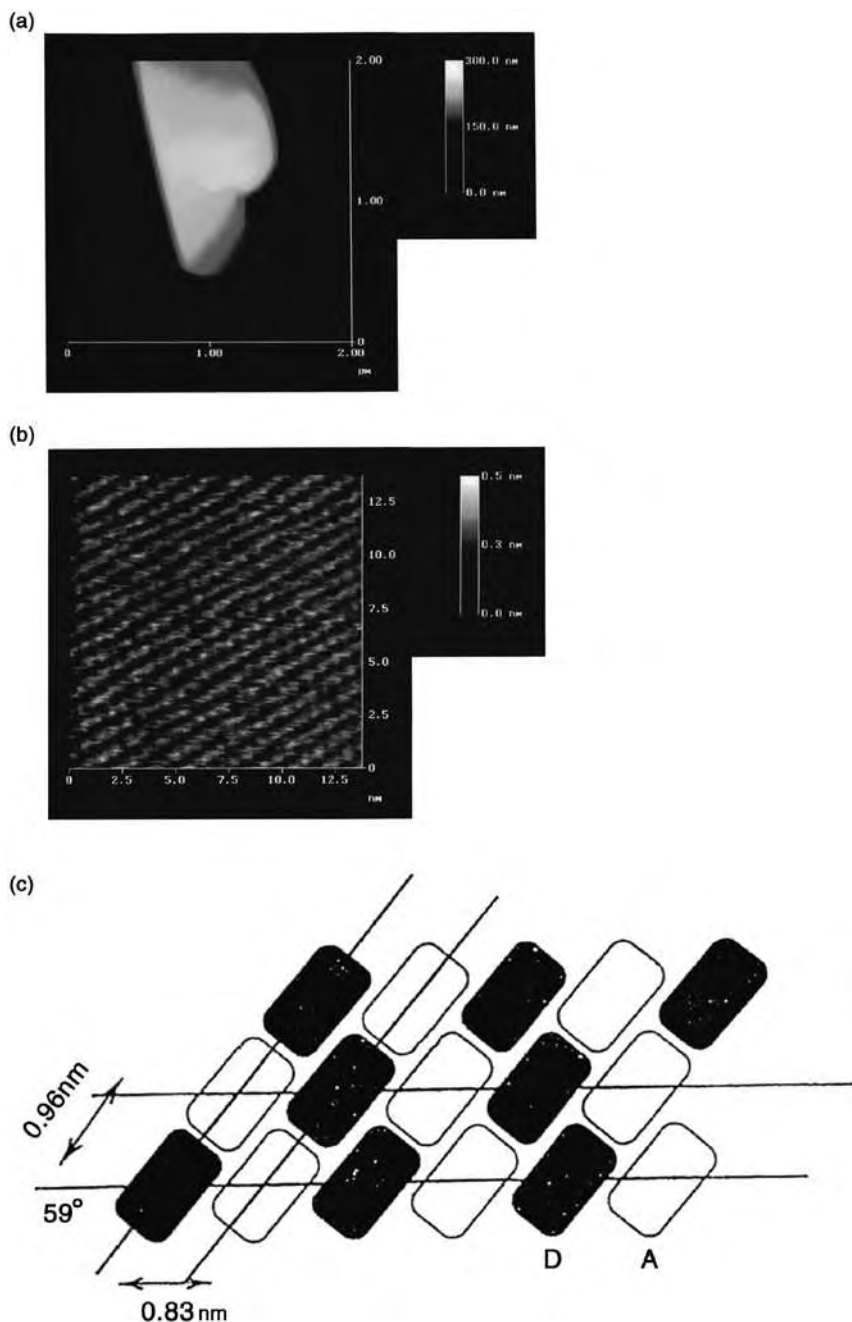
hydrocarbon chains are no longer lying on the surface but tilted a little from it. The dependence of the molecular orientation on the number of layers may be attributed to the direct interaction between the first layer and the substrate in the one-layer CT films and to the longitudinal interactions between the sheets of two-dimensional microcrystals in the multi-layer CT films. Fig. 10 illustrates schematic models for the molecular orientation and stacking pattern of D and A molecules in the mixed-stack CT films of octadecyl-TCNQ doped by (Me)<sub>2</sub>P [28]. The degree of CT (P) was determined to be 0.5 by a shift of a B<sub>1u</sub> C≡N stretching band of the TCNQ chromophore, suggesting that the complex is close to the N-I boundary [28].

Fig. 11(a) shows the AFM image of an 11-layer mixed-stack CT film of octadecyl-TCNQ and (Me)<sub>2</sub>P scanned at room temperature with a scan area of  $2 \times 2 \mu\text{m}^2$  [29]. It can be seen from the image that the CT film consists of platelet microcrystal domains of a few micrometers in size in which a multi-layered structure with many steps is observed. An analysis of the cross-sectional profile revealed that the layered platelet microcrystal domains have a step of 3.3 nm thickness [29]. This is in good agreement with the *d* value measured by the X-ray diffraction method [28]. Therefore, it seemed that the X-ray diffraction peaks originate from the multi-layered structure inside the domains. Each layer in the domains apparently consists of biomolecular layers of octadecyl-TCNQ and (Me)<sub>2</sub>P because the layer thickness of 3.3 nm is larger than the molecular length (3.0 nm) of octadecyl-TCNQ. The biomolecular layer structure also supports that the CT film is in a mixed-stack pattern.

Fig. 11(b) depicts a highly resolved AFM image ( $13 \times 13 \text{ nm}^2$ ) scanned on the surface of the platelet microcrystal domain in the 11-layer mixed-stack CT film (Fig. 11(a)) [29]. A highly ordered periodic molecular arrangement on D and A can be observed in the image. The parallel ridges are considered to be due to the stacks of D and A in the mixed-stack CT film. The interstack period across the parallel ridges was calculated to be 0.96 nm, while the intrastack period along the CT stacks was found to be 0.83 nm. The angle between the inter- and intrastack axes was measured to be 59°. These three parameters of molecular arrangement are described as (0.96 nm × 0.83 nm, angle 59°) hereafter. Fig. 11(c) illustrates a schematic model for the molecular arrangement of D and A in the CT film [29]. The above AFM images provide morphological evidence for the result obtained by the X-ray measurement, i.e., the mixed-stack CT films have the well-ordered layered structure in which the highly crystalline structure exists. This is a good example for demonstrating the utility of the combined infrared spectroscopy and AFM.

### 3. SERS STUDIES ON MONOLAYER FILMS

As a sensitive analytical tool, SERS spectroscopy can greatly increase both sensitivity and specificity of Raman spectroscopy. Hitherto, it has been considered that two mechanisms should be responsible for the SERS enhancement.



**Fig. 11.** (a) A high-resolution AFM image scanned on the surface of the platelet microcrystal domain in Fig. 1(a). (b) Molecular arrangement of acceptor (octadecyl-TCNQ) and donor ((Me)<sub>2</sub>P) inside the platelet microcrystal domains of the CT films. (Reproduced with permission from Ref. [29]. Copyright (1997) American Chemical Society.)

The first one is electromagnetic in origin and is associated with the large electric field that emerges when the roughened surface of a metal is illuminated with electromagnetic radiation. The other is chemical in nature and is associated with a resonance effect involving the charge transfer of metal [37–40]. SERS can provide unique information about the structure and orientation of molecules adsorbed on a metal surface and the interaction between different components in LB and SAM films [41–44]. SERS has several advantages to study monolayer films. For example, the structure and orientation of molecules adsorbed on a substrate can be investigated by “*in situ*” observation, and ultrahigh sensitivity of SERS makes it possible to detect the adsorbates adsorbed from a solution with a concentration of as low as  $10^{-12}$  M on a metal substrate [45,46].

### 3.1. SERS Studies on Metallophthalocyanine Self-Assembled Films on Different Organic-Monolayer-Modified Films

Li et al. [47] fabricated SAMs of ruthenium phthalocyanine (RuPc) on a silver substrate precoated with an SAM of 4-mercaptopyridine (PySH) or 1,4-bis[2-(4-pyridyl)ethenyl]-benzene (BPENB). SERS spectroscopy was used to explore the structure and orientation of the self-assembled films, and they successfully observed Raman bands due to vibrational modes of the pigment molecules in the composite films in the SERS spectra.

Fig. 12 depicts SERS spectra of (a) an SAM film of PySH and (b) an alternating bilayer self-assembly film of PySH and RuPc, and (c) a Raman spectrum of RuPc in bulk [47]. The SERS spectrum of RuPc–PySH composite film is very similar to that of PySH adsorbed on the silver substrate except for the appearance of three new bands at 1336, 674, and  $596\text{ cm}^{-1}$  (one can observe the corresponding bands in the Raman spectrum of RuPc in bulk (Fig. 12(e))). The band at  $1336\text{ cm}^{-1}$  is due to the C–N stretching mode and the two bands at 674 and  $596\text{ cm}^{-1}$  are assigned to the out-of-plane C–H bending modes of the RuPc moiety, implying that RuPc is successfully assembled on the PySH-modified silver surface. The appearance of new bands in the SERS spectra also shows that SERS is powerful in detecting molecular vibrations in a long range. Furthermore, according to the SERS selection rules [48–51], only when a molecule is orientated parallel to a metal surface, the intensity of out-of-plane vibrations will be enhanced. Thus, the appearance of the out-of-plane vibrations suggests the parallel orientation of RuPc molecules in the composite film.

It is also noted that the SERS bands arising from the SAM of PySH on the silver film before and after the binding of RuPc do show obvious changes in the frequency and relative intensity (Fig. 12(a) and (b)). A band due to the C=C stretching vibration of PySH shifts from  $1606\text{ cm}^{-1}$  to  $1609\text{ cm}^{-1}$ , the relative intensity of the band at  $1606\text{ cm}^{-1}$  to that at  $1574\text{ cm}^{-1}$ , which is sensitive to an environmental change in the N atom of PySH, increases [50,51], and a band at  $1530\text{ cm}^{-1}$  due to the C=C/C=N stretching vibration shifts to  $1509\text{ cm}^{-1}$  in the composite film, implying that the RuPc molecules are adsorbed on the PySH

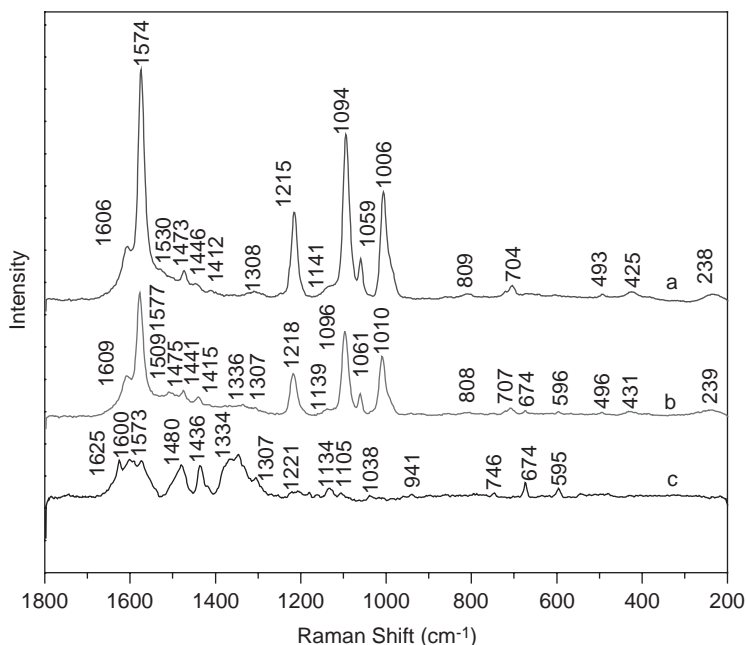


**Fig. 12.** SERS spectra of (a) an SAM film of PySH and (b) an alternating bilayer self-assembly film of PySH and RuPc, and (c) a Raman spectrum of RuPc in bulk. The laser power at the sample position was 1.0 mW for (a) and (b), and the data acquisition time was 90 s. The laser power at the sample position was 4.0 mW for (c) and the data acquisition time was 150 s. (Reproduced with permission from Ref. [47]. Copyright (2004) Elsevier.)

film through the Ru–N interaction [47]. Significant shifts are also observed in the 1100–1000  $\text{cm}^{-1}$  region, where three bands are shifted from 1094, 1059, and 1006  $\text{cm}^{-1}$  to 1096, 1061, and 1010  $\text{cm}^{-1}$ , respectively. Yamada and Yamamoto [52] observed substantial spectral changes in the same region of Raman spectra of pyridine adsorbed on a metal oxide surface and assigned these changes to different binding types of pyridine on the metal oxide surface. Therefore, the shifts observed for the three bands in the 1000–1100  $\text{cm}^{-1}$  region imply the binding of the metal ion of RuPc to the N atom of the pyridyl group, that is, RuPc is successfully assembled on the PySH film.

Fig. 13 shows (a) a Raman spectrum of BPENB in bulk and SERS spectra of (b) an SAM of BPENB on a silver substrate and (c) an alternating bilayer self-assembly film of BPENB and RuPc [47]. As is known, when molecules are chemisorbed on a metal surface, there is an overlap between a molecular orbital and a metal orbital, the molecular structure being changed, and in consequence, the positions and relative intensities of SERS bands are dramatically changed. On the other hand, an SERS spectrum of physisorbed molecules is practically the same as that of corresponding free molecules, small changes being observed

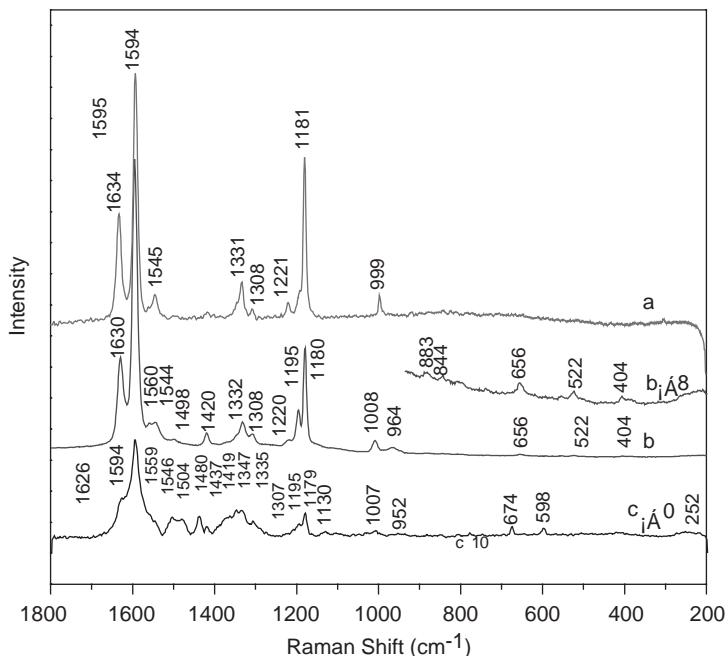


**Fig. 13.** A Raman spectrum of (a) BPENB in bulk, and SERS spectra of (b) an SAM film of BPENB and (c) an alternating bilayer self-assembly film of BPENB and RuPc. The laser power at the sample position was 1.0 mW for (b) and (c), and the data acquisition time was 10 s. (Reproduced with permission from Ref. [47]. Copyright (2004) Elsevier.)

only for bandwidths. From comparison between the spectra in Fig. 13(a) and (b), it is clear that the BPENB molecules are chemically bonded to the metal surface. This can also be confirmed by the band at 1008 cm<sup>-1</sup>, which is characteristic of the ring breathing mode of chemisorbed pyridine molecules. Considering the structure of BPENB, Li et al. [47] concluded that BPENB is chemisorbed on the silver surface through the Ag–N interaction. Thus, they proposed a nearly perpendicular orientation of BPENB molecules on the silver film due to the molecular rigidity [47]. For RuPc bound to the SAM of BPENB, the SERS spectrum shows bands from both RuPc and BPENB moieties (Fig. 13(c)). To facilitate further structural analysis, the possible band assignments for RuPc and BPENB are given in Tables 2 and 3, respectively [47]. The SAM of RuPc formed on the top of BPENB-modified silver surface exhibits six new bands at 1480, 1437, 1347, 1130, 674, and 598 cm<sup>-1</sup>, which are ascribed to vibrational modes of the RuPc moiety (Fig. 13(c), Table 2). The results confirm the ability of SERS in detecting molecular vibrations in a long range again. Additionally, it is interesting to point out that the SERS bands arising from the SAM of BPENB on the silver substrate before and after the

**Table 2**

Wavenumbers and assignments for the SERS bands of RuPc in bulk (from Ref. [47])

Wavenumbers ( $\text{cm}^{-1}$ )	Assignments	Wavenumbers ( $\text{cm}^{-1}$ )	Assignments
1625	C=N stretching	1221	C-H deformation
1600	Benzene ring stretching	1180	C-H deformation
1591	Benzene ring stretching	1162	C-H deformation
1573	C=C stretching	1134	Pyrrrole ring breathing
1480	Isoindole ring stretching	1105	C-H deformation
1436	C-H deformation	1038	C-H deformation
1419	C-H deformation	941	Macrocycle deformation
1368	C-H deformation	746	Macrocycle deformation
1347	C-N stretching	674	Out-of-plane C-H bending
1334	C-N stretching	595	Out-of-plane C-H bending
1307	C-H deformation		

**Table 3**

Wavenumbers and assignments for the SERS bands of BPENB film (from Ref. [47])

Wavenumbers ( $\text{cm}^{-1}$ )	Assignments	Wavenumbers ( $\text{cm}^{-1}$ )	Assignments
1630	Phe and vinyl stretching	1195	Phe and vinyl-C-H deformation
1595	Phe and vinyl C-H stretching	1180	Py-C-H stretching
1560	Py-C-H deformation	1008	Ring breathing
1544	Py-C-H deformation	964	Ring breathing
1498	Py-C-H and vinyl-C-H deformation	883	Py-out-of-plane C-H deformation
1420	C-H deformation	844	Phe-out-of-plane C-H deformation
1332	C-H deformation	656	In-plane ring deformation
1308	C-H* deformation	522	C-H deformation
1220	Phe-C-H deformation	404	Out-of-plane ring bending

Phe, phenyl ring; Py, pyridine ring.

\*Includes benzene C-H, vinyl C-H, and pyridine C-H near the N atom.

binding of RuPc also show significant changes in the frequencies and relative intensities. This indicates that SERS is powerful in detecting the interaction of different molecules. From the above results, Li et al. [47] concluded that RuPc is assembled on the BPENB film successfully.

The method used by Li et al. [47] for grafting RuPc on a silver substrate modified by an organic monolayer is based on the formation of an axial coordination bond between the pyridyl group of PySH or BPENB and RuPc. They reported two parallel studies on PySH- or BPENB-modified silver substrates [47,53]. In both cases, the results indicate that RuPc can be assembled on the top of PySH- or BPENB-modified silver films. There is no doubt that the orientation of RuPc is largely dependent on that of PySH or BPENB on the silver surface, namely, on the direction of the lone pair electrons of the pyridine N atom that coordinates to the central metal, Ru of the phthalocyanine core. Osawa and co-workers [54] reported based on scanning tunneling microscopy (STM) measurements that the pyridine plane of 4-mercaptopyridine SAM on Au (111) lies nearly parallel to the gold surface. Another Japanese group [55], however, based also on their STM observation of 4-mercaptopyridine SAM on Au (111), proposed that the pyridine ring is oriented almost vertical to the Au(111) surface, and that the molecular axis passing through the N and S atoms is tilted appreciably with respect to the surface normal. The latter conclusion is in good agreement with other previous literature results for the SAMs of 4-pyridinethiolate and related compounds on gold or silver surfaces [56–59]. Considering the geometry of metallophthalocyanine and the M–N bond length of about 1.9–2.2 Å for the central metal (M) and the N atom of the axial ligand [60–62], the ligation of the Ru atom of phthalocyanine core with the N atom of the pyridine moiety indicates that the pyridine plane is not oriented parallel to the surface. The N atom of pyridine should be in a position that allows the access of RuPc to it. In the RuPc–PySH composite film, both the pyridine plane and the axis through the N and S atoms are tilted, at least to some extent, with respect to the silver surface.

Comparing the SERS spectra of the two kinds of composite films, it can be seen that the six new bands due to the vibrational modes of RuPc appear in the SERS spectrum of the RuPc–BPENB composite film (Fig. 13(c)) while only three new bands appear for the RuPc–PySH composite film (Fig. 12(b)). These observations may be ascribed to the differences in the conjugation system, structure, and orientation between the two kinds of SAMs and to the different interaction between PySH/BPENB and RuPc. According to the SERS selection rules [48–51], SERS enhancement always emerges from the vibrations that have depolarizable components perpendicular to a metal surface, and the magnitude of the enhancement will be proportional to the projection of the dipole moment perpendicular to the surface. The spectral changes observed in the two kinds of composite films led Li et al. [47] to conclude that the orientations of PySH and BPENB on the silver substrates are different, and that BPENB should be oriented nearly perpendicular to the silver surface while PySH is tilted with respect to the silver surface, as shown in Fig. 14.

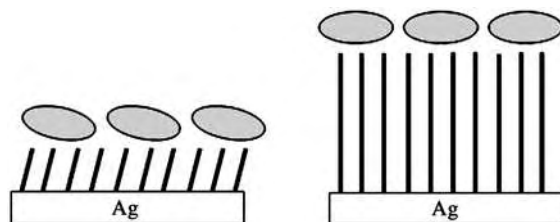


**Fig. 14.** Possible sketches for the RuPc–PySH (left) and RuPc–BPENB (right) composite films. (Reproduced with permission from Ref. [47]. Copyright (2004) Elsevier.)

### 3.2. SERS Studies on Metalloporphyrin Self-Assembled Films on Organic-Monolayer-Modified Substrates

Li *et al.* [63] investigated effects of a central metal on the formation of metalloporphyrin SAMs linked by an axial ligand on PySH-modified silver substrates. A porphyrin monolayer can be formed by chemical linkage between the central metal of a metalloporphyrin hydroxyl (MOH) compound and a modified silver substrate. PySH is very much favorable to realize the graft of MOH because it not only modifies the silver substrate but also delivers a pyridyl group anchoring on the surface. Thus, the key point is to form a coordination bond between the nitrogen atom of the pyridyl group and the central metal of a porphyrin compound. Li *et al.* [63] studied two metalloporphyrin SAMs on the PySH-modified silver substrates and focused their attention on the effects of the central metal on the structure and orientation of metalloporphyrin composite films.

Fig. 15 shows SERS spectra of (a) an SAM film of PySH and (b) an alternating bilayer self-assembly film of PySH and TbOH, and (c) a Raman spectrum of TbOH in bulk [63]. The SERS spectrum of the SAM film of PySH presents a band at  $243\text{ cm}^{-1}$ , which is characteristic of the Ag–S stretching mode, indicating that PySH is bounded on the silver substrate through the sulfur atom of pyridine group. The assignments for PySH adsorbed on a silver substrate can be referred to Refs. [64,65] and the possible assignments for TbOH (and LuOH) in bulk are listed in Table 4. A band at  $1612\text{ cm}^{-1}$  arising from the ring stretching mode of PySH disappears in the SERS spectrum of the bilayer self-assembly film of PySH and TbOH (Fig. 15(b)). It is known that this band is sensitive to the environmental changes in the N atom of PySH. Therefore, its disappearance implies that the porphyrin molecules are anchored on the N atoms of the pyridyl groups. Two pair of bands are observed at  $1597$  and  $1583\text{ cm}^{-1}$  and  $1030$  and  $1012\text{ cm}^{-1}$  in the same spectrum (Fig. 15(b)), suggesting that there are at least two kinds of different phenyl rings in the composite film or that not all the phenyl rings are in the same plane. In the present case, the bands at  $1597$  and  $1030\text{ cm}^{-1}$  can be attributed to the ring stretching and

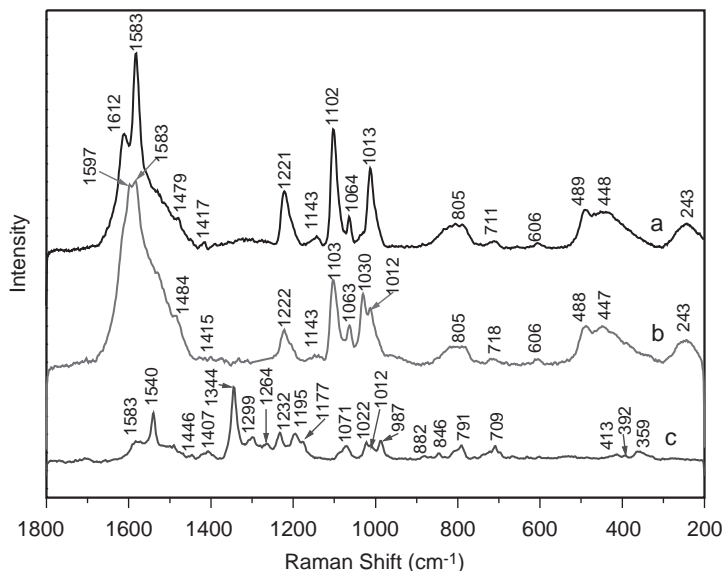


**Fig. 15.** SERS spectra of (a) an SAM film of PySH and (b) an alternating bilayer self-assembly film of PySH and TbOH, and (c) a Raman spectrum of TbOH in bulk. The laser power incident upon the samples was 4.0 mW and the data acquisition time was 250 s for (a) and (b). The laser power at the sample was 2.0 mW and the data acquisition time was 120 s for (c). (Reproduced with permission from Ref. [63]. Copyright (2004) Society for Applied Spectroscopy.)

breathing vibrations of four phenyl rings of TbOH, which are rotated by about  $80^\circ$  to the plane of the porphyrin macrocycle, and the bands at  $1583$  and  $1012\text{ cm}^{-1}$  to the corresponding vibrations of the pyridyl ring of PySH. Moreover, it is noted that the SERS bands arising from the SAM of PySH on the silver substrate before and after the binding of TbOH show clear changes in the frequencies and relative intensities (Fig. 15(a) and (b)). Especially, the band at  $711\text{ cm}^{-1}$  shows a significant upward shift to  $718\text{ cm}^{-1}$ . All these changes indicate that TbOH is successfully assembled on the PySH-modified silver surface. It is known that the pyridyl ring of PySH is tilted with respect to the surface when it is adsorbed on a metal surface. There is not enough evidence that indicates that the pyridyl ring orientation changes upon the formation of the TbOH–PySH composite film.

Fig. 16 shows SERS spectra of (a) an SAM film of PySH and (b) an alternating bilayer self-assembly film of PySH and LuOH, and (c) a Raman spectrum of LuOH in bulk [63]. The assignments for LuOH in bulk are also listed in Table 4 [63]. The spectrum in Fig. 16(b) shows SERS bands arising from both LuOH and PySH moieties, suggesting the formation of the LuOH–PySH composite film. The SAM of LuOH formed on the top of the

**Table 4**

Wavenumbers and assignments for the Raman bands of (a) TbOH in bulk and (b) LuOH in bulk (from Ref. [63])

Wavenumbers (cm <sup>-1</sup> )		Assignments
TbOH	LuOH	
1583	1577	$\nu(\text{C}_\beta\text{-C}_\beta)$
1540	1543	$\nu(\text{C}_\alpha\text{-C}_m)$
1446	1450	$\nu(\text{C}_\alpha\text{-C}_\beta)/\delta(\text{C}_\beta\text{-H})$
1407	1409	$\nu(\text{C}_\alpha\text{-N})/\nu(\text{C}_\beta\text{-C}_\beta)$
1344	1348	$\nu(\text{C}_\alpha\text{-N})/\nu(\text{C}_\beta\text{-C}_\beta)$
1299	1297	$\nu(\text{C}_\alpha\text{-N})/\nu(\text{C}_\beta\text{-C}_\beta)$
1264	1261	$\nu(\text{C}_\alpha\text{-N})/\nu(\text{C}_\beta\text{-C}_\beta)$
1232	1233	$\nu(\text{C}_m\text{-Ph})$
1195	1195	$\delta(\text{C}_\beta\text{-H})$
1177	1171	$\delta(\text{C}_\beta\text{-H})$
1071	1068	$\delta(\text{C}_\beta\text{-H})$
1022	1025	Phenyl
1012	1012	$\nu(\text{C}_\alpha\text{-N})/\nu(\text{C}_\alpha\text{-C}_\beta)$
987	990	$\nu(\text{C}_\alpha\text{-N})/\nu(\text{C}_\alpha\text{-C}_\beta)$
882	880	$\delta(\text{Pyr. def.})$
846	846	$\delta(\text{Pyr. def.})$
791	791	$\delta(\text{Pyr. def.})$
709	710	$\gamma(\text{C}_\beta\text{-H})$
413	414	$\nu(\text{N-M})$
392	395	$\nu(\text{N-M})$
359	367	$\delta(\text{Pyr. def.})$

PySH-modified silver film shows two new bands at 1544 and 1349 cm<sup>-1</sup> in comparison with the spectrum of the SAM film of PySH (Fig. 16(a)); these bands are obviously due to vibrational modes of the LuOH moiety (Fig. 16(c)). Furthermore, the frequencies and relative intensities of SERS bands arising from the PySH-modified silver film show significant changes after the binding of LuOH. The relative intensity of two bands at 1611 and 1581 cm<sup>-1</sup> changes very much upon the formation of the composite film, implying that LuOH is adsorbed on the N atom of the PySH molecules. Bands at 1611, 1581, 1099, and 1062 cm<sup>-1</sup> shift to 1613, 1584, 1102, and 1065 cm<sup>-1</sup>, respectively, indicating the strong interaction between PySH and LuOH molecules in the composite film. Of note is that a band at 1221 cm<sup>-1</sup> due to the in-plane C-H bending mode of the PySH molecules disappears in the SERS spectrum of the composite film. This indicates that the orientation of the PySH molecules changes. According to the SERS selection rules [48–51], the disappearance of the band at 1221 cm<sup>-1</sup> due to the in-plane C-H bending mode of PySH suggests that the PySH plane becomes more parallel to the silver substrate upon the formation of the composite film.

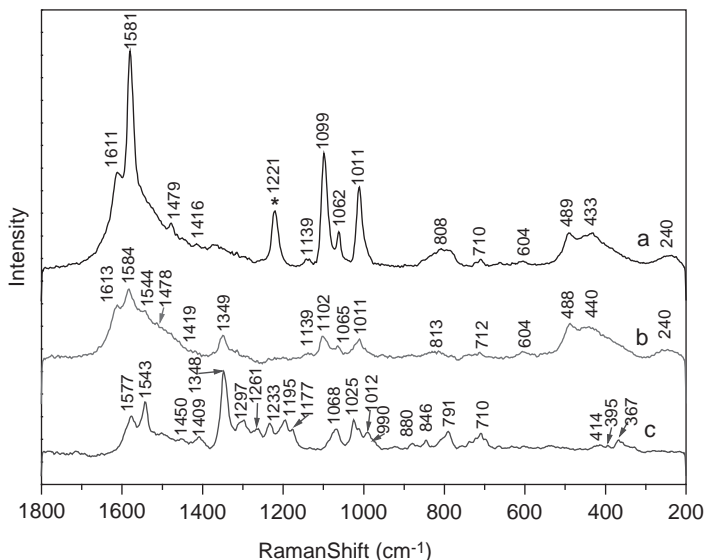


**Fig. 16.** SERS spectra of (a) an SAM film of PySH and (b) an alternating bilayer self-assembly film of PySH and LuOH, and (c) a Raman spectrum of LuOH in bulk. The laser power incident upon the samples was 4.0 mW and the data acquisition time was 150 s for (a) and (b). The laser power at the sample position was 0.4 mW and the data acquisition time was 40 s for (c). (Reproduced with permission from Ref. [63]. Copyright (2004) Society for Applied Spectroscopy.)

### 3.3. An SERS Study on the Orientation of an Atactic Poly(methyl methacrylate) Thin Film on a Silver Substrate

Zhang et al. [66] investigated the orientation of an atactic poly(methyl methacrylate) (a-PMMA) thin film on a silver substrate by SERS. Fig. 17(a) and (b) show a SERS spectrum of a-PMMA dip-coated onto the top of a silver substrate and a Raman spectrum of the solid powder of a-PMMA, respectively. Remarkable spectral changes can be observed between the two spectra. A band at  $1602\text{ cm}^{-1}$ , which is very weak in the normal Raman spectrum, is the strongest band in the SERS spectrum. Similarly, a band near  $1003\text{ cm}^{-1}$  is of medium strength in the Raman spectrum of a-PMMA but becomes very strong in the SERS spectrum. The  $1003\text{ cm}^{-1}$  band was assigned to the O-CH<sub>3</sub> rocking vibration interacting with the stretching vibration of the C-O-C group. Dybal and Krimm [67] have confirmed this assignment by the normal-coordinate calculations, and the potential energy distribution (PED) has indicated the large contribution from the C-O-C stretching vibration. However, it is difficult to assign the band near  $1602\text{ cm}^{-1}$ . The appearance of the strong band near  $1600\text{ cm}^{-1}$  is most likely due to chemical adsorption; in other words, there is some interaction between the a-PMMA thin film and the

**Table 5**

Assignments of bands in SERS spectra of a-PMMA (from Ref. [66])

Wavenumber (cm <sup>-1</sup> )	Relative intensity <sup>a</sup>	Tentative assignment of the bands discussed <sup>b</sup>	Polarization to interface <sup>c</sup>
1732	Vm	$\nu(\text{C}=\text{O})$	
1602	Vs	?	⊥
1452	W	$\delta(\text{CH}_2)$	
1380	M	$\delta_s(\alpha\text{-CH}_3)$	⊥
1003	Vs	$\nu_s(\text{C}-\text{O}-\text{C})$	⊥
837	M	r(CH <sub>2</sub> )	⊥

<sup>a</sup>s, strong; m, medium; w, weak; and v, very.<sup>b</sup> $\nu_s$ , symmetric stretching;  $\delta$ , bending;  $\delta_s$ , symmetric bending; and r, rocking.<sup>c</sup>The symbol || indicates that the polarizability change associated with the band is parallel to the interface between polymer and metal; ⊥ indicates that the polarizability change is perpendicular to the interface.

silver substrate, although the mechanism of the chemical adsorption is still unclear [66].

The tentative assignment of the SERS spectrum of the a-PMMA film is shown in Table 5 [66]. It can be seen from the SERS spectrum (Fig. 17(a)) of the a-PMMA film that the bands near 1380 and 837 cm<sup>-1</sup> show great enhancement compared with those in the Raman spectrum. Thus, the polarizability changes associated with these bands are perpendicular to the interface between the polymer and the metal. The bands near 1380 and 837 cm<sup>-1</sup> are assigned to the R-CH<sub>3</sub> symmetric bending and CH<sub>2</sub> rocking vibrations, respectively (Table 5), and both involve considerable motion perpendicular to the long axis of the molecules. Assuming that a-PMMA is adsorbed with the molecular axes mostly parallel to the surface, the corresponding bands should appear with considerable intensity, and that is what has been observed. The band near 1452 cm<sup>-1</sup> is assigned to the CH<sub>2</sub> symmetric bending vibration that involves a motion mostly parallel to the long axis of the molecules. In the SERS spectrum in Fig. 17(a), Zhang et al. [66] found that the intensity of the band near 1452 cm<sup>-1</sup> decreases largely. Thus, it is very likely that a-PMMA is adsorbed with the molecular axes mostly parallel to the substrate. Moreover, from the relative intensity of perpendicular bands and parallel bands, it is obvious that the molecular chain of a-PMMA is aligned more parallel to the substrate at the interface than in the bulk. A relatively strong band near 1732 cm<sup>-1</sup> in the Raman spectrum is very weak in the SERS spectrum. This band has been assigned to the C=O stretching mode. However, the band near 1003 cm<sup>-1</sup>, which has been assigned to the C-O-C stretching vibration, is enhanced in the SERS spectrum. Both of the two bands are concerned with the ester group of a-PMMA. It is believed that in this case, the differences are related to a geometry structure caused by the presence of the metal surface [66]. When an a-PMMA film is dip-coated on a silver mirror substrate,

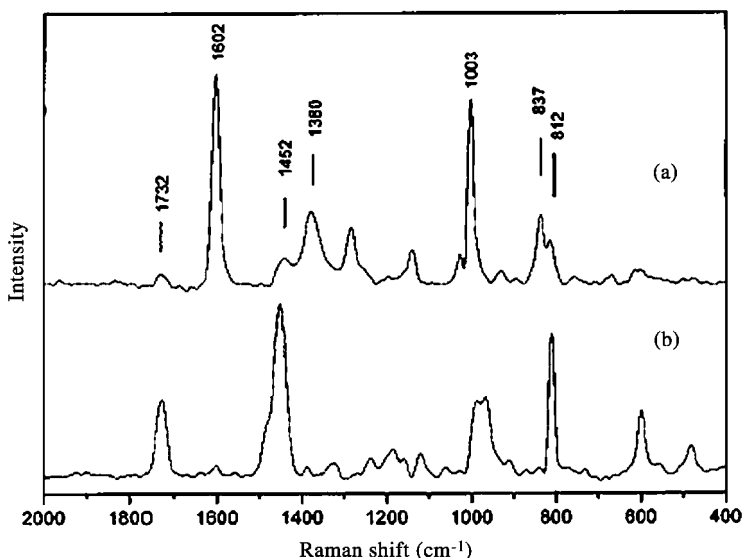


**Fig. 17.** (a) An SERS spectrum from a-PMMA dip-coated onto the top side of the substrate. (b) A Raman spectrum of the bulk a-PMMA. (Reproduced with permission from Ref. [66]. Copyright (2002) American Chemical Society.)

molecules in the first monolayer have a conformation with one ester group in contact with the surface. According to the SERS selection rules [48–51], C=O stretching modes are likely to be parallel to the metal surface and the corresponding SERS band should be weak; meanwhile, the C–O–C stretching modes are likely to be perpendicular to the metal, and the corresponding SERS bands should be strong.

The effect of annealing temperature on the configuration of a-PMMA adsorbed onto the silver surface was also investigated. Fig. 18(a) shows the SERS spectrum of a-PMMA dip-coated onto the top of a silver substrate before annealing and Fig. 18(b) and (c) depict those after annealing at 120 and 150 °C for 1 h, respectively [66]. Compared with the SERS spectrum before annealing, the intensity of the band near 1003 cm<sup>-1</sup> decreases largely with the increase in the annealing temperature. In the earlier discussion of RA infrared spectra of a-PMMA, Zhang et al. [66] suggested that there is a conformational transition of ester groups in the a-PMMA thin film. Upon annealing above the glass transition temperature, the structure of the ester group changes from *gauche* conformer into *trans* conformer (Fig. 19). In such case, the direction of C–O–C stretching mode changes from normal into parallel to the surface of substrate. This is in accordance with the decrease in the intensity of the strong band near 1003 cm<sup>-1</sup> in the SERS spectra after annealing.

It is also interesting to note that there is a change in the relative intensity of two bands at 837 and 812 cm<sup>-1</sup> when increasing the annealing temperature.

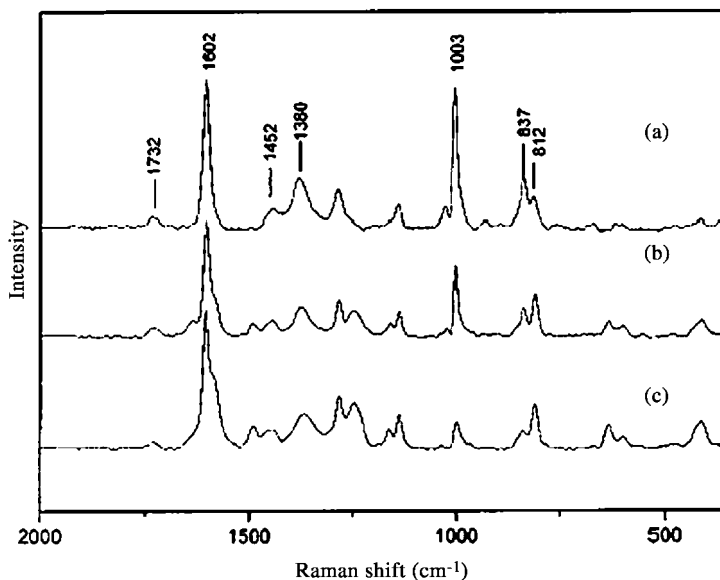


**Fig. 18.** SERS spectra from a-PMMA dip-coated on the top of the substrate (a) without annealing, (b) after annealing at temperature 120 °C for 1 h, and (c) after annealing at 150 °C for 1 h. (Reproduced with permission from Ref. [66]. Copyright (2002) American Chemical Society.)

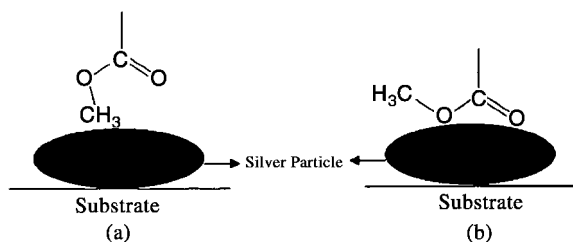


**Fig. 19.** Possible structures of adsorbed ester group of a-PMMA on a silver particle: (a) *gauche* conformer and (b) *trans* conformer. (Reproduced with permission from Ref. [66]. Copyright (2002) American Chemical Society.)

There have been hot debates about the assignment of the Raman band at  $812\text{ cm}^{-1}$  of a-PMMA. However, the band at  $837\text{ cm}^{-1}$ , as discussed above, is assigned to the  $\text{CH}_2$  rocking vibration that involves a motion perpendicular to the long axis of the a-PMMA molecule. Its decrease in the intensity indicates that the molecular chains of a-PMMA deviate from the surface after annealing. When annealing at a higher temperature (above the  $T_g$ ), the molecular chains begin to relax, which is also in accordance with the change in the SERS spectrum.

## 4. AFM STUDIES ON MONOLAYER FILMS

### 4.1. AFM Studies on Metalloporphyrin LB Films

For a mixed LB film, AFM is a powerful tool to investigate the miscibility and phase separation of component molecules. Li et al. [68] studied the structural characterization of rare earth metalloporphyrin (TbOH/GdOH) Langmuir/LB monolayers and their mixtures with stearic acid (SA) on solid surfaces by use of surface pressure–molecular area ( $\pi$ - $A$ ) isotherm measurement, AFM, and spectroscopy techniques. They studied molecular aggregation and stacking in the TbOH and GdOH LB films, and the influences of added SA on the monolayer organization and interactions between the metalloporphyrin macrocycles.

Fig. 20(a) and (b) show AFM images of one-layer LB films deposited from TbOH and TbOH/SA monolayers, respectively [68]. The TbOH LB film exhibits a heterogeneous surface with some aggregates on the mica, while the TbOH/SA LB film shows obvious phase separation between Phase 1 and Phase 2. The height of Phase 1 in the TbOH/SA LB film is about two times higher than that of Phase 2 in the AFM image in Fig. 20(b) and almost comparable with that of the TbOH LB film (Fig. 20(a)). As is well known, the porphyrin–porphyrin overlap occurs during compression. Thus, it is very likely that the TbOH LB film consists of overlapped porphyrins. For the TbOH/SA LB film, the introduction of SA seems to break the stacking  $\pi$ - $\pi$  interaction between TbOH molecules, and thus some monolayers with preferable mutual miscibility are formed. Consequently, Li et al. [68] concluded that Phase 1 consists of the stacking porphyrins while Phase 2 is composed of porphyrin monolayers. Fig. 20(c) and (d) show AFM images of one-layer LB films deposited from GdOH and GdOH/SA monolayers, respectively. The two LB films on the mica surfaces contain some porphyrin aggregates, indicating that the mutual miscibility of GdOH and SA is preferable.

The AFM images of the TbOH and GdOH LB films show some porphyrin aggregates. However, the image of the TbOH/SA LB film shows an obvious phase separation while the GdOH/SA LB film exhibits similar morphology to the GdOH LB film. Though the alkyl chains of SA almost have no influence on the porphyrin ring orientation, they have great influence on the packing of the molecules. In contrast to the TbOH/SA LB film due to much stronger  $\pi$ - $\pi$  interactions between GdOH molecules, the introduction of SA cannot break them, and thus the monolayers cannot be formed in the GdOH/SA LB film. Accordingly, Li et al. [68] did not observe the phase separation in the GdOH/SA LB film. This result is consistent with the BAM observations of TbOH, GdOH, TbOH/SA, and GdOH/SA Langmuir films and further demonstrates the important effects of a porphyrin central metal on the organization and formation of the mixed films.

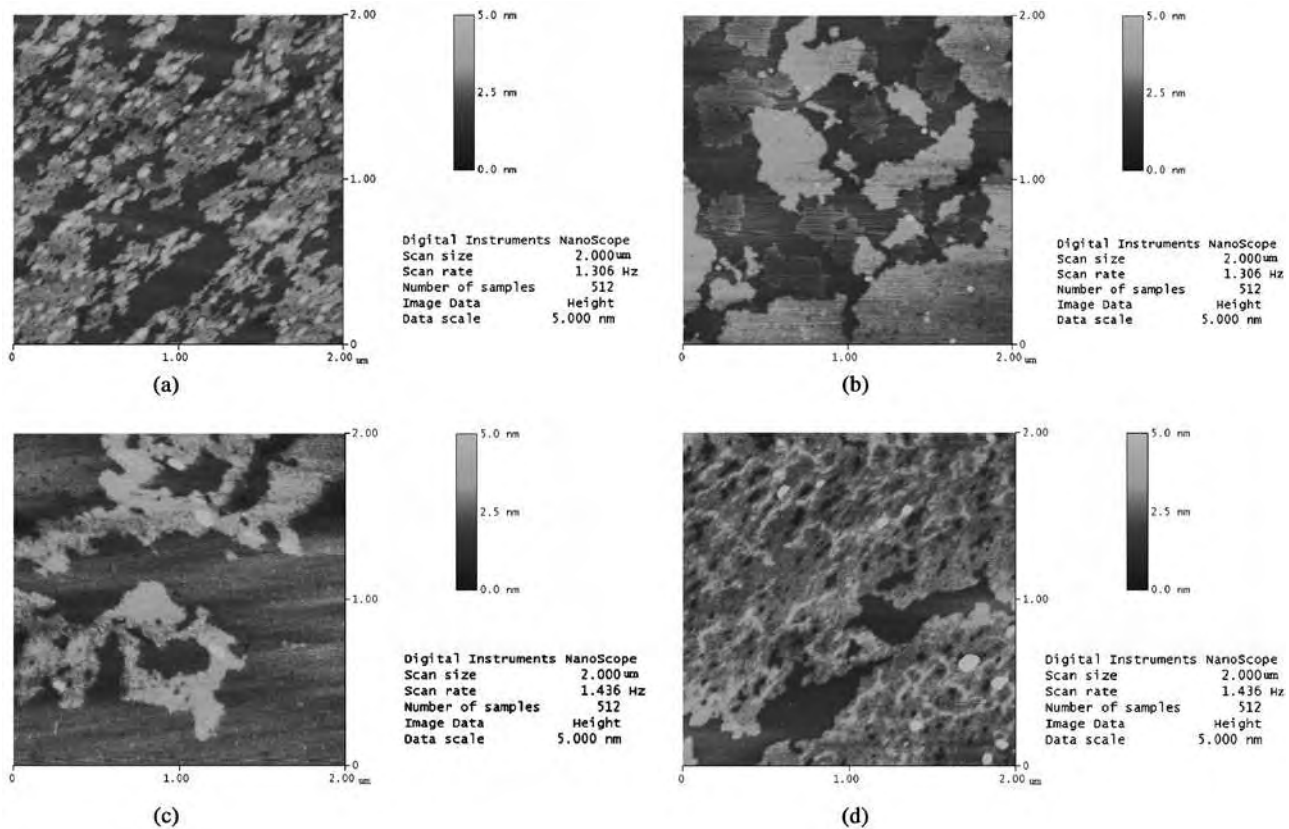


**Fig. 20.** AFM images of one-layer LB films deposited from (a) TbOH, (b) TbOH/SA, (c) GdOH, and (d) GdOH/SA monolayers. (Reproduced with permission from Ref. [68]. Copyright (2005) Elsevier.)

#### 4.2. An *In Situ* AFM Study on Morphological Changes in an LB Film of Cadmium 10,12-Pentacosadiynoate during Polymerization

Tachibana et al. [69] explored the morphological changes in an LB film of cadmium 10,12-pentacosadiynoate during polymerization by *in situ* AFM. Fig. 21 shows *in situ* AFM images of the one-layer DA(12-8) LB film during the polymerization by the irradiation of UV light [69]. Before the irradiation of UV light, several three-dimensional structures with a height of 5 nm above the planar surface are evident (Fig. 21(a)). The morphology of the DA(12-8) LB film remains unchanged in the initial regime where the film is in the blue phase (Fig. 21(b)). In the second regime, a number of three-dimensional domains begin to appear from the planar surface (Fig. 21(c)). *Ex situ* AFM gave similar results. With increasing the irradiation time, the number of three-dimensional domains increases slightly and each domain grows (Fig. 21(d) and (e)). In the

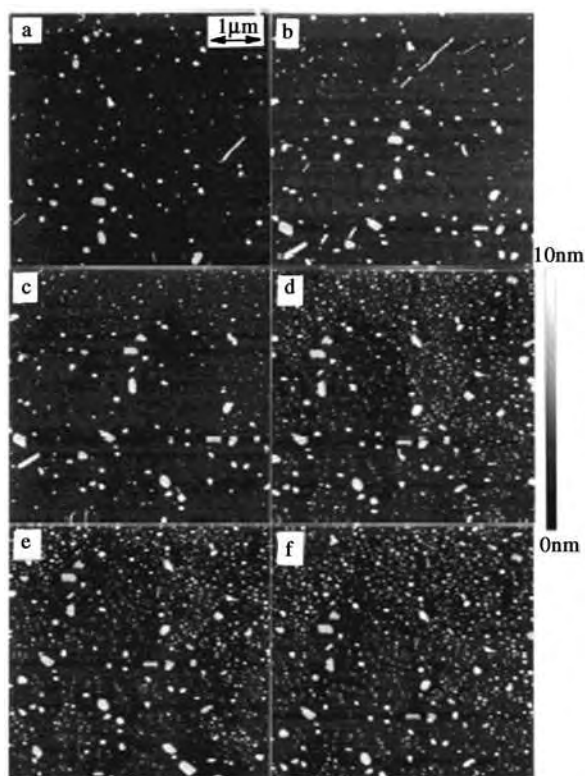


**Fig. 21.** AFM images ( $5 \times 5 \mu\text{m}^2$ ) of a one-layer LB film of DA(12-8) with different irradiation times of UV light: (a) before irradiation, (b) irradiation time of 5 min, (c) 15 min, (d) 30 min, (e) 50 min, and (f) 90 min. (Reproduced with permission from Ref. [69]. Copyright (2000) American Chemical Society.)

final regime, the number of three-dimensional domains does not change significantly and each domain increases its size slightly (Fig. 21(f)).

They assumed the following processes [69]: when the polymerization proceeds, the propagation of the polymer backbone will impose a significant stress on the structure of the LB films. When this stress exceeds a certain threshold, a structural change associated with a color change will occur to release a part of the stress accumulated in the film. This color change shows a decrease in the effective conjugation length of the polydiacetylene backbone, which could be caused by the disruption of the conjugation due to the displacement of some of the atoms in the polymer backbone. The color change caused by the stress in the film will lead to the modification of the structure of the LB film. This should be responsible both for the order–disorder transition of the alkyl chains and for the morphological change of the film. In the final regime, the morphology of the film changes only slightly until a saturated state is reached. This is a good example of an *in situ* AFM study on morphological changes in an LB film.

## 5. INFRARED AND VISIBLE ABSORPTION SPECTROSCOPY STUDIES ON J- AND H-AGGREGATES IN LB FILMS OF MEROCYANINE DYE

A great deal of attention has recently been paid to potential applications of thin films containing synthetic dyes to various devices including photovoltaic cells, optical waveguides, and ultrafast optical switches, aiming at the realization of the devices with novel functions that cannot be performed by using thin films composed of inorganic materials [70–73]. When the thin films are fabricated using dyes, a variety of dye aggregates are often formed through various non-covalent interactions such as permanent dipole, hydrophobic, coordination,  $\pi$ – $\pi$  stacking and hydrogen-bonding interactions [73,74]. Among them, it is well known that there are two limiting types of dye aggregates categorized by the orientation of transition dipole moments and the spectral characteristics [73]. One is J-aggregates that exhibit a red-shifted sharp absorption from a monomer electronic transition and an intense emission with a small or zero Stokes shift. The other is H-aggregates showing a blue-shifted sharp absorption and no or a weak emission with an appreciable Stokes shift.

The J- and H-aggregates have been found to possess the usefulness according to their respective aggregates for the device applications [70–73,75,76]. Therefore, studies on the control of the dye aggregate formation and the formation mechanism of their aggregates in thin films are of great importance for practical use as well as for basic research of assembled dye molecules to understand their phenomena.

In this section, infrared and visible spectroscopy studies on the structure and the formation mechanism of the J- and H-aggregates in LB films of

merocyanine dye (MS, 3-carboxy-methyl-5-[2-(3-octadecyl-benzothiazolin-2-ylidene)-ethylidene]rhodanine, see Fig. 22(a)) are described. For the LB films of MS, the J- and H-aggregates can be easily controlled [77–84].

When a mixed LB film composed of an MS–arachidic acid ( $C_{20}$ ) binary system is prepared using an aqueous subphase containing  $Cd^{2+}$  ions, a red-shifted sharp absorption peak is observed at 590 nm, which is red-shifted from that of the MS monomer peak at around 540 nm. The red-shifted sharp absorption band at 590 nm is called J-band, and is ascribed to the specific alignments of MS, i.e., J-aggregates. There have been so far many reports as to the LB films of the MS J-aggregates not only for functions such as photoconduction [85], photoelectric conversion [86], and nonlinear optics [87] but also for structures including in-plane orientation [88] and formation mechanism [89–95]. On the other hand, there was only one example as to a blue-shifted band of the MS LB films. Nakahara and Möbius observed a blue-shifted sharp absorption band at around 500 nm for the monolayers of an MS–methyl arachidate–*n*-hexadecane ternary system formed on an air/water interface [89]. However, no discussion was given for the assignment and the origin of the blue-shifted band.

Hirano et al. [77–84] found that a blue-shifted H-band is induced at 505 nm when a mixed LB film is fabricated by adding a small amount of *n*-alkane species ( $AL_n$ ) including *n*-octadecane ( $AL_{18}$ ) to the MS– $C_{20}$  binary system. Furthermore, they explored a structural factor governing the aggregation states by characterizing the MS structures in the J- and H-aggregates in the mixed LB films of the binary and ternary systems towards the elucidation of the formation mechanism of the blue-shifted H-aggregates. The structural characterization of MS in both aggregates studied by means of infrared and visible absorption spectroscopy is outlined below.

## 5.1. Formation and Assignments of Red- and Blue-Shifted Bands in LB Films of MS

Fig. 22(b) shows polarized visible absorption spectra of mixed LB films of MS– $C_{20}$  binary and MS– $C_{20}$ – $AL_{18}$  ternary systems prepared by using an aqueous subphase containing  $Cd^{2+}$  ions, where the ratio in the mixed system is  $[MS]:[C_{20}]:[AL_{18}] = 1:2:x$  ( $x = 0$  and 1) [77–84]. The thick and thin lines in Fig. 22(b) refer to the spectra,  $A_{\parallel}$  and  $A_{\perp}$ , measured by linearly polarized light with the electric vector parallel and perpendicular to the dipping direction of the substrate, respectively. For  $x = 0$ , a sharp absorption peak is observed at 590 nm, which is red-shifted from the MS monomer peak at around 540 nm. The dichroic ratio  $R$  of the 590 nm band is  $R > 1$ , where  $R$  is defined as  $A_{\parallel}/A_{\perp}$ . For  $x = 1.0$ , on the other hand, a sharp blue-shifted band with  $R < 1$  appears at 505 nm. Fig. 22(c) refers to the cases of the corresponding binary and ternary systems fabricated under the subphase without the  $Cd^{2+}$  ions [84]. Unlike the results in Fig. 22(b), remarkably red- and blue-shifted bands are not observed

with their  $R$  being unity. Therefore, it could be recognized that the  $\text{Cd}^{2+}$  ions mixed into the subphase are of significance for the formation of the bands in Fig. 22(b).

The formation of the red- and blue-shifted bands and their dichroic behaviors in Fig. 22(b) could be interpreted referring to the excitation energy

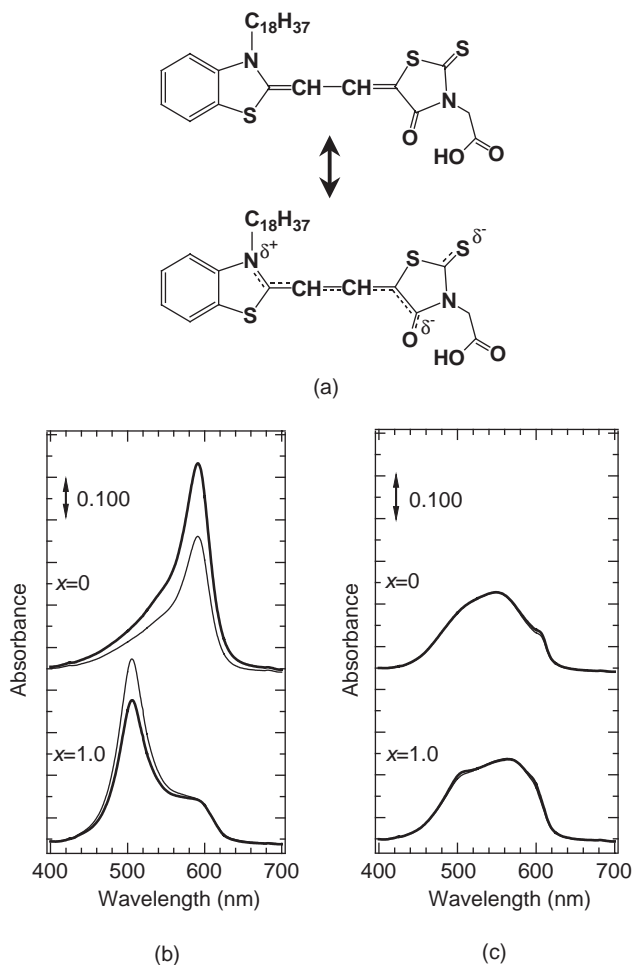


**Fig. 22.** (a) Chemical structure of MS and a schematic representation of the intramolecular charge transfer in MS. Polarized visible absorption spectra of the mixed LB films of the MS-C<sub>20</sub> binary and MS-C<sub>20</sub>-AL<sub>18</sub> ternary systems with the molar mixing ratios of [MS]:[C<sub>20</sub>]:[AL<sub>18</sub>] = 1:2:x (x = 0 and 1) fabricated under a subphase (b) with and (c) without Cd<sup>2+</sup> ions. The thick and thin lines represent A<sub>||</sub> and A<sub>⊥</sub> measured by linearly polarized light with the electric vector parallel and perpendicular to the dipping direction of substrates, respectively. (Reproduced with permission from Ref. [84]. Copyright (2006) Elsevier.)

shift due to the dye aggregation and the flow orientation effect of the aggregates during the LB vertical dipping process. As shown in Fig. 23(a), the J-aggregate has head-to-tail alignment of transition dipole moments characterized by a red-shift from the monomer. On the other hand, the H-aggregate is characterized by side-by-side alignment of transition dipole moments, showing a blue-shifted absorption. In addition, it is well known that a sharp and narrow absorption is observed due to motional narrowing, when the size of both aggregates is larger [73].

The dichroic behaviors of both red- and blue-shifted bands could be interpreted by the flow orientation effect proposed by Minari et al. [88] who formulated the transfer process of dye aggregates by introducing a complex velocity potential as representing the flow of a monolayer at an air/water interface. In Fig. 23(b), during the vertical-dipping process using a conventional LB trough, the long axes of the dye aggregates, elongated in shape at the air/water interface, tend to align parallel to the dipping direction of a substrate. The orientation of dye aggregates is governed by the velocity gradient and the rotatory Brownian motion at the air/water interface during the deposition process. Consequently, the tendency to align parallel to the dipping direction of the substrate is more prominent for longer aggregates.

The results in Fig. 22(b) are in good agreement with the above prediction that the red-shifted J-bands and the blue-shifted H-bands, being sharp in shape, should show  $R > 1$  and  $R < 1$ , respectively, if both aggregates are elongated. Therefore, the 590 and 505-nm bands are assigned to the J- and H-bands, respectively. Thus, Hirano et al. [77–84] found that the formation of the J- and H-aggregates can be easily controlled by the simple method of whether a small amount of AL<sub>18</sub> is added to the MS–C<sub>20</sub> binary system or not.

## 5.2. Out-of-Plane and In-Plane Orientations of MS Transition Dipole Moments in J- and H-Aggregates

Let us consider the out-of-plane and in-plane orientations of the MS transition dipole moments in the J- and H-aggregates investigated by polarized visible absorption spectroscopy. Here, a simple geometrical model [96] was applied, where only refraction due to an LB film is taken into account. As shown in Fig. 24(a),  $\beta'$  and  $\beta$  are incident and refractive angles, respectively.  $\alpha$  denotes an angle between the  $x$ -axis and the electric vector of light, and  $\alpha = 0^\circ$  and  $90^\circ$  correspond to s- and p-polarizations, respectively. Based on the intensity  $A(\alpha, \beta')$  of an absorption peak due to the transition dipole moment of  $m$ , following two parameters concerning the molecular orientation can be given as

$$\langle \sin^2 \theta \sin^2 \phi \rangle = \left[ \frac{A(0^\circ, 0^\circ)}{A(90^\circ, 0^\circ)} \left( 1 + \frac{A(90^\circ, \beta')}{A(0^\circ, \beta') \sin^2 \beta} \right) - \cot^2 \beta + 1 \right]^{-1} \quad (1)$$

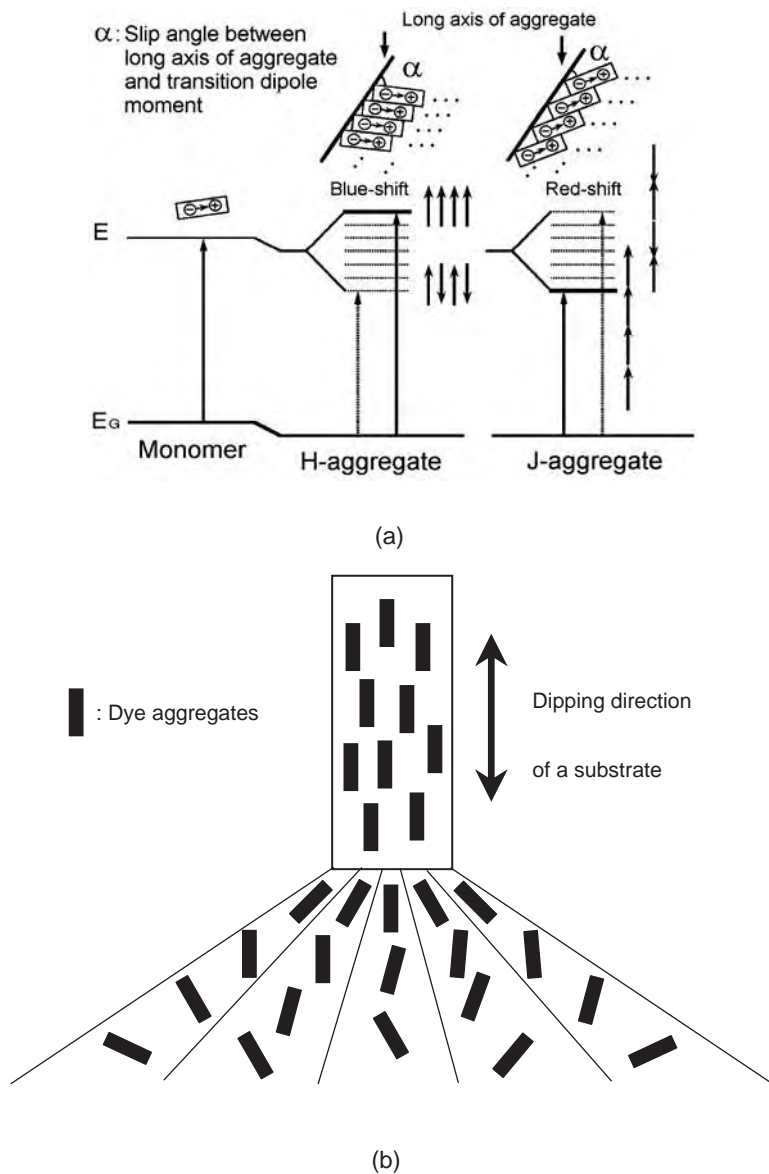


**Fig. 23.** (a) The correlation between the alignment of the transition dipole moments of dyes in the J- and H-aggregates and the excitation energy shift;  $\alpha$  denotes a slip angle between the long axis of the aggregates elongated in shape and the vector of the transition dipole moments. (b) A schematic representation of the flow orientation effect of the one-dimensionally developed aggregates at an air/water interface during LB vertical dipping process.

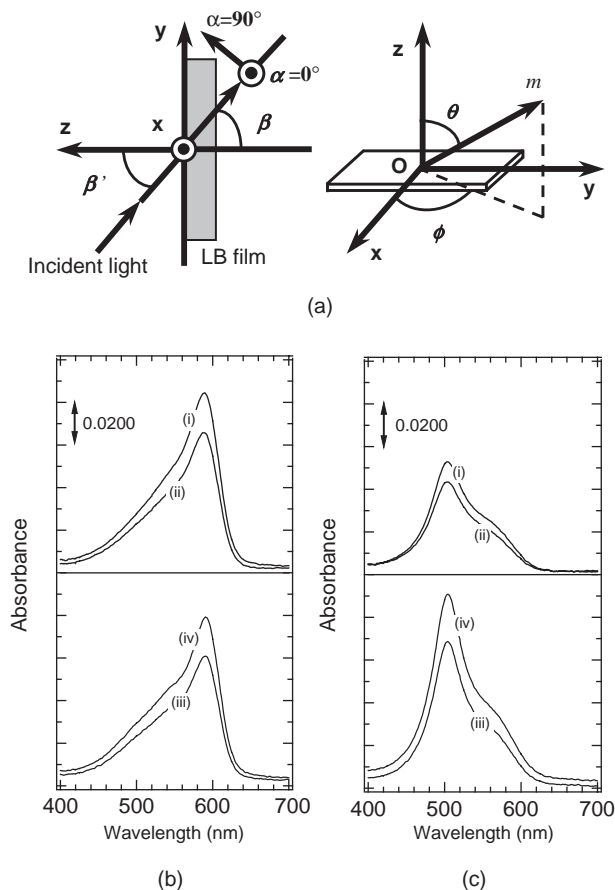


**Fig. 24.** (a) A simple geometrical model [96] for determining the orientation of the MS transition dipole moment  $m$  by means of visible absorption spectroscopy with linearly polarized light; only refraction due to an LB film is taken into account. Polarized visible absorption spectra of mixed LB films of (b) MS-C<sub>20</sub> binary and (c) MS-C<sub>20</sub>-AL<sub>18</sub> ternary systems with the molar mixing ratios of [MS]:[C<sub>20</sub>]:[AL<sub>18</sub>] = 1:2: $x$  ( $x = 0$  and 1). (i), (ii), (iii), and (iv) correspond to  $A(90^\circ, 0^\circ)$ ,  $A(90^\circ, 45^\circ)$ ,  $A(0^\circ, 0^\circ)$ , and  $A(0^\circ, 45^\circ)$ , respectively. (Reproduced with permission from Ref. [83]. Copyright (2006) Taylor & Francis.)

and

$$\langle \sin^2 \theta \rangle = \langle \sin^2 \theta \sin^2 \phi \rangle \left( \frac{A(0^\circ, 0^\circ)}{A(90^\circ, 0^\circ)} + 1 \right) \quad (2)$$

where  $\cos \beta = A(0^\circ, 0^\circ)/A(0^\circ, \beta')$ .  $\theta$  and  $\phi$  represent polar angles defining the direction of  $m$  shown in Fig. 24(a) (right side). The angular brackets  $\langle \rangle$  denote

the average over  $\theta$  and  $\phi$ . Eq. (2) is the parameter representing the out-of-plane orientation of  $m$ . The parameter showing the in-plane orientation of the projection of  $m$  using Eqs. (1) and (2) can be written as

$$p = \frac{\langle \sin^2 \theta \sin^2 \phi \rangle}{\langle \sin^2 \theta \rangle} \quad (3)$$

In the application of the above model, the two-layer LB films of MS deposited on both sides of a substrate were used, and it was assumed that  $m$  is parallel to the MS chromophore. Fig. 24(b) and (c) show polarized visible absorption spectra of the MS-C<sub>20</sub> binary and MS-C<sub>20</sub>-AL<sub>18</sub> ternary systems; (i), (ii), (iii), and (iv) correspond to  $A(90^\circ, 0^\circ)$ ,  $A(90^\circ, 45^\circ)$ ,  $A(0^\circ, 0^\circ)$ , and  $A(0^\circ, 45^\circ)$ , respectively [83]. The thick and thin lines in Fig. 24(b) and (c) refer to the p- and s-polarizations, respectively. Referring to the results in Fig. 24(b),  $\beta$  is estimated to be  $39.2^\circ$  when  $\beta'$  is set to be  $45^\circ$ , and  $\langle \sin^2 \theta \sin^2 \phi \rangle$ ,  $\langle \sin^2 \theta \rangle$ , and  $p$ -values are 0.571, 0.976, and 0.585, respectively. In Fig. 24(c),  $\beta$ ,  $\langle \sin^2 \theta \sin^2 \phi \rangle$ ,  $\langle \sin^2 \theta \rangle$ , and  $p$ -values are  $39.6^\circ$ , 0.417, 0.972, and 0.429, respectively. Therefore, the  $\langle \sin^2 \theta \rangle$  values suggested that  $m$  lies in the film plane for both cases. Furthermore, the estimated  $p$ -values suggested that  $m$  in the J-aggregates is preferentially oriented towards the  $y$ -axis rather than the  $x$ -axis, and that  $m$  in the H-aggregates is towards the  $x$ -axis rather than the  $y$ -axis. It was also noted that no peak but those at 590 and 505 nm are observed, when  $\beta' = 45^\circ$ , indicating no other aggregation states occur in the out-of-plane. Thus, it was most likely that the change in the MS aggregation states induced by AL<sub>18</sub> occurs in the in-plane of the films.

### 5.3. Intramolecular Charge Transfer of MS in J- and H-Aggregates

To be examined next were the electronic structures of MS in both aggregates to explore structural changes of MS. Fig. 25 shows polarized infrared absorption spectra of 10-layer LB films of the MS-C<sub>20</sub> binary and MS-C<sub>20</sub>-AL<sub>18</sub> ternary systems, respectively [84]. Here, the thick and thin lines refer to the spectra,  $A_{\parallel}$  and  $A_{\perp}$ , measured by using linearly polarized light with the electric vector parallel and perpendicular to the dipping direction of a substrate, respectively. The dichroic behaviors of the infrared spectra in Fig. 25 were comparable to those of the visible spectra in Fig. 22(b). According to the result of *ab initio* calculation based on the density functional theory (DFT) for the MS chromophore [93,94], peaks at around 1500 and 1190 cm<sup>-1</sup> are assigned to the stretching mode of the central conjugated system (referred to as  $\nu(\text{C}=\text{C})$ ,  $\text{N}^{\delta+}=\text{C}^-\text{C}=\text{C}-\text{C}=\text{C}-\text{O}^{\delta-}$ , Fig. 22(a)) and the C=S stretching mode of the rhodanine ring (or simply  $\nu(\text{C}=\text{S})$ ,  $\text{C}=\text{S} \leftrightarrow \text{C}-\text{S}^{\delta-}$ , Fig. 22(a)), respectively. Therefore, these peaks could be utilized as the makers to examine the MS electronic states in both aggregates.

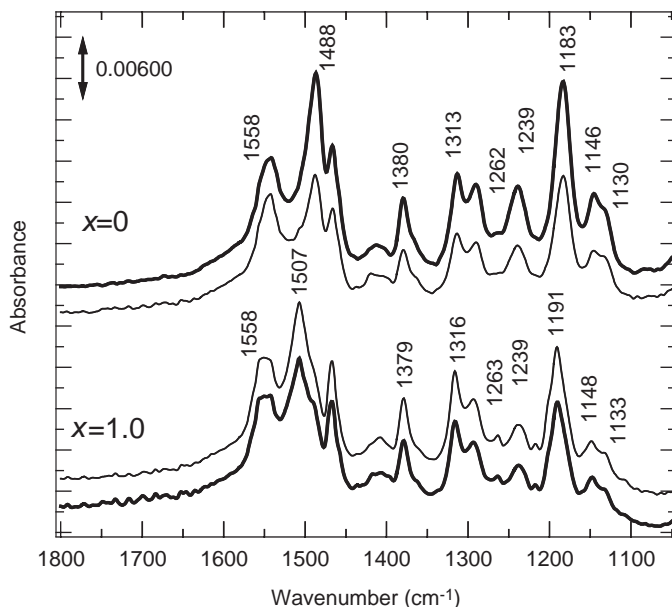


**Fig. 25.** Polarized infrared absorption spectra of the mixed LB films of the MS- $C_{20}$  binary and MS- $C_{20}$ - $AL_{18}$  ternary systems with the molar mixing ratios of  $[MS]:[C_{20}]:[AL_{18}] = 1:2:x$  ( $x = 0$  and  $1$ ). The thick and thin lines refer to spectra  $A_{\parallel}$  and  $A_{\perp}$  measured by linearly polarized light with the electric vector parallel and perpendicular to the dipping direction of substrates, respectively. (Reproduced with permission from Ref. [84]. Copyright (2006) Elsevier.)

For  $x = 0$ , sharp absorption peaks are observed at  $1488$  and  $1183\text{ cm}^{-1}$  in the spectra of the J-aggregates. These peaks are markedly red-shifted from those of the non-aggregation state (see Table 6), reflecting softening of the bond alternation in the MS central conjugated system [92–94]. For  $x = 1.0$ , on the other hand, the corresponding peaks of the H-aggregates appear at  $1507$  and  $1191\text{ cm}^{-1}$ . Their peak positions were fairly close to those of the non-aggregation state (see Table 6). For both J- and H-aggregates, it should be noted that the peaks due to the carboxylic and carbonyl groups of MS, and those assigned to the carboxylic group of  $C_{20}$  were not observed in the  $1800\text{--}1600\text{ cm}^{-1}$  region, indicating the complete chelation between MS and  $C_{20}$  molecules, and  $Cd^{2+}$  ions.

These results could be interpreted as follows: For the J-aggregates ( $x = 0$ ), the red-shifts of the peak positions are ascribed to the increase in the intramolecular charge transfer of MS caused by (1) the chelation between the MS chromophore and the  $Cd^{2+}$  ion, and (2) the formation of the J-aggregates [92–94]. Furthermore, Ikegami et al. interpreted that the intramolecular charge transfer enhanced by the latter case decreases the total energy in the aggregation, once the J-aggregates are produced [92,94].

**Table 6**

Wavenumbers of infrared bands of the MS chromophore in the J- and H-aggregates, and the non-aggregation states

Wavenumbers of MS LB films containing Cd <sup>2+</sup> (cm <sup>-1</sup> )		
H-aggregate	Non-aggregate <sup>a</sup>	J-aggregate
1558		1558
1507	(1512)	1488
1379	1381	1380
1316	1317	1313
1263		1262
1239		1239
1191	1190	1183
1148		1146
1133	1130	1130

<sup>a</sup>From Ref. [84].

The result for the H-aggregates ( $x = 1.0$ ) indicated that the degree of the MS intramolecular charge transfer is fairly close to that in the non-aggregation state. Consequently, it was expected that the dominant interaction in the H-aggregates is not the MS permanent dipole interaction but an other interaction. In this respect, the intermolecular hydrogen bonding between the carboxylic group of MS and carbonyl groups of the neighboring MS is one of the candidates for the H-aggregation, but it is very unlikely due to the chelation between MS and C<sub>20</sub> molecules, and Cd<sup>2+</sup> ions. The other possibility is a  $\pi$ - $\pi$  interaction, which should be more favorable for the aggregation with a side-by-side alignment rather than a head-to-tail alignment. Therefore, the  $\pi$ - $\pi$  interaction between the MS chromophores seems to dominate in the MS H-aggregation. In this way, it was found that the degree of the MS intramolecular charge transfer is quite different between the J- and H-aggregates, and that the H-aggregates are formed without the stabilization based on the drastic increase of the intramolecular charge transfer seen in the J-aggregates.

#### 5.4. Conformation and Orientation of Hydrocarbon Chains of MS in J- and H-Aggregates

Furthermore, the conformation and orientation of the hydrocarbon chains of MS in the MS-C<sub>20</sub> binary and MS-C<sub>20</sub>-AL<sub>18</sub> ternary systems were investigated by using infrared absorption spectroscopy. In this respect, deuterated arachidic acid (C<sub>20</sub>-*d*) and deuterated *n*-octadecane (AL<sub>18</sub>-*d*) were utilized to separate infrared bands due to the hydrocarbon chains of MS from those arising from C<sub>20</sub> and AL<sub>18</sub>. Fig. 26 shows polarized infrared spectra  $A_{||}$  of 10-layer LB films of pure cadmium arachidate (CdC<sub>20</sub>), MS-C<sub>20</sub>-*d* binary and MS-C<sub>20</sub>-*d*-AL<sub>18</sub>-*d*

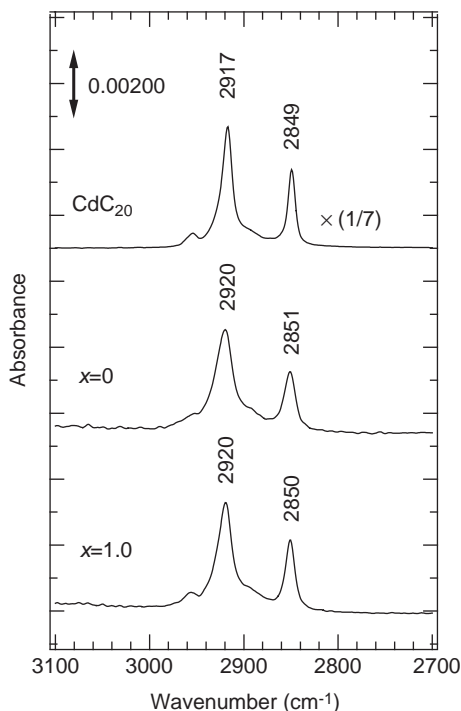


**Fig. 26.** Polarized infrared absorption spectra  $A_{\parallel}$  of the LB films of  $\text{CdC}_{20}$ , the 1:2 mixture of the MS-deuterated arachidic acid ( $\text{C}_{20}\text{-}d$ ) and (c) the 1:2:1 mixture of the MS- $\text{C}_{20}\text{-}d$ -deuterated  $n$ -octadecane ( $\text{AL}_{18}\text{-}d$ ). (Reproduced with permission from Ref. [84]. Copyright (2006) Elsevier.)

ternary systems [81]. For the  $\text{CdC}_{20}$  LB films, absorption peaks at 2954, 2917, and  $2849\text{ cm}^{-1}$  are assigned to the  $\text{CH}_3$  asymmetric, the  $\text{CH}_2$  antisymmetric, and symmetric stretching modes of the hydrocarbon chain, respectively. The peak positions of the  $\text{CH}_2$  stretching bands are characteristic of the all-*trans* conformation of the hydrocarbon chain, as in the case of cadmium stearate ( $\text{CdC}_{18}$ ) LB films [97].

The corresponding peaks due to the  $\text{CH}_2$  antisymmetric and symmetric stretching modes are observed at 2920 and  $2851\text{ cm}^{-1}$ , respectively, in the infrared spectrum of the MS- $\text{C}_{20}$  binary system (J-aggregates;  $x = 0$ ), while those in the MS- $\text{C}_{20}$ - $\text{AL}_{18}$  ternary system (H-aggregates;  $x = 1.0$ ) appear at 2920 and  $2850\text{ cm}^{-1}$ . These results suggested the presence of a few *gauche* conformers in the MS hydrocarbon chains of both mixed LB films.

The intensity ratio and the ratio of the full widths of the half height (FWHH) of the  $\text{CH}_2$  antisymmetric and symmetric stretching bands for  $x = 0$  and 1.0 are 1:1.08 and 1:1.19 (intensity ratio) and 1:0.813 and 1:0.813 (FWHH ratio), respectively. In addition, the intensity of the  $\text{CH}_3$  asymmetric stretching band for  $x = 0$  is appreciably lower than that for  $x = 1.0$ . These results

suggested that the long axis of the MS hydrocarbon chain in the J-aggregates is more parallel to the film surface than that in the H-aggregates.

Moreover, Hirano et al. applied a model proposed by Chollet [98] to the quantitative estimation of the orientation of the long axis of the hydrocarbon chain. In the model, not only the refraction and reflection at air/LB film and LB film/substrate interfaces but also the optical rotation of electromagnetic wave due to the LB films is taken into account to obtain quantitative information about the molecular orientation.

As shown in Fig. 27(a) (left side), the direction of the incident beam of linearly polarized light is along the  $z$ -axis with its electric vector in the  $x$ - $y$  plane, where  $i = \angle zoz' = \angle xox'$  is an inclination angle. The polar angle of the vector  $m$  corresponding to the sum of the transition moments of the CH<sub>2</sub> antisymmetric (or symmetric) stretching mode is defined by  $\theta$ , where  $m$  is assumed to be distributed uniformly against the  $z'$ -axis (right side). In such a case, the dichroic ratio  $R (= A_{\parallel}/A_{\perp})$  can be expressed as

$$R = \frac{A_{\parallel}}{A_{\perp}} = \frac{(1/2)(\sin^2 \theta) \langle n_3 \cos i + n_1 \sqrt{1 - (n_1/n_3)^2 \sin^2 i} \rangle}{\langle n_1 \cos i + n_3 \sqrt{1 - (n_1/n_3)^2 \sin^2 i} \rangle \{(1/2) \cos i (\sin^2 \theta) \sqrt{1 - (n_1/n_3)^2 \sin^2 i} + (n_3 n_1^2/n_3^2) \sin^2 i (\cos^2 \theta)\}} \quad (4)$$

where  $n_1$ ,  $n_2$ , and  $n_3$  refer to the refractive indices of air, an LB film, and a substrate, respectively. In the present study, we used the appropriate values of  $n_1 = 1.0$ ,  $n_2 = 1.5$ , and  $n_3 = 1.4$ . The angular brackets  $\langle \rangle$  denote the average of the zenith angle. It should be noted that unlike the definition in the model of the visible region in Fig. 24(a),  $A_{\parallel}$  and  $A_{\perp}$  correspond to s- and p-polarizations, respectively. Moreover, we used the following approximation [97] based on the orthogonal relation being represented as

$$\langle \cos^2 \theta \rangle + \langle \cos^2 \theta' \rangle + \langle \cos^2 \gamma \rangle = 1 \quad (5)$$

where  $\theta$  and  $\theta'$  represent the tilt angles of  $m$  estimated from the CH<sub>2</sub> antisymmetric and symmetric stretching bands, respectively, and  $\gamma$  refers to the tilt angle of the long axis of the MS hydrocarbon chain from the film normal.

Let us investigate the orientation of the alkyl chains in the CdC<sub>20</sub> LB film shown in Fig. 26 as reference. Fig. 27(b) shows the dichroic ratio  $R (= A_{\parallel}/A_{\perp})$  of the CH<sub>2</sub> antisymmetric stretching band for the CdC<sub>20</sub> LB film plotted against the inclination angle  $i$  [81]. The solid curves refer to the inclination-angle-dependence calculated using Eq. (4): (i)  $\theta = 10.0^\circ$ , (ii)  $\theta = 30.0^\circ$ , (iii)  $\theta = 50.0^\circ$ , (iv)  $\theta = 70.0^\circ$ , and (v)  $\theta = 83.0^\circ$ . It is noted that the  $R$ -value is 1.05 at  $i = 0^\circ$ , which is consistent with the assumption that  $m$  is uniformly distributed around the  $z$ -axis. As shown in Fig. 27(b), the best least-squares fit is  $\theta = 83.0^\circ$ . In addition,  $\theta' = 81.0^\circ$  is obtained from the CH<sub>2</sub> symmetric stretching band by the same procedure. Therefore, the  $\langle \cos^2 \gamma \rangle$  value is estimated to be 0.961 ( $\gamma = 11.5^\circ$ ) using Eq. (5).

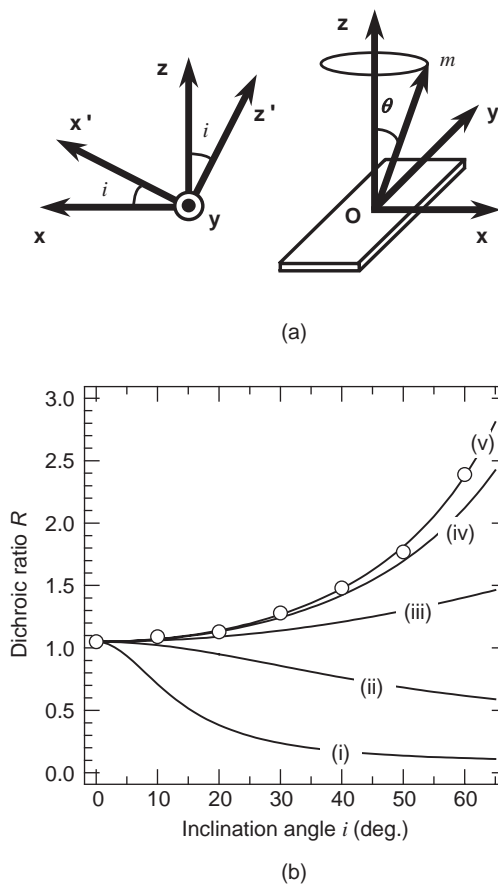


**Fig. 27.** (a) A model proposed by P. Chollet et al. [98] for determining the orientation of a hydrocarbon chain by means of infrared absorption spectroscopy with linearly polarized light; not only the refraction and reflection at air/LB film and LB film-substrate interfaces but also the optical rotation of electromagnetic wave due to an LB film is taken into account. (b) The dichroic ratio  $R$  ( $= A_{\parallel}/A_{\perp}$ ) of the  $\text{CH}_2$  antisymmetric stretching band of the LB films of  $\text{CdC}_{20}$  plotted against the inclination angle  $i$ . The solid curves refer to the inclination-angle-dependence of  $R$  calculated using Eq. (5): (i)  $\theta = 10.0^\circ$ , (ii)  $\theta = 30.0^\circ$ , (iii)  $\theta = 50.0^\circ$ , (iv)  $\theta = 70.0^\circ$ , and (v)  $\theta = 83.0^\circ$ . (Reproduced with permission from Ref. [84]. Copyright (2006) Elsevier.)

The  $\langle \cos^2 \gamma \rangle$  values of the MS hydrocarbon chains in the MS- $\text{C}_{20}$ - $d$  binary and MS- $\text{C}_{20}$ - $d$ -AL $_{18}$ - $d$  ternary systems were similarly estimated, although a few *gauche* conformers are contained in both systems. It is also noted that the  $R$ -value remains approximately unity at  $i = 0^\circ$  for both mixed systems. The  $\langle \cos^2 \gamma \rangle$  value is 0.522 ( $\gamma = 43.8^\circ$ ) for the binary system, whereas the value of 0.613 ( $\gamma = 38.5^\circ$ ) is obtained for the ternary system [81]. The results of the

orientation obtained, and the estimates from the intensity and FWHH ratios indicated that the long axis of the MS hydrocarbon chain in the J-aggregates is more parallel to the film surface than that in the H-aggregates. Thus, the orientation of the MS hydrocarbon chains is significantly different between the two aggregates. So far, in the J-aggregation of an analogous MS, Ikegami [95] pointed out, on the basis of the *ab initio* calculation of the optimization for the geometrical structure, that the slippage of the alignment between the adjacent dye chromophores in the J-aggregation can be regulated by the hydrocarbon chain. Considering the results of the orientation of the MS hydrocarbon chains for the J- and H-aggregates, and the role of the hydrocarbon chain pointed out by Ikegami, the regulation of the slippage of the chromophore by the MS hydrocarbon chain in the H-aggregates was expected to be restricted compared to that in the J-aggregates.

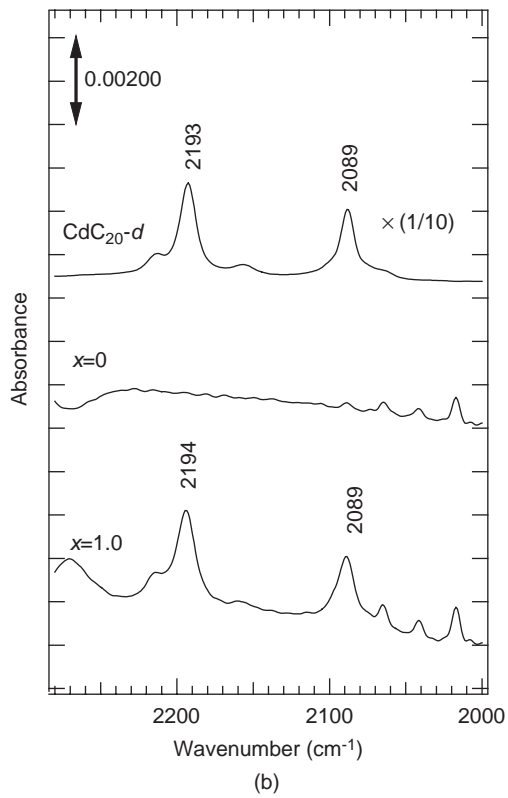
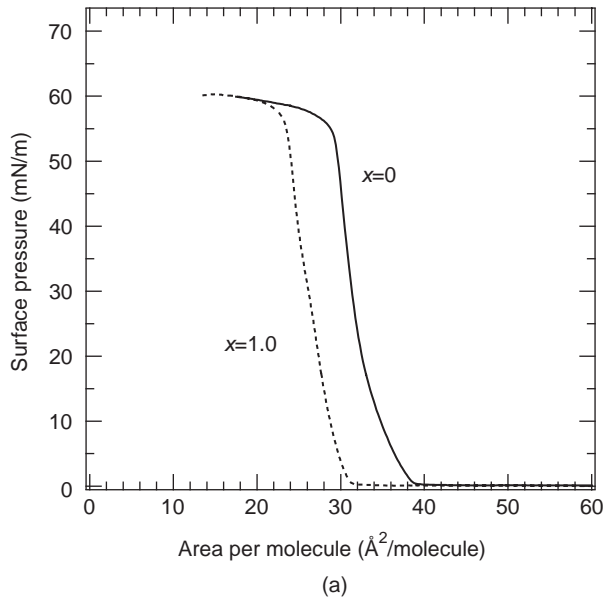
### 5.5. Whereabout, Conformation, and Orientation of AL<sub>18</sub> Added as a Third Component in Mixed LB Films

As seen in Fig. 22(b), the aggregation states of the J- and H-aggregates in the MS LB films was easily tuned by adding a small amount of AL<sub>18</sub>. Here, there arises a question as follows: where do AL<sub>18</sub> molecules which act as “trigger molecules” [97,99] exist in the monolayers or the LB films of the MS–C<sub>20</sub>–AL<sub>18</sub> ternary system? Accordingly, Hirano et al. [78,80,82] investigated the whereabout, conformation, and orientation of AL<sub>18</sub> added as a third component in the MS–C<sub>20</sub>–AL<sub>18</sub> ternary system using the surface–pressure isotherms and infrared spectroscopy.

Fig. 28(a) shows the surface pressure ( $\pi$ )–area ( $A$ ) isotherms of the MS–C<sub>20</sub> binary and MS–C<sub>20</sub>–AL<sub>18</sub> ternary systems [77]. The abscissa refers to the average value of the area per molecule for the binary and ternary systems at the air/water interface. From the  $\pi$ – $A$  isotherm of the binary system, the occupied area of MS is estimated to be 56 Å<sup>2</sup>/molecule, assuming that the occupied area of C<sub>20</sub> is 20 Å<sup>2</sup>/molecule at 25 mN/m. The result suggested the side-on structure that the long axis of the MS chromophore is nearly parallel to the air/water interface. In addition, MS has the empty space of 36 Å<sup>2</sup>/molecule on its chromophore, if the area of the hydrocarbon chain substituted to the

---

**Fig. 28.** (a) Surface pressure ( $\pi$ )–area ( $A$ ) isotherms of mixed monolayers of the MS–C<sub>20</sub> binary and MS–C<sub>20</sub>–AL<sub>18</sub> ternary systems with the molar mixing ratios of [MS]:[C<sub>20</sub>]:[AL<sub>18</sub>] = 1:2: $x$  ( $x = 0$  and 1.0) on a subphase with Cd<sup>2+</sup> ions. (Reproduced with permission from Ref. [78]. Copyright (1999) The Japan Society of Applied Physics.) (b) Polarized infrared spectra  $A_{||}$  of LB films of CdC<sub>20</sub>- $d$ , MS–C<sub>20</sub> binary and MS–C<sub>20</sub>–AL<sub>18</sub>- $d$  ternary systems with the molar mixing ratios of [MS]:[C<sub>20</sub>]:[AL<sub>18</sub>- $d$ ] = 1:2: $x$  ( $x = 0$  and 1). (Reproduced with permission from Ref. [82]. Copyright (2004) American Institute of Physics.)



MS chromophore is simply  $20 \text{ \AA}^2/\text{molecule}$ . Using these values (56 and  $20 \text{ \AA}^2/\text{molecule}$ ), the occupied area of  $\text{AL}_{18}$  could be estimated for the ternary system.

The estimated area per molecule of  $\text{AL}_{18}$  in the  $\text{MS-C}_{20}\text{-AL}_{18}$  ternary system is  $5.85 \pm 6.51 \text{ \AA}^2/\text{molecule}$ . This result could be interpreted based on the following assumptions. Each MS molecule has the empty space, which can roughly accommodate two straight-chain hydrocarbons. The occupied area by  $\text{AL}_{18}$  should be zero if the empty space on the MS chromophore is fully filled with  $\text{AL}_{18}$ . On the other hand, the  $\text{AL}_{18}$  area should be  $20 \text{ \AA}^2/\text{molecule}$  if the long axis of  $\text{AL}_{18}$  exists perpendicular to the air/water interface at the outside of the MS empty space. Comparing the experimental results with the assumptions, it was suggested that the added  $\text{AL}_{18}$  molecules tend to fill the MS empty space in the monolayer of the ternary system.

Fig. 28(b) depicts polarized infrared absorption spectra of 10-layer LB films of pure  $\text{CdC}_{20-d}$ , and the  $\text{MS-C}_{20}$  binary and  $\text{MS-C}_{20}\text{-AL}_{18-d}$  ternary systems [80,82]. In the case of  $\text{CdC}_{20-d}$  LB film, peaks at  $2193$  and  $2089 \text{ cm}^{-1}$  are assigned to the  $\text{CD}_2$  antisymmetric and symmetric stretching modes of the hydrocarbon chain, respectively, and their peak positions are characteristic of the all-*trans* conformation of the hydrocarbon chain. The LB film of the  $\text{MS-C}_{20}$  binary system does not show the peak, as a matter of course. The film of the  $\text{MS-C}_{20}\text{-AL}_{18}$  ternary system yields the peaks at  $2194$  and  $2089 \text{ cm}^{-1}$ , suggesting the presence of  $\text{AL}_{18-d}$  with the all-*trans* conformation.

Using the Chollet's model shown in Fig. 27(a), the estimation of the orientations of the  $\langle \cos^2 \gamma \rangle$  values were  $0.952$  ( $\gamma = 12.6^\circ$ ) and  $0.978$  ( $\gamma = 8.51^\circ$ ) for the LB films of the  $\text{CdC}_{20-d}$  and the  $\text{MS-C}_{20}\text{-AL}_{18}$  ternary system, respectively [82]. Thus, it was well comprehended that the long axis of  $\text{AL}_{18}$  with the all-*trans* conformation in the MS empty space is perpendicular to the film surface. Consequently, the differences in the orientation of the MS hydrocarbon chains between the binary and the ternary systems (Section 5.4) may be caused by the close packing between the MS hydrocarbon chains and the  $\text{AL}_{18}$  molecules in the MS empty space, and this packing might bring about the stabilization of the formation energy in the H-aggregation.

As already seen, it was found by Hirano et al. [77–84] that the aggregation states of MS can be easily controlled in the mixed LB films of the  $\text{MS-C}_{20}$  binary and  $\text{MS-C}_{20}\text{-AL}_{18}$  ternary systems. And, they characterized the MS structures in the J- and the H-aggregates to explore the structural factors governing both aggregation states towards the elucidation of the formation mechanism of the H-aggregates induced by  $\text{AL}_{18}$ . Fig. 29(a) and (b) depict a schematic representation of the MS structure in the J- and the H-aggregates, and their in-plane structural models where the carboxylic group of MS and the carbonyl group of the neighboring MS are connected one after another by

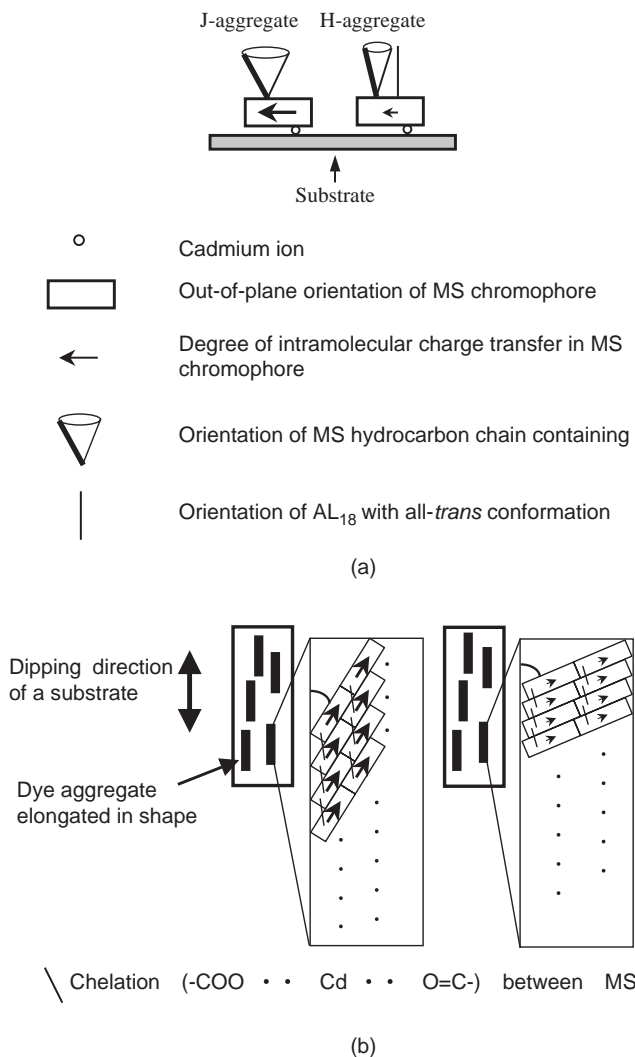


**Fig. 29.** (a) A schematic representation of the MS structure in the J- and H-aggregates formed in LB films of the MS-C<sub>20</sub> binary and MS-C<sub>20</sub>-AL<sub>18</sub> ternary systems with the molar mixing ratios of [MS]:[C<sub>20</sub>]:[AL<sub>18</sub>] = 1:2:*x* (*x* = 0 and 1). (b) An in-plane structural model for the J- and H-aggregates of MS, where the carboxylic group of MS and the carbonyl group of the neighboring MS are connected one after another by Cd<sup>2+</sup> ions.

Cd<sup>2+</sup> ions, respectively. Therefore, it was suggested that the degree of the orientation of the hydrocarbon chain substituted to MS are of importance for determining the formation of the J- and the H-aggregates observed in the mixed LB films of MS.

## REFERENCES

- [1] P. R. Griffiths and J. A. deHaseth, *Fourier Transform Infrared Spectroscopy*, Wiley-Interscience, New York, 1986.
- [2] T. Takenaka and J. Umemura, in *Vibrational Spectra and Structure*, Vol. 19 (J. R. Durig, ed.), Elsevier, Amsterdam, 1991, p. 215.
- [3] A. A. Christy, Y. Ozaki and V. G. Gregoriou, *Modern Fourier Transform Infrared Spectroscopy*, Elsevier, Amsterdam, 2001.
- [4] I. R. Lewis and H. G. M. Edwards, *Handbook of Raman Spectroscopy*, Marcel Dekker, New York, 2001.
- [5] J. G. Grasselli and B. J. Bulkin (eds.), *Analytical Raman Spectroscopy*, Wiley, New York, 1991.
- [6] A. Ulman, *An Introduction to Ultrathin Organic Films from Langmuir–Blodgett to Self-Assembly*, Academic Press, San Diego, 1991.
- [7] T. Hasagawa, V. Konka and R. M. Leblanc, in *Vibrational Spectroscopy of Biological and Polymeric Materials* (V. G. Gregoriou and M. S. Braiman, eds.), Taylor & Francis, Boca Raton, 2006, p. .
- [8] J. Umemura, in *Handbook of Vibrational Spectroscopy*, Vol. 2 (J. M. Chalmers and P. R. Griffiths, eds.), Wiley, Chichester, 2002, p. 982.
- [9] J. Lipkowski and P. N. Ross (eds.), *Imaging of Surfaces and Interfaces*, Wiley-VCH, Weinheim, 1999.
- [10] D. Sarid, *Scanning Force Microscopy*, Oxford University Press, Oxford, 1994.
- [11] J. Umemura, T. Kamata, T. Kawai and T. Takenaka, *J. Phys. Chem.*, 94 (1990) 62.
- [12] J. Umemura, D. G. Cameron and H. H. Mantsch, *Biochim. Biophys. Acta*, 602 (1980) 32.
- [13] H. Shapper, D. G. Cameron and H. H. Mantsch, *Can. J. Chem.*, 59 (1981) 2543.
- [14] M. Tasumi, T. Shimonouchi and T. Miyazawa, *J. Mol. Struct.*, 9 (1962) 261.
- [15] R. G. Snyder and J. H. Schachtschneider, *Spectrochim. Acta*, 19 (1963) 85.
- [16] P. A. Chollet, J. Messier and C. Rosilio, *J. Chem. Phys.*, 64 (1976) 1042.
- [17] P. A. Chollet, *Thin Solid Films*, 52 (1978) 343.
- [18] T. Nakamura, (H. S. Nalwa, ed.), *Handbook of Organic Conductive Molecules and Polymers*, Wiley, Chichester, UK, 1997, p. .
- [19] J. M. Williams, J. R. Ferrano, R. J. Thorn, K. D. Carson, U. Geiser, H. H. Wang, A. M. Kini and M. Whangbo, *Organic Superconductors*, Prentice Hall, Englewood Cliffs, NJ, 1992.
- [20] N. Kubota, Y. Ozaki, T. Araki, S. Ohki and K. Iriyama, *Langmuir*, 7 (1991) 774.
- [21] S. Terashita, K. Nakatsu, Y. Ozaki, T. Mochida, T. Araki and K. Iriyama, *Langmuir*, 8 (1992) 3051.
- [22] S. Terashita, Y. Ozaki and K. Iriyama, *J. Phys. Chem.*, 97 (1993) 10454.
- [23] Y. Wang, Y. Ozaki and K. Iriyama, *Langmuir*, 11 (1995) 705.
- [24] Y. Wang, K. Nichogi, S. Terashita, K. Iriyama and Y. Ozaki, *J. Phys. Chem.*, 100 (1996) 368.
- [25] Y. Wang, K. Nichogi, K. Iriyama and Y. Ozaki, *J. Phys. Chem.*, 100 (1996) 374.
- [26] Y. Wang, K. Nichogi, K. Iriyama and Y. Ozaki, *J. Phys. Chem.*, 100 (1996) 17232.
- [27] Y. Wang, K. Nichogi, K. Iriyama and Y. Ozaki, *J. Phys. Chem.*, 100 (1996) 17238.

- [28] Y. Wang, K. Nichogi, K. Iriyama and Y. Ozaki, *J. Phys. Chem. B*, 101 (1997) 6367.
- [29] Y. Wang, K. Nichogi, K. Iriyama and Y. Ozaki, *J. Phys. Chem. B*, 101 (1997) 6372.
- [30] Y. Wang, K. Nichogi, K. Iriyama and Y. Ozaki, *J. Phys. Chem. B*, 101 (1997) 6379.
- [31] H. Wang and Y. Ozaki, *Langmuir*, 16 (2000) 7070.
- [32] S. Morita, Y. Ozaki and I. Noda, *Appl. Spectrosc.*, 55 (2001) 1618.
- [33] S. Morita, Y. Ozaki and I. Noda, *Appl. Spectrosc.*, 55 (2001) 1622.
- [34] S. Morita, K. Iriyama and Y. Ozaki, *J. Phys. Chem. B*, 104 (2000) 1183.
- [35] S. Morita, K. Nichogi and Y. Ozaki, *J. Phys. Chem. B*, 108 (2004) 7871.
- [36] H. Wang and Y. Ozaki, *Langmuir*, 18 (2005) 10243.
- [37] R. K. Chang and T. E. Furtak (eds.), *Surface Enhanced Raman Scattering*, Plenum, New York, 1982.
- [38] G. C. Schatz and R. P. VanDuyne, in *Handbook of Vibrational Spectroscopy*, Vol. 1 (J. M. Chalmers and P. R. Griffiths, eds.), Wiley, Chichester, 2005, p. 759.
- [39] K. Kneipp, M. Moskovits and H. Kneipp (eds.), *Surface Enhanced Raman Scattering—Physics and Applications*, Springer, Berlin, 2006.
- [40] R. Aroca, *Surface-Enhanced Vibrational Spectroscopy*, Wiley, New York, 2006.
- [41] Z. J. Zhang, T. Imae, H. Sato, A. Watanabe and Y. Ozaki, *Langmuir*, 17 (2001) 4564.
- [42] K. Niwa, M. Furukawa and K. Niki, *J. Electrochem.*, 245 (1988) 275.
- [43] C. Hinnen and J. Niki, *J. Electrochem.*, 264 (1989) 157.
- [44] D. Hobara, K. Niki, C. Zhou, G. Chumanov and T. M. Cotton, *Colloid Interfaces A: Physicochem. Eng. Aspects*, 93 (1994) 241.
- [45] K. Kneipp, H. Kneipp, R. Manoharan, I. Itzkan, R. R. Dasari and M. S. Feld, *J. Raman Spectrosc.*, 29 (1998) 743.
- [46] P. Hilderbrandt and M. Stockburger, *J. Phys. Chem.*, 88 (1984) 5935.
- [47] X. Li, W. Xu, H. Jia, X. Wang, B. Zhao, B. Li and Y. Ozaki, *Thin Solid Films*, 457 (2004) 372.
- [48] J. W. Hu, B. Zhao, W. Q. Xu, B. F. Li and Y. G. Fan, *Spectrochim. Acta A*, 58A (2002) 2827.
- [49] D. S. Wang and M. Kerker, *Phys. Rev. B*, 24 (1982) 1777.
- [50] M. Moskovits and J. S. Suh, *J. Phys. Chem.*, 92 (1988) 6327.
- [51] J. S. Suh and M. Moskovits, *J. Am. Chem. Soc.*, 108 (1986) 4711.
- [52] H. Yamada and Y. Yamamoto, *J. Chem. Soc. Faraday Trans.*, 75 (1979) 1215.
- [53] J. Cheng, X. Li, W. Song, W. Xu, B. Zhao and G. Zhang, *Chem. Phys. Lett.*, 344 (2005) 405.
- [54] L. J. Wan, Y. Hara, H. Noda and M. Osawa, *J. Phys. Chem. B*, 102 (1998) 5943.
- [55] T. Sawaguchi, F. Mizutani and I. Taniguchi, *Langmuir*, 14 (1998) 3565.
- [56] H. Han, S. W. Han, S. W. Joo and K. Kim, *Langmuir*, 15 (1999) 6868.
- [57] J. Y. Gui, F. Lu, D. A. Stern and T. A. Hubbard, *J. Electroanal. Chem.*, 245 (1990) 292.
- [58] P. A. Christensen and A. Hamnet, *J. Electroanal. Chem.*, 407 (1991) 318.
- [59] T. Zhu, X. Zhang, J. Wang, X. Y. Fu and Z. F. Liu, *Thin Solid Films*, 327 (1998) 595.

- [60] A. Capobianchi, A. M. Paoletti, G. Pennesi, G. Rossi, R. Caminiti and C. Ercolani, *Inorg. Chem.*, 4635 (1994) 33.
- [61] R. Caminti, M. P. Donzello, C. Ercolani and C. C. Sandun, *Inorg. Chem.*, 3027 (1999) 38.
- [62] R. Salzmann, C. J. Ziegler, N. Godbou, M. T. McMahon, K. S. Suslick and E. Oldfield, *J. Am. Chem. Soc.*, 11323 (1998) 120.
- [63] X. Li, W. Xu, H. Jia, X. Wang, B. Zhao, B. Li and Y. Ozaki, *Appl. Spectrosc.*, 58 (2004) 287.
- [64] J. A. Baldwin, B. Vlckova, M. P. Andrews and I. S. Butler, *Langmuir*, 13 (1997) 3744.
- [65] S. Z. Zou, C. T. Williams, E. K. Y. Chen and M. J. Weaver, *J. Am. Chem. Soc.*, 120 (1998) 3811.
- [66] J. M. Zhang, D. H. Zhang and D. Y. Shen, *Macromolecules*, 35 (2002) 5140.
- [67] J. Dybal and S. Krimm, *Macromolecules*, 23 (1990) 1301.
- [68] X. Li, W. Xu, T. Itoh, A. Ikehata, B. Zhao, B. Li and Y. Ozaki, *J. Colloid Interface Sci.*, 284 (2005) 582.
- [69] H. Tachibana, Y. Yamanaka, H. S. Masahiko Abe and M. Matsumoto, *Langmuir*, 16 (2000) 2975.
- [70] H. Kuhn, *Thin Solid Films*, 178 (1989) 1.
- [71] G. G. Roberts, *Langmuir–Blodgett Films*, Plenum Press, New York, London, 1990.
- [72] H. Kuhn and D. Moebius, in *Physical Methods of Chemistry* (B. W. Rossiter and R. C. Baetzold, eds.), Second Edition, Wiley, New York, 1993.
- [73] T. Kobayashi, *J-Aggregates*, World Scientific, Singapore, 1996.
- [74] H. Yao, K. Domoto, T. Isohashi and K. Kimura, *Langmuir*, 21 (2005) 1067.
- [75] K. Saito, *J. Phys. Chem. B*, 105 (2001) 4235.
- [76] T. Wakamatsu, K. Watanabe and K. Saito, *Appl. Opt.*, 44 (2005) 906.
- [77] Y. Hirano, H. Sano, J. Shimada, H. Chiba, J. Kawata, Y. F. Miura, M. Sugi and T. Ishii, *Mol. Cryst. Liq. Cryst.*, 294 (1997) 161.
- [78] Y. Hirano, K. N. Kamata, Y. S. Inadzuki, J. Kawata, Y. F. Miura, M. Sugi and T. Ishii, *Jpn. J. Appl. Phys.*, 38 (1999) 6024.
- [79] Y. Hirano, T. M. Okada, Y. F. Miura, M. Sugi and T. Ishii, *J. Appl. Phys.*, 88 (2000) 5194.
- [80] Y. Hirano, Y. S. Inadzuki, Y. F. Miura, M. Sugi and T. Ishii, *Trans. Mater. Res. Soc. Jpn.*, 27 (2002) 521.
- [81] S. Morita, Y. F. Miura, M. Sugi and Y. Hirano, *J. Appl. Phys.*, 94 (2003) 4368.
- [82] Y. Hirano, T. N. Murakami, Y. K. Nakamura, Y. Fukushima, Y. Tokuoka and N. Kawashima, *J. Appl. Phys.*, 96 (2004) 5528.
- [83] Y. Hirano, M. A. Ohkubo, Y. Tokuoka, N. Kawashima and Y. Ozaki, *Mol. Cryst. Liq. Cryst.*, 445 (2006) 383.
- [84] Y. Hirano, Y. Tokuoka, N. Kawashima and Y. Ozaki, *Vibrational Spectroscopy*, in press.
- [85] M. Sugi and S. Iizima, *Thin Solid Films*, 68 (1980) 199.
- [86] K. Saito, *Jpn. J. Appl. Phys.*, 34 (1995) 3832.
- [87] N. Kato, K. Saito, T. Serata, H. Aida and Y. Uesu, *J. Chem. Phys.*, 115 (2001) 1473.

- [88] N. Minari, K. Ikegami, S. Kuroda, K. Saito, M. Saito and M. Sugi, *J. Phys. Soc. Jpn.*, 58 (1989) 222.
- [89] H. Nakahara and D. Möbius, *J. Colloid Interface Sci.*, 114 (1986) 363.
- [90] Y. Ozaki, K. Iriyama, T. Iwasaki and H. Hamaguchi, *Appl. Surf. Sci.*, 33/34 (1988) 1317.
- [91] Y. Fijimoto, Y. Ozaki and K. Iriyama, *J. Chem. Soc. Faraday Trans.*, 92 (1996) 413.
- [92] K. Ikegami, C. Mingotaud and M. Lan, *Thin Solid Films*, 393 (2001) 193.
- [93] N. Kato, M. Yamamoto, K. Itoh and Y. Uesu, *J. Phys. Chem. B*, 107 (2003) 11917.
- [94] K. Ikegami and S. Kuroda, *Chem. Phys.*, 295 (2003) 205.
- [95] K. Ikegami, *J. Chem. Phys.*, 121 (2004) 2337.
- [96] K. Ikegami, S. Kuroda, Y. Tabe, K. Saito, M. Sugi, M. Matsumoto, T. Nakamura and Y. Kawabata, *Jpn. J. Appl. Phys.*, 31 (1992) 1206.
- [97] R. Azumi, M. Matsumoto, S. Kuroda and M. J. Crossley, *Langmuir*, 11 (1995) 4495.
- [98] P. A. Chollet, *Thin Solid Films*, 68 (1980) 13.
- [99] R. Azumi, M. Matsumoto, Y. Kawabata, S. Kuroda, M. Sugi, L. G. King and M. J. Crossley, *J. Am. Chem. Soc.*, 114 (1992) 10662.

This page intentionally left blank

## Subject Index

- 2-(11-mercaptopundecanamido)benzoic acid 239
- 3-mercaptopropionic acid (MPA) SAM 223, 230
- 10,12-pentacosadiynoic acid 221
- 11-mercaptopundecanol 239
- 12-hydroxydodecanoic acid 221
- $\pi$ - $\pi$  interaction 14
- $\pi$ - $\pi$  stacking interaction 227
- n*-dodecanethiol 239
  
- accumulation 221, 224, 226
- active esterification 232
- adhesion 35, 37, 39–40
- adlayer 221–222
  - thickness 221–222
- adsorbate 223, 232
- adsorbed firm 224
- adsorption 32, 41, 44, 47, 220–224, 229–236
  - film 220, 224–226
  - kinetics 231
- adsorption–desorption profile 222
- aggregation 223–224, 226, 235
  - kinetics 303
- AHAPS 147
  - SAM 147
- air/water interface 219–221, 223, 226–227, 236
- alkaline phosphatase 240
- alkyl thiol SAM 221
- amide I and II bands 231
- amide linkage 231, 234
- aminoundecanethiol SAM 239
- amphiphile 221, 223
- amphiphilic compound 219
- anisotropic wetting 206
- anthracenyl focal point 224
- antigen–antibody reaction 239
- antioxidant 224
- assembling 168
- atomic force microscope (AFM) 156, 232, 311, 313, 321, 337, 339
  
- avidin–biotin interaction 239
- avidity 65
- azacrown core 235–236
  
- base-pair 231
- bilayer 221, 224
- binary mixture 13
- bio-affinity analysis 62
- biocompatible 220, 227
- biomacromolecule-detection sensing 227, 239
- biomolecular
  - recognition 240
  - sensing 239
- biosensing
  - array technology 240
  - device 240
- biosensitive surface 240
- biotin ligand 239
- block copolymer 227
- bottom-up approach 219
- bridging
  - attraction 39
  - ligand 221
- brush 42, 44–46
- building block 220, 234, 238
  
- cadmium stearate 311
- carbosilane dendrimer 221
- catalysis 219
- centrifugal liquid membrane method 280
- charge transfer 321, 346
- chemical vapor adsorption (CVA) method 194
- chemical vapor deposition (CVD) 144
- chemisorbed adlayer 221
- chirality 12
- circuit formation 169
- circular dichroism (CD) 287
- clay 220
- cleaning 147
- CLM/CD 287
- CLM/Raman microscope spectrometry 284
- colloidal metal 219

- column-like structure 221
- complexation 227, 229
- confocal Raman spectrometer 20
- constant
  - current mode 4
  - height mode 4
- contact angle 148, 239
- contact-mode AFM 159
- copolymer 227
- core-shell block dendrimer 221
- coupling reagent 232
- critical aggregation 303
  
- denaturation degree 231–232
- dendrimer 220–224, 227, 229–240
  - activated surface 240
- dendritic
  - branch 238
  - Polymer 219–221, 223–225, 227, 229, 231, 233–235, 237–239, 241, 243, 245
- dendron 220, 223–227, 239
  - thiol 221, 240
- desorbed 12
- desorption 222, 231–232
  - equilibrium 222
- DFM-AFM 160
- diffraction 60
- dip pen nanolithography 234
- discotic monolayer domain 225
- DNA 227, 229–232, 234, 239–240
  - strand 231
- DNA–DNA interaction 239
- domino-like molecular reorientation 13
- donor–acceptor complex 14
- double-layer force 37, 39, 41, 44
- dynamic force mode 160
  
- edge-on configuration 221
- electrochemical 224
  - etching 7
- electron avalanche 17
- electronics 219, 235
- electrostatic interaction 223, 227, 229, 234–235, 239
- ellipsometry 148, 150
- enhancement factor 18
- exchange process 13
- excimer lamp 147
- excited state dynamics 21
  
- face-on configuration 236
- face-to-face stacking 224
- FAS3 147
- FAS17 147
- fast interfacial reaction 281
- fatty acid 248, 250–251, 266, 268
- Fermi level 3
- fluctuation dynamics 13
- fluorescence 30–31, 58
  - correlation spectroscopy 31
  - lifetime 282
- fluorinated amphiphile 177, 181, 186, 188
- fluorocarbon 177, 181, 184, 187–188
  - block 227
- focal point 225
- force 35, 37
- friction 28–29, 31
- fullerene 224
- fullerodendrion 224–225
- functional group 238, 240
- fused silica 223
  
- gene delivery 227
- generation 221–226, 234–240
- Gibbs
  - adsorption 219
  - monolayer 177, 180–181
- gold electrode 239
- grazing incident X-ray diffraction 208
- guest molecule 238
  
- H-aggregate 340, 346
- helical PGA 234
- helix random-coil transition 234
- hexagonal lattice ordering 236
- hexylene spacer 236–237
- hierarchical structure 240
- high-speed stirring method 278
- HOMO 9
- HOPG 7
- hybrid 220, 228, 235–238
- hybridization 220, 235–236, 238
- hydration 35, 37
- hydrogen bonding 223, 229, 234
- hydrophilic 221, 223–224, 227, 234
  - core 224
- hydrophobic 34, 220–221, 223, 227, 236
  - interaction 32
- hydrosilation 223

- image contrast 9
- immobilization surface 168, 239–240
- immuno-assay 69
- in-plane ordering 224
- inelastic tunneling 18
- infrared absorption spectra 223, 230
- infrared reflection absorption spectroscopy (IRRAS) 248–255, 257–264, 273
- infrared spectroscopy 311, 321, 323
- inner void 238
- interaction 239
- interface 220, 229, 236–238
- interfacial
  - aggregation 301
  - catalysis 295
  - formation constant 302
  - magnetic susceptibility 294
  - reflection spectrometry 281
- interferometry 24, 26, 29, 31
- inverse
  - decay length 4
  - type microscopy 19
- ion association extraction 299
- ionic additive 16
- ITO 7
  
- J-aggregate 340, 346
  
- Kelvin force microscope (KFM) 160
  
- label-free 56
- Langmuir monolayer 177–179, 181, 183–188, 219, 226, 247, 266
- Langmuir–Blodgett (LB) film 32, 159, 193, 195, 219, 311, 313, 321, 337, 339, 340, 346
- lateral
  - diffusion coefficient 291
  - force microscope 156
  - interaction 223
- layer-by-layer 68
- LFM 156
- light-harvesting complex 73
- limit of detection 68
- lipid 23, 31, 37
- liquid crystal 220
- liquid–liquid interface 277
- lithography 235
  
- local density of state 9
- LUMO 9
  
- magnetic susceptibility 292
- magnetophoretic velocimetry 292
- MD simulation 297
- medical therapy 220
- memory effect 235
- merocyanine dye 340–341
- metal ion 305
- metal nanoparticle 220, 234, 236
- metal substrate 219, 221
- metalloporphyrin 330
- mica 32, 34, 36, 39
- micelle 219
- micro-two-phase sheath flow method 281
- micro/nanofabrication 143
- micro/nanolithography 141
- micro/nanostructured SAM 167
- microcontact printing method 234
- microsensor 224
- mimetic processing 227
- miscibility 184, 186
- modified 36
- molecular
  - arrangement 223–228
  - chain length 153
  - dynamics simulation 297–298
  - layer 223–224
  - recognition 229, 239
- monodisperse 220
- monolayer 193, 219–221, 223–225, 227–228, 234, 236, 239–240
- morphology 224
- MPA SAM 223, 235
- multilayer 220–221, 224, 226
  
- n-octadecyltrimethoxysilane (ODS) 232
- nano-capsule 220
- nano-reactor 220
- nano-technology 219
- nanodevice 220
- nanofunctionality 20
- nanoparticle 234–236
- nanopattern 168
- nanosensor 220
- nanowire 14
- neutron and X-ray reflectivity 237

- non-contact AFM (NC-AFM) 160  
nonlinear optical spectroscopy 30  
non-specific binding 63
- octadecanethiolate monolayer 223  
ODS 147  
oleophilic 227  
oligonucleotide hybridization 81  
optics 219  
optoelectronic device 224  
organosilane 193  
organosilane  
  compound 142  
  molecule 146  
  SAM 142  
orientation 343, 348  
Ostwald ripening process 12
- patterning 167, 203, 206  
peptide 255, 257–258  
perfluorinated block 227  
perfluorooctadecanoic acid 227–228  
phase separation 177–178, 183–185  
phospholipid 32, 35–36, 248, 251, 255,  
  266, 268  
photo mask 232  
photodegradation 151  
photoelectrochemical property 224  
photolithographic 232  
photonics 235  
photopatterning 156  
photoreaction 235  
photoresist 143  
physisorbed organic molecule 8  
piezoelectric material 4  
plasma-polymerized film 159  
plasmon band 236  
PM-IRRAS 248, 263–273  
PNA 74  
poly(amido amine) (PAMAM) dendrimer  
  222  
poly(benzyl ether) monodendron 221  
poly(iminopropane-1,3-diyl) 220  
Poly(methyl methacrylate) 333  
poly(phenylene sulfide) dendrimer 224  
poly(propyleneimine) (PPI) dendrimer 220,  
  233  
polyelectrolyte 39–46, 227, 229–232, 234  
polymer casting film 159  
polymerization reaction 14–15  
primary amine 229  
protein 248–249, 255–258, 261, 266,  
  268, 271–273  
  chip 240  
  immobilization 239  
  ligand 239  
Prussian Blue 239
- quantum dot 235
- Raman spectroscopy 283, 309–310, 323  
rapid interfacial reaction 299  
re-adsorbed 12  
reflection–absorption 310  
reflective type 19  
residence time 13
- SAM 141, 219–221, 223–224, 229–232,  
  234, 236, 239–240  
sapphire 24, 31  
scaffold 220, 235  
scanning probe microscope 143  
scanning probe nanolithography (SPNL)  
  158  
scattering length density (SLD) 228, 237  
SEIRAS 230–232  
selective adsorption 234  
self-adsorbed monolayer 8  
self-assembled monolayer 63, 141, 311  
self-assembly 106, 219, 221, 235  
SERS 285–286, 311, 323, 330, 333  
SFA 26–30  
SHG/CD 288  
silicon wafer 220, 223  
silver nanoparticle 236  
single molecule probing 289  
single strand 231  
singlet oxygen sensitizer 224  
site-specific immobilization 212  
site-specific polymerization 210–211  
sodium poly-L-glutamate 227  
solid substrate 219–221, 223, 227, 238  
solid–liquid interface 7  
solvent extraction kinetics 278  
solvophilic moiety 224  
solvophobic 227  
solvophobicity-to-solvophilicity balance  
  227

- spatial resolution 1
- specific interaction 23
- spectroscopy 30
- spherical structure 220
- spontaneous aggregation 220
- SPR 234
- steric force 37, 39–41, 45, 47
- sum-frequency generation 30
- superhydrophilic 239
- superhydrophobic 239
- surface
  - acoustic wave 239
  - coverage 223, 226, 239
  - enhanced infrared absorption spectra (SEIRAS) 222, 229
  - enhanced Raman scattering (SERS) 18
  - forces apparatus 23–25
  - plasmon resonance (SPR) 18, 55, 231
  - potential 164
  - pressure–molecular area isothermal curve 237
  - structure 92, 97, 102, 106–108, 112
  - tension 221
- surfactant 23, 28, 30, 31–32, 40, 177, 178–181, 184–187
  - adsorption 87–91, 93, 95–101, 103–105, 107, 109, 111–113, 115
  - micelle 227
- synergic extraction rate 283
  
- template 167, 235–236
- tertiary amine 229
- tetracyanoquinodimethane 313
- thermo-annealing 224
- thiol SAM 219–220, 223, 234, 239
- tilt angle 350
  
- tip enhanced Raman spectroscopy 18
- top-down approach 219
- tunneling
  - current 2
  - spectroscopy 17
- two-dimensional ordering 236
- two-layer structure 224
- two-phase stopped flow method 280
- two-photon excitation fluorescence 283
  
- UV–vis absorption band 229, 231
- UV/ozone cleaning 147
  
- vacuum ultra-violet (VUV) light 143, 232
- van der Waals force 33, 35, 37
- vibrational spectroscopy 310
- visible absorption spectroscopy 340
- VOC 238–239
- VUV 143
  
- water
  - contact angle 155
  - droplet 148
  - subphase 221, 227–228, 236
- wettability 223
- wiring 169
  
- X-ray
  - diffraction 321
  - reflectivity 225
- Xe excimer light 148
- XPS 154
  
- zone texture 227